Université Paris Cité en cotutelle avec University of Glasgow

École doctorale Bio Sorbonne Paris Cité (ED 562)

PARIS CENTRE DE RECHERCHE CARDIOVASCULAIRE (PARCC, INSERM U970)

Genetics and Genomics of Primary Aldosteronism

Par **May FAYAD**

Thèse de doctorat de **Physiologie et Physiopathologie**

Dirigée par **Maria-Christina ZENNARO**

Et co-dirigée par **Eleanor DAVIES**

Présentée et soutenue publiquement

le 10/12/2025

Devant un jury composé de :

Andreas SCHEDL, DR, Université Cote d'Azur	Rapporteur
Say VIENGCHAREUN, IR, Université Paris-Saclay	Rapporteur
Laurence AMAR, PU-PH, Université Paris Cité	Examinatrice
David PENTON RIBAS, PU, University of Zurich	Examinateur
Annabel BERTHON, CR, Université Paris Cité	Membre invitée
Eleanor DAVIES, PU, University of Glasgow	Co-Directrice de thèse
Maria-Christina ZENNARO, DR, Université Paris Cité	Directrice de thèse



GA 954798





The study has received funding from the European Union's Horizon2020 research and innovation programme under the Marie Sklodowska-Curie grant agreement No 954798, and from the Fondation pour la Recherche Médicale (FRM, grant number FDT202404018696) for the fourth year of doctoral studies.

Acknowledgements

I would like to begin by sincerely thanking the members of the jury for accepting to evaluate my thesis work:

- **Dr. Andreas SCHEDL** and **Dr. Say VIENGCHAREUN**, who took the time to carefully examine my work as reviewers.
- **Pr. Laurence AMAR**, **Dr. Annabel BERTHON** and **Pr. David PENTON RIBAS**, who took the time to evaluate my work as examiners.
- **Pr. Eleanor Davies**, my thesis co-supervisor.
- **Dr. Maria-Christina Zennaro**, who directed my thesis.

I want to take the time to thank each person who took part of this journey.

To Christina, you made this journey look easier than it is. Thank you for your support and guidance since day 1, from my first day as a master's student to my PhD and the journey continues. Thank you for giving me the chance to be part of this lab, especially as your student, and for trusting in me. You taught me what leadership looks like. I am so grateful for having you as my supervisor and for sharing so many conference trips with you, even when we had to run to catch trains! Thank you for being very natural and humble, always listening and understanding. You set the bar so high for a mentee-mentor relationship, that all my friends are jealous.

To Sheerazed and Fabio, thank you for being there whenever I needed you. I couldn't count the times I jumped into your office to ask for help and always found you there for me. Thank you for the scientific discussions and the small talk.

To Pr. Eleanor, my co-supervisor, thank you for your heartwarming welcome into your lab for my secondment and for the discussions. This experience inspired me to learn R programming, which is now part of my daily routine.

To Isabelle, thank you for always being there and managing everything. Thank you for the small morning chats and for checking on me when you felt that I was tired.

To old and current lab mates, with whom I shared so much time and so much meals, I am grateful to each one of you for sharing this journey with you : Alaa, Coralie, Daniel, Dhekra, Jimmy, Johanna, Linghui, Marguerite, Nicolo, Ourida, Rami, Rim, Rita, Parisa, Romane, Teresa, Xiaomin.

To Team 13, thank you for all the time we shared together, even though I will never forgive you for leaving me halfway and moving out. I am sure that you will never find better neighbours!

To my colleagues and FRIENDS at the BDE, you made each day more bearable. Thank you for the funny moments we shared in this "chaotic" BDE (P.S. Investigations are still ongoing to find out who's responsible for all the noise). Thank you for supporting me when I'm tired and in my "laughing/crying" phase. I am grateful for each one of you : Amandine, Sara, Nicolo, Becky, Julie and Tom.

To Nicolò, my fellow Italian Mindshifter, thank you for all the discussions and the time we spent together. We shared this journey since day 1 with all the meetings, the "long" trainings and the failed experiments, but it could have been better with a spritz.

To Dhekra, thank you for the time we spent together and the chats with your very good Lebanese accent. Thank you for teaching me how to use THE "Ferrari".

To Daniel, the other half of the always-tired duo. Thank you for the laughs, the meals and chouquettes we shared. We definitely agree on one thing : Makhlouf always wins.

To Amandine, my office ex-neighbour and the master negotiator, thank you for all the laughs, support and good humour you put in the room. Thanks for never giving up on correcting my excellent French (P.S. I miss my marble office).

To Sara, thank you for your good humour and the good times we spent in the BDE and beyond. I will always cherish those moments.

To Julie and Becky, even though you were not officially part of the BDE, you never failed to join the fun. Thank you for the sleepovers and good times.

To Rami, my Lebanese colleague and friend, thank you for your support. Even though we didn't have the chance to cross paths in the lab, you never hesitated to help me. You handed me your project and I hope I took good care of it.

To the Mindshift family, thank you for the good memories throughout this period. I am grateful for this opportunity and to have met each one of you. I will hold this experience in my heart forever and hope that our paths cross again one day.

To the ECR family, thank you for the fun times at afterwork drinks and parties we spent together, and for always bringing good vibes.

To Corinne and Mathilde, merci pour l'aide que vous m'avez accordée et surtout merci de m'avoir accueilli dans votre bureau pour des longues heures sur HALO.

À Corina, Imène et Gwendoline, merci d'avoir pris soin des souris et de toutes mes demandes, et merci d'avoir été si patientes pour recevoir les listes de sacrifices.

To my Parisian family, thank you for always being there and for making me feel at home. I am really happy that in some way we all ended up in Paris : Christian, Cynthia, Elie, Joya, Léa N, Léa S, Nicole, Rym, Teresa.

To Léa, sorry I meant Dr. Nabhan, I am grateful to have you in my life. Thank you for all the good times we shared in Paris, from long hours looking for a master's internship to years of Parisian PhD life and a lot of fajitas. I couldn't imagine Paris without you.

To Christian and Elie, thank you for all the time we shared in Paris. Here's to many more cookies and calorie counting.

To Teresa, Cynthia and Léa S, thank you for all the coffee dates and endless conversations in Parisian cafés.

To my long-distance best friends,

To Maria, thank you for being the person you are, caring and always positive. We shared so many memories since the first day at Franciscaine dorm, from wine tasting (I'm not sure if we were tasting or drinking), to trips in Europe and I couldn't be happier to have you in my life.

To Tracy, thank you for the good times I always have around you. You spread so much joy and positivity wherever you are. Thank you for the long nights we spent studying, and yet here we are still on our computers !

To Jana, my cousin and best friend, you're more like a sister. Thank you for being there for me, for all the video calls and gossip. I'm grateful for your presence.

To my parents, thank you for pushing me to be the best version of me. I would never be here if it wasn't for your support and sacrifices. Thank you for everything you did and still do for me. Words will never be enough to express my gratitude for everything you've given me. I hope I've made you proud.

To my brother and sister, thank you for being part of my life at every step. I've always counted the days until I could be with you again and cherish every moment we spend together.

To Alain, last but not least, my partner and support system, thanking you would never be enough. Thank you for always being here for me no matter what. Thank you for supporting me at every step of the way. I am forever grateful for you. Even thousands of miles away, you never failed to be the strength I need.

Génétique et génomique de l'hyperaldostéronisme primaire

L'hyperaldostéronisme primaire (HAP) est une cause majeure d'hypertension artérielle secondaire, caractérisé par une production autonome d'aldostérone. Des études pangénomiques ont identifié CASZ1, un facteur de transcription à doigts de zinc et corépresseur du récepteur des minéralocorticoïdes (MR), comme gène de susceptibilité à l'HAP régulant la biosynthèse d'aldostérone. Le MR lie l'aldostérone et est exprimé dans les cellules productrices d'aldostérone de la zone glomérulée (ZG) et dans les adénomes produisant de l'aldostérone (APA).

L'objectif de ce projet est d'étudier comment le MR et *CASZ1* influencent la structure, fonction et régulation de l'aldostérone dans le cortex surrénalien, conduisant au développement de l'HAP. Nous avons généré des modèles murins knockout cellule-spécifiques, avec inactivation de Mr ($MRKO^{Ad}$) ou Casz1 ($Casz1^{Ad}$) dans les cellules ZG exprimant l'aldostérone synthase, en croisant Cyp11b2-Cre avec Nr3c2fl/fl ou Casz1fl/fl. À 12 semaines, les souris $MRKO^{Ad}$ présentaient des phénotypes sexe-spécifiques : expansion de la ZG et réduction de la zone X (ZX) chez les femelles, augmentation du poids corporel chez les mâles. Les deux sexes montraient une expression réduite de *Cyp11b2* mais une aldostérone plasmatique normale. Ces changements étaient associés à une diminution de la prolifération et une activation PKA, révélée par CREB et pCREB augmentés et expression élevée des sous-unités PKA chez les mâles. Les souris rapporteuses $MRKO^{Ad}$::mTmG à 5 semaines ont révélé une dynamique de lignée ZG altérée chez les femelles. Le régime pauvre en sel (LSD) a révélé des réponses adaptatives altérées chez les $MRKO^{Ad}$ Ad. Bien que l'aldostérone augmentait après 2 semaines de LSD dans les deux génotypes, la réponse était atténuée chez les MRKOZG, avec élévation compensatoire de corticostérone. L'expansion ZG (Dab2+) et l'induction de Cyp11b2 étaient atténuées chez les $MRKO^{Ad}$. Les mâles montraient une régulation positive de Cyp11b1 durant le LSD, absente chez les femelles, révélant une activation stéroïdogénique sexe-spécifique. L'analyse en composantes principales des profils stéroïdiens a démontré des réponses plus prononcées chez les WT. Chez les femelles, les $MRKO^{Ad}$ montraient une conversion de lignée ZX altérée avec cellules double-positives augmentées après récupération. L'analyse de séquençage d'ARN sur noyaux isolés a révélé des changements importants dans la réponse transcriptionnelle surrénalienne au régime pauvre en sel après l'inactivation du MR dans les cellules de la ZG. Notamment, les souris $MRKO^{Ad}$ ont montré une expression de Ren1 considérablement réduite et n'ont pas réussi à activer correctement le système rénine-angiotensine local pendant la restriction sodée. Nous avons également observé une

reprogrammation perturbée de la ZF et une expression altérée des enzymes stéroïdogéniques clés (Cyp11b2/Cyp11b1), soulignant le rôle critique du MR dans le maintien de la plasticité du cortex surrénalien

En parallèle, les souris Casz1^{Ad} à 12 semaines n'ont montré aucune altération significative de la morphologie, poids corporel, architecture corticale ou profils hormonaux, bien que des tendances vers augmentation ZG Dab2+ et diminution ZX 20alpha-HSD+ ont été observées chez les femelles. L'aldostérone plasmatique montrait une réduction non significative chez les femelles knockout.

Ces résultats établissent une base pour investiguer CASZ1 sous défis physiologiques et son interaction avec le MR dans les doubles KO MRKO^{Ad}::Casz1^{Ad}. En conclusion, la délétion du MR provoque des altérations sexe-spécifiques de l'architecture surrénalienne, prolifération et expression enzymatique stéroïdogénique. Des mécanismes compensatoires maintiennent l'aldostérone basale mais limitent les réponses adaptatives à la restriction sodée, révélant le rôle critique du MR dans l'homéostasie, plasticité et régulation sexe-spécifique de la ZG, via un mécanisme autocrine-paracrine. La délétion CASZ1 a montré des changements minimes en conditions basales, soulignant la nécessité d'investigations sous défis physiologiques. Ces modèles murins fournissent des aperçus sur les mécanismes moléculaires régulant l'homéostasie surrénalienne, élargissant notre compréhension de la physiopathologie de l'HAP avec implications pour les stratégies diagnostiques et thérapeutiques.

Mots clés : Hyperaldostéronisme primaire, Récepteur minéralocorticoïde, *CASZ1*, Zone glomérulée, Cortex surrénalien, Aldostérone, Stéroïdogenèse, Régime sodé

Genetics and genomics of primary aldosteronism

Primary aldosteronism (PA) is a major cause of secondary arterial hypertension, characterized by autonomous aldosterone production. Genome-wide association studies identified CASZ1, a zinc-finger transcription factor and mineralocorticoid receptor (MR) corepressor, as a PA susceptibility gene regulating aldosterone biosynthesis in the adrenal gland. The MR binds aldosterone and is expressed in aldosterone-producing cells of the adrenal zona glomerulosa (ZG) and in aldosterone-producing adenomas (APA).

The aim of this project was to investigate how MR and CASZ1 influence adrenal cortex structure, function, and aldosterone regulation, eventually leading to the development of PA. We generated different cell-specific knockout mouse models, with inactivation of Mr ($MRKO^{Ad}$) or Casz1 ($Casz1^{Ad}$) in ZG cells expressing aldosterone synthase and their descendants, by crossing Cyp11b2-Cre mice with Nr3c2 fl/fl or Casz1fl/fl mice. At 12 weeks, $MRKO^{Ad}$ mice exhibited sex-specific phenotypes: females showed significant ZG expansion and reduced X zone (ZX), while males displayed increased body weight without altered ZG architecture. Both sexes showed reduced Cyp11b2 expression, but normal plasma aldosterone levels. These changes were associated with decreased proliferation as well as activation of the PKA signaling pathways, revealed by increased CREB and Pcreb protein levels and elevated expression of PKA subunits in males. At 5 weeks of age, $MRKO^{Ad}$::mTmG reporter mice revealed altered ZG lineage dynamics in females, with increased GFP+ cells. Low salt diet (LSD) revealed impaired adaptive responses in $MRKO^{Ad}$ mice. While aldosterone increased as expected after 2 weeks of LSD in both WT and $MRKO^{Ad}$ mice, the response was significantly blunted in $MRKO^{Ad}$ mice, with a compensatory elevation in corticosterone. ZG expansion (Dab2+ cells) and Cyp11b2 induction were also attenuated in MRKO mice. Males showed coordinated Cyp11b1 upregulation during LSD, absent in females, revealing sex-specific steroidogenic activation. Principal component analysis of comprehensive steroid profiles demonstrated WT mice displaying more pronounced responses than $MRKO^{Ad}$ mice. In females, $MRKO^{Ad}$ mice showed altered ZX lineage conversion dynamics with increased double-positive cells after 1-week recovery. Single-nucleus RNA sequencing analysis revealed important changes in the adrenal transcriptional response to low-salt diet after MR inactivation in ZG cells. Most notably, $MRKO^{Ad}$ mice showed dramatically reduced Ren1 expression and failed to properly activate the local renin-angiotensin system during salt restriction. We also observed disrupted ZF reprogramming and altered expression of key steroidogenic enzymes (Cyp11b2/Cyp11b1), highlighting MR's critical role in maintaining adrenal cortex plasticity. In

parallel, investigation of Casz1^{Ad} mice at 12 weeks under standard condition showed no significant alterations in adrenal morphology, body weight, cortical architecture, or hormonal profiles in either sex, though trends toward increased Dab2+ ZG and decreased 20-alpha-HSD+ ZX were observed in females. Plasma aldosterone showed non-significant reduction in knockout females.

These results establish a baseline for investigating CASZ1's role under physiological challenges such as salt modulation, and its interaction with the MR in MRKO^{Ad}::Casz1^{Ad} double KO mice. In conclusion, MR deletion in the adrenal cortex causes sex-specific alterations in adrenal architecture, proliferation, and steroidogenic enzyme expression. Compensatory mechanisms maintain basal aldosterone but limit adaptive responses to salt restriction, revealing MR's critical role in ZG homeostasis, plasticity, and sex-specific regulation, via an autocrine-paracrine mechanism. *CASZ1* deletion showed minimal phenotypic changes under basal conditions, highlighting the need for investigations under diverse physiological challenges. Together, these mouse models provide insights into molecular mechanisms regulating adrenal homeostasis, expanding our understanding of PA pathophysiology with potential implications for diagnostic and therapeutic strategies.

Mots clés : Primary aldosteronism, Mineralocorticoid receptor, CASZ1, Zona glomerulosa, Adrenal cortex, Aldosterone, Steroidogenesis, Salt diet

List of abbreviations

A

- **ACE** - Angiotensin-Converting Enzyme
- **ACTH** - Adrenocorticotropic Hormone
- **AE1** - Chloride/Bicarbonate Exchanger
- **AF-1** - Transcriptional Activation Function 1
- **AF-2** - Activation Function 2
- **AGP** - Adrenogonadal Primordium
- **Akr1c18** - Aldo-Keto Reductase Family 1 Member C18
- **Ang II** - Angiotensin II
- **AP** - Adrenal Primordium
- **APA** - Aldosterone-Producing Adenomas
- **APC** - Adenomatous Polyposis Coli
- **AR** - Androgen Receptor
- **ARR** - Aldosterone to Renin Ratio
- **AS** - Aldosterone Synthase
- **ASDN** - Aldosterone-Sensitive Distal Nephron
- **AT1** - Angiotensin II Type 1 Receptor
- **AT2** - Angiotensin II Type 2 Receptor
- **ATP1A1** - ATPase Na+/K+ Transporting Subunit Alpha 1
- **ATP2B3** - ATPase Plasma Membrane Ca^{2+} Transporting 3
- **AVP** - Vasopressin
- **Axin2** - Axis Inhibition Protein 2

B

- **B2m** - β2-Microglobulin
- **BAH** - Bilateral Adrenal Hyperplasia

C

- **CACNA1D** - Calcium Voltage-Gated Channel Subunit Alpha1 D
- **CACNA1H** - Calcium Voltage-Gated Channel Subunit Alpha1 H
- **CADM1** - Cell Adhesion Molecule 1
- **CaMKs** - Calcium/Calmodulin-Dependent Protein Kinases
- **cAMP** - Cyclic Adenosine Monophosphate
- **CASZ1** - Castor Zinc Finger 1
- **CaV3.2** - Voltage-Gated Calcium Channel Type 3.2
- **CBP** - CREB Binding Protein
- **CDF** - Cation Diffusion Facilitator
- **ChIP-seq** - Chromatin Immunoprecipitation Sequencing
- **CK1** - Casein Kinase 1
- **CLCN2** - Chloride Voltage-Gated Channel 2
- **CREB** - cAMP Response Element-Binding Protein
- **CRH** - Corticotropin-Releasing Hormone
- **CTNNB1** - Catenin Beta 1
- **CYP** - Cytochrome P450

- **CYP11A1** - Cytochrome P450 Family 11 Subfamily A Member 1
- **Cyp11b1** - 11β-Hydroxylase
- **Cyp11b2** - Aldosterone Synthase
- **CYP17A1** - 17α-Hydroxylase/17,20-Lyase
- **CYP21A2** - 21-Hydroxylase

D

- **Dab2** - Disabled Homolog 2
- **DAPI** - 4′,6-Diamidino-2-Phenylindole
- **DBD** - DNA-Binding Domain
- **DHEA** - Dehydroepiandrosterone
- **DNA** - Deoxyribonucleic Acid
- **DNase** - Deoxyribonuclease
- **DRC** - Direct Renin Concentration
- **DZ** - Definitive Zone

E

- **ENaC** - Epithelial Sodium Channel
- **ER** - Endoplasmic Reticulum / Estrogen Receptor
- **ERK1/2** - Extracellular Signal-Regulated Kinase 1/2
- **EVC** - Ellis-van Creveld Syndrome Protein
- **EVC2** - Ellis-van Creveld Syndrome Protein 2

F

- **FH** - Familial Hyperaldosteronism
- **FKBP51** - FK506-Binding Protein 51
- **FKBP52** - FK506-Binding Protein 52
- **Frzb** - Frizzled-Related Protein
- **FZ** - Foetal Zone
- **FZD** - Frizzled Receptor

G

- **GILZ** - Glucocorticoid-Induced Leucine Zipper
- **GLI** - Glioma-Associated Oncogene
- **GLI1** - Glioma-Associated Oncogene 1
- **GNA11** - G Protein Subunit Alpha 11
- **GNAQ** - G Protein Subunit Alpha Q
- **GPCR** - G Protein-Coupled Receptor
- **GR** - Glucocorticoid Receptor
- **GRA** - Glucocorticoid-Remediable Aldosteronism
- **GREs** - Glucocorticoid Response Elements
- **GSK3β** - Glycogen Synthase Kinase-3β
- **GTP** - Guanosine Triphosphate
- **GWAS** - Genome-Wide Association Study

H

- **H295R** - Human Adrenocortical Carcinoma Cell Line
- **HEK-293** - Human Embryonic Kidney 293 Cells
- **HEK293F** - Human Embryonic Kidney 293F Cells
- **HES** - Hematoxylin, Eosin, and Saffron
- **hMRα** - Human Mineralocorticoid Receptor Alpha
- **hMRβ** - Human Mineralocorticoid Receptor Beta
- **HPA** - Hypothalamic-Pituitary-Adrenal Axis
- **HREs** - Hormone Response Elements
- **HSP70** - Heat Shock Protein 70
- **HSP90** - Heat Shock Protein 90

I

- **IRES** - Internal Ribosomal Entry Site

J

- **JNK** - c-Jun N-terminal Kinase

K

- **KCNJ5** - Potassium Inwardly Rectifying Channel Subfamily J Member 5
- **KCNK3** - Potassium Two Pore Domain Channel Subfamily K Member 3
- **K^+** - Potassium
- **KO** - Knock-Out

L

- **LBD** - Ligand-Binding Domain
- **LC-MS/MS** - Liquid Chromatography-Tandem Mass Spectrometry
- **LEF** - Lymphoid Enhancer Binding Factor
- **Lef1** - Lymphoid Enhancer Binding Factor 1
- **LRP5/6** - Low-Density Lipoprotein Receptor-Related Protein 5/6

M

- **MC2R** - Melanocortin 2 Receptor
- **MCOLN3** - Mucolipin 3
- **MR** - Mineralocorticoid Receptor
- **MRA** - Mineralocorticoid Receptor Antagonists
- **MREs** - Mineralocorticoid Response Elements

N

- **Na+/K+-ATPase** - Sodium-Potassium ATPase
- **NCoR** - Nuclear Receptor Co-Repressor
- **NDS** - Normal Donkey Serum
- **Nedd4-2** - Neural Precursor Cell Expressed Developmentally Down-Regulated Protein 4-2
- **NGS** - Next-Generation Sequencing

- **NLS1** - Nuclear Localization Signal 1
- **NR3C2** - Nuclear Receptor Subfamily 3 Group C Member 2
- **NR4A1** - Nuclear Receptor Subfamily 4 Group A Member 1
- **Nr4a1** - Nuclear Receptor Subfamily 4 Group A Member 1
- **NR4A2** - Nuclear Receptor Subfamily 4 Group A Member 2
- **Nr4a2** - Nuclear Receptor Subfamily 4 Group A Member 2
- **NR5A1** - Nuclear Receptor Subfamily 5 Group A Member 1
- **NDRG2** - N-Myc Downstream-Regulated Gene 2 Protein
- **NTD** - N-Terminal Domain
- **NUR77** - Nuclear Receptor Subfamily 4 Group A Member 1
- **NURR1** - Nuclear Receptor Related 1

P

- **p23** - Cochaperone Protein p23
- **p48** - Immunophilin p48
- **p300** - Binding Protein 300
- **PA** - Primary Aldosteronism
- **PBS** - Phosphate-Buffered Saline
- **PCA** - Principal Component Analysis
- **PCP** - Planar Cell Polarity
- **PFA** - Paraformaldehyde
- **pH** - Potential of Hydrogen
- **PKA** - Protein Kinase A
- **PKC** - Protein Kinase C
- **PMCA3** - Plasma Membrane Ca^{2+}-Transporting ATPase 3
- **PR** - Progesterone Receptor
- **PRA** - Plasma Renin Activity
- **pRb** - Retinoblastoma Protein
- **PRKACA** - Protein Kinase cAMP-Activated Catalytic Subunit Alpha
- **Prkar1a** - Protein Kinase cAMP-Dependent Type I Regulatory Subunit Alpha
- **PTCH1** - Patched 1

R

- **RAAS** - Renin-Angiotensin-Aldosterone System
- **RAR** - Retinoic Acid Receptor Alpha
- **Rho GTPases** - Rho Family of GTPases
- **RNA** - Ribonucleic Acid
- **ROR2** - Receptor Tyrosine Kinase Like Orphan Receptor 2
- **Rspo3** - R-Spondin 3
- **RT-qPCR** - Real-Time Quantitative PCR
- **RXFP2** - Relaxin Family Peptide Receptor 2
- **RXR** - Retinoid X Receptor
- **RYK** - Receptor-Like Tyrosine Kinase

S

- **SCNN1A** - Sodium Channel Epithelial 1 Alpha Subunit
- **SF1** - Steroidogenic Factor 1

- **SGK1** - Serum and Glucocorticoid Regulated Kinase 1
- **Shh** - Sonic Hedgehog
- **SHH** - Sonic Hedgehog
- **SLC30A1** - Solute Carrier Family 30 Member 1
- **SMO** - Smoothened
- **snRNAseq** - Single-Nucleus RNA Sequencing
- **SRC-1** - Steroid Receptor Co-Activator 1
- **Star** - Steroidogenic Acute Regulatory Protein
- **StAR** - Steroidogenic Acute Regulatory Protein
- **SuFu** - Suppressor of Fused

T

- **TASK-1** - TWIK-Related Acid-Sensitive Potassium Channel 1
- **TCF** - T Cell Factor
- **TR** - Thyroid Hormone Receptor
- **TRPML** - Transient Receptor Potential Mucolipin

U

- **Ubc** - Ubiquitin C

V

- **VDR** - Vitamin D Receptor

W

- **WES** - Whole Exome Sequencing
- **Wnt4** - Wnt Family Member 4

Z

- **ZF** - Zona Fasciculata
- **ZG** - Zona Glomerulosa
- **ZnT1** - Zinc Transporter 1
- **ZR** - Zona Reticularis
- **ZX** - Zona X

Numbers

- **3β-HSD** - 3β-Hydroxysteroid Dehydrogenase
- **14-3-3** - 14-3-3 Proteins
- **18S** - 18S Ribosomal RNA
- **20α-HSD** - 20α-Hydroxysteroid Dehydrogenase

List of figures

Figure 1: Summary of aldosterone stimulation by components of the renin–angiotensin-aldosterone system 23
Figure 2: Overview of Mutations in the KCNJ5 Gene and Their Structural Localization in the GIRK4 Channel 26
Figure 3: Summary of Somatic Mutations in ATP1A1 and ATP2B3 Found in Aldosterone-Producing Adenomas (APAs) 27
Figure 4: Somatic and germline CACNA1D mutations associated with human diseases.....28
Figure 5: Overview of the molecular mechanisms driving aldosterone-producing adenomas (APAs).....31
Figure 6: Genetic and pathogenic mechanisms of familial hyperaldosteronism and targeted treatment 35
Figure 7: Adrenal gland anatomical and histological structure 38
Figure 8: Comparison between mouse and human adrenal gland structure 38
Figure 9: Summary of the major steroidogenic pathways of the human adrenal cortex within the three adrenocortical zones.....40
Figure 10: Regulation of aldosterone production in response to K+ or AngII stimulation 42
Figure 11: Regulation of glucocorticoid production and its physiological roles.....43
Figure 12 : Overview of canonical and non-canonical Wnt signalling pathways. 46
Figure 13: Schematic representation of activation of the cyclic adenosine monophosphate (cAMP) signalling pathway in normal adrenocortical cells 48
Figure 14 : Paracrine communication between zona glomerulosa and capsule cells. 50
Figure 15 : Schematic illustration of the cellular rearrangements during adrenal development in mice and humans. 51
Figure 16 : Homeostatic tissue renewal in the mouse adult adrenal cortex and capsule.....53
Figure 17 : Adrenal cortex renewal in female mice and interplay with androgens 55
Figure 18 : Phylogenetic tree of the nuclear receptor superfamily.....57
Figure 19 : Structure of nuclear receptor superfamily 58
Figure 20 : Schematic diagram of the domain structure of the 984 amino acid human MR, with the hinge region between the DBD and LBD 59
Figure 21 : MR-dependent regulation of volume and electrolyte balance in the aldosterone-sensitive distal nephron.....62
Figure 22 : Mineralocorticoid receptor structure and regulation 64

Figure 23 : MR at the cross-road of metabolic functions 67
Figure 24 MR expression and structural alterations in control and pathological adrenal tissue 68
Figure 26 : Schematic diagram of CASZ1-nucleosome remodeling and deacetylase (NuRD) co-repressor complex for MR. 80
Figure 27 : Body weight and adrenal gland weight in wild-type and Casz1 knockout mice ..88
Figure 28 : Morphological characterization of the adrenal cortex in wild-type and Casz1 knockout mice.....90
Figure 29 : Principal component analysis and hierarchical clustering of plasma steroid profiles 92
Figure 30 : Principal component analysis decomposition and variable contributions.....94
Figure 31 : Gene expression analysis in adrenal cortex.....96

Table of contents

INTRODUCTION 21

1. Arterial hypertension 21
2. Blood pressure and the Renin-Angiotensin-Aldosterone system 21
3. Primary aldosteronism 23
4. The genetics of PA 24
   - 4.1 Somatic mutations in APA 24
     - 4.1.1 KCNJ5 mutations 25
     - 4.1.2 ATP1A1 and ATP2B3 mutations 26
     - 4.1.3 CACNA1D mutations 28
     - 4.1.4 Mutations affecting CTNNB1 alone or co-occurring with GNAQ/GNA11 mutations 29
     - 4.1.5 CADM1 mutations 29
     - 4.1.6 SLC30A1 mutations 30
     - 4.1.7 MCOLN3 mutations 30
   - 4.2 Familial forms of primary aldosteronism 31
     - 4.2.1 Familial hyperaldosteronism type I (FH-I) 31
     - 4.2.2 Familial hyperaldosteronism type II (FH-II) 32
     - 4.2.3 Familial hyperaldosteronism type III (FH-III) 32
     - 4.2.4 Familial hyperaldosteronism type IV (FH-IV) 33
   - 4.3 Genetic susceptibility to PA 34
5. Anatomy of the adrenal gland 37
   - 5.1 Adrenal gland structure and function 37
   - 5.2 Differences in the adrenal cortex structure between species 38
   - 5.3 Vascularisation of the adrenal gland 39
   - 5.4 Adrenal gland innervation 39
6. Steroidogenesis 40
   - 6.1 Aldosterone biosynthesis 40
   - 6.2 Cortisol biosynthesis 42
7. Signalling pathways and transcription factors in adrenal gland development and steroidogenesis 44
   - 7.1 Wnt signalling pathway 44
   - 7.2 PKA signalling pathway 46
   - 7.3 Glioma-associated oncogene 1 - GLI1 and Sonic HedgeHog – SHH pathways 48
8 Adrenal cortex development and remodelling 50
   - 8.1 Development of the foetal adrenal gland 50

8.2 Sexual dimorphism in adrenal cortex renewal 53
9 The Mineralocorticoid Receptor 56
9.1 The Nuclear Receptor Superfamily of Transcription Factors 56
9.2 Mineralocorticoid Receptor Structure and Mechanism of Action 58
9.3 Regulation of the Mineralocorticoid Receptor Activity 63
9.4 Tissue Distribution of the Mineralocorticoid Receptor 64
9.4.1 Mineralocorticoid Receptor in the Cardiovascular System 64
9.4.2 Mineralocorticoid Receptor in the Brain 65
9.4.3 Mineralocorticoid Receptor in Adipose Tissue and Metabolic Regulation 66
9.4.4 MR Expression in other tissues 66
9.5 MR expression in the adrenal cortex 67
9.6 Experimental Models and MR Knockout Studies 68
9.7 Therapeutic Targeting of MR 70
Overall hypothesis and objectives 72
THESIS PROJECT 73
10 Part I: An aldosterone-mineralocorticoid receptor regulatory loop maintains ZG homeostasis and plasticity 73
10.1 Thesis paper introduction 73
11 Part II: Role of *Casz1* in Adrenal Cortex Development 76
11.1 Introduction 76
11.1.1 General Characteristics of Castor Zinc Finger 1 (CASZ1) 76
11.1.2 CASZ1 in Adrenocortical Physiology 78
11.1.2.1 Developmental and Adult Expression in Adrenal Tissue 78
11.1.2.2 Negative Regulation of Aldosterone Production 79
11.1.3 CASZ1b Functions as a Mineralocorticoid Receptor Corepressor 79
11.1.4 Regulation of Ion Channel Gene Expression 80
11.1.5 CASZ1 Genetic Variants and Primary Aldosteronism 81
11.1.6 CASZ1 in Cardiovascular Development and Disease 82
11.1.7 CASZ1 in Other Biological Contexts 82
11.2 Investigation of the role of CASZ1 in the adrenal cortex 83
11.3 Material and methods 83
11.3.1 Generation of Zona Glomerulosa-Specific *Casz1* Knockout Mice 83
11.3.2 Genotyping 84
11.3.3 Tissue Collection and Processing 84
11.3.4 Histological Examination and Immunostaining 84
11.3.4.1 Histological Staining 84

11.3.4.2 Immunofluorescence 84
11.3.4.3 Image Acquisition 85
11.3.4.4 Image Analysis 85
11.3.5 RNA Extraction and RT-qPCR Analysis 85
11.3.6 Steroid Profiling and Analysis 86
11.4 Results 87
11.4.1 General Characterization of the *Casz1* mouse model 87
11.4.2 Morphological Characterization of Casz1KO^{Ad} Adrenal Cortex 88
11.4.3 Steroid profile analysis 90
11.4.4 Gene Expression Analysis in Casz1KO^{Ad} Adrenal Glands 94
11.5 Discussion 96
11.6 Conclusion 99
General conclusion 101
Bibliography 103
Appendix 128
12 Scientific papers 128
12.1 Sexually dimorphic interzonal crosstalk reshapes the adrenal cortex in response to pathophysiological challenges 128
12.2 Mineralocorticoid receptor inhibition in parietal epithelial cells 129
12.3 Modulation of Calcium Signaling on Demand to Decipher the 130
13 Book Chapter 131
13.1 MicroRNAs in aldosterone production and action 131
14 Scientific review 132
14.1 Genetics mechanisms of primary aldosteronism 132
15 Hot off the press 133
15.1 Insights into the mechanisms of inhibition of aldosterone production by mutant atrial natriuretic peptide (MANP) 133

INTRODUCTION

1. Arterial hypertension

Arterial hypertension, also known as high blood pressure, is one of the most frequent chronic conditions affecting populations worldwide. According to the 2024 ESC Guidelines, the diagnosis of hypertension requires confirmed measurements showing systolic pressure reaching 140 mmHg or higher, or diastolic pressure at 90 mmHg or above. The guidelines now recognize an additional category termed "elevated blood pressure", which encompasses systolic readings between 120-139 mmHg or diastolic readings between 70-89 mmHg. For individuals in this elevated range who face substantial cardiovascular disease risk, initiating blood pressure reduction therapy may be beneficial (McEvoy et al., 2024). High systolic blood pressure is the leading risk factor globally for attributable deaths, accounting for 10.8 million deaths (GBD 2019 Meningitis Antimicrobial Resistance Collaborators, 2023). The World Health Organization estimates that 54% of strokes and 47% of ischemic heart disease are a direct consequence of hypertension (Lawes et al., 2008). Arterial hypertension has an estimated overall prevalence of 24.1% in adult men and 20.1% in adult women (NCD Risk Factor Collaboration (NCD-RisC), 2017). Arterial hypertension may be asymptomatic in patients before it leads to damages in vital organs such as the heart, kidneys and brain. Hypertension is classified into two types: primary (essential) hypertension, which has no clear cause, influenced by genetic and environmental factors; and secondary hypertension which occurs due to specific medical conditions, including renal and endocrine disorders (Unger et al., 2020).

2. Blood pressure and the Renin-Angiotensin-Aldosterone system

The renin-angiotensin-aldosterone system (RAAS) plays a central role in regulating blood pressure. Renin, an enzyme crucial to this system, is produced and stored in juxtaglomerular cells, specialized smooth muscle-derived cells located in the afferent arterioles of the kidneys. These cells are located within the juxtaglomerular apparatus, which is a specialised structure regulating blood pressure and glomerular filtration rate. It is located near the glomerulus, where the distal convoluted tubule of the nephron comes into close contact with the afferent arteriole. Renin release is triggered by several physiological conditions (Yamaguchi et al., 2023):

- A decrease in renal perfusion pressure, detected by baroreceptors in the afferent arteriole of the kidney.
- Decreased sodium levels detected by the macula-densa, specialised cells in the distal convoluted tubule which are part of the juxtaglomerular apparatus, capable of sensing sodium concentrations in the distal tubule of the kidney and to transfer the information to juxtaglomerular cells, in what is known as the tubuloglomerular feedback.
- Activation of the sympathetic nervous system through β-adrenergic receptors.

Once released, renin enters the circulation where it acts on its substrate, angiotensinogen, a protein produced and secreted by the liver. Renin cleaves angiotensinogen to form angiotensin I, an inactive precursor that is rapidly converted into the active peptide angiotensin II (Ang II) in the lungs by the angiotensin-converting enzyme (ACE) (MacKenzie et al., 2024) (Fig. 1).

Ang II, one of the primary downstream effectors of the RAAS, is a potent vasoconstrictor that acts on arterioles. Systemic vasoconstriction caused by Ang II increases total peripheral resistance, thereby raising blood pressure without altering blood volume. Ang II mediates its physiological effects by binding to specific cell surface receptors, particularly on organs like the heart, kidneys, blood vessels, adrenal glands, liver, and regions of the brain involved in cardiovascular control. Ang II acts mainly through two types of G-protein coupled receptors: angiotensin II type 1 (AT1) and type 2 (AT2) receptors. Most of Ang II's known actions, including vasoconstriction, occur through the AT1 receptor. In contrast, the AT2 receptor generally promotes vasodilation and blood pressure reduction, indicating that the two receptors often have opposite effects (Gembardt et al., 2008; Lavoie and Sigmund, 2003).

In addition to promoting vasoconstriction, Ang II stimulates the adrenal cortex to release aldosterone, a key hormone in blood pressure regulation. Aldosterone is one of the most effective agents in conserving sodium within the body. It is typically secreted in response to low blood pressure, reduced sodium levels, or elevated potassium concentrations. Aldosterone acts on the aldosterone-sensitive distal nephron, where it enhances sodium reabsorption and potassium secretion in the aldosterone sensitive distal nephron (Pearce et al., 2003). These effects are mediated via the mineralocorticoid receptor (MR), a transcription factor belonging to the nuclear receptor family. The reabsorption of sodium also leads to water retention, which increases both blood volume and blood pressure. Angiotensin II also directly stimulates sodium reabsorption in the proximal tubule of the nephron, and stimulates release of vasopressin from

the pituitary gland, further contributing to sodium and water retention and increased blood pressure.

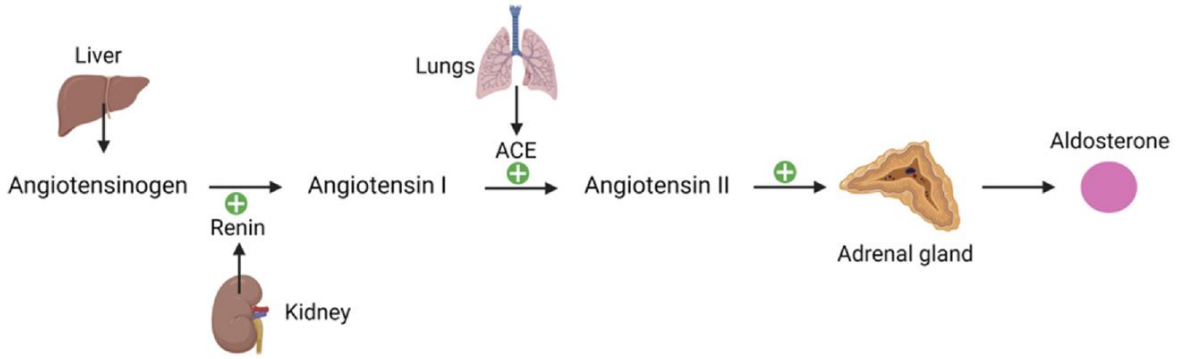

Figure 1: Summary of aldosterone stimulation by components of the renin–angiotensin-aldosterone system (Extracted from MacKenzie et al., 2024).

3. Primary aldosteronism

Primary aldosteronism (PA), also known as Conn's syndrome, was first described by Jerome W. Conn in 1955 in a patient presenting muscle weakness along with intermittent muscle spasms. These symptoms were accompanied by hypertension resistant to treatment as well as polydipsia, polyuria, hypokalaemia, proteinuria and high aldosterone levels. These symptoms were found to be associated to an aldosterone producing adenoma (CONN and LOUIS, 1956; Conn and Louis, 1955).

PA is the most common form of secondary hypertension with a prevalence of 5% in hypertensive subjects in primary care and up to 20% in patients with treatment resistant hypertension (Hannemann and Wallaschofski, 2012; Silvia Monticone et al., 2017; Zennaro et al., 2020). It is particularly frequent in patients under 40 years referred to specialised centers, where it accounts for 16% of cases (de Freminville et al., 2024) PA is characterized by high plasma aldosterone levels due to an autonomous production of aldosterone by the adrenal gland, renin suppression associated with an elevated aldosterone to renin ratio (ARR) and hypokalaemia in 9 to 37% of the cases (Adler et al., 2025).The two mains causes of PA are either unilateral aldosterone producing adenomas (APA) or bilateral adrenal hyperplasia (BAH, also called idiopathic hyperaldosteronism – IHA), which account for 90-95% of cases (Adler et al., 2025; Boulkroun et al., 2015; Fagugli and Taglioni, 2011).

PA remains largely underdiagnosed due to its complex workup, contributing to significant cardiovascular burden. Indeed, elevated aldosterone increases cardiovascular risk beyond that of essential hypertension due to its damaging effects on heart and vessels, independent of blood pressure levels (Monticone et al., 2018). This is due to direct effects of aldosterone in various tissues that drive end-organ damage and cardiovascular disease (Yang et al., 2023). Given the high prevalence of PA and the severe cardiovascular consequences of aldosterone excess, the 2025 Endocrine Society guidelines suggest screening of all hypertensive patients for primary aldosteronism. The screening protocol requires morning blood collection while patients are in a seated position, with normal dietary sodium intake maintained beforehand. Testing includes concurrent measurement of both aldosterone and renin levels. Diagnostic criteria for a positive screen include renin suppression below specific thresholds (PRA ≤1 ng/mL/h or DRC ≤8.2 mU/L) combined with elevated aldosterone levels that vary by assay method used (≥10 ng/dL via immunoassay; ≥7.5 ng/dL via LC-MS/MS). A significant departure from prior guidelines is that confirmatory suppression testing is now reserved for select patients: those with moderate likelihood of unilateral disease who are potential surgical candidates. The guidelines also emphasize repeat screening if clinical deterioration occurs, including worsening blood pressure control, development of hypokalemia, or new-onset atrial fibrillation without structural cardiac abnormalities (Adler et al., 2025).

4. The genetics of PA

The emergence of high-throughput sequencing technologies, such as whole exome sequencing (WES), over the past fifteen years has significantly advanced our understanding of the genetic basis of PA, allowing to identify inherited germline mutations in familial forms of PA and somatic mutations in APA.

4.1 Somatic mutations in APA

Recurrent somatic mutations in different genes have been identified in APA. The use of aldosterone synthase (AS) immunohistochemistry guided next-generation sequencing (NGS) for genetic screening has enabled precise detection of somatic mutations in APA, revealing that approximately 90% of tumors carry mutations in genes involved in ionic transport and membrane potential regulation within zona glomerulosa (ZG) cells. Notably, mutations have been frequently identified in *KCNJ5, CACNA1D, ATP1A1*, and *ATP2B3*, which encode potassium and calcium channels as well as ATPase pumps essential for maintaining ionic homeostasis. Additional genes such as *CTNNB1, GNAQ/GNA11, CLCN2, CACNA1H,*

CADM1, *SLC30A1* and *MCOLN3* have also been implicated, highlighting additional molecular mechanisms leading to APA development (De Sousa et al., 2020, p. 20; Fernandes-Rosa et al., 2023; Nanba et al., 2018; Rege et al., 2023; Wu et al., 2021).

4.1.1 KCNJ5 mutations

The *KCNJ5* gene encodes the G protein-activated inward rectifier potassium channel 4 (GIRK4), which is expressed in the ZG of the adrenal gland (Barrett et al., 2021). Choi and colleagues identified two somatic mutations in *KCNJ5* in 8 out of 22 APAs (Choi et al., 2011). *KCNJ5* mutations are the most common somatic mutations found APAs (Boulkroun et al., 2012; Fernandes-Rosa et al., 2014). They affect residues critical for channel function, leading to a loss of potassium selectivity, allowing sodium to enter the cells. Sodium influx causes membrane depolarization, followed by opening voltage-gated calcium channels, and increases intracellular calcium levels, thereby activating the calcium signalling pathway that stimulates expression of *CYP11B2*, coding for AS, and aldosterone production. However, while these mutations lead to excessive aldosterone biosynthesis, they do not promote cell proliferation and may even reduce cell viability through sodium-induced toxicity (Zennaro et al., 2018). This has recently been confirmed by our laboratory in a newly established cell model, in which increased sodium influx leads to reduced proliferation and increased apoptosis (Fedlaoui et al., 2024). *KCNJ5* mutations are more frequently observed in younger individuals and women and are often associated with larger tumours, higher aldosterone levels, and distinct histological features, such as lipid-rich cells resembling those of the ZF. Additionally, these tumours tend to produce elevated levels of hybrid steroids, including 18-hydroxycortisol and 18-oxocortisol (De Sousa et al., 2020; Fernandes-Rosa et al., 2017; Scholl et al., 2012).

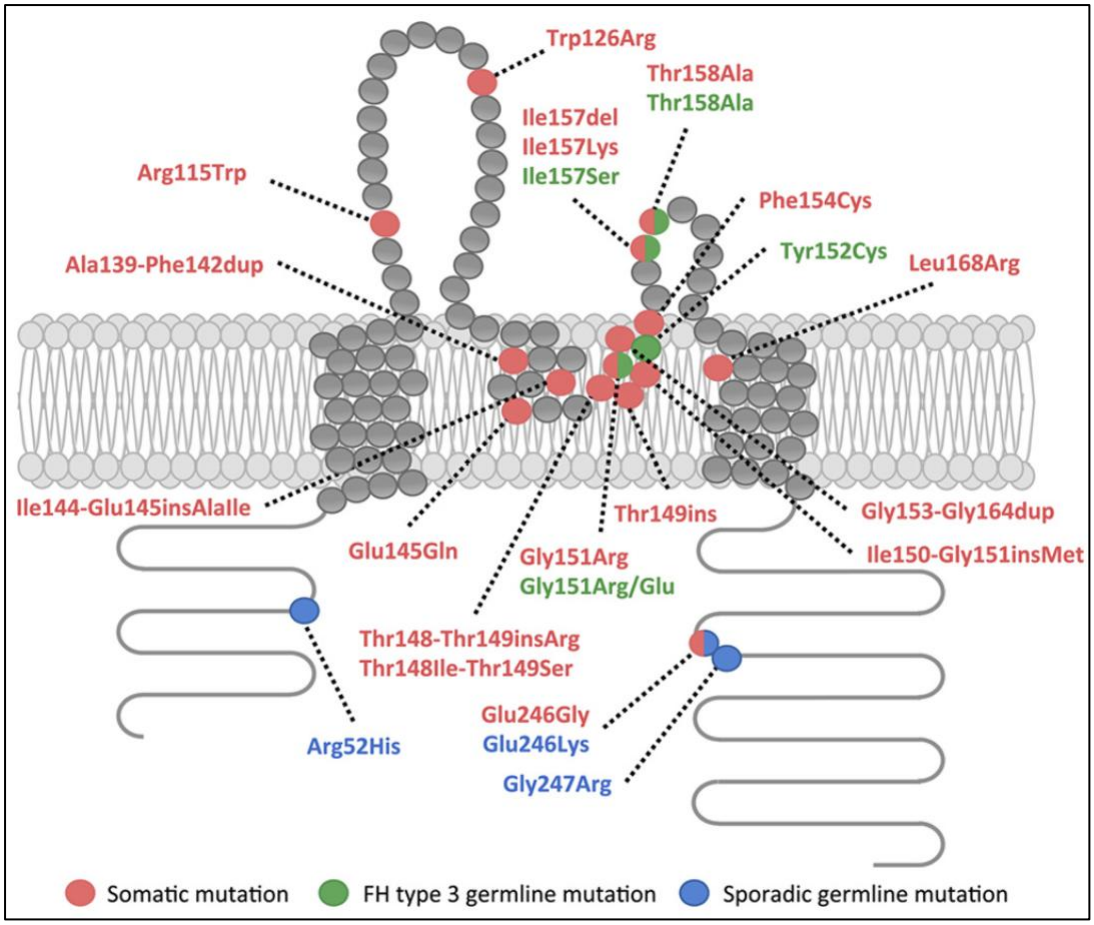

Figure 2: ***Overview of Mutations in the KCNJ5 Gene and Their Structural Localization in the GIRK4 Channel.*** *These mutations lead to a loss of channel selectivity for potassium (K+), specifically by affecting its transport to the extracellular space in favour of sodium (Na+), which enters and depolarises the cell, activating the calcium signalling pathway and leading to the production of aldosterone. Other mutations, not localised in the selectivity filter and in its proximity, such as sporadic germline variants, decrease the expression of the channel at the plasma membrane (Extracted from (Prada et al., 2017)).*

4.1.2 ATP1A1 and ATP2B3 mutations

ATP1A1 and *ATP2B3* genes code respectively for the Na^+/K^+-ATPase alpha-1 subunit and plasma membrane transporting ATPase 3 (PMCA3), which both belong to the P-type family of ATPases. These pumps consist of 10 transmembrane domains (M1-M10) and intracellular C- and N- termini. The Na^+/K^+-ATPase pump maintains the electrochemical gradient essential for various physiological processes by exchanging three intracellular Na^+ ions for two extracellular K^+ ions. The *PMCA3* maintains intracellular calcium balance by actively transporting calcium ions out of the cell. WES sequencing of tumours and control tissue from nine males with hypokalaemia without *KCNJ5* mutations lead to the identification of somatic variants of *ATP1A1* in three out of nine patients and somatic variants of *ATP2B3* in two tumour tissues (Azizan et al., 2013; Beuschlein et al., 2013; Fernandes-Rosa et al., 2014; Gomez-Sanchez et al., 2015). Several disease-associated somatic variants have been identified within *ATP1A1*,

especially in transmembrane domains critical for ion binding and pump function. Mutations affecting M1 and M4 reduce K^+ affinity, compromising pump activity, while variants in M9 disrupt Na^+ coordination. Expression of mutant proteins in adrenocortical H295R cells induces partial membrane depolarization and altered potassium sensitivity. They lead to a loss of function of the pump and also induce a proton leak, which induces cell membrane depolarization and increased Ca^{2+} influx (Stindl et al., 2015). In contrast, mutations in *ATP2B3* often involve in-frame deletions within the M4 domain, such as the p.Leu425_Val426del mutations, which impair the protein ability to effectively extrude Ca^{2+} from the cell. Functional studies using HEK-293 and H295R cells carrying these deletions revealed enhanced aldosterone secretion linked to dysregulated intracellular calcium signalling (Beuschlein et al., 2013; Tauber et al., 2016).

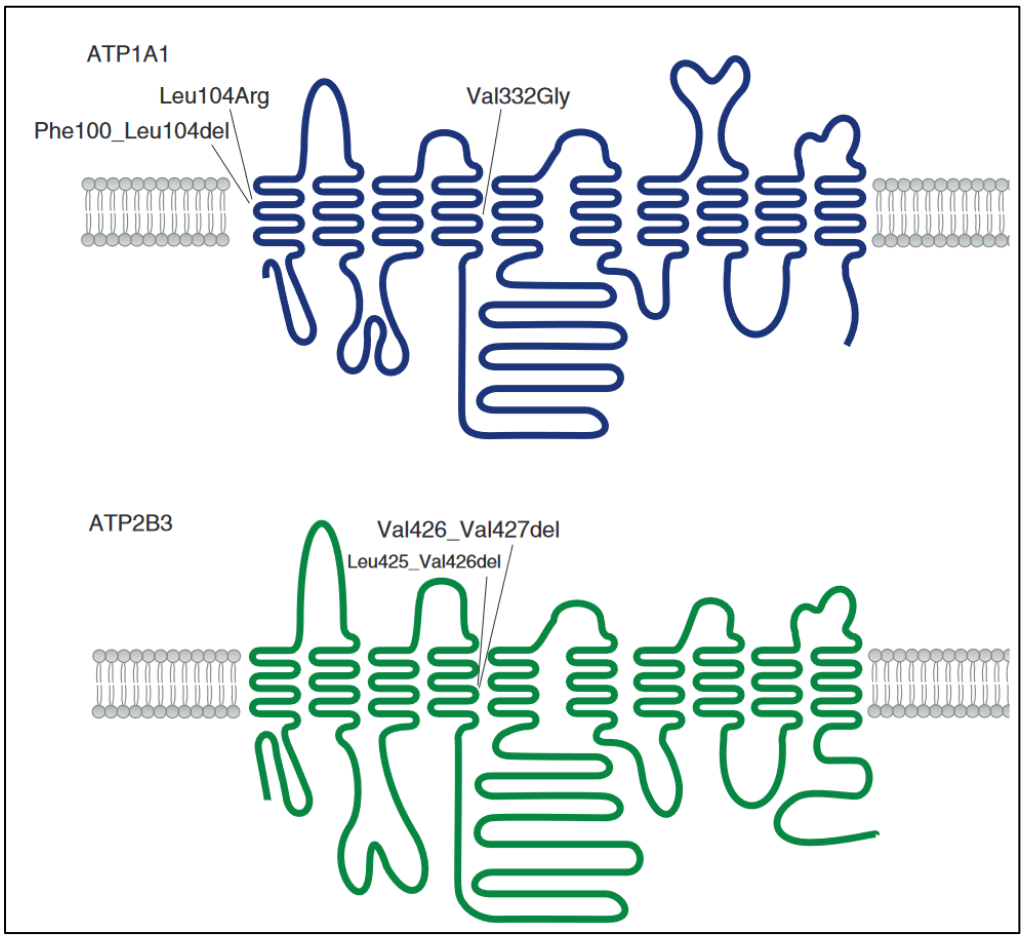

Figure 3: ***Summary of Somatic Mutations in ATP1A1 and ATP2B3 Found in Aldosterone-Producing Adenomas (APAs).*** *The ATP1A1 and ATP2B3 proteins contain ten transmembrane segments (M1 to M10), with M1 positioned at the N-terminal end. Ion transport is facilitated by specific amino acid residues located within M4, M5, M6, and M8—among which M4 plays a particularly crucial role. ATP and phosphate molecules bind within the large cytoplasmic loop that connects M4 and M5. Additionally, the smaller cytoplasmic loop situated between M2 and M3 is essential for the conformational shifts involved in the energy transduction process (Extracted from (Beuschlein et al., 2013)) .*

4.1.3 CACNA1D mutations

The *CACNA1D* (calcium voltage-gated channel subunit α1D) gene encodes for the pore-forming α_1 subunit of the Cav1.3 L-type voltage-gated calcium channel. WES studies in patients with APAs identified recurrent heterozygous mutations in this gene (Azizan et al., 2013; Scholl et al., 2013). The α_1 subunit of Cav1.3 is composed of four homologous domains (I–IV), each containing six transmembrane segments (S1–S6), with the S5–S6 loop playing an important role in delimiting the pore of the channel (Scholl et al., 2013). Mutations were identified in highly conserved regions involved in voltage sensing, notably p.Val259Asp and p.Pro1336Arg, and in the channel activation domains, such as p.Gly403Arg and p.Ile750Met. These are gain-of function mutations, which lead to channel activation at a less depolarized cell membrane potential and delay channel inactivation, leading to increased calcium signalling in the cell and induction of aldosterone biosynthesis (Azizan et al., 2013; Pinggera and Striessnig, 2016; Scholl et al., 2013). *CACNA1D* mutations represent the second most frequent somatic event in APAs, with a reported prevalence of approximately 27% (De Sousa et al., 2020) and a higher prevalence in subjects from Sub-Saharan African ancestry (K et al., 2019). Histologically, APAs harboring *CACNA1D* mutations tend to resemble ZG cells, contrasting with *KCNJ5*-mutant APAs, which have a zona fasciculata-like morphology (Azizan et al., 2013; Fernandes-Rosa et al., 2014).

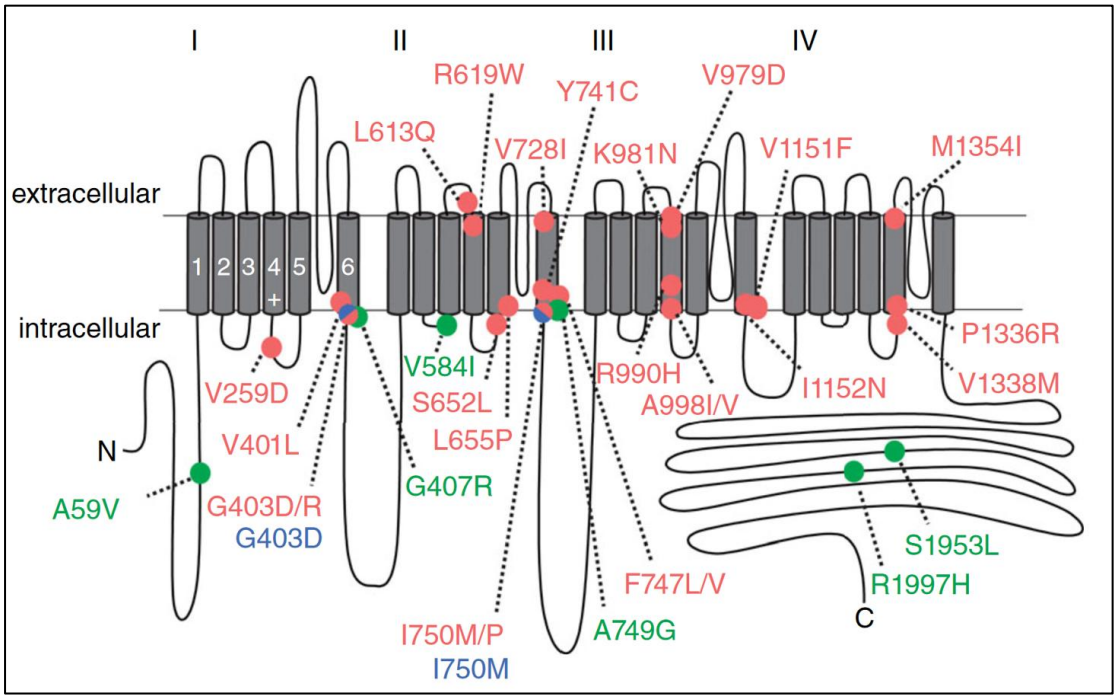

Figure 4: ***Somatic and germline CACNA1D mutations associated with human diseases.*** *Missense mutations in CACNA1D are depicted as circles. Somatic mutations identified in APAs are shown in red. Of these, only V259D, G403D/R, I750M, and P1336R have been functionally characterized, all exhibiting strong gain-of-*

function effects. Germline mutations G403R and I750M, shown in blue, were identified as de novo variants in patients with primary aldosteronism, seizures, and neurological abnormalities (PASNA). Mutations associated with autism spectrum disorder (ASD) are indicated in green (Extracted from (Pinggera and Striessnig, 2016)).

4.1.4 Mutations affecting *CTNNB1* alone or co-occurring with *GNAQ/GNA11* mutations

Mutations in the *CTNNB1* gene, which encodes the β-catenin protein, are frequently implicated in adrenal cortical pathologies, including APAs and adrenocortical carcinomas. The screening of a cohort of 198 APA found *CTNNB1* mutations in approximately 5.1% of tumors with a higher prevalence in women (Åkerström et al., 2016; Wu et al., 2017). These mutations often affect exon 3, disrupting phosphorylation sites that normally regulate β-catenin degradation. As a result, β-catenin accumulates in the nucleus and aberrantly activates WNT/β-catenin signalling, promoting uncontrolled cell proliferation and tumorigenesis (Maharjan et al., 2018). Recent studies have identified gain-of-function mutations in *GNA11* and its homolog *GNAQ*, which encode the α-subunit of the Gq protein, in APAs that also carry *CTNNB1* mutations. These *GNAQ/11* mutations are notably associated with cases of PA diagnosed during hormonally dynamic periods such as puberty, pregnancy, or menopause. In the ZG, Gq/11 proteins mediate the response to angiotensin II, activating calcium signalling and stimulating aldosterone production. In vitro experiments have demonstrated an additive effect of *CTNNB1* and *GNAQ*/*GNA11* mutations on aldosterone biosynthesis and gene expression profiles. Notably, APAs with these double mutations show increased expression of *LHCGR*, the gene encoding the luteinizing hormone/choriogonadotropin receptor, which may explain the hormonal sensitivity observed in affected patients. Evidence suggests that *GNA11/Q* mutations may occur first, creating a permissive environment for subsequent *CTNNB1* mutations, a hypothesis supported by mosaic *GNAQ/11* mutations found in hyperplastic ZG issue adjacent to APAs (Zhou et al., 2021).

4.1.5 CADM1 mutations

Recent studies have identified somatic mutations in the *CADM1* gene, which encodes a Cell Adhesion Molecule 1 that is located at gap junction (GJ) and plays an important role in cell communication. The mutations p.Val380Asp and p.Gly379Asp, were discovered by WES of APA and mutant proteins were shown to significantly upregulate *CYP11B2* expresison by 10- to 25-fold in adrenocortical H295R cells. Functionally, CADM1 mutations impair GJ mediated communication between adrenal ZG cells, a new mechanism that was shown to suppress aldosterone production. Pharmacological inhibition of GJs using Gap27 mimicked the effects of CADM1 mutations, further supporting the role of intercellular communication in regulating aldosterone biosynthesis. The findings suggest that *CADM1* mutations disrupt physiological

aldosterone regulation by interfering with GJ-mediated signalling, revealing a previously unknown mechanism in APA development and PA (Azizan et al., 2023; Wu et al., 2023).

4.1.6 SLC30A1 mutations

Recent genomic analyses have identified somatic mutations in the *SLC30A1* gene (Solute Carrier Family 30 Member 1), which encodes the zinc efflux transporter ZnT1 (Zinc Transporter 1). ZnT1 functions as a Zn^{2+}/Ca^{2+} and/or Zn^{2+}/H^{+} exchanger and plays a key role in maintaining intracellular zinc homeostasis. *SLC30A1* is part of the Cation Diffusion Facilitator (CDF) superfamily, specifically within the SLC30 subfamily, which comprises ten members grouped based on gene sequence homology. The ZnT1 protein contains six transmembrane domains and features a histidine- and serine-rich intracellular loop between the fourth and fifth transmembrane segments. Both the N-terminal and C-terminal regions are located on the cytoplasmic side of the membrane (Huang and Tepaamorndech, 2013). Mutations in *SLC30A1*, particularly in-frame deletions such as p.L51_A57del and p.L49_L55del, are situated near the zinc-binding domain and are believed to impair ZnT1's ion transport function. These alterations lead to abnormal sodium influx, causing membrane depolarization and activation of voltage-gated calcium channels. The resulting increase in intracellular calcium stimulates *CYP11B2* expression, thereby enhancing aldosterone biosynthesis. Clinically, these mutations are associated with elevated aldosterone and 18-oxocortisol levels, and appear to be more prevalent in male patients (Rege et al., 2023).

4.1.7 MCOLN3 mutations

In a recent study, *van Rooyen et al.* have identified somatic mutations in the *MCOLN3* gene as a novel molecular mechanism underlying a subset of APAs. The *MCOLN3* gene encodes mucolipin-3, a protein that functions as a cation-selective channel with inward rectification, and is part of the transient receptor potential mucolipin (TRPML) family. It is primarily localized to endolysosomal membranes, where it regulates intracellular calcium and other ion fluxes. These mutations were shown to enhance intracellular calcium signalling, a key driver of *CYP11B2* expression and aldosterone synthesis in adrenal ZG cells. Functional assays demonstrated that mutant *MCOLN3* channels increased calcium influx, leading to upregulated aldosterone production. Moreover, transcriptomic profiling revealed that *MCOLN3*-mutant APAs exhibit a distinct gene expression signature, suggesting a unique molecular subtype within primary aldosteronism (van Rooyen et al., 2025).

The molecular mechanisms of somatic mutations in APA are summarized in Figure 5.

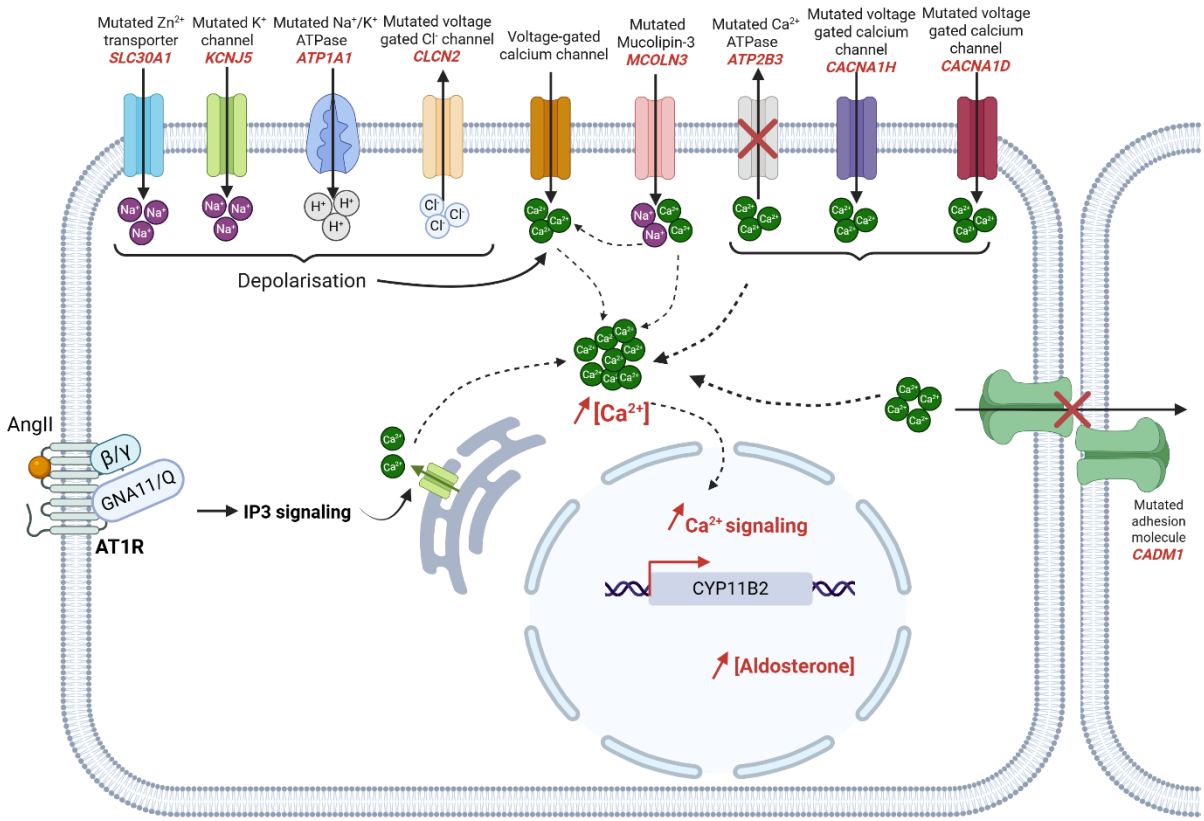

Figure 5: ***Overview of the molecular mechanisms driving aldosterone-producing adenomas (APAs).*** *Somatic mutations in genes such as KCNJ5, ATP1A1, CLCN2, SLC30A1 and MCOLN3 disrupt ion transport, leading to membrane depolarization and increased intracellular calcium, which stimulates aldosterone synthesis. Activating mutations in calcium channel genes (CACNA1D, CACNA1H) or pumps (ATP2B3) directly promote increased intracellular calcium concentrations and upregulate CYP11B2 expression. Alterations in GNA11 and GNAQ result in constitutive G-protein signalling, while CTNNB1 mutations activate Wnt/β-catenin pathways, contributing to both hormone production and cell proliferation. CADM1 mutations increase aldosterone production by interfering with cell–cell communication. (Fayad*, Faedda* et al, under submission).*

4.2 Familial forms of primary aldosteronism

Different hereditary mutations define four subtypes of familial hyperaldosteronism (FH I-IV), rare conditions that are transmitted as autosomal dominant traits. While most cases of PA occur sporadically, familial forms account for approximately 1–5% of diagnoses (Fernandes-Rosa et al., 2017). The different forms of FH and their underlying genetic defects are summarised in Figure 6.

4.2.1 Familial hyperaldosteronism type I (FH-I)

Familial Hyperaldosteronism Type I (FH-I), also known as glucocorticoid-remediable aldosteronism (GRA), is a rare autosomal dominant form of PA caused by a chimeric gene formed through unequal crossing-over between the *CYP11B1* gene, which encodes 11β-

hydroxylase responsible for cortisol biosynthesis, and the *CYP11B2* gene which encodes AS (Fernandes-Rosa et al., 2017; Scholl, 2022). This genetic rearrangement results in the expression of AS under the control of the *CYP11B1* promoter, making aldosterone production dependent on the adrenocorticotropic hormone (ACTH) rather than regulated by the renin-angiotensin system (Lifton et al., 1992). Consequently, aldosterone is produced in the ZF instead of the ZG, following the circadian rhythmicity of corticol, leading to hypertension, suppressed plasma renin activity, and elevated aldosterone levels. Clinically, patients often exhibit elevated levels of hybrid steroids, such as 18-hydroxycortisol and 18-oxocortisol, which are considered diagnostic markers of FH-I. A defining feature of FH-I is its suppressibility by exogenous glucocorticoids. Administration of low-dose dexamethasone suppresses ACTH secretion, thereby reducing aldosterone synthesis and normalizing blood pressure and potassium levels (Stowasser et al., 2000; Sutherland et al., 1966; Zennaro et al., 2020).

4.2.2 Familial hyperaldosteronism type II (FH-II)

Familial Hyperaldosteronism Type II (FH-II) is an inherited form of PA that is not responsive to glucocorticoid therapy. It was initially mapped to chromosome 7p22 through linkage analysis in several affected families (Gordon et al., 1991; Stowasser et al., 1992). The condition is inherited in an autosomal dominant manner and presents with variable severity, ranging from mild hypertension to early-onset, treatment-resistant forms. The molecular basis of FH-II was clarified with the identification of heterozygous mutations in the *CLCN2* gene, which encodes the ClC-2 chloride channel, in a large Australian family (Scholl et al., 2018), with another mutation described in parallel in a case of early onset PA (Fernandes-Rosa et al., 2018). Mutations are typically located within a short aminoacid segment of ClC-2 called the inactivation domain, resulting in constitutive activation and loss of normal regulatory responses to voltage, pH, or cell volume. The persistent chloride efflux leads to membrane depolarization, activation of voltage-gated calcium channels, and increased *CYP11B2* transcription, thereby stimulating aldosterone production (Fernandes-Rosa et al., 2018). A certain degree of phenotypic variability and incomplete penetrance observed in FH-II is thought to reflect the diversity of *CLCN2* mutations, which can affect different functional domains of the channel (Scholl et al., 2018) (Dutta et al., 2019).

4.2.3 Familial hyperaldosteronism type III (FH-III)

Familial Hyperaldosteronism Type III (FH-III) is a rare autosomal dominant form of primary aldosteronism caused by recurrent germline mutations in the *KCNJ5* gene. Similar to mutations

responsible for APA. these mutations disrupt the ion selectivity filter of the channel, allowing sodium to enter ZG cells. This abnormal influx leads to membrane depolarization, activation of voltage-gated calcium channels, and an increase in intracellular calcium levels. The elevated calcium concentration stimulates the expression of *CYP11B2*, resulting in excessive aldosterone production (Choi et al., 2011; Mulatero et al., 2013). Clinically, FH-III typically presents with early-onset hypertension, often during childhood or adolescence, and is frequently accompanied by hypokalemia. Imaging may reveal bilateral adrenal hyperplasia, with some cases showing significant glandular enlargement. Biochemical findings include elevated plasma aldosterone, suppressed renin activity, and increased levels of hybrid steroids such as 18-oxocortisol and 18-hydroxycortisol (Azizan et al., 2023; S. Monticone et al., 2017). Two clinical forms of FH-III have been described. In severe cases, patients develop drug-resistant hypertension due to bilateral adrenal hyperplasia at a young age, often requiring bilateral adrenalectomy to cure hypertension, followed by lifelong hormone replacement therapy (Choi et al., 2011). In contrast, milder forms of the disease may be managed effectively with mineralocorticoid receptor antagonists (MRA) such as spironolactone or eplerenone (Azizan et al., 2023; Mulatero et al., 2012; Scholl et al., 2012).

4.2.4 Familial hyperaldosteronism type IV (FH-IV)

Familial Hyperaldosteronism Type IV (FH-IV) is a rare autosomal dominant form of primary aldosteronism caused by mutations in the *CACNA1H* gene, which encodes the α1 subunit of the voltage gated CaV3.2 T-type calcium channel. These mutations were first identified in two independent studies, which together described five distinct variants in patients with differing clinical presentations of PA (Daniil et al., 2016; Scholl et al., 2015).

Electrophysiological characterization of these variants revealed a gain-of-function phenotype, with altered channel kinetics that include activation at more negative membrane potentials and delayed inactivation. These changes result in enhanced calcium influx, which promotes sustained intracellular calcium signalling. This, in turn, stimulates the expression of *CYP11B2*, leading to increased aldosterone production. Functional studies using H295R-S2 adrenocortical cells expressing the mutant CaV3.2 channels confirmed that these mutations enhance aldosterone biosynthesis, especially in response to potassium stimulation (Daniil et al., 2016). The clinical phenotype associated with FH-IV is variable. Some individuals present with early-onset hypertension and developmental abnormalities, while others exhibit features resembling FH-II. This phenotypic diversity suggests that CACNA1H mutations may contribute to a

spectrum of aldosterone-related disorders, depending on the specific mutation and its functional impact (Daniil et al., 2016).

4.3 Genetic susceptibility to PA

Beyond rare germline and somatic mutations, our laboratory has highlighted the role of common genetic variants in predisposing individuals to PA. By applying a genome-wide association study (GWAS) to a large cohort with PA, Le Floch et al identified several genetic risk loci for PA on chromosomes 1, 13, and X. The loci on chromosome 1 and 13, including the genes *CASZ1* (Castor Zinc Finger 1) and *RXFP2* (Relaxin Family Peptide Receptor 2), were subsequently replicated on a large German cohort and two additional smaller cohorts (Le Floch et al., 2022). Overexpression of *CASZ1* and *RXFP2* in adrenocortical cells reduced mineralocorticoid output without affecting cortisol production, under both basal and stimulated conditions following treatment with angiotensin II or potassium (Le Floch et al., 2022). The SNPs were found associated to both APA and BAH, supporting the hypothesis of a genetic and pathophysiological continuum between these two subtypes of PA. Remarkably, theses loci had previously been associated with blood pressure related loci and resistant hypertension, supporting clinical evidence of a continuum between dysregulated aldosterone production and hypertension in the general population (Brown et al., 2020). Genetic risk loci have subsequently been replicated in a Japanese cohort and cross-ancestry meta-analysis (Inoue et al., 2024; Naito et al., 2023), with some heterogeneity indicating a possible heterogeneity across different populations. Altogether this discovery represents a paradigm shift in our understanding of the genetics of PA, indicating that common genetic variants may predispose to aldosterone dysregulation in the general population, by modifying adrenocortical function and mineralocorticoid output in the adrenal gland. This could lead to a propitious environment for the appearance of somatic mutations and the development of PA in extreme cases (Le Floch et al., 2022).

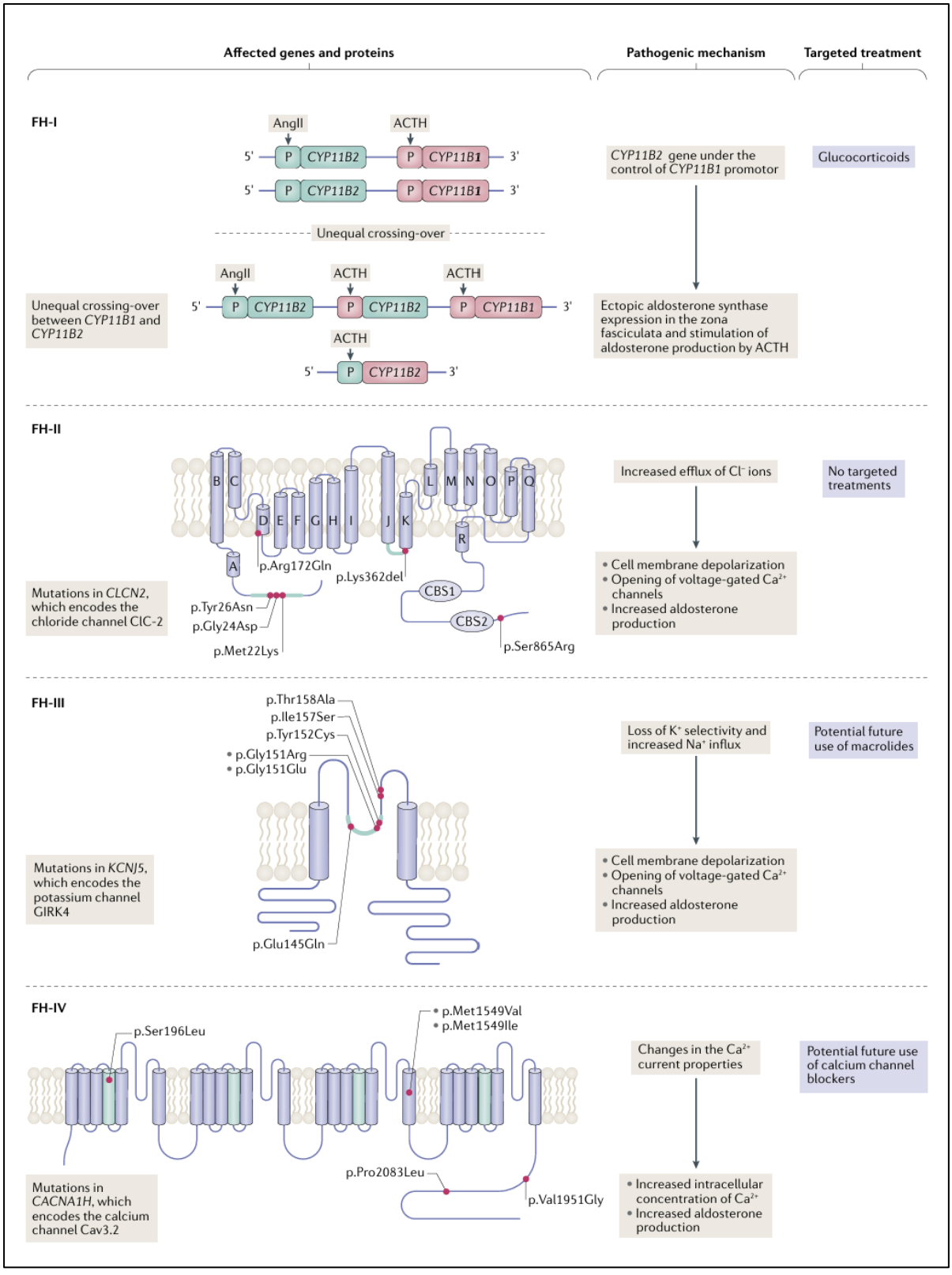

Figure 6: ***Genetic and pathogenic mechanisms of familial hyperaldosteronism and targeted treatment****. Familial hyperaldosteronism type I (FH-I) is due to unequal crossing-over between the CYP11B1 and CYP11B2 genes, resulting in the fusion of the regulatory sequences of CYP11B1 to the coding sequence of CYP11B2. This unequal crossing-over leads to ectopic aldosterone synthase expression in the zona fasciculata and stimulation of aldosterone production by adrenocorticotropic hormone (ACTH). Targeted treatment is based on the use of glucocorticoids. FH-II is due to mutations in the CLCN2 gene, which encodes the chloride channel ClC-2, resulting in an increased efflux of Cl– ions, leading to cell membrane depolarization, opening of voltage-gated calcium channels and increased aldosterone*

production. No targeted treatments for FH-II are currently available. FH-III is due to mutations in the potassium channel GIRK4, encoded by KCNJ5. These mutations are responsible for a change in the channel selectivity, with a loss of potassium selectivity and an increased sodium influx, leading to cell membrane depolarization, opening of voltage-gated calcium channels and increased aldosterone production. No targeted treatments for FH-III are available so far, but macrolides specifically block the mutated channels and might represent potential pharmacological options. Mutations in CACNA1H, encoding the calcium channel Cav3.2, are responsible for FH-IV. These mutations result in changes in calcium current properties, leading to an increased intracellular concentration of calcium and aldosterone production. Specific calcium channel blockers acting on mutated Cav3.2 channels could be a useful development for patients with FH-IV. AngII, angiotensin II (Extracted from (Zennaro et al., 2020)).

5. Anatomy of the adrenal gland

5.1 Adrenal gland structure and function

The adrenals are paired endocrine organs positioned at the superior pole of each kidney. Each gland comprises two developmentally and functionally distinct compartments: a central medulla derived from neural crest cells that secretes catecholamines, and a peripheral cortex of mesodermal origin that produces steroid hormones. A fibrous capsule composed of fibroblasts and myofibroblasts surrounds both compartments. The adrenal cortex is divided itself in three functionally different layers: the ZG, the zona fasciculata (ZF) and the zona reticularis (ZR) (Figure 7). Thanks to a peculiar functional zonation, each of these zones is responsible for the secretion of specific steroid hormones. Although each zone uses cholesterol as a precursor for steroid hormone synthesis, the production of zone-specific steroids results from differential enzyme expression.

The mineralocorticoids, primarily aldosterone, are synthesized in the ZG. The ZG is the outer layer of the cortex and it accounts for 5-10% of its size with small cells arranged in clusters. The cells have round, dense nuclei with a lightly basophilic cytoplasm.

The glucocorticoids, with cortisol being the most prominent in human and corticosterone in mice and rats, are produced in the ZF. The ZF is the second and largest layer and is formed of lipid-rich polygonal cells that are arranged in radial columns.

Additionally, androgens, specifically dehydroepiandrosterone (DHEA), are synthesized in the ZR. On the other hand, the adrenal medulla produces catecholamines, primarily epinephrine and norepinephrine. Each of these hormones plays a distinct role in regulating various physiological processes (Yates et al., 2013).

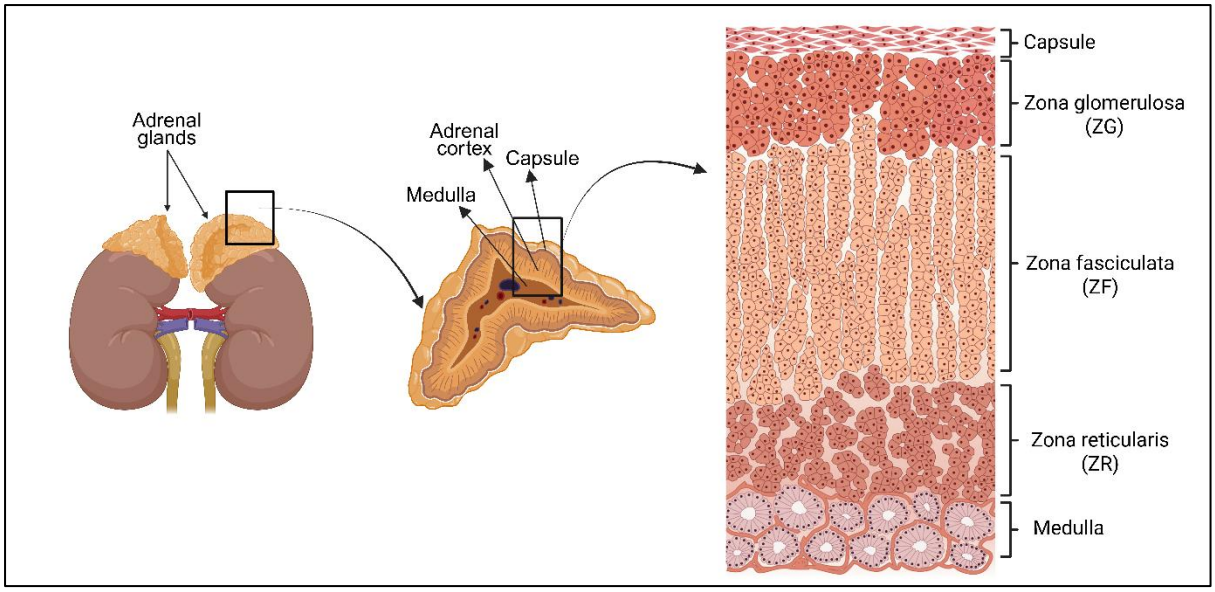

Figure 7: ***Adrenal gland anatomical and histological structure.*** *The adrenal gland consists of a central medulla, surrounded by the cortex and then the capsule. The cortex itself is divided into three zones, from the outermost to the innermost: the zona glomerulosa, zona fasciculata, and zona reticularis. Each of these zones synthesizes different steroid hormones, thanks to the expression of enzymes specific to each region (generated with BioRender).*

5.2 Differences in the adrenal cortex structure between species

The adrenal gland structure is slightly different between human and mouse, with the absence of the ZR in mice and the presence of another zone called X zone (ZX) at the corticomedullary boundary (Fig.2). The ZX is not well characterized and its function is not clear until now. The ZX has a dimorphic phenotype, with its regression after puberty in males and after the first pregnancy or at late stage of life in females (Hershkovitz et al., 2007; Kang et al., 2024; Pihlajoki et al., 2015). In addition, the mouse ZF does not express the 17α-hydroxylase and is therefore uncapable of converting pregnenolone and progesterone to its 17α-hydroxylated derivatives, which are essential precursors of glucocorticoids and adrenal androgens.

Species	Mouse	Human
Anatomy	cap zG zF X med	cap zG zF zR med
CYP17A1 expressed	No	Yes
Major glucocorticoid	Corticosterone	Cortisol
Adrenal androgens	No	Yes

Figure 8: Comparison between mouse and human adrenal gland structure (Edited from (Pihlajoki et al., 2015)).

5.3 Vascularisation of the adrenal gland

The adrenals are highly vascularised endocrine organs, where every single cell is in contact with a blood vessel. This vascularisation is important due to the role of the adrenals in the production of different hormones vital for the body functions. The primary suppliers of blood flow to the adrenal glands are the adrenal arteries, which are divided into three groups: superior adrenal arteries which originate from the inferior phrenic arteries; the middle adrenal arteries that are bilateral and arise from the abdominal aorta; and the inferior adrenal arteries which stem from the renal arteries(Megha et al., 2025; Wright and Burns, 2025).

The arteries branch out at the surface of the adrenal gland, beneath the capsule, into a network of small blood vessels called the subcapsular capillary plexus. This network supplies the capsule and gives rise to two major arterial networks: cortical capillaries, which perfuse the three cortical zones before draining into medullary sinusoids, and the medullary arteries, which penetrate directly through the cortex to supply the medulla (Bassett and West, 1997; Kikuta and Murakami, 1982).

5.4 Adrenal gland innervation

Adrenal innervation involves both sympathetic and parasympathetic autonomic inputs, enabling the gland to respond dynamically to stress signals. Preganglionic sympathetic fibers, predominantly from spinal segments T5-T11, reach the adrenal via the splanchnic nerves. Upon entering through the capsule, these fibers arborize extensively, creating a subcapsular neural plexus that penetrates into both cortical and medullary compartments.

The medulla receives dense sympathetic innervation, with preganglionic cholinergic fibers directly synapsing onto chromaffin cells. These neuroendocrine cells function as modified postganglionic neurons, rapidly secreting catecholamines (epinephrine and norepinephrine) into the circulation during acute stress responses. Parasympathetic fibers from the vagus nerve also innervate the gland, though their physiological role remains incompletely understood.

The adrenal also contains intrinsic ganglia—sympathetic neurons that bypass the celiac ganglion and reside within the gland itself across subcapsular, cortical, and medullary zones. These intraglandular neurons send axons to blood vessel pericytes and medullary chromaffin cells, suggesting local neuromodulatory circuits that may fine-tune adrenal function independently of central nervous system input (Parker et al., 1993).

6. Steroidogenesis

Adrenal steroids are synthesized from cholesterol by a series of enzymatic steps involving cytochrome P450 (CYP) family enzymes and hydroxysteroid dehydrogenases. These reactions take place either in the mitochondrial membrane or in the endoplasmic reticulum (ER) (Fig.4).

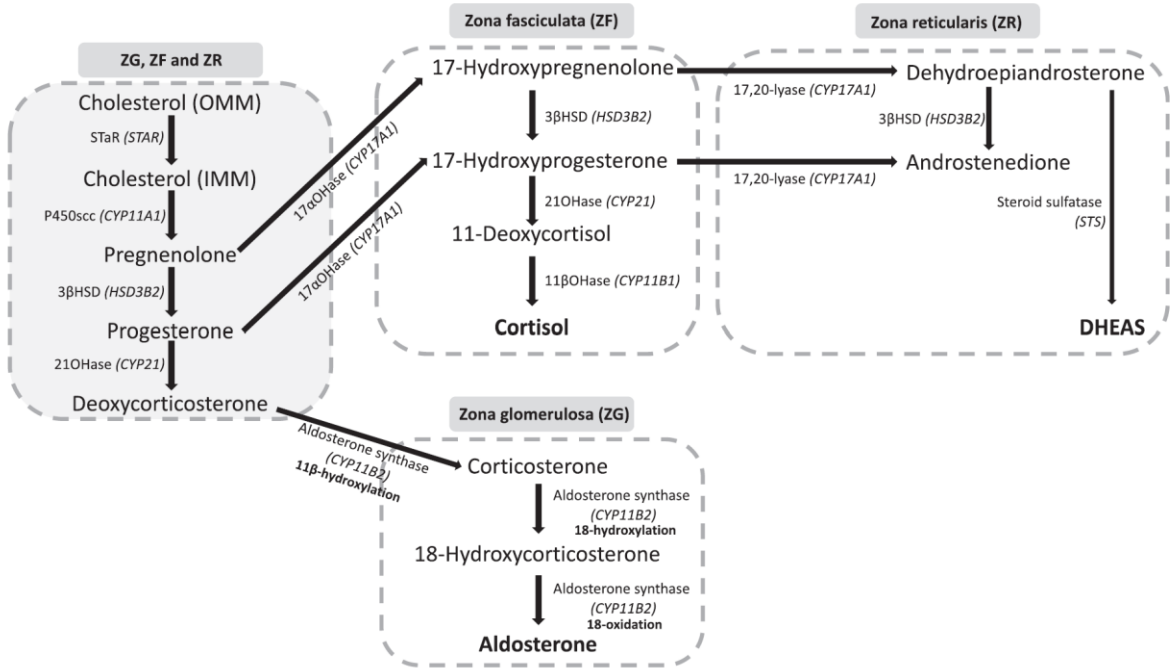

Figure 9: ***Summary of the major steroidogenic pathways of the human adrenal cortex within the three adrenocortical zones.*** *Names of the enzymes mediating each stage are shown alongside the name of the corresponding gene in brackets (Extracted from (MacKenzie et al., 2024)).*

6.1 Aldosterone biosynthesis

Aldosterone is synthesized in the ZG of the adrenal cortex, where AS, encoded by the *CYP11B2* (cytochrome P450 family 11 subfamily B member 2) gene, catalyzes the final steps of its production. The biosynthetic pathway begins with the transport of cholesterol to the inner mitochondrial membrane by the steroidogenic acute regulatory protein (StAR). There, *CYP11A1* catalyzes the cleavage of the cholesterol side chain to form pregnenolone, which is then transferred to the endoplasmic reticulum (ER). In the ER, 3β-hydroxysteroid dehydrogenase (3β-HSD) converts pregnenolone into progesterone, which is hydroxylated by 21-hydroxylase (*CYP21A2*) to produce 11-deoxycorticosterone. This intermediate returns to the mitochondria, where aldosterone synthase catalyzes three sequential reactions: the 11β-hydroxylation of 11-deoxycorticosterone to form corticosterone, followed by 18-hydroxylation of corticosterone to produce 18-hydroxycorticosterone, and finally, an 18-oxidation step converting 18-hydroxycorticosterone into aldosterone (Connell and Davies, 2005; Pignatti and

Flück, 2021). Aldosterone plays a key role in regulating blood pressure and electrolyte balance by promoting sodium reabsorption and potassium excretion, primarily in the distal nephron. It also exerts effects on other tissues such as the colon, salivary and sweat glands, heart, brain, and adipose tissue. However, excess aldosterone is associated with cardiac hypertrophy, fibrosis, vascular remodelling, insulin resistance, and inflammation in adipose tissue (van der Heijden et al., 2020). Aldosterone production is primarily regulated by the RAS, extracellular potassium levels, and to a lesser extent, ACTH (Connell and Davies, 2005). Ang II binds to the AT1 receptor on ZG cells, a G protein-coupled receptor (GPCR) linked to Gαq, activating phospholipase C and generating inositol 1,4,5-trisphosphate (IP3) and diacylglycerol (DAG). IP3 stimulates calcium release from the ER, increasing intracellular calcium and activating calcium/calmodulin-dependent protein kinases (CaMKs), which phosphorylate transcription factors such as NR4A1 (*NUR77*), NR4A2 (*NURR1*), and CREB, enhancing *CYP11B2* expression. Ang II also inhibits potassium channels such as TASK1, TASK3, and GIRK4 (*KCNJ5*), and the Na^+/K^+-ATPase, leading to membrane depolarization and opening of voltage-gated calcium channels (Spät and Hunyady, 2004). ZG cells are highly sensitive to extracellular potassium due to their high expression of potassium channels. Elevated K^+ levels reduce potassium conductance, depolarize the membrane, and activate calcium signaling (Spät and Hunyady, 2004). Beyond these primary regulators (angiotensin II and potassium), ACTH can acutely stimulate aldosterone synthesis via the MC2R receptor, a GPCR linked to Gαs, which activates adenylate cyclase and the PKA pathway. PKA phosphorylates StAR directly (at Ser194 in mice, Ser195 in humans) or indirectly via CREB, increasing cholesterol transport to mitochondria. ACTH also upregulates *CYP11A1*, enhancing precursor availability (Ruggiero and Lalli, 2016). Chronic ACTH exposure, however, suppresses aldosterone production and promotes transdifferentiation of ZG cells into ZF-like cells (Fuchs-Hammoser et al., 1980).

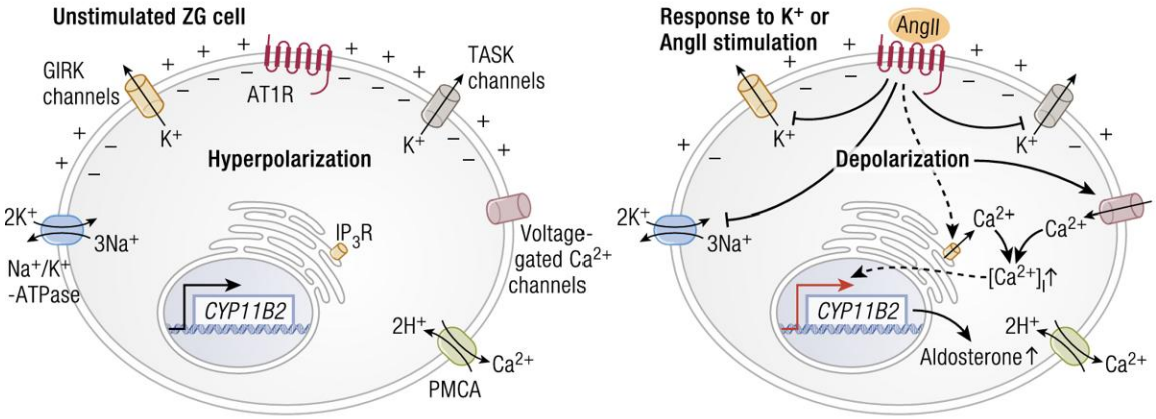

Figure 10: ***Regulation of aldosterone production in response to K+ or AngII stimulation.*** *In absence of stimulation (AngII or K+), ZG cells are hyperpolarized owing to the presence of a large number of K+ channels. In response to an increase of extracellular K+ concentration or to the binding of AngII to its receptor (AT1R), inhibition of K+ channels leads to cell membrane depolarization, opening of voltage gated Ca2+ channels, increased intracellular calcium concentrations, and activation of Ca2+ signaling, the major trigger for aldosterone biosynthesis. Moreover, binding of AngII to AT1R leads to inhibition of the Na+/K+-ATPase, increasing cell depolarization. In addition, signaling through Gaq promotes the release of Ca2+ from the endoplasmatic reticulum through binding of IP3 to its receptor, again stimulating aldosterone biosynthesis. (Extracted from (Zennaro et al., 2017)).*

6.2 Cortisol biosynthesis

Cortisol biosynthesis occurs in the ZF of the adrenal cortex and is regulated by circadian rhythms and stress stimuli via the hypothalamic-pituitary-adrenal (HPA) axis. In response to stress, corticotropin-releasing hormone (CRH) and vasopressin (AVP) are secreted by the hypothalamus, synergistically stimulating the release of ACTH from the anterior pituitary. ACTH binds to the melanocortin 2 receptor (MC2R) on adrenocortical cells leading to the activation of the cAMP/PKA signalling pathway, which promotes the transcription of genes coding for steroidogenic enzymes such as StAR and CYP11B1, thereby enhancing cortisol synthesis (Gallo-Payet et al., 2017).

In humans, the presence of 17α-hydroxylase (encoded by *CYP17A1*) in the ER of the ZF and the ZR cells allows the conversion of progesterone into 17-hydroxyprogesterone. Hydroxylation by the 21-hydroxylase generates 11-deoxycortisol, which is then hydroxylated in the mitochondria by the 11β-hydroxylase (*CYP11B1*) at the C11 position to form cortisol. However, in rodents such as mice, *Cyp17a1* is not expressed in the adrenal cortex, due to epigenetic repression mechanisms including DNA methylation of the *Cyp17a1* promoter. As a result, the steroidogenic pathway skips the 17α-hydroxylation and proceeds from progesterone

to 11-deoxycorticosterone, which is converted to corticosterone by 11β-hydroxylase. Corticosterone thus becomes the dominant glucocorticoid in mice, whereas in humans it serves primarily as a precursor to aldosterone (Yates et al., 2013).

Despite structural differences, corticosterone in mice has similar physiological roles to cortisol, including regulation of metabolism, immune responses, and stress adaptation (Figure 11). It binds both the glucocorticoid receptor (GR) and the MR, contributing to its regulatory functions. The absence of *Cyp17a1* also explains the lack of adrenal androgen production in rodents, further distinguishing their adrenal steroid profile from that of humans (Missaghian et al., 2009).

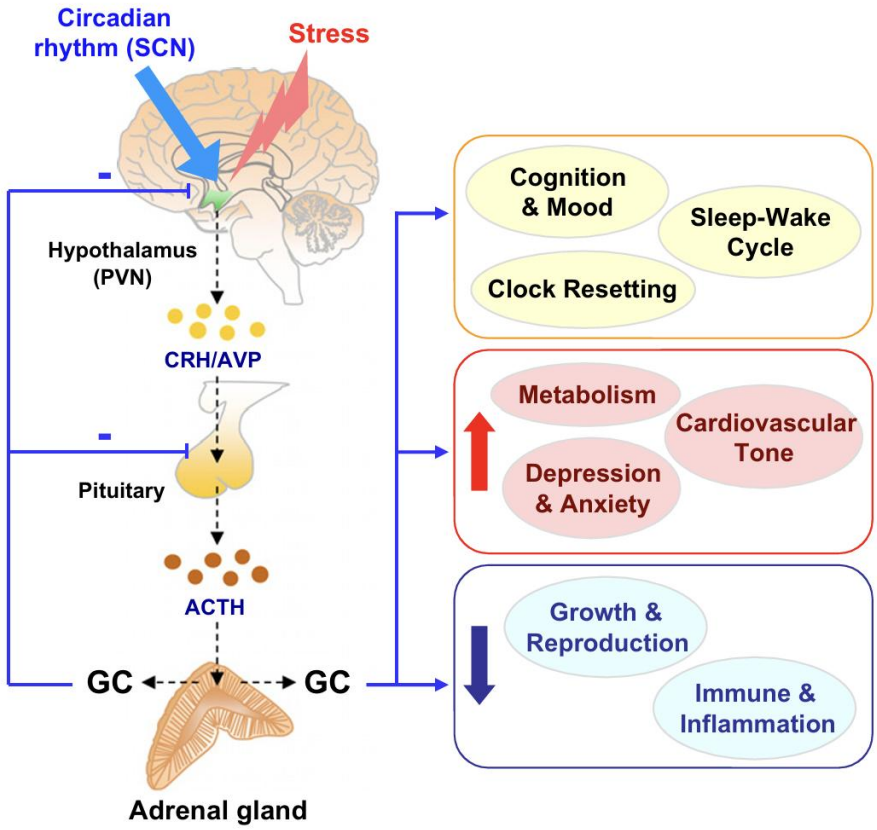

Figure 11: ***Regulation of glucocorticoid production and its physiological roles.*** Glucocorticoids (GC) are primarily regulated by the hypothalamus–pituitary–adrenal gland (HPA) axis, a major neuroendocrine circuit of the stress response system. When certain neurochemical signals related to either circadian rhythm or stress are received by the hypothalamus, a subset of neurosecretory cells in the paraventricular nucleus (PVN) releases corticotrophin-releasing hormone (CRH) and arginine vasopressin (AVP) to stimulate adrenocorticotropic hormone (ACTH) synthesis and secretion from the pituitary. ACTH then induces adrenocortical cells to produce and secrete GC in circulation. GC turns off the HPA axis activity by negative feedback. In addition, GC exerts widespread effects in the body to restore and maintain physiological homeostasis *(Extracted from (Son et al., 2011))*.

7. Signalling pathways and transcription factors in adrenal gland development and steroidogenesis

Adrenal gland homeostasis is maintained by a number of major signaling pathways and transcription factors, which regulate its development, cell lineage, regeneration and function. Among them, the Wnt, PKA, GLI1 and Sonic HedgeHog (Shh) pathways are major players involved in adrenal gland physiology.

7.1 Wnt signalling pathway

The Wnt signalling pathway contributes to adrenal cortex development and function, by influencing progenitor cell proliferation, polarity, differentiation, apoptosis and inflammatory responses. In the adrenal cortex, it plays a critical role from embryonic development through adult tissue maintenance and steroid hormone production. Two major branches of Wnt signalling are recognized: the canonical (β-catenin-dependent) and the non-canonical (β-catenin-independent) pathways (Tai and Shang, 2023) (Figure 12). Depending on the Wnt-receptor complex, one of the two pathways is activated. In the canonical pathway, in the absence of Wnt ligands, β-catenin is phosphorylated by a "destruction" complex that consists of CK1 (casein kinase 1), GSK3β (glycogen synthase kinase-3β), APC (adenomatous polyposis coli), and the scaffolding protein Axin. Wnt signalling is activated following the binding of Wnt ligands to the Frizzled (FZD) receptors and LRP5/6 co-receptors, leading to inhibition of the β-catenin destruction complex. This inhibition allows β-catenin to accumulate in the cytoplasm and translocate into the nucleus, where it interacts with T cell factor (TCF)/lymphoid enhancer binding factor (LEF) transcription factors to activate target genes involved in cell fate and steroidogenesis (Berthon et al., 2012; Nusse and Clevers, 2017; Rim et al., 2022). The non-canonical pathways, which do not involve β-catenin, include the PCP (planar cell polarity) pathway and the Wnt/Ca^{2+} pathway. These are initiated by Wnt ligands binding to alternative co-receptors such as ROR2 (Receptor Tyrosine Kinase Like Orphan Receptor 2) and RYK (Receptor-like Tyrosine Kinase), leading to activation of JNK (c-Jun N-terminal kinase), Rho GTPases, and intracellular calcium signalling cascades (El Wakil and Lalli, 2011; Rao and Kühl, 2010; Slusarski et al., 1997). These pathways regulate tissue morphogenesis, cell migration, and immune responses, and can antagonize canonical Wnt signalling under certain conditions (Yuzugullu et al., 2009).

In the adrenal cortex, canonical Wnt signalling is predominantly active in the ZG, where it supports aldosterone production and zonal identity. Wnt4, a key ligand in this zone, is co-expressed with β-catenin and is essential for proper ZG development and *CYP11B2* expression. Wnt4 deficient mice exhibit impaired ZG formation and ectopic migration of adrenal-like cells to the gonads, suggesting a role in progenitor cell sorting during development. These mice show a decreased *Cyp11b2* expression as well as a reduction in aldosterone levels (Heikkilä et al., 2002). Similarly, mice with *Rspo3* inactivation, which leads to decreased Wnt/β-catenin signalling, showed a decreased ZG size and proliferation (Berthon et al., 2010; Vidal et al., 2016). In vitro experiments using the H295R adrenocortical cell line have shown that β-catenin can directly interact with an enhancer region of the *AT1R* gene, promoting its transcription. This upregulation of *AT1R* subsequently enhances the expression of *CYP11B2*, through the transcriptional activation of the nuclear receptors NUR77 (Nuclear Receptor Subfamily 4 Group A Member 1) and NURR1 (Nuclear Receptor Related 1). These receptors, members of the NUR orphan nuclear receptor family, are known to regulate genes involved in steroidogenesis, including *CYP11B2*. Interestingly, NUR77 and NURR1 also participate in a feedback mechanism that limits β-catenin activity, either by promoting its degradation or by reducing its function as a transcriptional coactivator (Berthon et al., 2014).

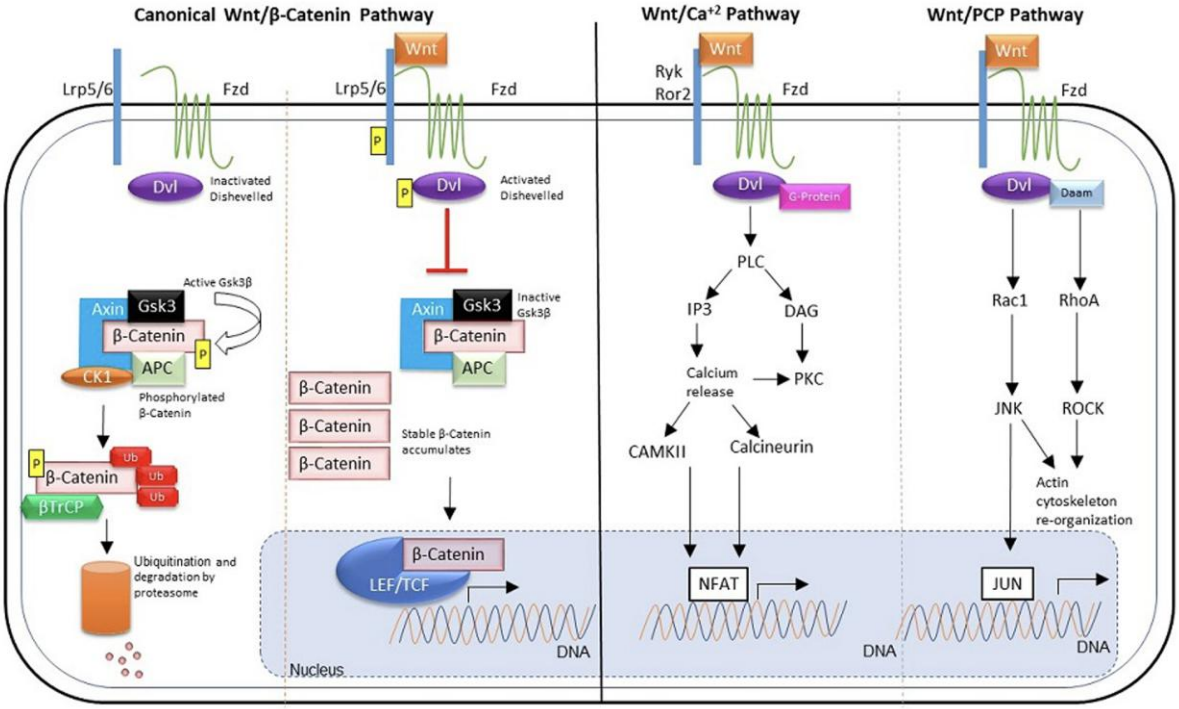

Figure 12 : Overview of canonical and non-canonical Wnt signalling pathways. *(Left) Unstimulated Wnt pathway results in constitutive β-catenin degradation. Wnt stimulation stabilizes β-catenin leading to lymphoid enhancer factor 1 (LEF1)/T-cell factor (TCF) target gene expression. (Center) Wnt/Calcium pathway stimulated through Ryk and Ror2 co-receptor leading to cytoplasmic calcium release from the endoplasmic reticulum and NFAT mediated gene expression. (Right) Wnt/planar cell polarity pathway activates small GTPases leading to actin cytoskeleton re-organization. LRP5/6: lipoprotein receptor related protein 5 or 6; Fzd: Frizzled; Dvl: Dishev elled; APC: adenomatous polyposis coli; CK1: casein kinase 1; Gsk3: glycogen synthase kinase 3; βTrcp: beta-transducin repeats-containing protein; Ror2: receptor tyrosine kinase-like orphan receptor 2; IP3: inositol 1,4,5-triphosphate; PKC: protein kinase C; NFAT: nuclear factor of activated T-cells; CaMKII: CaM kinase II; RhoA: Ras homolog gene family, member A (Extracted from (Garcia et al., 2018)).*

7.2 PKA signalling pathway

The protein kinase A (PKA) pathway is a central regulator of steroid hormone production in the adrenal cortex, particularly in response to ACTH. PKA signalling pathway has been shown to be important in the homeostasis and differentiation of the ZF and its function. Activation of this pathway is crucial for the conversion of ZG cells into ZF cells and for the normal zonation of the cortex (Drelon et al., 2016). PKA is a tetramer complex, consisting of two catalytic subunits (PRKACA) that are inactive due to their binding to two regulatory subunits (PRKARA) (Figure 13). Following ACTH binding to MC2R, the adenylate cyclase enzyme is activated which leads to an increase in intracellular cyclic AMP (cAMP). Elevated cAMP levels trigger the dissociation of the PKA regulatory subunits from the complex, releasing the catalytic subunits, which then phosphorylate transcription factors such as CREB (cAMP response element-binding protein), which interacts with CREB binding protein (CBP) and

p300 to regulate target gene expression (Mayr and Montminy, 2001). In addition to transcriptional regulation, PKA signalling enhances the acute phase of steroidogenesis by facilitating the movement of cholesterol into mitochondria, where the first enzymatic step occurs by converting the cholesterol to pregnenolone. This step is tightly regulated by StAR, whose expression and activity are directly influenced by PKA-dependent phosphorylation (Clark, 2016). Interestingly, the overactivation of PKA signalling by knocking out the regulatory subunit of PKA (*Prkar1a*) specifically in the mice adrenal induces disorganized zonation and Cushing's syndrome (Sahut-Barnola et al., 2010). PKA has been also shown to accelerate the regeneration of the adult adrenal cortex and to favour ZF differentiation (Dumontet et al., 2018). It has been suggested that PKA acts as a tumor suppressor in the adrenal cortex by repressing the activity of Wnt signalling (Drelon et al., 2016). Modifications in PKA signalling are frequently reported in adrenal gland disorders, including cortisol-producing adenomas and Carney complex. In Carney complex, inactivating mutations of the regulatory subunit PRKAR1A lead to constitutive PKA activation, while cortisol-producing adenomas can harbor activating mutations of the catalytic subunit PRKACA, both resulting in cortisol excess (Zilbermint and Stratakis, 2015). Wnt and PKA play essential and complementary roles in the functional zonation of the adrenal cortex, with Wnt signalling favouring a ZG phenotype, while PKA activation promotes a ZF phenotype (Drelon et al., 2016) (Fig. 14).

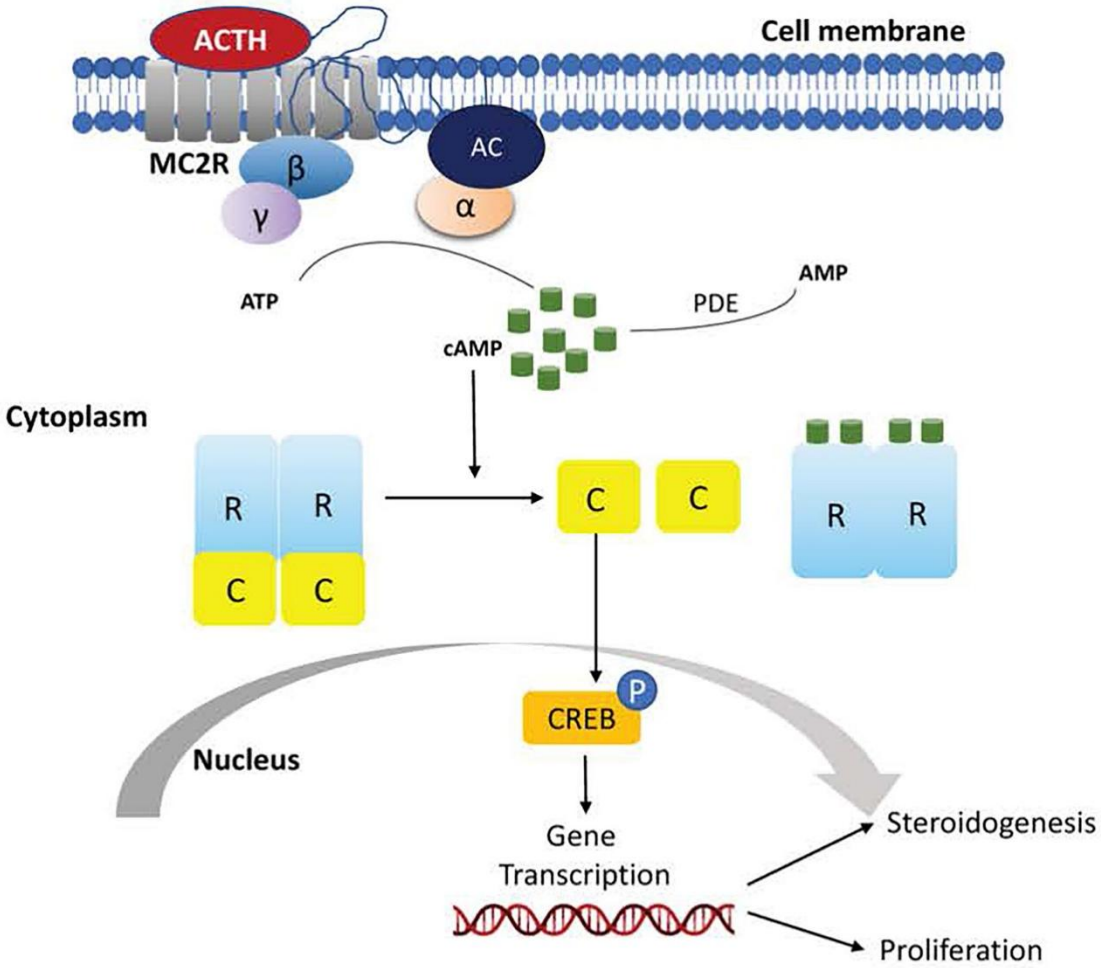

Figure 13: Schematic representation of activation of the cyclic adenosine monophosphate (cAMP) signalling pathway in normal adrenocortical cells. *ACTH (adrenocorticotropic hormone) binds to the melanocortin 2 receptor (MC2R) at the cell membrane, activating adenylyl cyclase (AC) via Gs protein subunits (α, β, γ). AC converts ATP to cAMP, which can be degraded to AMP by phosphodiesterases (PDE). cAMP binds to the regulatory subunits (R) of protein kinase A (PKA), releasing the active catalytic subunits (C). Active PKA catalytic subunits translocate to the nucleus and phosphorylate the transcription factor CREB (cAMP response element-binding protein), which then binds to DNA to activate gene transcription. This pathway regulates both steroidogenesis and cell proliferation in adrenocortical cells (Extracted from (Pitsava et al., 2022)).*

7.3 Glioma-associated oncogene 1 - GLI1 and Sonic HedgeHog – SHH pathways

The Sonic Hedgehog (SHH) signalling pathway is a highly conserved molecular cascade that plays a crucial role in embryonic development, tissue patterning, and stem cell maintenance. In the adrenal gland, SHH signalling contributes to both its development and long-term maintenance, particularly through the regulation of progenitor cells located in the adrenal capsule. SHH is secreted by subcapsular ZG cells and acts on neighbouring capsular cells by binding to its receptor, Patched (PTCH1), which normally inhibits the transmembrane protein

Smoothened (SMO). Ligand binding relieves this inhibition, allowing SMO to initiate a signalling cascade that culminates in the transcriptional activation of GLI1 (Glioma-Associated Oncogene 1), which is expressed in capsular cells and functions as a transcriptional activator. A key modulator of this pathway is Suppressor of Fused (SuFu), which sequesters GLI proteins in the cytoplasm and promotes their processing into repressors. When SHH signalling is active, SuFu inhibition is lifted, enabling GLI1 to translocate into the nucleus and activate genes involved in cell proliferation, differentiation, and survival (King et al., 2009; Lee et al., 2017; Lyraki and Schedl, 2021b).

A subpopulation of GLI1-positive progenitor cells resides in the adrenal capsule and remains active under homeostatic conditions. These cells, which lack SF1 expression, are considered stem-like and respond to paracrine SHH signals from subcapsular SHH^+ cells. SHH is the only Hedgehog ligand expressed in the adrenal gland, and its signalling depends on the presence of a primary cilium in capsular cells. SHH is secreted by clusters of subcapsular cells interspersed among $CYP11B2^+$ zona glomerulosa cells and diffuses to nearby mesenchymal capsular cells. Upon binding to PTCH1 at the base of the primary cilium, SMO accumulates at the ciliary tip and recruits the cilial proteins EVC (Ellis-van Creveld) and EVC2 (also known as Limbin), facilitating GLI activation by antagonizing SuFu. This cascade stabilizes GLI2 and GLI3, promoting GLI1 expression and the transcription of SHH target genes. These $GLI1^+$ capsular cells are part of a bidirectional paracrine loop that governs adrenal cortex renewal and zonal identity. Once activated, they secrete RSPO3, a Wnt pathway enhancer that stimulates underlying ZG cells to express Wnt4 and SHH in both steroidogenic and progenitor populations. SHH then signals back to the capsule, recruiting new progenitor cells and guiding their differentiation into cortical cells. Notably, while SHH knockout mice retain normal adrenal zonation, *Rspo3* deletion disrupts ZG identity, indicating that *Rspo3* also acts through SHH-independent mechanisms. This reciprocal signalling highlights the role of the capsule as a central hub for adrenal cortex cell renewal and zonal maintenance (Huang et al., 2010; Lyraki and Schedl, 2021a; Vidal et al., 2016) (Figure 14).

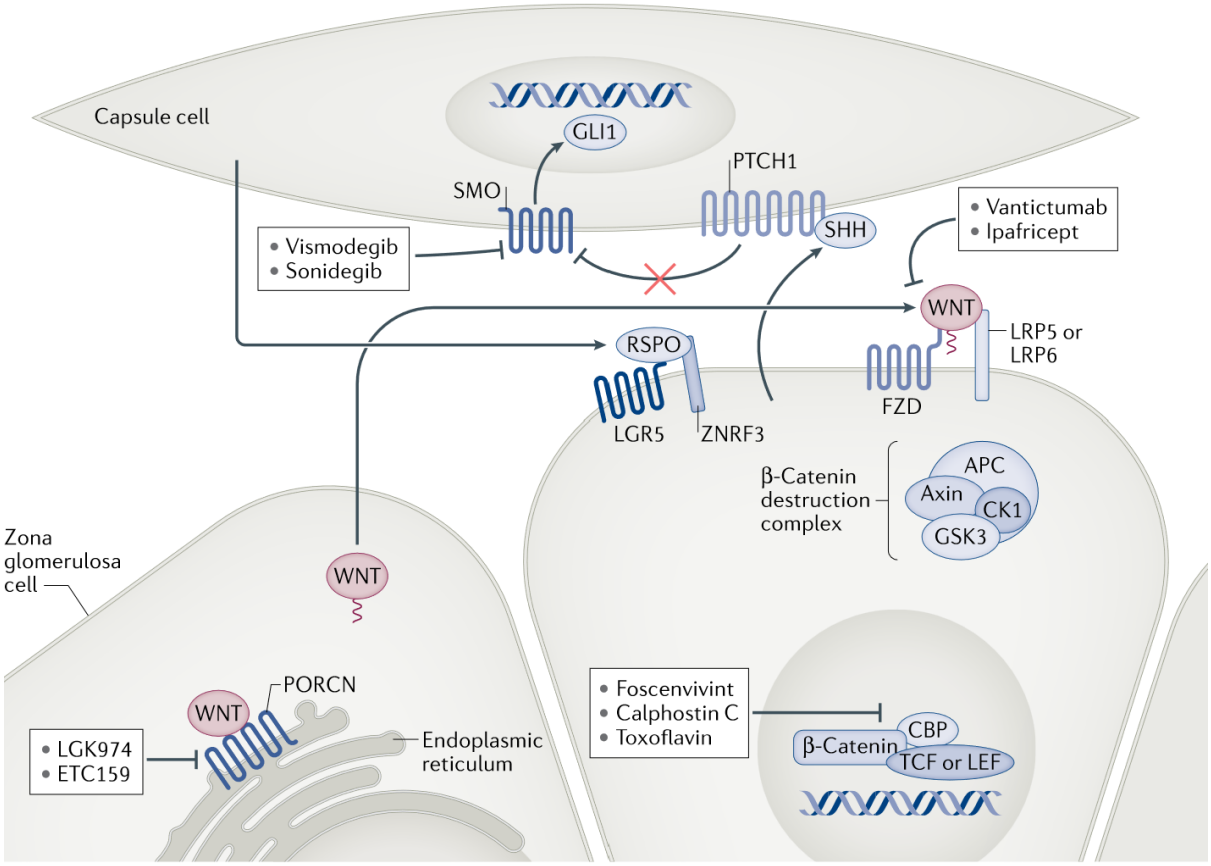

Figure 14 : Paracrine communication between zona glomerulosa and capsule cells. *Secreted sonic hedgehog (SHH) ligands from the zona glomerulosa activate Hedgehog signalling in a subpopulation of capsule cells that includes the capsular progenitors. Binding of SHH to its receptor patched 1 (PTCH1) abolishes the inhibition of smoothened (SMO), which culminates in activation of GLI-mediated transcription. Activation of canonical WNT–β- catenin signalling in zona glomerulosa cells requires WNT ligands (mainly WNT4 and WNT5a), which originate in nearby zona glomerulosa cells, and R-spondin ligands (such as RSPO3 and RSPO1), which are secreted by capsular cells. Binding of these ligands to their cognate receptors culminates in cytoplasmic accumulation and nuclear translocation of β- catenin, which acts as a transcriptional cofactor for T cell-specific transcription factor (TCF) and lymphoid enhancer-binding factor (LEF) proteins. Of note, WNT ligands must be lipidated by porcupine (PORCN) acyltransferases in the originating cells, which enables their secretion and receptor recognition. The Hedgehog and WNT–β- catenin pathways are depicted in their activated state. (Extracted from (Lyraki and Schedl, 2021b)).*

8 Adrenal cortex development and remodelling

8.1 Development of the foetal adrenal gland

During embryogenesis, the adrenal cortex arises from distinct developmental origins in mice and humans. In mice, the adrenal cortex and gonads share a common origin, the adrenogonadal primordium (AGP), a structure derived from the coelomic epithelium, which separates into adrenal and gonadal lineages around embryonic day 9.5 (E9.5). The AGP originates from a thickened region of the intermediate mesoderm located between the coelomic epithelium and the dorsal aorta. By E10.5, the AGP separates into the gonadal primordium and the adrenal primordium (AP). The adrenal primordium then migrates dorsomedially and begins to express

high levels of NR5A1 (SF1), which is essential for steroidogenic differentiation. Around E12.5, chromaffin cells derived from neural crest precursors invade the AP to form the adrenal medulla, while mesenchymal cells contribute to capsule formation. In humans, however, the adrenocortical lineage arises independently from the adrenogenic coelomic epithelium at 3-4 weeks of gestation, in a temporally and spatially distinct manner from gonad formation (Figure 15) (Abou Nader and Boyer, 2021; Cheng et al., 2022; Kim and Choi, 2020).

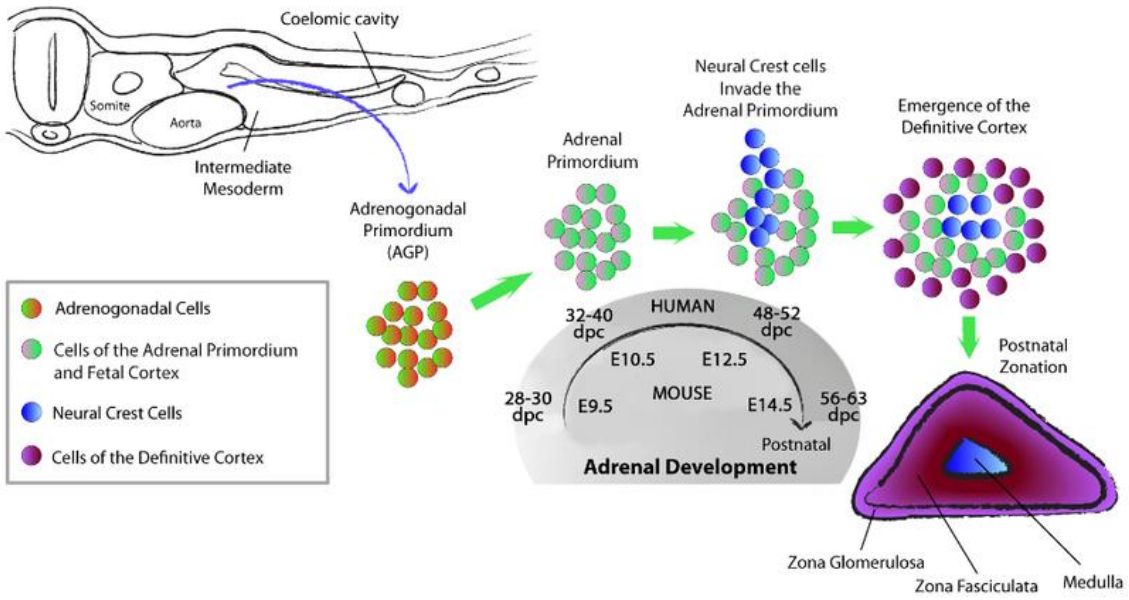

Figure 15 : Schematic illustration of the cellular rearrangements during adrenal development in mice and humans. *The adrenogonadal primordium (AGP) originates from cells localized between the coelomic epithelium and the dorsal aorta (blue arrow) at around 28–30 dpc (E9.5 in the mouse). At 32–40 dpc (E10.5 in the mouse), the adrenal primordium separates from the AGP. Between 48 and 52 dpc (E12.5), neural crest cells, precursors of the chromaffin cells of the medulla, invade the AGP. From 56 dpc (E14.5) onward, the fetal cortical cells are replaced by the definitive cortex, which gives rise to the adult zG and zF around the time of birth (Extracted from (Pignatti et al., 2023)).*

The foetal adrenal cortex consists of two main zones: the outer definitive zone (DZ) and the larger inner foetal zone (FZ). The DZ remains relatively quiescent until late gestation, while the FZ is highly active, producing dehydroepiandrosterone (DHEA) and its sulfated form (DHEAS), which serve as precursors for placental estrogen synthesis (Kim and Choi, 2020). After birth, the FZ undergoes rapid involution via apoptosis, and the DZ differentiates into the ZG and ZF. The ZR emerges later, around 6–8 years of age, marking the onset of adrenarche (Dumontet et al., 2018). The adrenal cortex is a highly dynamic organ, undergoing continuous renewal throughout life. Stem/progenitor cells located in the adrenal capsule and subcapsular ZG contribute to this turnover. These cells proliferate and migrate centripetally, differentiating into ZG and subsequently into ZF cells, before undergoing apoptosis at the corticomedullary

junction (Abou Nader and Boyer, 2021). This centripetal model of zonation, first proposed by Salmon and Zwemer in 1941, has been supported by lineage tracing studies showing radial migration of Shh and Gli1-expressing progenitor cells (Kim and Choi, 2020). An alternative model, proposed by Deane and Greep, suggests independent development of each zone, though recent evidence favours the centripetal model (Greep and Deane, 1949). Transcriptional regulators play a crucial role in cell fate determination. Steroidogenic Factor 1 (SF1/NR5A1) is essential for adrenal development and steroidogenic gene expression. Sf1 knockout mice lack adrenal glands entirely, and heterozygous mice show impaired compensatory growth following unilateral adrenalectomy. SF1 also facilitates lineage conversion, enabling mesenchymal stem cells to differentiate into steroid-producing cells. Freedman et al. demonstrated that ZG cells can convert into ZF cells postnatally, and that ZF differentiation can occur independently of ZG lineage when SF1 is absent (Freedman et al., 2013; Schimmer and White, 2010). In mice, a transient layer known as the X-zone (ZX) persists postnatally as a remnant of the fetal adrenal cortex and is considered analogous to the human FZ. The ZX regresses at puberty in males and during the first pregnancy in females, but persists in castrated animals, indicating a role for sex hormones in its regulation. The adrenal cortex exhibits sexual dimorphism, with female mice showing larger glands, higher hormone levels, and faster cell turnover compared to males (Lyraki and Schedl, 2021c). Homeostatic renewal of the cortex is regulated by RSPO/Wnt/β-catenin and SHH signaling pathways (Figure 16). RSPO3 from capsular cells activates Wnt signaling in subcapsular progenitors, which express Shh and Wnt4, promoting their differentiation into steroidogenic cells. As proliferation occurs mostly in the capsule and outer cortex, newly generated cells undergo differentiation into ZG cells, which then undergo centripetal migration and lineage conversion into ZF cells. These processes are regulated by the mutually antagonistic WNT–β-catenin and cAMP–PKA signaling pathways, with WNT signaling promoting ZG identity and cAMP–PKA signaling promoting ZF differentiation (Dumontet et al., 2018; Lyraki and Schedl, 2021a).

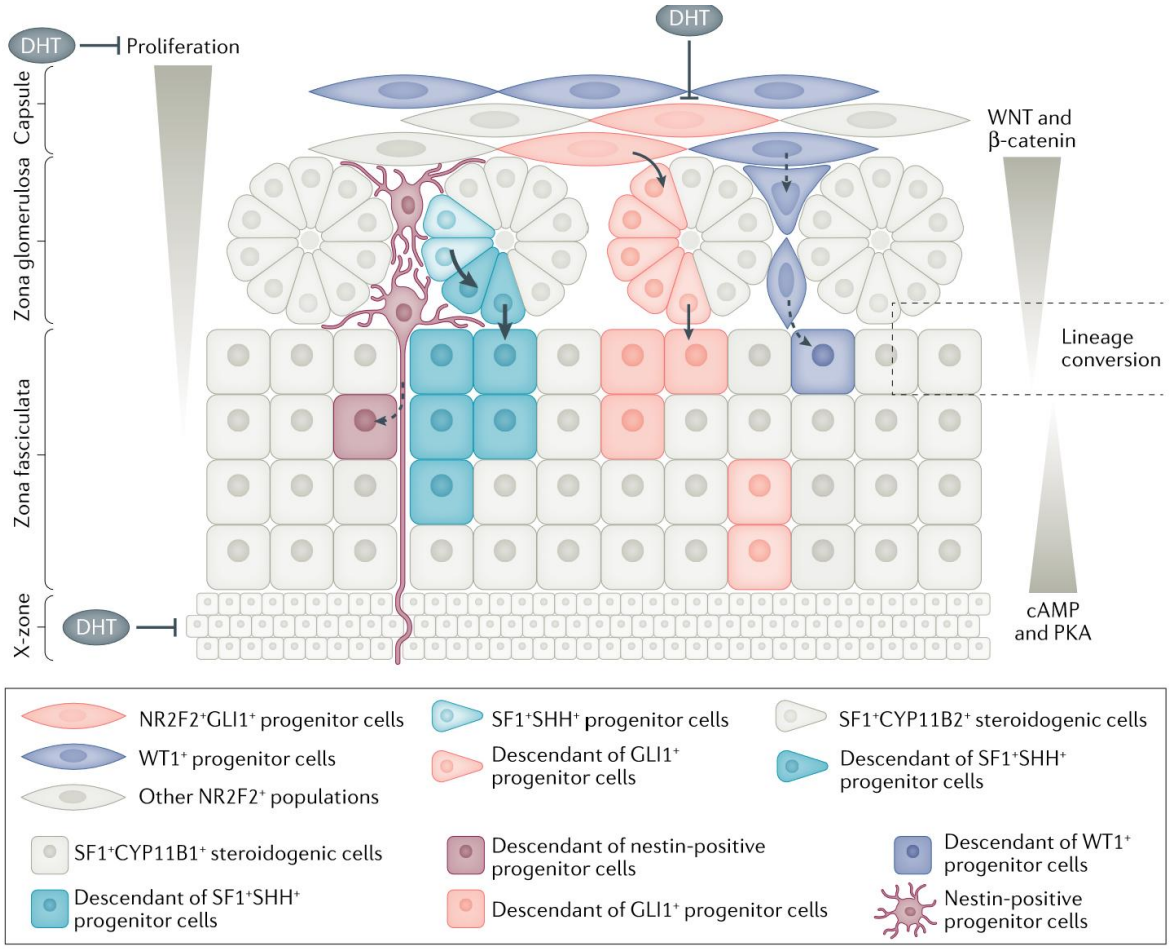

Figure 16 : Homeostatic tissue renewal in the mouse adult adrenal cortex and capsule. *Steroidogenic cells in the mouse adrenal cortex are predominantly derived from GLI1+ progenitor cell populations in the capsule (pink) and steroidogenic factor 1-positive (SF1+) sonic hedgehog-positive (SHH+) progenitors in the subcapsular zona glomerulosa (light blue). Wilms tumour protein homologue-positive (WT1+) progenitor populations in the outer capsule and nestin-positive progenitor populations in the cortex also contribute to the replenishment of cortical cells, especially after gonadectomy or under conditions such as stress. As proliferation occurs mostly in the capsule and the outer cortex, the newly generated cells undergo differentiation into zona glomerulosa cells, which undergo centripetal migration and lineage conversion into zona fasciculata cells. These processes are regulated by levels of activity of the WNT–β- catenin and cAMP–protein kinase A (PKA) signalling pathways, which are mutually antagonistic. Alternative, as yet uncharacterized, pathways can also generate zona fasciculata cells (not shown). Finally, a transient zone exists between the zona fasciculata and the medulla, termed the X-zone, which regresses after puberty in male mice and after pregnancy in female mice. Androgens, exemplified by dihydrotestosterone (DHT), exert a suppressive influence on cortical cell turnover (Extracted from (Lyraki and Schedl, 2021b)).*

8.2 Sexual dimorphism in adrenal cortex renewal

Sex-specific differences in adrenal cortex renewal contribute to the distinct morphological and functional characteristics observed between males and females. In adult female mice, the adrenal cortex shows a significantly higher regenerative capacity compared to males, with renewal rates estimated to be approximately three times greater. This enhanced turnover is

closely linked to hormonal regulation, as it is sensitive to gonadectomy and androgen replacement in males (Grabek et al., 2019; Levasseur et al., 2019).

The increased renewal in females is driven by elevated proliferative activity both within the cortex and the surrounding capsule. Notably, progenitor cells expressing Axin2 and Wnt4, located along the ZG, are more active in females. Additionally, $Gli1^{+}$ stem cells in the adrenal capsule play a crucial role in female adrenal regeneration, but this contribution is largely absent in males. Lineage tracing studies have shown that after puberty, androgens suppress the activity of Gli1+ cells, limiting renewal in males to Shh+ progenitors within the ZG only (Grabek et al., 2019; Levasseur et al., 2019).

These differences are primarily driven by hormonal influences rather than chromosomal sex. For instance, ovariectomized females treated with dihydrotestosterone (DHT) show reduced recruitment of $Gli1^{+}$ progenitors and diminished capsular proliferation. In contrast, females maintain the ability to recruit both Gli1+ cells from the capsule and Shh+ cells from the subcapsular region. This dual recruitment mechanism supports their higher renewal capacity and may explain the increased incidence of adrenal hyperplasia and neoplasia observed in women (Lyraki and Schedl, 2021c).

Androgens also modulate adrenal renewal through the Wnt signalling pathway. By downregulating *Frzb*, a gene encoding a Wnt antagonist, androgens enhance canonical Wnt activity. This shift favours the maintenance of ZG identity and inhibits processes such as transdifferentiation and centripetal migration, which lead to a reduced cortical renewal (Berthon et al., 2010; Pignatti et al., 2020). In females, the low androgen environment supports renewal via the PKA signalling pathway, further contributing to sex-specific differences in adrenal homeostasis (Dumontet et al., 2018; Levasseur et al., 2019) (Figure 17).

While rodent models have provided valuable insights, the role of androgen receptor (AR) signalling in regulating adrenal stem cell dynamics and tissue renewal remains incompletely understood and warrants further investigation (Lyraki and Schedl, 2021c). In humans, sex differences in adrenal gland structure and renewal are less well characterized. Some post-mortem studies suggest that men may have larger adrenal glands, although age-related trends show a decline in adrenal weight in older men, while it remains stable in women. Interestingly,

ZF cells in older men exhibit shorter telomeres compared to those in women, though the implications of this observation remain unclear (Nonaka et al., 2020).

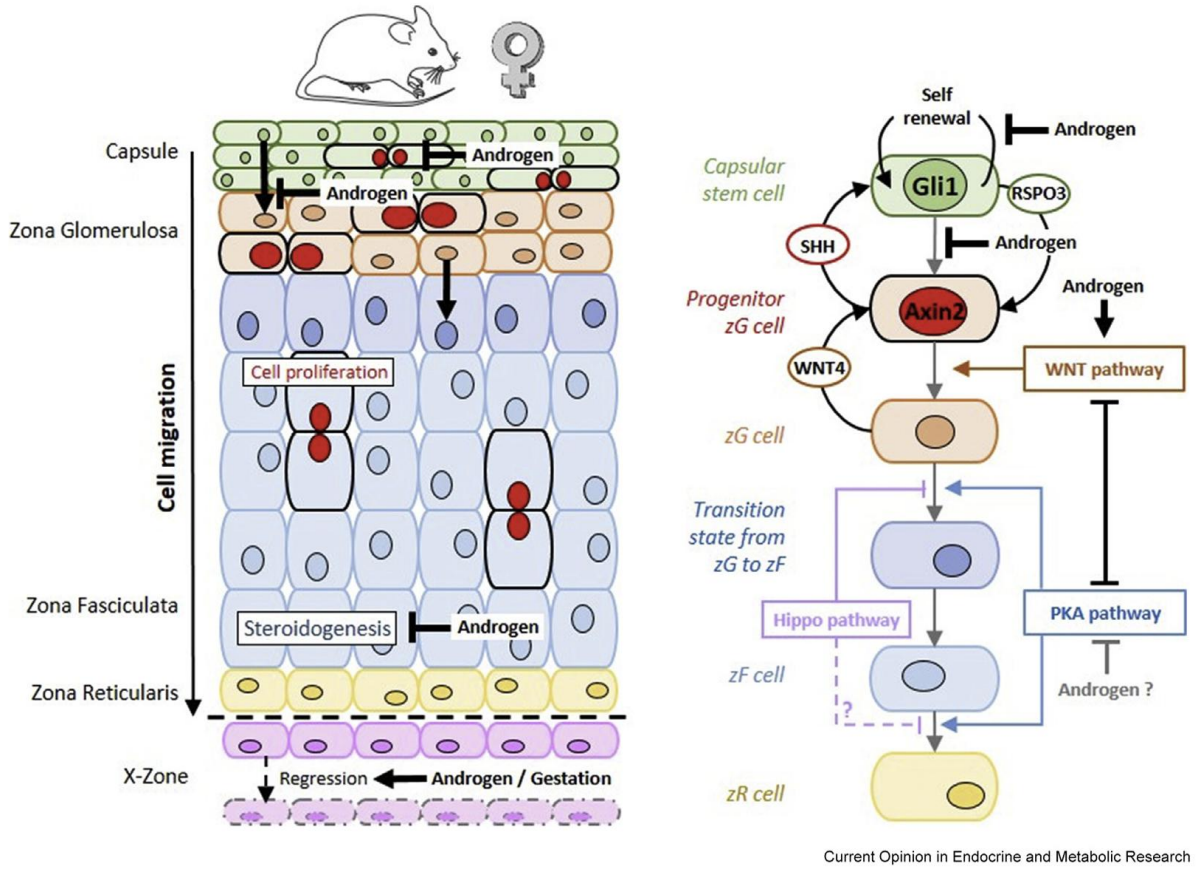

Figure 17 : ***Adrenal cortex renewal in female mice and interplay with androgens (Adapted from (Dumontet et al., 2018; Grabek et al., 2019)).*** *Scheme of female adrenal cortex cell renewal dynamics: Gli1+ stem cells and Axin2+/Shh+ progenitor cells residing within the capsule and ZG, respectively, that can either proliferate or be recruited to ensure cell renewal of the definitive/adult cortex. Centripetal migration and zonal differentiation result from the antagonistic interplay between WNT and PKA signaling pathways, with the WNT pathway promoting ZG identity, whereas the PKA pathway stimulates cell turnover and favors conversion to ZF identity and eventually to ZR identity. In the ZF, the Hippo pathway exerts a repressive role in ZF differentiation/maintenance and therefore potentially in that of the ZR. The X-zone regresses during the midgestation in females and at puberty in males. The androgenic milieu tones down cortex replenishment by yet unclear mechanisms. Indeed, testicular androgens impede capsular stem cell recruitment and proliferation that only occur in females or prepubescent males. Moreover, androgens sustain the WNT pathway, which restrains the PKA pathway, leading to lower cortical cell renewal in males. Steroidogenic cells in the ZF could also be negatively affected by androgens, resulting in lower steroidogenic activity in males than in females. PKA, cAMP-dependent protein kinase; ZF, zona fasciculata; ZG, zona glomerulosa; ZR, zona reticularis (Extracted from (Levasseur et al., 2019)).*

9 The Mineralocorticoid Receptor

9.1 The Nuclear Receptor Superfamily of Transcription Factors

The MR is a member of the nuclear receptor superfamily that represents the largest family of transcription factors in eukaryotes, comprising 48 members in humans. These receptors are ligand-activated transcription factors that respond to small, lipophilic molecules such as steroid hormones, thyroid hormones, retinoids, fatty acids, and vitamins A and D2. Unlike membrane-bound receptors that require signal transduction cascades, nuclear receptors can directly bind DNA and regulate gene expression, making them uniquely suited for rapid and direct genomic responses (Carlberg, 2024).

The nuclear receptor superfamily is organized into six phylogenetic groups based on evolutionary relationships and DNA-binding characteristics (Figure 18). The MR belongs to subfamily 3C of the steroid hormone receptors, along with the glucocorticoid receptor (GR), androgen receptor (AR), and progesterone receptor (PR). This phylogenetic clustering reflects their shared evolutionary origin and high sequence homology, particularly within their DNA-binding domains. In contrast, the estrogen receptors (ER) form a separate subfamily (3A), while other groups include thyroid hormone receptors (group 2), retinoic acid receptors (group 2), and orphan receptors with unknown or no ligands (groups 0, 4, 5, and 6) (Nuclear Receptors Nomenclature Committee, 1999).

Structurally, nuclear receptors share a conserved modular architecture composed of six functional domains (Figure 19): a variable N-terminal domain (N-ter) containing a transcriptional activation function (AF-1), a highly conserved DNA-binding domain (DBD) containing 2 zinc finger motifs, a hinge region, a conserved ligand-binding domain (LBD) with a second activation function (AF-2), and a variable C-terminal domain. The DBD allows receptors to recognize specific hormone response elements (HREs) in the promoter regions of target genes, while the LBD mediates ligand binding and co-regulator recruitment (Kim and Fang, 2018). Within the DBD, the P-box motif plays a critical role in determining DNA-binding specificity. In steroid hormone receptors such as the MR, GR, androgen receptor (AR), and progesterone receptor (PR), the P-box enables recognition of the AGAACA sequence. In contrast, receptors like retinoic acid receptor alpha (RAR), retinoid X receptor (RXR), vitamin D receptor (VDR), thyroid hormone receptor (TR), and estrogen receptor (ER) possess a slightly different P-box that facilitates binding to AGGTCA elements. These sequence preferences underpin the functional diversity of nuclear receptors in gene regulation (Umesono

and Evans, 1989). Functionally, nuclear receptors are classified into Type I and Type II. Type I receptors are the ones that reside in the cytoplasm and translocate to the nucleus upon ligand binding, whereas Type II receptors are constitutively nuclear and often form heterodimers with retinoid X receptors. Upon activation, nuclear receptors recruit coactivator or corepressor complexes that modify chromatin structure through histone acetylation or deacetylation, thereby regulating transcription (Weikum et al., 2018).

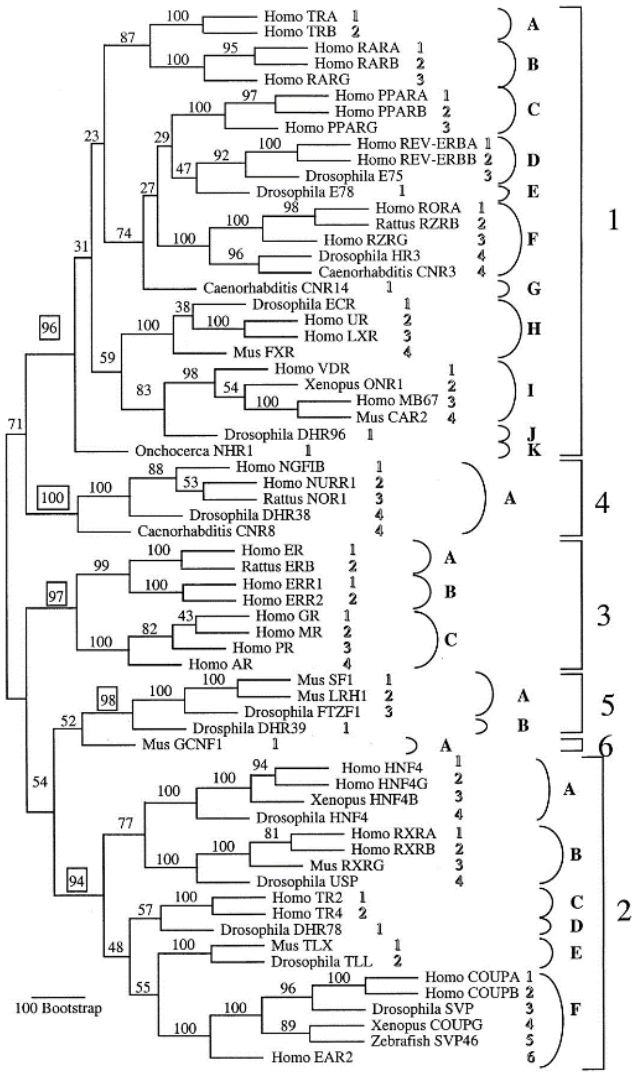

Figure 18 : Phylogenetic tree of the nuclear receptor superfamily. *The 48 human nuclear receptors are organized into six groups (0-6) based on evolutionary relationships. Numbers at nodes indicate bootstrap confidence values. The mineralocorticoid receptor (MR) belongs to subfamily 3C with the glucocorticoid receptor (GR), androgen receptor (AR), and progesterone receptor (PR), reflecting their shared evolutionary origin and structural similarities. SF1 (steroidogenic factor 1) in group 5 is the master regulator of adrenal development. Numbers after receptor names indicate species: 1 = human, 2 = mouse, 3 = rat, 4 = other species. Adapted from Nuclear Receptors Nomenclature Committee (1999).*

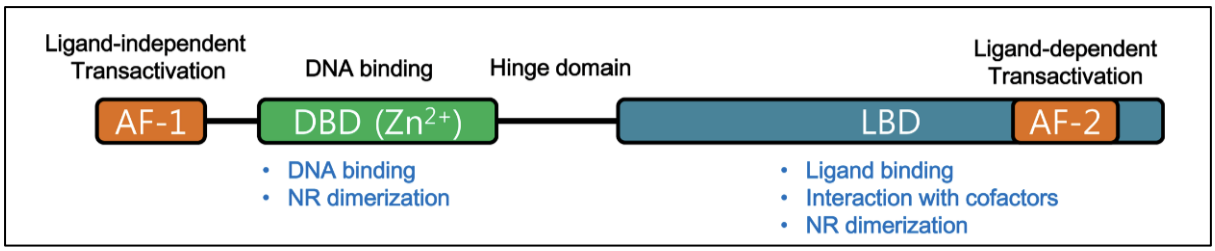

Figure 19 : Structure of nuclear receptor superfamily (Extracted from (Kim and Fang, 2018)).

9.2 Mineralocorticoid Receptor Structure and Mechanism of Action

Within the nuclear receptor superfamily, the MR, encoded by the *NR3C2* gene, is specifically classified within the steroid receptor subfamily 3, group C. It functions as a ligand-dependent transcription factor, mediating the effects of mineralocorticoids such as aldosterone, and also binds glucocorticoids like cortisol with comparable affinity (Mangelsdorf et al., 1995).

The human *NR3C2* gene is located on chromosome 4q31.23, spanning approximately 366 kb and composed of 10 exons, of which eight are translated (Zennaro et al., 1995). Alternative promoter usage and splicing generate multiple transcript variants, including hMRα and hMRβ, which are co-expressed in target tissues (Zennaro et al., 2001, 1996) .

The MR protein consists of 984 amino acids and is organized into modular domains typical of nuclear receptors (Figure 19) (Viengchareun et al., 2007; Yang et al., 2023):

- N-terminal domain (NTD): Contains AF-1, which mediates ligand-independent transcriptional activity and is highly variable among nuclear receptors.
- DNA-binding domain (DBD): Composed of two zinc finger motifs, this domain enables MR to bind specific mineralocorticoid response elements (MREs) in the promoter regions of target genes. The C-terminus of the DBD contains a nuclear localization signal (NLS1) (Hudson et al., 2014).
- Hinge region: Provides flexibility between the DBD and LBD. The NLS1 from the DBD extends into this region.
- Ligand-binding domain (LBD): Responsible for ligand recognition and binding, and contains AF-2, which recruits co-regulators upon ligand binding.

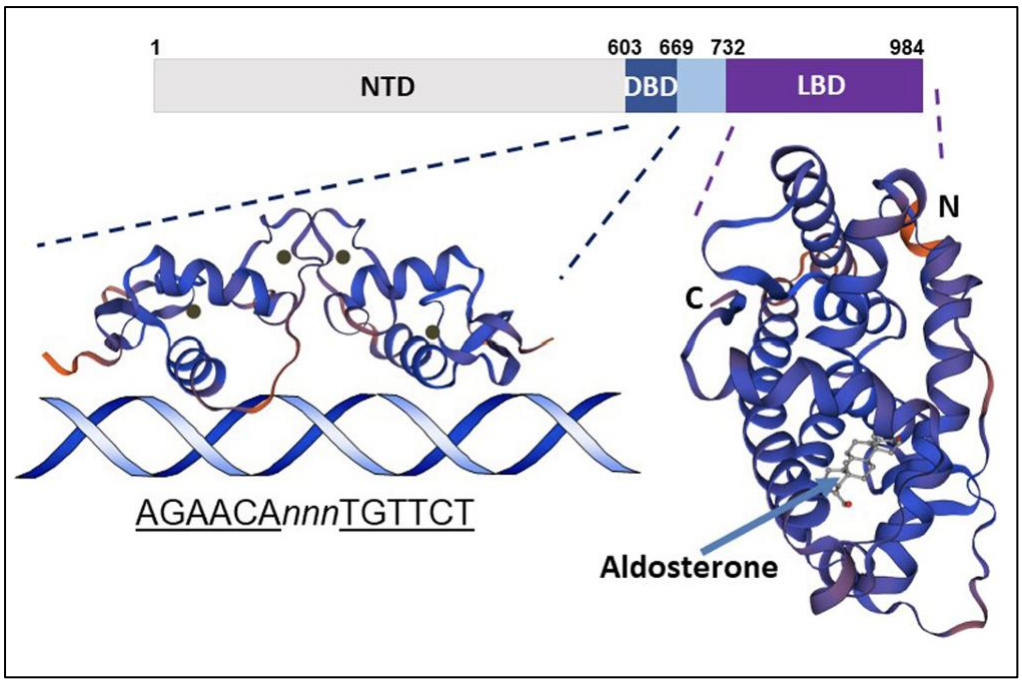

Figure 20 : Schematic diagram of the domain structure of the 984 amino acid human MR, with the hinge region between the DBD and LBD. Below the linear schematic is the crystal structure of two DBD monomers with the hormone response element shown below the DNA. The DBD is composed of two subdomains, each containing four cysteine residues that tetra-coordinate a zinc ion, forming the classic zinc finger structure essential for DNA interaction. Each zinc finger is followed by an amphipathic helix and a peptide loop. The first subdomain includes the DNA-recognition helix, which engages the major groove of DNA to establish base-specific contacts. In contrast, the helix in the second subdomain interacts non-specifically with the DNA backbone. This subdomain's peptide loop contains the distal box, or "D box," which harbors key residues involved in receptor dimerization. DBD, DNA-binding domain; LBD, ligand-binding domain; NTD, N-terminal domain (Extracted from (Yang et al., 2023)).

In the absence of ligand, MR is predominantly located in the cytoplasm, where it is maintained in an inactive state through association with a multi-protein chaperone complex. This complex includes heat shock proteins such as HSP90 (heat shock protein 90), HSP70, p23, and immunophilins like FKBP51 and p48, which stabilize the receptor and preserve its ligand-binding conformation (Binart et al., 1995; Bruner et al., 1997). Upon aldosterone binding, MR undergoes a conformational change that leads to the dissociation of heat shock proteins and the replacement of FKBP51 with FKBP52 (Galigniana et al., 2010). This exchange facilitates the translocation of the receptor complex into the nucleus via the nuclear pore complex. Once inside the nucleus, MR dissociates from the chaperone proteins and forms homodimers or heterodimers which enables it to bind to specific hormone response elements (HREs), such as glucocorticoid or mineralocorticoid response elements (GREs/MREs), in the regulatory regions of target genes. Recent data have also suggested that the MR can engage in higher order multimeric homo- or heterocomplexes to regulate gene transcription, with agonist-bound MR forming tetramers in the nucleoplasm and larger oligomers upon DNA binding (Fettweis et al., 2024). DNA binding is followed by the recruitment of transcriptional co-activators such as

SRC-1 (steroid receptor co-activator 1), p300 (binding protein 300)/CBP (CREB binding protein) and others, which possess histone acetyltransferase activity. DNA binding is followed by the recruitment of transcriptional co-activators such as SRC-1 (steroid receptor co-activator 1), p300 (binding protein 300)/CBP (CREB binding protein) and others, which possess histone acetyltransferase activity. These co-regulators remodel chromatin structure, allowing access to the transcriptional machinery. MR then facilitates the recruitment of RNA polymerase II, initiating transcription of target genes. Genome-wide chromatin immunoprecipitation followed by sequencing (ChIP-seq) in human kidney cells has shown that MR binding sites are often located in distal enhancer regions, typically around 10 kb from transcription start sites (Le Billan et al., 2015). MR binding is dynamic and occurs in oscillatory cycles, with receptor occupancy detectable as early as 15 minutes after aldosterone stimulation. These cycles are closely followed by RNA polymerase II recruitment, with a temporal delay of approximately 8 minutes, suggesting a tightly coordinated transcriptional response (Le Billan et al., 2018). The transcriptional output of MR is highly tissue-specific. In epithelial tissues such as the kidney, MR regulates genes involved in sodium reabsorption and electrolyte balance, including SCNN1A (sodium channel epithelial 1 alpha subunit), ATP1A1, SGK1 (serum and glucocorticoid regulated kinase 1), and NDRG2 (N-Myc downstream-regulated gene 2 protein) (Boulkroun et al., 2002; Fernandes-Rosa et al., 2011). In contrast, in non-epithelial tissues such as the heart, vasculature, and brain, MR modulates genes involved in inflammation, fibrosis, vascular remodelling, and behavioural responses (El Mouhayyar et al., 2025; Sierra-Ramos et al., 2021).

In the aldosterone-sensitive distal nephron (ASDN), the MR plays a key role in regulating sodium reabsorption by modulating the expression of genes that control the trafficking and activity of the epithelial sodium channel (ENaC) (Figure 20, (Zennaro et al., 2012)). Upon aldosterone stimulation, MR rapidly induces the transcription of several target genes, including *SGK1*, *GILZ* (glucocorticoid induced leucine zipper), *NDRG2*, and *14-3-3* proteins (Chen et al., 1999; Liang et al., 2006; Muller et al., 2003). ENaC channels are subject to continuous turnover through endocytosis and exocytosis. Newly synthesized ENaC is transported from the endoplasmic reticulum to the apical membrane via the Golgi apparatus. Once at the membrane, ENaC is regulated by the E3 ubiquitin ligase Nedd4-2, which binds to the channel and tags it with ubiquitin, leading to its internalization and either recycling or degradation depending on the type of ubiquitination (Fakitsas et al., 2007; Staub and Rotin, 2006). *SGK1* enhances ENaC stability at the membrane by phosphorylating Nedd4-2. This phosphorylation promotes the

interaction of Nedd4-2 with *14-3-3* proteins, which prevents Nedd4-2 from binding to ENaC, thereby reducing channel removal. *GILZ* further supports this process by facilitating the association of *SGK1* with the ENaC regulatory complex, increasing Nedd4-2 phosphorylation (Debonneville et al., 2001; Soundararajan et al., 2010). In addition to its genomic actions, aldosterone can exert rapid non-genomic effects in ASDN cells occurring within minutes. These include the activation of large conductance potassium (BK) channels, which contributes to membrane potential regulation (ref), and rapid activation of signalling cascades such as PKC and ERK1/2 pathways. Beyond sodium transport, aldosterone also regulates acid-base homeostasis through genomic mechanisms. Aldosterone promotes hydrogen ion secretion through increased H^+-ATPase expression and activity in intercalated cells of the distal tubule. This process is coupled with bicarbonate reabsorption into the bloodstream via the chloride/bicarbonate exchanger (AE1) located on the basolateral membrane. Together, these transcriptional and post-transcriptional effects on both sodium and acid-base transport contribute to overall fluid, electrolyte, and pH homeostasis (Ruhs et al., 2017).

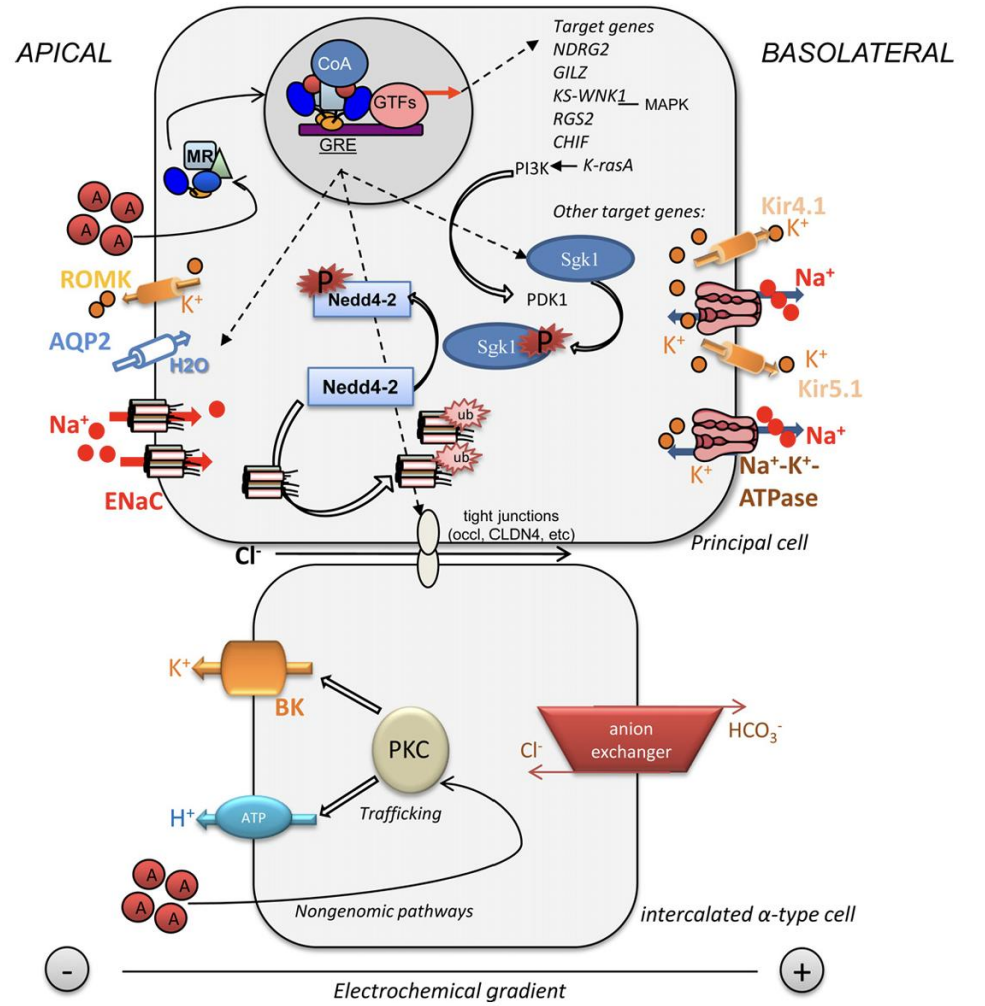

Figure 21 : MR-dependent regulation of volume and electrolyte balance in the aldosterone-sensitive distal nephron. In aldosterone target cells, such as the late connecting tubule, the connecting tubule and collecting duct, aldosterone binding to the MR is followed by receptor activation, nuclear translocation and binding to regulatory regions of hormone responsive genes (GRE, glucocorticoid responsive element). MR dimers recruit transcriptional coregulators (CoA) to activate the transcriptional machinery (GTPs, general transcription factors) leading to the expression of aldosterone target genes mainly involved in sodium transport. These include the epithelial sodium channel ENaC and the Na+–K+-ATPase, as well as several regulatory proteins, among them the serum and glucocorticoid-induced kinase 1 (sgk1), N-myc downregulated gene 2 (NDRG2), channel inducing factor (CHIF), and glucocorticoid induced leucine zipper (GILZ). For simplicity, only the principal MR-regulated genes are shown. Dotted arrows represent MR-induced effects on different aldosterone-dependent cellular functions. Double arrows represent actions (phosphorylation, ubiquitylation), full arrows represent movements (aldosterone entry and MR binding, nuclear translocation). In the absence of aldosterone, ENaC interacting with Nedd4-2, an ubiquitin ligase, is ubiquitilated and degraded by the proteasome. Upon aldosterone exposure, PDK1 (itself activated by different phosphorylation cascades involving MAPK, k-rasA and PI3 K) phosphorylates sgk1 which in turn phosphorylates Nedd4-2. Phosphorylated Nedd4-2 is no more able to interact with ENaC, increasing its localization to the apical membrane. Sodium exits cells across the basolateral membrane to the interstitial fluid via the ubiquitous Na+–K+-ATPase, providing the driving force for Na+ transport. Basolateral K+ channels (Kir4.1 and Kir5.1) participate in generating cell membrane potential and in K+ recycling, while apical K+ channels, mainly ROMK1, are responsible for K+ secretion. In the intercalated cells, aldosterone rapidly stimulates H+ excretion into urine via H+-ATPase coupled with the basolaterally expressed chloride-bicarbonate exchanger that releases bicarbonate into blood through the PKC-dependant trafficking of the proton pump to the apical membrane. Aldosterone also stimulates large conductance K+ channel (BK) activity. AQP2, aquaporin 2 (Extracted from (Zennaro et al., 2012)).

9.3 Regulation of the Mineralocorticoid Receptor Activity

The MR is subject to complex regulatory mechanisms that fine-tune its activity in response to physiological and environmental cues. Beyond its ligand-dependent activation, MR function is modulated by post-translational modifications, ligand specificity, co-regulator interactions, and systemic factors such as salt intake, stress, and circadian rhythms. Post-translational modifications such as phosphorylation, SUMOylation, and ubiquitination play critical roles in shaping MR behaviour (Pascual-Le Tallec and Lombès, 2005). Phosphorylation by kinases like ERK1/2 can influence the nuclear translocation of the MR and its interaction with transcriptional co-regulators. SUMOylation generally suppresses MR activity by promoting the recruitment of transcriptional repressors, while ubiquitination marks the receptor for degradation via the proteasome, thereby limiting its signalling duration and intensity (Faresse, 2014; Shibata et al., 2013).

Although MR binds aldosterone with high affinity, it also has similar affinity for glucocorticoids such as cortisol and corticosterone. In aldosterone-sensitive tissues, the enzyme 11β-hydroxysteroid dehydrogenase type 2 (11β-HSD2) protects MR from glucocorticoid activation by converting cortisol into its inactive form, cortisone (in human) and corticosterone (in mice). This enzymatic barrier ensures that aldosterone remains the dominant ligand for MR in epithelial tissues like the kidney, allowing for precise regulation of sodium and water balance (Funder et al., 1973; Jiménez-Canino et al., 2017)

The transcriptional activity of MR is further shaped by its interaction with co-regulators. Co-activators such as SRC-1 enhance MR-mediated gene expression by facilitating chromatin remodelling and recruitment of the transcriptional machinery, while co-repressors like NCoR inhibit MR activity by promoting chromatin condensation. The availability and expression of these co-regulators vary across tissues, contributing to the tissue-specific effects of MR signalling (Pascual-Le Tallec and Lombès, 2005; Yang and Young, 2009).

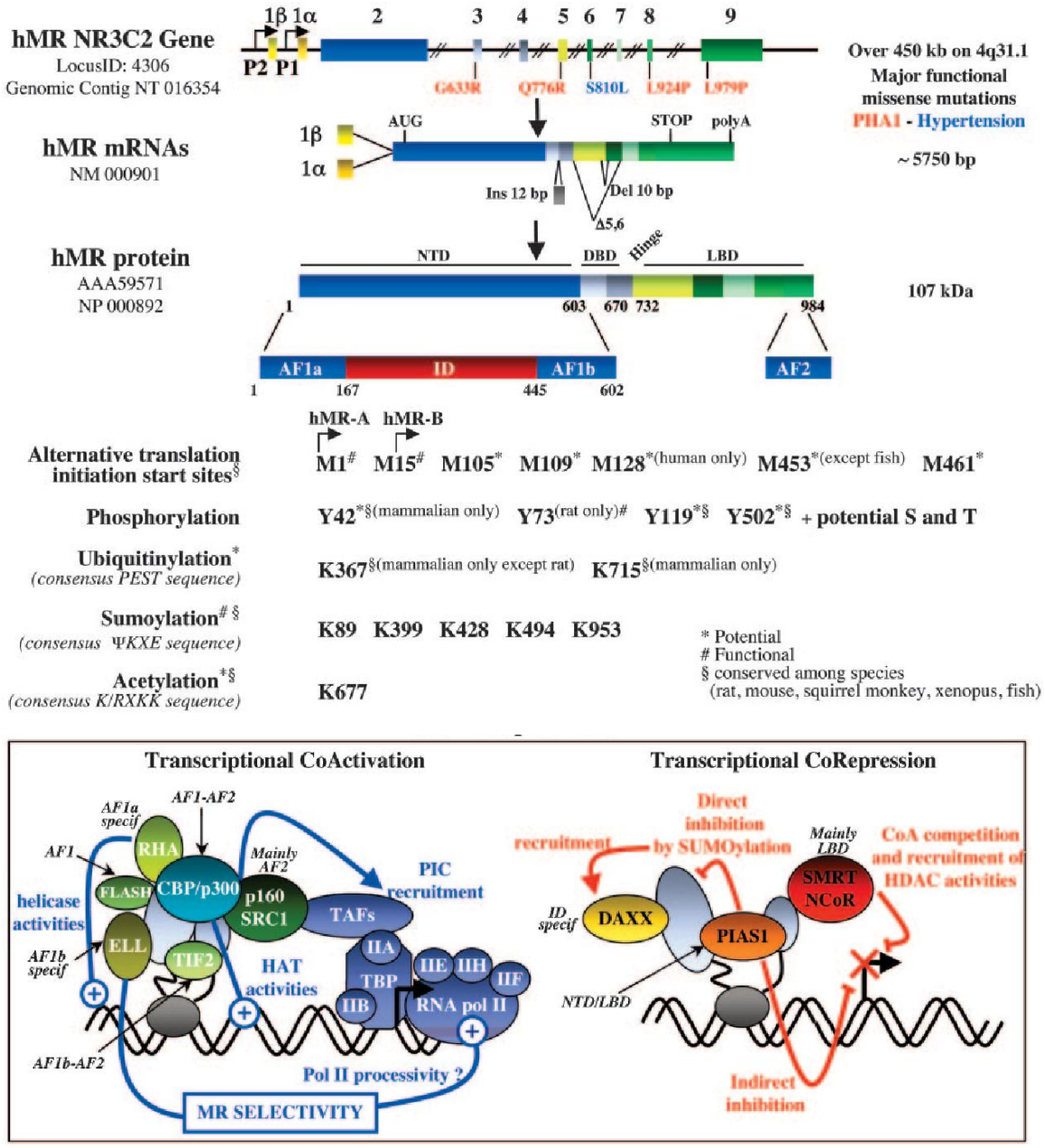

Figure 22 : Mineralocorticoid receptor structure and regulation. (A) Domain organization of the human MR gene (NR3C2), mRNA isoforms, protein structure showing functional domains (NTD, DBD, Hinge, LBD), and post-translational modifications including phosphorylation, ubiquitination, sumoylation, and acetylation sites. (B) Mechanisms of MR transcriptional regulation showing coactivation (left) and corepression (right) pathways. Adapted from Pascual-Le Tallec & Lombès, Mol Endocrinol 2005.

9.4 Tissue Distribution of the Mineralocorticoid Receptor

9.4.1 Mineralocorticoid Receptor in the Cardiovascular System

Cardiomyocytes, vascular smooth muscle cells, endothelial cells, and cardiac fibroblasts all express MR, though notably without substantial 11β-HSD2 activity (Gomez-Sanchez et al., 2006), except for smooth muscle cells where colocalization of aldosterone-binding capacity with 11β-HSD2 activity has been demonstrated (Kornel, 1994). This absence in most

cardiovascular tissues means that cardiovascular MR can respond to both aldosterone and glucocorticoids, complicating the interpretation of the role of MR in these tissues. In the heart, MR overactivation has been implicated in pathological cardiac remodelling. Experimental studies in rodents demonstrated that aldosterone infusion, particularly when combined with high salt intake or uninephrectomy, produces severe cardiac fibrosis, inflammation, and left ventricular hypertrophy which can be prevented by MRA (Brilla et al., 1993; Rocha et al., 2000). These findings suggested that inappropriate cardiac MR activation contributes to heart failure progression independently of blood pressure effects. These results have been substantiated further in clinical trials, where use of MRA on top of standard therapy improves mortality and morbidity in patients with heart failure (Pitt et al., 2003, 1999).

The MR is also expressed in endothelial cells and vascular smooth muscle cells. In smooth muscle cells, MR contributes to modulating vasomotor tone and blood pressure, driving vascular remodelling in response to factors such as hypertension, vascular injury, obesity, and aging, and promoting cardiovascular diseases, including aortic aneurysms, heart valve abnormalities, and heart failure (Mitchell et al., 2024).

9.4.2 Mineralocorticoid Receptor in the Brain

The brain represents another major site of non-epithelial MR expression. Studies in the 1960s first identified high-affinity corticosteroid binding sites in the hippocampus, which were later recognized as MR (McEwen et al., 1968; Reul and de Kloet, 1985). MR is highly expressed in limbic structures, particularly the hippocampus, amygdala, and prefrontal cortex. Like cardiovascular tissues, these brain regions lack 11β-HSD2, meaning that MR is predominantly occupied by glucocorticoids under basal conditions (De Kloet et al., 1998). The MR in the brain works in tandem with the GR to regulate the HPA axis and coordinate behavioural and neuroendocrine responses to stress. The balance between MR (high affinity, low capacity receptor) and GR (low affinity, high capacity receptor) activation appears crucial for maintaining appropriate stress responses and cognitive function. MR, which is activated at low glucocorticoid concentrations typical of the circadian nadir, helps maintain basal HPA axis tone and influences processes such as threat detection and memory consolidation (Joëls et al., 2008). GR, activated during stress when glucocorticoid levels rise, mediates negative feedback and stress-induced behavioural adaptations. Disruption of this MR/GR balance has been implicated in stress-related psychiatric disorders (de Kloet et al., 2005). MR expression in the hippocampus plays a particularly important role in cognitive function. Studies in rodents have shown that MR influences synaptic plasticity, neuronal excitability, and memory formation

(Oitzl and de Kloet, 1992). MR activation enhances memory consolidation and retrieval, while MR blockade impairs these processes. In humans, polymorphisms in the *NR3C2* gene have been associated with differences in memory performance and stress reactivity, suggesting that individual variation in MR function may influence cognitive and emotional phenotypes (van Leeuwen et al., 2011).

9.4.3 Mineralocorticoid Receptor in Adipose Tissue and Metabolic Regulation

The MR is also expressed in both white and brown adipocytes and evidence indicates that MR activation in fat tissue influences whole-body metabolic homeostasis. In vitro studies showed that glucocorticoids, acting through MR, can promote adipocyte differentiation and lipid accumulation (Caprio et al., 2007). This raised the possibility that MR might contribute to metabolic dysfunction, particularly in the context of obesity and metabolic syndrome where both glucocorticoid levels and adiposity are often elevated.

Deletion of the MR in the adipocytes in mice protects against high fat diet induced obesity, insulin resistance, and metabolic dysfunction (Urbanet et al., 2015). Conversely, transgenic mice overexpressing MR in adipocytes develop metabolic abnormalities. Pharmacological MR blockade with spironolactone or eplerenone improves metabolic parameters in rodent models of obesity, including enhanced insulin sensitivity, reduced adipose inflammation, and improved glucose tolerance (Guo et al., 2008; Hirata et al., 2009).

9.4.4 MR Expression in other tissues

Beyond the major organs discussed above, MR has been detected in numerous other tissues. In the eye, MR is expressed in the retina and has been implicated in the pathogenesis of retinal vascular diseases (Zhao et al., 2012). In the skin, MR influences wound healing and may contribute to inflammation in certain dermatological conditions (Tiganescu et al., 2013). The colon expresses both MR and 11β-HSD2, where MR regulates electrolyte absorption similar to its renal function. Immune cells, including macrophages and T cells, also express MR, which modulates inflammatory responses and immune cell polarization (Rickard et al., 2009).

This widespread tissue distribution underscores that MR is far more than a simple regulator of renal sodium transport. Rather, MR represents a versatile transcription factor that coordinates diverse physiological processes across multiple organ systems, with important implications for both normal physiology and disease.

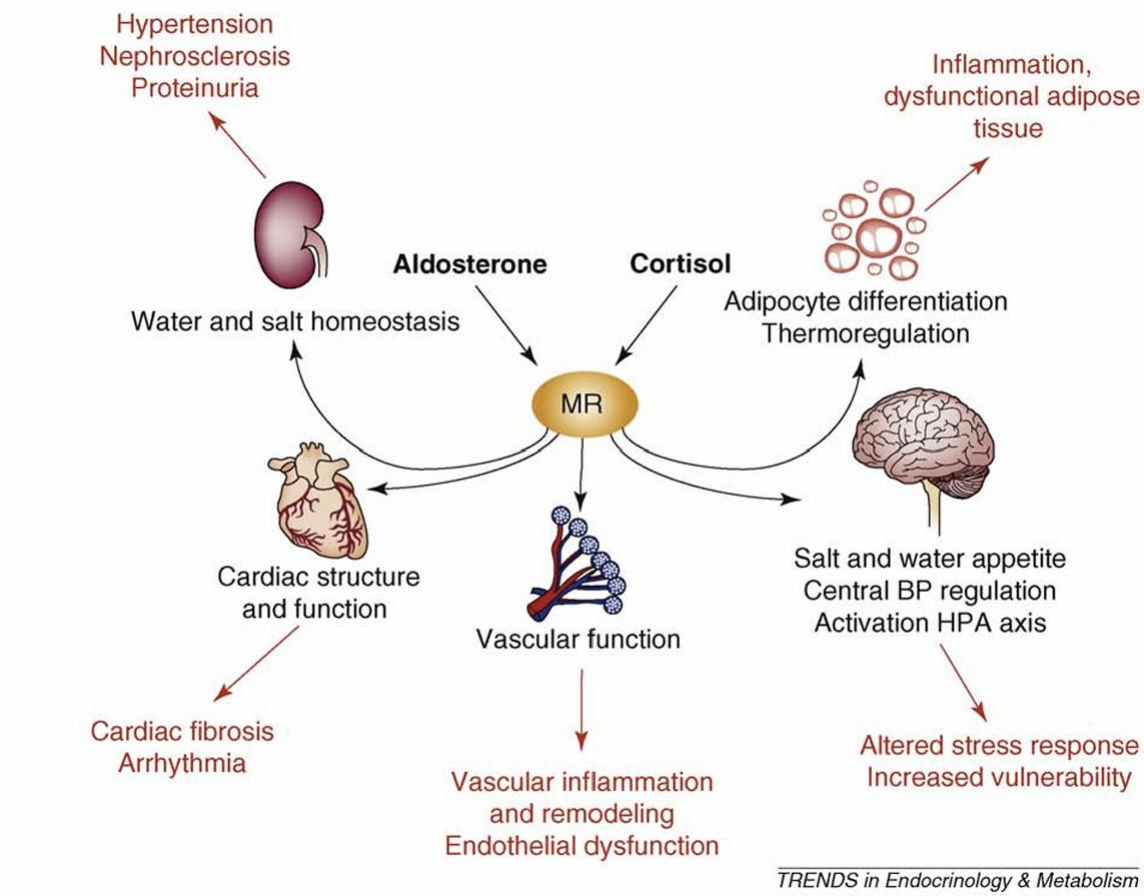

Figure 23 : MR at the cross-road of metabolic functions. *MR activation by either aldosterone or cortisol (corticosterone) is involved in several physiological processes in different tissues. Inappropriate activation of the MR by environmental or genetic factors might trigger deleterious responses in various tissues, which ultimately lead to the development of hypertension, obesity, insulin resistance and cardiovascular injury (Extracted from (Zennaro et al., 2009)).*

9.5 MR expression in the adrenal cortex

While the MR is expressed in multiple tissues, its role in the adrenal cortex may be particularly relevant to aldosterone signalling and adrenal gland homeostasis. Within the adrenal cortex, MR expression has been detected predominantly in the ZG, where 11β-HSD2 is also expressed (Boulkroun et al., 2010; Burton et al., 2009). The functional significance of MR in the ZG extends beyond classical aldosterone responsiveness. Some evidence suggests that MR may participate in autocrine or paracrine regulatory loops within the ZG itself, where locally produced aldosterone could activate MR to modulate steroidogenic enzyme expression (Chong et al., 2017). This hypothesis is supported by observations that MR activation can influence the expression of genes involved in aldosterone biosynthesis and potassium channel function, creating potential feedback mechanisms that modulate aldosterone output in response to physiological demands (Chong et al., 2017).

A study by Boulkroun et al. (2010) demonstrated that MR is expressed in human adrenal cortex, mainly in the ZG, and in APAs (Figure 22). Their investigation of adrenal tissue from patients with APAs revealed significant structural alterations in the peritumoral cortex, including adrenal cortex remodelling characterized by ZG hyperplasia, increased nodulation, and decreased vascularization. These changes in the tissue adjacent to the adenoma suggest that the pathological process in PA extends beyond the discrete tumour itself to affect the surrounding adrenal architecture. The increased nodulation observed in the peritumoral tissue indicates an abnormal proliferative environment that may contribute to the development and progression of APAs (Boulkroun et al., 2010).

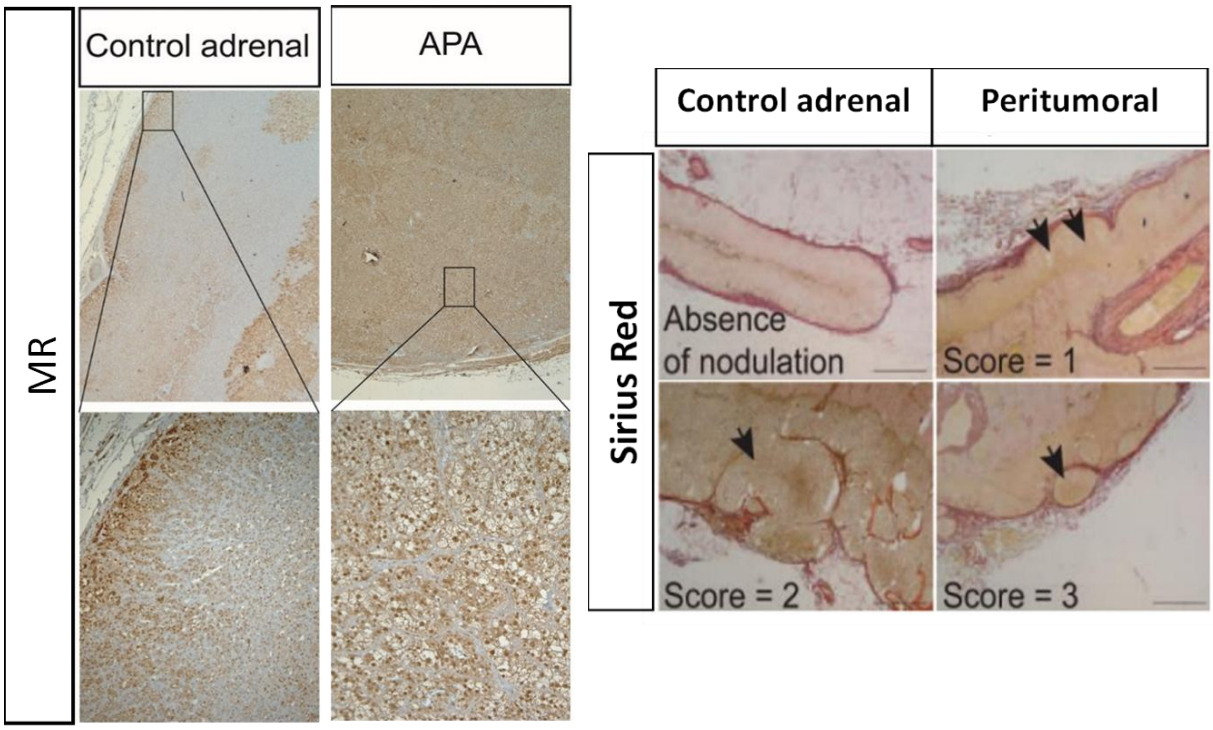

Figure 24 MR expression and structural alterations in control and pathological adrenal tissue. *Left panel: MR immunohistochemistry (brown) performed on control adrenal and aldosterone-producing adenoma (APA). Nuclei were counterstained with hematoxylin (blue). MR is expressed predominantly in the zona glomerulosa of control adrenal cortex and throughout the APA tissue. Right panel: Sirius Red staining demonstrating the degree of nodulation in control adrenal (showing absence of nodulation) compared to peritumoral tissue adjacent to APAs. Nodulation was scored from 0 (absence) to 3 (severe), with black arrowheads indicating nodular structures. Peritumoral tissue shows increased nodulation (scores 1-3) characteristic of adrenal cortex remodelling in primary aldosteronism. (Adapted from (Boulkroun et al., 2010)).*

The development of genetically modified mouse models has been instrumental in dissecting the physiological and pathophysiological roles of the MR. The first global MR knockout mouse was generated in the late 1990s and provided fundamental insights into the essential functions of the receptor (Berger et al., 1998). Homozygous MR-null mice (MR-/-) die within the first

two weeks of postnatal life due to severe renal salt wasting, hyperkalemia, and dehydration, demonstrating the critical role of MR in maintaining sodium and potassium homeostasis (Berger et al., 1998). These animals exhibit profound urinary sodium losses despite elevated plasma aldosterone levels, confirming that MR mediates the classical aldosterone-dependent sodium reabsorption in the distal nephron. Supplementation with high-salt diet can partially rescue the lethal phenotype, allowing some animals to survive into adulthood, though they remain severely growth-retarded and exhibit persistent electrolyte abnormalities (Berger et al., 2000). The early lethality of global MR knockout mice necessitated the development of tissue-specific conditional knockout models using the Cre-loxP system. These models have enabled researchers to investigate MR function in specific cell types and organs without the confounding effects of systemic electrolyte disturbances. Cardiomyocyte-specific MR knockout mice have revealed that cardiac MR contributes to pathological remodelling following myocardial infarction and pressure overload, independent of blood pressure changes (Fraccarollo et al., 2011). Similarly, endothelial cell-specific deletion of MR has demonstrated protective effects against vascular inflammation and dysfunction in models of hypertension and metabolic syndrome (Schäfer et al., 2013). In the central nervous system, brain-specific MR knockout models have highlighted the receptor's role in cognitive function, stress responses, and emotional regulation. Forebrain-specific MR deletion results in impaired hippocampal function, altered stress-coping behaviors, and enhanced anxiety-like responses, underscoring the importance of MR in maintaining the balance of the hypothalamic-pituitary-adrenal axis (Berger et al., 2006). Conversely, selective deletion of MR in specific neuronal populations has revealed region-specific functions in memory consolidation and behavioral adaptation to stress (Kretz et al., 1999).

Beyond knockout models, gain-of-function approaches have also provided valuable insights. Transgenic mice overexpressing MR in specific tissues, such as the heart or vasculature, develop exaggerated pathological responses to injury or stress, further supporting a causal role for MR in tissue damage (Qin et al., 2003). In a transgenic mouse model, in which expression of the human MR was placed under the control of its proximal P1 promoter, resulted in the appearance of mild dilated cardiomyopathy associated with increased heart rate, as well as nephropathy with decreased renal potassium excretion, underscoring the major role of MR in regulating cardiac and renal function (Le Menuet et al., 2001).

9.7 Therapeutic Targeting of MR

The therapeutic targeting of the MR has evolved significantly since the introduction of the first MR antagonists in the 1950s, with these agents now recognized as essential components in the treatment of cardiovascular and renal diseases. Spironolactone, a steroidal MR antagonist derivative of progesterone discovered in 1957, was initially developed as a potassium-sparing diuretic for the management of PA (Kagawa et al., 1957). Its mechanism of action involves competitive inhibition of aldosterone binding to MR, thereby preventing MR-mediated sodium reabsorption and potassium excretion in the distal nephron (Overdiek and Merkus, 1987). Clinical trials demonstrated that spironolactone significantly reduces mortality and hospitalization in patients with severe heart failure, establishing MR antagonists as an essential therapy in cardiovascular medicine (Pitt et al., 1999).

Despite its clinical efficacy, spironolactone's lack of selectivity for MR presents significant limitations. Due to its steroidal structure, spironolactone exhibits cross-reactivity with other steroid hormone receptors, including the androgen receptor and progesterone receptor, leading to dose-dependent endocrine side effects such as gynecomastia, erectile dysfunction, and menstrual irregularities (Jeunemaitre et al., 1987). These adverse effects limit patient adherence and led to the development of more selective MR antagonists. Eplerenone represents a second-generation steroidal MR antagonist with substantially improved receptor selectivity compared to spironolactone, although less potency (de Gasparo et al., 1987; Delyani et al., 2001). However, both spironolactone and eplerenone carry risks of hyperkalemia, particularly in patients with impaired renal function or those receiving renin-angiotensin system inhibitors, necessitating careful monitoring and limiting their use in patients with advanced chronic kidney disease (Vardeny et al., 2012).

The limitations of both MR antagonists have driven the development of third-generation nonsteroidal MR antagonists with improved pharmacological profiles. Finerenone, the most clinically advanced of these novel agents, is a nonsteroidal dihydropyridine-based MR antagonist that exhibits high selectivity for MR with balanced distribution between renal and cardiac tissues (Kolkhof et al., 2014). Preclinical studies demonstrated that finerenone provides comparable or superior end-organ protection compared to eplerenone in experimental models of heart failure, hypertension, and diabetic nephropathy, with a reduced propensity for hyperkalemia (Barrera-Chimal et al., 2018). The unique pharmacokinetic and

pharmacodynamic properties of finerenone, including its shorter plasma half-life and distinct tissue distribution, may contribute to its differentiated clinical profile (Pitt et al., 2013).

Overall hypothesis and objectives

Genome-wide association studies identified *CASZ1*, a zinc-finger transcription factor and MR corepressor, as a PA susceptibility gene regulating aldosterone biosynthesis in adrenocortical cells. The MR binds aldosterone and is expressed in aldosterone-producing cells of the ZG and in APA. We made the hypothesis that CASZ1, on its own or interacting with the MR, may affect adrenocortical homeostasis, including cell renewal, cell lineage conversion, and function, contributing to the development of PA in carriers of *CASZ1* risk alleles.

The aim of this project was to investigate how MR and *CASZ1* influence adrenal cortex structure, function, and aldosterone regulation, by developing and investigating different genetically modified mouse models.

THESIS PROJECT

10 Part I: An aldosterone-mineralocorticoid receptor regulatory loop maintains ZG homeostasis and plasticity

10.1 Thesis paper introduction

Primary aldosteronism (PA) is the most frequent form of secondary arterial hypertension, with a prevalence of 5% in hypertensive individuals in the general population and reaching up to 20% in those with treatment-resistant hypertension. PA is characterized by autonomous aldosterone production from the adrenal cortex, typically originating from either an aldosterone-producing adenoma (APA) or bilateral adrenal hyperplasia (BAH). Beyond driving hypertension through enhanced sodium reabsorption in the kidney, excess aldosterone causes direct cardiovascular damage. This elevates risks for myocardial infarction, cardiac arrhythmias, and heart failure independently of blood pressure levels[1].

Somatic and germline mutations have been identified in APA and familial forms of PA, helping to elucidate key disease mechanisms. Recurrent somatic mutations affect ion channels and pumps (*KCNJ5, CACNA1D, ATP1A1, ATP2B3, CLCN2, CACNA1H, SLC30A1* and *MCOLN3*) as well as other pathways (*CTNNB1, GNAQ/GNA11, CADM1*), and these have been identified as drivers of autonomous aldosterone production[2–4]. Beyond these genetic drivers, genome-wide association studies (GWAS) have identified common genetic variants within different chromosomal regions associated with increased PA risk across both unilateral and bilateral forms[5–7]. Genes within these risk loci modulate aldosterone output from adrenocortical cells and were previously associated with blood pressure-related traits and hypertension. This represents a shift in our understanding of PA. It suggests that subtle genetic variation may modify adrenocortical homeostasis, ultimately leading to aldosterone dysregulation in the general population and PA in extreme cases.

The mineralocorticoid receptor (MR), encoded by *NR3C2*, is a nuclear hormone receptor that functions as a ligand-dependent transcription factor within classical target organs including kidney, colon, and cardiovascular tissues[18,19]. In the aldosterone-sensitive distal nephron of the kidney, MR regulates electrolyte transport and fluid homeostasis, making it a major regulator

of blood pressure. When excessively activated in cardiovascular tissues, MR promotes pathological remodelling including cardiac fibrosis and vascular dysfunction[20]. This provides the therapeutic rationale for MR antagonists such as spironolactone and eplerenone in treating PA and heart failure[21]. Importantly, MR expression extends beyond these classical targets. It is also found in the aldosterone-producing zona glomerulosa (ZG) itself and in APAs[22,23]. This coincidence of aldosterone production and MR expression in the same cells suggests potential autocrine or paracrine regulatory loops, where locally secreted aldosterone might influence ZG homeostasis through MR-mediated mechanisms.

The adrenal cortex displays a characteristic layered organization where each concentric zone has a distinct endocrine function. Aldosterone biosynthesis occurs exclusively in the outermost ZG through expression of aldosterone synthase (AS), the enzyme encoded by CYP11B2 that catalyzes the final steps of conversion from corticosterone to aldosterone. The adjacent zona fasciculata (ZF) synthesizes glucocorticoids using 11β-hydroxylase (CYP11B1), while the human zona reticularis (ZR) produces androgenic precursors in the innermost cortical region[8]. Mice differ from humans in this organization. They lack a constitutive ZR and instead display a sexually dimorphic X zone (ZX) that regresses with sexual maturation in males and after the first pregnancy in females[9,10]. These zones respond to separate regulatory inputs - the renin-angiotensin-aldosterone system (RAAS) and extracellular potassium concentration primarily regulate ZG activity, while pituitary-derived ACTH drives glucocorticoid output from the ZF[11].

Despite relatively low rates of cell proliferation, the adrenal cortex is remarkably adaptive and regenerative. This enables the tissue to modify both its structure and function in response to environmental signals, with significant sex-specific differences[30]. Recent evidence demonstrates substantial adrenocortical plasticity and cell lineage conversion. Mature ZG cells migrate inward while progressively adopting ZF characteristics during physiological cortical renewal[12–14]. This dynamic cell fate transition is orchestrated by different signaling cascades, including sonic hedgehog from subcapsular cells within the ZG[15,16]. Under low salt diet, the adrenal cortex undergoes cellular and functional remodeling. ZG cell proliferation increases and aldosterone synthesis is enhanced, demonstrating the plasticity of the cortex[17].

Several observations support the hypothesis of aldosterone-MR autocrine signaling within the adrenal cortex. First, MR transcripts and protein are detected specifically in ZG cells, confirming these cells possess functional receptor machinery[22,23]. The ZG also expresses 11β-hydroxysteroid dehydrogenase type 2 (11β-HSD2)[23], which protects MR from glucocorticoid

activation by converting corticosterone (in mice) into its inactive form. Intra-adrenal aldosterone concentrations substantially exceed circulating levels, providing adequate local ligand to engage MR. In non-adrenal tissues, MR participates in proliferative control and structural remodeling across diverse cell types, suggesting similar roles might exist in the ZG[25],[26]. Clinical observations show that PA patients exhibit ZG hyperplasia and increased nodulation in the cortex adjacent to APA, potentially reflecting local MR-dependent processes[22]. Additionally, CASZ1, one of the PA susceptibility genes identified in GWAS studies, acts as a transcriptional corepressor for the MR[24]. This further supports a role for MR in regulating adrenal cortex homeostasis.

Previous investigations have faced significant challenges. Constitutive MR knockout animals show embryonic lethality, while systemic MR blockade triggers compensatory RAAS activation that confounds interpretation of ZG-specific effects[27]. Any observed alterations in aldosterone production following MR disruption could represent indirect consequences of perturbed renal sodium handling rather than direct effects within steroidogenic cells. The ZG also operates within a complex signaling environment, integrating systemic hormones (angiotensin II, potassium, ACTH) with local paracrine factors from capsular progenitors and adjacent cortical zones. To distinguish cell-autonomous MR actions from these intersecting regulatory inputs, cell-type-selective genetic manipulation strategies are necessary.

Based on this evidence, we hypothesized the existence of an autocrine-paracrine loop of aldosterone regulation of ZG homeostasis via the MR. To investigate the cell-autonomous functions of MR in aldosterone-producing cells, we generated cell-specific knockout mice employing Cyp11b2-Cre[14] to ablate MR selectively in ZG and derived cells. We tested whether aldosterone regulates ZG structure and function through MR by evaluating these animals under baseline conditions and during sodium restriction, a physiological stressor that stimulates the RAAS and promotes ZG growth. To comprehensively map cellular heterogeneity, define plasticity mechanisms, and identify MR-dependent transcriptional programs, we performed single-nucleus RNA sequencing (snRNAseq). This work aimed to elucidate the role of MR in regulating adrenal cortex homeostasis and plasticity, with potential implications for understanding the pathophysiology of PA.

11 Part II: Role of *Casz1* in Adrenal Cortex Development

11.1 Introduction

11.1.1 General Characteristics of Castor Zinc Finger 1 (CASZ1)

CASZ1 (Castor Zinc Finger 1) is encoded by the *CASZ1* gene located in human at the chromosomal position 1p36.22, extending across roughly 160 kb and comprising 21 distinct exons (Liu et al., 2006). The significance of this genomic region extends beyond *CASZ1* itself, as chromosome 1p36.22 has emerged as a critical locus in numerous GWAS examining blood pressure regulation and predisposition to hypertensive disorders(Kato et al., 2011; Levy et al., 2009). Through alternative splicing mechanisms, the *CASZ1* gene generates two principal protein variants that differ substantially in size and functional domain composition. *CASZ1* belongs to the large family of C2H2-type zinc finger transcription factors, proteins characterized by their ability to recognize and bind specific DNA sequences through zinc-coordinated finger-like domains. The designation C2H2 refers to the conserved cysteine-cysteine-histidine-histidine amino acid motifs that coordinate zinc ions, creating stable structures for DNA interaction (Jian and Poetsch, 2023).

- The long isoform (CASZ1a, also known as CASZ11) represents the full-length protein product, consisting of 1,759 amino acid residues with an approximate molecular weight of 190 kDa. This variant incorporates all 21 exons and features an impressive array of 11 zinc finger domains distributed throughout its structure. Beyond the zinc fingers, CASZ1a contains numerous regulatory elements including nuclear localization signals for nuclear import, a second C-terminal nuclear localization sequence, and extended regions particularly rich in alanine, glutamine, and asparagine residues that may serve regulatory functions (Liu et al., 2006).
- The short isoform (CASZ1b, also known as CASZ5) arises through alternative splicing that terminates the transcript at exon 16, yielding a 1,166 amino acid protein of approximately 125 kDa. This truncated form retains only five zinc finger domains and lacks the extensive C-terminal region present in CASZ1a (Liu et al., 2006; Yokota et al., 2021).

The N-terminal 1,166 amino acids are identical between both isoforms, encompassing the first five zinc fingers, one nuclear localization signal, proline-rich domains implicated in protein-protein interactions, and a conserved ATP/GTP-binding motif of unclear function. Notably, each zinc finger module is preceded by a conserved para-zinc finger sequence. The key structural difference lies in the six additional C-terminal zinc fingers in Casz1a and associated regulatory sequences (Liu et al., 2006).

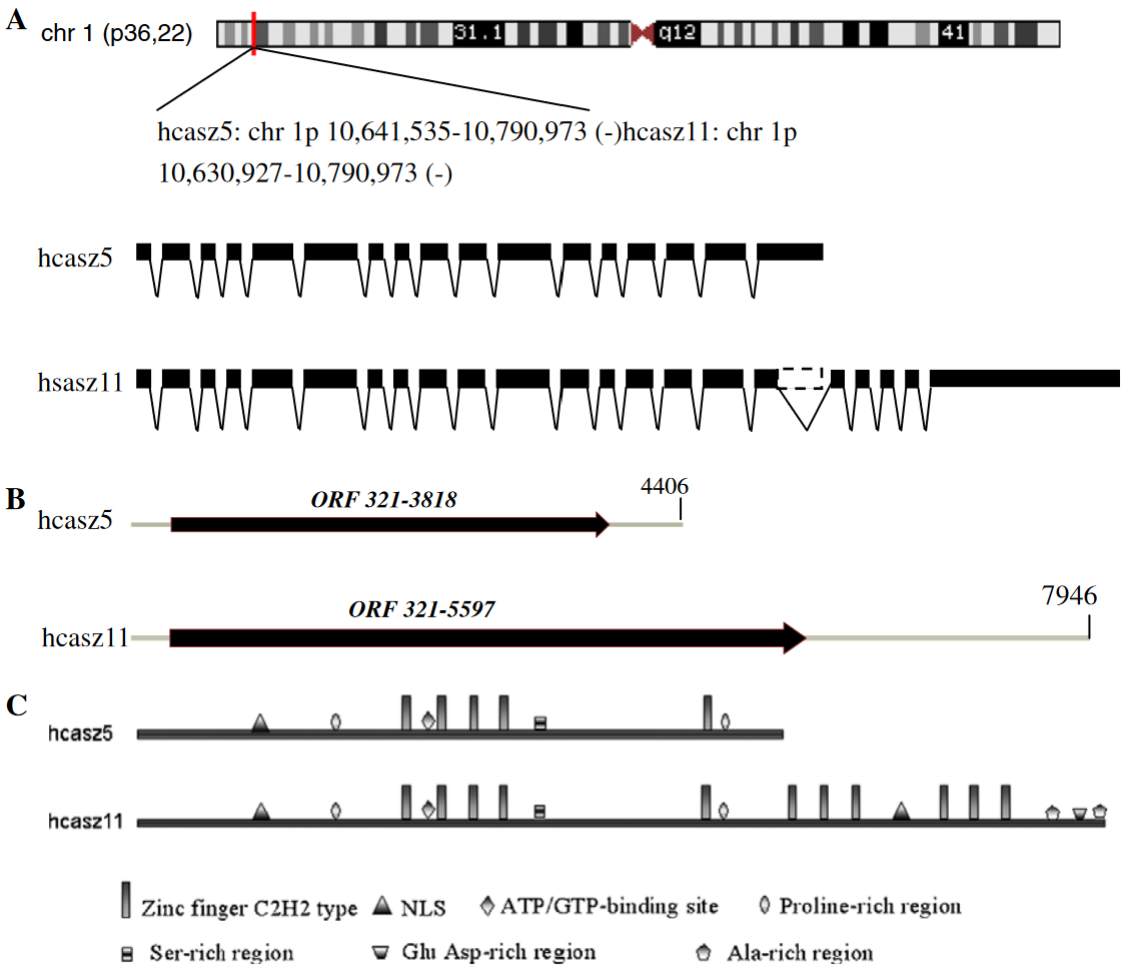

Figure 25 : Genomic structure, cDNA information, and the predicted protein motifs of CASZ1. *(A) Representation of genomic structure for CASZ1. The human CASZ1 gene is located on chr1p 36.22. The gene encodes two transcripts, hcasz5 and hcasz11. Exon 16 is differently spliced to produce these two transcripts. (B) The assembled CASZ1 comprises a 50 UTR region/30 UTR region, start/stop-codon, and poly(A) signal. Within the 30 UTR there are two putative consensus polyadenylation signals (ATAAA) for both hcasz5 (nt: 4380–4384; 4389–4393) and hcasz11 (nt: 7618–7622; 7919–7923). There is one RNA instability motif (ATTTA) for hcasz5 (nt: 4401–4405) and there are four for hcasz11 (nt: 6661–6665; 7824–7828; 7841–7845; 7859–7863). (C) Both hcasz5 and hcasz11 proteins have motifs such as zinc finger, NLS, ATP-binding site, Ser-rich region, and proline-rich domain, hcasz11 also has Glu Asp-rich region and Ala-rich region (Extracted from (Liu et al., 2006)).*

Beyond DNA-binding capabilities conferred by its zinc finger domains, *CASZ1* possesses several other functional regions whose roles are gradually being elucidated. Nuclear localization signals ensure proper trafficking of the protein to the nucleus where it can access

its genomic targets. Proline-rich regions are typically associated with protein-protein interactions, suggesting CASZ1 functions within multi-protein regulatory complexes. A serine-rich domain represents a potential substrate for phosphorylation-based regulation, though the responsible kinases and functional consequences remain largely unexplored. The ATP/GTP-binding motif is conserved but its functional significance awaits experimental validation (Jian and Poetsch, 2023; Liu et al., 2006). Northern blot analyses have revealed *CASZ1* transcripts in multiple human tissues, with major mRNA species of approximately 8.0 kb and minor transcripts around 4.4 kb (Liu et al., 2006). Abundant expression characterizes several organs including the heart, lung, skeletal muscle, pancreas, testis, small intestine, and stomach. Interestingly, brain tissue shows negligible *CASZ1* expression. As will be discussed extensively below, *CASZ1* is also present in the adrenal cortex, particularly within the ZG where aldosterone synthesis occurs.

11.1.2 CASZ1 in Adrenocortical Physiology

11.1.2.1 Developmental and Adult Expression in Adrenal Tissue

Investigation of gene expression datasets from human fetal adrenal development have shown *CASZ1* expression during early gestation, specifically between 42.5 and 73.5 days post-conception (Le Floch et al., 2022). Unlike certain tissue-restricted transcription factors, *CASZ1* shows relatively stable expression throughout adrenal development and maintains expression in mature adult tissue. Modern single-nucleus RNA sequencing approaches applied to adult human adrenocortical samples have revealed *CASZ1* transcripts across multiple cellular populations, including the aldosterone-secreting cells of the ZG. Spatial gene expression using RNAscope in situ hybridization technology has precisely localized *CASZ1* mRNA within adrenal tissue, demonstrating its presence in steroid-producing cells of both the ZG and ZF (Le Floch et al., 2022). Importantly, *CASZ1* expression is maintained in pathological tissue, including APAs and the surrounding non-tumoral adrenal cortex. The spatial overlap between *CASZ1* expression and key steroidogenic enzymes is particularly important, including colocalization with *CYP11B2* (Le Floch et al., 2022). Additionally, *CASZ1* shows coordinated expression with the MR in aldosterone-responsive tissues including renal tubular epithelium and ZG cells, suggesting potential involvement in modulating hormonal responses (Yokota et al., 2021).

11.1.2.2 Negative Regulation of Aldosterone Production

Functional studies in human adrenocortical H295R-S2 cells have provided crucial mechanistic insights into the role of *CASZ1* in aldosterone regulation. When *CASZ1* is experimentally overexpressed in these cells, aldosterone biosynthesis is significantly reduced under both baseline conditions and following stimulation with angiotensin II (Le Floch et al., 2022). Multiple complementary measurements confirm this inhibitory effect, where mass spectrometry quantification shows decreased aldosterone secretion, Western blot analysis reveals reduced AS protein levels, and quantitative PCR demonstrates diminished *CYP11B2* mRNA abundance. While *CASZ1* overexpression suppresses mineralocorticoid production, it has minimal impact on cortisol biosynthesis (Le Floch et al., 2022). This selectivity indicates that *CASZ1* specifically targets ZG steroidogenic pathways rather than causing generalized suppression of adrenocortical steroid production. The mechanism likely involves direct transcriptional repression of *CYP11B2* through CASZ1 binding to regulatory elements in the *CYP11B2* gene, though the precise DNA binding sites and cofactor requirements remain to be fully characterized (Yokota et al., 2023). These findings suggest *CASZ1* functions physiologically as a brake on aldosterone production, preventing excessive mineralocorticoid secretion (Yokota et al., 2023). In this model, normal *CASZ1* expression maintains aldosterone output within appropriate physiological ranges, while reduced *CASZ1* function, whether from genetic variation, epigenetic silencing, or other mechanisms, could permit pathological aldosterone excess. This regulatory mechanism appears particularly important in the ZG, where tight control of aldosterone production is essential for maintaining electrolyte balance and normal blood pressure (Le Floch et al., 2022; Yokota et al., 2023).

11.1.3 CASZ1b Functions as a Mineralocorticoid Receptor Corepressor

A major advance in understanding CASZ1 biology came from Yokota and colleagues discovery that CASZ1b, the shorter isoform, acts as a transcriptional corepressor for the MR (Yokota et al., 2021). Using mass spectrometry-based proteomics combined with biochemical co-immunoprecipitation approaches, these investigators identified CASZ1b in protein complexes containing MR and demonstrated direct physical interaction between the two proteins. CASZ1b exerts its corepressor function through multiple mechanisms. Physical protein-protein interaction between CASZ1b and MR occurs via specific binding interfaces. In the presence of aldosterone, CASZ1b reduces the ability of the MR to activate transcription

from target gene promoters. The strength of this repression depends on cellular context, the specific promoter sequences involved, and the presence of other coregulatory proteins (Yokota et al., 2023, 2021). The tissue distribution of CASZ1b mirrors that of MR across all major aldosterone target tissues. Both proteins are co-expressed in renal distal convoluted tubule and collecting duct epithelial cells, in aldosterone-producing ZG cells, and in cardiovascular tissues including vascular smooth muscle and cardiac myocytes (Yokota et al., 2021). This widespread co-expression pattern suggests CASZ1b tunes aldosterone sensitivity across multiple organ systems. In the kidney, CASZ1b may fine-tune the magnitude of sodium reabsorption in response to aldosterone, while in the adrenal gland, it could participate in local feedback loops regulating aldosterone biosynthesis (Yokota et al., 2023). Experimental depletion of *CASZ1* through RNA interference enhanced MR-dependent transcriptional responses in HEK293F cells, suggesting that endogenous CASZ1b normally constrains aldosterone signalling (Yokota et al., 2021). Conversely, increasing CASZ1b expression attenuates cellular responses to aldosterone without changing MR protein abundance or aldosterone-binding affinity. These observations indicate CASZ1b acts as a selective modulator of MR transcriptional activity rather than affecting receptor expression or ligand recognition.

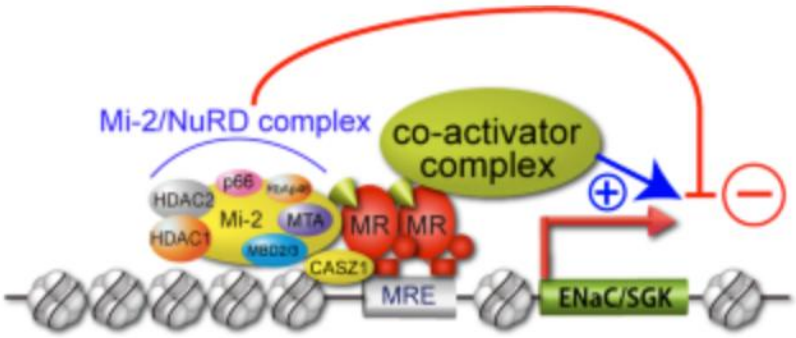

Figure 26 : Schematic diagram of CASZ1-nucleosome remodeling and deacetylase (NuRD) co-repressor complex for MR. Upon aldosterone binding to MR, the CASZ1-NuRD co-repressor and co-activator complexes are recruited to the MR bound to the target gene promoter. These complexes cooperatively regulate transcription

11.1.4 Regulation of Ion Channel Gene Expression

The regulatory influence of *CASZ1* extends beyond *CYP11B2* expression and MR corepression to include other genes critical for adrenocortical function. Notably, CASZ1 regulates expression of *CACNA1D* and *KCNK3*, genes encoding ion channels with established roles in human and experimental PA pathogenesis (Bandulik et al., 2010; Le Floch et al., 2022). As previously mentioned, somatic gain-of-function mutations in *CACNA1D,* which encodes the

Cav1.3 L-type voltage-gated calcium channel, have been identified in APAs, where they drive autonomous aldosterone secretion through enhanced calcium entry (Azizan et al., 2023). The regulation of *CACNA1D* through CASZ1 suggests a mechanism whereby diminished *CASZ1* function could promote aberrant calcium signalling in ZG cells (Liu et al., 2014). *KCNK3* encodes the TASK-1 potassium channel, which controls ZG membrane potential and aldosterone production. These channels are essential for maintaining appropriate resting membrane potential in ZG cells, and their dysfunction has been linked to dysregulated aldosterone production in rodent models (Bandulik et al., 2010). CASZ1-mediated control of potassium channel expression represents another layer through which this transcription factor may influence aldosterone biosynthesis (Liu et al., 2014).

11.1.5 CASZ1 Genetic Variants and Primary Aldosteronism

A GWAS performed by the host laboratory has identified different genetic loci associated with PA, including a region containing *CASZ1* on chromosomal locus 1p36.22 (Le Floch et al., 2022). The discovery cohort included 562 PA patients and 950 controls, with subsequent validation in an independent cohort and meta-analysis combining 1,162 cases with 3,296 controls, demonstrating robust and reproducible association of *CASZ1* variants with PA risk. The association of *CASZ1* to PA has been replicated across multiple ancestries, including Japanese, UK Biobank European, and FinnGen cohorts, with consistent effects observed in both European and East Asian populations (Inoue et al., 2024; Naito et al., 2023). This cross-ancestry replication substantially strengthens confidence that *CASZ1* represents a genuine susceptibility locus and suggests the causal variant may be ancient in human evolutionary terms. An important observation is that *CASZ1* polymorphisms, also associated with blood pressure traits in previous GWAS, show larger effect sizes for PA risk compared to their associations with essential hypertension in the general population, suggesting specific involvement in pathological aldosterone excess as an underlying pathogenic mechanism (Naito et al., 2023). In the adrenal gland in situ hybridization and snRNAseq studies demonstrated *CASZ1* expression in both APAs and adjacent non-neoplastic adrenal cortex (Le Floch et al., 2022), with enrichment in aldosterone producing cell clusters (also called aldosterone producing micronodules), which are particular groups of cells in the human adrenal cortex displaying autonomous aldosterone production and somatic mutations in PA driver genes (De Sousa et al., 2020; Nishimoto et al., 2015).

11.1.6 CASZ1 in Cardiovascular Development and Disease

CASZ1 plays indispensable roles in cardiomyocyte differentiation and cardiac morphogenesis during embryonic development. Initial work in Xenopus identified the vertebrate *CASZ1* ortholog as essential for differentiation of cardiac progenitor cells at the ventral midline (Christine and Conlon, 2008). Subsequent mammalian studies confirmed the requirement of Casz1 for proper heart formation (Liu et al., 2014). Mouse models with *Casz1* deficiency exhibit embryonic lethality associated with cardiac edema, structural cardiac defects including ventricular septal defects, and impaired cardiac contractile function (Jian and Poetsch, 2023; Liu et al., 2014). The severity of this cardiac phenotype highlights the essential role of *CASZ1* in heart development and explains why homozygous loss-of-function mutations would likely be lethal in humans. Loss-of-function mutations in *CASZ1* have been identified in patients with various congenital cardiac malformations, including ventricular septal defects (the most common form of congenital heart disease), hypoplastic left heart syndrome, left ventricular noncompaction, and dilated cardiomyopathy (Jian and Poetsch, 2023). These mutations typically affect zinc finger domains or cause protein truncation, disrupting the transcriptional and protein interaction functions critical for proper heart development. These findings across diverse cardiac malformations underscore the essential role of *CASZ1* in heart development.

11.1.7 CASZ1 in Other Biological Contexts

Beyond cardiovascular and adrenocortical functions, CASZ1 participates in neuronal development, consistent with its discovery through homology to Drosophila castor. In mammalian systems, CASZ1 regulates neuroblast lineage specification and neurite outgrowth (Liu et al., 2006). *CASZ1* expression increases during neuronal differentiation, and the protein localizes to nuclei in differentiating neuronal cells. In cancer biology, CASZ1 exhibits context-dependent effects that have been termed a "double-agent" phenomenon (Jian and Poetsch, 2023). In neuroblastoma, CASZ1 functions as a tumor suppressor through transcriptional reprogramming that inhibits cell cycle progression and restores retinoblastoma protein (pRb) activity (Liu et al., 2013, 2011). Loss of CASZ1 expression or function in neuroblastoma correlates with more aggressive disease and worse prognosis. Conversely, in certain other malignancies such as ovarian cancer, CASZ1 has been reported to promote metastasis, suggesting its effects on cancer biology depend heavily on cellular context, cooperating oncogenes or tumor suppressors, and tissue of origin (Wu et al., 2016). These apparently

An aldosterone-mineralocorticoid receptor regulatory loop maintains ZG homeostasis and plasticity

May Fayad[1,2], Rami M. El Zein[1], Nicolo Faedda[1], Rita Chamoun[1,3], Parisa Rezvanisanijouybari[1,2], Ourida Koual[1], Linghui Kong[1], Isabelle Giscos-Douriez[1], Stéphanie Baron[4], Oliver Domenig[5], Marko Poglitsch[5], Fabio L. Fernandes-Rosa[1], Eleanor Davies[2], Sheerazed Boulkroun[1], Maria-Christina Zennaro[1,6]

[1]Université Paris Cité, Inserm, PARCC, Paris, France
[2]School of Cardiovascular and Metabolic Health, BHF Glasgow Cardiovascular Research Centre, University of Glasgow, Glasgow, United Kingdom
[3]Maastricht University Medical Center, Maastricht Limburg, The Netherlands
[4]Assistance Publique-Hôpitaux de Paris, Hôpital Européen Georges Pompidou, Service de Physiologie, Paris, France
[5]Attoquant Diagnostics, Vienna, Austria
[6]Assistance Publique-Hôpitaux de Paris, Hôpital Européen Georges Pompidou, Service de Génétique, Paris, France

#Corresponding author
Address correspondence to:
Maria-Christina Zennaro, MD, PhD
Inserm, U970
Paris Cardiovascular Research Center – PARCC
56, rue Leblanc,
75015 Paris – France
Tel : +33 (0)1 53 98 80 42
Fax : + 33 (0)1 53 98 79 52
e-mail : maria-christina.zennaro@inserm.fr

Declaration of interest

The authors have nothing to disclose

Abstract

Background: The mineralocorticoid receptor (MR) plays a major role in regulating sodium homeostasis and blood pressure. Recent studies have shown that MR is expressed in the aldosterone producing cells of the zona glomerulosa (ZG) of the adrenal cortex, but its role in adrenocortical homeostasis has not been investigated.

Objectives: To define the cell-autonomous roles of MR in aldosterone-producing cells using ZG-specific MR knockout mice combined with single-nucleus transcriptomics.

Methods: We generated Cyp11b2-Cre-driven MR knockout ($MRKO^{Ad}$) mice and performed morphological, hormonal and molecular phenotyping under standard and low-salt diets. Single-nucleus RNA sequencing (snRNAseq) across four conditions was analyzed to define population-specific MR functions and plasticity mechanisms.

Results: MR deletion reduced *Cyp11b2* and aldosterone synthase (AS) expression in the adrenal cortex, with sex-specific effects on ZG architecture, but no change in basal aldosterone levels. This was associated with reduced proliferation and PKA activation, without modification of Wnt/β-catenin signaling. Under low salt diet, increased aldosterone production was accompanied by ZG expansion and increased AS expression in wild type mice, which was abolished in $MRKO^{Ad}$ mice of both sexes. snRNAseq analysis revealed three mechanistically distinct plasticity programs following LSD: (1) ZG maintained identity through MR-dependent proliferation; (2) ZG_ZF transition zone showed robust plasticity driven by environmental signals (10% MR-dependent); and (3) zona fasciculata resolved into two subpopulations - ZF1 underwent authentic MR-dependent ZG transdifferentiation supported by constitutive metabolic priming, while ZF2 showed *Cyp11b2* induction without acquiring ZG identity. MR-dependent genes, representing 28% of plasticity genes, accounted for 69% of functional ZG signature changes and converged on metabolic pathways (oxidative phosphorylation, ATP synthesis, steroid biosynthesis), establishing MR as an orchestrator of metabolic reprogramming.

Conclusions: MR plays distinct, cell-population-specific roles across the adrenal cortex. MR maintains ZG function in an autocrine-paracrine loop under basal conditions and regulates proliferative capacity, ZG architecture sex-specifically, and orchestrates metabolic transformation required for adrenal cortex plasticity following a salt challenge.

Introduction

Among secondary causes of arterial hypertension, primary aldosteronism (PA) is the most frequent one, with a prevalence of 5% in hypertensive individuals in the general population and reaching up to 20% in those with treatment-resistant hypertension. PA is due to autonomous aldosterone production from the adrenal cortex, typically originating from either an aldosterone-producing adenoma (APA) or bilateral adrenal hyperplasia. Beyond its role in driving hypertension through enhanced sodium reabsorption, via its binding to the mineralocorticoid receptor (MR) in the kidney, excess aldosterone triggers direct cardiovascular damage, elevating risks for myocardial infarction, cardiac arrhythmias, and heart failure independently of blood pressure levels[1]. Somatic and germline mutations have been identified in APA and familial forms of PA, allowing to elucidate disease mechanisms. Recurrent somatic mutations affecting ion channels and pumps (*KCNJ5, CACNA1D, ATP1A1, ATP2B3, CLCN2, CACNA1H, SLC30A1* and *MCOLN3*) and other pathways (*CTNNB1, GNAQ/GNA11, CADM1*) have been identified as key drivers of autonomous aldosterone production [2–4]. Beyond these genetic drivers, genome-wide association studies (GWAS) have identified common genetic variants within different chromosomal regions associated with increased PA risk across both unilateral and bilateral forms[5–7]. Genes within these risk loci have been shown to modulate aldosterone output from adrenocortical cells and had previously been associated with blood pressure related traits and hypertension. This represents a paradigm shift in our understanding of PA, suggesting that subtle genetic variation may modify adrenocortical homeostasis, ultimately leading to aldosterone dysregulation in the general population and PA in extreme cases.

Within the adrenal gland, the cortex displays a characteristic layered organization wherein each concentric zone has a distinct endocrine function. Aldosterone biosynthesis occurs exclusively in the outermost ZG through expression of aldosterone synthase (AS), the enzyme encoded by *CYP11B2* that catalyzes the final steps of conversion from corticosterone to aldosterone. Adjacent to this, the zona fasciculata (ZF) synthesizes glucocorticoids using 11β-hydroxylase (*CYP11B1*), while the human zona reticularis (ZR) produces androgenic precursors in the innermost cortical region[8]. Unlike humans, mice lack a constitutive ZR and instead display a sexually dimorphic X zone (ZX) that regresses with sexual maturation in males and after the first pregnancy in females, highlighting important species-specific differences in adrenal architecture[9,10]. These zones respond to separate regulatory inputs. The renin-angiotensin-aldosterone system (RAAS) and extracellular potassium concentration are the main regulators of ZG activity. In contrast, pituitary-derived ACTH drives glucocorticoid output from the ZF[11]. Understanding how these functionally distinct zones maintain stable boundaries while retaining adaptive flexibility represents a central question in adrenal biology. Emerging evidence demonstrates substantial adrenocortical plasticity and cell lignage conversion, with mature ZG cells migrating inward while progressively adopting ZF characteristics during physiological cortical renewal[12–14]. This dynamic cell fate transition is orchestrated by different signalling cascades. These include sonic hedgehog from subcapsular cells within the ZG[15,16]. Under low salt diet, the adrenal cortex undergoes a cellular and functional remodeling, with ZG cell proliferation and enhanced aldosterone synthesis, demonstrating the plasticity of the cortex[17].
The MR, encoded by *NR3C2*, is a nuclear hormone receptor that acts as a ligand dependent transcription factor within target organs including kidney, colon, and cardiovascular tissues [18,19]. In the aldosterone sensitive distal nephron of the kidney, MR regulates electrolyte

transport and fluid homeostasis, thus being a major regulator of blood pressure. Excessive MR activation in cardiovascular tissues promotes pathological remodelling including cardiac fibrosis and vascular dysfunction[20]. This establishes the therapeutic rationale for MR antagonists like spironolactone and eplerenone in treating PA and heart failure[21]. Notably, MR expression extends beyond these classical targets to include the aldosterone-producing ZG itself and APAs[22,23]. This anatomical coincidence of aldosterone production and MR expression suggests potential autocrine or paracrine regulatory loops. Locally secreted aldosterone might influence ZG homeostasis through MR-mediated mechanisms. Such local signalling could govern adrenal structure, cellular proliferation, or steroidogenic output, yet this possibility remains largely unexplored. Remarkably, CASZ1, encoded by one of the candidate genes identified in GWAS studies on chromosome 1[5], acts as a transcriptional corepressor for the MR [24]. This further supports the hypothesis of a role of the MR in regulating adrenal cortex homeostasis.

Multiple observations support the hypothesis of aldosterone-MR autocrine signalling within the adrenal cortex. Detection of MR transcripts and protein specifically in ZG cells confirms these cells possess functional receptor machinery[22,23]. The ZG also expresses 11β-hydroxysteroid dehydrogenase type 2 (11β-HSD2)[23], which protects MR from glucocorticoid activation by converting cortisol into its inactive form, cortisone (in human) and corticosterone (in mice). Intra-adrenal aldosterone concentrations substantially exceed circulating levels, providing adequate local ligand to engage MR. Studies in non-adrenal tissues demonstrate MR participation in proliferative control and structural remodelling across diverse cell types including vascular smooth muscle, cardiac fibroblasts, and renal epithelia[25,26]. This suggests analogous roles might exist in the ZG. Clinical observations reveal that PA patients exhibit ZG hyperplasia and increased nodulation in the cortex adjacent to APA, potentially reflecting local MR-dependent processes[22].

Previous investigations using constitutive MR knockout animals encountered embryonic lethality, while systemic MR blockade triggers compensatory RAAS activation that confounds interpretation of ZG-specific effects[27]. Observed alterations in aldosterone production following MR disruption could represent indirect consequences of perturbed renal sodium handling rather than direct effects within steroidogenic cells. Additionally, the ZG operates within a complex signalling environment, integrating systemic hormones (angiotensin II, potassium, ACTH) with local paracrine factors from capsular progenitors and adjacent cortical zones. Distinguishing cell-autonomous MR actions from these intersecting regulatory inputs necessitates cell-type-selective genetic manipulation strategies.

Based on this evidence, we make the hypothesis of the existence of an autocrine-paracrine loop of aldosterone regulation of ZG homeostasis via the MR. To investigate cell-autonomous MR functions in aldosterone-producing cells and directly test whether aldosterone regulates ZG structure and function through MR, we generated cell-specific knockout mice employing Cyp11b2-Cre[14] to ablate MR selectively in ZG and derived cells. We evaluated these animals under baseline conditions and during sodium restriction, a physiological stressor stimulating the RAAS and promoting ZG growth. To comprehensively map cellular heterogeneity, define plasticity mechanisms, and identify potential cellular origins of APAs, we performed single-nucleus RNA sequencing (snRNAseq). We show that MR ablation in the ZG reduces *Cyp11b2*

and AS expression in both sexes under basal conditions, but had only minor consequences on circulating aldosterone levels. MR knock-out affected the proliferative activity and zonal architecture in a sex-divergent manner, with females exhibiting ZG enlargement. This was associated with activation of PKA pathways, but no modification of canonical Wnt/β-catenin signaling. scRNAseq revealed cell-specific adaptation to a low salt challenge, involving MR-dependent and independent functions in distinct cellular subpopulations. These findings indicate that while MR in the ZG is non-essential for aldosterone biosynthesis itself under basal conditions, it significantly influences proliferation, structural organization, and responses to environmental challenges.

Results

Generation and characterization of Cyp11b2-Cre::Nr3c2 and Cyp11b2-Cre::Nr3c2::mTmG mice

To achieve cell-specific MR deletion in aldosterone-producing cells, we crossed our previously characterized Cyp11b2-Cre mouse line, in which Cre recombinase is inserted within the Cyp11b2 locus (exon 9) downstream of the stop codon in the 3' untranslated region (3' UTR) after an Internal Ribosome Entry Site (IRES) (Faedda et al., 2025), with Nr3c2-flox/flox mice provided by IGBMC (Strasbourg). The Nr3c2-flox/flox allele contains loxP sites flanking exons 5 and 6 of the *Nr3c2* gene (Figure 1A). This strategy allows bicistronic translation of both *Cyp11b2* and Cre recombinase from a single mRNA transcript, preserving functional aldosterone synthase expression while enabling MR deletion in Cyp11b2-expressing cells (Figure 1A.1).

To confirm tissue-specific excision, we performed PCR amplification on genomic DNA isolated from adrenal cortex, heart, kidney, and tail (Figure 1B). A 214 bp band corresponding to the excised *Nr3c2* allele was detected exclusively in the adrenal cortex, while other tissues expressing *Nr3c2* (kidney, heart) showed only the 454 bp band corresponding to the intact floxed allele, confirming efficient and specific genomic excision in the adrenal cortex. Quantitative PCR on isolated adrenal glands demonstrated significant reduction in *Nr3c2* mRNA expression in Cyp11b2-Cre::Nr3c2 (hereafter MRKO^{Ad}) mice compared to wild-type controls (Figure 1C), confirming successful MR deletion at the transcriptional level. RNAscope in situ hybridization further validated the loss of *Nr3c2* mRNA specifically in the ZG of MRKO mice (Figure 1D).

To enable lineage tracing of Cyp11b2-expressing cells, MRKO^{Ad} mice were crossed with Gt(ROSA)$^{26Sortm4(ACTB-tdTomato-EGFP)Luo/J}$ (mTmG) reporter mice to generate the Cyp11b2-Cre::Nr3c2::mTmG (MRKO^{Ad}::mTmG) line (Figure 1A.2). In this system, Cre-recombined cells switch from membrane-targeted Tomato (mTomato, red) to membrane-targeted GFP (mGFP, green) expression, allowing permanent marking of aldosterone-producing cell lineages.

MR deletion causes sex-specific morphological changes in the adrenal cortex

To characterize the phenotypic consequences of MR deletion in aldosterone-producing cells under basal conditions, we examined 12-weeks old mice for morphological and zonal architecture changes. Male MRKO^{Ad} mice exhibited significantly increased body weight compared to wild-type controls, while female MRKO^{Ad} mice showed no difference (Figure 2A, left). Adrenal gland weights, normalized to body weight, were comparable between genotypes in both sexes (Figure 2A, middle and right).

Histological examination by hematoxylin-eosin-saffron (HES) staining revealed no obvious morphological abnormalities in adrenal cortical architecture in either sex (Figure 2B, upper panels). However, immunofluorescence analysis using zone-specific markers uncovered sex-specific alterations in cortical zonation. Dab2 immunostaining, which marks the ZG, revealed significant expansion of the Dab2+ area in female MRKO^{Ad} mice compared to wild-type controls (Figure 2B, middle panels; Figure 2C). In contrast, male MRKO^{Ad} mice showed no significant change in Dab2+ ZG area despite their increased body weight (Figure 2C).

Analysis of the sexually dimorphic ZX, located at the innermost boundary between ZF and medulla in female mice, revealed zone-specific effects of MR deletion. Immunofluorescence

for 20α-HSD, a marker of ZX identity, showed significant reduction in the 20α-HSD+ area in female MRKO^{Ad} mice compared to controls (Figure 2B, lower panels; Figure 2D). As expected, 20α-HSD staining was absent in male adrenals of both genotypes (Figure 2B, lower panels), confirming its physiological regression after puberty in males.

These data demonstrate that MR regulates adrenal zonation in a sex-specific manner, with female mice showing ZG expansion accompanied by ZX reduction, while males exhibit increased body weight without alterations in adrenal cortical architecture.

Functional characterization of MRKO^{Ad} mice reveals maintained hormone levels despite reduced *Cyp11b2* expression

To assess the functional consequences of MR deletion in aldosterone-producing cells, we examined steroidogenic enzyme expression, proliferation, and hormone production in 12-week-old mice under basal conditions.

AS expression was reduced in MRKO^{Ad} mice. Immunofluorescence analysis of adrenal cortex revealed a decreased number of AS+ cells in the ZG of MRKO^{Ad} mice compared to wild-type controls in both sexes (Figure 3A). Quantification confirmed significantly reduced AS+ area over total cortical area in MRKO^{Ad} mice (Figure 3B). Quantitative RT-PCR validated these findings, demonstrating reduced *Cyp11b2* mRNA levels in MRKO^{Ad} adrenals (Figure 3C, left). *Cyp11b1* expression was significantly increased in male MRKO^{Ad} mice, while Star expression remained unchanged in both sexes (Figure 3C, middle and right), suggesting zone-specific and sexually dimorphic compensatory responses to MR ablation.

Comprehensive steroid profiling by liquid chromatography-tandem mass spectrometry (LC-MS/MS) was performed to assess steroidogenic output in MRKO^{Ad} mice (Figure 3D). Principal component analysis (PCA) demonstrated that steroid profiles in MRKO^{Ad} mice largely overlapped with wild-type controls in both sexes, indicating preserved overall steroidogenic capacity despite reduced *Cyp11b2* and AS expression (Figure 3D; Supplementary Figure S1). The first principal component (Dim1) captured the major sources of variation in steroid metabolism: in males, Dim1 (35% variance) was driven by progesterone, 11-hydroxy-11-doc and corticosterone levels (Supplementary Figure S1A), while in females, Dim1 (41.7% variance) was driven mainly by 18-hydroxycorticosterone, aldosterone and corticosterone (Supplementary Figure S1B). This dimensional separation reflects the distinct steroidogenic pathways characterizing male and female adrenal function under basal conditions.

Plasma hormone levels are maintained despite reduced *Cyp11b2* expression (Supplementary Tables S4, S5). Despite significant reductions in *Cyp11b2* expression, plasma aldosterone levels showed no significant differences between MRKO^{Ad} and wild-type mice in either sex (Figure 3E, top left), although a slight decrease was detected in male mice. Corticosterone levels were comparable between genotypes (Figure 3E, top right), and plasma renin activity (PRA) showed no significant differences (Figure 3E, bottom left). Comprehensive profiling of angiotensin peptides (Ang I, Ang II, Ang III, Ang IV, Ang 1-5, Ang 1-7) revealed no significant differences between genotypes in either sex (Supplementary Table S6), further supporting maintained RAAS homeostasis. However, the aldosterone-to-angiotensin II (AA2) ratio was significantly reduced in male MRKO^{Ad} mice while remaining unchanged in females (Figure 3E, bottom right), suggesting a compensated phenotype in males allowing to maintain aldosterone output.

Cell proliferation was reduced in the adrenal cortex MRKO^{Ad}. Immunofluorescence analysis of Ki67, a marker of proliferating cells, revealed decreased proliferation in MRKO^{Ad} adrenal

cortex compared to wild-type controls in both sexes (Figure 3F). Quantification of immunofluorescence signals demonstrated significantly reduced $Ki67^{+}$ cells as percentage of total cortical nuclei in both male and female mice (Figure 3G), indicating that MR signaling supports adrenocortical proliferation.

To investigate potential signaling mechanisms underlying maintained aldosterone production despite reduced *Cyp11b2* and AS expression, we examined components of the PKA pathway, a key regulator of steroidogenesis that plays a role in ZF identity maintenance. Western blot analysis revealed increased levels of both total CREB and phosphorylated CREB (pCREB) in $MRKO^{Ad}$ adrenals from both sexes (Figure 3H), suggesting enhanced PKA activity. Quantitative PCR analysis of PKA pathway components showed sex-specific upregulation, with both the regulatory subunit *Prkar1a* and catalytic subunit *Prkaca* significantly increased specifically in male $MRKO^{Ad}$ mice (Figure 3I).

These results demonstrate that MR deletion in aldosterone-producing cells reduces AS and *Cyp11b2* expression, and proliferation, yet circulating aldosterone levels are maintained through compensatory mechanisms. Male mice exhibit more pronounced molecular compensation, including enhanced PKA subunit expression at the transcriptional level, while both sexes show PKA-CREB pathway activation at the protein level and females also display slight ZG expansion. Expression of Wnt/β-catenin pathway genes (*Lef1*, *Wnt4*) showed no differences between genotypes in either sex at baseline (Supplementary Figure S2A), suggesting that Wnt signalling does not mediate the compensatory responses observed under basal conditions. These findings suggest that under basal conditions, MR in aldosterone-producing cells regulates proliferative capacity and ZG maintenance, with consequences on aldosterone production being compensated for by activation of alternative mechanisms.

Salt restriction reveals impaired aldosterone response with compensatory mechanisms in $MRKO^{Ad}$ mice

To determine whether MR becomes essential under conditions of increased aldosterone demand, and to assess the plasticity of the adrenal cortex, we subjected male and female mice to a low salt diet (LSD, <0.03% Na+) for 2 weeks, starting at 3 weeks of age until 5 weeks of age, designated as time point T1(Figure 4A; Supplementary Figure S3A). To study the ability of the adrenal cortex to reverse the effects of salt restriction, mice were then returned to standard diet for one week of recovery until 6 weeks of age, designated as time point T2 (Figure 4A; Supplementary Figure S3A). All analyses were performed at T1 (5 weeks, after LSD) and T2 (6 weeks, after recovery), with age-matched controls maintained on standard diet at both timepoints.

Hormonal Responses to Salt Restriction. Plasma aldosterone measurements revealed that wild-type males responded robustly to salt restriction, showing significantly elevated aldosterone levels during LSD compared to age-matched controls at T1 (Figure 4B, left). Similarly, wild-type females exhibited significant aldosterone elevation during LSD (Supplementary Figure S3B, left). This confirms the expected adaptive response to sodium deprivation in both sexes. $MRKO^{Ad}$ mice showed a significantly blunted aldosterone response. $MRKO^{Ad}$ mice of both sexes increased aldosterone production in response to LSD compared to their respective baseline controls, demonstrating retained capacity to respond to salt deprivation (Figure 4B; Supplementary Figure S3B, left panels). However, this response was significantly blunted compared to wild-type mice under LSD conditions in both males (Figure 4B, left) and females

(Supplementary Figure S3B, left), indicating that MR signaling in aldosterone-producing cells is required for maximal aldosterone response to sodium restriction.

Notably, MRKO^{Ad} mice of both sexes exhibited significantly elevated plasma corticosterone levels during LSD compared to both their own baseline controls and to wild-type mice under LSD conditions (Figure 4B, right; Supplementary Figure S3B, right), suggesting a compensatory shift toward corticosterone production when aldosterone synthesis is impaired. This glucocorticoid elevation may partially compensate for reduced mineralocorticoid activity through mineralocorticoid receptor activation in target tissues.

Recovery responses show sex-specific patterns. Following the one-week recovery period at T2, both wild-type and MRKO^{Ad} males showed significant decreases in aldosterone levels compared to LSD (Figure 4B, left), demonstrating normalization of the aldosterone response. Wild-type females similarly showed decreased aldosterone after recovery (Supplementary Figure S3B, left). However, females displayed more persistent genotype effects: even under basal conditions at T2, MRKO^{Ad} females showed reduced aldosterone compared to wild-type controls, and following recovery from LSD, MRKO^{Ad} females remained significantly below wild-type females (Supplementary Figure S3B, left), suggesting less complete recovery in females. Corticosterone levels in MRKO^{Ad} mice of both sexes normalized after recovery, decreasing significantly compared to LSD (Figure 4B, right; Supplementary Figure S3B, right), indicating that the compensatory corticosterone elevation was reversible. The reduced aldosterone production at T2 in control female mice of 6-weeks of age, not visible at 5 weeks (T1) nor at 12 weeks of age (Figure 3), suggests a compensated hormonal phenotype in MRKO^{Ad} mice, which is sex-specific and age dependent.

Morphological and Molecular Responses. Immunofluorescence analysis of Dab2, a ZG marker, revealed major changes in ZG architecture during salt restriction. In males, wild-type mice showed significant expansion of Dab2+ area during LSD compared to baseline controls, with partial normalization after recovery (Figure 4D; Figure 4F, left). Notably, wild-type males showed reduced Dab2+ ZG area at the T2 baseline compared to T1 baseline, indicating age-dependent changes in ZG architecture similarly to those previously described[14]. MRKO^{Ad} males showed reduced Dab2+ area at baseline, increased Dab2+ area during LSD compared to their baseline, but remained significantly below wild-type males during LSD (Figure 4D; Figure 4F, left), confirming impaired ZG expansion. Females showed similar patterns, with wild-type mice exhibiting ZG expansion during LSD with normalization after recovery, and reduced ZG area at T2 baseline compared to T1 (Supplementary Figure S3D; Supplementary Figure S3F, left). MRKO^{Ad} females showed blunted ZG expansion during LSD compared to their control (Supplementary Figure S3D; Supplementary Figure S3F, left).

AS immunofluorescence paralleled the Dab2 findings in both sexes. In males, wild-type mice showed increased number of AS+ cells during LSD with normalization after recovery (Figure 4C; Figure 4F, middle). MRKO^{Ad} males also elevated AS protein during LSD compared to baseline, but remained significantly lower than wild-type males under LSD (Figure 4C; Figure 4F, middle). Following recovery, MRKO^{Ad} males showed decreased AS expression below baseline levels (Figure 4F, middle). Females demonstrated similar patterns, with wild-type mice increasing AS expression during LSD and normalizing after recovery, while MRKO^{Ad} females showed reduced expression compared to wild-type during LSD (Supplementary Figure S3C; Supplementary Figure S3F, middle).

Quantitative PCR validated these observations. In males, *Cyp11b2* mRNA increased significantly in wild-type mice during LSD, while MRKO^{Ad} males showed blunted *Cyp11b2*

induction compared to wild-type LSD (Figure 4G, left). Interestingly, *Cyp11b1* mRNA was also significantly increased in wild-type males during LSD, but not in MRKO^{Ad} (Figure 4G, right), suggesting coordinated activation of steroidogenic capacity across cortical zones in response to salt restriction. In females, wild-type mice similarly increased *Cyp11b2* mRNA during LSD with normalization after recovery (Supplementary Figure S3G, left). However, unlike males, females showed no significant changes in *Cyp11b1* expression (Supplementary Figure S3G, right), revealing sex-specific differences in ZF activation during salt stress.

Body and adrenal weight changes reflect metabolic stress and compensatory growth. Body weight measurements revealed that male MRKO^{Ad} mice were heavier than wild-type controls at baseline (Supplementary Figure S5, upper left), consistent with our findings at 12 weeks of age. Both genotypes showed weight loss during LSD (Supplementary Figure S5, upper left). In males, both wild-type and MRKO^{Ad} mice showed increased left adrenal weight after recovery (Supplementary Figure S5, upper middle), suggesting compensatory organ growth. In females, MRKO^{Ad} mice showed bilateral adrenal enlargement during LSD (Supplementary Figure S5, lower middle and right), consistent with compensatory organ growth in response to impaired aldosterone synthesis and activation of the RAAS.

Lineage Tracing Reveals Sex-Specific ZG Dynamics. Cell lineage tracing was investigated in MRKO^{Ad}::mTmG mice, where mGFP marks cells with a history of *Cyp11b2* expression. In males, quantification of mGFP^{+} cells within the cortex showed no significant changes across conditions (Figure 4E; Figure 4F, right), suggesting that the proportion of cortical cells derived from the ZG lineage remains stable despite salt restriction and recovery in males.

In contrast, female MRKO^{Ad} mice showed a higher percentage of mGFP^{+} cells at baseline compared to wild-type controls (Supplementary Figure S3E; Supplementary Figure S3F, right), consistent with the expanded Dab2^{+} ZG observed at 12 weeks in MRKO^{Ad} females (Figure 2C). Interestingly, following recovery in LSD-fed mice, mGFP+ cell percentage decreased significantly in MRKO^{Ad} females (Supplementary Figure S3F, right), suggesting ZG lineage dynamics or increased centripetal migration of ZG-derived cells in female MRKO^{Ad} mice during recovery from salt stress.

Wnt/β-Catenin Pathway Dynamics Correlate with Sex-Specific Recovery Patterns. To investigate potential mechanisms underlying the sex-specific ZG expansion and recovery patterns, we examined expression of Wnt/β-catenin pathway genes, which are critical regulators of adrenal zonation and ZG maintenance. qPCR analysis revealed striking sex-specific differences in Wnt pathway dynamics that parallel the observed morphological changes (Supplementary Figure S2B-C).

In females, salt restriction activated Wnt signalling, with *Lef1* expression significantly increased in WT LSD compared to baseline controls, consistent with the observed ZG expansion. Notably, during recovery, Wnt signalling was actively suppressed: *Lef1* significantly decreased in WT LSD+REC compared to WT LSD, and *Axin2* similarly decreased. *Wnt4* expression showed no significant changes across conditions. This pattern of Wnt activation during stress followed by active suppression during recovery aligns with the complete normalization of ZG size and aldosterone production observed in females.

In contrast, males showed persistent Wnt pathway activation during the recovery phase. *Lef1* expression was significantly elevated in WT LSD+REC compared to both age-matched controls and to WT LSD, indicating sustained Wnt signalling during recovery. Similarly, *Axin2* expression increased during recovery. This persistent Wnt activation in males correlates with

the partial normalization of ZG size observed after recovery, in contrast to the complete normalization seen in females. The continued Wnt signaling may slow or limit the rate of ZG regression, preventing full return to baseline architecture and potentially maintaining the ZG in a primed state for rapid re-expansion upon future salt restriction.

Interestingly, MRKO^{Ad} males showed increased *Wnt4* expression during LSD compared to their baseline controls, suggesting potential compensatory Wnt pathway activation in the absence of functional MR signalling in aldosterone-producing cells. No other genotype-specific differences in Wnt pathway genes reached significance.

These findings reveal that Wnt/β-catenin signalling dynamics differ fundamentally between sexes during adaptation to salt restriction: females show transient Wnt activation that is actively turned off during recovery, while males exhibit prolonged Wnt activation during recovery. This sex-specific temporal regulation of Wnt signalling provides a molecular mechanism underlying the differential recovery kinetics observed in ZG morphology, aldosterone production, and steroid pathway profiles between males and females. MR knock-out appears to affect the Wnt/β-catenin response both during the challenge and at recovery.

Steroid Profiling Reveals Distinct Steroidogenic Responses and Sex-Specific Recovery. Comprehensive steroid profiling by LC-MS/MS revealed distinct steroidogenic responses to LSD in both sexes (Figure 4H-I; Supplementary Figure S3H-I; Supplementary Tables S7-S14). PCA in males showed clear separation between control and LSD groups along the first (Dim1, 55.9 % variance) with 11-hydroxy-11-DOC, progesterone, 11-DOC and corticosterone as the primary contributors to this separation (Supplementary Figure S4A). In females, Dim1 (38.9 % variance) was driven by 18-hydroxycorticosterone, aldosterone and pregnelenone, (Supplementary Figure S4B), revealing sex-specific steroidogenic profiles during salt restriction. Wild-type LSD samples showed greater displacement along Dim1 than MRKO^{Ad} LSD samples in both sexes, indicating more pronounced steroidogenic activation in wild-type mice. The second dimension (Dim2) in males (23.2% variance) was primarily driven by 18-hydroxycorticosterone and aldosterone, while in females Dim2 (29.6 % variance) was driven by 11-DOC, corticosterone and 18-hydroxy-11-DOC (Supplementary Figure S4). Hierarchical clustering confirmed these patterns, with LSD samples forming a distinct cluster with elevated pathway steroids, while recovery samples clustered with baseline controls, demonstrating reversibility of the hormonal phenotype (Figure 4H-I; Supplementary Figure S3H-I).

Males showed complete normalization with no persistent genotype differences after recovery (all comparisons: ns; Supplementary Table S10). In contrast, females displayed incomplete recovery, with MRKO^{Ad} females showing persistently reduced aldosterone (during recovery: P=0.015; at T2: P=0.004) and 18-hydroxycorticosterone (P=0.040; P=0.010) compared to wild-type (Supplementary Table S14).

Together, these results demonstrate that MR signaling regulates multiple steps in the aldosterone synthesis pathway simultaneously, coordinating the complete steroidogenic response to salt restriction. MRKO^{Ad} mice retain capacity to respond but show blunted aldosterone production with compensatory corticosterone elevation. The responses are largely reversible in males but show persistent genotype effects in MRKO^{Ad} females, revealing sex-specific consequences of disrupted MR signalling.

X-Zone Lineage Conversion Shows Altered Dynamics in MRKO^{Ad} Females

To investigate potential alterations in ZF-to-ZX lineage conversion during salt restriction, we performed detailed analysis of the sexually dimorphic ZX in female mice. The ZX, located at

the innermost boundary between the ZF and medulla, contains a subset of cells derived from the Cyp11b2^{+} ZG lineage that have migrated centripetally through the ZF and undergo conversion to ZX identity, as previously described (Faedda et al., bioRxiv 2025).

Overall ZX size remains stable during salt restriction. Co-immunofluorescence of mGFP (Cyp11b2-lineage traced cells) and 20αHSD (ZX marker) allowed visualization of cells at different stages of lineage conversion (Figure 5A-B). Quantification of total 20αHSD^{+} area as percentage of cortex showed no significant changes across conditions in either genotype (Figure 5C), indicating that overall ZX size remained stable during the LSD challenge and recovery period. However, analysis of mGFP^{+}20αHSD^{+} double-positive cells, which represent ZF cells actively converting to ZX identity, revealed altered conversion dynamics in MRKO^{Ad} females. The proportion of double-positive cells within the total cortex was significantly increased in MRKO^{Ad} females after recovery from LSD compared to T1 LSD itself (Figure 5D), suggesting enhanced lineage conversion following salt stress. When examining double-positive cells specifically as a percentage of the ZX area, MRKO females showed an age-dependent increase from T1 to T2 (Figure 5E), indicating progressive accumulation of cells undergoing active ZF-to-ZX conversion during this developmental period.

Quantitative PCR analysis of *Akr1c18* (encoding 20αHSD) revealed that wild-type females increased ZX marker expression during LSD, with persistent elevation after recovery (Figure 5E), indicating transcriptional activation of ZX identity during salt stress. This suggests that salt restriction may influence not only ZG expansion but also the dynamics of centripetal cell migration and ZX formation.

These results demonstrate that MR regulates the rate of ZF-to-ZX lineage conversion in female mice. MRKO^{Ad} females show increased conversion dynamics, particularly after recovery from salt challenge, suggesting that MR normally restrains or modulates the centripetal migration and conversion of ZF cells to ZX identity. This may represent an adaptive response to altered steroidogenic demands or ZG architecture in the absence of functional MR in aldosterone-producing cells.

Single-nuclei transcriptomic atlas reveals heterogeneity within the adrenal cortex and following LSD

Building on the morphological evidence of MR-dependent cortical remodeling (Figure 4D-F, Supplementary Figure S3D-F), we performed single-nucleus RNA sequencing (snRNA-seq) of male mouse adrenal glands across four experimental conditions: wild-type mice on standard diet (WT SD), wild-type mice on low-salt diet (WT LSD), ZG-specific MR knockout mice on standard diet (MKO SD), and MKO mice on low-salt diet (MKO LSD) (Figure 6A).

Unsupervised graph-based clustering on Harmony-corrected principal components identified eight distinct populations: ZG (11.0%), ZG-ZF transition zone (ZG_ZF, 14.6%), ZF cluster 0 (ZF1, 23.1%), ZF clusters 1-10 (ZF2, 27.9%), adrenal medulla (6.4%), endothelial cells (11.4%), fibroblasts (1.9%), and macrophages (3.7%) (Figure 6A-B, Supplementary Figure S8A). Each population expressed canonical marker genes consistent with their identity: ZG cells expressed *Cyp11b2* and *Dab2*; ZF cells expressed *Cyp11b1*; medullary cells expressed *Th* and *Pnmt*; and endothelial cells expressed *Pecam1* (Figure 6D, Supplementary Figure S8B-C). Notably, the ZF resolved into two transcriptionally distinct subpopulations. The first, designated ZF1 (Seurat cluster 0, 23.1% of nuclei), occupied a spatially separated region in UMAP space and exhibited distinct gene expression patterns (Supplementary Figure S9A). The remaining ZF cells (Seurat clusters 1-10, collectively designated ZF2, 27.9%) formed a

cohesive cluster sharing canonical ZF identity. The existence of two ZF subpopulations with distinct transcriptional programs suggested potential differences in their functional capacity and plasticity responses.

Salt restriction induced significant shifts in cortical cell type composition in wild-type mice. In accordance to morphological observations, the ZG population expanded from 9.3% to 14.6% of cortical cells under LSD, while the ZG_ZF transition zone increased from 12.0% to 18.3% (Figure 6C). These changes were markedly attenuated in $MRKO^{Ad}$ mice (ZG: 9.6% → 11.5%; ZG_ZF: 14.9% → 13.3%), suggesting that MR signalling drives cortical remodelling in response to sodium restriction. These single-nuclei transcriptomic findings align with the morphological measurements of ZG expansion and centripetal migration patterns observed histologically (Figure 4D-F, Supplementary Figure S3D-F), providing independent validation at single-cell resolution.

snRNAseq reveals Cyp11b2 induction within the ZF. Given the robust Cyp11b2+ cortical expansion observed morphologically with salt restriction (Figure 4D-F), we sought to define which specific adrenocortical cell populations contribute to this increase at single-cell resolution. UMAP visualization of *Cyp11b2* expression across all cortical populations revealed an unexpected pattern: salt restriction induced robust *Cyp11b2* expression not only in the ZG and transition zone as anticipated, but deep within a distinct ZF subpopulation (ZF1) that normally produces only glucocorticoids (Figure 7A). Under baseline conditions, ZF1 cells showed minimal *Cyp11b2* expression, consistent with their ZF identity. However, salt restriction triggered *Cyp11b2* upregulation specifically in ZF1, while the adjacent ZF2 subpopulation showed minimal response. This finding was unexpected: zona fasciculata cells are canonically defined by Cyp11b1 expression and corticosterone production, not aldosterone synthesis. Moreover, ZF1 robustly induced *Cyp11b2* while ZF2 remained largely unresponsive despite both subpopulations occupying the same anatomical layer and experiencing identical systemic signals, suggesting fundamental differences in plasticity capacity between these subpopulations.

Integration of marker co-expression and gene signature analysis reveals MR-dependent plasticity of adrenocortical cell populations. To define MR's role across all cortical populations beyond ZG, and determine which subpopulations possess plasticity capacity, we quantified cells co-expressing both *Cyp11b1* and *Cyp11b2* across all populations and conditions, revealing striking heterogeneity in plasticity capacity with differential MR-dependence (Figure 7A-B). As double-positive status does not reflect authentic ZG identity, and to distinguish genuine transdifferentiation from partial marker induction, we calculated a comprehensive ZG gene signature score encompassing six canonical markers: *Cyp11b2*, *Dab2*, *Wnt4* (Wnt ligand essential for ZG maintenance), *Shh* (sonic hedgehog, ZG developmental marker), *Rspo3* (R-spondin 3, Wnt pathway enhancer), and *Axin2* (direct Wnt target gene indicating active Wnt signalling). This gene set represents the core transcriptional program that distinguishes ZG from ZF cells and includes both effector genes for aldosterone production and upstream signalling components that maintain ZG identity. Module scores above zero indicate cells with expression profiles characteristic of the ZG state, while negative scores indicate lack of ZG identity. Integration of double-positive cell quantification with ZG signature score analysis revealed striking heterogeneity in plasticity mechanisms and MR function across cortical populations (Figure 7B-D). In WT animals**,** multiple populations showed increased double-positive cells under salt restriction with distinct signature score patterns: ZG cells maintained

consistently positive scores (mean range: 0.55-0.61 across all four conditions); ZG_ZF and ZF1 cells both achieved positive signature scores under salt restriction (0.47 and 0.39, respectively); while ZF2 cells showed substantial *Cyp11b2* induction yet failed to achieve positive signature scores (mean range: -0.20 to -0.02 across all conditions) (Figure 7C). In MRKO^{Ad} mice**,** ZG cells maintained positive signature scores across both dietary conditions and ZG_ZF cells similarly retained positive scores; in contrast, ZF1 cells failed to achieve positive signature scores under salt restriction, remaining negative; ZF2 cells maintained negative scores in both WT and MRKO^{Ad}. These findings demonstrate that MR plays fundamentally different roles across cortical populations, controlling proliferation in established ZG cells while regulating transdifferentiation in ZF subpopulations.

ZG maintains identity through MR-dependent proliferation. ZG cells maintained their aldosterone-producing identity across all conditions, with ZG signature scores remaining consistently positive (mean: 0.57 wild type SD, 0.61 wild type LSD, 0.55 MRKO^{Ad} SD, 0.58 MRKO^{Ad} LSD; Figure 7C, Supplementary Figure S10A). Under salt restriction, ZG cells showed 2,375 differentially expressed genes (adjusted $p < 0.05$, Supplementary Figure S10B), including enhanced expression of canonical ZG markers (*Cyp11b2, Dab2, Wnt4*) alongside genes involved in ZG maintenance and metabolic reprogramming, reflecting enhanced aldosterone production capacity. Analysis of MR-dependent genes in ZG revealed 1,247 genes requiring MR for normal expression under salt restriction (wild type LSD vs MRKO^{Ad} LSD, adjusted $p < 0.05$, Supplementary Figure S10C; Supplementary Table S6), with 734 genes MR-enhanced (higher in wild type) and 513 genes MR-repressed (higher in MRKO^{Ad}). This MR-dependent transcriptional activity explains the attenuated ZG expansion in MRKO^{Ad} mice (9.6% → 11.5%) compared to wild-type (9.3% → 14.6%): this indicates that MR is not required for ZG identity maintenance but supports proliferative expansion of the ZG layer during salt restriction.

The ZG_ZF transition zone demonstrates robust, position-driven plasticity with minimal MR-dependence. At baseline, 13.2% of ZG_ZF cells were *Cyp11b1-Cyp11b2* double-positive in wild-type mice, reflecting their anatomical position at the zonal boundary and transitional nature from ZG to ZF (Supplementary Figure S10D). Under salt restriction, this cell component increased to 63.0% in wild-type mice, and 50.7% in MRKO^{Ad} mice (Figure 7B). This translates to only 10.3% MR-dependence, indicating that ZG_ZF plasticity is not primarily driven by cell-autonomous MR signaling. Remarkably, ZG_ZF cells achieved robustly positive ZG signature scores under salt restriction (mean: 0.47), confirming shift towards a ZG identity (Figure 7C). Under salt restriction, ZG_ZF cells showed the largest transcriptional response among all cortical populations, with 2,247 differentially expressed genes (adjusted $p < 0.05$, Supplementary Figure S10E). This massive transcriptional remodelling was accompanied by coordinate upregulation of ZG identity genes (*Cyp11b2, Dab2, Wnt4, Rspo3*), distinguishing ZG_ZF's response from incomplete conversion. Remarkably, this plasticity showed minimal MR-dependence: comparison of wild-type versus MRKO^{Ad} mice under LSD revealed 1,977 MR-dependent genes (WT LSD vs MRKO^{Ad} LSD, adjusted $p < 0.05$, Supplementary Figure S10F), yet these accounted for only 10% of the phenotypic change in ZG signature acquisition. While 1,977 genes represents substantial MR transcriptional activity, the core ZG identity genes (*Cyp11b2, Dab2, Wnt4, Rspo3*) that define the ZG signature score were largely MR-independent in ZG_ZF cells. The high baseline double-positive percentage, robust salt response independent of MR, and positive ZG signature score collectively demonstrate that proximity

to the ZG microenvironment enables these cells to readily adopt aldosterone-producing cell characteristics.

ZF1 exhibits strongly MR-dependent transdifferentiation with authentic ZG identity acquisition. Double-positive cells increased from 5.79% at baseline to 37.4% in wild-type mice under LSD but only reached 18.7% in $MRKO^{Ad}$ mice, demonstrating 48.6% MR-dependence (Figure 7B). This indicates that approximately half of ZF1's plasticity capacity requires cell-autonomous MR signaling. Critically, ZF1 showed marked acquisition of ZG identity in wild-type mice, with mean ZG signature scores increasing from 0.09 (WT SD) to 0.39 (WT LSD) ($\Delta = +0.30$, $p < 2.2\times10^{-16}$, Figure 7C). This change represents ZF1 crossing from near-zero to robustly positive ZG signature, indicating acquisition of ZG transcriptional identity rather than merely increased expression of individual genes. For comparison, established ZG cells maintained signature scores of 0.57 (WT SD) to 0.61 (WT LSD). In $MRKO^{Ad}$ mice, the ZG signature response in ZF1 was reduced by 69% (WT change: +0.30 vs MKO change: +0.09, $p < 10^{-50}$), demonstrating that MR signaling drives the majority of ZF transdifferentiation (Figure 7C). Analysis of individual ZG marker genes confirmed this pattern. *Cyp11b2* showed 8.6-fold induction in wild-type ZF1 cells but only 1.0-fold induction in $MRKO^{Ad}$ cells, confirming MR-dependent regulation. *Wnt4, Rspo3*, and *Dab2* showed comparable MR-dependent patterns, with WT mice achieving substantially higher expression under salt restriction than $MRKO^{Ad}$ mice. Interestingly, *Ren1* (renin) was one of the most upregulated genes in wild type mice, increased 157-fold in WT but being markedly blunted in $MRKO^{Ad}$ mice. These findings establish ZF1 as the ZF subpopulation capable of MR-driven transdifferentiation with authentic ZG identity acquisition.

ZF2 shows paradoxical Cyp11b2 induction without acquisition of ZG identity. Despite being the most abundant ZF subpopulation (27.9% of nuclei), ZF2 cells demonstrated limited plasticity in response to LSD. Double-positive cells increased from 5.3% at baseline to 40.8% in wild-type mice under salt restriction, superficially similar to ZF1's response (Figure 7B). However, in contrast to ZF1, ZF2 showed substantial *Cyp11b2* induction (12.5-fold increase) yet failed to acquire positive ZG gene signature, with scores remaining negative across all conditions (mean range: -0.20 to -0.02, Figure 7C). This dissociation between *Cyp11b2* induction and acquisition of comprehensive ZG identity demonstrates that co-expression of individual ZG markers is insufficient for authentic transdifferentiation. ZF2 appears capable of partial, likely paracrine-driven *Cyp11b2* upregulation, potentially responding to elevated circulating ACTH or local angiotensin II, without achieving the coordinated transcriptional reprogramming that defines true ZG identity. These findings establish the ZG signature score as a critical tool for distinguishing genuine cellular plasticity from simple marker co-expression.

Together, these analyses establish that MR plays distinct, population-specific roles across the adrenal cortex (Figure 7D): (1) in ZG, MR controls proliferative expansion rather than identity maintenance; (2) in ZG_ZF transition zone, cellular plasticity operates largely independent of MR (10.3% MR-dependent), possibly mediated by microenvironmental Wnt signals from the adjacent ZG layer; (3) in ZF1, cell-autonomous MR-driven transdifferentiation requires MR-dependent signals to achieve full ZG identity (48.6% MR-dependent); and (4) in ZF2, incomplete conversion shows *Cyp11b2* induction without coordinated transcriptional reprogramming, possibly reflecting paracrine responses to systemic hormonal changes without capacity for authentic transdifferentiation.

Baseline Transcriptional Priming Predisposes ZF1 to Plasticity

Having established that ZF1 undergoes authentic MR-dependent transdifferentiation while ZF2 lacks this capacity despite exposure to identical hormonal signals, we next sought to understand the molecular basis for this differential plasticity. To identify baseline features that predispose ZF1 to plasticity, we performed comprehensive transcriptomic comparison between ZF1 and ZF2 subpopulations at baseline (wild-type mice, standard diet; 6,859 ZF1 cells, 7,328 ZF2 cells). This analysis revealed 5,580 significantly differentially expressed genes (adjusted $p < 0.05$, Wilcoxon rank-sum test), with 2,511 genes higher in ZF1 and 3,069 genes higher in ZF2, demonstrating that these subpopulations represent distinct functional states within the ZF (Supplementary Figure S9A-B).

Volcano plot analysis revealed ZF1's enrichment for mitochondrial electron transport chain components (mt-Nd1, mt-Nd2, mt-Co1, mt-Cytb), secretory granule proteins (*Chgb*, 3.2 $\log_2$FC; *Chga*, 2.8 $\log_2$FC), steroidogenic enzymes (*Hsd3b1*, 2.1 $\log_2$FC; *Cyp11b1*, 1.8 $\log_2$FC), and translation machinery (Supplementary Figure S9B). Heatmap analysis of the top 60 differentially expressed genes confirmed these patterns remained stable across all experimental conditions, indicating constitutive rather than condition-dependent differences between the subpopulations (Supplementary Figure S9C). Gene Ontology enrichment analysis confirmed ZF1's transcriptional priming for high metabolic activity, with the top enriched pathways including ribonucleoprotein complex biogenesis (p.adj = 8.4×10^{-98}), cytoplasmic translation (p.adj = 2.1×10^{-67}), RNA splicing (p.adj = 1.8×10^{-54}), ribosome biogenesis (p.adj = 3.1×10^{-32}), and oxidative phosphorylation (p.adj = 1.2×10^{-45}) (Supplementary Figure S9D). Module score analysis quantified this metabolic advantage: ZF1 cells showed significantly higher OXPHOS scores (mean: 0.89 vs -0.35 in ZF2, $p < 10^{-300}$), ribosome scores (mean: 0.92 vs -0.38, $p < 10^{-300}$), and mitochondrial gene content (mean: 6.2% vs 4.1%, $p < 10^{-300}$) (Supplementary Figure S9E). This constitutive metabolic infrastructure positions ZF1 to rapidly respond to plasticity cues and meet the energetic demands of aldosterone biosynthesis.

In contrast, ZF2 showed enrichment for structural and maintenance functions rather than biosynthetic capacity. The top ZF2-enriched pathways included small GTPase-mediated signal transduction (p.adj = 2.3×10^{-28}), positive regulation of cellular catabolic processes, regulation of autophagy, regulation of GTPase activity, and macroautophagy (Supplementary Figure S9D), alongside elevated expression of extracellular matrix components (*Col1a1, Col3a1, Col5a1*), basement membrane proteins (*Lamb2, Lamc1*), and cell adhesion molecules. This transcriptional signature suggests ZF2 plays a more structural, tissue-maintenance role within the ZF, with gene expression programs optimized for cellular homeostasis and extracellular matrix remodelling rather than dynamic steroidogenic responses. These baseline transcriptional differences explain ZF2's inability to undergo authentic transdifferentiation: the observation that ZF2 can induce *Cyp11b2* without coordinate upregulation of metabolic support programs demonstrates that plasticity competence requires pre-existing biosynthetic infrastructure that cannot be rapidly assembled in response to acute signals. Together, these findings establish that ZF1 represents a metabolically primed, biosynthetically competent ZF subpopulation predisposed to transdifferentiation, while ZF2 serves a distinct structural-maintenance role that lacks the capacity for authentic ZG conversion.

scRNAseq reveals MR-dependent transcriptional programs underlying ZF1 plasticity. Having established that ZF1 undergoes transdifferentiation in an MR-dependent manner, we next sought to define the transcriptional programs underlying this plasticity at the molecular level.

We performed differential expression analysis comparing ZF1 cells from wild-type mice under salt restriction versus standard diet. This analysis identified 452 significantly upregulated genes and 389 downregulated genes (adjusted $p < 0.05$, Wilcoxon rank-sum test). Heatmap visualization of the top 60 differentially expressed genes revealed a coordinated transcriptional response (Figure 8A). Upregulated genes included key ZG markers (*Cyp11b2*, 3.4 $\log_2$FC; *Ren1*, 7.3 $\log_2$FC; *Dab2*, *Wnt4*, *Rspo3*) alongside metabolic reprogramming genes (Slc16a3, 9.5 $\log_2$FC; *Eno3*, 3.6 $\log_2$FC; *Gpha2*, 3.8 $\log_2$FC), indicating acquisition of both aldosterone-producing identity and enhanced metabolic capacity. Downregulated genes included ZF-associated transcripts and cell cycle regulators, consistent with a shift from proliferative ZF identity toward differentiated ZG function. Gene Ontology enrichment analysis of upregulated genes revealed significant enrichment for oxidative phosphorylation, mitochondrial ATP synthesis, electron transport chain, and steroid hormone biosynthesis, indicating that ZF1 transdifferentiation requires substantial metabolic reprogramming. To determine which plasticity genes require MR, we compared ZF1 transcriptomes between wild-type and MRKO^{Ad} mice under LSD (WT LSD vs MRKO^{Ad} LSD; 5,431 cells WT LSD, 4,344 cells MRKO^{Ad} LSD). This identified 186 MR-enhanced genes (higher in WT) and 297 MR-repressed genes (higher in MRKO^{Ad}, adjusted $p < 0.05$). Heatmap analysis of the top 60 MR-dependent genes revealed robust expression differences across genotypes, with MR-enhanced genes including critical aldosterone pathway components (*Cyp11b2, Ren1, Agtr1b, Inha*), Wnt signaling modulators (*Wnt4, Rspo3, Dkk3*), and metabolic regulators (*Slc16a3, Gpha2, Slc2a4*) (Figure 8B). Notably, MR-enhanced genes showed strong upregulation specifically under salt restriction in wild-type mice but failed to reach comparable levels in MRKO^{Ad} mice, demonstrating that MR is required for their salt-induced expression.

MR-dependent genes are functionally concentrated among the highest fold-change plasticity genes. To quantify MR's contribution to the plasticity program, we identified genes that were both salt-induced and MR-dependent. Of the 452 upregulated plasticity genes, 127 (28%) were significantly reduced in MRKO^{Ad} mice (Figure 8C), indicating these genes require MR for their salt-induced expression. Notably, while this represented a minority of plasticity genes by count, these 127 MR-dependent genes were highly enriched among the most robustly induced transcripts. Specifically, 28 of the top 30 plasticity genes (93%) showed MR-dependence, and 18 genes appeared in both top 30 lists (plasticity and MR-dependent), including the highest fold-change inducers *Slc16a3* (9.5 $\log_2$FC), *Ren1* (7.3 $\log_2$FC), *Cyp11b2* (3.4 $\log_2$FC), and *Inha* (3.4 $\log_2$FC). This selective enrichment explains how 28% of genes by count account for 69% of the functional ZG signature score change (Figure 7C), demonstrating that MR preferentially controls genes with the largest effects on cell identity. In contrast, the 325 MR-independent plasticity genes showed enrichment for immediate-early stress response genes (*Fos, Jun, Egr1*), general transcriptional machinery, and structural proteins that may represent initial adaptive responses to salt restriction independent of MR-mediated transdifferentiation programs.

MR-dependent genes converge on core metabolic and steroidogenic pathways. To understand the biological processes controlled by MR during plasticity, we performed Gene Ontology enrichment analysis on salt-induced and MR-dependent gene sets. The top 20 enriched pathways revealed striking convergence: 17 of 20 pathways (85%) were significantly enriched in both analyses (Figure 8D). These shared pathways were predominantly metabolic, including oxidative phosphorylation, ATP synthesis coupled electron transport, mitochondrial ATP

synthesis coupled electron transport, and aerobic respiration, alongside steroid hormone biosynthetic processes. Notably, these convergent pathways included ATP metabolic processes, mitochondrial electron transport chain components (NADH to ubiquinone, cytochrome c to oxygen), and energy derivation by oxidation of organic compounds, all critical for sustaining the increased energetic demands of aldosterone biosynthesis. Aldosterone synthesis via *Cyp11b2* requires three sequential enzymatic reactions (11β-hydroxylation, 18-hydroxylation, and 18-oxidation), each consuming NADPH and oxygen, in contrast to corticosterone synthesis which requires only 11β-hydroxylation. The enrichment of mitochondrial ATP synthesis and oxidative phosphorylation pathways demonstrates the metabolic reprogramming required for this transition from corticosterone to aldosterone production.

Together, these single-cell transcriptomic analyses reveal that MR plays distinct, population-specific roles across the adrenal cortex. In ZG, MR supports proliferative expansion without controlling identity. In ZG_ZF, environmental signals drive plasticity largely independent of MR. In ZF1, MR acts as a master regulator of the metabolic reprogramming required for transdifferentiation, with MR-dependent genes selectively enriched among high fold-change transcripts and convergent on core metabolic pathways.

Discussion

In this work, we investigated the cell-autonomous functions of MR in aldosterone-producing cells of the ZG of the adrenal cortex using a Cyp11b2-Cre knockout model combined with morphological and functional investigations, comprehensive steroid profiling and single-nucleus transcriptomics. Our findings show that the MR is involved in regulating ZG function and aldosterone synthase expression in an autocrine-paracrine loop. Importantly, they reveal that MR acts as a central coordinator that modulates adaptive responses, enables specific cell populations for transdifferentiation, and regulates proliferative capacity in zone-specific and sex-specific manner.

Under basal conditions, our study revealed a dissociation between ZG architecture and aldosterone production in $MRKO^{Ad}$ mice. Female $MRKO^{Ad}$ mice show expanded Dab2+ ZG area but reduced AS+ cells, while males maintain normal ZG dimensions. Both sexes exhibit reduced *Cyp11b2* expression, reduced number of AS+ cells, and reduced cell proliferation. Despite these changes, circulating aldosterone levels are comparable to wild type mice under basal conditions in both sexes. Comprehensive profiling of angiotensin peptides and plasma renin activity revealed normal levels of RAS components, although a slight decrease of the AA2R may indicated a compensated phenotype in male mice. These results indicate that MR is involved in regulating aldosterone production in the ZG via an autocrine-paracrine feedback loop regulating *Cyp11b2* and AS expression and that cell-autonomous mechanisms rather than systemic feedback loops may be involved in maintaining appropriate aldosterone levels in $MRKO^{Ad}$ mice.

The mechanism underlying maintained aldosterone output may involve compensatory PKA pathway activation. $MRKO^{ZG}$ mice of both sexes show increased phosphorylated CREB, while males additionally upregulate PKA catalytic subunit expression. This compensation is consistent with known PKA functions to enhance steroidogenic capacity post-translationally by directly phosphorylating StAR, increasing cholesterol transfer to the inner mitochondrial membrane without requiring increased gene expression[28,29]. Consistent with this mechanism, *Star* mRNA levels remain unchanged despite increased steroidogenic output per cell. Our data also show sexually dimorphic mechanisms to maintain hormonal output, including architectural compensation with enlarged ZG in females and possibly a metabolic enhancement in males, allowing to increase the steroid output per cell. Remarkably, female mice show expanded ZG area but reduced number of AS+ aldosterone-producing cells. This may reflect a cell-autonomous, autocrine regulation of *Cyp11b2* expression by the MR, with a compensatory recruitment of progenitor cells into the ZG attempting to restore the depleted AS+ cell pool. The selective occurrence of this expansion in females, who exhibit higher baseline adrenal turnover rates, may reflect their capacity of engaging both subcapsular and ZG progenitors[30] for adrenal regeneration, whereas males, are devoid of the capacity for such expansion and instead may rely on metabolic adaptations within existing cells.

Salt restriction induced important morphological changes in the adrenal cortex, with substantial ZG expansion and increased AS+ cell populations in both sexes, with reduced dynamic plasticity in $MRKO^{ZG}$ mice. snRNAseq analysis revealed considerable cellular heterogeneity

in adaptive mechanisms. Indeed, three mechanistically distinct plasticity strategies were observed in different cell populations: position-dependent plasticity at the ZG_ZF transition zone, cell-autonomous MR-driven transdifferentiation in metabolically a primed ZF subset, and incomplete marker induction without real functional conversion in other ZF subpopulations.

The ZG_ZF transition zone represents a specialized microenvironment where potential positional signals may drive plasticity, this phenomenon being largely independent of MR. Double *Cyp11b2/Cyp11b1*-positive cell numbers increased substantially under salt restriction in both genotypes, with modest MR-dependence. Integration of *Cyp11b2/Cyp11b1* co-expression quantification with ZG signature score analysis revealed that these cells achieve authentic ZG identity, with positive signature scores indicating complete transcriptional reprogramming of ZG_ZF transitional cells. Transcriptional profiles in this cell population suggest that local signaling factors, such as Wnt, Shh, or Rspo gradients, may drive plasticity independently of MR.

Remarkably, a specific ZF subpopulation (ZF1 cells) exhibited strong MR-dependent ZF to ZG plasticity despite their ZF identity. Under LSD, wild-type ZF1 cells dramatically increased the percentage of *Cyp11b2/Cyp11b1* double-positive cells and achieved positive ZG signature scores, indicating authentic transdifferentiation. MRKO^{Ad} mice showed marked impairment of this response, revealing MR requirement. ZF1 cells show selective plasticity based on pre-existing necessary steroidogenic machinery. They express high levels of mitochondrial biosynthetic enzymes and have enhanced oxidative phosphorylation capacity. This metabolic priming enables rapid aldosterone production upon appropriate signals, but requires MR to coordinate the transcriptional program. ZF2 cells in contrast, despite showing substantial *Cyp11b2* induction, failed to achieve positive ZG signature scores and maintained low aldosterone biosynthetic capacity, revealing incomplete conversion without the metabolic foundation required for functional aldosterone biosynthesis.

Pathway enrichment analysis comparing MR-dependent genes with plasticity-associated genes revealed substantial functional convergence. The high degree of pathway overlap (85%) despite modest gene count overlap (28%) indicates that MR-dependent genes are functionally concentrated in rate-limiting metabolic programs required for aldosterone biosynthesis. Pathways unique to the plasticity analysis included protein folding and cellular stress responses, likely representing general adaptation to transcriptional reprogramming, while MR-specific pathways were minimal, further supporting that MR controls the core functional output of the plasticity program rather than parallel processes. Among shared pathways, steroid hormone biosynthetic process enrichment directly confirmed MR controls aldosterone synthesis enzymes and energy metabolism pathways, both of which are needed for steroidogenesis.

MRKO^{Ad} mice showed compensatory corticosterone elevation during salt restriction, which has functional significance: corticosterone binds MR with affinity similar to aldosterone[31], and several-fold elevation may partially overcome 11β-HSD2 protection, providing substitute mineralocorticoid activity. This compensation suggests the adrenal can reroute steroid biosynthesis when the aldosterone pathway is impaired. Alternatively, MR absence may lead

to cellular reprogramming and modified engagement of the ZF. Indeed, we have previously shown that the adrenocortical response to a LSD involves major transcriptional changes in the ZF[14]. The reversibility upon recovery indicates acute metabolic adaptation rather than permanent reprogramming. Recovery from salt restriction revealed sex-specific dynamics with distinct underlying mechanisms revealed by Wnt/β-catenin pathway analysis. Females showed transient Wnt activation with complete recovery: wild-type mice increased *Lef1* during salt restriction, then actively suppressed Wnt signalling during recovery with decreased *Lef1* and *Axin2*, paralleling complete normalization of ZG size, *Cyp11b2* expression, and aldosterone production. Males showed a different pattern: sustained elevation of *Lef1* and *Axin2* during recovery, correlating with incomplete normalization of ZG architecture yet complete hormonal normalization. This apparent contradiction suggests prolonged Wnt activation maintains the ZG in a primed state for rapid re-expansion without necessarily maintaining elevated steroid output. MRKO^{Ad} females showed persistent genotype-specific reductions in aldosterone and 18-hydroxycorticosterone at recovery, indicating MR plays a sustained role in maintaining optimal ZG capacity even after challenges resolve. MRKO^{Ad} males showed compensatory *Wnt4* upregulation during salt restriction, suggesting Wnt pathway activation can partially substitute for MR signalling. The difference between transient activation with active suppression in females versus persistent activation in males indicates that Wnt/β-catenin signalling may be involved in regulating recovery dynamics.

An important consideration is the developmental stage at which we initiated salt restriction compared to other studies. LSD was started at 3 weeks of age, immediately post-weaning, whereas our previous lineage tracing study using the same genetic model initiated at 4 weeks of age[14]. Despite similar experimental durations and genetic models, the current study observed greater ZG expansion. This likely reflects enhanced adrenal plasticity at 3 weeks when the ZG is still developmentally active and progressiely decreasing in size, compared to 4 weeks when architecture has stabilized[14]. This difference in plasticity response over just one week of development suggests a developmental critical window for maximal adrenal plasticity immediately post-weaning.

In conclusion, our study reveals that MR in aldosterone-producing cells of the ZG serves different roles in regulating aldosterone biosynthesis, proliferation, metabolic priming, and adaptive responses with zone-specific and sex-specific differences. Although MR seems not essential for maintaining basal aldosterone production, despite major effects on AS expression, it coordinates maximal steroidogenic responses through metabolic transformation. The adrenal cortex employs three mechanistically distinct plasticity strategies, with compensatory mechanisms including PKA activation and corticosterone elevation maintaining ZG function when MR is absent. Sex-specific Wnt/β-catenin signalling dynamics provide a mechanistic basis for differential recovery patterns. These findings advance our understanding of adrenocortical function, revealing a central role of the MR in regulating ZG homeostasis via an autocrine-paracrine loop as well as novel sex-specific mechanisms of adrenal adaptation to environmental stimulation.

Materials and methods

Handling and generation of *Cyp11b2-Cre::Mr* and *Cyp11b2-Cre::Mr::mTmG* mouse model

Animal studies were conducted according to the guidelines and regulations formulated by the European Commission for experimental use (Directive 2010/63/EU). The use of animals and experimental protocols were approved by the local Ethics Committee of Université Paris Cité (N° 17-020) and by the French Ministère de l'Enseignement Supérieur, de la Recherche et de l'Innovation (APAFIS authorization number #11509-201703281427107 v4). All animals were group-housed and bred in a dedicated specific pathogen-free (SPF) facility with 12h/12h light-dark cycles, ad libitum access to food and water, and were checked daily. Health status was routinely monitored to maintain SPF grade. Nr3c2-flox/flox mice (exons 5 and 6 flanked by loxP sites) were obtained from Institut Clinique de la Souris (ICS-PHENOMIN, IGBMC, Illkirch-Graffenstaden, France). These mice were crossed with Cyp11b2-Cre mice (previously characterized by Faedda et al., bioRxiv, 2025) to generate aldosterone-producing cell-specific mineralocorticoid receptor knockout mice ($MRKO^{Ad}$). To enable lineage tracing, $MRKO^{Ad}$ mice were further crossed with $Gt(ROSA)^{26Sortm4(ACTB-tdTomato,-EGFP)Luo/J}$ (mTmG) reporter mice (The Jackson Laboratory, stock #007676) to generate Cyp11b2-Cre::Nr3c2::mTmG ($MRKO^{Ad}$::mTmG) mice. In the mTmG system, cells constitutively express membrane-targeted tdTomato (mT) fluorescence. Upon Cre-mediated recombination, cells switch to express membrane-targeted EGFP (mG), permanently labeling Cyp11b2-expressing cell**s,** providing permanent lineage tracing of Cyp11b2-expressing cells**.** All experiments were conducted using male and female mice carrying one copy of the Cre recombinase allele (Cyp11b2+/Cre). Control mice were heterozygous for Cre with wild-type Nr3c2 alleles (Cyp11b2+/Cre::Nr3c2+/+), while $MRKO^{Ad}$ mice were heterozygous for Cre and homozygous for the floxed Nr3c2 allele (Cyp11b2+/Cre::Nr3c2fl/fl).

Genotyping

Genomic DNA was extracted from tail biopsies and genotyping was performed by PCR. For Cre recombinase detection, primers were: Forward 5'-GCTCCTGCTTCACCATGTGAGCAG-3' and Reverse 5'-GGACCAGCTATAGAGACCTCACCAACAC-3'. For Nr3c2 floxed alleles, four primers were used: F1 5'-CCACTTGTATCGGCAATACAGTTTAGTGTC-3', F2 5'-CACATTGCATGGGGACAACTGACTTC-3', R1 5'-GGAGATCGTACAAACATACGAACAGC-3', and R2 5'-CTGTGATGCGCTCGGAAACGG-3'. PCR products were visualized on 2% agarose gels.

Diets

Male and female mice were fed different diets for a period of two weeks, from 3 weeks of age until reaching 5 weeks of age (Figure 4a and 5a, time point 1, T1): Standard diet (SD, 0.28% Na+; 0.86% K+, A03SP-10, SAFE, Augy, France) or low salt diet (LSD, <0.03% Na+; 0.8% K+, E15430-247, Ssniff, Soest, Germany). Half of the mice were sacrificed at the end of the two-week period (T1, 5 weeks of age), while the others were returned to standard diet and housed under normal conditions for one week and sacrificed at 6 weeks of age (time point 2, T2). For all timepoints, corresponding age-matched control animals fed standard diet throughout were investigated (Ctrl T1, Ctrl T2).

Western Blot

Western blot analysis was performed on adrenal glands from 12-week-old wild-type and MRKO^{Ad} male and female mice. Total proteins were extracted using RIPA buffer (RB 4475, BioBasic, Canada) supplemented with EDTA-free protease and phosphatase inhibitor cocktail (Bimake). Samples were rotated for 30 min at 4°C and centrifuged at 13,000 rpm for 15 min. Protein concentration in the supernatant was determined using Bradford protein assay (Bio-Rad). Ten micrograms of total protein were loaded on 10% acrylamide SDS-PAGE gels, transferred onto nitrocellulose membranes, and incubated overnight at 4°C with the following primary antibodies: phospho-CREB (Ser133; 1:1000, #9198, Cell Signaling Technology), CREB (1:1000, #9197, Cell Signaling Technology), and β-actin (1:5000, #2228, Sigma-Aldrich). Membranes were then incubated with HRP-conjugated secondary antibodies: anti-rabbit IgG (1:2000, #7074, Cell Signaling Technology) or anti-mouse IgG (1:5000, #A90-146P, Bethyl Laboratories). Signals were developed using Clarity Max™ Western ECL substrate (Bio-Rad, Hercules, CA) and detected with a Fujifilm LAS-4000 mini luminescent image analyzer (Fujifilm, Tokyo, Japan). Band intensities were quantified using Multi Gauge software (Fujifilm). Expression of phospho-CREB and total CREB were normalized to β-actin.

Histological Examination and Immunostaining

Tissue Collection and Processing

Mice were anesthetized with isoflurane (3%) and, after confirming the absence of paw-pinch reflex, sacrificed by cervical dislocation following blood sampling. Right adrenals were snap-frozen in liquid nitrogen for molecular analysis.
For LSD diets on MRKO::mTmG mice, left adrenals were fixed in 4% paraformaldehyde (PFA) overnight at 4°C and cryoprotected through successive immersions in 10%, 20%, and 30% sucrose solutions for 24 hours each. Adrenals were then embedded in optimal cutting temperature (OCT) compound using isopentane and stored at −80°C. Sections (10 µm) were cut using an Epredia™ CryoStar™ NX70 cryostat at −20°C, mounted on Superfrost Plus™ microscope slides, and stored at −80°C. For basal characterization experiments (12-week-old mice): Left adrenals were fixed in 4% PFA overnight at 4°C, dehydrated through graded ethanol series, cleared in xylene, and embedded in paraffin. Sections (6 µm) were cut using a microtome, mounted on Superfrost Plus™ microscope slides, and stored at room temperature.

Histological Staining

For histological analysis of paraffin-embedded sections, slides were deparaffinized in xylene and rehydrated through graded ethanol. Hematoxylin, eosin, and saffron (HES) staining was performed using standard protocols. Paraffin sections were deparaffinized and rehydrated by xylene and graded ethanol, respectively, then mounted using Pertex mounting medium (Histolab, #00840). For frozen sections, hematoxylin and eosin (H&E) staining was performed using the Rapid Frozen Sections H&E staining kit (Bio-Optica, #04-061010) following the manufacturer's instructions, followed by dehydration and mounting as described above.

Immunofluorescence

For immunofluorescence on frozen sections, tissues were permeabilized for 15 min with either TBS containing 0.1% Triton X-100 (for Cyp11b2 and Ki67) or PBS containing 0.1% Triton X-100 (for 20α-HSD and Dab2). For paraffin sections, slides were first deparaffinized and

rehydrated, then subjected to heat-induced antigen unmasking with citric-acid based antigen unmasking solution from Vector laboratories (H-3300) for 30 min at 98°C before permeabilization. Sections were blocked for 2 hours at room temperature with blocking buffer containing 5% BSA and 10% normal donkey serum (NDS) in TBS with 0.05% Triton X-100 (for Cyp11b2 and Ki67) or 10% NDS in PBS with 0.1% Triton X-100 (for 20α-HSD and Dab2). Primary antibodies were diluted in 3% BSA and 3% NDS in TBS with 0.05% Triton X-100 (for Cyp11b2 and Ki67) or in 1% NDS in PBS with 0.1% Triton X-100 (for 20α-HSD and Dab2) and incubated overnight at 4°C. The following primary antibodies were used: mouse Cyp11b2 (1:100, generous gift from Dr. C.E. Gomez-Sanchez), Dab2 (1:1600, #D709T, Cell Signaling Technology), Ki67 (1:1000, #ab15580, Abcam), and 20α-HSD (1:500, generous gift from Dr. Yacob Weinstein). Sections were then incubated with donkey anti-rabbit Alexa Fluor 647 secondary antibody (1:1000 in 3% BSA or 3% NDS in PBS/TBS with 0.05% Triton X-100) for 2 hours at room temperature. Nuclei were counterstained with 4′,6-diamidino-2-phenylindole (DAPI, 1:5000, Roche Diagnostics GmbH). Whole slide imaging was performed using an Olympus SlideView VS200 digital slide scanner (Olympus Corporation, Tokyo, Japan) with the UPlanXApo 20×/0.80 objective lens. Regions of interest (ROIs) and focus points were automatically recognized by the scanner and manually updated as needed to ensure optimal image quality.

Image Analysis

Quantitative analysis of immunofluorescence images was performed using HALO software (version 3.6.4134, Indica Labs) with the HighPlex FL v4.2.14 module. Fluorescence TIFF images were imported and background correction was applied to reduce non-specific fluorescence and autofluorescence. All channels (DAPI, Alexa Fluor 488, Alexa Fluor 594, and Alexa Fluor 647) were aligned for accurate signal quantification. ROIs corresponding to adrenal cortex were manually annotated, with artifacts, surrounding adipose tissue, and medulla manually excluded from analysis. DAPI was used for nuclear segmentation within ROIs. In $MRKO^{Ad}$::mTmG mice, Alexa Fluor 488 detected GFP^{+} membranes and Alexa Fluor 594 detected mTomato. Cyp11b2-, Dab2-, Ki67-, and 20α-HSD-positive cells were identified using Alexa Fluor 647. Fluorescence intensity thresholds were set for all channels based on signal intensity.

RNAscope In Situ Hybridization

RNAscope in situ hybridization was performed on 10 µm frozen adrenal sections using the RNAscope 2.5 HD Detection Kit - RED (Cat. No. 322360, Advanced Cell Diagnostics, Bio-Techne) for single target detection of Nr3c2, and the RNAscope 2.5 HD Duplex Reagent Kit (Cat. No. 322430, Advanced Cell Diagnostics, Bio-Techne) for dual detection of Cyp11b1 and Cyp11b2.

Single target detection (*Nr3c2*):

Briefly, frozen slides were heated for 30 min at 60°C and post-fixed with 4% PFA in 1× PBS for 15 min at 4°C. Tissues were dehydrated through consecutive immersions in 50%, 70%, and 100% ethanol for 5 min each and air-dried for 5 min at room temperature. Slides were then immersed in pre-heated 1× Target Retrieval solution for 5 min, washed with ultrapure water, rinsed in fresh 100% ethanol, and air-dried. RNAscope Protease Plus solution was applied to slides, which were then incubated for 30 min at 40°C.

The Mm-Nr3c2 probe (Cat. No. 456331, Advanced Cell Diagnostics) was hybridized to sections for 2 hours at 40°C. Signal amplification was performed through 6 sequential AMP

cycles (AMP 1-6), each incubated for 30 min at 40°C. Signal detection was achieved using Fast Red substrate (alkaline phosphatase-based chromogen) for 10 min at room temperature, producing a red signal.

Dual target detection (*Cyp11b1* and *Cyp11b2*):

Frozen slide pretreatment was performed as described above. Dual probe hybridization was performed using Mm-Cyp11b1-C2 (Cat. No. 564431-C2, Channel C2, Advanced Cell Diagnostics) and Mm-Cyp11b2 (Cat. No. 505851, Channel C1, Advanced Cell Diagnostics) probes for 2 hours at 40°C. Following probe hybridization, 6 sequential AMP cycles (AMP 1-6) were performed at 40°C. The C2 target (*Cyp11b1*) was then detected using Fast Red substrate (alkaline phosphatase-based chromogen) for 10 min at room temperature, producing a red signal. Subsequently, 4 additional AMP cycles (AMP 7-10) were performed, followed by detection of the C1 target (*Cyp11b2*) with HRP-based Green chromogen for 10 min at room temperature.

All slides were counterstained with 50% Gill's Hematoxylin I for 30 sec at room temperature, briefly rinsed with tap water, immersed in 0.02% ammonia water for bluing, washed with tap water, and dried in a 60°C oven for 15 min. Slides were briefly dipped in fresh xylene and mounted with VectaMount Permanent Mounting Medium (Cat. No. H-5000, Vector Laboratories). Images were acquired using a Leica microscope system with 40× oil immersion objective.

RNA Extraction and RT-qPCR Analysis

Total RNA was isolated from whole adrenal glands using a Janke and Kunkel Ultra-Turrax T25 homogenizer (IKA Technologies, Staufen, Germany) and TRIzol reagent (Invitrogen, #15596018). Following DNase I treatment (Invitrogen, #18068-015), cDNA was synthesized from 0.5 µg of RNA using the iScript™ cDNA Synthesis Kit (Bio-Rad, #1708891).

For the 12-week experiment, quantitative PCR was performed in duplicate using the CFX Opus 96 Real-Time PCR System (Bio-Rad) with SYBR Green Supermix (Bio-Rad, #1725274). Normalization for RNA quantity and reverse transcriptase efficiency was performed against three reference genes: ribosomal 18S RNA, β2-microglobulin, and ubiquitin C (geometric mean of expression). Relative quantification was performed using the standard curve method. Primer sequences are listed in Supplementary Table S3.

For the LSD experiment, quantitative PCR was performed using a custom pre-spotted 384-well plate with TaqMan Gene Expression Assays (Thermo Fisher Scientific) for 12 genes including *Cyp11b2, Cyp11b1, Star, Nr4a2, Nr4a1, Wnt4, Axin2, Lef1*, and *Akr1c18*. Plate organization and configuration were performed using QuantStudio 12K Flex Real-Time PCR Software (Thermo Fisher Scientific), and reactions were run on the QuantStudio™ 12K Flex Real-Time PCR System (Thermo Fisher Scientific). Normalization was performed against three housekeeping genes: ribosomal 18S RNA, β2-microglobulin, and ubiquitin C (geometric mean of expression). Relative quantification was performed using the $2^{-\Delta\Delta Ct}$ method. TaqMan assay IDs are listed in Supplementary Table S2.

Steroid Profiling and Analysis

Plasma steroids (pregnenolone, progesterone, 11-deoxycorticosterone, corticosterone, 18-hydroxy-11-deoxycorticosterone, 18-hydroxycorticosterone, aldosterone, and 18-hydroxycortisol) were simultaneously measured in a 13-minute run by liquid chromatography-tandem mass spectrometry (LC-MS/MS) as previously described [2].

Heatmap analysis of steroid hormone concentrations was based on a Z-score normalized matrix of hormone variables, using the pheatmap package (v1.0.12) in R, with hierarchical clustering applied to the variables. Z-scores were calculated by subtracting the mean of each variable from individual data points and dividing by the corresponding standard deviation. A diverging color scale was used to represent the Z-score normalized hormone concentrations, ranging from deep blue ($Z \leq -1$), through white ($Z = 0$), to deep red ($Z \geq +1$). Values outside this range were capped and mapped to the deepest blue or red to minimize the influence of extreme values on the color gradient.
Principal component analysis (PCA) was performed on the original data using the FactoMineR package (v2.11) with default standardization and visualized with the factoextra package (v1.0.7). All analyses were performed in R (v4.4.2).

Single-Nucleus RNA Sequencing

Sample Preparation and Nuclei Isolation

Adrenal glands were collected from four experimental conditions: wild-type mice on standard diet (MWT_SD), wild-type mice on low-sodium diet (MWT_LSD), mineralocorticoid receptor knockout mice on standard diet (MKO_SD), and mineralocorticoid receptor knockout mice on low-sodium diet (MKO_LSD). For each condition, three adrenal glands were pooled to generate sufficient biological material. Nuclei were isolated using the Chromium Nuclei Isolation Kit with RNase Inhibitor (PN-1000494, 10x Genomics) according to the manufacturer's protocol.

Library Preparation and Sequencing

Single-nucleus libraries were prepared using the Chromium GEM-X Single Cell 3' Reagent Kits v4 (10x Genomics) on the 10x Genomics Chromium Controller platform following the manufacturer's instructions. Libraries were sequenced on an Illumina NovaSeq 6000 system at the Institut Imagine genomics platform (Paris, France). Sequencing metrics for each sample are summarized in Table S1.

Data Processing and Quality Control

Raw sequencing reads were processed using Cell Ranger version 9.0.1 (10x Genomics). Reads were aligned to the mouse reference genome GRCm39-2024-A (mm39) with intronic reads included to capture nascent transcripts characteristic of nuclear RNA. Gene expression matrices were generated for each sample using the standard Cell Ranger pipeline.
Downstream analysis was performed using Seurat version version 5.3.0 in R version 4.4.1. For each sample, Seurat objects were created with initial filtering parameters requiring a minimum of 3 cells per gene and a minimum of 200 features per nucleus. Quality control filtering was applied to remove low-quality nuclei based on the following criteria: nuclei with 200 to 6,000 detected genes and less than 5% mitochondrial gene content were retained for analysis. Each sample was processed independently through quality control, doublet removal, and initial clustering before integration.

Doublet Removal

Doublets were identified and removed using DoubletFinder (v2.0.6) independently for each sample. For each sample, data were first normalized using the LogNormalize method with default parameters (scale factor = 10,000). The top 2,000 highly variable genes were identified using variance stabilizing transformation (vst method) implemented in the

FindVariableFeatures function. Data were scaled using ScaleData, and principal component analysis (PCA) was performed. Pre-clustering was performed using FindNeighbors and FindClusters with the first 9 principal components and resolution parameter of 0.2 to facilitate homotypic doublet proportion estimation.

For doublet detection, the optimal pK parameter was determined through parameter sweep analysis (paramSweep function) using the first 9 principal components with sct = FALSE. The best pK value was selected based on the highest mean bimodality coefficient (BCmetric). The expected doublet rate was set at 15% of nuclei, adjusted for homotypic doublets based on pre-clustering results using the modelHomotypic function with pN = 0.25. Doublets were classified using doubletFinder with the optimized pK parameter specific to each sample (ranging from 0.005 to 0.01 across samples), and only singlets were retained for downstream analysis.

After doublet removal, 105,400 nuclei were retained across all four samples. Each sample was re-normalized and re-processed through the same normalization, scaling, PCA, and clustering pipeline before integration.

Data Normalization and Sample Integration

After individual sample processing, quality control, and doublet removal, the four samples were merged into a single Seurat object with unique cell identifiers. Gene expression data were normalized using the LogNormalize method with default parameters (scale factor = 10,000). The top 2,000 highly variable genes were identified using variance stabilizing transformation implemented in the FindVariableFeatures function. Data were scaled using the ScaleData function on the identified variable features.

To account for technical variation between samples while preserving biological differences between experimental conditions, the merged dataset was integrated using Harmony (v1.2.3). Principal component analysis (PCA) was performed on the normalized expression matrix of variable features. Integration was performed on the PCA embedding using 20 principal components with the IntegrateLayers function and HarmonyIntegration method, with sample identity as the batch variable. This generated a batch-corrected "harmony" dimensional reduction for downstream analysis.

Dimensionality Reduction and Clustering

Following Harmony integration, Uniform Manifold Approximation and Projection (UMAP) was performed on the harmony-corrected embeddings for two-dimensional visualization using default Seurat parameters. Unsupervised clustering was performed using the Louvain algorithm implemented in the FindNeighbors and FindClusters functions. The first 15 dimensions of the batch-corrected harmony reduction were used for clustering analysis with a resolution parameter of 0.3 to identify distinct cell populations. Integration quality was assessed by visualizing sample distribution across clusters to ensure biological variation was preserved while technical batch effects were minimized.

Cell Type Annotation

Cell type identities were assigned to clusters based on expression of canonical marker genes using module scoring and manual curation. Module scores were calculated using Seurat's AddModuleScore function with the following marker gene sets: ZG (ZG: *Cyp11b2, Dab2, Wnt4, Shh*), Zona fasciculata (ZF: *Cyp11b1, Hsd3b6, Nr4a1*), Adrenal medulla (*Th, Ddc, Pnmt*), Endothelial cells (*Pecam1, Cdh5, Vwf*), Fibroblasts (*Col1a1, Dcn, Lum*), Macrophages (*Cd68, Csf1r, Adgre1*).

For each cluster, the average module score for each cell type was calculated, and clusters were assigned to the cell type with the highest average score. Marker gene expression was validated using FeaturePlot visualization to confirm appropriate assignment.
The ZG-zona fasciculata transition zone (ZG_ZF) was identified as a distinct population expressing both *Cyp11b2* and *Cyp11b1* with intermediate expression of zona-specific markers, consistent with cells at the anatomical boundary between these zones.
The zona fasciculata population was subdivided into ZF1 (cluster 0) and ZF2 (clusters 1-10) based on spatial separation in UMAP space and distinct baseline transcriptional profiles. Despite both subpopulations expressing canonical zona fasciculata markers (*Cyp11b1, Hsd3b6, Nr4a1*), differential expression analysis revealed that ZF1 was characterized by higher expression of mitochondrial genes, translation machinery, and secretory granule proteins compared to ZF2 (2,341 differentially expressed genes at baseline, adjusted $p < 0.05$).
After final annotation, eight distinct populations were identified: ZG (ZG), ZG-zona fasciculata transition zone (ZG_ZF), zona fasciculata cluster 0 (ZF1), zona fasciculata clusters 1-10 (ZF2), adrenal medulla, endothelial cells, fibroblasts, and macrophages.

Double-Positive Cell Quantification

To quantify cellular plasticity, we identified cells co-expressing both zona fasciculata and ZG markers. For each population (ZG, ZG_ZF, ZF1, ZF2) and experimental condition, cells were classified as double-positive if they expressed both Cyp11b1 (zona fasciculata marker) and Cyp11b2 (ZG marker) with normalized expression values greater than 0.5 in the RNA assay. The percentage of double-positive cells was calculated as (number of double-positive cells / total cells in population) × 100 for each condition. MR-dependence was calculated as: [(WT change - MKO change) / WT change] × 100, where "change" represents the difference in double-positive percentage between low-sodium diet and standard diet within each genotype.

ZG Signature Score Calculation

A comprehensive ZG gene signature score was calculated to assess acquisition of aldosterone-producing cell identity beyond individual marker expression. The signature comprised six canonical ZG markers representing distinct aspects of ZG biology: Cyp11b2 (aldosterone synthase), Dab2 (ZG structural marker), Wnt4 (Wnt ligand essential for ZG maintenance), Shh (sonic hedgehog developmental marker), Rspo3 (R-spondin 3 Wnt pathway enhancer), and Axin2 (direct Wnt target gene indicating active signaling). Module scores were calculated using Seurat's AddModuleScore function with default parameters (ctrl = 100 randomly selected control genes, seed = 1). For each cell, the score represents the average expression of signature genes minus the average expression of control genes, scaled to a mean of zero across all cells. Positive scores indicate expression profiles characteristic of ZG identity, while negative scores indicate lack of ZG identity. Statistical comparisons of signature scores between conditions were performed using the Wilcoxon rank-sum test.

Gene Ontology Enrichment Analysis

Gene Ontology (GO) enrichment analysis was performed to identify biological processes enriched in differentially expressed gene sets. Gene symbols were converted to Entrez IDs using the org.Mm.eg.db annotation package (v3.19.1). GO enrichment for Biological Process terms was performed using the enrichGO function from clusterProfiler (v4.12.0) with the following parameters: ont = "BP", pAdjustMethod = "BH" (Benjamini-Hochberg), pvalueCutoff = 0.05, qvalueCutoff = 0.05, readable = TRUE to return gene symbols. The mouse genome annotation was used as the background (OrgDb = org.Mm.eg.db). Significantly

enriched pathways (adjusted $p < 0.05$) were ranked by adjusted p-value, and the top 15 pathways from each analysis were selected for comparative visualization. For pathway comparison analysis, pathways were considered enriched in both analyses if they appeared in the top 15 lists from both plasticity gene and MR-dependent gene enrichments.

Venn Diagram and Gene Overlap Analysis

To identify genes requiring MR for their plasticity-induced expression, we performed overlap analysis between salt-induced plasticity genes (upregulated in ZF1 WT LSD vs WT SD, adjusted $p < 0.05$) and MR-enhanced genes (upregulated in ZF1 WT LSD vs MKO LSD, adjusted $p < 0.05$). Venn diagrams were generated using the VennDiagram package (v1.7.3) to visualize gene set overlaps. For genes appearing in the overlap, both the plasticity fold change and MR-dependent fold change were extracted to assess their relative magnitude of induction and MR-dependence. The percentage of plasticity genes requiring MR was calculated as (number of overlap genes / total plasticity upregulated genes) × 100.

Differential Gene Expression Analysis

Differential gene expression analysis was performed using Seurat's FindMarkers function, which implements a Wilcoxon rank-sum test. For each comparison, cells were subset to the populations of interest, and the RNA assay (normalized data) was used for testing. Genes were tested if they were detected in at least 10% of cells in either group (min.pct = 0.1) and showed a minimum $\log_2$ fold change threshold of 0.25 (logfc.threshold = 0.25). Genes were considered significantly differentially expressed if adjusted p-value < 0.05. P-values were adjusted for multiple testing using the Bonferroni correction.

Visualization and Heatmap Generation

Data visualization was performed using ggplot2 (v3.5.2), ComplexHeatmap (v2.20.0), ggrepel (v0.9.6), and Seurat's built-in plotting functions. Volcano plots were generated using ggplot2 with ggrepel for gene label placement to avoid overlapping text. Points were colored by significance and fold change thresholds. Key genes of biological interest were labeled on the plots. For heatmap visualization of top differentially expressed genes, the top 30 upregulated and top 30 downregulated genes were selected for each comparison, ranked by a combination of adjusted p-value and absolute $\log_2$ fold change. For display, average expression per condition was calculated for cells within the population of interest across all four experimental conditions (WT SD, WT LSD, MKO SD, MKO LSD). Expression values were scaled by gene using z-score normalization, and extreme values were capped at ±2.5 for visualization to prevent outliers from dominating the color scale. Heatmaps were generated using ComplexHeatmap with hierarchical clustering applied within gene direction groups (upregulated genes clustered separately from downregulated genes) to maintain clear visual separation of transcriptional programs, while conditions were displayed in biological order (WT SD, WT LSD, MKO SD, MKO LSD) without clustering.

Statistical Analysis

All statistical analyses were performed in R version 4.4.1. Sample sizes represent pooled adrenal glands from 3 mice per condition, with statistical comparisons performed at the single-cell level. For comparisons of continuous variables (e.g., ZG signature scores, gene expression levels), the Wilcoxon rank-sum test (Mann-Whitney U test) was used for two-group comparisons. Multiple testing correction for differential gene expression was performed using the Bonferroni method. Statistical significance was defined as $p < 0.05$ unless otherwise

specified. In figures, significance levels are indicated as: *p < 0.05, **p < 0.01, ***p < 0.001. All tests were two-sided.

Software and Packages

All analyses were performed in R version 4.4.1. Key R packages and versions used include: Seurat (v5.3.0) for single-cell RNA sequencing analysis, DoubletFinder (v2.0.6, github.com/chris-mcginnis-ucsf/DoubletFinder) for doublet detection, harmony (v1.2.3) for batch correction and data integration, ggplot2 (v3.5.2) for data visualization, dplyr (v1.1.4) for data manipulation, ComplexHeatmap (v2.20.0) for heatmap generation, ggrepel (v0.9.6) for non-overlapping text labels in plots, patchwork (v1.3.0) for figure assembly and multi-panel layouts, tidyr (v1.3.1) for data reshaping, clusterProfiler (v4.12.0) for Gene Ontology enrichment analysis, org.Mm.eg.db (v3.19.1) for mouse genome annotation and gene ID conversion, VennDiagram (v1.7.3) for gene set overlap visualization. Cell Ranger version 9.0.1 (10x Genomics) was used for initial sequence alignment and gene quantification.

Acknowledgments

This work was funded through the European Union's Horizon 2020 research and innovation 813 programme under the Marie Sklodowska-Curie grant agreement No. 954798 (MINDSHIFT804 814 ITN) institutional support from INSERM, by the Agence Nationale pour la Recherche (ANR-815 18-CE93-0003-01), the Fondation pour la Recherche Médicale (EQU201903007864).

Bibliography

1. Monticone, S. *et al.* Prevalence and Clinical Manifestations of Primary Aldosteronism Encountered in Primary Care Practice. *J Am Coll Cardiol* **69**, 1811–1820 (2017).
2. De Sousa, K. *et al.* Genetic, Cellular, and Molecular Heterogeneity in Adrenals With Aldosterone-Producing Adenoma. *Hypertension* **75**, 1034–1044 (2020).
3. Fernandes-Rosa, F. L. *et al.* New advances in endocrine hypertension: from genes to biomarkers. *Kidney Int* **103**, 485–500 (2023).
4. Scholl, U. I. *et al.* Hypertension with or without adrenal hyperplasia due to different inherited mutations in the potassium channel KCNJ5. *Proc Natl Acad Sci U S A* **109**, 2533–2538 (2012).
5. Le Floch, E. *et al.* Identification of risk loci for primary aldosteronism in genome-wide association studies. *Nat Commun* **13**, 5198 (2022).
6. Naito, T. *et al.* Genetic Risk of Primary Aldosteronism and Its Contribution to Hypertension: A Cross-Ancestry Meta-Analysis of Genome-Wide Association Studies. *Circulation* **147**, 1097–1109 (2023).
7. Inoue, K. *et al.* Primary Aldosteronism and Risk of Cardiovascular Outcomes: Genome-Wide Association and Mendelian Randomization Study. *J Am Heart Assoc* **13**, e034180 (2024).
8. Zennaro, M.-C., Boulkroun, S. & Fernandes-Rosa, F. Genetic Causes of Functional Adrenocortical Adenomas. *Endocr Rev* **38**, 516–537 (2017).
9. Pihlajoki, M., Dörner, J., Cochran, R. S., Heikinheimo, M. & Wilson, D. B. Adrenocortical zonation, renewal, and remodeling. *Front Endocrinol (Lausanne)* **6**, 27 (2015).
10. Hershkovitz, L., Beuschlein, F., Klammer, S., Krup, M. & Weinstein, Y. Adrenal 20α-Hydroxysteroid Dehydrogenase in the Mouse Catabolizes Progesterone and 11-Deoxycorticosterone and Is Restricted to the X-Zone. *Endocrinology* **148**, 976–988 (2007).
11. Miller, W. L. & Auchus, R. J. The molecular biology, biochemistry, and physiology of human steroidogenesis and its disorders. *Endocr Rev* **32**, 81–151 (2011).
12. King, P., Paul, A. & Laufer, E. Shh signaling regulates adrenocortical development and identifies progenitors of steroidogenic lineages. *Proc Natl Acad Sci U S A* **106**, 21185–21190 (2009).
13. Freedman, B. D. *et al.* Adrenocortical zonation results from lineage conversion of differentiated zona glomerulosa cells. *Dev Cell* **26**, 666–673 (2013).

14. Faedda, N. *et al.* Sexually dimorphic interzonal crosstalk reshapes the adrenal cortex in response to pathophysiological challenges. 2025.09.05.674435 Preprint at https://doi.org/10.1101/2025.09.05.674435 (2025).
15. Berthon, A. *et al.* Constitutive beta-catenin activation induces adrenal hyperplasia and promotes adrenal cancer development. *Hum Mol Genet* **19**, 1561–1576 (2010).
16. Vidal, V. *et al.* The adrenal capsule is a signaling center controlling cell renewal and zonation through Rspo3. *Genes Dev* **30**, 1389–1394 (2016).
17. Nishimoto, K., Harris, R. B. S., Rainey, W. E. & Seki, T. Sodium deficiency regulates rat adrenal zona glomerulosa gene expression. *Endocrinology* **155**, 1363–1372 (2014).
18. F, J. & N, F. Emerging Roles of the Mineralocorticoid Receptor in Pathology: Toward New Paradigms in Clinical Pharmacology. *Pharmacological reviews* **68**, (2016).
19. Zennaro, M. C. *et al.* Human mineralocorticoid receptor genomic structure and identification of expressed isoforms. *J Biol Chem* **270**, 21016–21020 (1995).
20. Zennaro, M.-C., Caprio, M. & Fève, B. Mineralocorticoid receptors in the metabolic syndrome. *Trends Endocrinol Metab* **20**, 444–451 (2009).
21. Bakris, G. L. *et al.* Effect of Finerenone on Chronic Kidney Disease Outcomes in Type 2 Diabetes. *N Engl J Med* **383**, 2219–2229 (2020).
22. Boulkroun, S. *et al.* Adrenal cortex remodeling and functional zona glomerulosa hyperplasia in primary aldosteronism. *Hypertension* **56**, 885–892 (2010).
23. Burton, T. J. *et al.* Expression of the epithelial Na(+) channel and other components of an aldosterone response pathway in human adrenocortical cells. *Eur J Pharmacol* **613**, 176–181 (2009).
24. Yokota, K. *et al.* CASZ1b is a novel transcriptional corepressor of mineralocorticoid receptor. *Hypertens Res* **44**, 407–416 (2021).
25. McCurley, A. & Jaffe, I. Z. Mineralocorticoid receptors in vascular function and disease. *Mol Cell Endocrinol* **350**, 256–265 (2012).
26. DuPont, J. J. & Jaffe, I. Z. 30 YEARS OF THE MINERALOCORTICOID RECEPTOR: The role of the mineralocorticoid receptor in the vasculature. *J Endocrinol* **234**, T67–T82 (2017).
27. Berger, S. *et al.* Mineralocorticoid receptor knockout mice: pathophysiology of Na+ metabolism. *Proc Natl Acad Sci U S A* **95**, 9424–9429 (1998).
28. Arakane, F. *et al.* Phosphorylation of steroidogenic acute regulatory protein (StAR) modulates its steroidogenic activity. *J Biol Chem* **272**, 32656–32662 (1997).

29. Manna, P. R., Dyson, M. T. & Stocco, D. M. Regulation of the steroidogenic acute regulatory protein gene expression: present and future perspectives. *Mol Hum Reprod* **15**, 321–333 (2009).
30. Grabek, A. *et al.* The Adult Adrenal Cortex Undergoes Rapid Tissue Renewal in a Sex-Specific Manner. *Cell Stem Cell* **25**, 290-296.e2 (2019).
31. Funder, J. W. Aldosterone and Mineralocorticoid Receptors-Physiology and Pathophysiology. *Int J Mol Sci* **18**, 1032 (2017).

Figure 1

A.

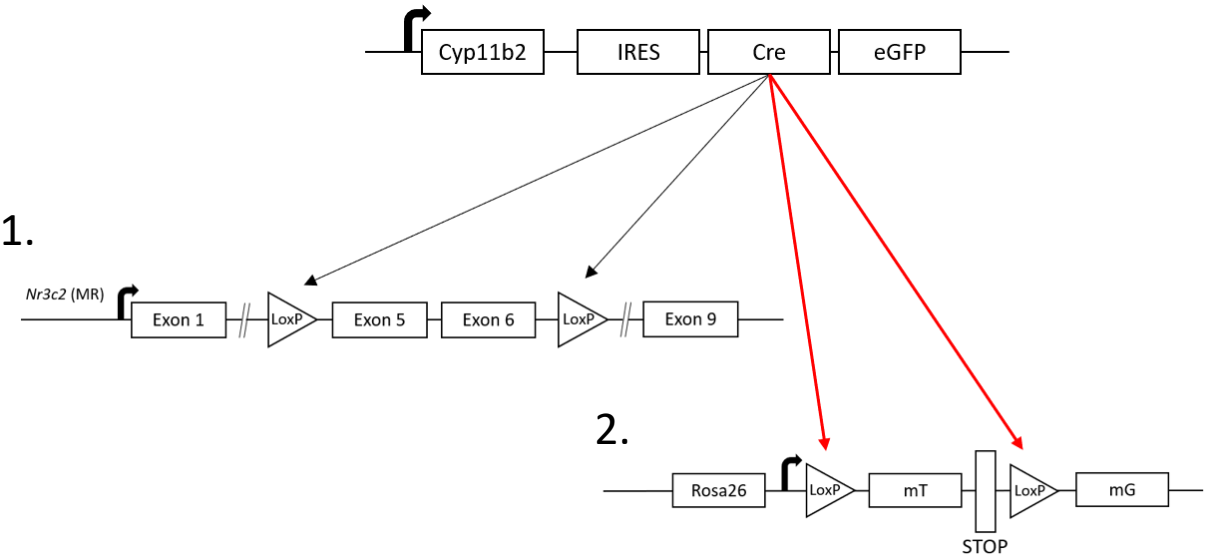

B.

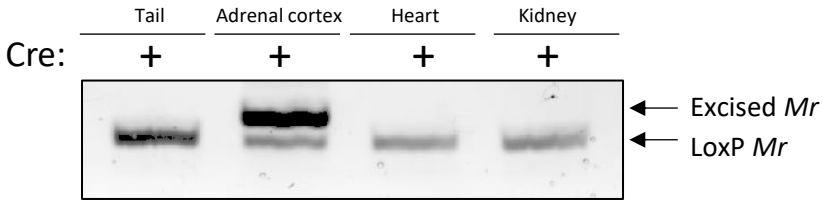

C.

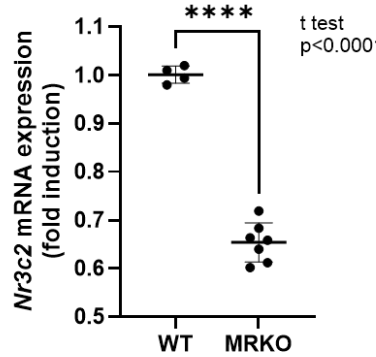

D.

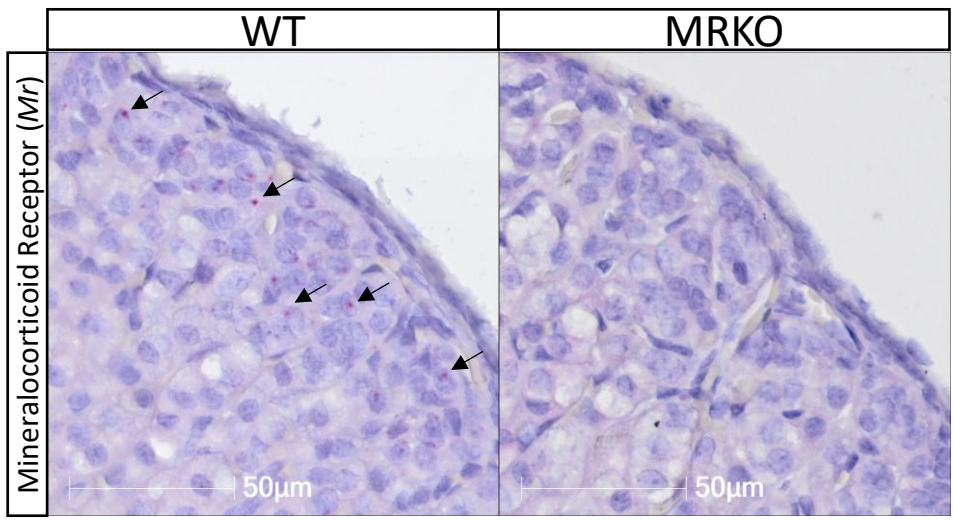

Figure 2

A.

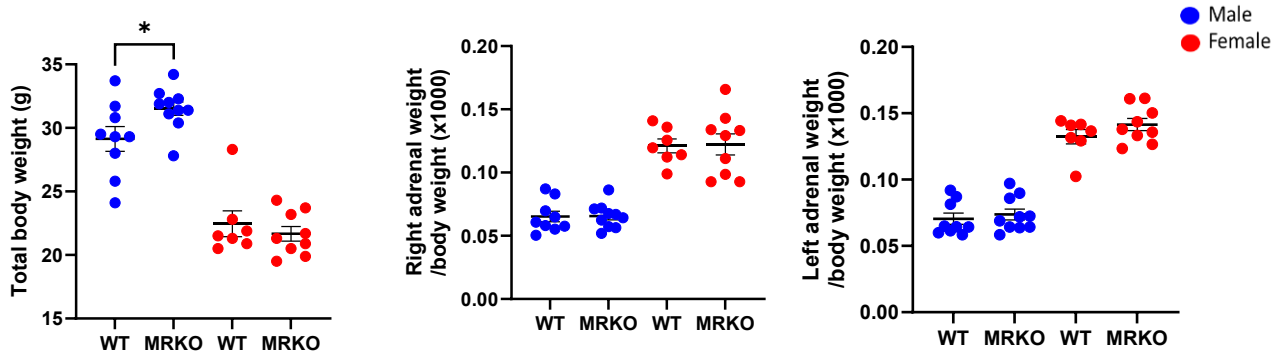

B.

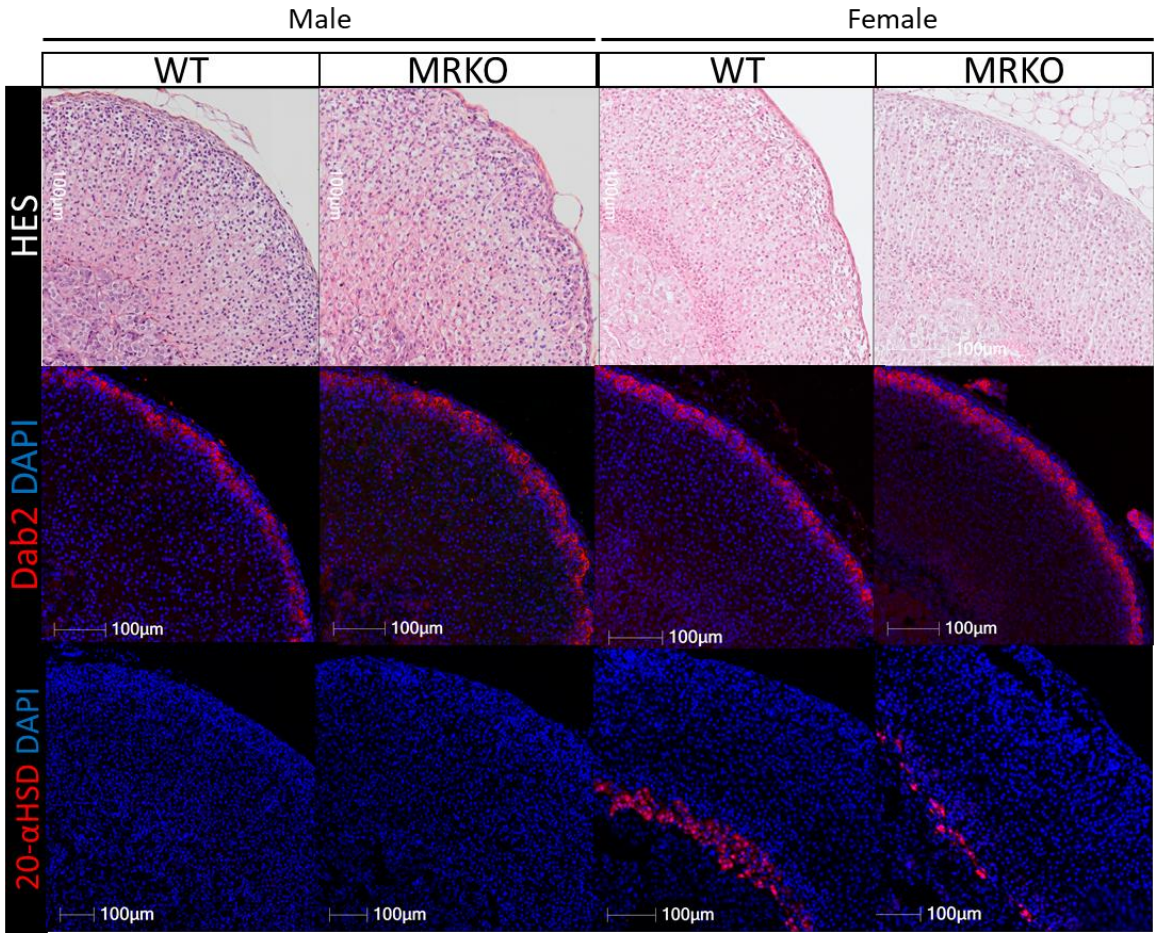

C.

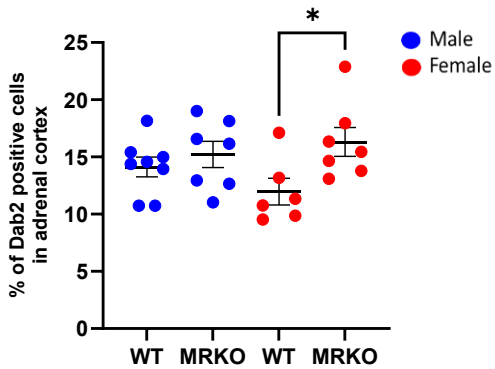

D.

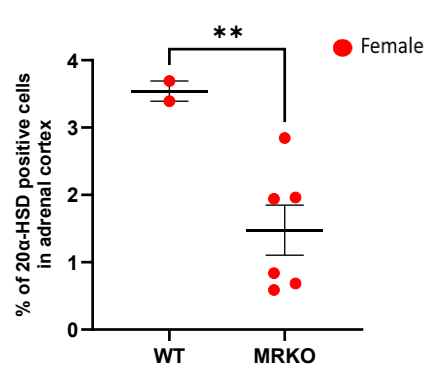

Figure 3

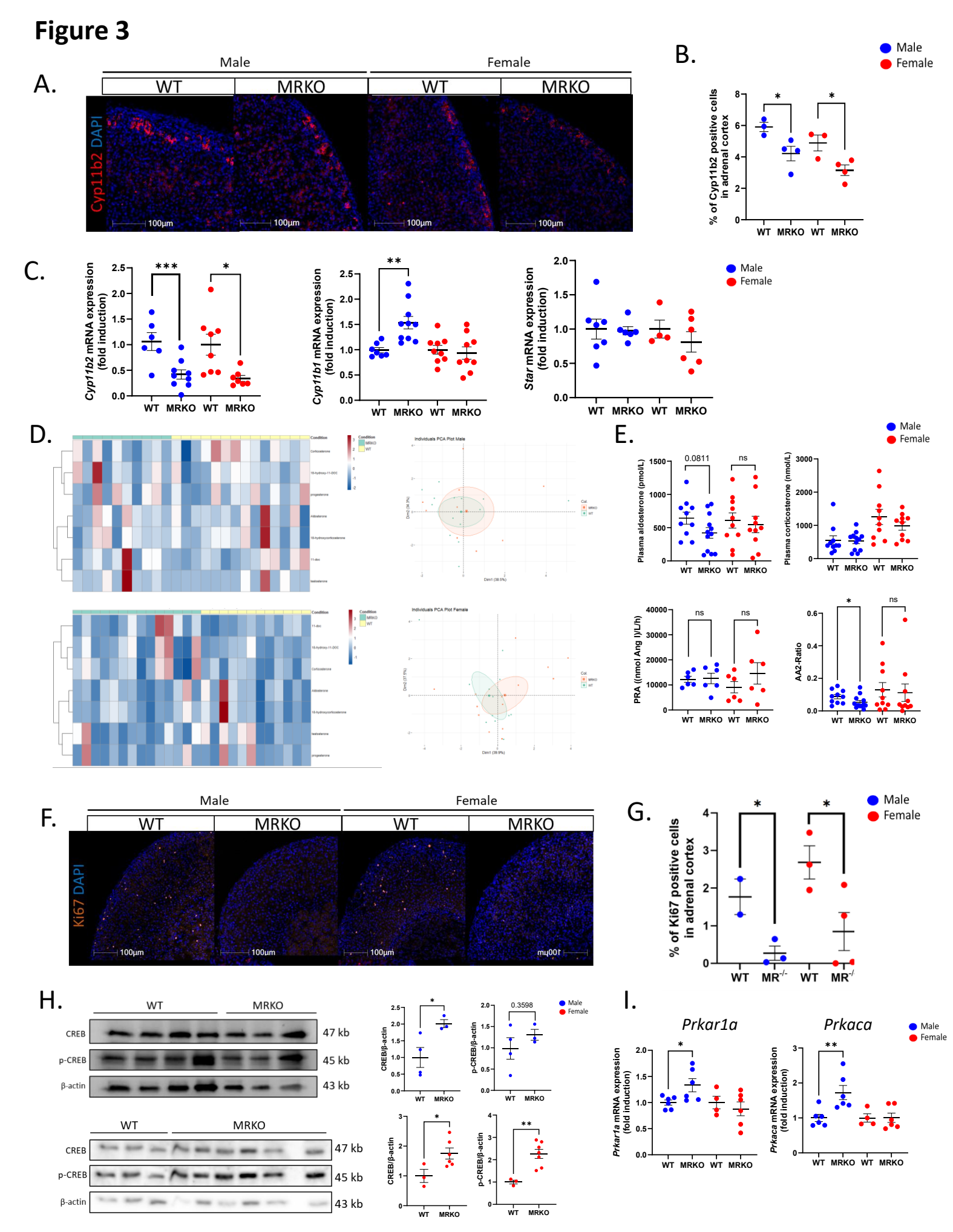
A.
Male
Female
WT
MRKO
WT
MRKO
Cyp11b2 DAPI
100µm
B.
Male
Female
% of Cyp11b2 positive cells in adrenal cortex
WT MRKO WT MRKO
C.
Cyp11b2 mRNA expression (fold induction)
Cyp11b1 mRNA expression (fold induction)
Star mRNA expression (fold induction)
WT MRKO WT MRKO
D.
Individuals PCA Plot Male
Individuals PCA Plot Female
E.
Plasma aldosterone (pmol/L)
0.0811
ns
Plasma corticosterone (nmol/L)
PRA ((nmol Ang I)/L/h)
AA2-Ratio
F.
Male
Female
WT
MRKO
Ki67 DAPI
100µm
G.
% of Ki67 positive cells in adrenal cortex
WT MR-/- WT MR-/-
H.
CREB
p-CREB
β-actin
47 kb
45 kb
43 kb
CREB/β-actin
p-CREB/β-actin
0.3598
I.
Prkar1a
Prkaca
Prkar1a mRNA expression (fold induction)
Prkaca mRNA expression (fold induction)

Figure 4

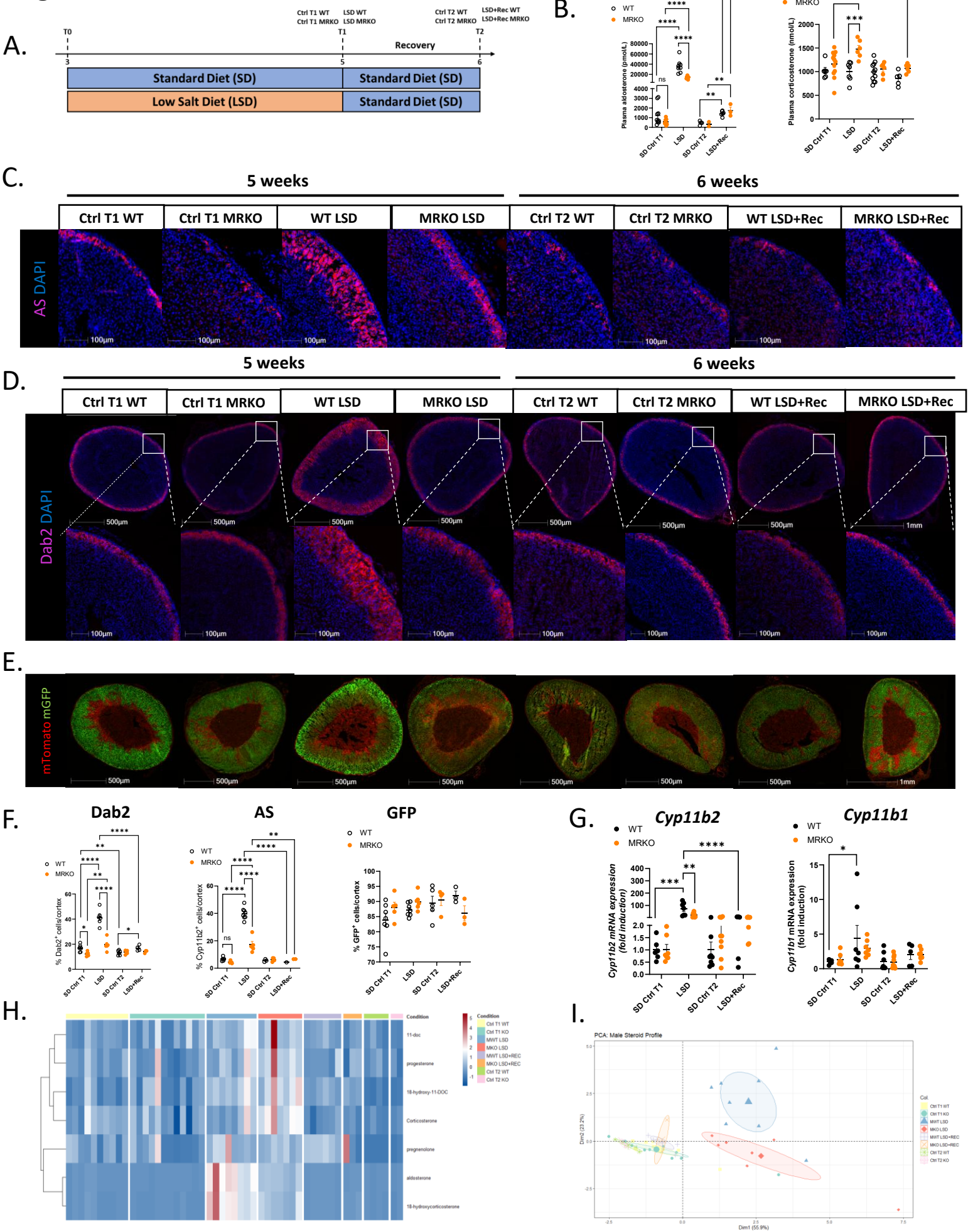
A.
T0
T1
T2
Recovery
Ctrl T1 WT
Ctrl T1 MRKO
LSD WT
LSD MRKO
Ctrl T2 WT
Ctrl T2 MRKO
LSD+Rec WT
LSD+Rec MRKO
Standard Diet (SD)
Low Salt Diet (LSD)
Standard Diet (SD)
B.
WT
MRKO
Plasma aldosterone (pmol/L)
Plasma corticosterone (nmol/L)
SD Ctrl T1
LSD
SD Ctrl T2
LSD+Rec
C.
5 weeks
6 weeks
Ctrl T1 WT
Ctrl T1 MRKO
WT LSD
MRKO LSD
Ctrl T2 WT
Ctrl T2 MRKO
WT LSD+Rec
MRKO LSD+Rec
AS DAPI
100µm
D.
Dab2 DAPI
500µm
1mm
E.
mTomato mGFP
F.
Dab2
AS
GFP
% Dab2+ cells/cortex
% Cyp11b2+ cells/cortex
% GFP+ cells/cortex
G.
Cyp11b2
Cyp11b1
Cyp11b2 mRNA expression (fold induction)
Cyp11b1 mRNA expression (fold induction)
H.
11-doc
progesterone
18-hydroxy-11-DOC
Corticosterone
pregnenolone
aldosterone
18-hydroxycorticosterone
I.
PCA: Male Steroid Profile

Figure 5

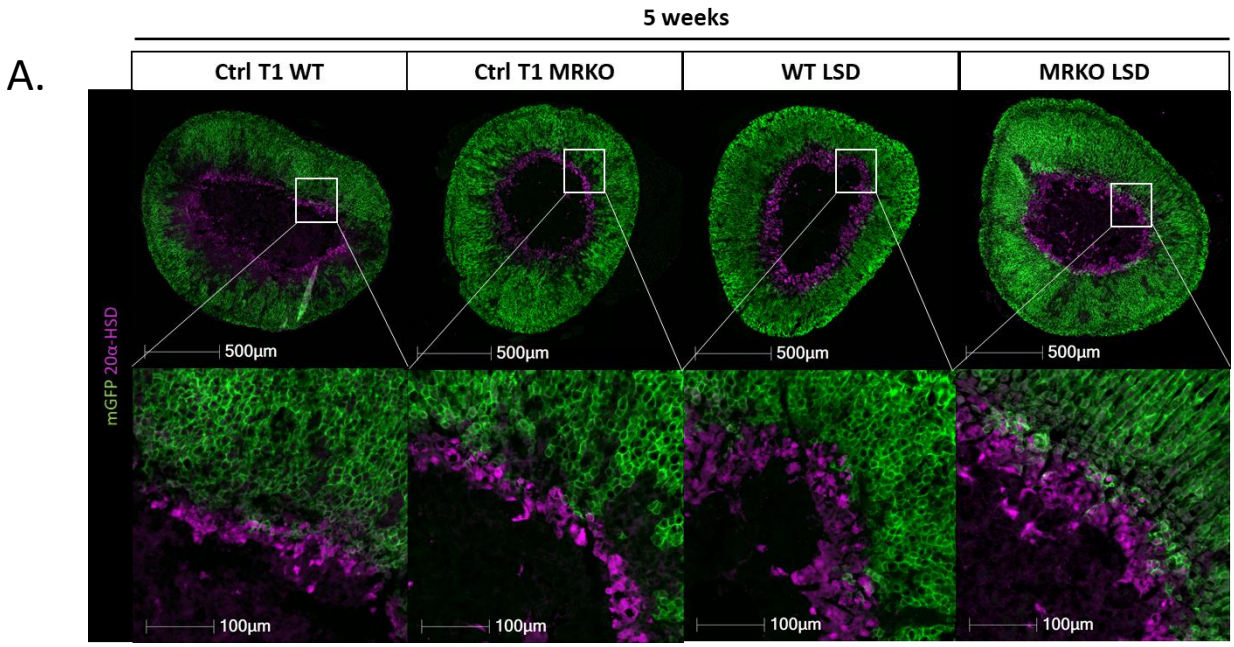
A.
5 weeks
Ctrl T1 WT
Ctrl T1 MRKO
WT LSD
MRKO LSD
mGFP 20α-HSD
500µm
100µm

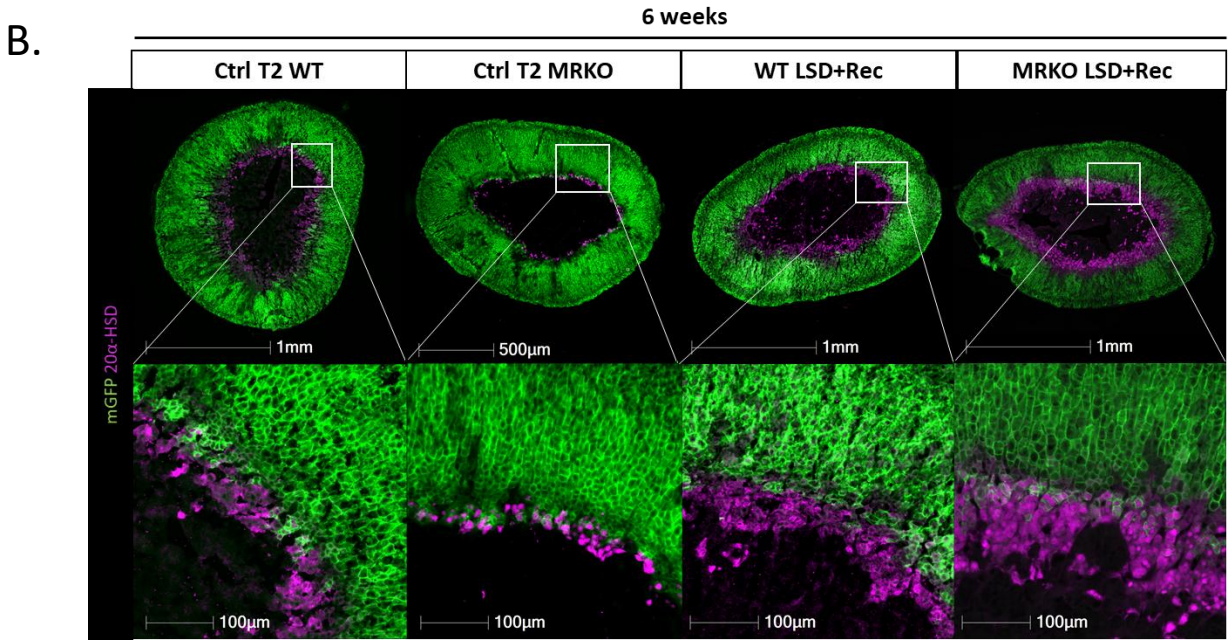
B.
6 weeks
Ctrl T2 WT
Ctrl T2 MRKO
WT LSD+Rec
MRKO LSD+Rec
mGFP 20α-HSD
1mm
500µm
100µm

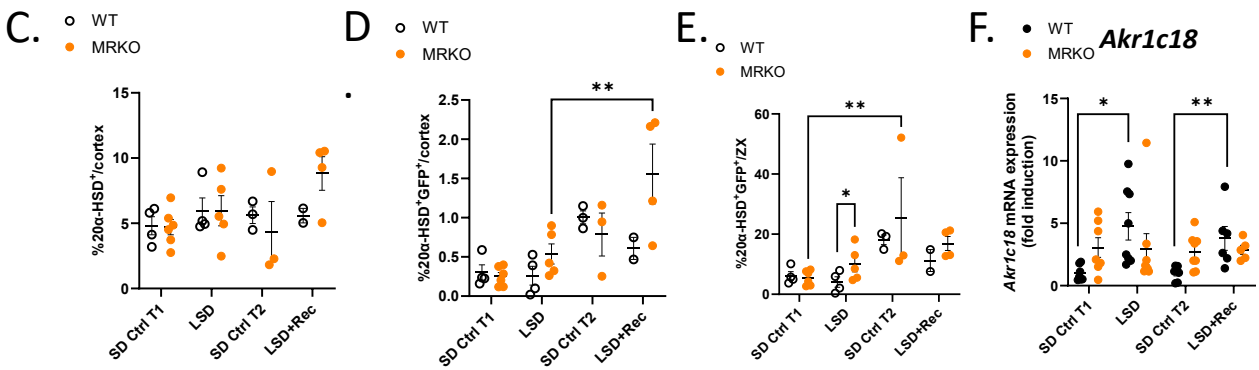
C.
WT
MRKO
%20α-HSD+/cortex
SD Ctrl T1
LSD
SD Ctrl T2
LSD+Rec
D
%20α-HSD+GFP+/cortex
**
E.
%20α-HSD+GFP+/ZX
*
F.
Akr1c18
Akr1c18 mRNA expression (fold induction)

Figure 6

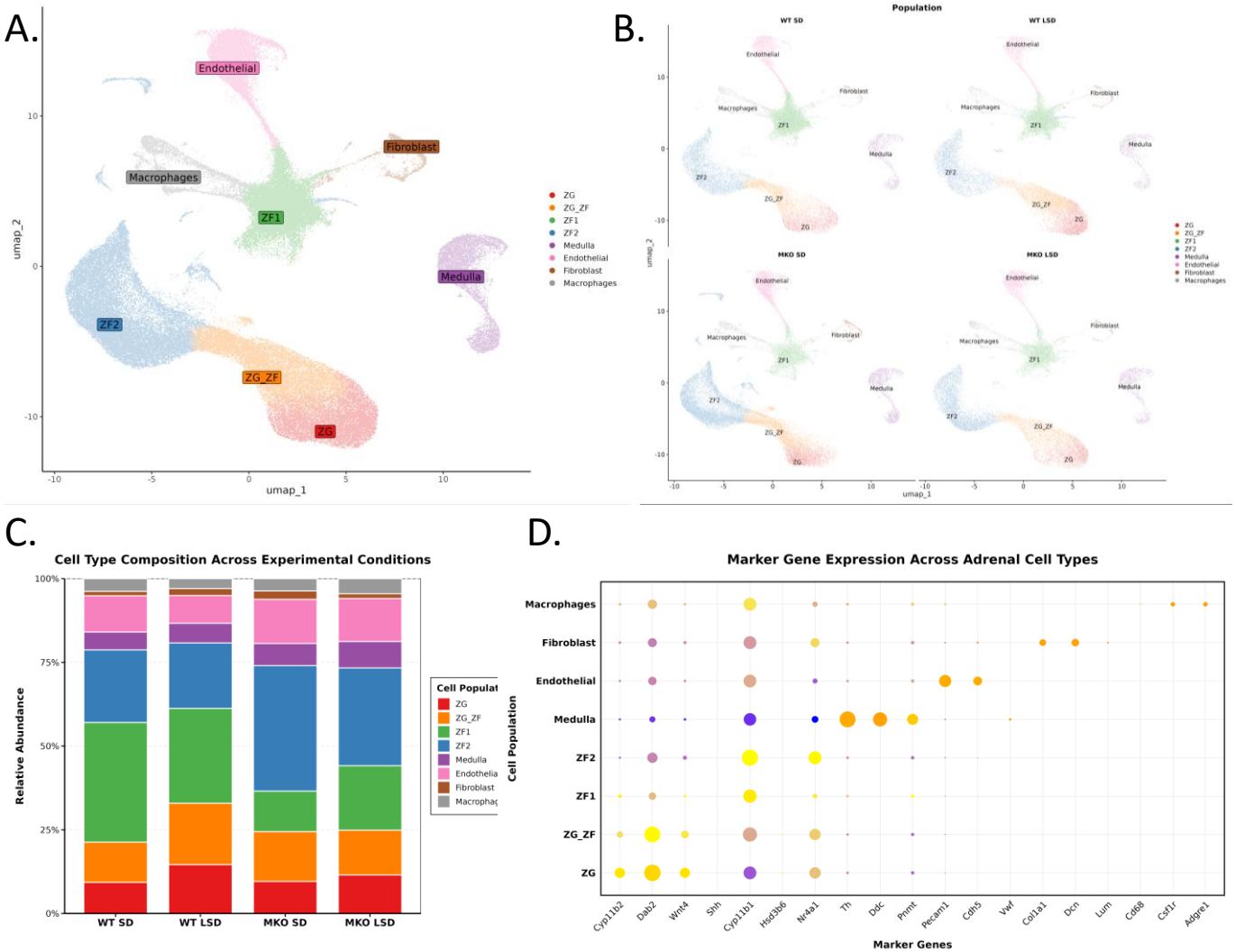
A.
Endothelial
Fibroblast
Macrophages
ZF1
Medulla
ZF2
ZG_ZF
ZG
umap_1
umap_2
ZG
ZG_ZF
ZF1
ZF2
Medulla
Endothelial
Fibroblast
Macrophages
B.
Population
WT SD
WT LSD
MKO SD
MKO LSD
C.
Cell Type Composition Across Experimental Conditions
Relative Abundance
100%
75%
50%
25%
0%
WT SD
WT LSD
MKO SD
MKO LSD
Cell Populat
ZG
ZG_ZF
ZF1
ZF2
Medulla
Endothelia
Fibroblast
Macropha
D.
Marker Gene Expression Across Adrenal Cell Types
Macrophages
Fibroblast
Endothelial
Medulla
ZF2
ZF1
ZG_ZF
ZG
Cell Population
Cyp11b2
Dab2
Wnt4
Shh
Cyp11b1
Hsd3b6
Nr4a1
Th
Ddc
Pnmt
Pecam1
Cdh5
Vwf
Col1a1
Dcn
Lum
Cd68
Csf1r
Adgre1
Marker Genes
% Expressed
25
50
75
Avg Expression
2
1
0
-1

Figure 7

A.

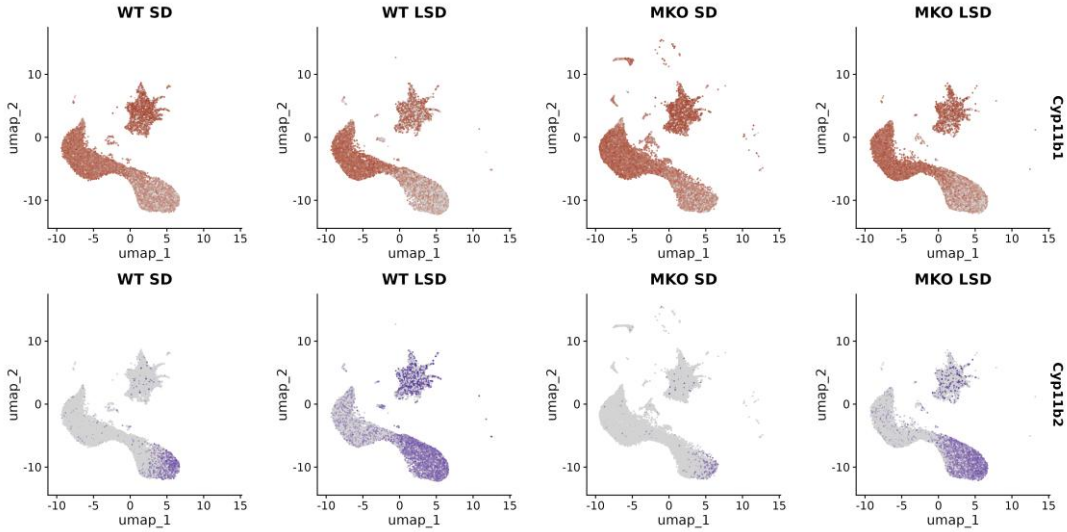

B.

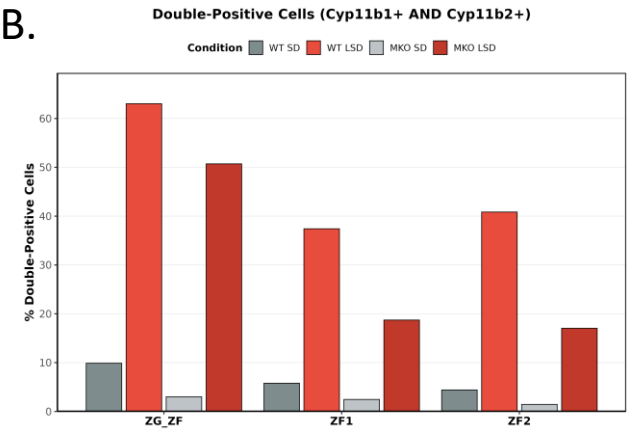

C.

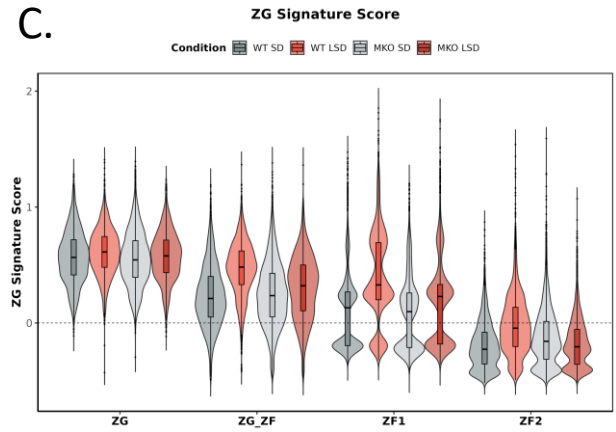

D.

Summary: Two Mechanisms of Cortical Plasticity

Population	Mechanism	WT_Response	MKO_Response	MR_Dependence	ZG_Identity	Key_Feature
ZG_ZF	Position-driven	9.9% → 63.0%	3.0% → 50.7%	10.3%	YES (0.467)	MR-independent Wnt/position
ZF1	MR-driven	5.8% → 37.4%	2.5% → 18.7%	48.6%	YES (0.393)	MR-required Transdifferentiation
ZF2	Partial/Indirect	4.4% → 40.8%	1.4% → 17.0%	57.2%	NO (-0.020)	Cyp11b2+ but no ZG identity

Figure 8

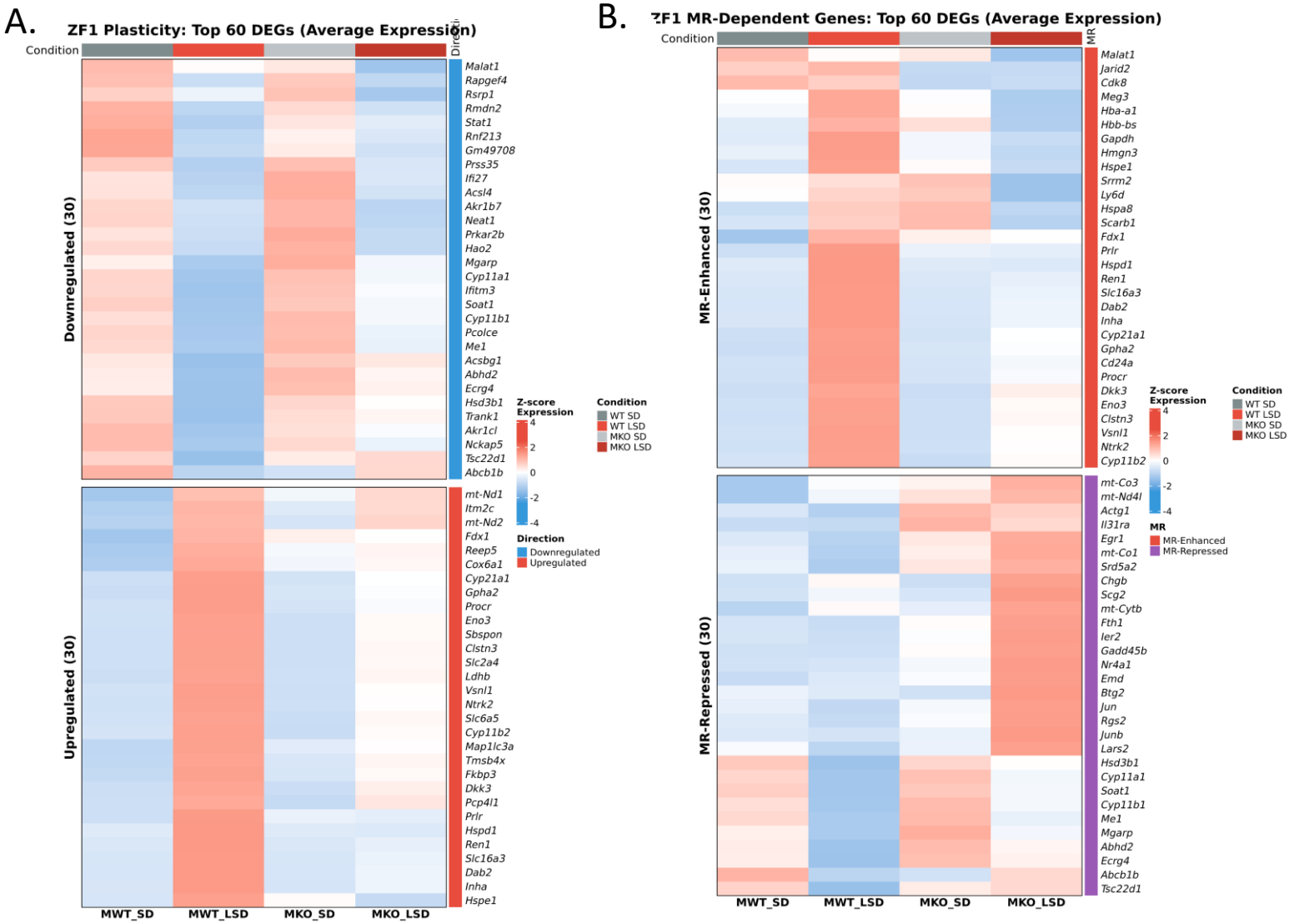

C.

ZF1 Plasticity Genes



D.

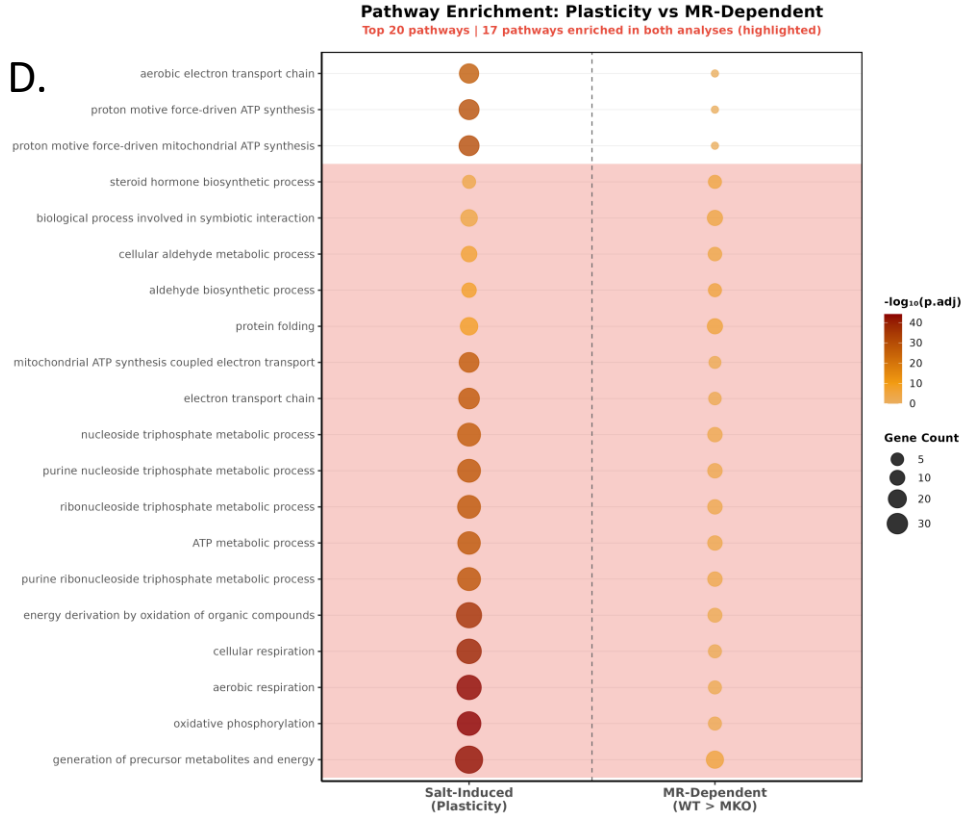

Supplementary Figure S1

A.

12 weeks
Male

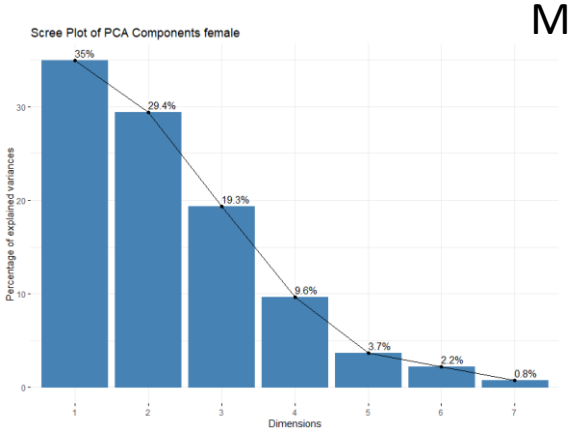

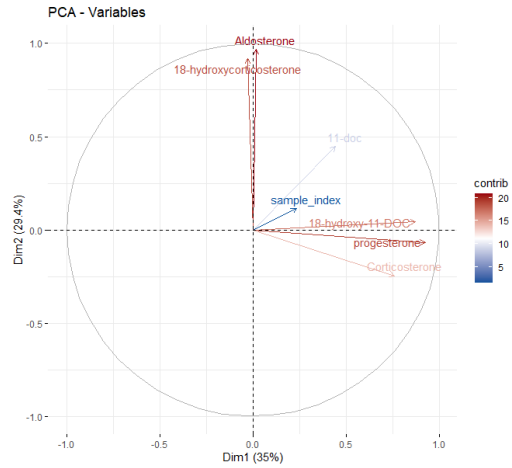

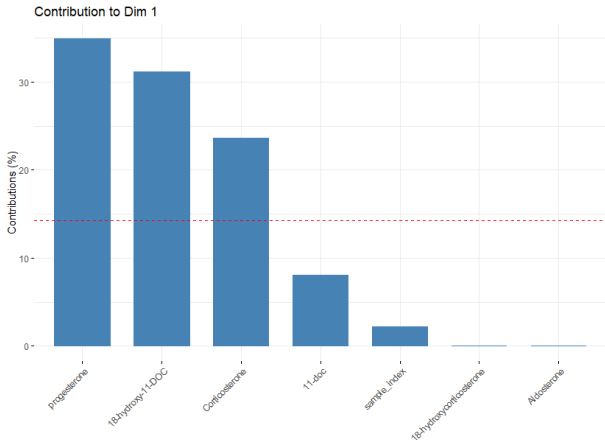

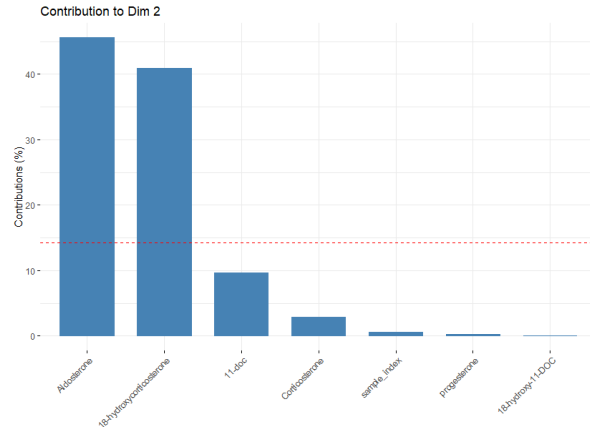

B.

Female

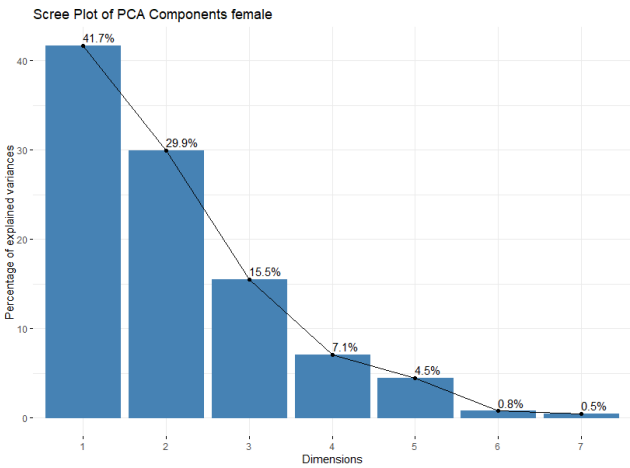

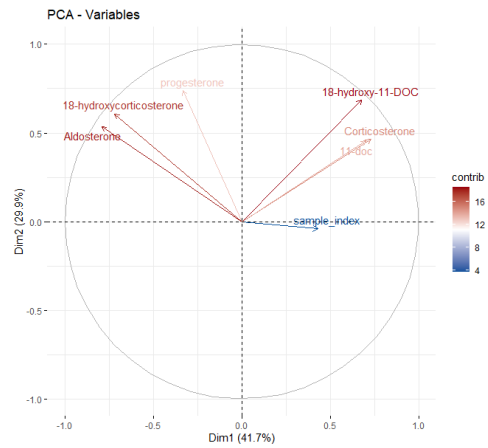

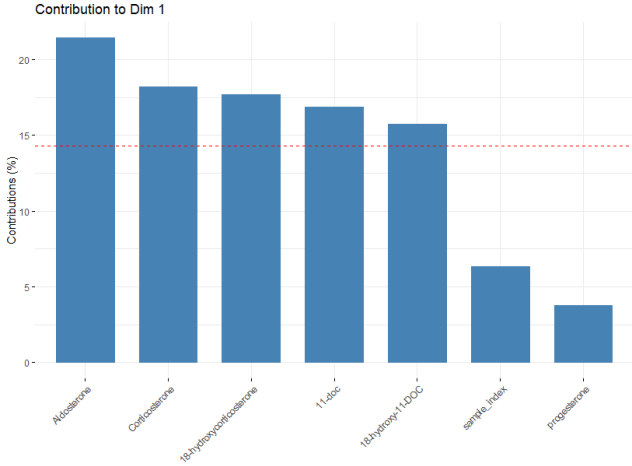

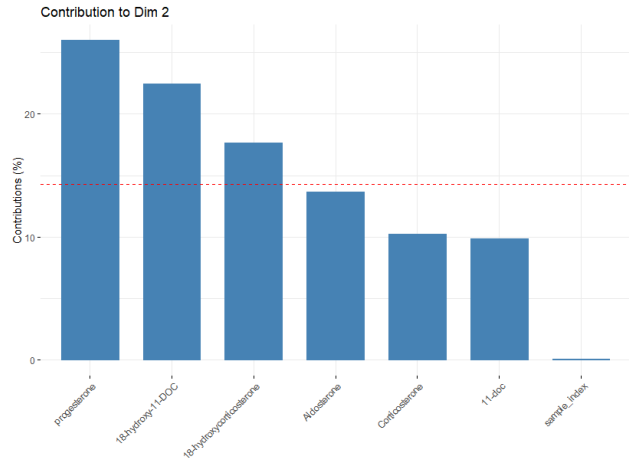

Supplementary Figure S2

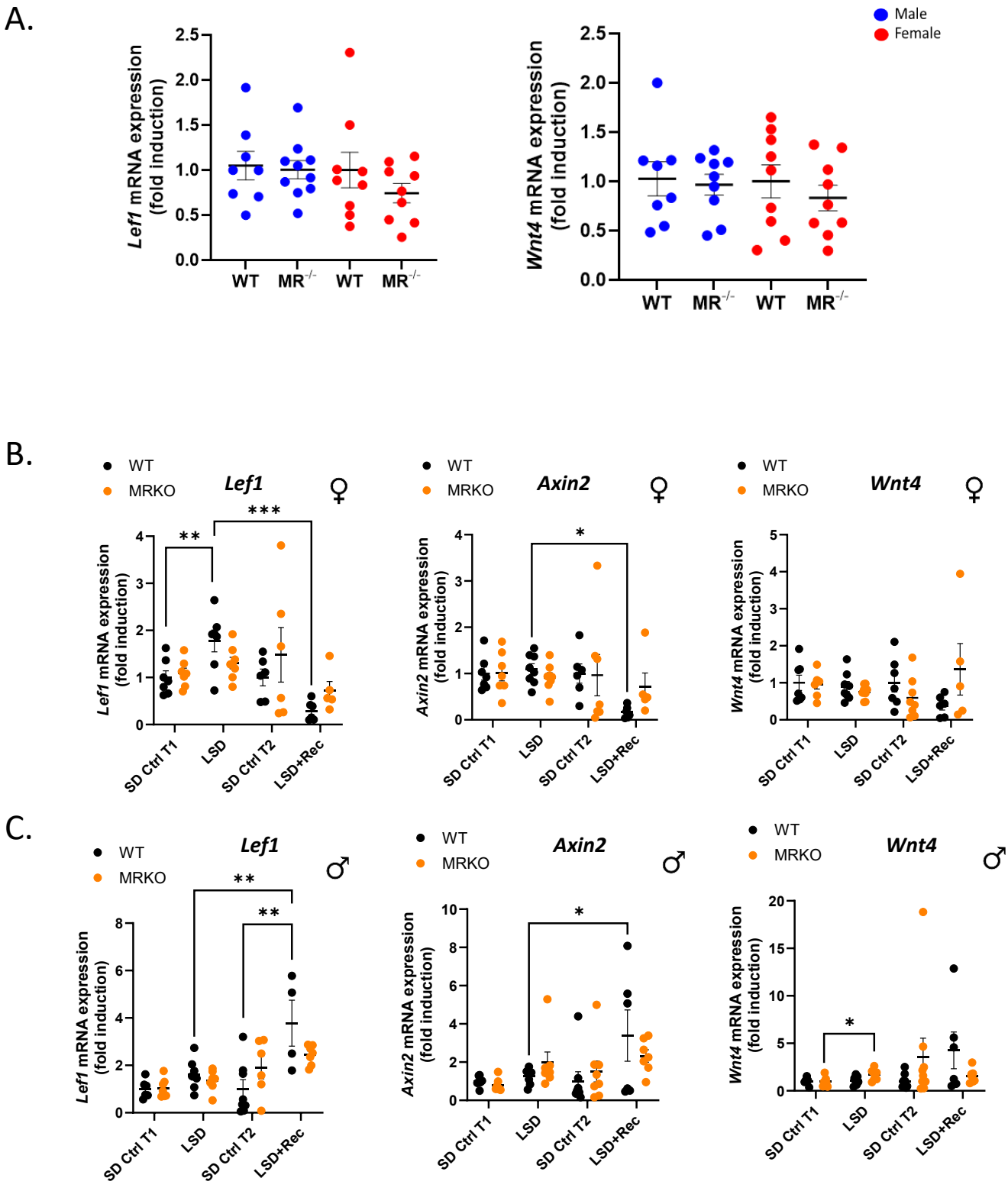

Supplementary Figure S3

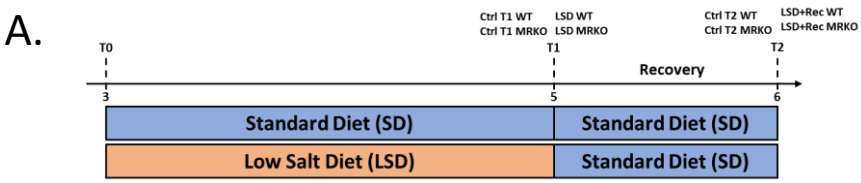

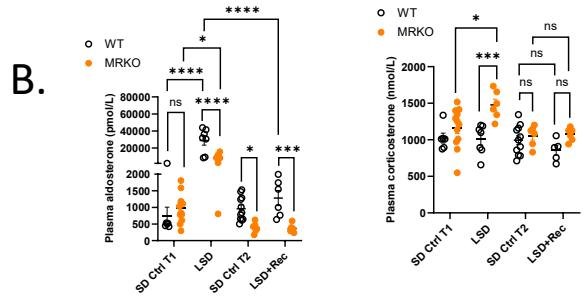

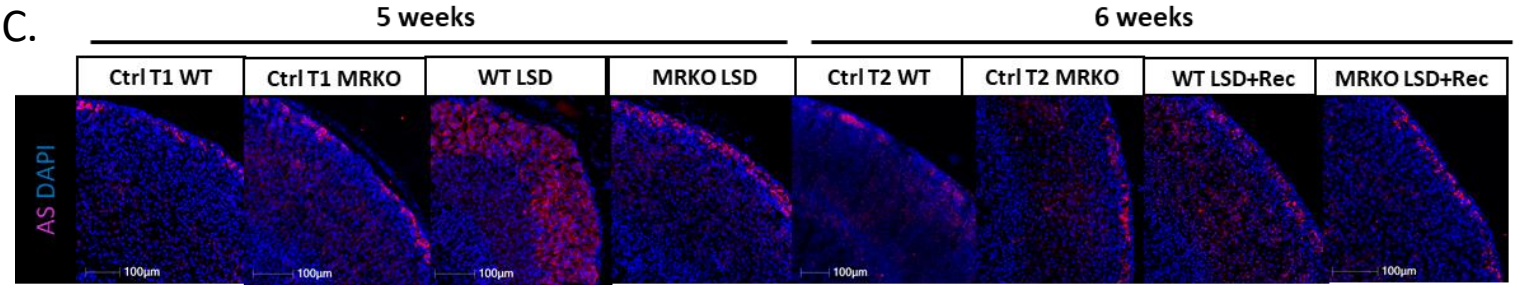

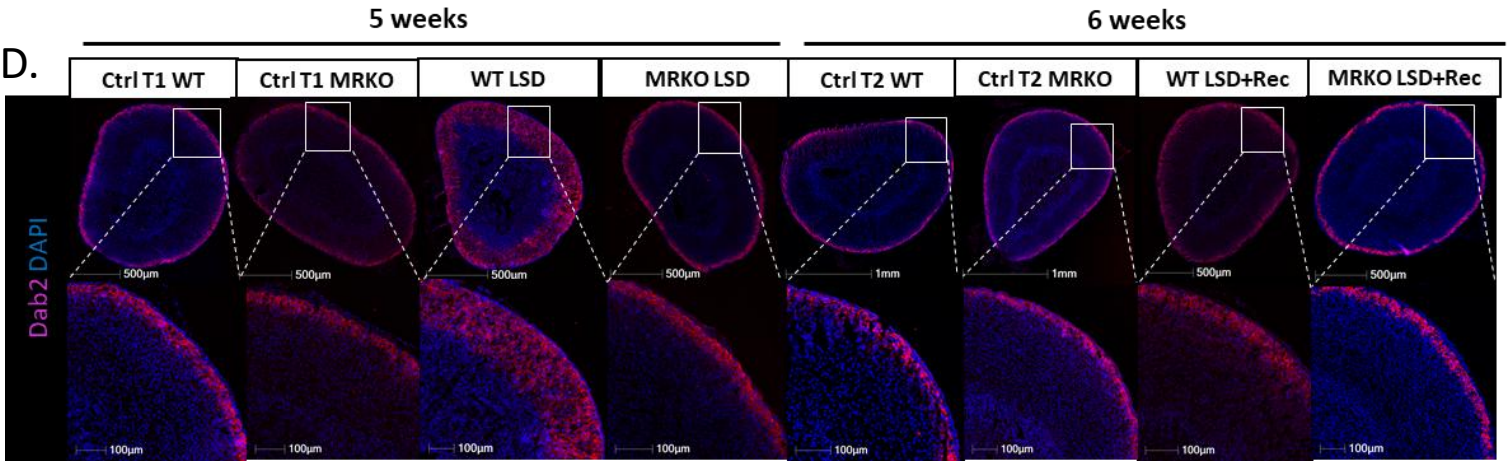

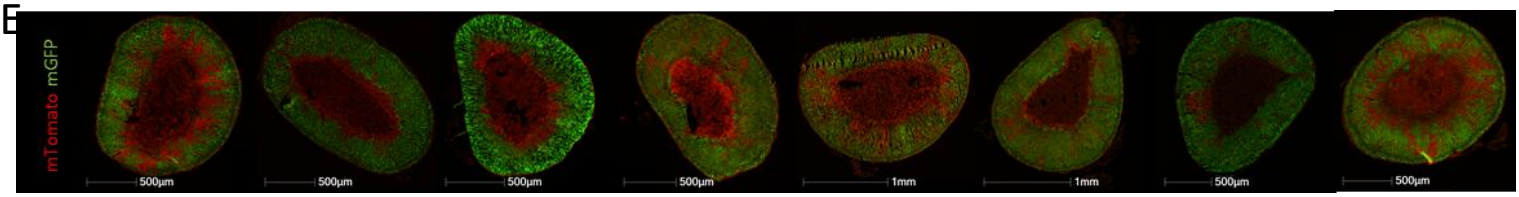

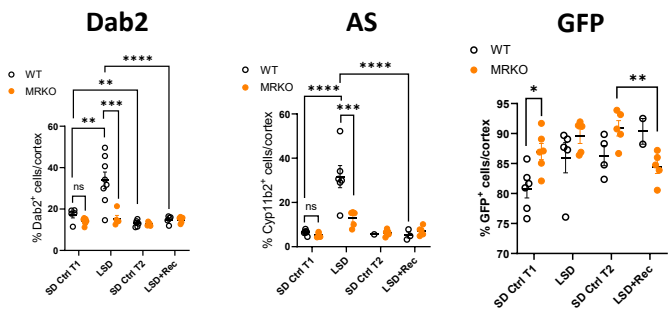

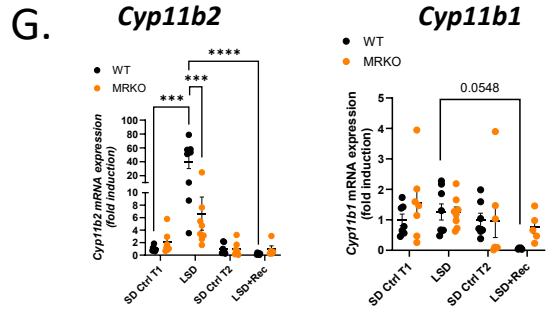

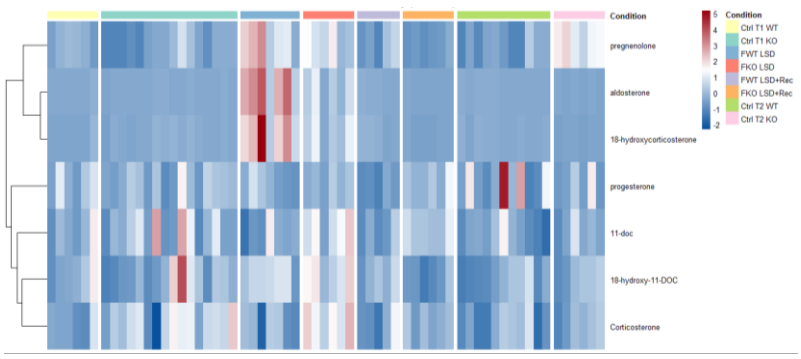

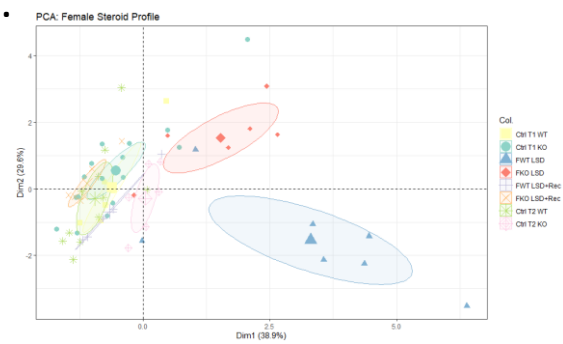

Supplementary Figure S4

Male

A.

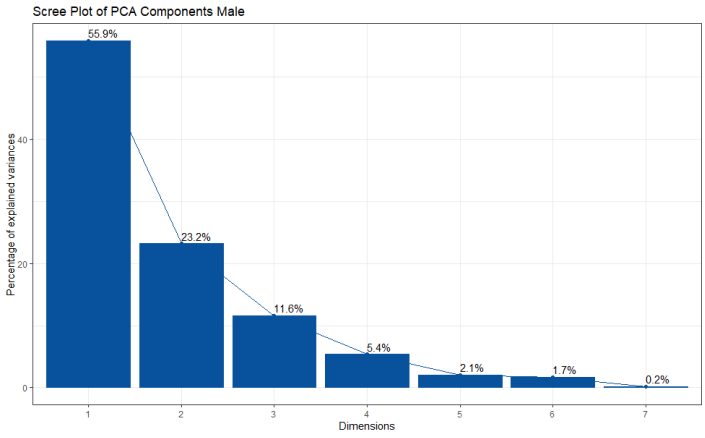

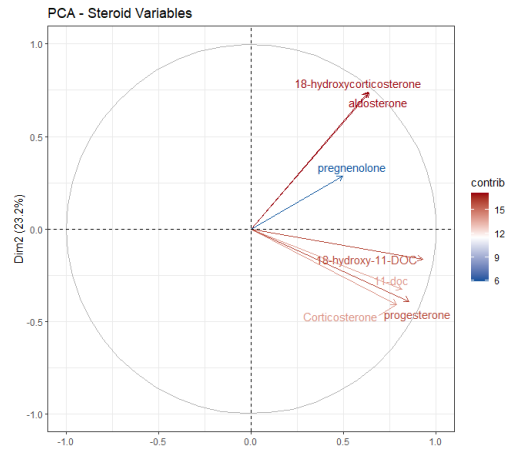

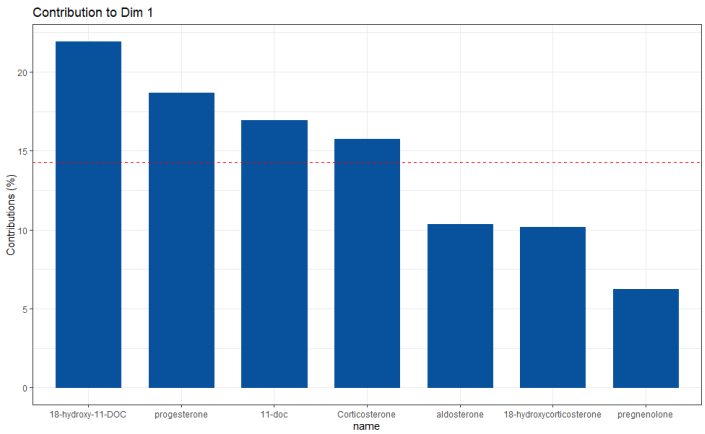

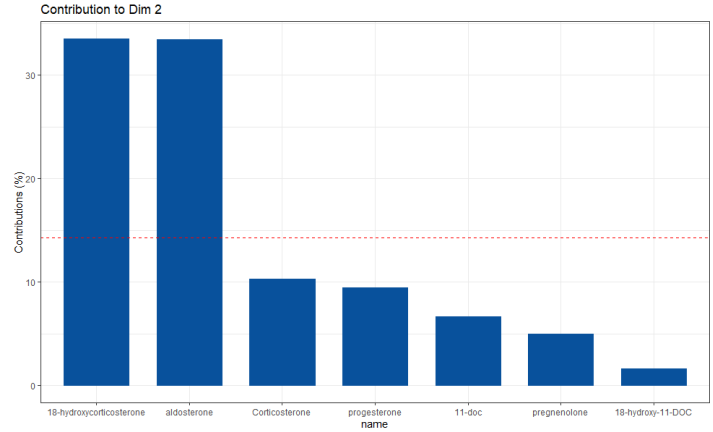

Female

B.

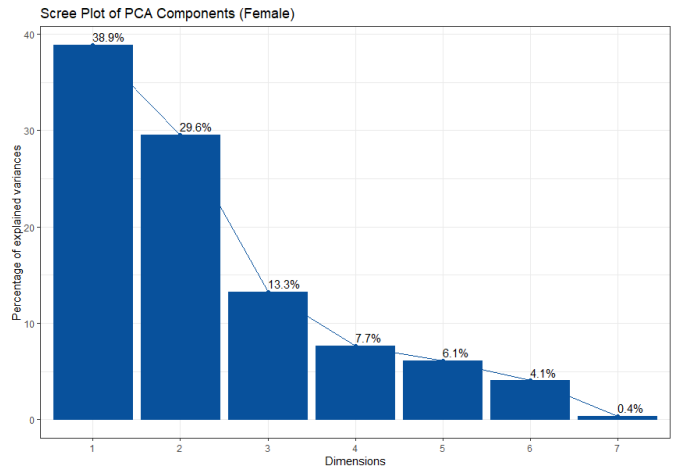

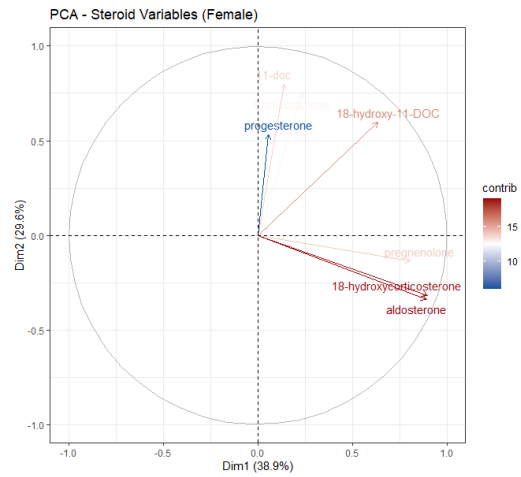

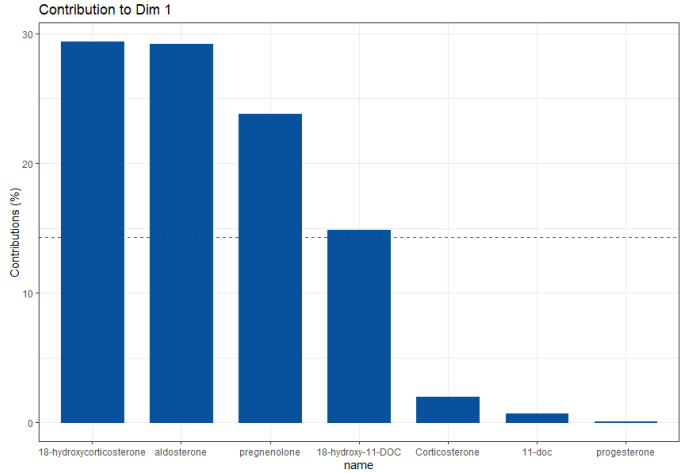

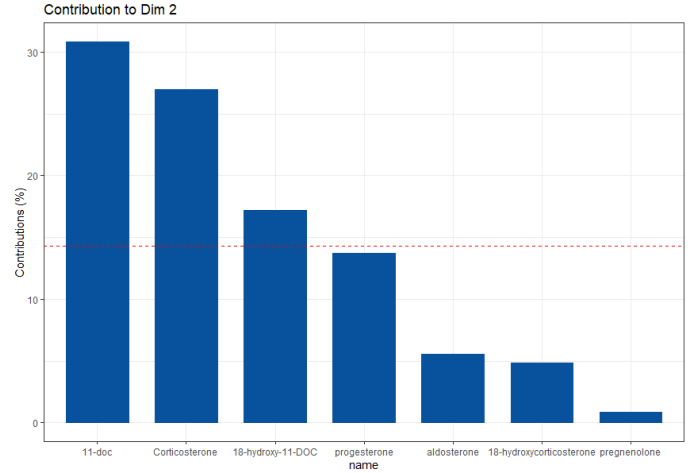

Supplementary Figure S5

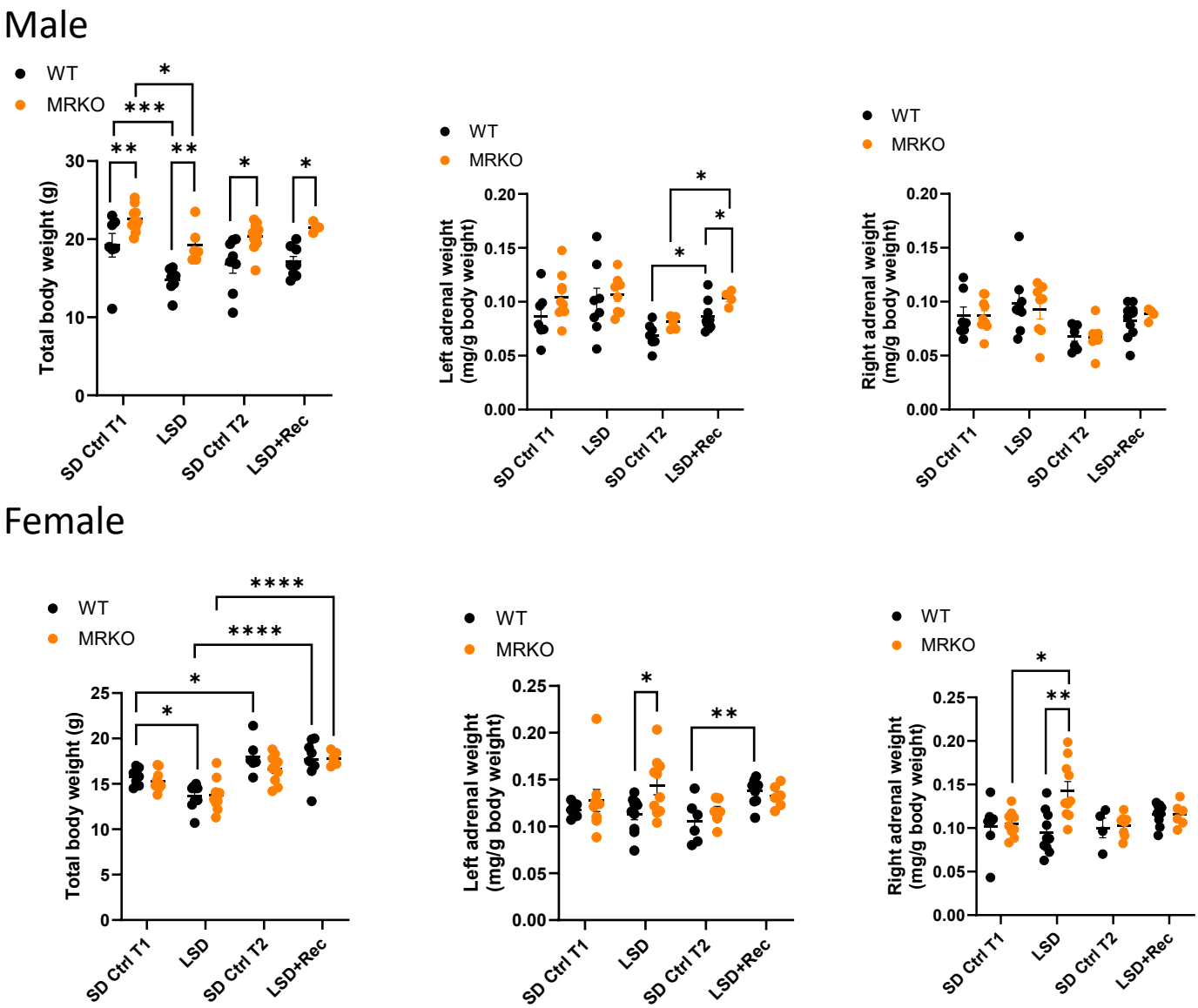

Supplementary Figure S6

A.

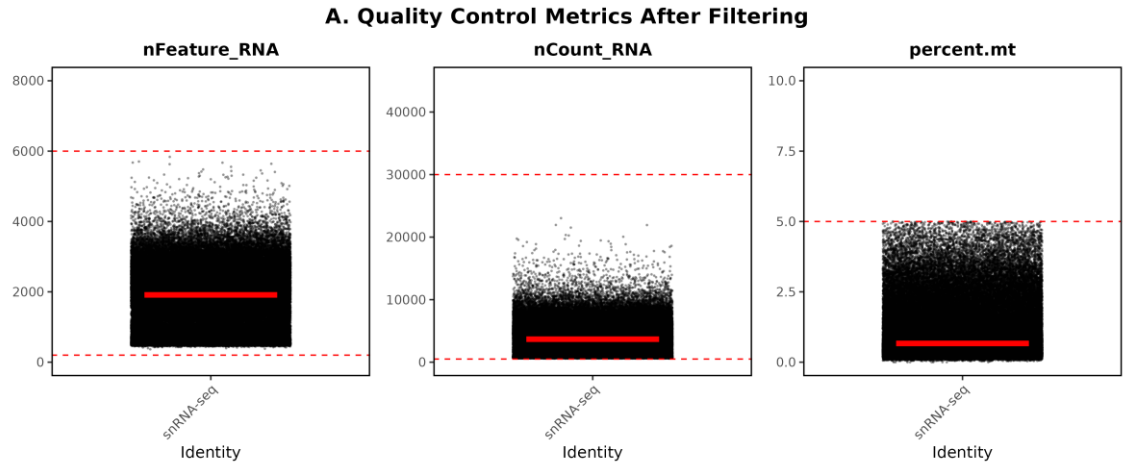

B.

sample	n_nuclei	mean_genes	median_genes	mean_UMI	median_UMI	mean_mito	median_mito
MKO_LSD	21687	1834	1992	4120	4404	1.21	0.71
MKO_SD	33951	1824	1906	3527	3489	0.84	0.57
MWT_LSD	23519	1861	2027	4045	4097	1.25	0.77
MWT_SD	26243	1688	1609	3629	2845	1.16	0.77

C.

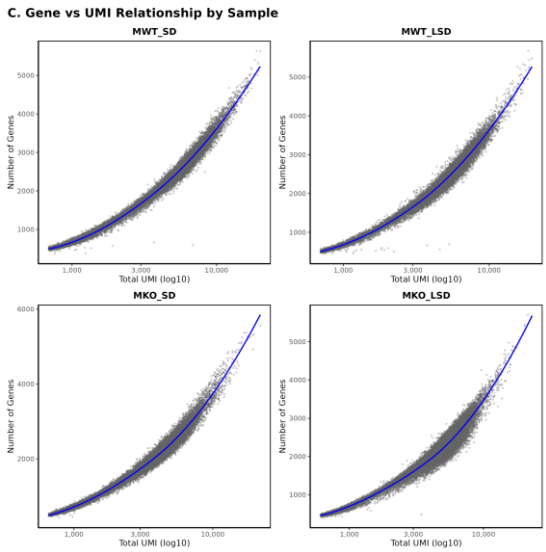

D.

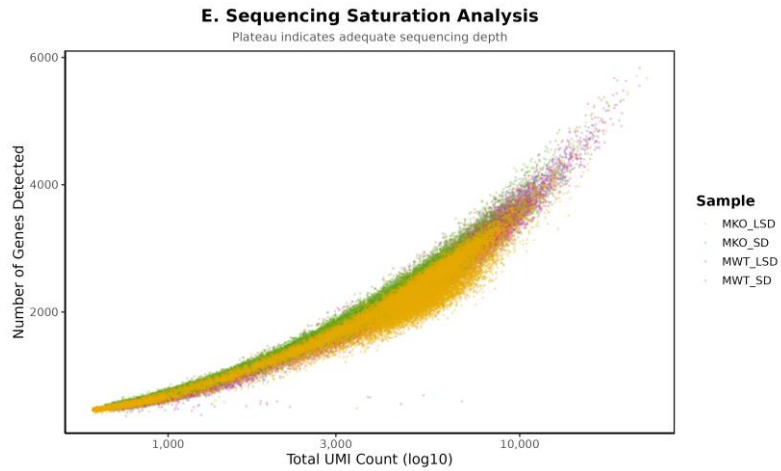

E.

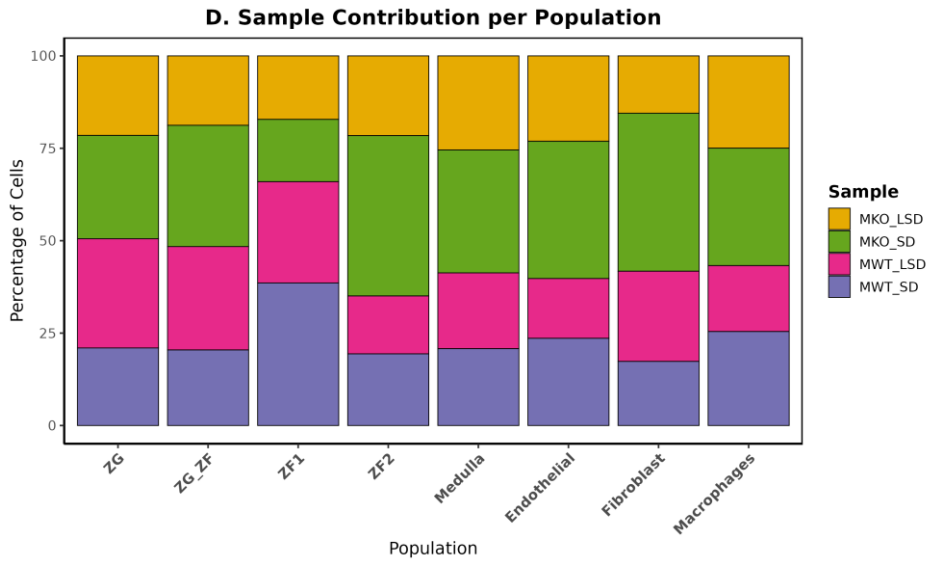

Supplementary Figure S8

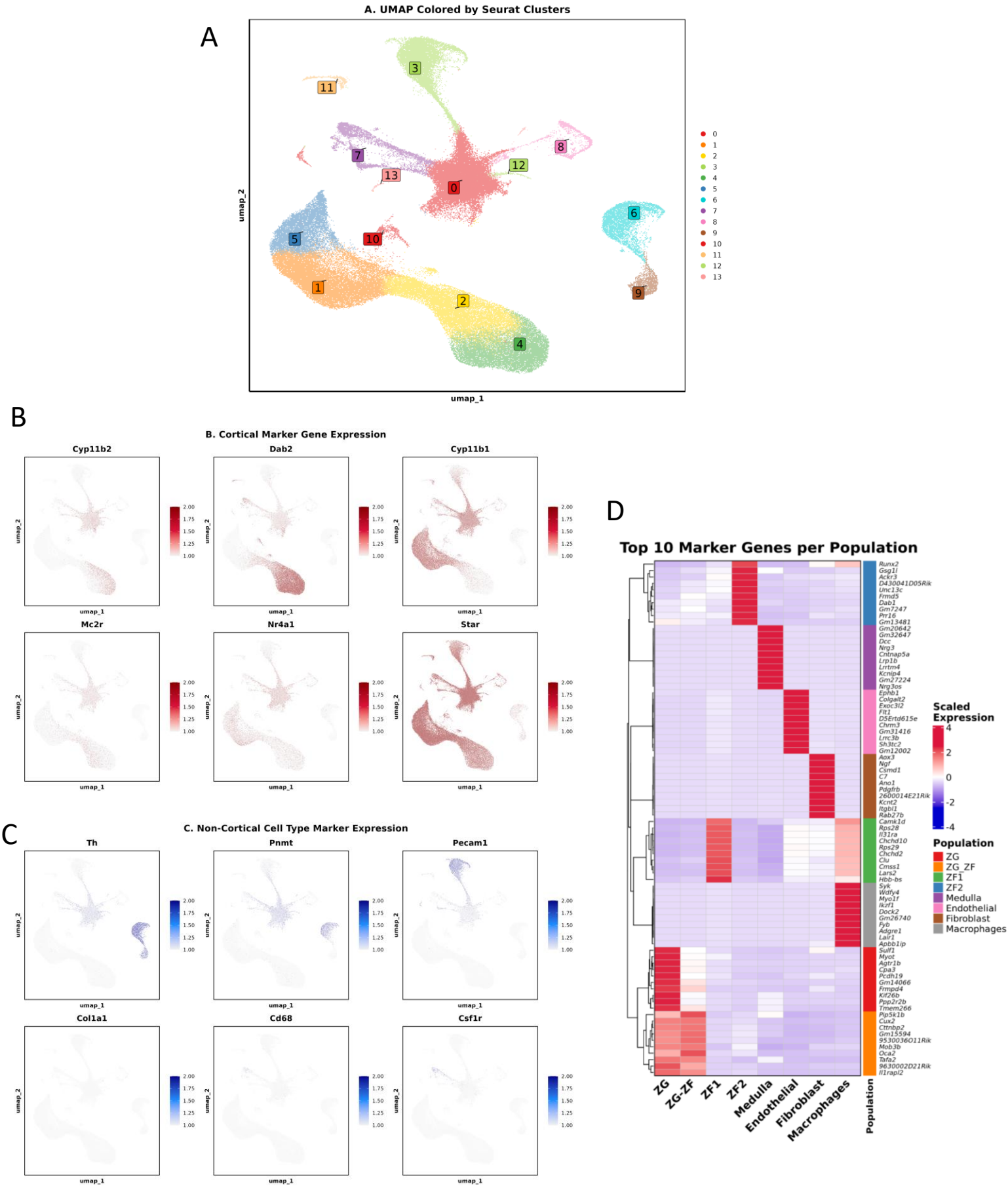

Supplementary Figure S9

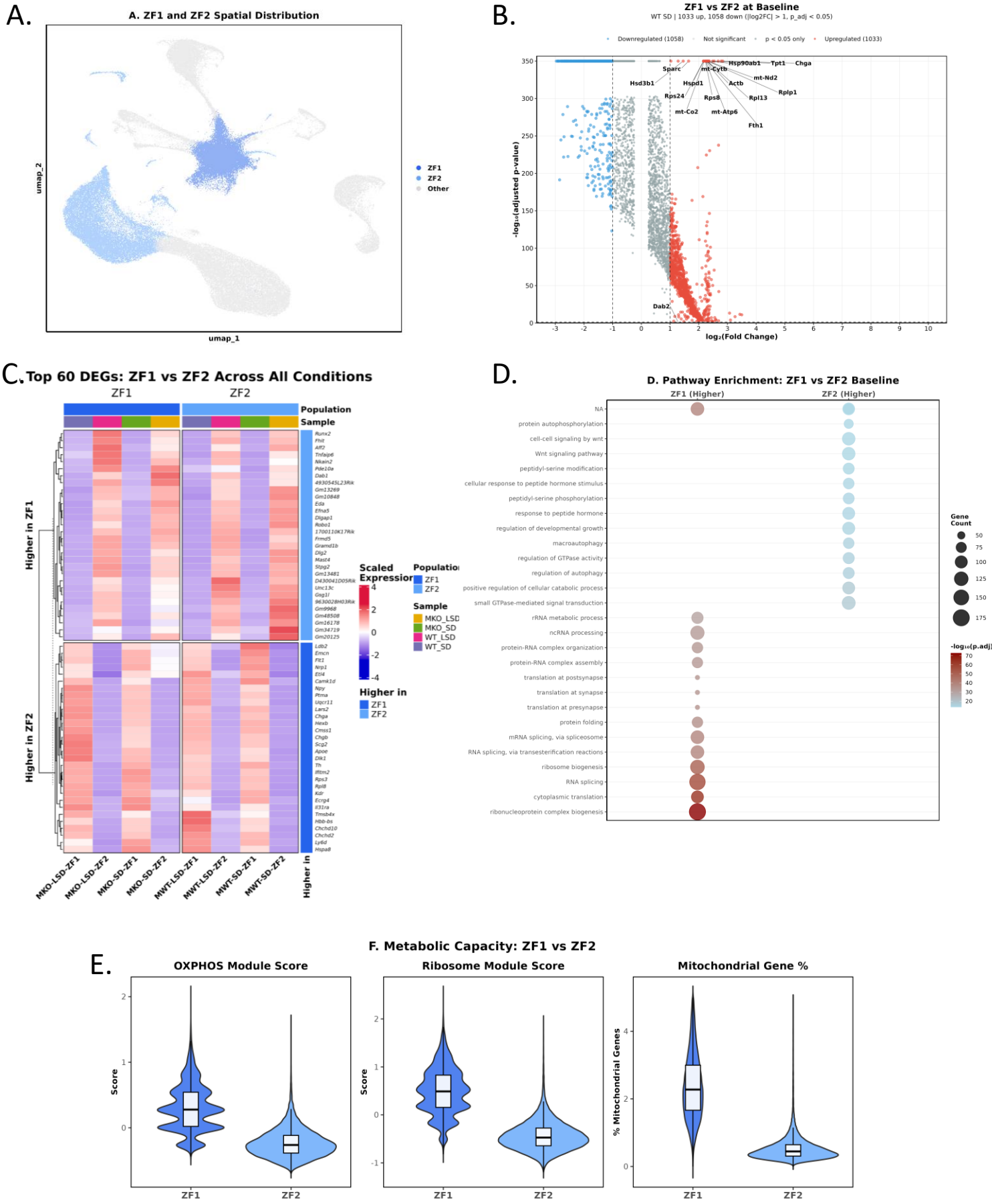

Supplementary Figure S10

A.

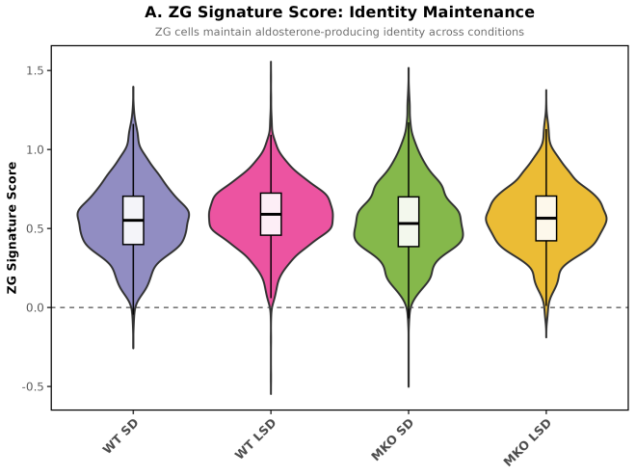

B.

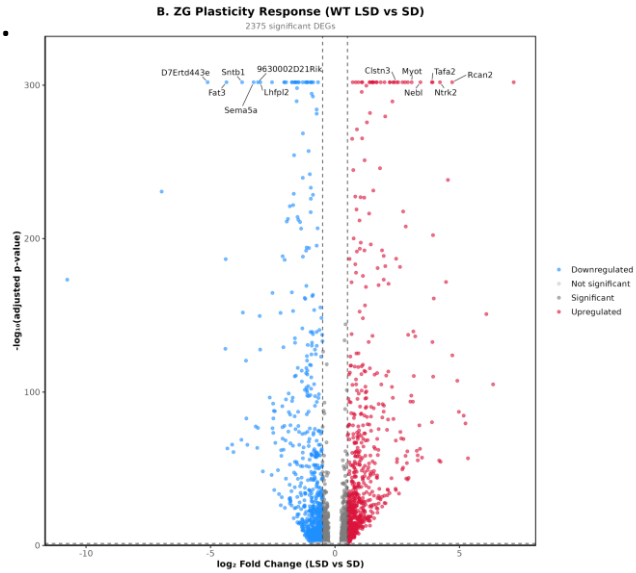

C.

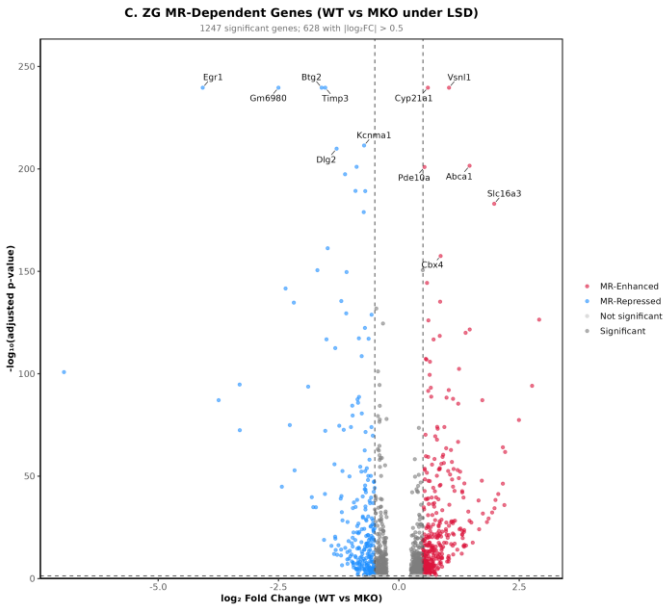

D.

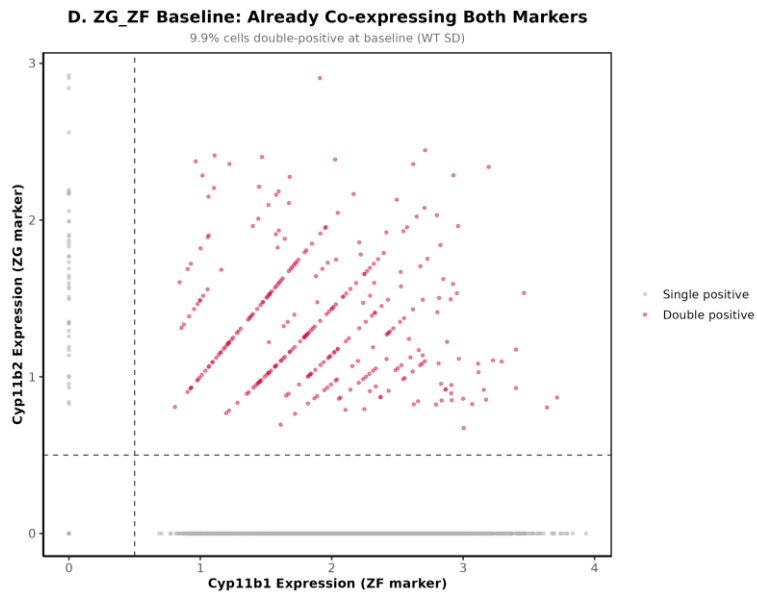

E.

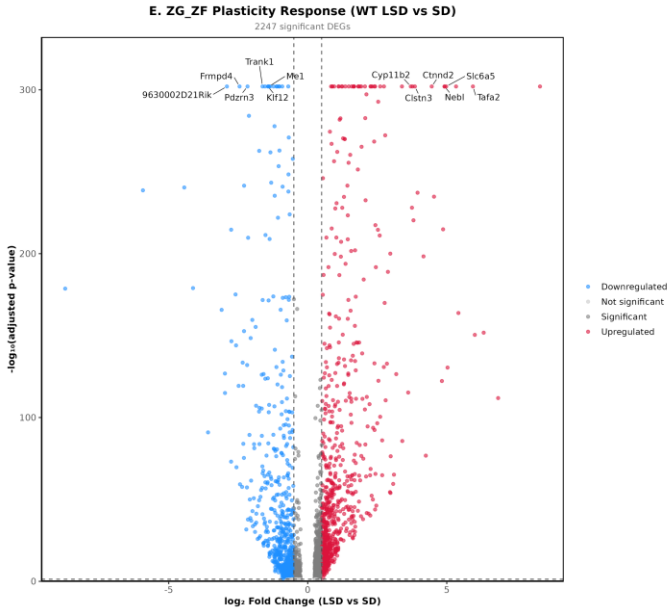

F.

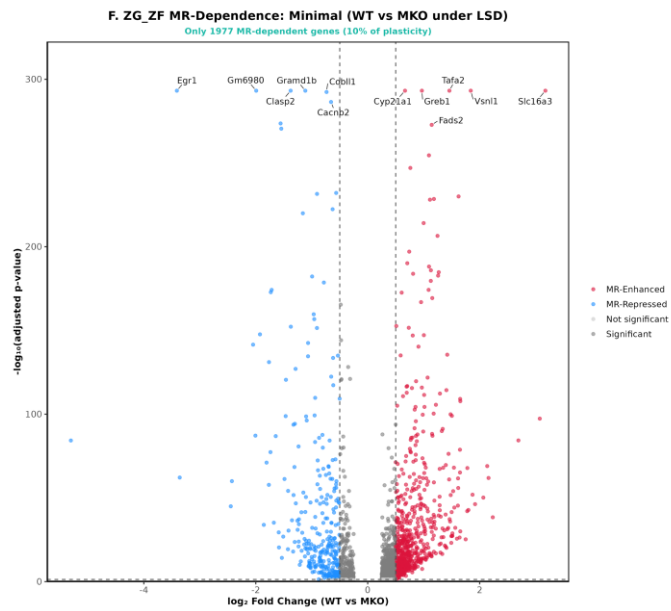

Figure 1. Generation and Characterization of Cyp11b2-Cre::Mr and Cyp11b2-Cre::Mr::mTmG Mouse Models

(A) Schematic representation of the genetic strategy. Cre recombinase was inserted into the 3' untranslated region of the Cyp11b2 gene after an internal ribosomal entry site (IRES). The IRES allows translation of two proteins (Cyp11b2 and Cre) from a single mRNA transcript, preserving functional aldosterone synthase expression. **(A.1)** Cyp11b2-Cre mice were crossed with Nr3c2-flox mice (exons 5 and 6 of Nr3c2 flanked by loxP sites) to generate MRKO mice with MR deletion specifically in Cyp11b2-expressing cells following Cre-Lox recombination. **(A.2)** MRKO mice were crossed with mTmG reporter mice (two-color fluorescent Cre-reporter allele) to generate the Cyp11b2-Cre::Nr3c2::mTmG (MRKO::mTmG) line for lineage tracing. **(B)** PCR analysis of genomic DNA from indicated tissues (tail, adrenal cortex, heart, kidney). Upper band (214 bp) represents the recombined allele (exons 5-6 excised); lower band (454 bp) represents the floxed allele. Adrenal cortex shows specific excision. **(C)** Quantitative PCR analysis of Nr3c2 mRNA expression in adrenal glands from wild-type and MRKO mice. Data normalized to housekeeping gene and expressed as fold change. **(D)** RNAscope in situ hybridization showing Nr3c2 mRNA expression (red dots) in adrenal cortex sections from wild-type and MRKO mice. Note absence of signal in zona glomerulosa of MRKO mice. Nuclei stained with [DAPI/hematoxylin, blue].Data are presented as mean ± SEM. ****p<0.0001 by unpaired t-test. Abbreviations: MWT, male wild type; MKO, $MRKO^{Ad}$ (male mineralocorticoid receptor knockout)

Figure 2. MR affects adrenal cortex morphology in 12-week-old male and female mice

(A) Total body weight and normalized weights of the right and left adrenal glands (relative to total body weight) in wild-type and MRKO male and female mice at 12 weeks of age. Blue dots = males, red dots = females. **(B)** Representative morphological characterization of adrenals from 12-week-old wild-type and MRKO mice. Upper panels: HES staining; Middle panels: Dab2 immunofluorescence (zona glomerulosa marker, magenta); Lower panels: 20α-HSD immunofluorescence (X zone marker, magenta). Nuclei stained with DAPI (blue). Scale bars: 100 µm. **(C)** Quantification of Dab2+ area in the adrenal cortex of wild-type and MRKO mice. Blue dots = males, red dots = females. **(D)** Quantification of 20α-HSD+ area in the adrenal cortex of wild-type and MRKO female mice. Red dots = females. Data are presented as mean ± SEM. *p<0.05; **p<0.01; ***p<0.001 by unpaired t-test or Mann-Whitney U test, as

appropriate based on normality testing. Abbreviations: MWT, male wild type; MKO, $MRKO^{Ad}$ (male mineralocorticoid receptor knockout)

Figure 3. Steroidogenic enzyme expression, proliferation, and hormone profiles in MRKO mice

(A) Representative immunofluorescence images of adrenal cortex from male and female wild-type and MRKO mice showing Cyp11b2 expression (magenta, aldosterone synthase). Nuclei stained with DAPI (blue). Scale bars: 100 μm. **(B)** Quantification of Cyp11b2+ area as percentage of total cortical area in male (blue dots) and female (red dots) mice. **(C)** Quantitative PCR analysis of steroidogenic enzyme expression in whole adrenal glands. Left: Cyp11b2 (aldosterone synthase); Middle: Cyp11b1 (11β-hydroxylase); Right: Star (steroidogenic acute regulatory protein). Values normalized to three housekeeping gene and expressed as fold change relative to sex-matched wild-type controls. Blue dots = males, red dots = females. **(D)** Comprehensive steroid profiling by liquid chromatography-tandem mass spectrometry (LC-MS/MS). Heatmaps show normalized steroid metabolite levels across the corticosteroid biosynthetic pathway in males (top) and females (bottom), with corresponding principal component analysis (PCA) plots (right) showing wild-type (circles) and MRKO (triangles) samples. **(E)** Plasma hormone and metabolite measurements at 12 weeks of age. Top row: Aldosterone (left), corticosterone (middle), and plasma renin activity/PRA (right). Bottom row: Aldosterone-to-angiotensin II ratio (AA2, left) and additional steroid metabolites (middle and right panels). Blue dots = males, red dots = females. **(F)** Representative immunofluorescence images of adrenal cortex showing Ki67 expression (orange, proliferation marker). Nuclei stained with DAPI (blue). Scale bars: 100 μm. **(G)** Quantification of Ki67+ proliferating cells as percentage of total cortical nuclei in male (blue dots) and female (red dots) mice **(H)** Western blot analysis of PKA signaling pathway activation. Representative blots showing total CREB (47 kDa), phosphorylated CREB (pCREB, 45 kDa), and β-actin (43 kDa, loading control) in adrenal lysates from wild-type and MRKO mice. Densitometric quantification of pCREB/total CREB ratio shown for males (top right) and females (bottom right). Blue dots = males, red dots = females. **(I)** Quantitative PCR analysis of PKA pathway components in adrenal glands. Left: PKA regulatory subunit (Prkar1a); Middle: PKA catalytic subunit (Prkaca); Right: Additional MR target genes. Values normalized to Actb housekeeping gene and expressed as fold change relative to sex-matched wild-type controls. Blue dots = males, red dots = females. All data presented as mean ± SEM. Statistical significance determined by unpaired t-test or Mann-Whitney U test following normality testing (Shapiro-Wilk test). *$p < 0.05$; **$p < 0.01$; ***$p <$

0.001. All mice analyzed at 12 weeks of age under standard diet conditions. Abbreviations: MWT, male wild type; MKO, MRKO^{Ad} (male mineralocorticoid receptor knockout)

Figure 4. Effect of LSD on Male MRKO Adrenal Gland

(A) Schematic representation of the low salt diet (LSD) administration protocol on male wild-type and MRKO mice from 3 weeks of age (T0) to 5 weeks (T1), followed by a one-week recovery period until 6 weeks of age (T2). **(B)** Plasma aldosterone and corticosterone levels measured by LC-MS/MS at T1 and T2 in male wild-type and MRKO mice. Black dots = wild-type, orange dots = MRKO. **(C)** Immunofluorescent labeling of Cyp11b2/AS (aldosterone synthase, magenta) in the adrenal cortex of male wild-type and MRKO mice at time points T1 and T2. Scale bars: 100 µm. **(D)** Immunofluorescent labeling of Dab2-positive cells (magenta) in the adrenal cortex of male wild-type and MRKO mice at T1 and T2. White squares represent the magnification area in the lower panel. Scale bars: 500 µm or 1 mm (upper), 100 µm (lower). **(E)** Co-immunofluorescence of mGFP (green) and mTomato (red) in male wild-type and MRKO mouse adrenals at T1 and T2. Scale bars: 100 µm. **(F)** Quantifications of Dab2+ cells, Cyp11b2+ cells, and mGFP+ cells in male wild-type and MRKO adrenals at T1 and T2. Black dots = wild-type, orange dots = MRKO. **(G)** Relative Cyp11b2 and Cyp11b1 mRNA expression measured by RT-qPCR in wild-type and MRKO mouse adrenals at T1 and T2. Black dots = wild-type, orange dots = MRKO. **(H)** Hierarchically clustered heatmaps of plasma steroid profiles of male wild-type and MRKO mice at T1 and T2. **(I)** Principal component analysis (PCA) of plasma steroid profiles of male wild-type and MRKO mice at T1 and T2. Data are presented as mean ± SEM. *$p<0.05$; **$p<0.01$; ***$p<0.001$ by two-way ANOVA followed by Sidak's post-hoc test. Abbreviations: MWT, male wild type; MKO, MRKO^{Ad} (male mineralocorticoid receptor knockout).

Figure 5. X-Zone Plasticity in MRKO Female Mice During LSD

(A) Representative co-immunofluorescence images of mGFP (green, Cyp11b2-lineage traced cells) and 20αHSD (purple, X zone marker) in adrenal cortex of wild-type and MRKO female mice under control conditions (Ctrl T1, Ctrl T2), following low salt diet (LSD), and after one week recovery (LSD+REC). White squares represent the magnification area shown in lower panels. Scale bars: 500 µm or 1 mm (upper panels), 100 µm (lower panels). **(B)** Quantification of 20αHSD+ area as percentage of total cortex. No significant differences were observed between genotypes or conditions. **(C)** Quantification of mGFP+20αHSD+ double-positive cells as percentage of total cortex. MRKO females showed significantly increased double-

positive cells after recovery compared to LSD. **(D)** Quantification of mGFP+20αHSD+ double-positive cells as percentage of X zone area. MRKO females showed age-dependent increase in double-positive cells (Ctrl T2 vs Ctrl T1). **(F)** Quantitative PCR analysis of Akr1c18 mRNA expression in adrenal glands. Wild-type females showed increased expression during LSD and after recovery compared to respective controls. Data are presented as mean ± SEM. Statistical analyses were performed using two-way ANOVA followed by Sidak's post-hoc test for multiple comparisons, with separate analyses conducted for T1 timepoint, T2 timepoint, and temporal comparisons (T1 vs T2). *p<0.05; **p<0.01. Abbreviations: MWT, male wild type; MKO, $MRKO^{Ad}$ (male mineralocorticoid receptor knockout).

Figure 6. Single-Nucleus Transcriptomic Atlas of the Mouse Adrenal Gland

(A) UMAP visualization of 105,400 nuclei from adult mouse adrenal glands, colored by cell type identity. Eight populations were identified through unbiased graph-based clustering and canonical marker expression: non-plastic zona fasciculata (ZF2, blue, 27.9%), plastic zona fasciculata (ZF1, green, 23.1%), ZG-ZF transition zone (orange, 14.6%), endothelial cells (pink, 11.4%), zona glomerulosa (ZG, red, 11.0%), medulla (purple, 6.4%), macrophages (gray, 3.7%), and fibroblasts (brown, 1.9%). Each point represents a single nucleus; spatial proximity indicates transcriptomic similarity. **(B)** UMAP visualization split by experimental condition showing cell type distribution across wild-type standard diet (MWT_SD, n=26,243 cells), wild-type low-sodium diet (MWT_LSD, n=23,519 cells), MR knockout standard diet (MKO_SD, n=33,951 cells), and MR knockout low-sodium diet (MKO_LSD, n=21,687 cells). Cell type colors correspond to panel A. **(C)** Stacked bar plot showing relative cell type proportions across experimental conditions. Each bar represents 100% of total cells captured in that condition. Bar segments are stacked from bottom to top in the following order: ZG (red), ZG_ZF (orange), ZF1 (green), ZF2 (blue), medulla (purple), endothelial (pink), fibroblast (brown), and macrophages (gray). Colors match cell type assignments in panels A and B. **(D)** Dot plot of canonical marker gene expression across cell populations. Dot size indicates the percentage of cells within each population expressing the indicated gene. Dot color represents average normalized expression level across all cells in that population (blue=low expression, yellow=intermediate, red=high expression). Marker genes shown: zona glomerulosa (*Cyp11b2, Dab2, Wnt4, Shh*); zona fasciculata (*Cyp11b1, Hsd3b6, Nr4a1*); medulla (*Th, Ddc, Pnmt*); endothelial (*Pecam1, Cdh5, Vwf*); fibroblast (*Col1a1, Dcn, Lum*); macrophages (*Cd68, Csf1r, Adgre1*). Gene names are italicized according to standard mouse nomenclature. Data represent n=12 mice (3 biological replicates per condition, 4 experimental conditions). Dimensionality

reduction was performed using UMAP on harmony-corrected principal components. Abbreviations: ZG, zona glomerulosa; ZF, zona fasciculata; MR, mineralocorticoid receptor; MWT, wild-type; MKO, MR knockout; SD, standard diet; LSD, low-sodium diet (14 days). Abbreviations: MWT, male wild type; MKO, $MRKO^{Ad}$ (male mineralocorticoid receptor knockout).

Figure 7. Heterogeneous mechanisms of cortical plasticity revealed by double-positive cell analysis and zona glomerulosa signature scores.

(A) UMAP feature plots showing scaled expression of *Cyp11b1* (top row, zona fasciculata marker) and *Cyp11b2* (bottom row, zona glomerulosa marker) across all four experimental conditions. Co-expression indicates plasticity. **(B)** Bar plot quantifying the percentage of double-positive cells (co-expressing *Cyp11b1* and *Cyp11b2*, expression threshold > 0.5) in ZG_ZF, ZF1, and ZF2 populations across all conditions. Error bars represent standard error of the mean. MR-dependence percentages are calculated as: [(WT change - MKO change) / WT change] × 100. **(C)** Violin plots with overlaid box plots showing ZG signature scores (6-gene module: *Cyp11b2*, *Dab2*, *Wnt4*, *Shh*, *Rspo3*, *Axin2*) across ZG, ZG_ZF, ZF1, and ZF2 populations in all four conditions. Dashed horizontal line at y = 0 indicates the threshold between ZG-positive (above) and ZG-negative (below) identity. ***$p < 0.001$, Wilcoxon rank-sum test. **(D)** Summary table comparing the mechanisms of plasticity in ZG_ZF (position-driven, 10.3% MR-dependent) versus ZF1 (MR-driven, 48.6% MR-dependent) populations, showing baseline double-positive percentages, salt-induced changes, and key distinguishing features. Abbreviations: MWT, male wild type; MKO, MRKOAd (male mineralocorticoid receptor knockout)**.**

Figure 8. MR-Dependent Transcriptional Programs in ZF1 Plasticity

(A-B) Heatmaps showing average scaled expression (z-score, capped at ±2.5) of top 60 differentially expressed genes in ZF1 cells. **(A)** Salt-induced plasticity genes (WT LSD vs WT SD): top 30 upregulated (red bar) and top 30 downregulated (blue bar) genes. **(B)** MR-dependent genes (WT LSD vs MKO LSD): top 30 MR-enhanced (red bar) and top 30 MR-repressed (purple bar) genes. Genes ranked by adjusted p-value and $\log_2$ fold change, clustered within each direction. **(C)** Venn diagram showing overlap between salt-induced plasticity genes (left) and MR-enhanced genes (right). Numbers indicate gene counts in each category. **(D)** Dot plot comparing GO Biological Process enrichment between gene sets. Top 20 pathways by combined significance shown. Dot size = gene count; dot color = $-\log_{10}$(adjusted p-value). Pink

shading highlights pathways enriched in both analyses. Single-nucleus RNA-seq from male mice (MWT_SD, MWT_LSD, MKO_SD, MKO_LSD). Differential expression by Wilcoxon test, adjusted $p < 0.05$. GO enrichment by clusterProfiler with Benjamini-Hochberg correction. Abbreviations: MWT, male wild type; MKO, MRKO^{Ad} (male mineralocorticoid receptor knockout).

Supplementary Figure S1. Principal Component Analysis Characteristics of Plasma Steroid Profiles in 12-Week-Old Mice

(A) Male steroid profile analysis. Top left: Scree plot showing the percentage of variance explained by each principal component (dimension). Top right: Variables factor map showing the relationship between individual steroids and principal components, with red and blue indicating opposing correlations. Bottom left: Bar plot showing the contribution of individual steroids to Dim1. Bottom right: Bar plot showing the contribution of individual steroids to Dim2. **(B)** Female steroid profile analysis. Top left: Scree plot showing the percentage of variance explained by each principal component (dimension). Top right: Variables factor map showing the relationship between individual steroids and principal components, with red and blue indicating opposing correlations. Bottom left: Bar plot showing the contribution of individual steroids to Dim1. Bottom right: Bar plot showing the contribution of individual steroids to Dim2. Abbreviations: MWT, male wild type; MKO, MRKO^{Ad} (male mineralocorticoid receptor knockout).

Supplementary Figure S2. Wnt/β-catenin pathway gene expression at baseline and during salt restriction challenge.

(A) qPCR analysis of Wnt/β-catenin pathway genes (*Lef1*, *Wnt4*) in adrenal glands from 12-week-old wild-type (WT) and zona glomerulosa-specific MR knockout (MRKO) mice under basal conditions (standard diet) for both male and female mice. **(B)** qPCR analysis of Wnt pathway target genes (*Lef1*, *Axin2*) and ligand (*Wnt4*) in female zona glomerulosa at baseline (Ctrl T1), after 14 days of low-salt diet (LSD), after 14 days recovery (LSD+REC), and age-matched recovery controls (Ctrl T2). **(C)** qPCR analysis of Wnt pathway genes (*Lef1*, *Axin2*, *Wnt4*) in male zona glomerulosa at baseline (Ctrl T1), after 14 days of low-salt diet (LSD), after 14 days recovery (LSD+REC), and age-matched recovery controls (Ctrl T2). Includes both wild-type and MRKO mice. Gene expression normalized to housekeeping genes *(Ubc, 18S, b2m)* and expressed as fold change relative to Ctrl T1 WT for each sex. Data represent mean ± SEM. Statistical analysis by two-way ANOVA (genotype × condition) with

Sidak's multiple comparisons test. *P < 0.05, **P < 0.01, ***P < 0.001; ns, not significant. Abbreviations: MWT, male wild type; MKO, MRKO^{Ad} (male mineralocorticoid receptor knockout).

Supplementary figure S3. Effect of LSD on female MRKO adrenal gland

(A) Schematic representation of the low salt diet (LSD) administration protocol on male wild-type and MRKO mice from 3 weeks of age (T0) to 5 weeks (T1), followed by a one-week recovery period until 6 weeks of age (T2). **(B)** Plasma aldosterone and corticosterone levels measured by LC-MS/MS at T1 and T2 in female wild-type and MRKO mice. Black dots = wild-type, orange dots = MRKO. **(C)** Immunofluorescent labeling of Cyp11b2/AS (aldosterone synthase, magenta) in the adrenal cortex of female wild-type and MRKO mice at time points T1 and T2. Scale bars: 100 µm. **(D)** Immunofluorescent labeling of Dab2-positive cells (magenta) in the adrenal cortex of female wild-type and MRKO mice at T1 and T2. White squares represent the magnification area in the lower panel. Scale bars: 500 µm or 1 mm (upper), 100 µm (lower). **(E)** Co-immunofluorescence of mGFP (green) and mTomato (red) in female wild-type and MRKO mouse adrenals at T1 and T2. Scale bars: 100 µm. **(F)** Quantifications of Dab2+ cells, Cyp11b2+ cells, and mGFP+ cells in female wild-type and MRKO adrenals at T1 and T2. Black dots = wild-type, orange dots = MRKO. **(G)** Relative Cyp11b2 and Cyp11b1 mRNA expression measured by RT-qPCR in wild-type and MRKO mouse adrenals at T1 and T2. Black dots = wild-type, orange dots = MRKO. **(H)** Hierarchically clustered heatmaps of plasma steroid profiles of female wild-type and MRKO mice at T1 and T2. **(I)** Principal component analysis (PCA) of plasma steroid profiles of female wild-type and MRKO mice at T1 and T2. Data are presented as mean ± SEM. *p<0.05; **p<0.01; ***p<0.001 by two-way ANOVA followed by Sidak's post-hoc test. Abbreviations: MWT, male wild type; MKO, MRKO^{Ad} (male mineralocorticoid receptor knockout).

Supplementary Figure S4. Principal Component Analysis Characteristics of Plasma Steroid Profiles Following Salt Restriction

(A) Male steroid profile analysis. Top left: Scree plot showing the percentage of variance explained by each principal component (dimension). Top right: Variables factor map showing the relationship between individual steroids and principal components, with red and blue indicating opposing correlations. Bottom left: Bar plot showing the contribution of individual steroids to Dim1. Bottom right: Bar plot showing the contribution of individual steroids to Dim2. **(B)** Female steroid profile analysis. Top left: Scree plot showing the percentage of

variance explained by each principal component (dimension). Top right: Variables factor map showing the relationship between individual steroids and principal components, with red and blue indicating opposing correlations. Bottom left: Bar plot showing the contribution of individual steroids to Dim1. Bottom right: Bar plot showing the contribution of individual steroids to Dim2. PCA analysis revealed clear separation between control and LSD groups along the first dimension (Dim1), which explained 50.5% of variance in males and 38.6% of variance in females. Abbreviations: MWT, male wild type; MKO, $MRKO^{Ad}$ (male mineralocorticoid receptor knockout).

Supplementary Figure S5. Body and Adrenal Weights During Salt Restriction Challenge

Total body weight (left panels), normalized left adrenal weight (middle panels), and normalized right adrenal weight (right panels) in wild-type and MRKO mice during the LSD protocol. Upper panels: males; Lower panels: females. Mice were assessed at baseline (SD Ctrl T1), after LSD treatment (LSD), at the second baseline timepoint (SD Ctrl T2), and after recovery (LSD+rec). Adrenal weights are normalized to total body weight and expressed as mg/g body weight. Black dots = wild-type, orange dots = MRKO. Data are presented as mean ± SEM. *p<0.05; **p<0.01; ***p<0.001; ****p<0.0001 by two-way ANOVA followed by Sidak's post-hoc test. Abbreviations: MWT, male wild type; MKO, $MRKO^{Ad}$ (male mineralocorticoid receptor knockout).

Supplementary Figure S6. Quality control metrics and technical validation of single-nucleus RNA sequencing data.

(A) Distribution of quality control metrics for all nuclei after filtering (n=105,400). Individual nuclei are shown as black points. Red dashed lines indicate filtering thresholds: nFeature_RNA (200-6,000 genes), nCount_RNA (500-30,000 UMI), and percent.mt (<5% mitochondrial content). Red bars indicate median values. All samples combined (MWT_SD, MWT_LSD, MKO_SD, MKO_LSD). **(B)** Summary statistics table showing nuclei count and quality metrics for each sample after filtering. Values include mean and median gene detection, UMI counts, and mitochondrial gene percentage per sample. **(C)** Relationship between total UMI count and number of genes detected for each sample individually. Scatter plots show individual nuclei (gray points) with loess smoothing curve (blue line). The plateau in the curves indicates adequate sequencing depth, with most nuclei achieving saturation in gene detection. **(D)** Sequencing saturation analysis across all samples. Individual nuclei are colored by sample identity. Black line represents loess fit across all data. The plateau demonstrates that sequencing

depth was sufficient to capture the majority of expressed genes per nucleus. **(E)** Sample contribution to each annotated cell population after Harmony batch correction. Stacked bar plots show the percentage of nuclei from each sample (color-coded) within each population. Balanced representation across samples within each population validates successful integration while preserving biological variation between experimental conditions. ZG, zona glomerulosa; ZG_ZF, zona glomerulosa-zona fasciculata transition zone; ZF1, zona fasciculata cluster 0; ZF2, zona fasciculata clusters 1-10. **All panels:** Data represent 105,400 high-quality nuclei from 4 samples representing four experimental conditions (wild-type standard diet [MWT_SD], wild-type LSD [MWT_LSD], MR knockout standard diet [MKO_SD], MR knockout LSD [MKO_LSD]). Each sample consists of 3 pooled adrenal glands from male mice of the same genotype and dietary treatment.

Supplementary Figure S7. Quality control metrics and technical validation of single-nucleus RNA sequencing data.

(A) Distribution of quality control metrics for all nuclei after filtering (n=105,400). Individual nuclei are shown as black points. Red dashed lines indicate filtering thresholds: nFeature_RNA (200-6,000 genes), nCount_RNA (500-30,000 UMI), and percent.mt (<5% mitochondrial content). Red bars indicate median values. All samples combined (MWT_SD, MWT_LSD, MKO_SD, MKO_LSD). **(B)** Summary statistics table showing nuclei count and quality metrics for each sample after filtering. Values include mean and median gene detection, UMI counts, and mitochondrial gene percentage per sample. **(C)** Relationship between total UMI count and number of genes detected for each sample individually. Scatter plots show individual nuclei (gray points) with loess smoothing curve (blue line). The plateau in the curves indicates adequate sequencing depth, with most nuclei achieving saturation in gene detection. **(D)** Sequencing saturation analysis across all samples. Individual nuclei are colored by sample identity. Black line represents loess fit across all data. The plateau demonstrates that sequencing depth was sufficient to capture the majority of expressed genes per nucleus. **(E)** Sample contribution to each annotated cell population after Harmony batch correction. Stacked bar plots show the percentage of nuclei from each sample (color-coded) within each population. Balanced representation across samples within each population validates successful integration while preserving biological variation between experimental conditions. ZG, zona glomerulosa; ZG_ZF, zona glomerulosa-zona fasciculata transition zone; ZF1, zona fasciculata cluster 0; ZF2, zona fasciculata clusters 1-10. **All panels:** Data represent 105,400 high-quality nuclei from 4 samples representing four experimental conditions (wild-type standard diet

[MWT_SD], wild-type low-sodium diet [MWT_LSD], MR knockout standard diet [MKO_SD], MR knockout low-sodium diet [MKO_LSD]). Each sample consists of 3 pooled adrenal glands from male mice of the same genotype and dietary treatment. Abbreviations: MWT, male wild type; MKO, $MRKO^{Ad}$ (male mineralocorticoid receptor knockout).

Supplementary Figure S8. Cell type identification and marker gene validation.

(A) UMAP visualization of all 105,400 nuclei colored by original Seurat cluster assignments (numbered 0-13) prior to biological annotation. Unsupervised graph-based clustering (Louvain algorithm, resolution = 0.3) on Harmony-corrected principal components identified 14 distinct clusters. Cluster numbers are displayed with labels. Each dot represents a single nucleus. **(B)** Feature plots showing expression of canonical cortical marker genes across all nuclei. Expression levels represent log-normalized counts, with color intensity indicating expression magnitude (gray = no/low expression; red = high expression). Genes shown: *Cyp11b2* (aldosterone synthase, zona glomerulosa marker), *Dab2* (disabled homolog 2, ZG structural marker), *Cyp11b1* (11β-hydroxylase, zona fasciculata marker), *Mc2r* (ACTH receptor, ZF marker), *Nr4a1* (nuclear receptor, ZF marker), and *Star* (steroidogenic acute regulatory protein, pan-steroidogenic marker). **(C)** Feature plots showing expression of non-cortical cell type markers. Color scale as in panel B (gray = no/low expression; blue = high expression). Genes shown: *Th* (tyrosine hydroxylase, medulla marker), *Pnmt* (phenylethanolamine N-methyltransferase, medulla marker), *Pecam1* (CD31, endothelial marker), *Col1a1* (collagen type I, fibroblast marker), *Cd68* (macrophage marker), and *Csf1r* (colony stimulating factor 1 receptor, macrophage marker). **(D)** Heatmap showing scaled expression of the top 10 differentially expressed marker genes for each annotated population. Marker genes were identified using Seurat FindAllMarkers with Wilcoxon rank-sum test (adjusted $p < 0.05$, minimum $\log_2$ fold change = 0.5, minimum percentage = 25%). Values represent scaled average expression per population (z-score normalized, capped at ±2.5). Rows are hierarchically clustered within each population. Right annotation bar indicates the population for which each gene is a marker. Abbreviations: MWT, male wild type; MKO, $MRKO^{Ad}$ (male mineralocorticoid receptor knockout).

(E) Module score distributions showing cell type-specific gene signature enrichment across all populations. Module scores were calculated using Seurat AddModuleScore with the following gene sets: ZG (*Cyp11b2*, *Dab2*, *Wnt4*, *Shh*); ZF (*Cyp11b1*, *Hsd3b6*, *Nr4a1*); Medulla (*Th*, *Ddc*, *Pnmt*); Endothelial (*Pecam1*, *Cdh5*, *Vwf*); Fibroblast (*Col1a1*, *Dcn*, *Lum*); Macrophage (*Cd68*,

Csf1r, *Adgre1*). Violin plots show score distributions with white boxplots indicating median and quartiles. Each population shows highest enrichment for its corresponding module, validating cell type assignments. Note that ZF1 shows elevated ZG module scores, reflecting its plasticity capacity. **All panels:** Data represent 105,400 high-quality nuclei from one sample per experimental condition (wild-type standard diet [MWT_SD], wild-type low-sodium diet [MWT_LSD], MR knockout standard diet [MKO_SD], MR knockout low-sodium diet [MKO_LSD]), with each sample consisting of 3 pooled adrenal glands. ZG, zona glomerulosa; ZG_ZF, zona glomerulosa-zona fasciculata transition zone; ZF1, zona fasciculata cluster 0 (plastic subpopulation); ZF2, zona fasciculata clusters 1-10 (non-plastic subpopulation). Abbreviations: MWT, male wild type; MKO, $MRKO^{Ad}$ (male mineralocorticoid receptor knockout).

Supplementary Figure S9. Baseline transcriptional differences between ZF1 and ZF2 subpopulations.

(A) UMAP highlighting ZF1 (dark blue) and ZF2 (light blue) spatial distribution. Other populations in gray. **(B)** Volcano plot of baseline DEGs (ZF1 vs ZF2, WT SD). 5,580 significant DEGs (adjusted $p < 0.05$). Genes higher in ZF1 (red), ZF2 (blue), or significant but smaller fold-change (gray). Key priming genes labeled. Dashed lines = significance thresholds. **(C)** Heatmap of top 60 DEGs (30 per direction) showing scaled average expression across all conditions. Rows split by direction (higher in ZF1 vs ZF2) and hierarchically clustered within groups. Top bars indicate population and condition. Expression patterns stable across conditions, indicating constitutive differences. **(D)** GO Biological Process enrichment for ZF1-enriched vs ZF2-enriched genes. Dot size = gene count; color = $-\log_{10}$(p.adj). ZF1 enriched for biosynthetic/metabolic processes (ribosome biogenesis, translation, RNA splicing). ZF2 enriched for regulatory processes (GTPase signaling, autophagy). **(E)** Metabolic capacity comparison via module scores. ZF1 shows higher OXPHOS, ribosome, and mitochondrial gene expression, supporting enhanced biosynthetic capacity. ZF1 n=24,343, ZF2 n=29,366 nuclei. Baseline analysis on WT_SD. Wilcoxon test, Benjamini-Hochberg correction. Abbreviations: MWT, male wild type; MKO, $MRKO^{Ad}$ (male mineralocorticoid receptor knockout).

Supplementary Figure S10. Zona glomerulosa and transition zone plasticity mechanisms.

(A) Violin plots showing ZG signature module scores across experimental conditions in zona glomerulosa cells. Module scores calculated using 6 ZG-specific genes (Cyp11b2, Dab2, Wnt4, Shh, Rspo3, Axin2). ZG cells maintain high aldosterone-producing identity across all

conditions (WT SD, WT LSD, MKO SD, MKO LSD), with slight enhancement under salt restriction that is largely MR-independent. White boxes indicate median and quartiles. n = 11,623 ZG nuclei. **(B)** Volcano plot of ZG plasticity response genes (WT LSD vs WT SD). Each point represents a gene, with x-axis showing $\log_2$ fold change and y-axis showing $-\log_{10}$(adjusted p-value). Red dots indicate significantly upregulated genes (adjusted $p < 0.05$, $\log_2FC > 0.5$); blue dots indicate downregulated genes (adjusted $p < 0.05$, $\log_2FC < -0.5$). ZG cells show 2,375 salt-responsive genes, including enhanced expression of canonical ZG markers (Cyp11b2, Dab2) and slight modulation of zona maintenance genes. Dashed lines indicate significance thresholds ($p = 0.05$, $|\log_2FC| = 0.5$). **(C)** Volcano plot of ZG MR-dependent genes (WT vs MKO under LSD). 1,247 genes require MR for normal expression under salt restriction (adjusted $p < 0.05$). MR-enhanced genes (red, 734 genes) are enriched for cell cycle and proliferation pathways, explaining the blunted ZG expansion in MKO mice (9.6% to 11.5%) compared to WT (9.3% to 14.6%). MR-repressed genes shown in blue (513 genes). Gene Ontology analysis reveals top enriched pathway is axon guidance, suggesting MR's role in tissue organization. Top differentially expressed genes labeled. **(D)** Scatter plot showing Cyp11b1 and Cyp11b2 co-expression in ZG_ZF transition zone cells at baseline (WT SD). Each dot represents a single nucleus. ZG_ZF cells show 9.9% double-positive status at baseline (red dots, expression threshold > 0.5 for both markers), indicating they already co-express zona fasciculata and zona glomerulosa markers due to their physical location at the zone boundary. This primes them for enhanced plasticity under salt restriction. Gray dots represent single-positive cells. Dashed lines indicate expression thresholds. **(E)** Volcano plot of ZG_ZF plasticity response (WT LSD vs WT SD). 2,247 genes change significantly in ZG_ZF cells under salt restriction, representing the largest plasticity response among cortical populations. The high baseline co-expression status (9.9% double-positive) enables rapid enhancement to 63.0% double-positive under salt. Red and blue dots indicate genes with $|\log_2FC| > 0.5$ and adjusted $p < 0.05$. ZG identity genes (Cyp11b2, Dab2) show strong upregulation. **(F)** Volcano plot of ZG_ZF MR-dependent genes (WT vs MKO under LSD). Only 1,977 genes show MR-dependent expression changes, but these account for merely 10% of the phenotypic plasticity (ZG signature acquisition). This minimal MR-dependence demonstrates that ZG_ZF plasticity is primarily driven by position-dependent niche signals (Wnt, retinoic acid) from the adjacent zona glomerulosa, rather than cell-intrinsic MR signaling. Gray dots indicate genes with significant p-values but small fold changes. This contrasts sharply with ZF1, where 49% of plasticity is MR-dependent, highlighting two distinct plasticity mechanisms: position-driven (ZG_ZF) versus cell-autonomous MR-driven (ZF1).

All panels: Analysis performed on zona glomerulosa (ZG, n=11,623) and zona glomerulosa-zona fasciculata transition zone (ZG_ZF, n=6,834) nuclei from four experimental conditions. Differential expression analysis performed using Seurat FindMarkers with Wilcoxon rank-sum test (adjusted $p < 0.05$, minimum $\log_2$ fold change = 0.25). Gene Ontology enrichment performed using clusterProfiler with Benjamini-Hochberg correction. Abbreviations: MWT, male wild type; MKO, $MRKO^{Ad}$ (male mineralocorticoid receptor knockout).

Supplementary Table S1. Quality control metrics and sample statistics. Single-nucleus RNA sequencing quality control statistics for all four experimental conditions. Each sample represents pooled adrenal glands from 3 mice. Nuclei were filtered to retain those with 200-6,000 detected genes, <20% mitochondrial content, and <1% hemoglobin contamination. Total analyzed: 105,400 high-quality nuclei. MWT, wild-type with MR; MKO, zona glomerulosa-specific MR knockout; SD, standard diet; LSD, low-sodium diet (14 days).

sample	Total_Nuclei	Mean_Genes	Median_Genes	Mean_UMI	Median_UMI	Mean_Percent_MT	Median_Percent_MT
MKO_LSD	21687	1834.2	1992	4119.7	4404	1.21	0.71
MKO_SD	33951	1823.8	1906	3526.9	3489	0.84	0.57
MWT_LSD	23519	1860.9	2027	4044.5	4097	1.25	0.77
MWT_SD	26243	1687.7	1609	3629.3	2845	1.16	0.77

Supplementary table S2 : TaqMan Gene Expression Assays used for low salt diet experiment

Gene Symbol	**TaqMan Assay ID**
Target genes	
Cyp11b2	Mm01204955_g1
Cyp11b1	Mm01204952_m1
Star	Mm00441558_m1
Nr4a2	Mm00443060_m1
Nr4a1	Mm01300401_m1
Wnt4	Mm01194003_m1
Axin2	Mm00443610_m1
Lef1	Mm00550265_m1
Akr1c18	Mm00506289_m1
Housekeeping genes	
18S	Mm02601777_g1
B2m	Mm00437762_m1
Ubc	Mm02525934_g1

Supplementary table S3 : SYBR Green primer sequences used for 12-week experiment

Gene	Direction	Primer Sequence (5′→3′)
Housekeeping genes		
18S	Forward	CCCTGCCCTTTGTACACACC
	Reverse	CGATCCGAGGGCCTCACTA
β2-microglobulin	Forward	ATTCACCCCCACTGAGACTG
	Reverse	TGCTATTTCTTTCTGCGTGC
Ubiquitin C	Forward	GTGCTTCATCCACTGGCTGGAA
	Reverse	GTCTGCGATAGGACCTGGTTGA
Target genes		
Star	Forward	TGCTCAACCTGCCTCCAGACTT
	Reverse	ACTGGCTGAAGTCTCGCTTCTG
Cyp11b1	Forward	TGTATCGAGAGCTGGCAGAG
	Reverse	CCTGGATGGCATCCATTGAC
Cyp11b2	Forward	ACCTACAGTGGCATTGTG
	Reverse	GATTGCTGTCGTGTCAAC
Wnt4	Forward	CCCTGTCTTTGGGAAGGTGGTG
	Reverse	CACCTGCTGAAGAGATGGCGTATAC
Lef1	Forward	AAATGGGTCCCTTTCTCCAC
	Reverse	TCGTCGCTGTAGGTGATGAG
Axin2	Forward	AGCCTAAAGGTCTTATGTGG
	Reverse	ATGGAATCGTCGGTCAGT
Prkar1a	Forward	CCCGAGATTATCCTGAGCAA
	Reverse	ATAGGCTGGTCAGCGAAGAA
Prkaca	Forward	TCCACAAATACTCAGGCAAAGAG
	Reverse	GCAGCTCCCTGGTCAGTAG
Akr1c18	Forward	GGCTTTGGCACCTATGCAAC
	Reverse	TGGGTCTGACCAACTCTGGA

Supplementary table S4. Plasma steroid profile in wild-type and MR knockout female mice.

Plasma steroid concentrations measured by LC-MS/MS in 12-week-old mice under basal conditions (standard diet). Values represent mean ± SEM. Aldosterone and 11-DOC are reported in pmol/L; all other steroids in nmol/L. Statistical comparisons between wild-type (WT) and zona glomerulosa-specific MR knockout (KO) mice were performed using Wilcoxon rank-sum test with Benjamini-Hochberg correction for multiple testing. *P < 0.05, **P < 0.01, ***P < 0.001; ns, not significant.

Steroid	Female WT	Female KO	P_value
11-doc (pmol/L)	26203.83 +/- 2007.45	34057.07 +/- 4793.44	ns
18-hydroxy-11-DOC (nmol/L)	691.00 +/- 44.35	822.57 +/- 102.39	ns
18-hydroxycorticosterone (nmol/L)	1.97 +/- 0.48	1.79 +/- 0.21	ns
Aldosterone (pmol/L)	868.58 +/- 171.34	739.36 +/- 105.42	ns
Corticosterone (nmol/L)	770.97 +/- 44.16	895.77 +/- 88.34	ns
Progesterone (nmol/L)	26.20 +/- 8.07	21.41 +/- 6.81	ns

Supplementary table S5. Plasma steroid profile in wild-type and MR knockout female mice.

Plasma steroid concentrations measured by LC-MS/MS in 12-week-old mice under basal conditions (standard diet). Values represent mean ± SEM. Aldosterone and 11-DOC are reported in pmol/L; all other steroids in nmol/L. Statistical comparisons between wild-type (WT) and zona glomerulosa-specific MR knockout (KO) mice were performed using Wilcoxon rank-sum test with Benjamini-Hochberg correction for multiple testing. *P < 0.05, **P < 0.01, ***P < 0.001; ns, not significant.

Steroid	Male WT	Male KO	P_value
11-doc (pmol/L)	10820.50 +/- 1313.36	12299.20 +/- 2262.40	ns
18-hydroxy-11-DOC (nmol/L)	234.29 +/- 19.02	257.10 +/- 36.76	ns
18-hydroxycorticosterone (nmol/L)	1.50 +/- 0.18	1.43 +/- 0.16	ns
Aldosterone (pmol/L)	691.36 +/- 87.02	690.20 +/- 76.70	ns
Corticosterone (nmol/L)	351.14 +/- 31.64	292.38 +/- 30.23	ns
Progesterone (nmol/L)	4.50 +/- 0.59	4.60 +/- 0.93	ns

Supplementary Table S6. Plasma angiotensin peptide profile in wild-type and MR knockout mice.

Circulating angiotensin peptide concentrations (pmol/L) measured by LC-MS/MS in 12-week-old mice under basal conditions (standard diet). Values represent mean ± SEM for normally distributed data, or median (interquartile range) for non-normally distributed data. Statistical comparisons between wild-type (WT) and zona glomerulosa-specific MR knockout (MRKO) mice were performed using appropriate tests (t-test or Mann-Whitney U test). *P < 0.05; ns, not significant (P ≥ 0.05). Ang, angiotensin.

Angiotensin	Male WT	Male MRKO	Male P value	Female WT	Female MRKO	Female P value
Ang II (pmol/L)	8222 ± 2983	8963 ± 4268	ns	9683 (3258 ~ 12333)	9650 ± 5424	ns
Ang 1-7 (pmol/L)	31.18 ± 11.48	26.00 (14.58 ~ 36.28)	ns	47.28 ± 26.77	56.07 ± 38.68	ns
Ang I (pmol/L)	679.9 ± 253.5	791.3 ± 396.0	ns	1730 (489.8 ~ 2050)	1518 ± 809.6	ns
Ang III (pmol/L)	1160 ± 526.9	1133 ± 667.6	ns	1029 ± 610.2	1273 ± 763.8	ns

Ang 1-5 (pmol/L)	1467 ± 683.9	1693 ± 885	ns	1546 ± 952.3	1686 ± 1042	ns
Ang IV (pmol/L)	320.7 ± 137.5	326.2 ± 188.5	ns	326.1 ± 191.5	392.3 ± 231.9	ns

Supplementary Table S7. Plasma steroid concentrations at baseline and during LSD in male mice.

Steroid hormone concentrations measured by LC-MS/MS in male mice at baseline (Ctrl T1, 12 weeks old) and after 14 days of LSD. Values represent mean ± SEM. Aldosterone and 11-DOC reported in pmol/L; all other steroids in nmol/L. WT, wild-type with MR; KO, zona glomerulosa-specific MR knockout (Cyp11b2-Cre; Nr3c2fl/fl); LSD, low-salt diet. Statistical comparisons shown in Table S21. N = 6-10 mice per group. 11-DOC, 11-deoxycorticosterone.

Steroid	Ctrl T1 WT	Ctrl T1 KO	MWT LSD	MKO LSD
11-doc (pmol/L)	16157.4 ± 1595.6	18674.9 ± 3142.0	27875.0 ± 3606.0	36997.6 ± 10143.8
18-hydroxy-11-DOC (nmol/L)	625.0 ± 72.3	736.1 ± 115.5	1060.5 ± 75.5	1328.9 ± 156.4
18-hydroxycorticosterone (nmol/L)	2.0 ± 0.4	1.3 ± 0.2	33.2 ± 4.5	14.6 ± 2.3
Corticosterone (nmol/L)	688.9 ± 43.9	614.0 ± 55.4	717.4 ± 73.7	1008.3 ± 76.0
Aldosterone (pmol/L)	1230.6 ± 328.9	552.0 ± 75.6	36016.1 ± 4657.0	13758.6 ± 1004.4
pregnenolone (nmol/L)	2.6 ± 0.3	2.3 ± 0.5	4.2 ± 0.7	3.5 ± 0.2
Progesterone (nmol/L)	7.2 ± 0.7	6.6 ± 1.4	10.5 ± 1.6	14.6 ± 2.4

Supplementary Table S8. Plasma steroid concentrations during recovery from LSD in male mice.

Steroid hormone concentrations measured by LC-MS/MS in male mice after 14 days recovery from low-sodium diet (LSD+REC) and age-matched controls (Ctrl T2, 15 weeks old). Recovery period consisted of return to standard sodium diet for 14 days following 14 days of low-sodium diet. Values represent mean ± SEM. Aldosterone and 11-DOC reported in pmol/L; all other steroids in nmol/L. WT, wild-type with MR; KO, zona glomerulosa-specific MR knockout; LSD+REC, low-salt diet followed by recovery. Statistical comparisons shown in Table S22. N = 3-6 mice per group. 11-DOC, 11-deoxycorticosterone.

Steroid	MWT LSD+REC	MKO LSD+REC	Ctrl T2 WT	Ctrl T2 KO
11-doc (pmol/L)	18923.0 ± 1621.8	14804.0 ± 3160.1	12927.5 ± 2885.3	10381.5 ± 623.5
18-hydroxy-11-DOC (nmol/L)	746.7 ± 43.7	763.3 ± 34.1	442.5 ± 34.0	439.5 ± 15.5
18-hydroxycorticosterone (nmol/L)	2.6 ± 0.2	3.4 ± 0.7	1.2 ± 0.2	0.8 ± 0.5
Corticosterone (nmol/L)	550.2 ± 36.0	546.0 ± 35.0	522.8 ± 27.8	542.5 ± 19.7
Aldosterone (pmol/L)	1440.7 ± 107.1	1731.0 ± 353.4	451.0 ± 105.6	334.0 ± 224.0
pregnenolone (nmol/L)	3.9 ± 0.2	4.3 ± 2.9	1.0 ± 0.0	1.1 ± 0.1
Progesterone (nmol/L)	6.9 ± 1.3	7.1 ± 2.6	5.8 ± 1.0	4.7 ± 1.7

Supplementary Table S9. Statistical comparisons of steroid concentrations at baseline and during LSD in male mice.

P-values from pairwise comparisons of plasma steroid concentrations between experimental groups. Statistical significance determined by Wilcoxon rank-sum test (Mann-Whitney U test) with Benjamini-Hochberg correction for multiple comparisons within each comparison type. Baseline_WT_vs_KO: Ctrl T1 WT vs Ctrl T1 KO (genotype effect at baseline); LSD_Effect_WT: Ctrl T1 WT vs MWT LSD (salt restriction response in wild-type); LSD_Effect_KO: Ctrl T1 KO vs MKO LSD (salt restriction response in knockout); Genotype_During_LSD: MWT LSD vs MKO LSD (genotype effect during salt restriction). ***P < 0.001, **P < 0.01, *P < 0.05; ns, not significant (adjusted P ≥ 0.05).

Steroid	Baseline_WT_vs_KO	LSD_Effect_WT	LSD_Effect_KO	Genotype_During_LSD
Aldosterone (pmol/L)	ns	0.0002***	0.0001***	0.002**
18-hydroxycorticosterone (nmol/L)	ns	0.0002***	0.0001***	0.008**
18-hydroxy-11-DOC (nmol/L)	ns	0.005**	0.005**	ns
Corticosterone (nmol/L)	ns	ns	0.0006***	0.033*
11-doc (pmol/L)	ns	0.005**	0.036*	ns
Progesterone (nmol/L)	ns	ns	0.002**	ns
pregnenolone (nmol/L)	ns	ns	0.033*	ns

Supplementary Table S10. Statistical comparisons of steroid concentrations during recovery from low-salt diet.

P-values from pairwise comparisons of plasma steroid concentrations during and after recovery from LSD. Statistical significance determined by Wilcoxon rank-sum test with Benjamini-Hochberg correction for multiple comparisons within each comparison type. Recovery_WT: MWT LSD vs MWT LSD+REC (recovery effect in wild-type); Recovery_KO: MKO LSD vs MKO LSD+REC (recovery effect in knockout); Genotype_During_Recovery: MWT LSD+REC vs MKO LSD+REC (genotype effect during recovery phase); Baseline_T2_WT_vs_KO: Ctrl T2 WT vs Ctrl T2 KO (genotype effect at recovery timepoint). ***P < 0.001, **P < 0.01, *P < 0.05; ns, not significant (adjusted P ≥ 0.05).

Steroid	Recovery_WT	Recovery_KO	Genotype_During_Recovery	Baseline_T2_WT_vs_KO
Aldosterone (pmol/L)	0.002**	0.023*	ns	ns
18-hydroxycorticosterone (nmol/L)	0.002**	0.023*	ns	ns
18-hydroxy-11-DOC (nmol/L)	0.011*	0.039*	ns	ns
Corticosterone (nmol/L)	ns	0.023*	ns	ns
11-doc (pmol/L)	ns	0.023*	ns	ns
Progesterone (nmol/L)	0.035*	0.023*	ns	ns
pregnenolone (nmol/L)	ns	ns	ns	ns

Supplementary Table S11. Plasma steroid concentrations at baseline and during LSD in female mice.

Steroid hormone concentrations measured by LC-MS/MS in female mice at baseline (Ctrl T1, 12 weeks old) and after 14 days of LSD. Values represent mean ± SEM. Aldosterone and 11-DOC reported in pmol/L; all other steroids in nmol/L. WT, wild-type with MR; KO, zona glomerulosa-specific MR knockout (Cyp11b2-Cre; Nr3c2fl/fl); LSD, low-salt diet. Statistical comparisons shown in Table S25. 11-DOC, 11-deoxycorticosterone.

Steroid	Ctrl T1 WT	Ctrl T1 KO	FWT LSD	FKO LSD
11-doc (pmol/L)	33954.7 ± 5032.1	37481.3 ± 4001.0	29903.1 ± 4937.3	47952.2 ± 5010.4
18-hydroxy-11-DOC (nmol/L)	1270.3 ± 160.0	1286.8 ± 145.3	1444.0 ± 95.2	1739.7 ± 145.0
18-hydroxycorticosterone (nmol/L)	1.8 ± 0.6	2.4 ± 0.2	26.5 ± 5.6	9.7 ± 2.3
Corticosterone (nmol/L)	1023.9 ± 67.4	1216.2 ± 66.8	1005.6 ± 77.4	1477.6 ± 78.9
Aldosterone (pmol/L)	746.5 ± 260.7	960.6 ± 95.9	28938.6 ± 5450.6	8064.7 ± 2268.4
pregnenolone (nmol/L)	3.1 ± 0.3	2.5 ± 0.3	7.5 ± 1.2	5.8 ± 0.7
Progesterone (nmol/L)	5.5 ± 0.9	4.8 ± 0.5	4.4 ± 0.7	4.8 ± 0.4

Supplementary Table S12. Plasma steroid concentrations during recovery from low-salt diet in female mice.

Steroid hormone concentrations measured by LC-MS/MS in female mice after 14 days recovery from low-salt diet (LSD+Rec) and age-matched controls (Ctrl T2, 15 weeks old). Recovery period consisted of return to standard sodium diet for 14 days following 14 days of low-salt diet. Values represent mean ± SEM. Aldosterone and 11-DOC reported in pmol/L; all other steroids in nmol/L. WT, wild-type with MR; KO, zona glomerulosa-specific MR knockout; LSD+Rec, low-salt diet followed by recovery. Statistical comparisons shown in Table S26. N = 5-11 mice per group. 11-DOC, 11-deoxycorticosterone.

Steroid	FWT LSD+Rec	FKO LSD+Rec	Ctrl T2 WT	Ctrl T2 KO
11-doc (pmol/L)	27893.2 ± 3486.9	39784.0 ± 2274.0	28505.4 ± 3374.4	31307.2 ± 3383.3
18-hydroxy-11-DOC (nmol/L)	1224.4 ± 108.7	943.3 ± 88.9	1055.5 ± 88.8	1191.8 ± 99.2
18-hydroxycorticosterone (nmol/L)	3.0 ± 0.5	1.1 ± 0.2	2.4 ± 0.2	1.1 ± 0.1
Corticosterone (nmol/L)	1008.2 ± 114.8	1073.3 ± 36.3	993.9 ± 61.0	1055.3 ± 57.4
Aldosterone (pmol/L)	1336.8 ± 270.0	366.7 ± 50.2	961.9 ± 110.6	392.7 ± 62.5

pregnenolone (nmol/L)	3.0 ± 0.8	2.1 ± 0.2	2.3 ± 0.4	7.2 ± 0.6
Progesterone (nmol/L)	2.5 ± 0.4	5.7 ± 0.7	6.7 ± 1.8	4.8 ± 1.2

Supplementary Table S13. Statistical comparisons of steroid concentrations at baseline and during low-salt diet in female mice.

P-values from pairwise comparisons of plasma steroid concentrations between experimental groups in female mice. Statistical significance determined by Wilcoxon rank-sum test (Mann-Whitney U test) with Benjamini-Hochberg correction for multiple comparisons within each comparison type. Baseline_WT_vs_KO: Ctrl T1 WT vs Ctrl T1 KO (genotype effect at baseline); LSD_Effect_WT: Ctrl T1 WT vs FWT LSD (salt restriction response in wild-type); LSD_Effect_KO: Ctrl T1 KO vs FKO LSD (salt restriction response in knockout); Genotype_During_LSD: FWT LSD vs FKO LSD (genotype effect during salt restriction). ***P < 0.001, **P < 0.01, *P < 0.05; ns, not significant (adjusted P ≥ 0.05).

Steroid	Baseline_WT_vs_KO	LSD_Effect_WT	LSD_Effect_KO	Genotype_During_LSD
Aldosterone (pmol/L)	ns	0.008**	0.008**	0.049*
18-hydroxycorticosterone (nmol/L)	ns	0.012*	0.008**	ns
18-hydroxy-11-DOC (nmol/L)	ns	ns	0.047*	ns
Corticosterone (nmol/L)	ns	ns	ns	0.008**
11-doc (pmol/L)	ns	ns	ns	ns
Progesterone (nmol/L)	ns	ns	ns	ns
pregnenolone (nmol/L)	ns	0.033*	0.008**	ns

Supplementary Table S14. Statistical comparisons of steroid concentrations during recovery from low-salt diet in female mice.

P-values from pairwise comparisons of plasma steroid concentrations during and after recovery from LSD in female mice. Statistical significance determined by Wilcoxon rank-sum test with Benjamini-Hochberg correction for multiple comparisons within each comparison type. Recovery_WT: FWT LSD vs FWT LSD+Rec (recovery effect in wild-type); Recovery_KO: FKO LSD vs FKO LSD+Rec (recovery effect in knockout); Genotype_During_Recovery: FWT LSD+Rec vs FKO LSD+Rec (genotype effect during recovery phase);

Baseline_T2_WT_vs_KO: Ctrl T2 WT vs Ctrl T2 KO (genotype effect at recovery timepoint). ***P < 0.001, **P < 0.01, *P < 0.05; ns, not significant (adjusted P ≥ 0.05).

Steroid	Recovery_WT	Recovery_KO	Genotype_During_Recovery	Baseline_T2_WT_vs_KO
Aldosterone (pmol/L)	0.009**	0.004**	0.015*	0.004**
18-hydroxycorticosterone (nmol/L)	0.009**	0.004**	0.040*	0.010**
18-hydroxy-11-DOC (nmol/L)	ns	0.006**	ns	ns
Corticosterone (nmol/L)	ns	0.004**	ns	ns
11-doc (pmol/L)	ns	ns	ns	ns
Progesterone (nmol/L)	ns	ns	0.015*	ns
pregnenolone (nmol/L)	0.041*	0.004**	ns	0.004**

12 Part II: Role of *Casz1* in Adrenal Cortex Development

12.1 Introduction

As described in the Introduction (Chapter 10), *CASZ1* was identified by GWAS within a region on chromosome 1 associated with an increased risk of developing PA (Le Floch et al., 2022). CASZ1 functions as a MR corepressor on transcriptional regulation. *In vitro* studies demonstrated that *CASZ1* overexpression in human adrenocortical cells completely suppresses aldosterone production, suggesting it may act as a negative regulator of mineralocorticoid signalling (Le Floch et al., 2022).

The physiological role of *CASZ1 in vivo*, particularly in the context of ZG homeostasis and aldosterone regulation under basal and challenged conditions, remains unexplored. Given the robust human genetic evidence linking *CASZ1* variants to PA susceptibility, and its established function as an MR corepressor, we hypothesized that *CASZ1* regulates aldosterone production in the adrenal cortex, either directly or in interaction with the MR, and that these effects may be modulated by common genetic variation.

To test this hypothesis and investigate *CASZ1* function in aldosterone-producing cells, we generated ZG-specific *Casz1* knockout mice using the Cyp11b2-Cre model crossed with Casz1$^{fl/fl}$ mice. This cell-specific approach allowed us to assess *CASZ1* function specifically in the ZG without the confounding effects of systemic *CASZ1* deletion in other tissues. We performed comprehensive phenotypic characterization of these mice at 12 weeks of age under standard conditions, examining adrenal morphology, steroidogenic enzyme expression, hormonal profiles, and cellular proliferation. This baseline characterization established the foundation for future experiments investigating the response to physiopathological challenges, in particular salt diets, to reveal the conditions under which *CASZ1* function becomes critical for aldosterone regulation.

The results of this initial characterization, presented in this section, establish essential tools and baseline data for investigating CASZ1's role in ZG biology and aldosterone homeostasis, with implications for understanding PA pathogenesis.

12.2 Investigation of the role of CASZ1 in the adrenal cortex

To investigate how this newly discovered susceptibility gene influences the regulatory transitions leading to PA, we have performed in vivo functional analyses using genetically

modified mouse models combined with molecular and biochemical approaches. The specific objectives were to evaluate the role of CASZ1 in PA development using mice with ZG-specific *Casz1* deletion and to elucidate the molecular mechanisms by which CASZ1 regulates adrenocortical function.

12.3 Material and methods

12.3.1 Generation of Zona Glomerulosa-Specific *Casz1* Knockout Mice

To achieve selective inactivation of *Casz1* in the ZG of the adrenal cortex, we employed a Cre-loxP conditional knockout strategy. Mice carrying a floxed *Casz1* allele (Casz1tm1.1Flc/Mmnc, MMRRC Stock No. 41176-UNC) were obtained from the Mutant Mouse Resource & Research Centers at the University of North Carolina at Chapel Hill. In this conditional allele, exon 6 of the *Casz1* gene are flanked by loxP sites, allowing for Cre recombinase-mediated excision. The $Casz1^{fl/fl}$ mice were crossed with transgenic mice expressing the Cre recombinase under the control of the *Cyp11b2* promoter (Cyp11b2-Cre mice). This Cyp11b2-Cre mouse line was generated and characterized in our laboratory (Faedda et al., 2025). The *Cyp11b2* gene encodes aldosterone synthase, which is exclusively expressed in ZG cells of the adrenal cortex, ensuring tissue-specific recombination and selective *Casz1* deletion in aldosterone-producing cells. The model has the advantage over other available models to maintain intact *Cyp11b2* and AS expression, as the Cre recombinase is inserted into the 3'UTR after an internal ribosomal entry site (IRES). All experiments were conducted using male and female mice carrying one copy of the Cre recombinase allele ($Cyp11b2^{+/Cre}$). Control mice were heterozygous for Cre with wild-type *Casz1* alleles ($Cyp11b2^{+/Cre}$::$Casz1^{+/+}$), while $Casz1KO^{ZG}$ mice were heterozygous for Cre and homozygous for the floxed *Casz1* allele ($Cyp11b2^{+/Cre}$::$Casz1^{fl/fl}$).

12.3.2 Genotyping

Genomic DNA was extracted from tail biopsies using the MyTaq Extract-PCR Kit (Meridian Bioscience) according to the manufacturer's instructions. Genotyping for the *Casz1* floxed allele was performed by polymerase chain reaction (PCR) using the following primers: Casz1 Forward (Cas41176F): 5'-CAGAGGAACTGTCTCCACTGTC-3' and Casz1 Reverse (Cas41176Rev): 5'-GTTTCTGTTGCTGGGTTAGGTT-3' (Eurogentec, Seraing, Belgium).

Cyp11b2-Cre genotyping was performed as previously described (Faedda et al., 2025). PCR products were analyzed by agarose gel electrophoresis.

12.3.3 Tissue Collection and Processing

Mice were anesthetized with isoflurane (3%) and, after confirming the absence of paw-pinch reflex, sacrificed by cervical dislocation after blood sampling. Right adrenal glands were snap-frozen in liquid nitrogen and stored at −80°C for molecular analysis. Left adrenal glands were fixed in 4% paraformaldehyde (PFA) overnight at 4°C, dehydrated through graded ethanol series (70%, 95%, 100%), cleared in xylene, and embedded in paraffin. Sections (6 µm) were cut using a microtome, mounted on Superfrost Plus™ microscope slides, and stored at room temperature until further processing.

12.3.4 Histological Examination and Immunostaining

12.3.4.1 Histological Staining

For histological analysis, paraffin-embedded sections were deparaffinized in xylene and rehydrated through graded ethanol (100%, 95%, 70%). Hematoxylin, eosin, and saffron (HES) staining was performed using standard protocols. Following staining, sections were dehydrated through graded ethanol, cleared in xylene, and mounted using Pertex mounting medium (Histolab, #00840).

12.3.4.2 Immunofluorescence

For immunofluorescence on paraffin sections, slides were first deparaffinized in xylene and rehydrated through graded ethanol. Heat-induced antigen retrieval was performed using citric acid-based antigen unmasking solution (Vector Laboratories, #H-3300) for 30 minutes at 98°C. After cooling, sections were permeabilized for 15 minutes with PBS containing 0.1% Triton X-100. Sections were blocked for 2 hours at room temperature with blocking buffer containing 10% normal donkey serum (NDS) in PBS with 0.1% Triton X-100. Primary antibodies were diluted in 1% NDS in PBS with 0.1% Triton X-100 and incubated overnight at 4°C. The following primary antibodies were used: 20α-HSD (1:500, gift from Dr. Yacov Weinstein), Dab2 (1:1600, #D709T, Cell Signaling Technology), and Ki67 (1:1000, #ab15580, Abcam). Following primary antibody incubation, sections were washed three times in TBS and incubated with donkey anti-rabbit Alexa Fluor 647 secondary antibody (1:1000 in 3% BSA and 3% NDS in TBS with 0.05% Triton X-100) for 2 hours at room temperature. Nuclei were

counterstained with 4′,6-diamidino-2-phenylindole (DAPI, 1:5000, Roche Diagnostics GmbH). Slides were mounted with appropriate mounting medium and stored at 4°C until imaging.

12.3.4.3 Image Acquisition

Whole slide imaging was performed using an Olympus SlideView VS200 digital slide scanner (Olympus Corporation, Tokyo, Japan) with the UPlanXApo 20×/0.80 objective lens. Regions of interest (ROIs) and focus points were automatically recognized by the scanner and manually adjusted as needed to ensure optimal image quality.

12.3.4.4 Image Analysis

Quantitative analysis of immunofluorescence images was performed using HALO software (version 3.6.4134, Indica Labs) with the HighPlex FL v4.2.14 module. Fluorescence TIFF images were imported and background correction was applied to reduce non-specific fluorescence and autofluorescence. All channels (DAPI, Alexa Fluor 488, Alexa Fluor 594, and Alexa Fluor 647) were aligned for accurate signal quantification. ROIs corresponding to adrenal cortex were manually annotated, with artifacts, surrounding adipose tissue, and medulla manually excluded from analysis. DAPI was used for nuclear segmentation within ROIs. 20α-HSD-, Dab2-, and Ki67-positive cells were identified using Alexa Fluor 647. Fluorescence intensity thresholds were set for all channels based on signal intensity distributions.

12.3.5 RNA Extraction and RT-qPCR Analysis

Total RNA was isolated from whole adrenal glands using a Janke and Kunkel Ultra-Turrax T25 homogenizer (IKA Technologies, Staufen, Germany) and TRIzol reagent (Invitrogen, #15596018) according to the manufacturer's instructions. Following chloroform extraction and isopropanol precipitation, RNA pellets were washed with 75% ethanol and resuspended in nuclease-free water. RNA concentration and purity were assessed using a NanoDrop spectrophotometer (Thermo Fisher Scientific), and RNA integrity was verified by agarose gel electrophoresis. RNA samples were treated with DNase I (Invitrogen, #18068-015) to eliminate genomic DNA contamination. Complementary DNA (cDNA) was synthesized from 0.5 µg of total RNA using the iScript™ cDNA Synthesis Kit (Bio-Rad, #1708891) according to the manufacturer's protocol. Quantitative real-time PCR (RT-qPCR) was performed using a

custom pre-spotted 384-well plate with TaqMan Gene Expression Assays (Thermo Fisher Scientific) for 12 target genes including *Cyp11b2, Cyp11b1, Star, Nr4a2, Nr4a1, Wnt4, Axin2, Lef1,* and *Akr1c18*. Plate organization and configuration were performed using QuantStudio 12K Flex Real-Time PCR Software (Thermo Fisher Scientific), and reactions were run on the QuantStudio™ 12K Flex Real-Time PCR System (Thermo Fisher Scientific). Gene expression was normalized against three housekeeping genes: 18S ribosomal RNA (18S), β2-microglobulin (B2m), and ubiquitin C (Ubc). The geometric mean of these reference genes was used as the normalization factor. Relative gene expression was calculated using the $2^{-\Delta\Delta Ct}$ method. TaqMan assay identification numbers are provided in Table 1:

Table 1 : TaqMan Gene Expression Assays used for qPCR experiment

Gene Symbol	TaqMan Assay ID
Target genes	
Cyp11b2	Mm01204955_g1
Cyp11b1	Mm01204952_m1
Star	Mm00441558_m1
Nr4a2	Mm00443060_m1
Nr4a1	Mm01300401_m1
Wnt4	Mm01194003_m1
Axin2	Mm00443610_m1
Lef1	Mm00550265_m1
Akr1c18	Mm00506289_m1
Housekeeping genes	
18S	Mm02601777_g1
B2m	Mm00437762_m1
Ubc	Mm02525934_g1

12.3.6 Steroid Profiling and Analysis

Blood samples were collected into heparinized tubes by retro-orbital puncture immediately following anesthesia and prior to sacrifice. Blood was centrifuged at 2000g for 15 minutes at 4°C to obtain plasma. Plasma samples were stored at −20°C until analysis. Plasma steroid concentrations (pregnenolone, progesterone, 11-deoxycorticosterone, corticosterone, 18-hydroxy-11-deoxycorticosterone, 18-hydroxycorticosterone, aldosterone, and 18-hydroxycortisol) were simultaneously measured by liquid chromatography-tandem mass spectrometry (LC-MS/MS) as previously described (De Sousa et al., 2020). Steroid hormone concentrations were visualized using heatmap analysis based on Z-score normalization. Z-scores were calculated by subtracting the mean of each variable from individual data points

and dividing by the corresponding standard deviation. Hierarchical clustering was applied to variables using the pheatmap package (v1.0.12) in R. A diverging colour scale was used to represent Z-score normalized hormone concentrations, ranging from deep blue ($Z \leq -1$) through white ($Z = 0$) to deep red ($Z \geq +1$). Values outside this range were capped to minimize the influence of extreme values on the colour gradient. Principal Component Analysis (PCA) was performed on the original steroid profiling data using the FactoMineR package (v2.11) with default standardization. Results were visualized using the factoextra package (v1.0.7).

12.4 Results

All experimental analyses were performed on 12-week-old male and female mice. Results were analysed separately by sex to account for potential sexual dimorphism in adrenal physiology. Throughout this section, the following group nomenclature is used: female wild-type (FWT), female *Casz1* knockout (FKO), male wild-type (MWT), and male *Casz1* knockout (MKO).

12.4.1 General Characterization of the *Casz1* mouse model

To assess whether ZG specific deletion of *Casz1* affects overall growth or adrenal gland size, body weight and adrenal weight were measured at the time of sacrifice. Body weight measurements revealed the expected sex difference, with male mice exhibiting significantly higher mean body weight compared to female mice, independent of genotype (Figure 27A). No statistically significant differences in body weight were observed between wild-type and knockout mice within either sex group. Similarly, adrenal weight normalized to body weight showed no statistically significant differences between wild-type and *Casz1* knockout mice in either males or females (Figure 27B-C). The overall distribution of normalized adrenal weights was consistent across genotype groups within each sex, with comparable mean values and variability. These findings indicate that ZG specific deletion of *Casz1* does not grossly affect adrenal gland development or size by 12 weeks of age.

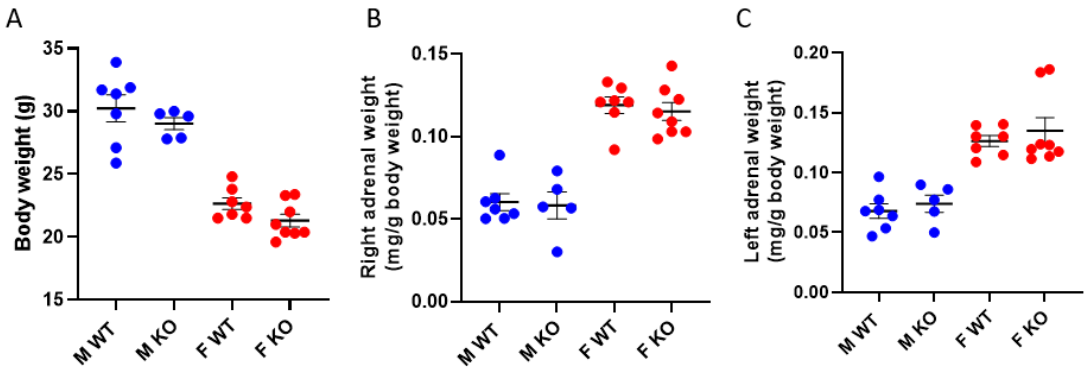

Figure 27 : Body weight and adrenal gland weight in wild-type and Casz1 knockout mice. *Total body weight (A), right adrenal weight (B), and left adrenal weight (C) in 12-week-old mice. Groups: male wild-type (M WT, blue), male knockout (M KO, blue), female wild-type (F WT, red), and female knockout (F KO, red). Individual values with mean ± SEM.*

12.4.2 Morphological Characterization of Casz1KO^{Ad} Adrenal Cortex

To evaluate whether loss of *Casz1* in the ZG results in structural alterations of the adrenal cortex, HES staining was performed on paraffin-embedded adrenal sections from all experimental groups. Visual examination of HES-stained sections revealed no major histological differences between *Casz1* knockout and wild-type mice in either sex. The typical organization of the adrenal cortex layers was preserved in all animals examined with no substantial changes in the overall architecture, cellular organization, or morphology of the adrenal cortex were noted across any of the experimental groups (Figure 28A).

Disabled homolog 2 (Dab2) is an established marker of ZG cells and has been implicated in cellular differentiation and signalling processes within the adrenal cortex. To assess whether *Casz1* deletion affects ZG identity or size, immunofluorescence staining for Dab2 was performed on adrenal sections from all groups. Visual inspection of Dab2 immunofluorescence images showed robust expression throughout the ZG in both wild-type and knockout mice of both sexes (Figure 28B). Quantitative analysis was performed by calculating the ratio of Dab2-positive cells to total DAPI-positive cells within the adrenal cortex. This analysis revealed a slight, non-significant increase in the proportion of Dab2-positive cells in *Casz1* knockout animals compared to wild-type controls in both males and females (Figure 28C). The lack of significant change in the number of Dab2+ cells suggests that ZG-specific deletion of *Casz1* does not substantially alter the number or identity of ZG cells at 12 weeks of age, although the analysis requires to be completed by increasing the number of mice.

20α-Hydroxysteroid dehydrogenase (20α-HSD), encoded by the *Akr1c18* gene, is a marker of the ZX, a transient region of the innermost adrenal cortex in mice. The ZX regresses in males around puberty but persists in females until first pregnancy. Immunofluorescence staining for 20α-HSD was performed to assess whether *Casz1* deletion affects ZX maintenance. 20α-HSD expression was detected exclusively in female mice, while no expression was observed in 12-week-old male mice of either genotype as expected. Within the female cohort, qualitative examination suggested a moderate decrease in 20α-HSD expression in *Casz1* knockout mice compared to wild-type controls (Figure 28D).

To determine whether *Casz1* deletion affects cellular proliferation within the adrenal cortex, immunofluorescence staining for the proliferation marker Ki-67 was performed. Ki-67 is expressed exclusively in actively cycling cells and provides a reliable index of proliferative activity. Immunofluorescence staining revealed Ki-67-positive cells scattered throughout the adrenal cortex in all experimental groups, with higher levels observed in females compared with males. Quantitative analysis of Ki-67^{+} cell number over cortex area showed no significant differences between *Casz1* knockout and wild-type mice in either sex (Figure 28E-F).

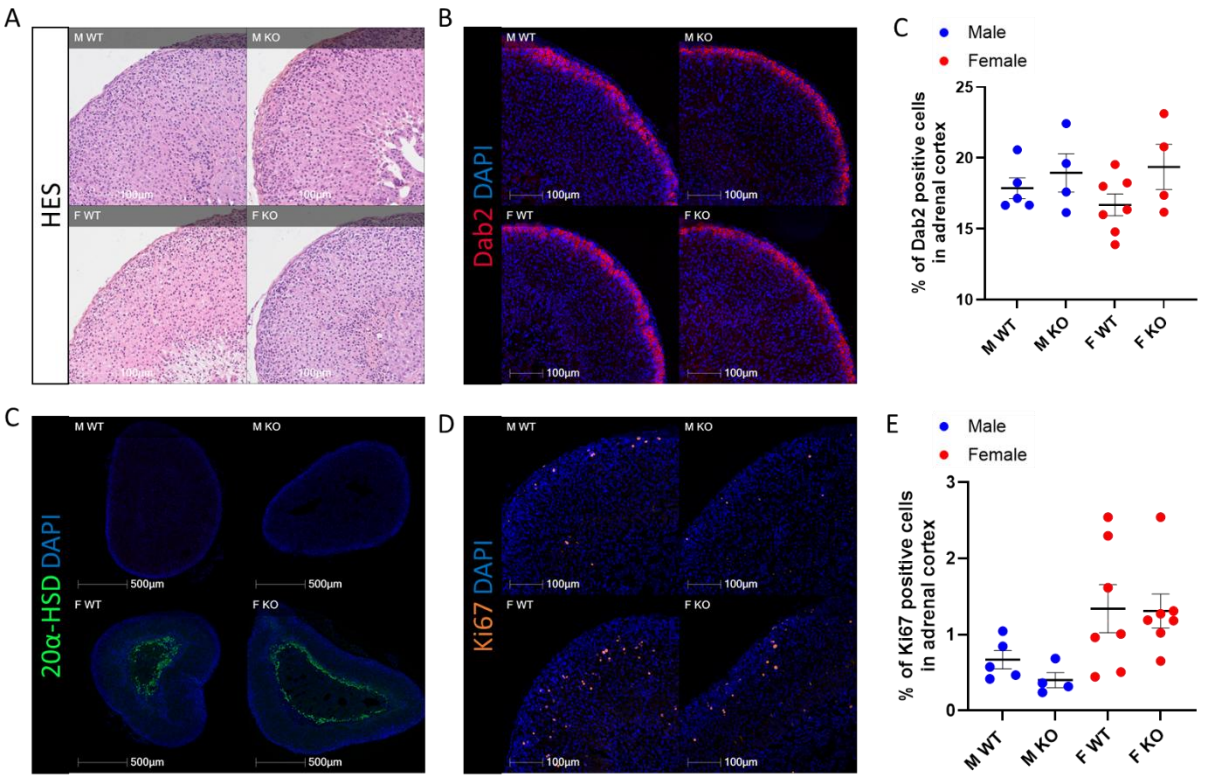

Figure 28 : Morphological characterization of the adrenal cortex in wild-type and Casz1 knockout mice. (A) Representative hematoxylin, eosin, and saffron (HES) staining of adrenal sections from male wild-type (M WT), male knockout (M KO), female wild-type (F WT), and female knockout (F KO) mice. (B) Representative immunofluorescence images showing Dab2 expression (magenta) and DAPI nuclear counterstaining (blue) in the adrenal cortex. (C) Quantification of Dab2-positive cells relative to total DAPI-positive cells in the adrenal cortex. Individual values with mean ± SEM. (D) Representative immunofluorescence images showing 20α-HSD expression (green) and DAPI nuclear counterstaining (blue). (E) Representative immunofluorescence images showing Ki67 expression (orange) and DAPI nuclear counterstaining (blue) in the adrenal cortex (F) Quantification of Ki67-positive cells relative to total DAPI-positive cells in the adrenal cortex. Individual values with mean ± SEM. Male groups in blue, female groups in red.

12.4.3 Steroid profile analysis

Comprehensive steroid profiling by LC-MS/MS was performed to assess whether *Casz1* inactivation affects circulating steroid hormone levels under basal conditions. Principal component analysis (PCA) revealed sex-specific steroidogenic profiles with distinct patterns between males and females.

In males, the first dimension (Dim1, 54.2% variance) was primarily driven by progesterone, 18-hydroxy-11-deoxycorticosterone, pregnenolone, and aldosterone (Figure 29B- 30C). The second dimension (Dim2, 20.6% variance) was predominantly influenced by 18-hydroxycorticosterone, aldosterone, and corticosterone (Figure 29B- 30D). PCA scatter plots showed substantial overlap between wild-type and Casz1KO^{ZG} mice, with no clear separation along either dimension, indicating similar overall steroid profiles between genotypes under basal conditions.

In females, Dim1 (42.2% variance) was driven by 18-hydroxy-11-deoxycorticosterone, progesterone, 11-deoxycorticosterone, corticosterone, and pregnenolone (Figure 29D- 30G), while Dim2 (31% variance) was primarily influenced by aldosterone and 18-hydroxycorticosterone (Figure 29D- 30H). Notably, PCA scatter plots showed partial separation between wild-type and Casz1KO^{ZG} mice along Dim1, with Casz1KO^{ZG} samples tending to cluster toward the negative side of this dimension and wild-type samples toward the positive side. This suggests that *Casz1* deletion in females may subtly affect the overall steroid profile, particularly involving the steroids that contribute most to Dim1. However, considerable individual variability was observed, resulting in overlapping confidence ellipses between groups.

Hierarchical clustering analysis of Z-score normalized steroid concentrations showed some interindividual variation but did not reveal consistent genotype-specific clustering patterns in

either sex (Figure 29A-29C). The heatmaps demonstrated that steroid profiles were primarily influenced by biological variability between individual animals. Individual measurements of key steroids including aldosterone, corticosterone, and their precursors showed overlapping distributions between wild-type and Casz1KO^{ZG} mice, with no statistically significant differences detected for any individual steroid measured (Table 2).

Collectively, these multivariate analyses indicate that the inactivation of *Casz1* does not substantially alter the overall plasma steroid profile in 12-week-old mice under basal unstimulated conditions, although subtle sex-specific differences may exist. The sex-specific patterns observed in steroid profiles reflect well-established differences in adrenal steroidogenic capacity between males and females.

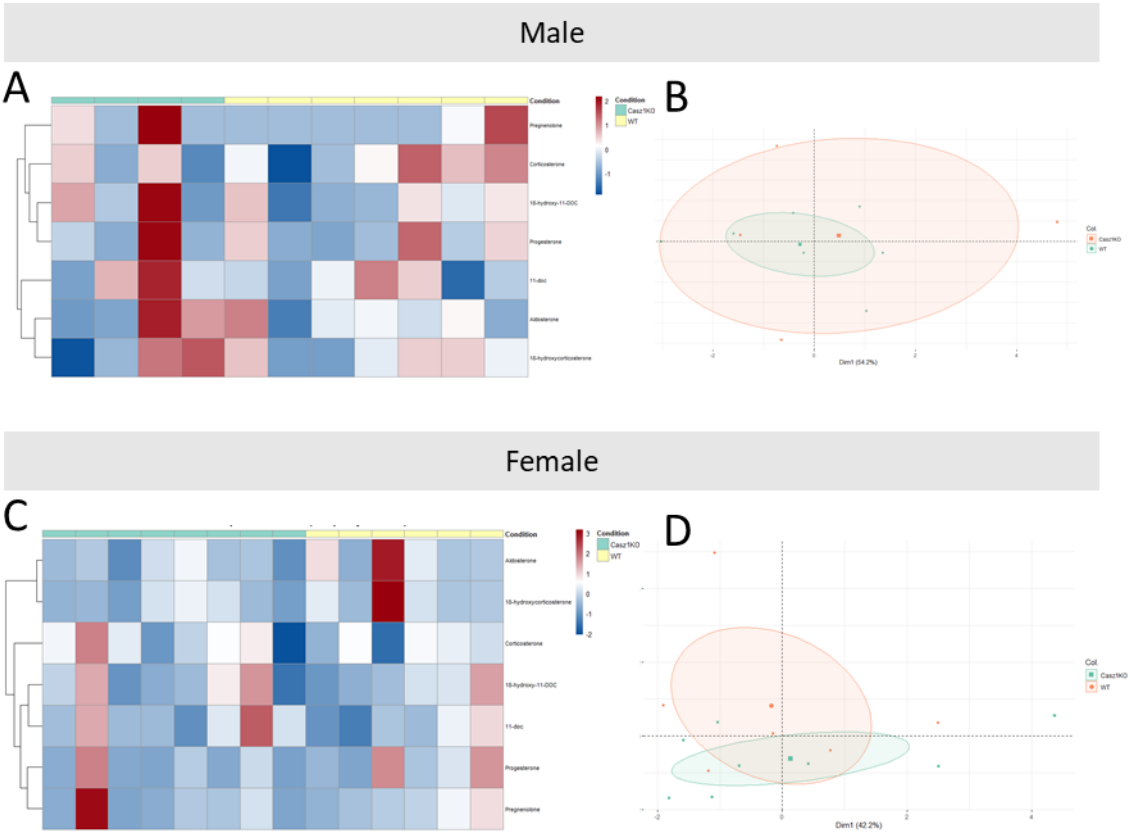

Figure 29 : Principal component analysis and hierarchical clustering of plasma steroid profiles. *Hierarchical clustering heatmaps of Z-score normalized steroid concentrations and PCA scatter plots for male (A-B) and female (C-D) mice. Heatmap color scale: blue (low, Z ≤ −2) to red (high, Z ≥ +2). PCA plots show wild-type (WT, green/teal) and Casz1KO^{ZG} (KO, orange/red) samples with 95% confidence ellipses. Dim1 and Dim2 percentages indicate variance explained. n = 6-8 per group.*

Male

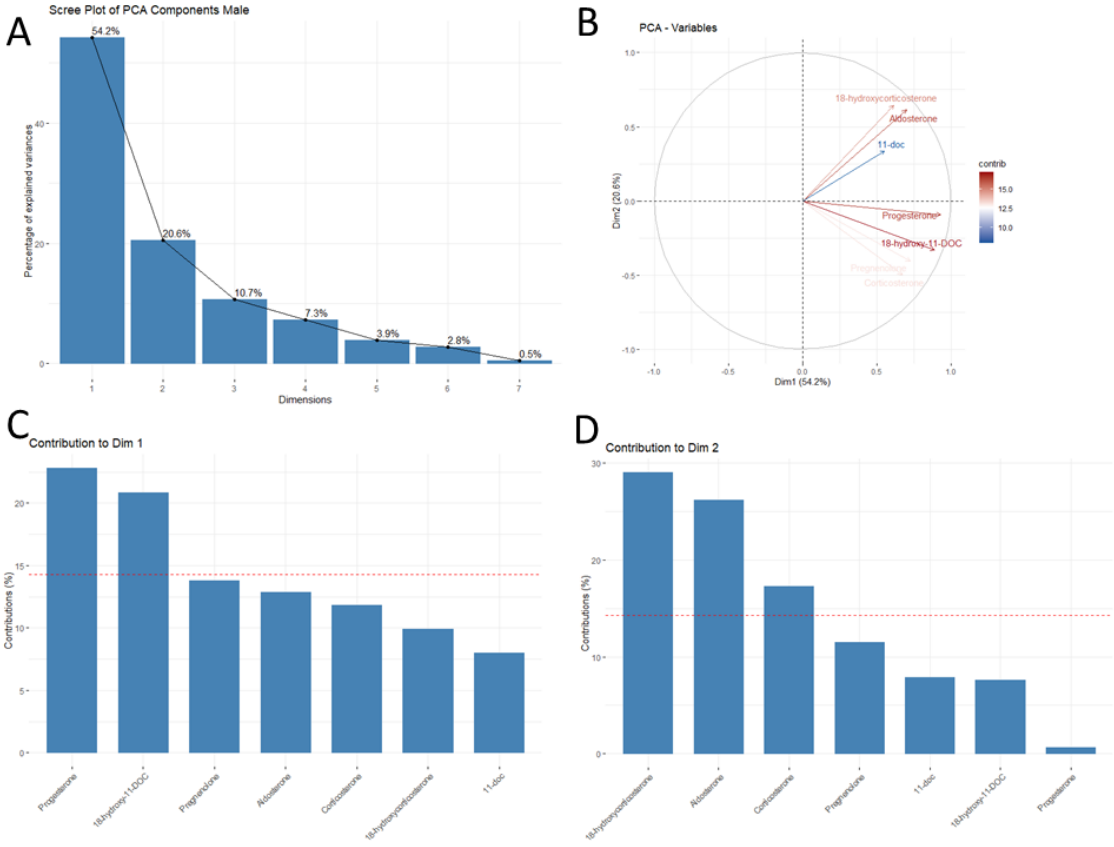
A
Scree Plot of PCA Components Male
Percentage of explained variances
Dimensions
54.2%
20.6%
10.7%
7.3%
3.9%
2.8%
0.5%
B
PCA - Variables
18-hydroxycorticosterone
Aldosterone
11-doc
Progesterone
18-hydroxy-11-DOC
Pregnenolone
Corticosterone
contrib
Dim2 (20.6%)
Dim1 (54.2%)
C
Contribution to Dim 1
Contributions (%)
Progesterone
18-hydroxy-11-DOC
Pregnenolone
Aldosterone
Corticosterone
18-hydroxycorticosterone
11-doc
D
Contribution to Dim 2
Contributions (%)
18-hydroxycorticosterone
Aldosterone
Corticosterone
Pregnenolone
11-doc
18-hydroxy-11-DOC
Progesterone

Female

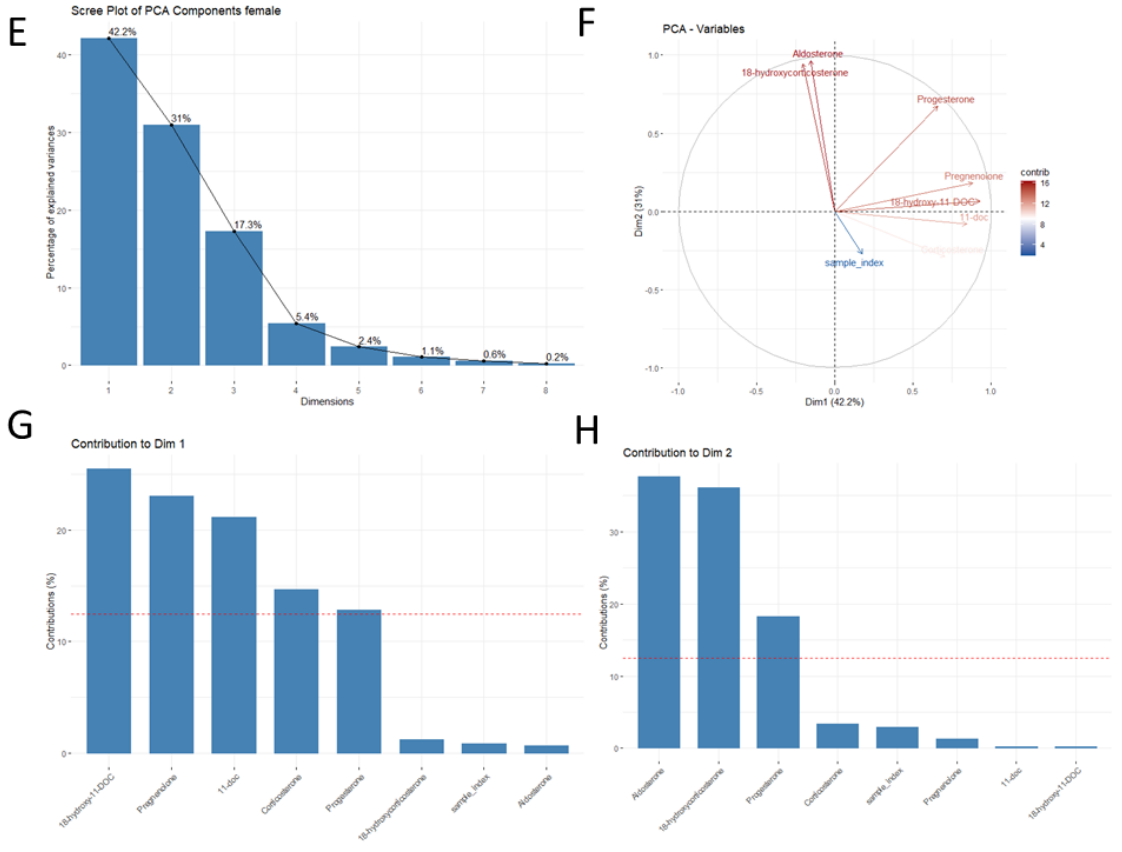
E
Scree Plot of PCA Components female
Percentage of explained variances
Dimensions
42.2%
31%
17.3%
5.4%
2.4%
1.1%
0.6%
0.2%
F
PCA - Variables
Aldosterone
18-hydroxycorticosterone
Progesterone
Pregnenolone
18-hydroxy-11-DOC
11-doc
Corticosterone
sample_index
contrib
Dim2 (31%)
Dim1 (42.2%)
G
Contribution to Dim 1
Contributions (%)
18-hydroxy-11-DOC
Pregnenolone
11-doc
Corticosterone
Progesterone
18-hydroxycorticosterone
sample_index
Aldosterone
H
Contribution to Dim 2
Contributions (%)
Aldosterone
18-hydroxycorticosterone
Progesterone
Corticosterone
sample_index
Pregnenolone
11-doc
18-hydroxy-11-DOC

Figure 30 : Principal component analysis decomposition and variable contributions. Scree plots (A, E), variable correlation circles (B, F), and contribution bar charts for Dim1 (C, G) and Dim2 (D, H) for male (A-D) and female (E-H) plasma steroid profiles. Scree plots show percentage of variance explained by each dimension. Variable plots display steroid vectors with color intensity indicating contribution strength (red = high, blue = low). Bar charts show individual steroid contributions with dashed lines indicating expected contribution if all variables contributed equally.

Steroid	F WT n=6	F KO n=8	M WT n=7	M KO n=4	P_Male	P_Female
11-doc (pmol/L)	22808.33 ± 2717.97	26753.00 ± 3075.68	7814.72 ± 972.11	9523.80 ± 1773.04	ns	ns
18-hydroxy-11-DOC (nmol/L)	756.00 ± 75.37	763.12 ± 84.86	228.62 ± 34.40	303.20 ± 86.38	ns	ns
18-hydroxycorticosterone (nmol/L)	2.89 ± 0.78	1.84 ± 0.23	1.49 ± 0.12	1.53 ± 0.35	ns	ns
Aldosterone (pmol/L)	1177.33 ± 266.93	730.62 ± 95.22	633.78 ± 59.52	708.95 ± 143.64	ns	ns
Corticosterone (nmol/L)	822.79 ± 57.83	857.87 ± 71.72	366.92 ± 60.76	313.36 ± 65.99	ns	ns
Pregnenolone (nmol/L)	5.08 ± 1.15	4.79 ± 2.36	0.79 ± 0.22	1.18 ± 0.46	ns	ns
Progesterone (nmol/L)	38.31 ± 14.83	19.76 ± 10.54	3.78 ± 0.84	4.08 ± 1.82	ns	ns

Table 2 : Plasma steroid hormone concentrations in wild-type and Casz1KO^{ZG} mice. Plasma concentrations of pregnenolone, progesterone, 11-deoxycorticosterone (11-doc), corticosterone, 18-hydroxy-11-deoxycorticosterone (18-hydroxy-11-DOC), 18-hydroxycorticosterone, and aldosterone measured by liquid chromatography-tandem mass spectrometry (LC-MS/MS) in 12-week-old mice. Data are presented as mean ± SEM for male wild-type (M WT), male Casz1KO^{ZG} (M KO), female wild-type (F WT), and female Casz1KO^{ZG} (F KO) groups. Statistical comparisons between wild-type and knockout mice were performed separately for each sex using the Mann-Whitney U test. n = 6-8 per group. ns, not significant ($p > 0.05$).

12.4.4 Gene Expression Analysis in Casz1KO^{Ad} Adrenal Glands

To gain molecular insight into the effects of *Casz1* deletion on adrenocortical function, quantitative real-time PCR (RT-qPCR) was performed on adrenal gland RNA samples to assess the expression of genes involved in steroidogenesis and Wnt/β-catenin signalling. Nine target genes were selected based on their established roles in adrenal physiology and aldosterone regulation (Figure 31).

The expression of key steroidogenic enzymes was evaluated, including *Cyp11b2*, *Cyp11b1*, and *Star*. Quantitative PCR analysis revealed no statistically significant differences in the expression levels of *Cyp11b2*, *Cyp11b1*, or *Star* between wild-type and Casz1KO^{ZG} mice in either sex. The relative expression values, calculated using the $2^{-\Delta\Delta Ct}$ method and normalized to the geometric mean of three housekeeping genes (18s, B2m, and Ubc), showed considerable

variability across individual samples. However, mean expression levels were comparable between genotypes within each sex group.

The nuclear receptors *Nr4a1* (*Nur77*) and *Nr4a2* (*Nurr1*) are key genes that play important roles in regulating steroidogenic gene expression in response to stimulation and have been implicated in ZG function. No significant differences in *Nr4a1* or *Nr4a2* expression were detected between wild-type and Casz1KO^{ZG} mice in either sex.

Expression of *Akr1c18*, encoding 20α-HSD, was analysed to complement the immunofluorescence findings described above. Consistent with the immunofluorescence results, which showed 20α-HSD protein expression exclusively in female mice, qPCR analysis revealed detectable *Akr1c18* mRNA expression in females, with lower or undetectable expression in males. However, no statistically significant differences in *Akr1c18* expression were observed between wild-type and Casz1KO^{ZG} mice within the female cohort.

The Wnt/β-catenin signalling pathway plays a critical role in ZG development, maintenance, and aldosterone production. To assess whether *Casz1* deletion affects this pathway, expression of *Wnt4*, *Axin2*, and *Lef1* was measured. No statistically significant differences in the expression of *Wnt4*, *Axin2*, or *Lef1* were detected between wild-type and Casz1KO^{ZG} mice in either sex. These findings suggest that under basal conditions at 12 weeks of age, *Casz1* inactivation does not substantially alter Wnt/β-catenin pathway activity, as assessed by the expression of these representative target genes.

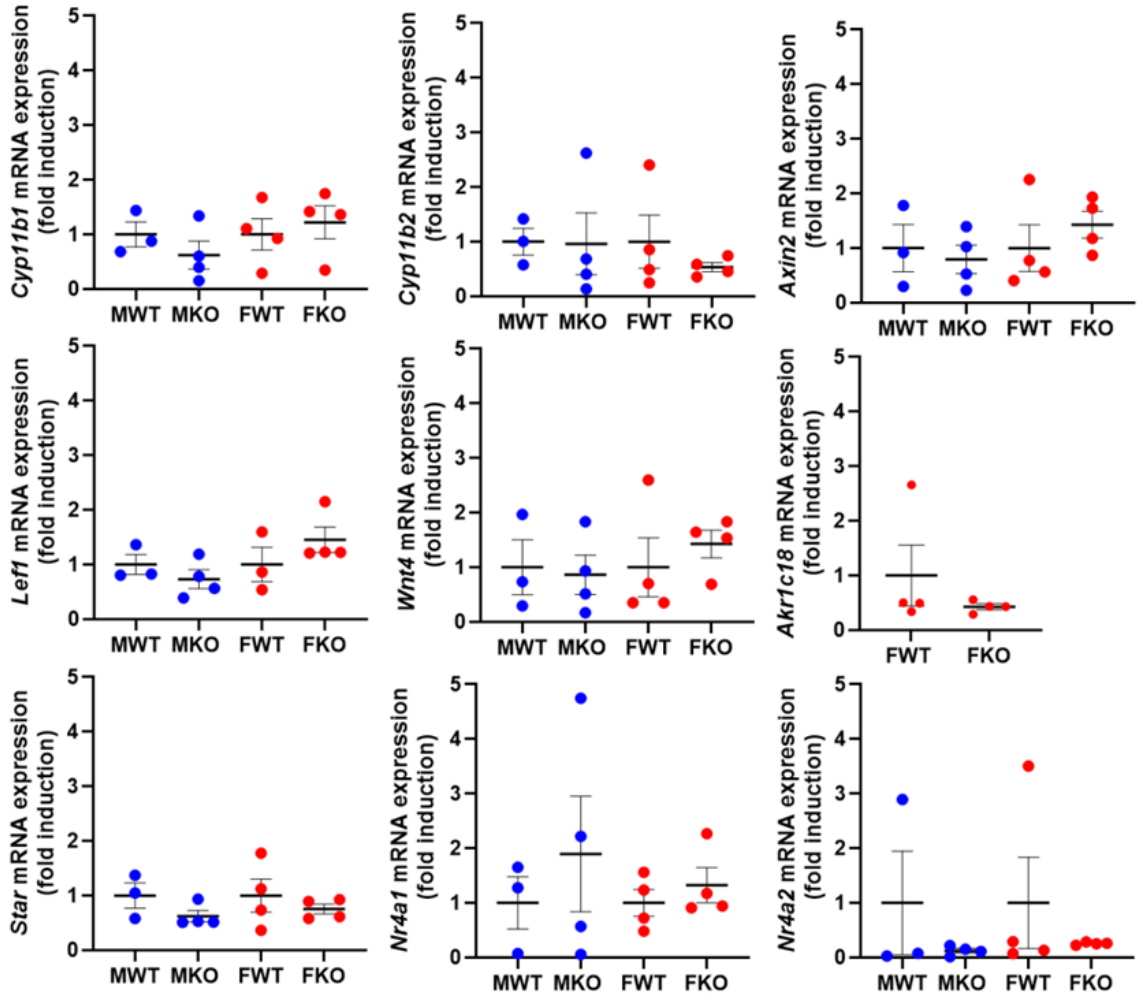

Figure 31 : Gene expression analysis in adrenal cortex. Relative mRNA expression of steroidogenic genes (*Cyp11b2, Cyp11b1, Star*), nuclear receptors (*Nr4a1, Nr4a2*), Wnt signalling genes (*Wnt4, Axin2, Lef1*), and *Akr1c18* by qPCR. Male (blue) and female (red) wild-type (WT) and Casz1KO^{ZG} mice. Fold change relative to WT ($2^{-\Delta\Delta Ct}$ method). Normalized to 18s, B2m, and Ubc. Individual values with mean ± SEM.

12.5 Discussion

This study aimed at investigating the role of *CASZ1* in adrenocortical function through ZG-specific gene inactivation in mice. The human GWAS study by Le Floch et al. (2022) identified *CASZ1* as a risk locus for PA and provided functional validation in human adrenocortical cells. Despite this compelling evidence, our initial characterisation of ZG-specific inactivation of *Casz1* in 12-week-old mice (Casz1KO^{ZG}) showed no clear phenotypic changes under basal conditions. Body weight, adrenal gland size, adrenocortical histology, cellular proliferation (Ki67) and steroidogenic gene expression (*Cyp11b2, Cyp11b1, Star*) were all comparable between wild-type and Casz1KO^{ZG} mice. Multivariate analysis of comprehensive steroid profiles revealed sex-specific patterns but only a minimal genotype-dependent separation.

While subtle differences were observed in females, including partial separation of steroid profiles in principal component analysis and qualitative reduction in 20α-HSD expression, these did not reach statistical significance.

The absence of a basal phenotype does not contradict the importance of *CASZ1* but suggests its function is context-dependent. The human GWAS data identified *CASZ1* variants as risk factors for PA (Le Floch et al., 2022) and *CASZ1* had previously been associated with blood pressure variation, suggesting an interaction between aldosterone dysregulation and hypertension in the general population. CASZ1 has been shown to act as both a transcriptional repressor of aldosterone biosynthesis and a mineralocorticoid receptor corepressor ((Le Floch et al., 2022; Yokota et al., 2021). In H295R-S2 cells, CASZ1 overexpression completely suppressed basal and angiotensin II-induced mineralocorticoid biosynthesis and significantly reduced aldosterone synthase expression, positioning it as a negative regulator of mineralocorticoid signalling. Such negative regulators may become functionally important primarily when the system is under stress or stimulation.

In humans, *CYP11B2* expression shows a complex pattern during development. The proportion of the definitive zone (DZ) or ZG relative to the total adrenal cortex begins to increase in the second trimester of pregnancy, then decreases in the third trimester, rises again after birth, reaches its highest point during infancy, and then gradually declines. Looking at AS^+ cells specifically, they remain relatively rare throughout the fetal period but become much more abundant after birth, peak during infancy, and then decline. When examining the proportion of AS^+ cells within just the DZ or ZG (rather than the whole adrenal), the pattern shows two distinct peaks, one during fetal life and another during the newborn period through infancy (Shironomae et al., 2024). In mice, the Cyp11b2-Cre driver initiates recombination during late embryonic or early postnatal development when *Cyp11b2* expression begins in the developing ZG, meaning *Casz1* deletion occurs during ZG development and remains absent throughout postnatal maturation. The absence of a basal phenotype in our model may reflect this early developmental timing. Deletion during adrenocortical differentiation could permit compensatory mechanisms to develop, masking CASZ1's function under basal conditions.

Female Casz1KO^{ZG} mice showed partial separation from wild-type females in principal component analysis of steroid profiles, while males showed complete overlap. Additionally, qualitative reduction in 20α-HSD expression was observed exclusively in females. The ZX regresses in males around puberty but persists in females until first pregnancy, representing a

transient fetal-type cortex with no clear human equivalent. These sex-specific patterns reflect fundamental differences in adrenocortical structure between male and female mice. The observation that *Casz1* deletion may affect X zone marker expression suggests *CASZ1* may play a role in adrenocortical zonation or maintenance of specific cell populations beyond effects on aldosterone biosynthesis. However, these observations remain preliminary and largely qualitative, requiring formal quantification and expanded sample sizes for confirmation.

The absence of clear phenotype under basal conditions prompted design of additional experiments to reveal *CASZ1* dependent functions under challenge conditions. Three complementary experimental strategies are currently underway or planned:

- **Low-sodium diet challenge:** Casz1KO^{ZG} mice will be subjected to two weeks of low-sodium diet (LSD) to test whether *CASZ1* constrains aldosterone production under sustained ZG stimulation. This classic physiological challenge activates the RAAS and tests adrenal cortex plasticity. If *CASZ1* normally constrains aldosterone production during prolonged activation, its absence should result in exaggerated aldosterone responses or enhanced ZG hypertrophy compared to wild-type controls.
- **Lineage tracing:** Crossing Casz1KO^{ZG} mice with mTmG reporter mice, already established in the host laboratory, will enable permanent lineage tracing of *Cyp11b2*-expressing ZG cells. The mTmG system permanently labels ZG cells, allowing them to be tracked over time. This will reveal whether *CASZ1* influences ZG cell distribution, transdifferentiation into ZF, or challenge-induced plasticity.
- **Double knockout studies:** Generating mice lacking both Casz1 and Mr specifically in ZG will dissect CASZ1 functions that depend on MR signalling from MR-independent mechanisms. Given that CASZ1b functions as a MR corepressor (Yokota et al., 2021), this addresses whether CASZ1 operates primarily through modulation of MR activity or has additional roles in aldosterone biosynthesis regulation. If CASZ1 functions primarily through MR, double knockout mice should resemble MR single knockout mice. If CASZ1 has MR-independent functions, double knockout mice might show additive or synergistic phenotypes.

This work illustrates important principles in translating human genetic findings to animal models. The observation that genetic deletion of a gene identified in human GWAS does not

produce a clear phenotype in a mouse model under basal conditions emphasizes the importance of comprehensive phenotyping under multiple conditions and the value of challenge experiments that simulate disease-relevant stresses. The subtle sex-specific effects observed suggest that CASZ1 function or its consequences may differ between males and females, consistent with known sexual dimorphism in adrenocortical structure and function.

12.6 Conclusion

This part of my thesis work established and characterized mice with ZG-specific *Casz1* inactivation. Despite evidence from GWAS studies identifying *CASZ1* as a risk locus for PA and functional validation in human adrenocortical cells demonstrating that CASZ1 overexpression completely suppresses mineralocorticoid biosynthesis, Casz1KO^{ZG} mice exhibited no overt phenotype under basal conditions at 12 weeks of age.

These findings indicate that CASZ1 is not essential for basal aldosterone production and ZG maintenance in young adult mice under standard conditions. However, these results do not refute *CASZ1's* importance in aldosterone regulation but rather suggest its function is context-dependent, becoming critical under specific physiological or pathological conditions. Several mechanisms could account for the absence of basal phenotype, including functional compensation by parallel regulatory pathways during development, species differences in adrenocortical biology and the difficulty of appropriately modelling slight changes in gene expression/function due to common genetic variation in mouse models.

Ongoing studies employing three complementary experimental strategies will test these hypotheses. LSD challenge for two weeks will test whether CASZ1 constrains aldosterone production under sustained renin-angiotensin system activation. Crossing *Casz1* knockout mice with mTmG reporter mice will enable lineage tracing of ZG-derived cells, revealing potential effects on cell fate, transdifferentiation, or ZG plasticity. Generation of double knockout mice lacking both CASZ1 and MR specifically in ZG will dissect CASZ1 functions that depend on MR signalling from MR-independent mechanisms.

This work establishes essential foundations for ongoing CASZ1 investigation. The Casz1KO^{ZG} mouse line has been validated through comprehensive morphological, molecular, and hormonal phenotyping. This baseline dataset defines normal adrenocortical parameters in the model, against which future manipulations can be compared. The demonstration that *Casz1*

deletion is well-tolerated under basal conditions establishes that any phenotypes emerging under challenge conditions reflect context-dependent functions rather than developmental abnormalities.

Understanding when and how CASZ1 influences aldosterone production and identifying conditions under which its loss becomes functionally significant, remains an important goal with implications for understanding PA pathogenesis. The work presented in this project, combined with the ongoing investigations described above, will contribute to comprehensive understanding of the role of CASZ1 in ZG biology and aldosterone regulation, potentially advancing our understanding of transcriptional networks governing aldosterone production and their perturbation in PA.

General discussion

The aim of this project was to investigate how MR and CASZ1 influence adrenal cortex structure, function, and aldosterone regulation, eventually leading to the development of PA. The first project examined the MR as a key player in adrenocortical plasticity and ZG maintenance. The second project investigated CASZ1, a zinc-finger transcription factor and MR corepressor identified through GWAS as a genetic risk factor for primary aldosteronism (PA).

Both projects employed ZG-specific Cre-mediated knockout strategies, providing directly comparable experimental results. Whereas MR knockout resulted in substantial morphological, molecular, and functional changes in basal conditions, no major modifications were observed in the *CASZ1* knockout model, underscoring different regulatory properties on adrenal cortex homeostasis. It therefore appears that MR functions as a transcriptional activator that drives metabolic reprogramming and cell fate decisions in the adrenal cortex, while CASZ1, although functioning as an MR corepressor and suppressor of aldosterone biosynthesis *in vitro*, may not be essential to adrenocortical function, at least under basal conditions.

Mineralocorticoid Receptor: A master regulator of adrenocortical plasticity

The MR study showed that MR plays distinct, cell-population-specific roles in coordinating three mechanistically different plasticity programs during low-salt challenge. First, MR directly maintains ZG identity and proliferative capacity, supporting baseline aldosterone production. Second, the ZG-ZF transition zone, representing approximately 10% of plasticity responses, shows robust MR-dependent responsiveness to a salt challenge at the boundary between the two zones. Third, the ZF resolves into two functionally distinct subpopulations: ZF1 undergoes authentic MR-dependent transdifferentiation to acquire ZG identity following LSD, supported by constitutive metabolic priming, while ZF2 shows *Cyp11b2* induction without full ZG identity acquisition.

The key mechanistic insight is that MR functions not simply by regulating individual steroidogenic genes, but rather by coordinating a comprehensive metabolic transformation necessary for cells to adopt aldosterone-producing identity. Despite representing only 28% of plasticity genes, MR-dependent genes accounted for 69% of functional ZG signature changes and converged on metabolic pathways including oxidative phosphorylation, ATP synthesis, and steroid biosynthesis.

This fundamentally revises our understanding of MR beyond its classical role in target tissues such as the kidney and cardiovascular system to include a critical role in the tissue that produces its ligand, creating an autocrine-paracrine regulatory loop. The demonstration of this local MR signalling system challenges the traditional view of the adrenal cortex as passively responding to external hormonal signals and instead positions it as an adaptive, self-regulating system.

Sex-specific effects on ZG architecture were observed in the MR knockout model, with MR deletion affecting ZG organization differently in males versus females. This likely reflects established sexual dimorphism in adrenal cortex structure, renewal mechanisms, and hormonal regulation. The adrenal cortex undergoes sex-specific remodelling at puberty, with distinct progenitor cell dynamics and proliferation rates between sexes. These observations suggest that sex hormones may modulate MR signalling, creating sex-specific regulatory networks in the adrenal cortex.

CASZ1: A context-dependent inhibitor of aldosterone production

In the light of the human genetic evidence linking *CASZ1* variants to PA susceptibility, the absence of a clear basal phenotype in *CASZ1* knockout mice is actually quite informative. The apparent difference between mouse models and human genetic studies offers important insights into how *CASZ1* functions and the nature of genetic risk factors for complex diseases.

CASZ1 likely functions as a negative regulator on aldosterone production that becomes critical only under specific circumstances. As a negative regulator and MR corepressor, *CASZ1* may suppress aldosterone synthesis primarily during prolonged stimulation or stress. Under basal conditions in young adult mice, aldosterone demand is modest and multiple redundant regulatory mechanisms may compensate for *CASZ1* absence. The Cyp11b2-Cre driver initiates recombination during late embryonic or early postnatal development, meaning *CASZ1* deletion occurs during ZG development. This early timing allows compensatory mechanisms to develop during adrenocortical differentiation, potentially masking CASZ1's function. This contrasts with acute *CASZ1* knockdown in mature human adrenocortical cells, which show dramatic suppression of aldosterone synthesis. Furthermore, human GWAS identified *CASZ1* variants associated with PA susceptibility in a population context involving lifelong exposure to environmental stressors such as dietary sodium variation. Young laboratory mice maintained under controlled conditions may not experience the cumulative stresses that reveal *CASZ1's* protective function.

The subtle sex-specific effects observed in female *CASZ1* knockout mice suggest a sexually dimorphic regulatory function of CASZ1. Female knockouts showed partial separation from wild-type females in principal component analysis of steroid profiles, while males showed complete overlap. In addition, *CASZ1* deletion reduced 20α-HSD expression in female mice. This enzyme marks the X zone, a transient remnant of the fetal adrenal cortex that regresses in males around puberty but persists in females until first pregnancy. These observations suggest that *CASZ1* may influence adrenocortical zonation beyond its effects on aldosterone biosynthesis. The fact that effects manifest in females but not males indicates that *CASZ1* function may be linked to sex hormones or female-specific adrenocortical structures. This is particularly interesting given that the X zone has no clear human equivalent, raising important questions about translational relevance while simultaneously suggesting that *CASZ1* may have broader roles in adrenocortical homeostasis than initially appreciated.

The MR-CASZ1 regulatory axis: balancing activation and inhibition

MR and CASZ1 may function as opposing forces in a finely tuned regulatory axis. CASZ1b physically interacts with MR to suppress its transcriptional activity, creating a direct negative feedback mechanism. When aldosterone production activates local MR, this could amplify aldosterone synthesis further, but CASZ1 may limit this amplification by repressing MR activity. This ensures that the aldosterone-MR autocrine loop identified in the first project operates within physiological boundaries rather than evolving into autonomous aldosterone production.

The contrasting phenotypes of the two knockout models demonstrate this regulatory relationship. MRKO^{Ad} eliminated the activating signal, resulting in reduced *Cyp11b2* expression, impaired ZG proliferation, and abolished LSD induced ZG expansion. CASZ1 knockout removes a negative inhibitory mechanism but shows minimal effect under basal conditions, suggesting that multiple brakes exist or that *CASZ1* becomes critical primarily under stimulation.

The single-nucleus RNA sequencing data from the MR study revealed that MR-dependent genes converge on metabolic pathways including oxidative phosphorylation, ATP synthesis, and steroid biosynthesis. *CASZ1*, as an MR corepressor, would be expected to suppress precisely these metabolic programs. The absence of *CASZ1* might therefore lead to excessive MR-driven metabolic activation under sustained RAAS stimulation, potentially explaining how genetic variation in *CASZ1* increases PA risk.

Three potential mechanisms could explain how genetic variation in *CASZ1* increases PA risk in humans. First, a quantitative effect: reduced *CASZ1* expression or function, as suggested by GWAS variants, weakens inhibitory control over MR-driven aldosterone synthesis. Under chronic stimulation from dietary sodium restriction, this would allow gradual expansion of aldosterone-producing cell populations and enhanced responsiveness to RAAS activation. Second, *CASZ1* may be particularly important during specific developmental windows or following sustained stimulation. Reduced *CASZ1* function during critical periods could predispose to altered ZG homeostasis that manifests as PA later in life. Third, CASZ1 function may become essential only when aldosterone production approaches upper physiological limits. Below this threshold, redundant mechanisms compensate, explaining the lack of basal phenotype in young mice. Above this threshold, CASZ1 absence permits transition to autonomous production.

Understanding the MR-CASZ1 axis has practical therapeutic implications. Current PA treatment relies on surgical removal of APAs or MR antagonists such as spironolactone and eplerenone that block MR in the whole body, causing systemic side effects. Therapies that specifically restore CASZ1 function in the adrenal cortex, or that modulate the balance between MR activation and CASZ1 repression, could offer more targeted interventions with fewer adverse effects.

General conclusion

My PhD work investigated two key regulatory factors in adrenal cortex function and aldosterone production: the MR and CASZ1, a zinc-finger transcription factor and MR corepressor identified through genome-wide association studies as a PA susceptibility gene. Using ZG-specific knockout mouse models and comprehensive single-nucleus RNA sequencing, I uncovered novel roles for MR in adrenocortical plasticity and performed the first functional characterization of CASZ1 in ZG biology.

The ZG-specific MR deletion revealed unexpected findings. Beyond its classical function in the kidney and cardiovascular system, the MR appears to play a critical role in maintaining adrenocortical zonation and plasticity. MR knock-out in the adrenal cortex results in altered ZG homeostasis, both under basal as well as stimulated conditions. In particular, snRNAseq analysis across different dietary conditions showed that MR deletion reprograms the ZF, altering cell identity and producing transitional populations between ZG and ZF. I also observed sex-specific effects, particularly in ZX marker expression in females. These results suggest that MR activation in the adrenal cortex not only regulates ZG function and aldosterone production in an autocrine paracrine loop, but also induces a transcriptional response regulating adrenocortical cell fate and zonation.

Investigation of the Casz1KO^{ZG} mice did not reveal major phenotypic or functional modifications. Despite clear human evidence that *CASZ1* variants increase PA risk and CASZ1 overexpression suppresses mineralocorticoid biosynthesis in adrenocortical cells, 12-weeks old Casz1KO^{ZG} mice showed no clear phenotypic change under basal conditions. Given that some of the MR dependent phenotypes are visible at 6 weeks of age but not at 12, such as reduced aldosterone production, or vice-versa, it may well be that CASZ1 function is age- and context-dependent, becoming critical under specific physiological or pathological stresses. Some minor sex-specific effects emerged in females, including partial separation of steroid profiles and reduced 20α-HSD expression, suggesting a possible ZX involvement. Three ongoing experimental approaches will clarify when CASZ1 becomes functionally important: LSD challenge, lineage tracing with mTmG reporter mice, and double knockout studies combining *Casz1* and *Mr* deletion to separate MR-dependent from MR-independent CASZ1 functions.

This work has revealed the role of MR in adrenocortical plasticity and ZF reprogramming for the first time, and established essential foundations for understanding CASZ1 function in ZG

biology. These findings open new perspectives on the molecular mechanisms underlying adrenal zonation, cell renewal and cell lineage conversion, providing a mechanistic explanation linking genetic variation in the general population to aldosterone dysregulation in the adrenal gland. Understanding these transcriptional networks regulating aldosterone production could ultimately identify new therapeutic targets for improved patient care and prevention of cardiovascular complications in PA.

Bibliography

Abou Nader, N., Boyer, A., 2021. Adrenal Cortex Development and Maintenance: Knowledge Acquired From Mouse Models. Endocrinology 162, bqab187. https://doi.org/10.1210/endocr/bqab187

Adler, G.K., Stowasser, M., Correa, R.R., Khan, N., Kline, G., McGowan, M.J., Mulatero, P., Murad, M.H., Touyz, R.M., Vaidya, A., Williams, T.A., Yang, J., Young, W.F., Zennaro, M.-C., Brito, J.P., 2025. Primary Aldosteronism: An Endocrine Society Clinical Practice Guideline. J Clin Endocrinol Metab 110, 2453–2495. https://doi.org/10.1210/clinem/dgaf284

Åkerström, T., Maharjan, R., Sven Willenberg, H., Cupisti, K., Ip, J., Moser, A., Stålberg, P., Robinson, B., Alexander Iwen, K., Dralle, H., Walz, M.K., Lehnert, H., Sidhu, S., Gomez-Sanchez, C., Hellman, P., Björklund, P., 2016. Activating mutations in CTNNB1 in aldosterone producing adenomas. Sci Rep 6, 19546. https://doi.org/10.1038/srep19546

Azizan, E.A.B., Drake, W.M., Brown, M.J., 2023. Primary aldosteronism: molecular medicine meets public health. Nat Rev Nephrol 19, 788–806. https://doi.org/10.1038/s41581-023-00753-6

Azizan, E.A.B., Poulsen, H., Tuluc, P., Zhou, J., Clausen, M.V., Lieb, A., Maniero, C., Garg, S., Bochukova, E.G., Zhao, W., Shaikh, L.H., Brighton, C.A., Teo, A.E.D., Davenport, A.P., Dekkers, T., Tops, B., Küsters, B., Ceral, J., Yeo, G.S.H., Neogi, S.G., McFarlane, I., Rosenfeld, N., Marass, F., Hadfield, J., Margas, W., Chaggar, K., Solar, M., Deinum, J., Dolphin, A.C., Farooqi, I.S., Striessnig, J., Nissen, P., Brown, M.J., 2013. Somatic mutations in ATP1A1 and CACNA1D underlie a common subtype of adrenal hypertension. Nat Genet 45, 1055–1060. https://doi.org/10.1038/ng.2716

Bandulik, S., Penton, D., Barhanin, J., Warth, R., 2010. TASK1 and TASK3 Potassium Channels: Determinants of Aldosterone Secretion and Adrenocortical Zonation. Horm Metab Res 42, 450–457. https://doi.org/10.1055/s-0029-1243601

Barrera-Chimal, J., Estrela, G.R., Lechner, S.M., Giraud, S., El Moghrabi, S., Kaaki, S., Kolkhof, P., Hauet, T., Jaisser, F., 2018. The myeloid mineralocorticoid receptor controls inflammatory and fibrotic responses after renal injury via macrophage interleukin-4 receptor signaling. Kidney Int 93, 1344–1355. https://doi.org/10.1016/j.kint.2017.12.016

Barrett, P.Q., Guagliardo, N.A., Bayliss, D.A., 2021. Ion Channel Function and Electrical Excitability in the Zona Glomerulosa: A Network Perspective on Aldosterone Regulation. Annu Rev Physiol 83, 451–475. https://doi.org/10.1146/annurev-physiol-030220-113038

Bassett, J.R., West, S.H., 1997. Vascularization of the adrenal cortex: its possible involvement in the regulation of steroid hormone release. Microsc Res Tech 36, 546–557. https://doi.org/10.1002/(SICI)1097-0029(19970315)36:6<546::AID-JEMT11>3.0.CO;2-O

Berger, S., Bleich, M., Schmid, W., Cole, T.J., Peters, J., Watanabe, H., Kriz, W., Warth, R., Greger, R., Schütz, G., 1998. Mineralocorticoid receptor knockout mice: pathophysiology of Na+ metabolism. Proc Natl Acad Sci U S A 95, 9424–9429. https://doi.org/10.1073/pnas.95.16.9424

Berger, S., Bleich, M., Schmid, W., Greger, R., Schütz, G., 2000. Mineralocorticoid receptor knockout mice: lessons on Na+ metabolism. Kidney Int 57, 1295–1298. https://doi.org/10.1046/j.1523-1755.2000.00965.x

Berger, S., Wolfer, D.P., Selbach, O., Alter, H., Erdmann, G., Reichardt, H.M., Chepkova, A.N., Welzl, H., Haas, H.L., Lipp, H.-P., Schütz, G., 2006. Loss of the limbic mineralocorticoid receptor impairs behavioral plasticity. Proc Natl Acad Sci U S A 103, 195–200. https://doi.org/10.1073/pnas.0503878102

Berthon, A., Drelon, C., Ragazzon, B., Boulkroun, S., Tissier, F., Amar, L., Samson-Couterie, B., Zennaro, M.-C., Plouin, P.-F., Skah, S., Plateroti, M., Lefèbvre, H., Sahut-Barnola, I., Batisse-Lignier, M., Assié, G., Lefrançois-Martinez, A.-M., Bertherat, J., Martinez, A., Val, P., 2014. WNT/β-catenin signalling is activated in aldosterone-producing adenomas and controls aldosterone production. Hum Mol Genet 23, 889–905. https://doi.org/10.1093/hmg/ddt484

Berthon, A., Martinez, A., Bertherat, J., Val, P., 2012. Wnt/β-catenin signalling in adrenal physiology and tumour development. Mol Cell Endocrinol 351, 87–95. https://doi.org/10.1016/j.mce.2011.09.009

Berthon, A., Sahut-Barnola, I., Lambert-Langlais, S., de Joussineau, C., Damon-Soubeyrand, C., Louiset, E., Taketo, M.M., Tissier, F., Bertherat, J., Lefrançois-Martinez, A.-M., Martinez, A., Val, P., 2010. Constitutive beta-catenin activation induces adrenal hyperplasia and promotes adrenal cancer development. Hum Mol Genet 19, 1561–1576. https://doi.org/10.1093/hmg/ddq029

Beuschlein, F., Boulkroun, S., Osswald, A., Wieland, T., Nielsen, H.N., Lichtenauer, U.D., Penton, D., Schack, V.R., Amar, L., Fischer, E., Walther, A., Tauber, P., Schwarzmayr, T., Diener, S., Graf, E., Allolio, B., Samson-Couterie, B., Benecke, A., Quinkler, M., Fallo, F., Plouin, P.-F., Mantero, F., Meitinger, T., Mulatero, P., Jeunemaitre, X., Warth, R., Vilsen, B., Zennaro, M.-C., Strom, T.M., Reincke, M., 2013. Somatic mutations in ATP1A1 and ATP2B3 lead to aldosterone-producing adenomas and secondary hypertension. Nat Genet 45, 440–444, 444e1-2. https://doi.org/10.1038/ng.2550

Binart, N., Lombès, M., Baulieu, E.E., 1995. Distinct functions of the 90 kDa heat-shock protein (hsp90) in oestrogen and mineralocorticosteroid receptor activity: effects of hsp90 deletion mutants. Biochem J 311 (Pt 3), 797–804. https://doi.org/10.1042/bj3110797

Boulkroun, S., Beuschlein, F., Rossi, G.-P., Golib-Dzib, J.-F., Fischer, E., Amar, L., Mulatero, P., Samson-Couterie, B., Hahner, S., Quinkler, M., Fallo, F., Letizia, C., Allolio, B., Ceolotto, G., Cicala, M.V., Lang, K., Lefebvre, H., Lenzini, L., Maniero, C., Monticone, S., Perrocheau, M., Pilon, C., Plouin, P.-F., Rayes, N., Seccia, T.M., Veglio, F., Williams, T.A., Zinnamosca, L., Mantero, F., Benecke, A., Jeunemaitre, X., Reincke, M., Zennaro, M.-C., 2012. Prevalence, clinical, and molecular correlates of KCNJ5 mutations in primary aldosteronism. Hypertension 59, 592–598. https://doi.org/10.1161/HYPERTENSIONAHA.111.186478

Boulkroun, S., Fay, M., Zennaro, M.-C., Escoubet, B., Jaisser, F., Blot-Chabaud, M., Farman, N., Courtois-Coutry, N., 2002. Characterization of rat NDRG2 (N-Myc downstream regulated gene 2), a novel early mineralocorticoid-specific induced gene. J Biol Chem 277, 31506–31515. https://doi.org/10.1074/jbc.M200272200

Boulkroun, S., Fernandes-Rosa, F.L., Zennaro, M.-C., 2015. Molecular and Cellular Mechanisms of Aldosterone Producing Adenoma Development. Front Endocrinol (Lausanne) 6, 95. https://doi.org/10.3389/fendo.2015.00095

Boulkroun, S., Samson-Couterie, B., Dzib, J.-F.G., Lefebvre, H., Louiset, E., Amar, L., Plouin, P.-F., Lalli, E., Jeunemaitre, X., Benecke, A., Meatchi, T., Zennaro, M.-C., 2010. Adrenal cortex remodeling and functional zona glomerulosa hyperplasia in primary aldosteronism. Hypertension 56, 885–892. https://doi.org/10.1161/HYPERTENSIONAHA.110.158543

Brilla, C.G., Matsubara, L.S., Weber, K.T., 1993. Anti-aldosterone treatment and the prevention of myocardial fibrosis in primary and secondary hyperaldosteronism. J Mol Cell Cardiol 25, 563–575. https://doi.org/10.1006/jmcc.1993.1066

Brown, J.M., Siddiqui, M., Calhoun, D.A., Carey, R.M., Hopkins, P.N., Williams, G.H., Vaidya, A., 2020. The Unrecognized Prevalence of Primary Aldosteronism: A Cross-sectional Study. Ann Intern Med 173, 10–20. https://doi.org/10.7326/M20-0065

Bruner, K.L., Derfoul, A., Robertson, N.M., Guerriero, G., Fernandes-Alnemri, T., Alnemri, E.S., Litwack, G., 1997. The unliganded mineralocorticoid receptor is associated with heat shock proteins 70 and 90 and the immunophilin FKBP-52. Recept Signal Transduct 7, 85–98.

Burton, T.J., Cope, G., Wang, J., Sim, J.C., Azizan, E.A.B., O'Shaughnessy, K.M., Brown, M.J., 2009. Expression of the epithelial Na(+) channel and other components of an aldosterone response pathway in human adrenocortical cells. Eur J Pharmacol 613, 176–181. https://doi.org/10.1016/j.ejphar.2009.04.005

Caprio, M., Fève, B., Claës, A., Viengchareun, S., Lombès, M., Zennaro, M.-C., 2007. Pivotal role of the mineralocorticoid receptor in corticosteroid-induced adipogenesis. FASEB J 21, 2185–2194. https://doi.org/10.1096/fj.06-7970com

Carlberg, C., 2024. A Key Transcription Factor Family: Nuclear Receptors, in: Carlberg, C. (Ed.), Gene Regulation and Epigenetics: How Science Works. Springer Nature Switzerland, Cham, pp. 59–71. https://doi.org/10.1007/978-3-031-68730-3_5

Chen, S.Y., Bhargava, A., Mastroberardino, L., Meijer, O.C., Wang, J., Buse, P., Firestone, G.L., Verrey, F., Pearce, D., 1999. Epithelial sodium channel regulated by aldosterone-induced protein sgk. Proc Natl Acad Sci U S A 96, 2514–2519. https://doi.org/10.1073/pnas.96.5.2514

Cheng, K., Seita, Y., Moriwaki, T., Noshiro, K., Sakata, Y., Hwang, Y.S., Torigoe, T., Saitou, M., Tsuchiya, H., Iwatani, C., Hosaka, M., Ohkouchi, T., Watari, H., Umazume, T., Sasaki, K., 2022. The developmental origin and the specification of the adrenal cortex in humans and cynomolgus monkeys. Sci Adv 8, eabn8485. https://doi.org/10.1126/sciadv.abn8485

Choi, M., Scholl, U.I., Yue, P., Björklund, P., Zhao, B., Nelson-Williams, C., Ji, W., Cho, Y., Patel, A., Men, C.J., Lolis, E., Wisgerhof, M.V., Geller, D.S., Mane, S., Hellman, P., Westin, G., Åkerström, G., Wang, W., Carling, T., Lifton, R.P., 2011. K+ channel mutations in adrenal aldosterone-producing adenomas and hereditary hypertension. Science 331, 768–772. https://doi.org/10.1126/science.1198785

Chong, C., Hamid, A., Yao, T., Garza, A.E., Pojoga, L.H., Adler, G.K., Romero, J.R., Williams, G.H., 2017. Regulation of aldosterone secretion by mineralocorticoid receptor-mediated signaling. J Endocrinol 232, 525–534. https://doi.org/10.1530/JOE-16-0452

Christine, K.S., Conlon, F.L., 2008. Vertebrate CASTOR is required for differentiation of cardiac precursor cells at the ventral midline. Dev Cell 14, 616–623. https://doi.org/10.1016/j.devcel.2008.01.009

Clark, B.J., 2016. ACTH Action on StAR Biology. Front. Neurosci. 10. https://doi.org/10.3389/fnins.2016.00547

CONN, J.W., LOUIS, L.H., 1956. Primary aldosteronism, a new clinical entity. Ann Intern Med 44, 1–15. https://doi.org/10.7326/0003-4819-44-1-1

Conn, J.W., Louis, L.H., 1955. Primary aldosteronism: a new clinical entity. Trans Assoc Am Physicians 68, 215–231; discussion, 231–233.

Connell, J.M.C., Davies, E., 2005. The new biology of aldosterone. J Endocrinol 186, 1–20. https://doi.org/10.1677/joe.1.06017

Daniil, G., Fernandes-Rosa, F.L., Chemin, J., Blesneac, I., Beltrand, J., Polak, M., Jeunemaitre, X., Boulkroun, S., Amar, L., Strom, T.M., Lory, P., Zennaro, M.-C., 2016. CACNA1H Mutations Are Associated With Different Forms of Primary Aldosteronism. EBioMedicine 13, 225–236. https://doi.org/10.1016/j.ebiom.2016.10.002

de Freminville, J.-B., Gardini, M., Cremer, A., Camelli, S., Baron, S., Bobrie, G., Gosse, P., Boulestreau, R., Gebara, N., Doublet, J., Dussartre, T., Grataloup, C., Lorthioir, A., Massien, C., Madjalian, A.-M., Riancho, J., Soulat, G., Postel-Vinay, N., Azizi, M., Rance, B., Amar, L., 2024. Prevalence and Risk Factors for Secondary Hypertension in Young Adults. Hypertension 81, 2340–2349. https://doi.org/10.1161/HYPERTENSIONAHA.124.22753

de Gasparo, M., Joss, U., Ramjoué, H.P., Whitebread, S.E., Haenni, H., Schenkel, L., Kraehenbuehl, C., Biollaz, M., Grob, J., Schmidlin, J., 1987. Three new epoxy-spirolactone derivatives: characterization in vivo and in vitro. J Pharmacol Exp Ther 240, 650–656.

de Kloet, E.R., Joëls, M., Holsboer, F., 2005. Stress and the brain: from adaptation to disease. Nat Rev Neurosci 6, 463–475. https://doi.org/10.1038/nrn1683

De Kloet, E.R., Vreugdenhil, E., Oitzl, M.S., Joëls, M., 1998. Brain corticosteroid receptor balance in health and disease. Endocr Rev 19, 269–301. https://doi.org/10.1210/edrv.19.3.0331

De Sousa, K., Boulkroun, S., Baron, S., Nanba, K., Wack, M., Rainey, W.E., Rocha, A., Giscos-Douriez, I., Meatchi, T., Amar, L., Travers, S., Fernandes-Rosa, F.L., Zennaro, M.-C., 2020. Genetic, Cellular, and Molecular Heterogeneity in Adrenals With Aldosterone-

Producing Adenoma. Hypertension 75, 1034–1044. https://doi.org/10.1161/HYPERTENSIONAHA.119.14177

Debonneville, C., Flores, S.Y., Kamynina, E., Plant, P.J., Tauxe, C., Thomas, M.A., Münster, C., Chraïbi, A., Pratt, J.H., Horisberger, J.D., Pearce, D., Loffing, J., Staub, O., 2001. Phosphorylation of Nedd4-2 by Sgk1 regulates epithelial Na(+) channel cell surface expression. EMBO J 20, 7052–7059. https://doi.org/10.1093/emboj/20.24.7052

Delyani, J.A., Rocha, R., Cook, C.S., Tobert, D.S., Levin, S., Roniker, B., Workman, D.L., Sing, Y.L., Whelihan, B., 2001. Eplerenone: a selective aldosterone receptor antagonist (SARA). Cardiovasc Drug Rev 19, 185–200. https://doi.org/10.1111/j.1527-3466.2001.tb00064.x

Drelon, C., Berthon, A., Sahut-Barnola, I., Mathieu, M., Dumontet, T., Rodriguez, S., Batisse-Lignier, M., Tabbal, H., Tauveron, I., Lefrançois-Martinez, A.-M., Pointud, J.-C., Gomez-Sanchez, C.E., Vainio, S., Shan, J., Sacco, S., Schedl, A., Stratakis, C.A., Martinez, A., Val, P., 2016. PKA inhibits WNT signalling in adrenal cortex zonation and prevents malignant tumour development. Nat Commun 7, 12751. https://doi.org/10.1038/ncomms12751

Dumontet, T., Sahut-Barnola, I., Septier, A., Montanier, N., Plotton, I., Roucher-Boulez, F., Ducros, V., Lefrançois-Martinez, A.-M., Pointud, J.-C., Zubair, M., Morohashi, K.-I., Breault, D.T., Val, P., Martinez, A., 2018. PKA signaling drives reticularis differentiation and sexually dimorphic adrenal cortex renewal. JCI Insight 3, e98394, 98394. https://doi.org/10.1172/jci.insight.98394

Dutta, R.K., Arnesen, T., Heie, A., Walz, M., Alesina, P., Söderkvist, P., Gimm, O., 2019. A somatic mutation in CLCN2 identified in a sporadic aldosterone-producing adenoma. Eur J Endocrinol 181, K37–K41. https://doi.org/10.1530/EJE-19-0377

El Mouhayyar, C., Chhikara, M., Tang, M., Nigwekar, S.U., 2025. Clinical implications of mineralocorticoid receptor overactivation. Clin Kidney J 18, sfae346. https://doi.org/10.1093/ckj/sfae346

El Wakil, A., Lalli, E., 2011. The Wnt/beta-catenin pathway in adrenocortical development and cancer. Mol Cell Endocrinol 332, 32–37. https://doi.org/10.1016/j.mce.2010.11.014

Faedda, N., Abdellatif, A.B., Carbone, F., Fayad, M., Fedlaoui, B., Chamoun, R., L'Héritier, R., Gaudio, I.D., Koual, O., Giscos-Douriez, I., Baron, S., Atkinson, B., Li, X., Kong, L., Xu, Y., Camerer, E., Menager, M., Fernandes-Rosa, F.L., Boulkroun, S., Zennaro, M.-C., 2025. Sexually dimorphic interzonal crosstalk reshapes the adrenal cortex in response to pathophysiological challenges. https://doi.org/10.1101/2025.09.05.674435

Fagugli, R.M., Taglioni, C., 2011. Changes in the perceived epidemiology of primary hyperaldosteronism. Int J Hypertens 2011, 162804. https://doi.org/10.4061/2011/162804

Fakitsas, P., Adam, G., Daidié, D., van Bemmelen, M.X., Fouladkou, F., Patrignani, A., Wagner, U., Warth, R., Camargo, S.M.R., Staub, O., Verrey, F., 2007. Early aldosterone-induced gene product regulates the epithelial sodium channel by deubiquitylation. J Am Soc Nephrol 18, 1084–1092. https://doi.org/10.1681/ASN.2006080902

Faresse, N., 2014. Post-translational modifications of the mineralocorticoid receptor: How to dress the receptor according to the circumstances? The Journal of Steroid Biochemistry and Molecular Biology 143, 334–342. https://doi.org/10.1016/j.jsbmb.2014.04.015

Fedlaoui, B., Cosentino, T., Sayed, Z.R.A., Giscos-Douriez, I., Faedda, N., Fayad, M., Hulot, J.-S., Magnus, C., Sternson, S.M., Travers-Allard, S., Baron, S., Fernandes-Rosa, F.L., Zennaro, M.-C., Boulkroun, S., 2024. Modulation of calcium signaling on demand to decipher the molecular mechanisms of primary aldosteronism. https://doi.org/10.1101/2024.04.29.591306

Fernandes-Rosa, F.L., Boulkroun, S., Fedlaoui, B., Hureaux, M., Travers-Allard, S., Drossart, T., Favier, J., Zennaro, M.-C., 2023. New advances in endocrine hypertension: from genes to biomarkers. Kidney Int 103, 485–500. https://doi.org/10.1016/j.kint.2022.12.021

Fernandes-Rosa, F.L., Boulkroun, S., Zennaro, M.-C., 2017. Somatic and inherited mutations in primary aldosteronism. J Mol Endocrinol 59, R47–R63. https://doi.org/10.1530/JME-17-0035

Fernandes-Rosa, F.L., Daniil, G., Orozco, I.J., Göppner, C., El Zein, R., Jain, V., Boulkroun, S., Jeunemaitre, X., Amar, L., Lefebvre, H., Schwarzmayr, T., Strom, T.M., Jentsch, T.J., Zennaro, M.-C., 2018. A gain-of-function mutation in the CLCN2 chloride channel gene causes primary aldosteronism. Nat Genet 50, 355–361. https://doi.org/10.1038/s41588-018-0053-8

Fernandes-Rosa, F.L., Hubert, E.-L., Fagart, J., Tchitchek, N., Gomes, D., Jouanno, E., Benecke, A., Rafestin-Oblin, M.-E., Jeunemaitre, X., Antonini, S.R., Zennaro, M.-C., 2011. Mineralocorticoid receptor mutations differentially affect individual gene expression profiles in pseudohypoaldosteronism type 1. J Clin Endocrinol Metab 96, E519-527. https://doi.org/10.1210/jc.2010-1486

Fernandes-Rosa, F.L., Williams, T.A., Riester, A., Steichen, O., Beuschlein, F., Boulkroun, S., Strom, T.M., Monticone, S., Amar, L., Meatchi, T., Mantero, F., Cicala, M.-V., Quinkler,

M., Fallo, F., Allolio, B., Bernini, G., Maccario, M., Giacchetti, G., Jeunemaitre, X., Mulatero, P., Reincke, M., Zennaro, M.-C., 2014. Genetic spectrum and clinical correlates of somatic mutations in aldosterone-producing adenoma. Hypertension 64, 354–361. https://doi.org/10.1161/HYPERTENSIONAHA.114.03419

Fettweis, G., Johnson, T.A., Almeida-Prieto, B., Weller-Pérez, J., Presman, D.M., Hager, G.L., Alvarez de la Rosa, D., 2024. The mineralocorticoid receptor forms higher order oligomers upon DNA binding. Protein Sci 33, e4890. https://doi.org/10.1002/pro.4890

Fraccarollo, D., Berger, S., Galuppo, P., Kneitz, S., Hein, L., Schütz, G., Frantz, S., Ertl, G., Bauersachs, J., 2011. Deletion of cardiomyocyte mineralocorticoid receptor ameliorates adverse remodeling after myocardial infarction. Circulation 123, 400–408. https://doi.org/10.1161/CIRCULATIONAHA.110.983023

Freedman, B.D., Kempna, P.B., Carlone, D.L., Shah, M., Guagliardo, N.A., Barrett, P.Q., Gomez-Sanchez, C.E., Majzoub, J.A., Breault, D.T., 2013. Adrenocortical zonation results from lineage conversion of differentiated zona glomerulosa cells. Dev Cell 26, 666–673. https://doi.org/10.1016/j.devcel.2013.07.016

Fuchs-Hammoser, R., Schweiger, M., Oelkers, W., 1980. The effect of chronic low-dose infusion of ACTH (1-24) on renin, renin-substrate, aldosterone and other corticosteroids in sodium replete and deplete man. Acta Endocrinol (Copenh) 95, 198–206. https://doi.org/10.1530/acta.0.0950198

Funder, J.W., Feldman, D., Edelman, I.S., 1973. The roles of plasma binding and receptor specificity in the mineralocorticoid action of aldosterone. Endocrinology 92, 994–1004. https://doi.org/10.1210/endo-92-4-994

Gadasheva, Y., Nolze, A., Grossmann, C., 2021. Posttranslational Modifications of the Mineralocorticoid Receptor and Cardiovascular Aging. Front. Mol. Biosci. 8. https://doi.org/10.3389/fmolb.2021.667990

Galigniana, M.D., Erlejman, A.G., Monte, M., Gomez-Sanchez, C., Piwien-Pilipuk, G., 2010. The hsp90-FKBP52 complex links the mineralocorticoid receptor to motor proteins and persists bound to the receptor in early nuclear events. Mol Cell Biol 30, 1285–1298. https://doi.org/10.1128/MCB.01190-09

Gallo-Payet, N., Martinez, A., Lacroix, A., 2017. Editorial: ACTH Action in the Adrenal Cortex: From Molecular Biology to Pathophysiology. Front Endocrinol (Lausanne) 8, 101. https://doi.org/10.3389/fendo.2017.00101

Garcia, A.L., Udeh, A., Kalahasty, K., Hackam, A.S., 2018. A growing field: the regulation of axonal regeneration by Wnt signaling. Neural Regen Res 13, 43–52. https://doi.org/10.4103/1673-5374.224359

GBD 2019 Meningitis Antimicrobial Resistance Collaborators, 2023. Global, regional, and national burden of meningitis and its aetiologies, 1990-2019: a systematic analysis for the Global Burden of Disease Study 2019. Lancet Neurol 22, 685–711. https://doi.org/10.1016/S1474-4422(23)00195-3

Gembardt, F., Heringer-Walther, S., van Esch, J.H.M., Sterner-Kock, A., van Veghel, R., Le, T.H., Garrelds, I.M., Coffman, T.M., Danser, A.H.J., Schultheiss, H.-P., Walther, T., 2008. Cardiovascular phenotype of mice lacking all three subtypes of angiotensin II receptors. The FASEB Journal 22, 3068–3077. https://doi.org/10.1096/fj.08-108316

Gomez-Sanchez, C.E., Kuppusamy, M., Gomez-Sanchez, E.P., 2015. Somatic mutations of the ATP1A1 gene and aldosterone-producing adenomas. Mol Cell Endocrinol 408, 213–219. https://doi.org/10.1016/j.mce.2014.12.004

Gordon, R.D., Stowasser, M., Tunny, T.J., Klemm, S.A., Finn, W.L., Krek, A.L., 1991. Clinical and Pathological Diversity of Primary Aldosteronism, Including a New Familial Variety. Clinical and Experimental Pharmacology and Physiology 18, 283–286. https://doi.org/10.1111/j.1440-1681.1991.tb01446.x

Grabek, A., Dolfi, B., Klein, B., Jian-Motamedi, F., Chaboissier, M.-C., Schedl, A., 2019. The Adult Adrenal Cortex Undergoes Rapid Tissue Renewal in a Sex-Specific Manner. Cell Stem Cell 25, 290-296.e2. https://doi.org/10.1016/j.stem.2019.04.012

Greep, R.O., Deane, H.W., 1949. Histological, cytochemical and physiological observations on the regeneration of the rat's adrenal gland following enucleation. Endocrinology 45, 42–56. https://doi.org/10.1210/endo-45-1-42

Guo, C., Ricchiuti, V., Lian, B.Q., Yao, T.M., Coutinho, P., Romero, J.R., Li, J., Williams, G.H., Adler, G.K., 2008. Mineralocorticoid receptor blockade reverses obesity-related changes in expression of adiponectin, peroxisome proliferator-activated receptor-gamma, and proinflammatory adipokines. Circulation 117, 2253–2261. https://doi.org/10.1161/CIRCULATIONAHA.107.748640

Hannemann, A., Wallaschofski, H., 2012. Prevalence of primary aldosteronism in patient's cohorts and in population-based studies--a review of the current literature. Horm Metab Res 44, 157–162. https://doi.org/10.1055/s-0031-1295438

Heikkilä, M., Peltoketo, H., Leppäluoto, J., Ilves, M., Vuolteenaho, O., Vainio, S., 2002. Wnt-4 deficiency alters mouse adrenal cortex function, reducing aldosterone production. Endocrinology 143, 4358–4365. https://doi.org/10.1210/en.2002-220275

Hershkovitz, L., Beuschlein, F., Klammer, S., Krup, M., Weinstein, Y., 2007. Adrenal 20α-Hydroxysteroid Dehydrogenase in the Mouse Catabolizes Progesterone and 11-Deoxycorticosterone and Is Restricted to the X-Zone. Endocrinology 148, 976–988. https://doi.org/10.1210/en.2006-1100

Hirata, A., Maeda, N., Hiuge, A., Hibuse, T., Fujita, K., Okada, T., Kihara, S., Funahashi, T., Shimomura, I., 2009. Blockade of mineralocorticoid receptor reverses adipocyte dysfunction and insulin resistance in obese mice. Cardiovasc Res 84, 164–172. https://doi.org/10.1093/cvr/cvp191

Huang, C.-C.J., Miyagawa, S., Matsumaru, D., Parker, K.L., Yao, H.H.-C., 2010. Progenitor cell expansion and organ size of mouse adrenal is regulated by sonic hedgehog. Endocrinology 151, 1119–1128. https://doi.org/10.1210/en.2009-0814

Huang, L., Tepaamorndech, S., 2013. The SLC30 family of zinc transporters - a review of current understanding of their biological and pathophysiological roles. Mol Aspects Med 34, 548–560. https://doi.org/10.1016/j.mam.2012.05.008

Hudson, W.H., Youn, C., Ortlund, E.A., 2014. Crystal structure of the mineralocorticoid receptor DNA binding domain in complex with DNA. PLoS One 9, e107000. https://doi.org/10.1371/journal.pone.0107000

Inoue, K., Naito, T., Fuji, R., Sonehara, K., Yamamoto, K., Baba, R., Kodama, T., Otagaki, Y., Okada, A., Itcho, K., Kobuke, K., Ohno, H., BioBank Japan, Morisaki, T., Hattori, N., Goto, A., Nishikawa, T., Oki, K., Okada, Y., 2024. Primary Aldosteronism and Risk of Cardiovascular Outcomes: Genome-Wide Association and Mendelian Randomization Study. J Am Heart Assoc 13, e034180. https://doi.org/10.1161/JAHA.123.034180

Jeunemaitre, X., Chatellier, G., Kreft-Jais, C., Charru, A., DeVries, C., Plouin, P.F., Corvol, P., Menard, J., 1987. Efficacy and tolerance of spironolactone in essential hypertension. Am J Cardiol 60, 820–825. https://doi.org/10.1016/0002-9149(87)91030-7

Jian, H., Poetsch, A., 2023. CASZ1: Current Implications in Cardiovascular Diseases and Cancers. Biomedicines 11, 2079. https://doi.org/10.3390/biomedicines11072079

Jiménez-Canino, R., Lorenzo-Díaz, F., Odermatt, A., Bailey, M.A., Livingstone, D.E.W., Jaisser, F., Farman, N., Alvarez de la Rosa, D., 2017. 11β-HSD2 SUMOylation Modulates Cortisol-Induced Mineralocorticoid Receptor Nuclear Translocation

Independently of Effects on Transactivation. Endocrinology 158, 4047–4063. https://doi.org/10.1210/en.2017-00440

Joëls, M., Karst, H., DeRijk, R., de Kloet, E.R., 2008. The coming out of the brain mineralocorticoid receptor. Trends Neurosci 31, 1–7. https://doi.org/10.1016/j.tins.2007.10.005

K, N., K, O., Ce, G.-S., Ca, S., Ap, D., M, S., Ldr, T., Dl, C., Jm, L., L, G., A, V., Ja, B., T, E., Tj, G., Sa, T., We, R., 2019. Genetic Characteristics of Aldosterone-Producing Adenomas in Blacks. Hypertension (Dallas, Tex. : 1979) 73. https://doi.org/10.1161/HYPERTENSIONAHA.118.12070

Kagawa, C.M., Cella, J.A., Van Arman, C.G., 1957. Action of new steroids in blocking effects of aldosterone and desoxycorticosterone on salt. Science 126, 1015–1016. https://doi.org/10.1126/science.126.3281.1015

Kang, Y., Laprocina, K., Zheng, H.S., Huang, C.-C.J., 2024. Current insight into the transient X-zone in the adrenal gland cortex. Vitam Horm 124, 297–339. https://doi.org/10.1016/bs.vh.2023.05.003

Kato, N., Takeuchi, F., Tabara, Y., Kelly, T.N., Go, M.J., Sim, X., Tay, W.T., Chen, C.-H., Zhang, Y., Yamamoto, K., Katsuya, T., Yokota, M., Kim, Y.J., Ong, R.T.H., Nabika, T., Gu, D., Chang, L.-C., Kokubo, Y., Huang, W., Ohnaka, K., Yamori, Y., Nakashima, E., Jaquish, C.E., Lee, J.-Y., Seielstad, M., Isono, M., Hixson, J.E., Chen, Y.-T., Miki, T., Zhou, X., Sugiyama, T., Jeon, J.-P., Liu, J.J., Takayanagi, R., Kim, S.S., Aung, T., Sung, Y.J., Zhang, X., Wong, T.Y., Han, B.-G., Kobayashi, S., Ogihara, T., Zhu, D., Iwai, N., Wu, J.-Y., Teo, Y.Y., Tai, E.S., Cho, Y.S., He, J., 2011. Meta-analysis of genome-wide association studies identifies common variants associated with blood pressure variation in east Asians. Nat Genet 43, 531–538. https://doi.org/10.1038/ng.834

Kikuta, A., Murakami, T., 1982. Microcirculation of the rat adrenal gland: a scanning electron microscope study of vascular casts. Am J Anat 164, 19–28. https://doi.org/10.1002/aja.1001640103

Kim, H., Fang, S., 2018. Crosstalk between FXR and TGR5 controls glucagon-like peptide 1 secretion to maintain glycemic homeostasis. Laboratory Animal Research 34, 140. https://doi.org/10.5625/lar.2018.34.4.140

Kim, J.-H., Choi, M.H., 2020. Embryonic Development and Adult Regeneration of the Adrenal Gland. Endocrinol Metab 35, 765–773. https://doi.org/10.3803/EnM.2020.403

Kolkhof, P., Delbeck, M., Kretschmer, A., Steinke, W., Hartmann, E., Bärfacker, L., Eitner, F., Albrecht-Küpper, B., Schäfer, S., 2014. Finerenone, a novel selective nonsteroidal

mineralocorticoid receptor antagonist protects from rat cardiorenal injury. J Cardiovasc Pharmacol 64, 69–78. https://doi.org/10.1097/FJC.0000000000000091

Kornel, L., 1994. Colocalization of 11 beta-hydroxysteroid dehydrogenase and mineralocorticoid receptors in cultured vascular smooth muscle cells. Am J Hypertens 7, 100–103. https://doi.org/10.1093/ajh/7.1.100

Kretz, O., Reichardt, H.M., Schütz, G., Bock, R., 1999. Corticotropin-releasing hormone expression is the major target for glucocorticoid feedback-control at the hypothalamic level. Brain Res 818, 488–491. https://doi.org/10.1016/s0006-8993(98)01277-3

Lavoie, J.L., Sigmund, C.D., 2003. Minireview: Overview of the Renin-Angiotensin System—An Endocrine and Paracrine System. Endocrinology 144, 2179–2183. https://doi.org/10.1210/en.2003-0150

Lawes, C.M.M., Vander Hoorn, S., Rodgers, A., International Society of Hypertension, 2008. Global burden of blood-pressure-related disease, 2001. Lancet 371, 1513–1518. https://doi.org/10.1016/S0140-6736(08)60655-8

Le Billan, F., Amazit, L., Bleakley, K., Xue, Q.-Y., Pussard, E., Lhadj, C., Kolkhof, P., Viengchareun, S., Fagart, J., Lombès, M., 2018. Corticosteroid receptors adopt distinct cyclical transcriptional signatures. FASEB J 32, 5626–5639. https://doi.org/10.1096/fj.201800391RR

Le Billan, F., Khan, J.A., Lamribet, K., Viengchareun, S., Bouligand, J., Fagart, J., Lombès, M., 2015. Cistrome of the aldosterone-activated mineralocorticoid receptor in human renal cells. FASEB J 29, 3977–3989. https://doi.org/10.1096/fj.15-274266

Le Floch, E., Cosentino, T., Larsen, C.K., Beuschlein, F., Reincke, M., Amar, L., Rossi, G.-P., De Sousa, K., Baron, S., Chantalat, S., Saintpierre, B., Lenzini, L., Frouin, A., Giscos-Douriez, I., Ferey, M., Abdellatif, A.B., Meatchi, T., Empana, J.-P., Jouven, X., Gieger, C., Waldenberger, M., Peters, A., Cusi, D., Salvi, E., Meneton, P., Touvier, M., Deschasaux, M., Druesne-Pecollo, N., Boulkroun, S., Fernandes-Rosa, F.L., Deleuze, J.-F., Jeunemaitre, X., Zennaro, M.-C., 2022. Identification of risk loci for primary aldosteronism in genome-wide association studies. Nat Commun 13, 5198. https://doi.org/10.1038/s41467-022-32896-8

Le Menuet, D., Isnard, R., Bichara, M., Viengchareun, S., Muffat-Joly, M., Walker, F., Zennaro, M.C., Lombès, M., 2001. Alteration of cardiac and renal functions in transgenic mice overexpressing human mineralocorticoid receptor. J Biol Chem 276, 38911–38920. https://doi.org/10.1074/jbc.M103984200

Lema, I., Amazit, L., Lamribet, K., Fagart, J., Blanchard, A., Lombès, M., Cherradi, N., Viengchareun, S., 2017. RNA-binding protein HuR enhances mineralocorticoid signaling in renal KC3AC1 cells under hypotonicity. Cell Mol Life Sci 74, 4587–4597. https://doi.org/10.1007/s00018-017-2594-x

Levasseur, A., Dumontet, T., Martinez, A., 2019. "Sexual dimorphism in adrenal gland development and tumorigenesis." Current Opinion in Endocrine and Metabolic Research, Adrenal Cortex 8, 60–65. https://doi.org/10.1016/j.coemr.2019.07.008

Levy, D., Ehret, G.B., Rice, K., Verwoert, G.C., Launer, L.J., Dehghan, A., Glazer, N.L., Morrison, A.C., Johnson, A.D., Aspelund, T., Aulchenko, Y., Lumley, T., Köttgen, A., Vasan, R.S., Rivadeneira, F., Eiriksdottir, G., Guo, X., Arking, D.E., Mitchell, G.F., Mattace-Raso, F.U.S., Smith, A.V., Taylor, K., Scharpf, R.B., Hwang, S.-J., Sijbrands, E.J.G., Bis, J., Harris, T.B., Ganesh, S.K., O'Donnell, C.J., Hofman, A., Rotter, J.I., Coresh, J., Benjamin, E.J., Uitterlinden, A.G., Heiss, G., Fox, C.S., Witteman, J.C.M., Boerwinkle, E., Wang, T.J., Gudnason, V., Larson, M.G., Chakravarti, A., Psaty, B.M., van Duijn, C.M., 2009. Genome-wide association study of blood pressure and hypertension. Nat Genet 41, 677–687. https://doi.org/10.1038/ng.384

Liang, X., Peters, K.W., Butterworth, M.B., Frizzell, R.A., 2006. 14-3-3 isoforms are induced by aldosterone and participate in its regulation of epithelial sodium channels. J Biol Chem 281, 16323–16332. https://doi.org/10.1074/jbc.M601360200

Lifton, R.P., Dluhy, R.G., Powers, M., Rich, G.M., Cook, S., Ulick, S., Lalouel, J.M., 1992. A chimaeric 11 beta-hydroxylase/aldosterone synthase gene causes glucocorticoid-remediable aldosteronism and human hypertension. Nature 355, 262–265. https://doi.org/10.1038/355262a0

Liu, Z., Li, W., Ma, X., Ding, N., Spallotta, F., Southon, E., Tessarollo, L., Gaetano, C., Mukouyama, Y.-S., Thiele, C.J., 2014. Essential role of the zinc finger transcription factor Casz1 for mammalian cardiac morphogenesis and development. J Biol Chem 289, 29801–29816. https://doi.org/10.1074/jbc.M114.570416

Liu, Z., Rader, J., He, S., Phung, T., Thiele, C.J., 2013. CASZ1 inhibits cell cycle progression in neuroblastoma by restoring pRb activity. Cell Cycle 12, 2210–2218. https://doi.org/10.4161/cc.25265

Liu, Z., Yang, X., Li, Z., McMahon, C., Sizer, C., Barenboim-Stapleton, L., Bliskovsky, V., Mock, B., Ried, T., London, W.B., Maris, J., Khan, J., Thiele, C.J., 2011. CASZ1, a candidate tumor-suppressor gene, suppresses neuroblastoma tumor growth through

reprogramming gene expression. Cell Death Differ 18, 1174–1183. https://doi.org/10.1038/cdd.2010.187

Liu, Z., Yang, X., Tan, F., Cullion, K., Thiele, C.J., 2006. Molecular cloning and characterization of human Castor, a novel human gene upregulated during cell differentiation. Biochem Biophys Res Commun 344, 834–844. https://doi.org/10.1016/j.bbrc.2006.03.207

Lyraki, R., Schedl, A., 2021a. Adrenal cortex renewal in health and disease. Nat Rev Endocrinol 17, 421–434. https://doi.org/10.1038/s41574-021-00491-4

Lyraki, R., Schedl, A., 2021b. Adrenal cortex renewal in health and disease. Nat Rev Endocrinol 17, 421–434. https://doi.org/10.1038/s41574-021-00491-4

Lyraki, R., Schedl, A., 2021c. The Sexually Dimorphic Adrenal Cortex: Implications for Adrenal Disease. Int J Mol Sci 22, 4889. https://doi.org/10.3390/ijms22094889

MacKenzie, S.M., Birch, L.A., Lamprou, S., Rezvanisanijouybari, P., Fayad, M., Zennaro, M.-C., Davies, E., 2024. MicroRNAs in aldosterone production and action. Vitam Horm 124, 137–163. https://doi.org/10.1016/bs.vh.2023.07.001

Maharjan, R., Backman, S., Åkerström, T., Hellman, P., Björklund, P., 2018. Comprehensive analysis of CTNNB1 in adrenocortical carcinomas: Identification of novel mutations and correlation to survival. Sci Rep 8, 8610. https://doi.org/10.1038/s41598-018-26799-2

Mangelsdorf, D.J., Thummel, C., Beato, M., Herrlich, P., Schütz, G., Umesono, K., Blumberg, B., Kastner, P., Mark, M., Chambon, P., Evans, R.M., 1995. The Nuclear Receptor Superfamily: The Second Decade. Cell 83, 835–839. https://doi.org/10.1016/0092-8674(95)90199-x

Mayr, B., Montminy, M., 2001. Transcriptional regulation by the phosphorylation-dependent factor CREB. Nat Rev Mol Cell Biol 2, 599–609. https://doi.org/10.1038/35085068

McEvoy, J.W., McCarthy, C.P., Bruno, R.M., Brouwers, S., Canavan, M.D., Ceconi, C., Christodorescu, R.M., Daskalopoulou, S.S., Ferro, C.J., Gerdts, E., Hanssen, H., Harris, J., Lauder, L., McManus, R.J., Molloy, G.J., Rahimi, K., Regitz-Zagrosek, V., Rossi, G.P., Sandset, E.C., Scheenaerts, B., Staessen, J.A., Uchmanowicz, I., Volterrani, M., Touyz, R.M., ESC Scientific Document Group, 2024. 2024 ESC Guidelines for the management of elevated blood pressure and hypertension. Eur Heart J 45, 3912–4018. https://doi.org/10.1093/eurheartj/ehae178

McEwen, B.S., Weiss, J.M., Schwartz, L.S., 1968. Selective retention of corticosterone by limbic structures in rat brain. Nature 220, 911–912. https://doi.org/10.1038/220911a0

Megha, R., Wehrle, C.J., Kashyap, S., Leslie, S.W., 2025. Anatomy, Abdomen and Pelvis: Adrenal Glands (Suprarenal Glands), in: StatPearls. StatPearls Publishing, Treasure Island (FL).

Missaghian, E., Kempná, P., Dick, B., Hirsch, A., Alikhani-Koupaei, R., Jégou, B., Mullis, P.E., Frey, B.M., Flück, C.E., 2009. Role of DNA methylation in the tissue-specific expression of the CYP17A1 gene for steroidogenesis in rodents. https://doi.org/10.1677/JOE-08-0353

Mitchell, G.F., Rong, J., Larson, M.G., Korzinski, T.J., Xanthakis, V., Sigurdsson, S., Gudnason, V., Launer, L.J., Aspelund, T., Hamburg, N.M., Gotal, J.D., Vasan, R.S., 2024. Vascular Age Assessed From an Uncalibrated, Noninvasive Pressure Waveform by Using a Deep Learning Approach: The AI-VascularAge Model. Hypertension 81, 193–201. https://doi.org/10.1161/HYPERTENSIONAHA.123.21638

Monticone, Silvia, Burrello, J., Tizzani, D., Bertello, C., Viola, A., Buffolo, F., Gabetti, L., Mengozzi, G., Williams, T.A., Rabbia, F., Veglio, F., Mulatero, P., 2017. Prevalence and Clinical Manifestations of Primary Aldosteronism Encountered in Primary Care Practice. J Am Coll Cardiol 69, 1811–1820. https://doi.org/10.1016/j.jacc.2017.01.052

Monticone, S., D'Ascenzo, F., Moretti, C., Williams, T.A., Veglio, F., Gaita, F., Mulatero, P., 2018. Cardiovascular events and target organ damage in primary aldosteronism compared with essential hypertension: a systematic review and meta-analysis. Lancet Diabetes Endocrinol 6, 41–50. https://doi.org/10.1016/S2213-8587(17)30319-4

Monticone, S., Tetti, M., Burrello, J., Buffolo, F., De Giovanni, R., Veglio, F., Williams, T.A., Mulatero, P., 2017. Familial hyperaldosteronism type III. J Hum Hypertens 31, 776–781. https://doi.org/10.1038/jhh.2017.34

Mulatero, P., Monticone, S., Rainey, W.E., Veglio, F., Williams, T.A., 2013. Role of KCNJ5 in familial and sporadic primary aldosteronism. Nat Rev Endocrinol 9, 104–112. https://doi.org/10.1038/nrendo.2012.230

Mulatero, P., Tauber, P., Zennaro, M.-C., Monticone, S., Lang, K., Beuschlein, F., Fischer, E., Tizzani, D., Pallauf, A., Viola, A., Amar, L., Williams, T.A., Strom, T.M., Graf, E., Bandulik, S., Penton, D., Plouin, P.-F., Warth, R., Allolio, B., Jeunemaitre, X., Veglio, F., Reincke, M., 2012. KCNJ5 mutations in European families with nonglucocorticoid remediable familial hyperaldosteronism. Hypertension 59, 235–240. https://doi.org/10.1161/HYPERTENSIONAHA.111.183996

Muller, O.G., Parnova, R.G., Centeno, G., Rossier, B.C., Firsov, D., Horisberger, J.-D., 2003. Mineralocorticoid effects in the kidney: correlation between alphaENaC, GILZ, and Sgk-1 mRNA expression and urinary excretion of Na+ and K+. J Am Soc Nephrol 14, 1107–1115. https://doi.org/10.1097/01.asn.0000061777.67332.77

Naito, T., Inoue, K., Sonehara, K., Baba, R., Kodama, T., Otagaki, Y., Okada, A., Itcho, K., Kobuke, K., Kishimoto, S., Yamamoto, K., BioBank Japan, Morisaki, T., Higashi, Y., Hinata, N., Arihiro, K., Hattori, N., Okada, Y., Oki, K., 2023. Genetic Risk of Primary Aldosteronism and Its Contribution to Hypertension: A Cross-Ancestry Meta-Analysis of Genome-Wide Association Studies. Circulation 147, 1097–1109. https://doi.org/10.1161/CIRCULATIONAHA.122.062349

Nanba, K., Omata, K., Else, T., Beck, P.C.C., Nanba, A.T., Turcu, A.F., Miller, B.S., Giordano, T.J., Tomlins, S.A., Rainey, W.E., 2018. Targeted Molecular Characterization of Aldosterone-Producing Adenomas in White Americans. J Clin Endocrinol Metab 103, 3869–3876. https://doi.org/10.1210/jc.2018-01004

NCD Risk Factor Collaboration (NCD-RisC), 2017. Worldwide trends in blood pressure from 1975 to 2015: a pooled analysis of 1479 population-based measurement studies with 19·1 million participants. Lancet 389, 37–55. https://doi.org/10.1016/S0140-6736(16)31919-5

Nishimoto, K., Tomlins, S.A., Kuick, R., Cani, A.K., Giordano, T.J., Hovelson, D.H., Liu, C.-J., Sanjanwala, A.R., Edwards, M.A., Gomez-Sanchez, C.E., Nanba, K., Rainey, W.E., 2015. Aldosterone-stimulating somatic gene mutations are common in normal adrenal glands. Proc Natl Acad Sci U S A 112, E4591-4599. https://doi.org/10.1073/pnas.1505529112

Nonaka, K., Aida, J., Takubo, K., Yamazaki, Y., Gao, X., Komatsu, A., Takakuma, S., Kakizaki, M., Inoshita, N., Gomi, F., Ishiwata, T., Chong, J.-M., Arai, T., Sasano, H., 2020. Correlation Between Telomere Attrition of Zona Fasciculata and Adrenal Weight Reduction in Older Men. J Clin Endocrinol Metab 105, dgz214. https://doi.org/10.1210/clinem/dgz214

Nuclear Receptors Nomenclature Committee, 1999. A unified nomenclature system for the nuclear receptor superfamily. Cell 97, 161–163. https://doi.org/10.1016/s0092-8674(00)80726-6

Nusse, R., Clevers, H., 2017. Wnt/β-Catenin Signaling, Disease, and Emerging Therapeutic Modalities. Cell 169, 985–999. https://doi.org/10.1016/j.cell.2017.05.016

Oitzl, M.S., de Kloet, E.R., 1992. Selective corticosteroid antagonists modulate specific aspects of spatial orientation learning. Behav Neurosci 106, 62–71. https://doi.org/10.1037//0735-7044.106.1.62

Overdiek, H.W., Merkus, F.W., 1987. The metabolism and biopharmaceutics of spironolactone in man. Rev Drug Metab Drug Interact 5, 273–302. https://doi.org/10.1515/dmdi.1987.5.4.273

Parker, T.L., Kesse, W.K., Mohamed, A.A., Afework, M., 1993. The innervation of the mammalian adrenal gland. J Anat 183, 265–276.

Pascual-Le Tallec, L., Lombès, M., 2005. The mineralocorticoid receptor: a journey exploring its diversity and specificity of action. Mol Endocrinol 19, 2211–2221. https://doi.org/10.1210/me.2005-0089

Pearce, D., Bhargava, A., Cole, T.J., 2003. Aldosterone: Its Receptor, Target Genes, and Actions, in: Vitamins & Hormones. Academic Press, pp. 29–76. https://doi.org/10.1016/S0083-6729(03)01002-1

Pignatti, E., du Toit, T., Flück, C.E., 2023. Development and function of the fetal adrenal. Rev Endocr Metab Disord 24, 5–21. https://doi.org/10.1007/s11154-022-09756-3

Pignatti, E., Flück, C.E., 2021. Adrenal cortex development and related disorders leading to adrenal insufficiency. Mol Cell Endocrinol 527, 111206. https://doi.org/10.1016/j.mce.2021.111206

Pignatti, E., Leng, S., Yuchi, Y., Borges, K.S., Guagliardo, N.A., Shah, M.S., Ruiz-Babot, G., Kariyawasam, D., Taketo, M.M., Miao, J., Barrett, P.Q., Carlone, D.L., Breault, D.T., 2020. Beta-Catenin Causes Adrenal Hyperplasia by Blocking Zonal Transdifferentiation. Cell Rep 31, 107524. https://doi.org/10.1016/j.celrep.2020.107524

Pihlajoki, M., Dörner, J., Cochran, R.S., Heikinheimo, M., Wilson, D.B., 2015. Adrenocortical zonation, renewal, and remodeling. Front Endocrinol (Lausanne) 6, 27. https://doi.org/10.3389/fendo.2015.00027

Pinggera, A., Striessnig, J., 2016. Cav 1.3 (CACNA1D) L-type Ca2+ channel dysfunction in CNS disorders. J Physiol 594, 5839–5849. https://doi.org/10.1113/JP270672

Pitsava, G., Maria, A.G., Faucz, F.R., 2022. Disorders of the adrenal cortex: Genetic and molecular aspects. Front. Endocrinol. 13. https://doi.org/10.3389/fendo.2022.931389

Pitt, B., Kober, L., Ponikowski, P., Gheorghiade, M., Filippatos, G., Krum, H., Nowack, C., Kolkhof, P., Kim, S.-Y., Zannad, F., 2013. Safety and tolerability of the novel non-steroidal mineralocorticoid receptor antagonist BAY 94-8862 in patients with chronic

heart failure and mild or moderate chronic kidney disease: a randomized, double-blind trial. Eur Heart J 34, 2453–2463. https://doi.org/10.1093/eurheartj/eht187

Pitt, B., Remme, W., Zannad, F., Neaton, J., Martinez, F., Roniker, B., Bittman, R., Hurley, S., Kleiman, J., Gatlin, M., Eplerenone Post-Acute Myocardial Infarction Heart Failure Efficacy and Survival Study Investigators, 2003. Eplerenone, a selective aldosterone blocker, in patients with left ventricular dysfunction after myocardial infarction. N Engl J Med 348, 1309–1321. https://doi.org/10.1056/NEJMoa030207

Pitt, B., Zannad, F., Remme, W.J., Cody, R., Castaigne, A., Perez, A., Palensky, J., Wittes, J., 1999. The effect of spironolactone on morbidity and mortality in patients with severe heart failure. Randomized Aldactone Evaluation Study Investigators. N Engl J Med 341, 709–717. https://doi.org/10.1056/NEJM199909023411001

Prada, E.T.A., Burrello, J., Reincke, M., Williams, T.A., 2017. Old and New Concepts in the Molecular Pathogenesis of Primary Aldosteronism. Hypertension 70, 875–881. https://doi.org/10.1161/HYPERTENSIONAHA.117.10111

Qin, W., Rudolph, A.E., Bond, B.R., Rocha, R., Blomme, E.A.G., Goellner, J.J., Funder, J.W., McMahon, E.G., 2003. Transgenic model of aldosterone-driven cardiac hypertrophy and heart failure. Circ Res 93, 69–76. https://doi.org/10.1161/01.RES.0000080521.15238.E5

Rao, T.P., Kühl, M., 2010. An updated overview on Wnt signaling pathways: a prelude for more. Circ Res 106, 1798–1806. https://doi.org/10.1161/CIRCRESAHA.110.219840

Rege, J., Bandulik, S., Nanba, K., Kosmann, C., Blinder, A.R., Plain, A., Vats, P., Kumar-Sinha, C., Lerario, A.M., Else, T., Yamazaki, Y., Satoh, F., Sasano, H., Giordano, T.J., Williams, T.A., Reincke, M., Turcu, A.F., Udager, A.M., Warth, R., Rainey, W.E., 2023. Somatic SLC30A1 mutations altering zinc transporter ZnT1 cause aldosterone-producing adenomas and primary aldosteronism. Nat Genet 55, 1623–1631. https://doi.org/10.1038/s41588-023-01498-5

Reul, J.M., de Kloet, E.R., 1985. Two receptor systems for corticosterone in rat brain: microdistribution and differential occupation. Endocrinology 117, 2505–2511. https://doi.org/10.1210/endo-117-6-2505

Rickard, A.J., Morgan, J., Tesch, G., Funder, J.W., Fuller, P.J., Young, M.J., 2009. Deletion of mineralocorticoid receptors from macrophages protects against deoxycorticosterone/salt-induced cardiac fibrosis and increased blood pressure. Hypertension 54, 537–543. https://doi.org/10.1161/HYPERTENSIONAHA.109.131110

Rim, E.Y., Clevers, H., Nusse, R., 2022. The Wnt Pathway: From Signaling Mechanisms to Synthetic Modulators. Annu Rev Biochem 91, 571–598. https://doi.org/10.1146/annurev-biochem-040320-103615

Rocha, R., Stier, C.T., Kifor, I., Ochoa-Maya, M.R., Rennke, H.G., Williams, G.H., Adler, G.K., 2000. Aldosterone: a mediator of myocardial necrosis and renal arteriopathy. Endocrinology 141, 3871–3878. https://doi.org/10.1210/endo.141.10.7711

Ruggiero, C., Lalli, E., 2016. Impact of ACTH Signaling on Transcriptional Regulation of Steroidogenic Genes. Front Endocrinol (Lausanne) 7, 24. https://doi.org/10.3389/fendo.2016.00024

Ruhs, S., Nolze, A., Hübschmann, R., Grossmann, C., 2017. 30 YEARS OF THE MINERALOCORTICOID RECEPTOR: Nongenomic effects via the mineralocorticoid receptor. J Endocrinol 234, T107–T124. https://doi.org/10.1530/JOE-16-0659

Sahut-Barnola, I., de Joussineau, C., Val, P., Lambert-Langlais, S., Damon, C., Lefrançois-Martinez, A.-M., Pointud, J.-C., Marceau, G., Sapin, V., Tissier, F., Ragazzon, B., Bertherat, J., Kirschner, L.S., Stratakis, C.A., Martinez, A., 2010. Cushing's syndrome and fetal features resurgence in adrenal cortex-specific Prkar1a knockout mice. PLoS Genet 6, e1000980. https://doi.org/10.1371/journal.pgen.1000980

Schäfer, N., Lohmann, C., Winnik, S., van Tits, L.J., Miranda, M.X., Vergopoulos, A., Ruschitzka, F., Nussberger, J., Berger, S., Lüscher, T.F., Verrey, F., Matter, C.M., 2013. Endothelial mineralocorticoid receptor activation mediates endothelial dysfunction in diet-induced obesity. Eur Heart J 34, 3515–3524. https://doi.org/10.1093/eurheartj/eht095

Schimmer, B.P., White, P.C., 2010. Minireview: Steroidogenic Factor 1: Its Roles in Differentiation, Development, and Disease. Molecular Endocrinology 24, 1322–1337. https://doi.org/10.1210/me.2009-0519

Scholl, U.I., 2022. Genetics of Primary Aldosteronism. Hypertension 79, 887–897. https://doi.org/10.1161/HYPERTENSIONAHA.121.16498

Scholl, U.I., Goh, G., Stölting, G., de Oliveira, R.C., Choi, M., Overton, J.D., Fonseca, A.L., Korah, R., Starker, L.F., Kunstman, J.W., Prasad, M.L., Hartung, E.A., Mauras, N., Benson, M.R., Brady, T., Shapiro, J.R., Loring, E., Nelson-Williams, C., Libutti, S.K., Mane, S., Hellman, P., Westin, G., Åkerström, G., Björklund, P., Carling, T., Fahlke, C., Hidalgo, P., Lifton, R.P., 2013. Somatic and germline CACNA1D calcium channel mutations in aldosterone-producing adenomas and primary aldosteronism. Nat Genet 45, 1050–1054. https://doi.org/10.1038/ng.2695

Scholl, U.I., Nelson-Williams, C., Yue, P., Grekin, R., Wyatt, R.J., Dillon, M.J., Couch, R., Hammer, L.K., Harley, F.L., Farhi, A., Wang, W.-H., Lifton, R.P., 2012. Hypertension with or without adrenal hyperplasia due to different inherited mutations in the potassium channel KCNJ5. Proc Natl Acad Sci U S A 109, 2533–2538. https://doi.org/10.1073/pnas.1121407109

Scholl, U.I., Stölting, G., Nelson-Williams, C., Vichot, A.A., Choi, M., Loring, E., Prasad, M.L., Goh, G., Carling, T., Juhlin, C.C., Quack, I., Rump, L.C., Thiel, A., Lande, M., Frazier, B.G., Rasoulpour, M., Bowlin, D.L., Sethna, C.B., Trachtman, H., Fahlke, C., Lifton, R.P., 2015. Recurrent gain of function mutation in calcium channel CACNA1H causes early-onset hypertension with primary aldosteronism. Elife 4, e06315. https://doi.org/10.7554/eLife.06315

Scholl, U.I., Stölting, G., Schewe, J., Thiel, A., Tan, H., Nelson-Williams, C., Vichot, A.A., Jin, S.C., Loring, E., Untiet, V., Yoo, T., Choi, J., Xu, S., Wu, A., Kirchner, M., Mertins, P., Rump, L.C., Onder, A.M., Gamble, C., McKenney, D., Lash, R.W., Jones, D.P., Chune, G., Gagliardi, P., Choi, M., Gordon, R., Stowasser, M., Fahlke, C., Lifton, R.P., 2018. CLCN2 chloride channel mutations in familial hyperaldosteronism type II. Nat Genet 50, 349–354. https://doi.org/10.1038/s41588-018-0048-5

Shibata, S., Rinehart, J., Zhang, J., Moeckel, G., Castañeda-Bueno, M., Stiegler, A.L., Boggon, T.J., Gamba, G., Lifton, R.P., 2013. Mineralocorticoid receptor phosphorylation regulates ligand binding and renal response to volume depletion and hyperkalemia. Cell Metab 18, 660–671. https://doi.org/10.1016/j.cmet.2013.10.005

Shironomae, T., Yamazaki, Y., Takeyama, J., Sakai, K., Sasano, H., Suzuki, T., 2024. Development of aldosterone biosynthesis during fetal and pediatric periods; Histological analysis of CYP11B2-positive cell distribution in the zona glomerulosa of human adrenal. The Journal of Steroid Biochemistry and Molecular Biology 244, 106593. https://doi.org/10.1016/j.jsbmb.2024.106593

Sierra-Ramos, C., Velazquez-Garcia, S., Keskus, A.G., Vastola-Mascolo, A., Rodríguez-Rodríguez, A.E., Luis-Lima, S., Hernández, G., Navarro-González, J.F., Porrini, E., Konu, O., Alvarez de la Rosa, D., 2021. Increased SGK1 activity potentiates mineralocorticoid/NaCl-induced kidney injury. Am J Physiol Renal Physiol 320, F628–F643. https://doi.org/10.1152/ajprenal.00505.2020

Slusarski, D.C., Yang-Snyder, J., Busa, W.B., Moon, R.T., 1997. Modulation of embryonic intracellular Ca2+ signaling by Wnt-5A. Dev Biol 182, 114–120. https://doi.org/10.1006/dbio.1996.8463

Son, G.H., Chung, S., Kim, K., 2011. The adrenal peripheral clock: glucocorticoid and the circadian timing system. Front Neuroendocrinol 32, 451–465. https://doi.org/10.1016/j.yfrne.2011.07.003

Soundararajan, R., Pearce, D., Hughey, R.P., Kleyman, T.R., 2010. Role of epithelial sodium channels and their regulators in hypertension. J Biol Chem 285, 30363–30369. https://doi.org/10.1074/jbc.R110.155341

Spät, A., Hunyady, L., 2004. Control of aldosterone secretion: a model for convergence in cellular signaling pathways. Physiol Rev 84, 489–539. https://doi.org/10.1152/physrev.00030.2003

Staub, O., Rotin, D., 2006. Role of ubiquitylation in cellular membrane transport. Physiol Rev 86, 669–707. https://doi.org/10.1152/physrev.00020.2005

Stindl, J., Tauber, P., Sterner, C., Tegtmeier, I., Warth, R., Bandulik, S., 2015. Pathogenesis of Adrenal Aldosterone-Producing Adenomas Carrying Mutations of the Na(+)/K(+)-ATPase. Endocrinology 156, 4582–4591. https://doi.org/10.1210/en.2015-1466

Stowasser, M., Bachmann, A.W., Huggard, P.R., Rossetti, T.R., Gordon, R.D., 2000. Treatment of Familial Hyperaldosteronism Type I: Only Partial Suppression of Adrenocorticotropin Required to Correct Hypertension. The Journal of Clinical Endocrinology & Metabolism 85, 3313–3318. https://doi.org/10.1210/jcem.85.9.6834

Stowasser, M., Gordon, R.D., Tunny, T.J., Klemm, S.A., Finn, W.L., Krek, A.L., 1992. Familial Hyperaldosteronism Type Ii: Five Families with a New Variety of Primary Aldosteronism. Clinical and Experimental Pharmacology and Physiology 19, 319–322. https://doi.org/10.1111/j.1440-1681.1992.tb00462.x

Sutherland, D.J., Ruse, J.L., Laidlaw, J.C., 1966. Hypertension, increased aldosterone secretion and low plasma renin activity relieved by dexamethasone. Can Med Assoc J 95, 1109–1119.

Tai, Y., Shang, J., 2023. Wnt/β-catenin signaling pathway in the tumor progression of adrenocortical carcinoma. Front Endocrinol (Lausanne) 14, 1260701. https://doi.org/10.3389/fendo.2023.1260701

Tauber, P., Aichinger, B., Christ, C., Stindl, J., Rhayem, Y., Beuschlein, F., Warth, R., Bandulik, S., 2016. Cellular Pathophysiology of an Adrenal Adenoma-Associated Mutant of the Plasma Membrane Ca(2+)-ATPase ATP2B3. Endocrinology 157, 2489–2499. https://doi.org/10.1210/en.2015-2029

Tiganescu, A., Tahrani, A.A., Morgan, S.A., Otranto, M., Desmoulière, A., Abrahams, L., Hassan-Smith, Z., Walker, E.A., Rabbitt, E.H., Cooper, M.S., Amrein, K., Lavery, G.G.,

Stewart, P.M., 2013. 11β-Hydroxysteroid dehydrogenase blockade prevents age-induced skin structure and function defects. J Clin Invest 123, 3051–3060. https://doi.org/10.1172/JCI64162

Umesono, K., Evans, R.M., 1989. Determinants of target gene specificity for steroid/thyroid hormone receptors. Cell 57, 1139–1146. https://doi.org/10.1016/0092-8674(89)90051-2

Unger, T., Borghi, C., Charchar, F., Khan, N.A., Poulter, N.R., Prabhakaran, D., Ramirez, A., Schlaich, M., Stergiou, G.S., Tomaszewski, M., Wainford, R.D., Williams, B., Schutte, A.E., 2020. 2020 International Society of Hypertension Global Hypertension Practice Guidelines. Hypertension 75, 1334–1357. https://doi.org/10.1161/HYPERTENSIONAHA.120.15026

Urbanet, R., Nguyen Dinh Cat, A., Feraco, A., Venteclef, N., El Mogrhabi, S., Sierra-Ramos, C., Alvarez de la Rosa, D., Adler, G.K., Quilliot, D., Rossignol, P., Fallo, F., Touyz, R.M., Jaisser, F., 2015. Adipocyte Mineralocorticoid Receptor Activation Leads to Metabolic Syndrome and Induction of Prostaglandin D2 Synthase. Hypertension 66, 149–157. https://doi.org/10.1161/HYPERTENSIONAHA.114.04981

van der Heijden, C.D.C.C., Ter Horst, R., van den Munckhof, I.C.L., Schraa, K., de Graaf, J., Joosten, L.A.B., Danser, A.H.J., Netea, M.G., Deinum, J., Rutten, J., Riksen, N.P., 2020. Vasculometabolic and Inflammatory Effects of Aldosterone in Obesity. J Clin Endocrinol Metab 105, 2719–2731. https://doi.org/10.1210/clinem/dgaa356

van Leeuwen, N., Bellingrath, S., de Kloet, E.R., Zitman, F.G., DeRijk, R.H., Kudielka, B.M., Wüst, S., 2011. Human mineralocorticoid receptor (MR) gene haplotypes modulate MR expression and transactivation: implication for the stress response. Psychoneuroendocrinology 36, 699–709. https://doi.org/10.1016/j.psyneuen.2010.10.003

van Rooyen, D., Bandulik, S., Coon, G.A., Laukemper, M., Kumar-Sinha, C., Udager, A.M., Lerario, A.M., Lee, C., Wachtel, H., Cohen, D.L., Luther, J.M., Giordano, T.J., Scholl, U.I., Butz, F., Popp, B., Turcu, A.F., Warth, R., Rainey, W.E., Rege, J., 2025. Somatic Mutations in MCOLN3 Are Associated With Aldosterone-Producing Adenomas. Hypertension 82, 1778–1788. https://doi.org/10.1161/HYPERTENSIONAHA.125.24909

Vardeny, O., Wu, D.H., Desai, A., Rossignol, P., Zannad, F., Pitt, B., Solomon, S.D., RALES Investigators, 2012. Influence of baseline and worsening renal function on efficacy of spironolactone in patients With severe heart failure: insights from RALES

(Randomized Aldactone Evaluation Study). J Am Coll Cardiol 60, 2082–2089. https://doi.org/10.1016/j.jacc.2012.07.048

Vidal, V., Sacco, S., Rocha, A.S., da Silva, F., Panzolini, C., Dumontet, T., Doan, T.M.P., Shan, J., Rak-Raszewska, A., Bird, T., Vainio, S., Martinez, A., Schedl, A., 2016. The adrenal capsule is a signaling center controlling cell renewal and zonation through Rspo3. Genes Dev 30, 1389–1394. https://doi.org/10.1101/gad.277756.116

Viengchareun, S., Le Menuet, D., Martinerie, L., Munier, M., Pascual-Le Tallec, L., Lombès, M., 2007. The mineralocorticoid receptor: insights into its molecular and (patho)physiological biology. Nucl Recept Signal 5, e012. https://doi.org/10.1621/nrs.05012

Viengchareun, S., Lema, I., Lamribet, K., Keo, V., Blanchard, A., Cherradi, N., Lombès, M., 2014. Hypertonicity Compromises Renal Mineralocorticoid Receptor Signaling through Tis11b-Mediated Post-Transcriptional Control. J Am Soc Nephrol 25, 2213–2221. https://doi.org/10.1681/ASN.2013091023

Vu, T.A., Lema, I., Hani, I., Cheval, L., Atger-Lallier, L., Souvannarath, V., Perrot, J., Souvanheuane, M., Marie, Y., Fabrega, S., Blanchard, A., Bouligand, J., Kamenický, P., Crambert, G., Martinerie, L., Lombès, M., Viengchareun, S., 2022. miR-324-5p and miR-30c-2-3p Alter Renal Mineralocorticoid Receptor Signaling under Hypertonicity. Cells 11, 1377. https://doi.org/10.3390/cells11091377

Weikum, E.R., Liu, X., Ortlund, E.A., 2018. The nuclear receptor superfamily: A structural perspective. Protein Sci 27, 1876–1892. https://doi.org/10.1002/pro.3496

Wright, N., Burns, B., 2025. Anatomy, Abdomen and Pelvis, Posterior Abdominal Wall Arteries, in: StatPearls. StatPearls Publishing, Treasure Island (FL).

Wu, C.-H., Peng, K.-Y., Hwang, D.-Y., Lin, Y.-H., Wu, V.-C., Chueh, J.S., 2021. Novel Mutations Detection with Next-Generation Sequencing and Its Association with Clinical Outcome in Unilateral Primary Aldosteronism. Biomedicines 9, 1167. https://doi.org/10.3390/biomedicines9091167

Wu, V.-C., Wang, S.-M., Chueh, S.-C.J., Yang, S.-Y., Huang, K.-H., Lin, Y.-H., Wang, J.-J., Connolly, R., Hu, Y.-H., Gomez-Sanchez, C.E., Peng, K.-Y., Wu, K.-D., 2017. The prevalence of CTNNB1 mutations in primary aldosteronism and consequences for clinical outcomes. Sci Rep 7, 39121. https://doi.org/10.1038/srep39121

Wu, X., Azizan, E.A.B., Goodchild, E., Garg, S., Hagiyama, M., Cabrera, C.P., Fernandes-Rosa, F.L., Boulkroun, S., Kuan, J.L., Tiang, Z., David, A., Murakami, M., Mein, C.A., Wozniak, E., Zhao, W., Marker, A., Buss, F., Saleeb, R.S., Salsbury, J., Tezuka, Y.,

Satoh, F., Oki, K., Udager, A.M., Cohen, D.L., Wachtel, H., King, P.J., Drake, W.M., Gurnell, M., Ceral, J., Ryska, A., Mustangin, M., Wong, Y.P., Tan, G.C., Solar, M., Reincke, M., Rainey, W.E., Foo, R.S., Takaoka, Y., Murray, S.A., Zennaro, M.-C., Beuschlein, F., Ito, A., Brown, M.J., 2023. Somatic mutations of CADM1 in aldosterone-producing adenomas and gap junction-dependent regulation of aldosterone production. Nat Genet 55, 1009–1021. https://doi.org/10.1038/s41588-023-01403-0

Wu, Y.-Y., Chang, C.-L., Chuang, Y.-J., Wu, J.-E., Tung, C.-H., Chen, Y.-C., Chen, Y.-L., Hong, T.-M., Hsu, K.-F., 2016. CASZ1 is a novel promoter of metastasis in ovarian cancer. Am J Cancer Res 6, 1253–1270.

Yamaguchi, H., Gomez, R.A., Sequeira-Lopez, M.L.S., 2023. Renin Cells, From Vascular Development to Blood Pressure Sensing. Hypertension 80, 1580–1589. https://doi.org/10.1161/HYPERTENSIONAHA.123.20577

Yang, J., Young, M.J., 2009. The mineralocorticoid receptor and its coregulators. https://doi.org/10.1677/JME-09-0031

Yang, J., Young, M.J., Cole, T.J., Fuller, P.J., 2023. Mineralocorticoid receptor signalling in primary aldosteronism. J Endocrinol 259, e220249. https://doi.org/10.1530/JOE-22-0249

Yates, R., Katugampola, H., Cavlan, D., Cogger, K., Meimaridou, E., Hughes, C., Metherell, L., Guasti, L., King, P., 2013. Adrenocortical development, maintenance, and disease. Curr Top Dev Biol 106, 239–312. https://doi.org/10.1016/B978-0-12-416021-7.00007-9

Yokota, K., Shibata, H., Kurihara, I., Itoh, H., Sone, M., 2023. CASZ1: a promising factor modulating aldosterone biosynthesis and mineralocorticoid receptor activity. Hypertens Res 46, 417–420. https://doi.org/10.1038/s41440-022-01131-8

Yokota, K., Shibata, H., Kurihara, I., Kobayashi, S., Murai-Takeda, A., Itoh, H., 2021. CASZ1b is a novel transcriptional corepressor of mineralocorticoid receptor. Hypertens Res 44, 407–416. https://doi.org/10.1038/s41440-020-00562-5

Yuzugullu, H., Benhaj, K., Ozturk, N., Senturk, S., Celik, E., Toylu, A., Tasdemir, N., Yilmaz, M., Erdal, E., Akcali, K.C., Atabey, N., Ozturk, M., 2009. Canonical Wnt signaling is antagonized by noncanonical Wnt5a in hepatocellular carcinoma cells. Mol Cancer 8, 90. https://doi.org/10.1186/1476-4598-8-90

Zennaro, M.-C., Boulkroun, S., Fernandes-Rosa, F.L., 2020. Pathogenesis and treatment of primary aldosteronism. Nat Rev Endocrinol 16, 578–589. https://doi.org/10.1038/s41574-020-0382-4

Zennaro, M.-C., Caprio, M., Fève, B., 2009. Mineralocorticoid receptors in the metabolic syndrome. Trends Endocrinol Metab 20, 444–451. https://doi.org/10.1016/j.tem.2009.05.006

Zennaro, M.-C., Fernandes-Rosa, F.L., Boulkroun, S., 2018. Overview of aldosterone-related genetic syndromes and recent advances. Curr Opin Endocrinol Diabetes Obes 25, 147–154. https://doi.org/10.1097/MED.0000000000000409

Zennaro, M.-C., Hubert, E.-L., Fernandes-Rosa, F.L., 2012. Aldosterone resistance: Structural and functional considerations and new perspectives. Molecular and Cellular Endocrinology, Mineralocorticoids and the Mineralocorticoid Receptor 350, 206–215. https://doi.org/10.1016/j.mce.2011.04.023

Zennaro, M.C., Keightley, M.C., Kotelevtsev, Y., Conway, G.S., Soubrier, F., Fuller, P.J., 1995. Human mineralocorticoid receptor genomic structure and identification of expressed isoforms. J Biol Chem 270, 21016–21020. https://doi.org/10.1074/jbc.270.36.21016

Zennaro, M.C., Le Menuet, D., Lombès, M., 1996. Characterization of the human mineralocorticoid receptor gene 5'-regulatory region: evidence for differential hormonal regulation of two alternative promoters via nonclassical mechanisms. Mol Endocrinol 10, 1549–1560. https://doi.org/10.1210/mend.10.12.8961265

Zennaro, M.C., Souque, A., Viengchareun, S., Poisson, E., Lombès, M., 2001. A new human MR splice variant is a ligand-independent transactivator modulating corticosteroid action. Mol Endocrinol 15, 1586–1598. https://doi.org/10.1210/mend.15.9.0689

Zhao, M., Célérier, I., Bousquet, E., Jeanny, J.-C., Jonet, L., Savoldelli, M., Offret, O., Curan, A., Farman, N., Jaisser, F., Behar-Cohen, F., 2012. Mineralocorticoid receptor is involved in rat and human ocular chorioretinopathy. J Clin Invest 122, 2672–2679. https://doi.org/10.1172/JCI61427

Zhou, J., Azizan, E.A.B., Cabrera, C.P., Fernandes-Rosa, F.L., Boulkroun, S., Argentesi, G., Cottrell, E., Amar, L., Wu, X., O'Toole, S., Goodchild, E., Marker, A., Senanayake, R., Garg, S., Åkerström, T., Backman, S., Jordan, S., Polubothu, S., Berney, D.M., Gluck, A., Lines, K.E., Thakker, R.V., Tuthill, A., Joyce, C., Kaski, J.P., Karet Frankl, F.E., Metherell, L.A., Teo, A.E.D., Gurnell, M., Parvanta, L., Drake, W.M., Wozniak, E., Klinzing, D., Kuan, J.L., Tiang, Z., Gomez Sanchez, C.E., Hellman, P., Foo, R.S.Y., Mein, C.A., Kinsler, V.A., Björklund, P., Storr, H.L., Zennaro, M.-C., Brown, M.J., 2021. Somatic mutations of GNA11 and GNAQ in CTNNB1-mutant aldosterone-producing adenomas presenting in puberty, pregnancy or menopause. Nat Genet 53, 1360–1372. https://doi.org/10.1038/s41588-021-00906-y

Zilbermint, M., Stratakis, C.A., 2015. Protein kinase A defects and cortisol-producing adrenal tumors. Curr Opin Endocrinol Diabetes Obes 22, 157–162. https://doi.org/10.1097/MED.0000000000000149

Appendix

13 Génétique et génomique de l'hyperaldostéronisme primaire (Résumé élaboré)

L'hypertension artérielle (HTA) touche environ 25 % de la population générale et constitue l'une des principales causes de maladies cardiovasculaires et de décès dans le monde. L'hyperaldostéronisme primaire (HAP) est la forme la plus fréquente d'HTA secondaire, avec une prévalence de 5% chez les individus hypertendus dans la population générale et atteignant jusqu'à 20% chez ceux présentant une hypertension résistante au traitement. L'HAP se caractérise par une production autonome d'aldostérone, due à un adénome produisant de l'aldostérone (APA) ou à une hyperplasie bilatérale des surrénales (BAH).

Des mutations somatiques et germinales ont été identifiées dans les APA et les formes familiales d'HAP. Des mutations somatiques récurrentes affectent les canaux ioniques et les pompes (*KCNJ5, CACNA1D, ATP1A1, ATP2B3, CLCN2, CACNA1H, SLC30A1 et MCOLN3*) ainsi que d'autres voies de signalisation (*CTNNB1, GNAQ/GNA11, CADM1*), conduisant à la production autonome d'aldostérone. Des études d'association pangénomique ont identifié *CASZ1*, un facteur de transcription à doigts de zinc et corépresseur du MR, comme gène de susceptibilité à l'HAP régulant la biosynthèse d'aldostérone dans les cellules corticosurrénaliennes. Le MR lie l'aldostérone et est exprimé dans les cellules productrices d'aldostérone de la ZG et dans les APA. Nous avons émis l'hypothèse que *CASZ1*, seul ou en interaction avec le MR, pourrait affecter l'homéostasie corticosurrénaliennes incluant le renouvellement cellulaire, la conversion du lignage cellulaire et la fonction, contribuant au développement de l'HAP chez les porteurs d'allèles de risque de *CASZ1*.

Le cortex surrénalien présente une organisation zonale où chaque zone concentrique a une fonction endocrine distincte. La biosynthèse de l'aldostérone se produit dans la zone glomérulée (ZG) externe par l'expression de l'aldostérone synthase (AS, codée par *CYP11B2*), enzyme catalysant les étapes finales de conversion de la corticostérone en aldostérone. La zone fasciculée (ZF) adjacente synthétise les glucocorticoïdes via la 11β-hydroxylase (*CYP11B1*), tandis que la zone réticulée (ZR) produit des précurseurs androgéniques. Chez la souris, la ZR est remplacée par une zone X (ZX) sexuellement dimorphique qui régresse avec la maturation sexuelle chez les mâles et après la première grossesse chez les femelles. Le système rénine-angiotensine-aldostérone (SRAA) et le potassium extracellulaire régulent l'activité de la ZG, tandis que l'ACTH hypophysaire stimule la production de glucocorticoïdes par la ZF.

Le cortex surrénalien présente une plasticité importante malgré des taux de prolifération cellulaire faibles. Les cellules matures de la ZG migrent vers l'intérieur et adoptent progressivement les caractéristiques de la ZF pendant le renouvellement cortical. Cette transition est orchestrée par différentes cascades de signalisation, incluant sonic hedgehog provenant des cellules sous-capsulaires. Sous régime pauvre en sel, le cortex surrénalien subit un remodelage cellulaire et fonctionnel avec augmentation de la prolifération des cellules de la ZG et renforcement de la synthèse d'aldostérone.

Le récepteur minéralocorticoïde (MR), codé par *NR3C2*, est un récepteur hormonal nucléaire fonctionnant comme facteur de transcription dépendant du ligand dans les organes cibles classiques incluant le rein, le côlon et les tissus cardiovasculaires. L'activation excessive du MR dans les tissus cardiovasculaires favorise le remodelage pathologique incluant la fibrose cardiaque et le dysfonctionnement vasculaire. L'expression du MR s'étend également à la zone glomérulée productrice d'aldostérone et aux APA, suggérant des boucles régulatrices autocrines ou paracrines où l'aldostérone sécrétée localement pourrait influencer l'homéostasie de la ZG via des mécanismes médiés par le MR.

L'objectif de ce projet était d'investiguer comment le MR et *CASZ1* influencent la structure, la fonction et la régulation de l'aldostérone dans le cortex surrénalien, en développant et étudiant différents modèles murins génétiquement modifiés. Des souris knockout cellule-spécifiques ont été générées utilisant Cyp11b2-Cre pour inactiver le MR ou *CASZ1* sélectivement dans la ZG et les cellules dérivées. Ces animaux ont été évalués dans des conditions basales et pendant la restriction sodée (pour les souris MRKO^{Ad}), un stress physiologique stimulant le SRAA et favorisant la croissance de la ZG. Un séquençage d'ARN à l'échelle du noyau cellulaire (snRNA-seq) a été réalisé pour cartographier l'hétérogénéité cellulaire, définir les mécanismes de plasticité et identifier les programmes transcriptionnels dépendants du MR. Ce travail visait à élucider le rôle du MR et de *CASZ1* dans la régulation de l'homéostasie et de la plasticité du cortex surrénalien, avec des implications pour la compréhension de la physiopathologie de l'HAP.

La caractérisation phénotypique des souris MRKO^{Ad} à 12 semaines en condition basale a révélé des phénotypes sexe-spécifiques. Chez les femelles, une expansion significative de la ZG a été observée avec réduction de la ZX. Les mâles MRKO^{Ad} présentaient une augmentation du poids corporel sans modifications majeures de l'architecture zonale. Les deux sexes montraient une expression réduite de *Cyp11b2* malgré le maintien de niveaux plasmatiques d'aldostérone

normaux, suggérant l'existence de mécanismes compensatoires préservant l'homéostasie minéralocorticoïde en conditions basales.

L'analyse des mécanismes moléculaires a révélé une diminution de la prolifération cellulaire dans le cortex surrénalien des souris MRKO^{Ad}. Une activation de la voie PKA a été détectée, avec augmentation des niveaux de CREB et pCREB ainsi qu'une expression élevée des sous-unités de la PKA, particulièrement chez les mâles. Ces résultats suggèrent que la perte du MR entraîne une reprogrammation des voies de signalisation intracellulaires, avec activation compensatoire de la voie PKA/CREB contribuant au maintien de la fonction stéroïdogénique basale.

Le régime pauvre en sel (LSD) a révélé un rôle critique du MR dans la réponse adaptative du cortex surrénalien. Bien que l'aldostérone augmentait après 2 semaines de LSD dans les deux génotypes, la réponse était significativement atténuée chez les souris MRKO^{Ad}. Une élévation compensatoire de la corticostérone a été observée chez les MRKO^{Ad}, suggérant un mécanisme de compensation par la ZF palliant la production insuffisante d'aldostérone par la ZG. L'expansion caractéristique de la ZG (cellules Dab2-positives) en réponse à la restriction sodée était atténuée chez les MRKO^{Ad}. L'induction de l'expression de *Cyp11b2* était significativement réduite chez les MRKO^{Ad}, indiquant que le MR est essentiel pour la réponse adaptative complète de la ZG à la restriction sodée.

Un dimorphisme sexuel marqué a été observé dans les réponses adaptatives au LSD. Les mâles montraient une régulation positive de *Cyp11b1* durant le LSD, absente chez les femelles, révélant des différences fondamentales dans les mécanismes de compensation en réponse au stress sodé. L'analyse en composantes principales (PCA) des profils stéroïdiens a démontré que les souris contrôles présentaient des réponses métaboliques plus prononcées au régime pauvre en sel que les souris MRKO^{Ad}, confirmant que l'absence de MR limite la capacité du cortex surrénalien à s'adapter métaboliquement à la restriction sodée.

Les expériences de traçage du lignage cellulaire chez les femelles ont révélé des altérations de la conversion du lignage cellulaire vers la ZX. Après récupération suivant le LSD, les souris MRKO^{Ad} femelles montraient une augmentation des cellules double-positives, suggérant une altération de la conversion normale du lignage vers la ZX. Ces résultats indiquent que le MR régule non seulement la fonction de la ZG, mais également la plasticité cellulaire entre les différentes zones du cortex surrénalien.

Une analyse par séquençage d'ARN à l'échelle du noyau cellulaire (snRNA-seq) du cortex surrénalien de souris contrôles et MRKO^{Ad} a été réalisée en condition basale et après régime pauvre en sel. L'analyse transcriptomique a révélé des changements importants dans la réponse du cortex surrénalien au régime pauvre en sel suite à l'inactivation du MR. Les souris MRKO^{Ad} ont montré une expression de Ren1 (rénine) considérablement réduite et n'ont pas activé correctement le système rénine-angiotensine local pendant la restriction sodée, révélant un rôle inattendu du MR dans la régulation du système rénine local, mécanisme potentiellement crucial pour l'adaptation à la restriction sodée.

L'analyse a également révélé une reprogrammation perturbée de la ZF en réponse à la restriction sodée chez les souris MRKO^{Ad}. Alors que les souris contrôles montrent des changements transcriptionnels coordonnés dans la ZF en réponse au LSD, cette plasticité adaptative était significativement altérée en l'absence de MR dans les cellules de la ZG, suggérant que le MR dans la ZG joue un rôle non-autonome cellulaire dans la régulation de la plasticité de la ZF, possiblement via des mécanismes paracrines. L'expression des enzymes stéroïdogéniques clés *Cyp11b2* et *Cyp11b1* était altérée chez les souris MRKO^{Ad} en réponse au LSD, expliquant en partie les altérations observées dans les profils stéroïdiens.

Ces analyses transcriptomiques ont démontré que le MR joue un rôle central dans le maintien de la plasticité du cortex surrénalien. Le MR régule non seulement la fonction intrinsèque des cellules de la ZG, mais coordonne également les réponses adaptatives de l'ensemble du cortex surrénalien à la restriction sodée, incluant l'activation du système rénine local, la reprogrammation de la ZF, et l'expression coordonnée des enzymes stéroïdogéniques zonales.

Le rôle de *CASZ1* a été étudié en générant des souris présentant une invalidation conditionnelle de *Casz1* spécifiquement dans les cellules de la ZG (souris Casz1Ad). La caractérisation phénotypique de ces souris à 12 semaines en condition basale a révélé un phénotype subtil sans altération significative de la morphologie générale du cortex surrénalien, du poids corporel, de l'architecture corticale ou des profils hormonaux. Des analyses morphologiques détaillées ont révélé des tendances chez les femelles, avec augmentation des cellules Dab2-positives de la ZG et diminution des cellules 20alpha-HSD-positives de la ZX. L'aldostérone plasmatique montrait une réduction non significative chez les femelles knockout, suggérant un effet subtil de *CASZ1* sur la production d'aldostérone qui pourrait devenir apparent dans des conditions de stimulation. Ces résultats établissent une base pour des investigations futures de *CASZ1* sous défis physiologiques. La génération de souris doubles knockout MRKO^{Ad}::Casz1KO^{Ad}

permettra d'explorer les interactions entre le MR et CASZ1 dans la régulation de la fonction du cortex surrénalien.

En conclusion, ce travail apporte des contributions majeures à la compréhension de la biologie du cortex surrénalien et de la pathogenèse de l'HAP. L'inactivation du MR spécifiquement dans les cellules de la ZG provoque des altérations sexe-spécifiques marquées de l'architecture surrénalienne, de la prolifération cellulaire et de l'expression des enzymes stéroïdogéniques. En condition basale, des mécanismes compensatoires incluant l'activation de la voie PKA/CREB permettent de maintenir des niveaux normaux d'aldostérone plasmatique. Ces mécanismes sont insuffisants lors de défis physiologiques, limitant les réponses adaptatives à la restriction sodée. Ces résultats révèlent le rôle critique du MR dans l'homéostasie, la plasticité et la régulation sexe-spécifique de la ZG, via un mécanisme autocrine-paracrine.

L'analyse par snRNA-seq a identifié des mécanismes moléculaires spécifiques par lesquels le MR régule la plasticité du cortex surrénalien. Le MR est essentiel pour l'activation du système rénine-angiotensine local, la reprogrammation coordonnée de la ZF en réponse au stress sodé, et le maintien de l'expression zonale des enzymes stéroïdogéniques. Les expériences de traçage du lignage cellulaire ont révélé que le MR régule la dynamique du lignage cellulaire de la ZG et la conversion des cellules vers la ZX, avec des différences sexuelles marquées. La caractérisation du modèle murin Casz1Ad a établi que la délétion de CASZ1 entraîne des changements minimes en conditions basales, soulignant la nécessité d'investigations sous défis physiologiques.

Une meilleure compréhension des mécanismes par lesquels le MR régule la production d'aldostérone et la plasticité du cortex surrénalien pourrait permettre l'identification de nouvelles cibles thérapeutiques pour le traitement de l'HAP. La régulation par le MR de l'expression locale de la rénine suggère l'existence d'un système rénine-angiotensine intra-surrénalien dont la dysrégulation pourrait contribuer au développement de l'HAP. Les modèles murins générés ($MRKO^{Ad}$ et $Casz1KO^{Ad}$), les données transcriptomiques produites, et les mécanismes de plasticité identifiés constituent une base pour de futures recherches visant à comprendre la pathogenèse de l'HAP et à développer de nouvelles approches thérapeutiques pour cette pathologie fréquente et sous-diagnostiquée.

14 Scientific papers

14.1 Sexually dimorphic interzonal crosstalk reshapes the adrenal cortex in response to pathophysiological challenges

Faedda N, Abdellatif AB, Carbone F, **Fayad M**, Fedlaoui B, Chamoun R, et al. Sexually dimorphic interzonal crosstalk reshapes the adrenal cortex in response to pathophysiological challenges. bioRxiv; 2025 [cited 2025 Sep 29]. p. 2025.09.05.674435. Available from: https://www.biorxiv.org/content/10.1101/2025.09.05.674435v1

Sexually dimorphic interzonal crosstalk reshapes the adrenal cortex in response to pathophysiological challenges

Nicolo Faedda[1], Alaa B Abdellatif[1], Francesco Carbone[2], May Fayad[1], Bakhta Fedlaoui[1], Rita Chamoun[3], Romane L'Héritier[1], Ilaria Del Gaudio[1], Ourida Koual[1], Isabelle Giscos-Douriez[1], Stéphanie Baron[1,4], Ben Atkinson[5], Xiaomin Li[1], Linghui Kong[1], Yunling Xu[1], Eric Camerer[1], Mickael Menager[2], Fabio L. Fernandes-Rosa[1], Sheerazed Boulkroun[1], Maria-Christina Zennaro[1,6#]

[1]Université Paris Cité, PARCC, Inserm, Paris, France
[2]Université Paris Cité, Imagine Institute, Laboratory of Inflammatory Responses and Transcriptomic Networks in Diseases, Atip-Avenir Team, INSERM UMR 1163, 75015 Paris, France
[3]Cardiovascular Research Institute Maastricht (CARIM) and Heart & Vessels Center, Maastricht University Medical Center, Maastricht, The Netherlands.
[4]Assistance Publique-Hôpitaux de Paris, Hôpital Européen Georges Pompidou, Service de Physiologie, Paris, France
[5]Intelligent Imaging Innovations Ltd, 17 Westbourne Studios, W10 5JJ, London, UK
[6]Assistance Publique-Hôpitaux de Paris, Hôpital Européen Georges Pompidou, Service de Génétique, Paris, France

[#]Corresponding author
Address correspondence to:
Maria-Christina Zennaro, MD, PhD
Inserm, U970
Paris Cardiovascular Research Center – PARCC
56, rue Leblanc,
75015 Paris – France
Tel : +33 (0)1 53 98 80 42
Fax : + 33 (0)1 53 98 79 52
e-mail : maria-christina.zennaro@inserm.fr

Declaration of interest

The authors have nothing to disclose

Abstract

Structured Abstract:

Background*:* Primary aldosteronism is the most common form of secondary arterial hypertension, due to autonomous aldosterone production from the adrenal cortex. Genome wide association studies discovered genetic risk loci associated with the disease, which may affect adrenal cortex renewal, differentiation and lineage conversion. Genetic susceptibility may be modulated by environmental challenges.

Method: Here we investigate how environmental cues affecting mineralocorticoid output modulate adrenal cortex homeostasis, cell lineage conversion and zone-specific transcriptional landscape. We have used a newly developed *Cyp11b2*^{Cre} mouse model and characterised its adaptation to a high or low salt diet (HSD, LSD**)**, as well as dexamethasone (DEX) treatment. To explore underlying mechanisms, deep functional and morphological phenotyping, lineage tracing and spatial transcriptomics of the adrenal cortex were performed.

Results: *Cyp11b2* expression was detected in *Cyp11b2*^{Cre}-*m*T*m*G mice as early as day P1 in different areas of the ZG, associated with high plasma aldosterone levels, with lineage conversion of zona glomerulosa (ZG) into zona fasciculata (ZF) cells progressing between 2 and 9 weeks of age and a progressive reduction of ZG size and evolution of cell components of the adrenal cortex over time. Transdifferentiation progressed into the X-zone (ZX) in females, revealing a previously unrecognized connection between ZF and ZX cells in adult mice. A sexually dimorphic, reciprocal interaction between the ZG and the ZF in adapting to salt diets or DEX treatment was observed, involving changes in cell composition and transcriptional reprogramming of the three zones.

Conclusion: HSD, LSD and DEX induce a sexually dimorphic cellular and transcriptional response, involving all layers of the adrenal cortex, and the reciprocal contribution of ZG and ZF cells, indicating functional interaction between adrenocortical zones in adapting to external cues.

Introduction

Primary aldosteronism (PA) is the most common form of secondary arterial hypertension, affecting up to 20% of hypertensive patients and contributing to increased cardiovascular risk[1–3]. It is due to excessive and autonomous aldosterone production by the adrenal gland, due in the majority of cases to a unilateral aldosterone producing adenoma (APA) or bilateral adrenal hyperplasia (BAH)[4]. Recent evidence suggests that abnormalities in aldosterone production may contribute to a significant fraction of hypertension in the general population[5]. While several germline and somatic mutations have been described in familial forms of PA and APA[5–7], recent genome wide association studies (GWAS) discovered genetic loci associated with increased risk of developing the disease[8–10]. These loci are shared between APA and BAH, revealing a hitherto unexpected common pathophysiology between unilateral and bilateral PA. Remarkably, PA risk loci also overlap with risk loci for hypertension traits, including resistant hypertension, providing genetic support to the clinical evidence of a pathophysiological continuum of aldosterone dysregulation throughout the spectrum of blood pressure, from normotension to PA[5]. Mechanistic studies have shown that genes located within risk loci for PA identified in GWAS modify adrenocortical function in cell and mouse models[8,11]. Experimental data on *CASZ1* and *RXFP2*, two PA susceptibility genes, suggest a potential pathogenic mechanism whereby a genetically determined reduction in aldosterone production by the ZG in carriers of PA risk alleles leads to PA due to lifelong increased stimulation of the adrenal cortex to maintain adequate mineralocorticoid output[8]. This chronic stimulatory drive may promote increased cell proliferation in the ZG, eventually resulting in a propitious environment for the appearance of somatic mutations within single or multiple aldosterone-producing areas in one or both adrenal glands[8]. On the other hand, *Wnt2b*, another PA susceptibility gene, is expressed in capsular cells of the adrenal cortex. Its inactivation in mice led to dysmorphic and hypocellular ZG, with impaired aldosterone production[11]. It therefore appears that risk loci for PA mainly affect adrenal cortex maintenance and cell differentiation, rather than directly aldosterone production. This raises the hypothesis that common genetic variation may modulate adrenal cortex renewal, differentiation and cell lineage conversion, eventually leading to hyperplasia, nodulation and PA in extreme cases.

The adrenal cortex consists of different concentric cell layers with different functional properties. The outermost layer, the zona glomerulosa (ZG), plays a key role in the renin-angiotensin-aldosterone system (RAAS) by producing mineralocorticoids, primarily aldosterone, which is essential for regulating salt and fluid balance in the kidney. The middle layer, the zona fasciculata (ZF), produces glucocorticoids, cortisol in humans and corticosterone in mice, under the influence of the hypothalamic-pituitary-adrenal (HPA) axis, affecting glucose homeostasis and the body's chronic stress response. The innermost layer, the zona reticularis (ZR) in humans, is responsible for androgen production. In mice, this layer is absent; instead, an X-zone (ZX) derived from the foetal adrenal cortex is present, which has an unknown function and regresses at puberty in males and after the first pregnancy in females[12–15]. This so-called “functional” zonation of the adrenal cortex results from the zone-specific expression of steroidogenic enzymes, including aldosterone synthase (AS, encoded by *CYP11B2*) in the ZG and 11β-hydroxylase (encoded by *CYP11B1*) in the ZF. The adrenal cortex is a highly dynamic and adaptive tissue, continuously renewing in adult mice and able to adapt its function and size to environmental requirements, with important sex-specific differences[16]. Renewal takes place in the outer layers of the adrenal cortex, with newly formed cells undergoing centripetal migration, differentiation, and lineage conversion to establish the distinct functional steroidogenic zones[17–19]. Undifferentiated progenitor cells located in the

subcapsular region develop into differentiated ZG cells, which subsequently transdifferentiate into ZF cells, although part of these progenitor cells may differentiate directly into ZF cells[18,19]. In mice, the ZX is considered to represent remnant tissue from the foetal cortex; lineage-tracing experiments have shown that the adult cortex derives from precursor cells in the fetal cortex, establishing a direct link between the adrenocortical zones[12–14]. Transdifferentiation has been described as the primary mechanism driving adult adrenal cortex renewal under physiological conditions, although the genes and pathways orchestrating these structural and metabolic changes remain a matter of investigation.

Genetic susceptibility may be modulated by environmental challenges. In particular, the adrenal cortex is constantly responding to pathophysiological demands with adaptations in hormone output and cellular plasticity[15,20,21]. Renewal and functional regeneration from glucocorticoid induced adrenocortical atrophy results from coordinated interplay between endocrine and paracrine regulation of growth and function involving different cell types and signalling pathways[22]. In the context of aldosterone homeostasis, salt diet is a major modulator of ZG homeostasis, leading to an adaptive hormonal and morphological response mediated mainly by the renin-angiotensin system[23,24], but detailed changes in cell lineage conversion and zonal gene expression programs remain to be determined. The aim of this study was to explore the role of environmental cues in modulating adrenal cortex homeostasis, transdifferentiation and zone-specific transcriptional landscape, with a particular attention to the ZG and mineralocorticoid homeostasis, as well as sexual dimorphism. We used a newly developed *Cyp11b2*^{Cre} mouse model, in which aldosterone production is conserved, and investigated its adaptation to different salt diets as well as dexamethasone (DEX) treatment, by deep functional and molecular phenotyping of male and female mice. Characterisation of the new mouse model revealed the morphological and functional evolution of the adrenal cortex with age, with transdifferentiation progressing into the X-zone (ZX) in females, revealing a previously unrecognized connection between ZF and ZX cells in adult mice. We further discover a sexually dimorphic interaction between the ZG and the ZF in adapting to a high (HSD) or low salt diet (LSD) or DEX treatment through changes in cell composition and transcriptional reprogramming of the adrenal cortex.

Results

Generation and characterization of *Cyp11b2*^{Cre} and *Cyp11b2*$^{+/Cre}$*-mTmG* mice

We developed a novel *Cyp11b2*^{Cre} mouse model in which the Cre recombinase is inserted within the *Cyp11b2* locus (exon 9) downstream of the stop codon located in the 3' untranslated region (3' UTR) of the gene, after an Internal Ribosome Entry Site (IRES) (Figure 1a). Insertion of the IRES allows the translation of two different proteins from a single mRNA transcript. The *Cyp11b2*$^{+/Cre}$ mice were crossed with *Gt(ROSA)26Sor*$^{tm4(ACTB-tdTomato-EGFP)Luo/J}$ reporter mice to generate the *Cyp11b2*^{Cre}::*m*T*m*G line. Investigation of Cre recombination in this reporter model showed efficient and specific recombination in the ZG only, with no leakage in other tissues, such as brain, kidney, visceral and subcutaneous adipose tissue, aorta and mesenteric vessels (Figure S1a). Measurements of circulating hormones in plasma by liquid chromatography tandem mass spectrometry (LC-MS/MS), performed on 6-weeks old mice of both sexes carrying heterozygous (*Cyp11b2*$^{+/Cre}$) or homozygous (*Cyp11b2*$^{Cre/Cre}$) Cre alleles, showed normal plasma aldosterone levels compared to wild type, indicating normal aldosterone production (Figure 1b), as well as no major differences in overall corticosteroid profiles (Figure S1b). Plasma Renin Activity (PRA) showed no significant difference across genotypes, confirming a conserved RAAS (Figure 1b). While Western blot analyses showed a reduction of Aldosterone Synthase (AS) expression in *Cyp11b2*$^{Cre/Cre}$ mice compared to WT and *Cyp11b2*$^{+/Cre}$ mice in both sexes (Figure S1c), a similar number of AS^{+} cells was detected by immunostaining across genotypes (Figure S1d). These results suggest that insertion of the Cre recombinase in the 3' UTR of the *Cyp11b2* gene may have affected mRNA-stabilising sequences present in this region, possibly leading to faster transcript degradation and decreased protein levels; however, this reduction does not lead to any change in aldosterone production and renin levels. Nevertheless, to exclude any RAAS and ZG physiological variability across groups, only heterozygous mice were used for subsequent experiments.

Lineage conversion progresses from ZF to ZX in *Cyp11b2*^{Cre}*::m*T*m*G mice

The kinetics of adrenal cortex cell lineage conversion was investigated in male and female *Cyp11b2*^{Cre}::*m*T*m*G mice from 2 weeks to 9 weeks of age by quantifying mGFP^{+} cells, which gradually replace mTomato^{+} cells as the cortex renewal process progresses[19]. During this time, adrenal weight increased progressively in both males and females (data not shown). At postnatal day 1 (P1), the surface of the adrenal showed large areas of mGFP^{+} cells (Figure S2a and S3a), whose localisation was restricted to the ZG (Figure S2a and S3b). At 2 weeks of age, the number of mGFP^{+} cells was 47.75±2.74% of adrenal cortex cells in males, increasing to 77.14±4.02% at 9 weeks of age (Figure 1c). In female mice, the mGFP^{+} cells similarly progressed from 41.54± 1.15% at 2 weeks to 75.12±3.93% at 9 weeks of age (Figure S2b). Comparing the evolution of mGFP^{+} cells in the cortex over time between sexes showed a significant difference at the age of 4 weeks, related to the major loss of ZX cells occurring at this age in males (Figure S2d). Quantification of Dab2^{+} cells, a marker of the ZG, showed a significant reduction of ZG size between 2 and 4 weeks of age in males, which was more progressive in females (Figure 1c and S2b). This was paralleled by a similar reduction of aldosterone levels over time (Figure S2c). Since the Cre recombinase is expressed under the control of the *Cyp11b2* promoter in the ZG, we also quantified the ratio of mGFP^{+} cells over Dab2^{+} cells, which showed a continuous increase between 2 and 7 weeks of age in both sexes (Figure 1c and S2b), with a slight but non significantly higher ratio after 6 weeks of age in females compared with males (Figure S2e).

Adrenal 3D reconstruction of 6 weeks old mice by lightsheet microscopy revealed uneven penetration of $mGFP^+$ cells in the adrenal cortex, suggesting spatially heterogenous transdifferentiation, as well as some columnar arrangements of mTomato cells in the ZF, connecting with the subcapsular region, in accordance with the alternative pathway of ZF differentiation moving directly from the subcapsular stem cell compartment to the ZF (Figure S1f). Remarkably, co-staining of mGFP and 20αHSD, a ZX marker ($mGFP^+/20\alpha HSD^+$), was observed starting from 6 weeks in female *Cyp11b2*$^{+/Cre}$-*m*T*m*G mice (Figure 1d), indicating a certain degree of lineage conversion between ZF and ZX.

Spatial transcriptomic (ST) analysis was performed on male and female *Cyp11b2*$^{+/Cre}$-*m*T*m*G mice at 2, 3, 6, 7 and 12 weeks of age. Using well defined markers for the different cell populations composing the adrenal gland (Figure S4, S5 and Table S1), we identified 11 cell clusters (Figure 1e-f, S5a-c), including the ZG, ZF, ZX and medulla, as well as cluster containing both ZG and ZF cells (ZG-ZF cluster), a cluster containing ZG and adrenal cortex progenitors, T cells, macrophages, and ZF clusters enriched for dendritic cells (ZF associated DC) and macrophages (ZF associated macrophages), representing a mixture of ZG and immune cells. Partitioning the overall uMAP of male and female mice at different ages revealed that the process of adrenal growth was associated with the expansion or regression of different cell clusters composing the adrenal cortex (Figure 1f and S5d). In particular, ST confirmed the reduction over time of the ZG observed by immunolabeling, and revealed an evolution of the ZF during growth with changes of the 3 ZF containing clusters (pure ZF, ZF Associated DC and ZF Associated Macrophages) in both males and females.

These results indicate that *Cyp11b2* expression is detectable at P1 in different areas of the ZG, associated with a large Dab^+ ZG as well as high aldosterone levels, both decreasing with age. Lineage conversion progresses into the ZX with time, becoming detectable around 6 weeks of age. These changes are associated with modifications in the cellular composition of the adrenal cortex.

Low salt diet (LSD) increases mineralocorticoid output by activating a sexually dimorphic transcriptional program

To assess the plasticity of the adrenal cortex in response to environmental requirements, we first stimulated the ZG by feeding male and female mice with a LSD (<0.03% Na^+) for 2 weeks, starting from 4 weeks until 6 weeks of age (Figure 2a, time point T_1). To study the ability of the adrenal cortex to reverse the effects of such stimulation, the mice were subjected to a one-week recovery period in which the mice are returned to a standard diet, referred to as T_2 (Figure 2a). LSD did not change total body weight or adrenal weight of treated mice compared to controls, with the exception of the left adrenal of LSD-fed females, which showed an increase in absolute weight (Figure S6a-b). No major histological changes were observed following treatment or recovery (Figure S6c). As expected, *Cyp11b2* mRNA expression increased significantly after two weeks of LSD, associated with an increase in plasma aldosterone levels (Figure 2b-c), without modification of *Cyp11b1* expression, but increased corticosterone levels in males (Figure 2d-e). After one week recovery (T_2), mice fed with a LSD had comparable *Cyp11b2* expression and plasma aldosterone levels to control (Ctrl T_2) mice (Figure 2b-c). RNAscope analysis confirmed increased mRNA expression of *Cyp11b2* in the ZG of mice following LSD, with no differences in *Cyp11b1* mRNA expression (Figure S7). Consistent with increased *Cyp11b2* expression and plasma aldosterone levels, immunostaining showed a significant increase in AS^+ cells in the ZG in both male and female mice following LSD and a decrease in AS^+ cells after recovery, with AS expression returning to levels comparable to Ctrl

T_2 (Figure 2f). Dab2 immunofluorescence revealed no changes in ZG size in both sexes after LSD or recovery (T_2) (Figure 2g). Steroid profiling of mice under LSD showed an increase of mineralocorticoids as well as steroid precursors, which returned to control values after one-week recovery in both sexes (Figure 2h). PCA of plasma steroids revealed clear separation between control and LSD-fed mice along the first Dimension (Dim1) (Figure 2i), which explained 51.1% in males and 44.9% in females of the total variance, driven mainly by aldosterone, pregnenolone, progesterone, 18-hydroxycorticosterone levels, with a sexually dimorphic contribution of each single steroid (Figure S8a and b). Cell lineage conversion following LSD was investigated in *Cyp11b2*$^{+/Cre}$-*m*T*m*G mice. Overall quantification of GFP$^+$ cells within the cortex showed a small, but not significant increase in both male and female mice (Figure S6d). Quantification following segmentation of the adrenal cortex in successive layers revealed an increased number of mGFP$^+$ cells in the external layers in males, corresponding to the ZG and compatible with the increased number of AS expressing cells, while in females a lower number of mGFP$^+$ cells were observed in the inner layers compared to Ctrl T_1 mice (Figure S6e).

ST data were interrogated to better detect changes in cell components and explore molecular changes underlying the response to LSD. In male mice, LSD induced an increase in clusters corresponding to ZG Adrenal Cortex Progenitors, ZG and the whole ZF (including the ZF, ZF associated macrophages and ZF associated DC clusters) at T_1 (Figure 3a). In the subsequent recovery week, a ZG Adrenal Cortex Progenitors and ZF clusters were reduced compared to the corresponding control animals, while the other clusters returned to control values (Figure 3c). Analysis of differentially expressed genes (DEG) performed in the ZG and ZF clusters revealed important transcriptional changes in the ZG, with increase in genes involved in steroid hormone biosynthesis and metabolism and ZG cell identity, such as *Cyp11b2, Dab2*, *Hsd3b1*, *Agtr1a*, and mitochondrial function (*Hspd1*, *Echs1*, *Fdx1, Atp5e*) (Figure 3b, f and Table S2). Remarkably, ZF appears to actively contribute to the response to LSD, as revealed by a large number of positive transcriptional changes (395 DEG, 352 upregulated, Figure 3b and Table S2). Among these genes are some that are directly linked with ZF cell identity and function, with increased expression of *Cyp11b1, Akr1b7, Scarb1* and *Fdx1* (Figure 3b and Table S2). Following one week of recovery the transcriptional activity of the ZG reverted to normal, whereas ZF still displays important transcriptional changes compared to Ctrl T_2 mice (Figure 3d). In female mice, a similar increase of the ZG cluster following LSD was observed, while the ZG Adrenal Cortex Progenitors and ZF clusters were reduced (Figure 3e). Recovery led to re-expansion of ZG Adrenal Cortex Progenitors and decrease of ZG (Figure 3g). LSD was associated with a limited number of transcriptional changes in the female ZG, including increased expression of *Cyp11b2* and *Fdx1*, while *Wnt4* was decreased (Figure 3f and Table S2). In contrast, an important transcriptional repression was observed in the ZF, in particular reduced expression of steroidogenic genes such as *Hsd3b1*, *Akr1b7*, *Scarb1*, and *Cyp21a1* (Figure 3f and Table S2). Recovery was associated to major changes in the ZF but not in the ZG, similar to what observed in males (Figure 3h and Table S2), with a recovery of positive transcriptional regulation (235 upregulated genes) and increased expression of *Hsd3b1*, *Cyp21a1*, and *Cyp11a1*. Overall, a higher number of DEG following LSD were observed in males compared to females, with major differences in the direction of regulation at both T1 and T2 particularly in the ZF (Figure 3i and S9, Table S2). Indeed, gene ontology revealed upregulation of KEGG pathways related to oxidative phosphorylation, steroid biosynthesis, and transcription in the ZF following LSD in males, while in females a majority of pathways was downregulated, including MAPK signalling, oxidative phosphorylation, extracellular matrix (ECM) receptor interaction and neurotrophin signaling (Figure S9 and Table S3). Following recovery, in males the main pathways were downregulated, including oxidative

phosphorylation and ECM receptor interaction, while in females recovery was associated with upregulation of ubiquitin mediated proteolysis, mitochondrial function, and apoptosis, and downregulation of calcium signalling, cell adhesion and hedgehog signalling. No modifications of Wnt/β-catenin genes were observed (Figure S6 f-g).

Altogether, these results suggest that the response of the adrenal cortex to a 2-weeks LSD, starting at 4-weeks of age, leads to increased mineralocorticoid output mediated by an increase in the number of AS^+ cells and *Cyp11b2* expression in both sexes, with only little increase of ZG cells revealed by ST. Adaptation to a LSD and the following recovery involves a major sexually dimorphic transcriptional response in the ZF, as well as different contributions of cell components of the adrenal cortex.

Adaptation of the adrenal cortex to a high salt diet (HSD) involves decrease of AS expression in the ZG and transcriptional changes in the ZF

Next, we investigated the effects of an inhibitory stimulus to the ZG on adrenal cortex plasticity, by feeding 4-weeks-old mice a HSD (3.2% Na^+) for a two-week period, followed by one week recovery (Figure 4a). Treatment induced a significant suppression of aldosterone levels in both sexes (Figure 4b-c), which was accompanied by a significant decrease of *Cyp11b2* mRNA expression in females (Fig. 4c). In males, although the reduction of *Cyp11b2* mRNA expression did not reach statistical significance when measured by RT-qPCR of the entire adrenal cortex (Figure 4b), ST revealed a significant reduction of *Cyp11b2* mRNA expression in the ZG (Table S4). One-week recovery restored *Cyp11b2* mRNA expression and plasma aldosterone levels in both sexes (Figure 4b-c). HSD and recovery did not modify body weight in male mice compared with controls (Figure S10a), while in females there was a significant increase in body weight after HSD that normalized after recovery (Figure S10b). Right and left adrenal weights showed no changes in both males and females at any time point of the diet (Figure S10a-b). H&E staining did not reveal any histological changes at T_1 nor at T_2 (Figure S10c). AS immunofluorescent showed a significant reduction of AS^+ cells in HSD fed mice versus controls (T_1, Figure 4d), confirmed also by RNAscope targeting *Cyp11b2* (Figure S7), which returned to normal levels after recovery (Figure 4d). These changes were not associated with any modification of ZG thickness, as quantified by the number of $Dab2^+$ cells (Figure 4e). HSD also led to increased plasma corticosterone levels (Figure 4f-g), which was accompanied by increased *Cyp11b1* mRNA expression in males only (Figure 4e), as also confirmed by ST (Table S4). These differences disappeared after recovery (Figure 4f-g). Steroid profiling showed an overall decrease in aldosterone and 18-hydroxycorticosterone levels and an increase in steroid precursors following HSD associated with an increase in glucocorticoid biosynthesis (Figure 4h). Recovery led to normalization of the steroid profile of HSD-fed mice. PCA showed clear separation between control and HSD-fed mice along Dim1 (Figure 4i), which explained 57% in males and 55.3% in females of the total variance, driven mainly by 18-hydroxy-11-DOC, pregnenolone, 11-deoxycorticosterone (only in females), corticosterone and progesterone (Figure 4i, S11a-b). Recovery was associated with a slight shift along the Dim2 driven by 18-hydrocorticosterone and aldosterone (Figure 4i and S11a-b). Analysis of *Cyp11b2*$^{+/Cre}$-*m*T*m*G mice revealed an increase of $mGFP^+$ cells following LSD in males (Figure S10d), which was distributed over all layers of the adrenal cortex (Figure S10f), suggesting that HSD may lead to increased lineage conversion from ZG to ZF, due to lack of stimulation to the ZG.

ST showed only a slight reduction in the ZG component, but revealed an enrichment in the ZG Adrenal Cortex Progenitors and ZF clusters compared with Ctrl T_1 in both sexes (Figure 5a, e).

After 1 week recovery, a slightly reduced ZG Adrenal Cortex Progenitor cell cluster was observed in males compared to control T_2, with normalization of the other cell clusters (Figure 5c). In females, recovery was followed by expansion of the ZG-ZF cluster and a minor expansion of ZG and ZF compared with Ctrl T_2 mice (Figure 5g). DEG analysis showed only a limited number of transcriptional changes after HSD or recovery in the ZG (Figure 5b, d, f, h and Table S4), including downregulation of *Cyp11b2* and *Kcnk9* (which did not reach statistical significance after Bonferroni correction in females). Remarkably, ZF once again showed significant gene expression changes after HSD (Figure 5b, f), as well as after recovery (Figure 5d, h), with important sex differences in the genes and direction of regulation (Figure S12 and Table S4). In males, upregulated genes following HSD are involved in steroid metabolism and mitochondrial function such as *Hsd3b1, Fdx1, Cyp11a1, Cyp11b1*, *Me1*, *Hspd1*, *Tspo, Sod1*, as well as ion homeostasis (*Kcnn2*, *Cacna2d1*, *Cacna1c*). In females, upregulated genes are also involved in steroidogenesis and mitochondrial metabolism (*Fdx1*, *Creb3*, *Scarb1*). Similar to what observed with LSD, only a limited number of genes were commonly regulated in males and females (Figure S12). GSEA again revealed opposite regulations in males and females, with KEGG terms related to oxidative phosphorylation being upregulated and neuroactive ligand receptor being downregulated following HSD in males, while females showed upregulation of neuroactive ligand receptor and downregulation of steroid biosynthesis; retinol metabolism was downregulated in both sexes (Table S2). After recovery, oxidative phosphorylation was the most significantly downregulated term in males, with upregulation of steroid hormone biosynthesis, while females showed mostly downregulation of KEGG terms, including calcium signalling, metabolism by cytochrome p450 and cell adhesion molecules. HSD induced only minor modifications of genes of the Wnt/β-catenin pathway (Figure S10e-f).

Altogether these data suggest that physiological response of aldosterone following a 2-week HSD, starting at 4 weeks of age, is mediated by a decrease in the number of AS expressing cells, reduced *Cyp11b2* expression, but only minor changes in ZG size. The response is associated with a sexually dimorphic transcriptional program involving mainly the ZF. In males, a small increase in GFP^+ cells distributed over all cortex layers was observed, suggesting that HSD may lead to accelerated lineage conversion from ZG to ZF.

Dexamethasone (DEX) treatment affects ZG function and accelerates ZG to ZF cell lineage conversion

To investigate whether challenges to the HPA axis similarly affect the interaction between adrenocortical zones, male and female mice underwent two weeks of DEX treatment starting at 4 weeks of age, followed by three weeks of recovery (Figure 6a). The efficacy of the treatment was confirmed by showing a significant reduction in *Cyp11b1* mRNA levels after two weeks of treatment, which returned to control levels after three weeks of recovery (T_2) (Figure 6b-c). Plasma corticosterone levels were significantly decreased following DEX treatment, returning to normal after recovery in both sexes (Figure 6b-c). DEX treated mice were found to have lower body weight compared with controls, with weight regained in females after recovery, but not in males (Figure S13a-b). This was also associated with a significant reduction in both right and left adrenal weights following DEX treatment, which reversed upon recovery, however without reaching control levels in male mice (Figure S13a-b). H&E staining shows an atrophic ZF with reduced cell density following treatment, with 3-weeks recovery allowing to restore adrenal cortex histology comparable to control (Figure S13c). RNAscope detection of *Cyp11b1* confirmed significant atrophy of the ZF after DEX treatment (Figure S7). When referred to the entire adrenal cortex, an increased number of AS^+ cells were measured by

immunofluorescence in male mice following DEX treatment (Figure 5d), which was associated with a non-significant increase in ZG thickness measured by the number of $Dab2^+$ cells (Figure 5e). This increase was however due to a decrease in the total adrenal cortex size due to regression of the ZF following DEX treatment, as indicated by quantification of AS^+ cells in the first 4 layers of the cortex only (Figure S13d). In females, no major changes in ZG size or number of AS^+ cells were observed, nor was any difference found after the recovery phase (Figure 5d-e).

Cyp11b2 expression was not different between treated animals and controls in males, but slightly increased in females following suppression and after recovery. In females, plasma aldosterone levels following DEX treatment were significantly reduced, but normalised after the 3-weeks recovery (Figure 6f-g), suggesting a compensatory increase of *Cyp11b2* mRNA expression to compensate for reduced aldosterone production following DEX treatment. In male mice, although a reduction of plasma aldosterone was observed, this did not reach statistical significance. Steroid profiling revealed an overall decreased production of glucocorticoids and mineralocorticoids as well as steroid precursors following DEX treatment in both sexes, which returned to normal values after the recovery weeks (Figure 6h). PCA of plasma steroids revealed clear separation between controls and DEX-treated mice along the first Dimension (Dim1), which explained 55.9% in males and 56.1% in females of the total variance, driven mainly by a reduction in corticosterone, 11-deoxycorticosterone, 18-hydroxy-11-DOC, progesterone (only in males) and 18-hydrocorticosterone (only in females) (Figure 6i, S14a-b). Steroid profiles completely normalised following 3 weeks of recovery (Figure 6i). Analysis of cell lineage conversion in *Cyp11b2*$^{+/Cre}$*-mTmG* mice showed a slight increase in total number of GFP^+ cells in the adrenal cortex in males, which was evenly distributed over all quantified layers (Figure S13e).

ST revealed a major transcriptional induction in the ZG in male mice (Figure 7a, Table S5), with 104 upregulated genes, together with an increase of the ZG Adrenal Cortex Progenitors and the ZG cluster, and a completely suppressed ZF cluster as expected. DEG analysis did not reveal any regulated genes in the ZF due to the severe atrophy following treatment. Among the most upregulated genes in the ZG were *Hsd3b1*, as well as *Fkbp4*, *Mc2r*, coding for the ACTH receptor, *Wnt5a*, a component of the Wnt/β-catenin pathway, and *Dlk*. *Nr4a1*, coding for NGFI-B, was one of the 5 downregulated genes, together with *Akr1b7* and *Vegfa*. Upregulated pathways included lysosome activity, PPAR signalling, and ABC transporters, which are associated with enhanced cellular metabolism and signalling, while the downregulated functions, including unsaturated fatty acid biosynthesis, steroid biosynthesis, retinol metabolism, indicate suppression of steroid metabolism (Figure S15). In female mice, DEX suppressed the ZF cluster as well as the ZG cluster (Figure 7e). DEG analysis following DEX treatment in females did show only slight changes in the ZG, but significant transcriptional regulation in the ZF (Figure 7d). Among the most upregulated genes were *Apoe*, *Nrep* and *Prkcd*, while down-regulated genes included *Cdkn1c*, *Kcnk3*, *Npr1*, *Cyp21a1*, and *Nr4a2*. In contrast to males, pathways related to steroid biosynthesis were upregulated in both ZG and ZF (Figure S15). RT-qPCR showed also activation of components of the Wnt/β-catenin pathways after DEX, which have suggestive significance in ST, such as *Wnt4* and *Lef1* in males, whereas increased expression of *Axin2* in both sexes was detected only by RT-qPCR (Figure 7c, f). In male mice, expression of *Tcf3* and *Axin2* were increased after recovery compared to Ctrl T2 (Figure 7c). DEX also induced an important increase of the Macrophage cluster mainly in male mice (Figure 7b). Those macrophages were localised at the border between the ZF and the medulla (Figure S4), as shown by CD68 immunostaining of adrenals from Cyp11b2$^{+/Cre}$-mTmG mice (Figure 7g). Those cells were lipid-laden, as shown by Oil Red O staining (Figure 7h), suggesting a "foam cell" phenotype. Finally, immunofluorescent staining of Ki67, a marker of

proliferation, showed a strong decrease of $Ki67^+$ nuclei in the adrenal cortex after DEX in both sexes, the only cells in active proliferation being located at the interface between the ZG and ZF (Figure 7i).

Altogether these results suggest that DEX treatment, similar to salt diets, affects both ZG and ZF, with an overall suppression of both glucocorticoid and mineralocorticoid axes as well as sexually dimorphic changes in gene expression, zone expansion and transdifferentiation**.**

LSD, HSD and DEX affect ZX regression and lineage conversion in female mice

Since our results indicated a certain degree of lineage conversion between the ZF and the ZX in female mice, we investigated whether the ZX is affected by a LSD, HSD or DEX treatment in female mice. The number of $20\alpha HSD^+$ cells did not change significantly following a HSD or LSD (Figure 8a). With the resolution of ST, an increase in the ZX cluster was observed following LSD compared to controls (Figure 8b). This was associated with a lower number of $GFP^+/20\alpha HSD^+$ cells in LSD mice compared with controls (Figure 8a and c). No major changes were observed following a HSD. While the number of $20\alpha HSD^+$ cells decreases between 6 (Ctrl T_1, Figure 8a) and 7 weeks (Ctrl T_2, Figure 8d and 8g) of age, no such decrease is observed in mice following a LSD after 1 week of recovery (Figure 8g) and the number of double positive $GFP^+/20\alpha HSD^+$ cells appears slightly, although not significantly, increased. Similar changes were also observed following a HSD (Figure 8g). These changes are confirmed by ST, with a larger ZX component at T2 following LSD or HSD (Figure 8f).

In mice treated with DEX, the ratio of the ZX $20\alpha HSD^+$ cells over the adrenal cortex is increased (Figure 8a), as also confirmed by ST (Figure 8b). Although DEX treated mice reduce the size of their ZX at 9 weeks of age after 3-weeks recovery, the number of $20\alpha HSD^+$/ZX cells is significantly higher in treated mice than in controls at T_2 (Figure 8h). The lineage conversion process is also significantly altered by DEX treatment, with an increased number of $GFP^+/20\alpha HSD^+$ cells following recovery, representing around 50% of ZX cells (Figure 8h).

Analysis of DEG in the ZX following treatments showed transcriptional changes mainly following recovery after LSD or HSD (Figure 8i, Table S6), with upregulation of genes involved in steroid metabolism *Me1* and *Hsd3b1* and downregulation of *Nr4a1* following LSD, and upregulation of genes involved in cholesterol and lipid metabolism following HSD (*Scd2*, *Hsd17b7*, *Cyp51*, *Msmo1*, *Fdps*).

Altogether, these results indicate that challenges affecting the ZG and ZF, such as salt diets and modulation of the HPA axis, also affect the ZX, in particular its regression with time and cell lineage conversion rate from the ZF.

Discussion

In this work we have explored how environmental cues affecting mineralocorticoid output, such as salt diets, modulate adrenal cortex homeostasis, cell lineage conversion and zone-specific transcriptional landscape. To this purpose, we have used multiple complementary morphological, functional and molecular investigations on a newly developed *Cyp11b2*^{cre} mouse model. This model, in which the Cre recombinase is inserted into the 3'UTR of the *Cyp11b2* gene, conserves normal ZG function, allowing its use to explore mineralocorticoid pathophysiology. We show that *Cyp11b2* expression is detectable as early as P1 in different areas of the ZG and a progressive reduction of ZG size and evolution of cell components of the adrenal cortex with age. Cell lineage conversion in *Cyp11b2*$^{+/Cre}$*-mTmG* mice showed the typical progressive transdifferentiation of ZG into ZF cells over time, progressing into the ZX in females, revealing a previously unrecognized connection between ZF and ZX cells in adult mice. A 2-weeks HSD or LSD, starting from 4 weeks of age, modulates mineralocorticoid output mainly by regulating steroidogenic gene expression, with little modifications of the number of ZG cells, but induces a major, sexually dimorphic, cellular and transcriptional remodelling in the ZF, which is also the major hallmark of recovery. A similar reciprocal response of the ZG is observed when challenging the ZF by DEX treatment, indicating a functional and molecular interaction between ZG and ZF to adapt to pathophysiological challenges.

Our study has allowed gaining insight into major processes involved in adrenal growth and reveals dynamic changes of adrenal cortex cell composition over time that are associated with functional and structural evolution and hormone production. GFP$^+$ cells were present in large areas of the adrenal surface already at P1, reflecting expression of *Cyp11b2,* and expanded into the entire ZG by two weeks of age, with cell lineage conversion proceeding into the entire ZF between 6 and 9 weeks of age in both males and females. These data are different from a previous model, in which the Cre recombinase was inserted into exon 2 of the *Cyp11b2* gene[19]. This may be due to a certain degree of *Cyp11b2* haploinsufficiency in the previous model, which, although without overt phenotype during postnatal life, may have modified *Cyp11b2* expression during embryonic development and subsequent expansion of AS expressing cells. We observed a progressive reduction of Dab2$^+$ cells between 2 and 6 weeks of age, which was paralleled by a reduction of plasma aldosterone levels. This is in agreement with the evolution of aldosterone levels in humans, where high aldosterone levels are observed in newborns, progressively decreasing with age[25–27]. Remarkably, our data show that lineage conversion in female mice progresses into the ZX, as evidenced by the coexpression of mGFP and 20αHSD, a ZX marker, in female 6- and 9-weeks old *Cyp11b2*$^{+/Cre}$*-mTmG* mice. Previous lineage tracing experiments have shown that the mouse adult cortex derives from precursor cells in the foetal cortex, demonstrating a direct link between the foetal and adult zones during development[14]. It has further been postulated that the foetal zone derives from the definitive zone through centripetal migration of cells[28]. Consistent with these models, recent data suggest a shared progenitor between the definitive and foetal zones in humans and cynomolgus monkey[29]. This "adrenal primordium" can differentiate into the definitive zone or the foetal zone through a direct pathway; in addition, an indirect pathway has been identified in which cells from the definitive zone differentiate further into the foetal zone, which thus represents the final stage of lineage conversion[29]. Our data indicate that, unlike the faster transdifferentiation observed between ZG and ZF, final lineage conversions from the ZF to the ZX proceeds much slower and never fully completes the process. Further investigations employing specific cell lineage tracing models may allow to further delineate this process.

Our results also suggest that the response of the ZG to a 2-week salt challenge with a LSD or HSD does not involve major modifications of ZG structure and cell lineage conversion, with only little modifications in ZG size, but is rather mediated by an effect on *Cyp11b2* expression, both by modulating its expression levels as well as the number of AS expressing ZG cells. Only a small increase in the ZG cluster was revealed by the resolution of ST. This is consistent with previous observations by Nishimoto et al, in which a short salt challenge to rats did not expand the ZG[24], while other models showed increased ZG following a low salt diet[23]. It is interesting to note that we show a progressive reduction of ZG size until 4 weeks of age, suggesting a reduced proliferative capacity of the adrenal ZG afterwards. This supports a hypothesis whereby timing of salt challenge, in addition to duration, may influence the expansive capacity of the ZG. Remarkably, we reveal a sexually dimorphic cellular and transcriptional adaptation to salt challenges, as well as interactions between the different cell layers of the adrenal cortex. Indeed, the resolution of ST allows to appreciate a small increase or decrease of the ZG cluster following a LSD or HSD respectively, associated with changes in the expression genes related to ZG cell identity and function. In addition, major modifications are observed in the ZF, which responds to salt challenges with changes in size and a large transcriptional and sexually dimorphic remodelling, which also contributes to recovery of the adrenal cortex after returning to normal salt diet. RAS modulation did not appear to affect the Wnt/β-catenin pathway in our experimental conditions. Previous studies have shown that changes in Wnt/β-catenin impact *Cyp11b2* expression and aldosterone production, as described in the Wnt4-deficient model ($Wnt4^{-/-}$)[30] and in studies using constitutive β-catenin activation (β-cat-GOF model)[31,32]. Our study indicates that, conversely, signals that increase (LSD) or decrease (HSD) *Cyp11b2* expression and aldosterone production do not affect Wnt/β-catenin signalling. Thus, salt diets do not appear to alter the main signalling pathway involved in maintaining the cellular identity and differentiation of the ZG, suggesting that RAS and Wnt/β-catenin pathways may regulate ZG through different, complementary mechanisms and that AS itself may be a component of ZG identity, whose expression is not only regulated towards maintaining salt and water homeostasis but may also play a role in more complex cellular functions.

DEX suppression is well known to suppress the endogenous HPA axis, inducing major changes in the adrenal cortex, including ZF atrophy with increased apoptosis, decreased *Cyp11b1* expression and corticosterone production. Recovery following DEX suppression involves cortical sonic hedgehog $(Shh)^+$ progenitor cells and Shh-responsive capsular cells, as well as WNT signalling[22]. Here we show that DEX treatment induces major ZF atrophy and infiltration of macrophages, which is more pronounced in males, as well as a general suppression of corticosteroid production, with reduced aldosterone levels particularly evident in females, which may be related to the role of ACTH in regulating aldosterone production. However, beyond this endocrine regulation, DEX suppression also led to an important transcriptional induction in the ZG in male mice, a process mirroring what is observed under HSD or LSD. This was accompanied by an activation of the Wnt/β-catenin pathway, as previously described[22]. Male mice appear to be more susceptible to DEX; possible explanations include the faster rate of adrenal cortex renewal in females and the capacity of females to replenish ZF from both subcapsular stem/precursor cells and ZG cells[18]. This would also explain why females do not increase their ZG cell pool, as seen in ST, to cope with cell loss and ZF atrophy, in contrast to what is observed in males.

Overall, our experiments also show only slight changes in cell lineage conversion following a LSD or HSD or following DEX treatment. Although this is in agreement with the lack of major structural modifications following a LSD or HSD, but not DEX treatment, one alternative explanation may be that the speed of lineage conversion in our model does not allow to well identify such changes, as transdifferentiation at the start of the treatment at 4 weeks of age has

well progressed into the entire adrenal cortex. An inducible model of Cre recombination allowing to activate the recombinase at the beginning or immediately before beginning of the challenge may allow to more precisely address the effect of challenges on cell lineage conversion. Indeed, our results show that both salt diets and DEX treatment affect the regression of the ZX with time and cell lineage conversion rate from the ZF, indicating that the ZX is affected by challenges affecting the ZG and ZF, and that effects on cell lineage conversion may become evident in a slower proliferating zone.

In conclusion, our study provides new insight into adrenal cortex cell lineage conversion and its dynamic adaptation to pathophysiological challenges. We reveal a sexually dimorphic cellular and transcriptional response to salt diets and DEX treatment, involving all layers of the adrenal cortex, and the reciprocal contribution of ZG and ZF cells to this response. Future investigations may allow to further define adrenal cortex cell dynamics and cell-specific transcriptional remodelling towards adaptation to environmental cues. In addition, these data may serve as a framework to better understand how genetic susceptibility may modulate this response, eventually leading to aldosterone dysregulation and PA in extreme cases.

Materials and methods

Handling and generation of Cyp11b2$^{+/Cre}$-*m*T*m*G mouse model

Animal studies were conducted according to the guidelines and regulations formulated by the European Commission for experimental use (Directive 2010/63/EU). The use of the animals and the experimental protocol were approved by the local Ethics committee of Paris Cité University (N° 17-020) and by the French Ministère de l'Enseignement Supérieur, de la Recherche et de l'Innovation (APAFIS authorization number #11509-201703281427107 v4) and were conducted in accordance with the relevant codes of practice for the care and use of animals for scientific purposes. All animals were group-housed and bred in a dedicated husbandry specific pathogen-free (SPF) facility with 12 h/12 h light-dark cycles, had ad libitum access to food and water, and were checked daily. Their health status was routinely checked to maintain SPF grade. The *Cyp11b2^{Cre}* mouse model was generated and validated on a C57BL/6J congenic background by GenOway (France). To generate the tissue specific reporter mouse model, the *Cyp11b2$^{+/Cre}$* mice were crossed with theGt(ROSA)$^{26Sortm4(ACTB-tdTomato-EGFP)Luo/J}$ reporter mouse model (Jackson:007676), bearing a two-color fluorescent Cre-reporter allele, to generate the *Cyp11b2^{Cre}*-*m*T*m*G line. In the absence of Cre recombination, tdTomato (*m*T) fluorescence is widespread in all cells/tissues. Cells expressing Cre recombinase and future cell lines derived from these cells exhibit eGFP (*m*G) expression located at the plasma membrane instead of *m*T fluorescence. All experiments were conducted on male and female heterozygous Cre mice. To respond to ethical requirement and reduce the number of animals used, the same control mice were used for different experiments: 4-weeks old mice for age studies and Ctrl T_1 LSD, HSD and DEX, 6-weeks old mice for age studies and Ctrl T_2 LSD and HSD, 7-weeks old mice for age studies and Ctrl T_2 DEX. For genotyping the following primers were used: Cre Forward: GCTCCTGCTTCACCATGTGAGCAG; Cre Reverse: GG ACCAGCTATAGAGACCTCACCAACAC.

Blood and plasma collection

Blood was collected from the retro-orbital venous plexus with heparin-coated capillaries under isoflurane (3%) anaesthesia. Blood was centrifugated at 2000 rcf for 15 minutes at 4°C to obtain plasma. Plasma was stored at -20°C for further analysis.

Diets

Male and female mice were fed different diets for a period of two weeks, from the age of 4 weeks until reaching 6 weeks of age (Figure 2a, and 4a, time point 1, T1): Standard (0.28% Na^+; 0.86% K^+, A03SP-10, SAFE, France), Low salt diet, LSD (<0.03% Na^+; 0.8% K^+, E15430-247, Ssniff, Soest, Germany), and High salt diet, HSD (3.2% Na^+; 0.97% K^+) (E15433-347, Ssniff, Soest, Germany). Half of the mice were sacrificed at the end of the period, while the others returned to a standard diet and were housed under normal conditions for 1 week and sacrificed at the age of 7 weeks (time point 2, T2). For all timepoints, the corresponding control animals were investigated (Ctrl T1, Ctrl T2).

Dexamethasone treatment

Male and female mice were subjected to dexamethasone (DEX) treatment from the age of 4 weeks for a period of two weeks until reaching the age of 6 weeks. Half of the mice were sacrificed at the end of the treatment (time point 1, T1) while the others were removed from the treatment and housed under normal conditions for 3 weeks of recovery and sacrificed at the age of 9 weeks (time point 2, T2). For both timepoints, the corresponding control animals were

investigated (Ctrl T1, Ctrl T2). DEX (DEXFREE eye drops, 1mg/ml) was administered via drinking water, protected from the light, at a concentration of 0.5% (m/v) ab libitum and changed every 48 hours to avoid compound degradation. The taste of water is not altered, and the volume of water consumed by mice under treatment was comparable to that of control mice. The mice under treatment were housed in cages of four animals maximum to avoid possible difficulties of access to water.

Western blot

6 weeks old WT, *Cyp11b2*$^{+/Cre}$ and *Cyp11b2*$^{Cre/Cre}$ female and male mice were used for western blot analysis. Total proteins were extracted using RIPA buffer (RB 4475, BioBasic Canada) with EDTA-free protease and phosphatase inhibitor (Bimake), Tissue lysates were then spinned down for 30 min at 4°C and centrifuged at 13000 rpm for 15 min at 4°C. Protein concentration was determined using Bradford protein essay (Biorad). 20 µg of total proteins were loaded on 10% Acrylamide SDS-PAGE gel, transferred onto nitrocellulose membrane and tagged with the following antibodies: mCyp11b2 (1:500 in TBS-T 5% milk, generous gift from CE Gomez-Sanchez), goat anti-rabbit IgG (H+L)-HRP conjugate antibody (1/5000, #1706515, Bio Rad), Vinculin (1/5000, V9131, Sigma-Aldrich) and anti-mouse IgG, HRP-linked antibody (1/2500, #1706516, Bio Rad). The signal was developed by Clarity Max™ Western ECL substrate (Biorad, Hercules, CA), detected by Fujifilm Las-4000 mini Luminescent image analyser (Fujifilm, Tokyo-Japan) and quantified by Multi gauge software (Fujifilm, Tokyo-Japan). The expression of total proteins was normalized to the expression of the housekeeping protein Vinculin.

Histological examination and immunostaining

Mice were anesthetized with isoflurane (3%) and after confirming the lack of paw-pinch reflex, sacrificed by cervical dislocation after blood sampling. Right adrenal was snap frozen in liquid nitrogen and left adrenal was processed for histology as following. The tissue was fixed in 4% PFA O/N and partially dehydrated through successive immersions into 10%, 20% and 30% sucrose solutions for 24 hours each. Adrenals were subsequently placed in embedding moulds and embedded with pure optimal cutting temperature (OCT) compound and isopentane and stored at −80 °C. Adrenals were sectioned in 10 µm cuts using an Epredia™ Cryostat CryoStar™ NX70, at a temperature of -30°C, transferred to a Superfrost Plus™ Microscope Slides and then stored at -80°C. For histological analysis H&S staining was performed using the Rapid Frozen Sections H&S staining kit (Bio-Optica, 04-061010) following the manufacturer's instructions and dehydrated through 10 immersions in 95% ethanol, 10 immersions in 100% ethanol and 20 immersions in Xylene. The sections were then mounted using Pertex (Histolab, 00840). For immunofluorescence studies tissues were permeabilized for 15 min either with TBS 0.1% Triton X100 (mCyp11b2 and Ki67) or PBS 0.1% Triton X100 (20αHSD and Dab2). The sections were then blocked with 5% BSA and 10% normal donkey serum (NDS) diluted in TBS 0.05% Triton X100 (mCyp11b2, Ki67) or 10% NDS in PBS 0.1% Triton X100 (20αHSD and Dab2) for 2 hours at room temperature. For mCyp11b2 and Ki67 detection primary antibodies were diluted in 3% BSA and 3% NDS diluted in TBS 0.05% Triton X100 and incubated overnight at 4°C whereas for 20αHSD and Dab2 detection, the primary antibodies were diluted in 1% NDS in PBS 0.1% Triton X100. The following primary antibodies were used: mouse Cyp11b2 (mCyp11b2, 1/100, generous gift from CE Gomez-Sanchez), Dab2 (1/1600, Cell Signalling, D709T), Ki67 (1/1000, Abcam, ab15580), 20αHSD (1/500, generous gift from Yacob Weinstein). Donkey anti-rabbit Alexa 647, diluted 1/1000 in 3% BSA or 3% NDS diluted in PBS/TBS 0.05% Triton X100 was used as secondary antibody for 2 hours at room temperature. Nuclei were counterstained using 4′,6-diamidino-2-phenylindole (DAPI) (1/5000, Roche Diagnostics GmbH). Whole slide imaging (WSI) was

performed for all the sections using the Olympus Slideview VS200 digital slide scanner (Olympus Corporation, Tokyo, Japan). The region of interests (ROIs) and focus points in the ROI were automatically recognized by the scanner and, in order to reach a high image quality, focus points were manually updated by the user. The slides were scanned using the UPlanXApo 20x/0.80 objective lens, which provides a high numerical aperture for superior resolution and image clarity.

Image analysis

The quantitative analysis of the immunofluorescence images was performed using HALO software (version 3.6.4134, Indica Labs) with the HighPlex Fl v4.2.14 module. The fluorescence TIFF images were imported into HALO. Background correction was applied to reduce non-specific fluorescence and autofluorescence in the tissue. All three channels (DAPI, Alexa Fluor 488, Alexa Fluor 594 and Alexa Fluor647) were aligned to ensure accurate signal quantification. ROIs corresponding to the adrenal tissue were manually annotated. Artefacts, left adipose tissue around the adrenal and the medulla were manually removed and excluded from the analysis. DAPI was used for traditional nuclear segmentation within the ROIs. Alexa Fluor 488 was used to detect the GFP^+ membrane and Alexa Fluor 594 to detect the mTomato in the Cyp11b2$^{+/Cre}$-*m*T*m*G mice. Cyp11b2-, Dab2-, Ki67- and 20αHSD- positive cells were identified using Alexa Fluor 647. Fluorescence intensity thresholds were set for all the channels based on the intensity of the signal.

Bi-photon imaging

The images were acquired with the Leica SP8-Dive biphoton. The tile scans were lunched with Z-stack 125um, Z step size 2um. and a 3D visualization and 3D reconstruction followed by the mosaic merge with LSA X software.

In situ mRNA analysis

In situ mRNA analysis was performed using the RNAscope assay (ACD, Biotechne). For RNAscope experiments, frozen slides were used of *Cyp11b2*$^{+/Cre}$-*m*T*m*G mice. RNAscope for mouse *Cyp11b2* and *Cyp11b1* was performed according to the manufacturers' instructions using the RNAscope 2.5 HD Duplex Detection kit (ACD, Biotechne). In brief, slides were heated for 30 min at 60°C and post-fixed with 4% PFA in 1x PBS for 15 min at 4°C. Tissues were dehydrated by consecutive baths in 50%, 70% and 100% ethanol for 5 min each and then air-dried for 5 min at room temperature. Slides were then immersed in the pre-heated 1x Target Retrieval solution for 5 min and then wash with MilliQ water. After rinsing in fresh 100% ethanol the slides were air-dried. RNAscope® Protease Plus solution was applied to the slides which were then incubated for 30 mins at 40°C. The hybridisation probe mixture (*Cyp11b1* and *Cyp11b2*) was added to the sections for 2hrs at 40°C. For amplification, AMP 1 solution was added to the slide and incubated for 30min at 40°C. The same steps were repeated for 6 cycles of amplification. A signal detection step is performed by adding Fast-RED substrate/slide for 10 min at room temperature. Four additional AMP hybridisation steps were performed for the second probe followed by a green signal detection step by adding GREEN substrate for 10min at RT. The slides were then counterstained with 50% haematoxylin for 2 min at room temperature and mounted.

RNA extraction and RT-qPCR analysis.

Total RNA was isolated from adrenal using Janke and Kunkel's Ultra-Turrax T25 (IKA technologies, Staufen DE) and TRIzol (Invitrogen, 15596018). After Deoxyribonuclease I treatment (Invitrogen, 18068-015), cDNA was generated from 0.5 µg of RNA with with iScript™ cDNA Synthesis Kit (Bio-Rad, 1708891). Duplicates of cDNA samples were then

amplified on the CFX Opus 96 Real-Time PCR System using SYBR Green Supermix (Bio-Rad, 1725274). Normalization for RNA quantity and reverse transcriptase efficiency was performed against three reference genes (geometric mean of the expression of Ribosomal 18S RNA, β2-microglobulin and Ubiquitin C). Quantification was performed using the $2^{\wedge-\Delta\Delta Ct}$ analysis. Sequences of primers are listed in following table.

Gene	Forward primer	Reverse primer
18S	5′-CCCTGCCCTTTGTACACACC-3′	5′-CGATCCGAGGGCCTCACTA-3′
mβ2-microglobulin	5′-ATTCACCCCCACTGAGACTG-3′	5′-TGCTATTTCTTTCTGCGTGC-3′
mUbiquitinC	5′-GTGCTTCATCCACTGGCTGGAA-3′	5′-GTCTGCGATAGGACCTGGTTGA-3′
mStAR	5′-GTGCTTCATCCACTGGCTGGAA-3′	5′-GTCTGCGATAGGACCTGGTTGA-3′
mCyp11b1	5′-TGTATCGAGAGCTGGCAGAG-3′	5′-CCTGGATGGCATCCATTGAC-3′
mCyp11b2	5′-ACCTACAGTGGCATTGTG-3′	5′-GATTGCTGTCGTGTCAAC-3′
mWnt4	5′-CCCTGTCTTTGGGAAGGTGGTG-3′	5′-CACCTGCTGAAGAGATGGCGTATAC-3′
mTcf3	5′-CAGATGGTGGCCTGGATACT-3′	5′-CATCCCTGCTGTAGCTGTCA-3′
mLef1	5′-AAATGGGTCCCTTTCTCCAC-3′	5′-TCGTCGCTGTAGGTGATGAG-3′
mAxin2	5′-AGCCTAAAGGTCTTATGTGG-3’	5′-ATGGAATCGTCGGTCAGT-3′
mBcl2	5’-GCCCTGTGGATGACTGAGTA-3’	5’-GCTGGGGCCATATAGTTCCA-3’
mTrp53	5’-ATTTCACCCTCAAGATCCGC-3’	5’-AACTCTAAGGCCTCATTCAGCT-3’
mCasp3	5’-TGGAGAACAACAAAACCTCAGT-3’	5’-TCCACTGACTTGCTCCCATG-3’

Steroid Profiling and analysis

Plasma steroids (pregnenolone, progesterone, 11-deoxycorticosterone, corticosterone, 18-hydroxy-11-deoxycorticosterone, 18-hydroxycorticosterone, aldosterone, 18-hydroxycortisol) were simultaneously measured in a 13-minute run by Liquid Chromatography coupled to tandem Mass Spectrometry as previously described[33]. Heatmap analysis of steroid hormone concentrations was based on a Z-score normalized matrix of hormone variables, using the *pheatmap* package (v1.0.12) in R, with hierarchical clustering applied to the variables. Z-scores were calculated by subtracting the mean of each variable from individual data points and dividing by the corresponding standard deviation. A diverging color scale was used to represent the Z-score normalized hormone concentrations, ranging from deep blue ($Z \leq -1$), through white ($Z = 0$), to deep red ($Z \geq +1$). Values outside this range were capped and mapped to the deepest blue or red, to minimize the influence of extreme values on the color gradient. Principal component analysis (PCA) was performed on the original data using the *FactoMineR* package (v2.11) with default standardization, and visualized with the *factoextra* package (v1.0.7). All analyses were performed in R (v4.4.2).

Spatial transcriptomics

Sample Preparation. 34 tissue sections (17 males, 17 females) were used for ST. Fluorescent images were acquired on a Vectra 3 Automated Quantitative Pathology Imaging System (Akoya Bioscience) and stitched using Halo software (Excilone). The spatial gene expression process including probe hybridization, probe ligation, enabled probe release with CytAssist and extension was performed using Visium CytAssist Spatial Gene Expression for FFPE, Mouse Transcriptome, 6.5mm, 4 rxns (1000521, 10X Genomics) according to the manufacturer's instructions. Briefly, sections were decrosslinked at 95°C for 60min, then Mouse WT pairs of probes, targeting 21000 genes, were incubated overnight. Paired probes were linked then transferred on the Visium slide using the Cytassist system. The spatial gene libraries were constructed using Probe-based Library Construction (10X Genomics). Library quantification and quality assessment was performed using Qubit fluorometric assay (Invitrogen) with dsDNA HS (High Sensitivity) Assay Kit, Bioanalyzer Agilent 2100 using a High Sensitivity DNA chip and KAPA Library Quantification Kit Illumina Platforms (Roche). Libraries were then sequenced on a NovaSeq 6000 (Illumina) using paired-end 28 x 50 bp with a depth of sequencing of 25,000 reads per spot.

Data analysis. Sequencing reads were demultiplexed and aligned to the mouse reference transcriptome (mm10-2020-A), using the spaceranger Pipeline (v2.0.0) in default mode. Loupe browser from 10X Genomics was used to align the barcoded spot patterns, perform spots selection on the tissue and do the pathological annotation. SpotClean (v1.4.1) was used to calculate the peer-spot contamination rates and to decontaminate the gene expression profiles from the spot swapping effect. The corrected UMI counts were loaded into Seurat (v5.10) for quality control, data integration and downstream analyses. Empty spots (nCount < 1) were removed and the data from each sample were log normalised and the effect of different number of counts (nCount) among samples was removed during scaling. For each sample, the top 3000 highly variable genes were selected using the FindVariableFeatures function. Batch effect between samples was corrected using Seurat's FindIntegratedAnchors, and the samples were integrated using cca reduction. On the integrated dataset, dimensionality reduction was performed using principal component (PC) analysis computed on the first 30 PC. FindNeighbors was used to compute the k-nearest neighbor graph on the low-dimensional embedding, and FindClusters was used to cluster the spots with multiple resolutions (from 0.8 to 2). Finally, the maximum resolution (r=2) was considered to better align with the expected cell populations, and it was used for visualisation and all downstream analyses. Cell type labels were assigned to resulting clusters based on a manually curated list of marker genes as well as previously defined signatures of the well-known adrenal gland subtypes (Table S1). All clusters were annotated, and 6589 spots were kept for further analysis.

Differential expression analysis was performed on log-normalized non-batch-corrected data using Wilcoxon testing with Bonferroni correction as implemented in the FindMarkers function. Only genes with adjusted p-values < 0.05 were selected as significant. The lists of differentially expressed genes were further divided into UP and DOWN regulated genes based on the avg_log2FC; avg_log2FC >0 for the UP regulated genes and 4avg_log2FC <0 for the DOWN regulated ones. The signature scores were calculated using the function AddModuleScore_UCell from UCell, and a combination of Scpubr (v2.0.2) and ggplot 2 was used in all the figures. GSEA analysis was performed using the fgsea package (v1.28.0) and the Kegg gene sets belonging to the Mouse MSigDB Collections (v2024.1). As each spot might contain a mixture of cell populations, deconvolution analysis using a reference-free approach was required to recover the correct organisation of the tissues. The deconvolution of the spatial spots was performed using the Stdeconvolve [] package. The spot coordinates, the raw counts and the cell annotation were extracted directly from the Seurat object and the pixels with less than 100 genes and 10 counts were removed. The deconvolution was performed assuming a

maximum of 9 cell populations and the parameters that led to the minimum perplexity of the LDA model were selected for downstream analysis. The pie charts and all the figures were generated using a combination of ggplot and the internal function vizAllTopics[34]. In total, we deconvolved 4 main populations, ZG, ZF, ZX and Medulla, with additional components associated with a mixture of the main populations and immune cells (Figure S17). We then compared the result of the deconvolution and the spatial expression patterns of the markers used for the annotation. In both cases, there was a good correlation with the spatial organisation observed in the histological images. In particular, the regions with a high degree of mixture were found either in the peripheral zones between distinct layers of the tissue or in sections where the tissues were folded and overlapped (Figure S17).

Statistical analyses

Each symbol in graphical representations show data Plot show mean ± SEM Quantitative variables are reported as means ± SEM when Gaussian distribution or medians and interquartile range when no Gaussian distribution. Parametric tests were applied only if normal distribution could be confirmed. Pairwise comparisons were done with unpaired t-test or Mann-Whitney test respectively; global comparison was evaluated using ANOVA or Kruskall Wallis test, followed by Sidak's or Dunn's multiple comparison test. A p value < 0.05 was considered significant for comparisons between 2 groups. Analyses were performed using Graphpad Prism 10 (GraphPad software Inc, San Diego, CA).

Acknowledgments

This work was funded through the European Union's Horizon 2020 research and innovation programme under the Marie Sklodowska-Curie grant agreement No. 954798 (MINDSHIFT804 ITN) institutional support from INSERM, by the Agence Nationale pour la Recherche (ANR-18-CE93-0003-01), the Fondation pour la Recherche Médicale (EQU201903007864).

References

1. Monticone, S. *et al.* Prevalence and Clinical Manifestations of Primary Aldosteronism Encountered in Primary Care Practice. *J. Am. Coll. Cardiol.* **69**, 1811–1820 (2017).
2. Mulatero, P. *et al.* Genetics, prevalence, screening and confirmation of primary aldosteronism: a position statement and consensus of the Working Group on Endocrine Hypertension of The European Society of Hypertension ∗. *J. Hypertens.* **38**, 1919–1928 (2020).
3. Rossi, G. P. *et al.* A Prospective Study of the Prevalence of Primary Aldosteronism in 1,125 Hypertensive Patients. *J. Am. Coll. Cardiol.* **48**, 2293–2300 (2006).
4. Adler, G. K. *et al.* Primary Aldosteronism: An Endocrine Society Clinical Practice Guideline. *J. Clin. Endocrinol. Metab.* **110**, 2453–2495 (2025).
5. Brown, J. M. *et al.* The Unrecognized Prevalence of Primary Aldosteronism: A Cross-sectional Study. *Ann. Intern. Med.* **173**, 10–20 (2020).
6. Zennaro, M.-C., Boulkroun, S. & Fernandes-Rosa, F. L. Pathogenesis and treatment of primary aldosteronism.
7. Azizan, E. A. B., Drake, W. M. & Brown, M. J. Primary aldosteronism: molecular medicine meets public health. *Nat. Rev. Nephrol.* **19**, 788–806 (2023).
8. Le Floch, E. *et al.* Identification of risk loci for primary aldosteronism in genome-wide association studies. *Nat. Commun.* **13**, 5198 (2022).
9. Naito, T. *et al.* Genetic Risk of Primary Aldosteronism and Its Contribution to Hypertension: A Cross-Ancestry Meta-Analysis of Genome-Wide Association Studies. *Circulation* **147**, 1097–1109 (2023).
10. Inoue, K. *et al.* Primary Aldosteronism and Risk of Cardiovascular Outcomes: Genome-Wide Association and Mendelian Randomization Study. *J. Am. Heart Assoc.* **13**, e034180 (2024).
11. Borges, K. S. *et al.* Non-canonical Wnt signaling triggered by WNT2B drives adrenal aldosterone production. Preprint at https://doi.org/10.1101/2024.08.23.609423 (2024).
12. Zubair, M., Ishihara, S., Oka, S., Okumura, K. & Morohashi, K. Two-Step Regulation of *Ad4BP/SF-1* Gene Transcription during Fetal Adrenal Development: Initiation by a Hox-Pbx1-Prep1 Complex and Maintenance via Autoregulation by Ad4BP/SF-1. *Mol. Cell. Biol.* **26**, 4111–4121 (2006).
13. Hershkovitz, L., Beuschlein, F., Klammer, S., Krup, M. & Weinstein, Y. Adrenal 20α-Hydroxysteroid Dehydrogenase in the Mouse Catabolizes Progesterone and 11-Deoxycorticosterone and Is Restricted to the X-Zone. *Endocrinology* **148**, 976–988 (2007).
14. Zubair, M., Parker, K. L. & Morohashi, K. Developmental Links between the Fetal and Adult Zones of the Adrenal Cortex Revealed by Lineage Tracing. *Mol. Cell. Biol.* **28**, 7030–7040 (2008).
15. Pihlajoki, M., DÃ¶rner, J., Cochran, R. S., Heikinheimo, M. & Wilson, D. B. Adrenocortical Zonation, Renewal, and Remodeling. *Front. Endocrinol.* **6**, (2015).
16. Grabek, A. *et al.* The Adult Adrenal Cortex Undergoes Rapid Tissue Renewal in a Sex-Specific Manner. *Cell Stem Cell* **25**, 290-296.e2 (2019).
17. Salmon, T. N. & Zwemer, R. L. A study of the life history of cortico-adrenal gland cells of the rat by means of trypan blue injections. *Anat. Rec.* **80**, 421–429 (1941).
18. Lyraki, R. & Schedl, A. Adrenal cortex renewal in health and disease. *Nat. Rev. Endocrinol.* **17**, 421–434 (2021).
19. Freedman, B. D. *et al.* Adrenocortical Zonation Results from Lineage Conversion of Differentiated Zona Glomerulosa Cells. *Dev. Cell* **26**, 666–673 (2013).

20. Simon, D. P. & Hammer, G. D. Adrenocortical stem and progenitor cells: Implications for adrenocortical carcinoma. *Mol. Cell. Endocrinol.* **351**, 2–11 (2012).
21. Pignatti, E., Leng, S., Carlone, D. L. & Breault, D. T. Regulation of zonation and homeostasis in the adrenal cortex. *Mol. Cell. Endocrinol.* **441**, 146–155 (2017).
22. Finco, I., Lerario, A. M. & Hammer, G. D. Sonic Hedgehog and WNT Signaling Promote Adrenal Gland Regeneration in Male Mice. *Endocrinology* **159**, 579–596 (2018).
23. Vohra, T. *et al.* Effect of Dietary Sodium Modulation on Pig Adrenal Steroidogenesis and Transcriptome Profiles. *Hypertension* **76**, 1769–1777 (2020).
24. Nishimoto, K., Harris, R. B. S., Rainey, W. E. & Seki, T. Sodium Deficiency Regulates Rat Adrenal Zona Glomerulosa Gene Expression. *Endocrinology* **155**, 1363–1372 (2014).
25. Bae, Y. J. *et al.* Reference intervals of nine steroid hormones over the life-span analyzed by LC-MS/MS: Effect of age, gender, puberty, and oral contraceptives. *J. Steroid Biochem. Mol. Biol.* **193**, 105409 (2019).
26. Miller, J. J. *et al.* Pediatric reference intervals for endocrine markers in healthy children and adolescents on the Liaison XL (DiaSorin) immunoassay system. *Clin. Biochem.* **120**, 110644 (2023).
27. Frederiksen, H. *et al.* Sex- and age-specific reference intervals of 16 steroid metabolites quantified simultaneously by LC-MS/MS in sera from 2458 healthy subjects aged 0 to 77 years. *Clin. Chim. Acta* **562**, 119852 (2024).
28. Ishimoto, H. & Jaffe, R. B. Development and Function of the Human Fetal Adrenal Cortex: A Key Component in the Feto-Placental Unit. *Endocr. Rev.* **32**, 317–355 (2011).
29. Cheng. The developmental origin and the specification of the adrenal cortex in humans and cynomolgus monkeys. *Sci. Adv.* (2022).
30. Heikkilä, M. *et al.* Wnt-4 Deficiency Alters Mouse Adrenal Cortex Function, Reducing Aldosterone Production. *Endocrinology* **143**, 4358–4365 (2002).
31. Pignatti, E. *et al.* Beta-Catenin Causes Adrenal Hyperplasia by Blocking Zonal Transdifferentiation. *Cell Rep.* **31**, 107524 (2020).
32. Berthon, A. *et al.* Constitutive β-catenin activation induces adrenal hyperplasia and promotes adrenal cancer development. *Hum. Mol. Genet.* **19**, 1561–1576 (2010).
33. De Sousa, K. *et al.* Genetic, Cellular, and Molecular Heterogeneity in Adrenals With Aldosterone-Producing Adenoma. *Hypertension* **75**, 1034–1044 (2020).
34. Miller, B. F., Huang, F., Atta, L., Sahoo, A. & Fan, J. Reference-free cell type deconvolution of multi-cellular pixel-resolution spatially resolved transcriptomics data. *Nat. Commun.* **13**, 2339 (2022).

Figures

Figure 1

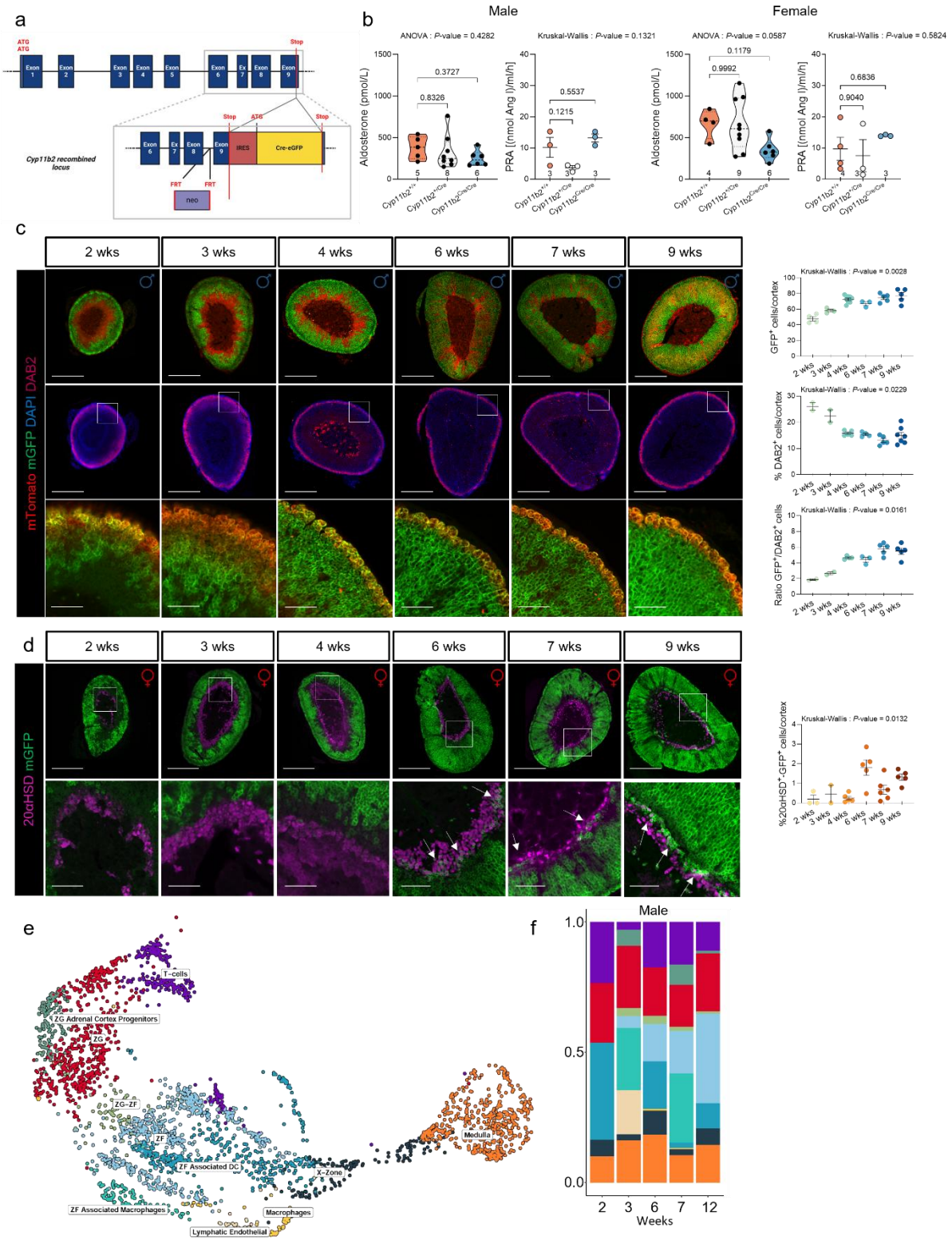

Figure 1. Characterization of the adrenal phenotype of the *Cyp11b2*^{Cre} mouse model. (a). Cre recombinase was inserted into the 3' untranslated region of the *Cyp11b2* gene, after an internal ribosomal entry site (IRES). The insertion of an IRES allows the translation of two different proteins from a single mRNA transcript, resulting in a functional aldosterone synthase

protein. **(b).** Plasma aldosterone levels (ordinary one-way ANOVA, followed by Šídák's multiple comparisons test) and Plasma Renin Activity (PRA, Kruskal-Wallis test followed by Dunn's multiple comparisons test) of *Cyp11b2* $^{+/+}$ (orange), *Cyp11b2*$^{+/Cre}$ (white) and *Cyp11b2*$^{Cre/Cre}$ (light blue) male (left) and female (right) 6 weeks old mice. **(c).** Co-immunofluorescence of mGFP (green) with mTomato (red) and DAB2 (ruby red) of male *Cyp11b2*$^{+/Cre}$-*m*T*m*G mouse adrenals at 2, 3, 4, 6, 7 and 9 weeks of age and quantification of mGFP^{+} cells and DAB2^{+} cells, with the analysis of cell lineage conversion expressed as the ratio of the number of cells expressing mGFP over the cortex area or the number of cells expressing DAB2. P values were obtained with Kruskal-Wallis test followed by Dunn's multiple comparisons test. **(d).** Co-immunofluorescence of mGFP (green) and 20αHSD (purple) of female *Cyp11b2*$^{+/Cre}$-*m*T*m*G mouse adrenals of 2, 3, 4, 6, 7 and 9 weeks of age. Quantification of 20αHSD positive cells and mGFP/20αHSD double-positive cells per cortex area (indicated by white arrows in the lower panel magnified image) at different time points. White squares represent the magnification area in the lower panel. The 7 weeks image has been used on Figure 8d. P values were obtained with Kruskal-Wallis test followed by Dunn's multiple comparisons test. Scale Bar: 500 μm upper panels with entire adrenals and 100 μm lower panels. **(e).** uMAP of adrenal cell clusters from male *Cyp11b2*$^{+/Cre}$-*m*T*m*G mice of 2, 3, 6, 7 and 12 weeks of age. **(f)**. Cell cluster proportions of male *Cyp11b2*$^{+/Cre}$-*m*T*m*G mice of 2, 3, 6, 7 and 12 weeks of age. Data are shown as mean ± SEM. *P value < 0.05; **P value < 0.01; ***P value < 0.001.

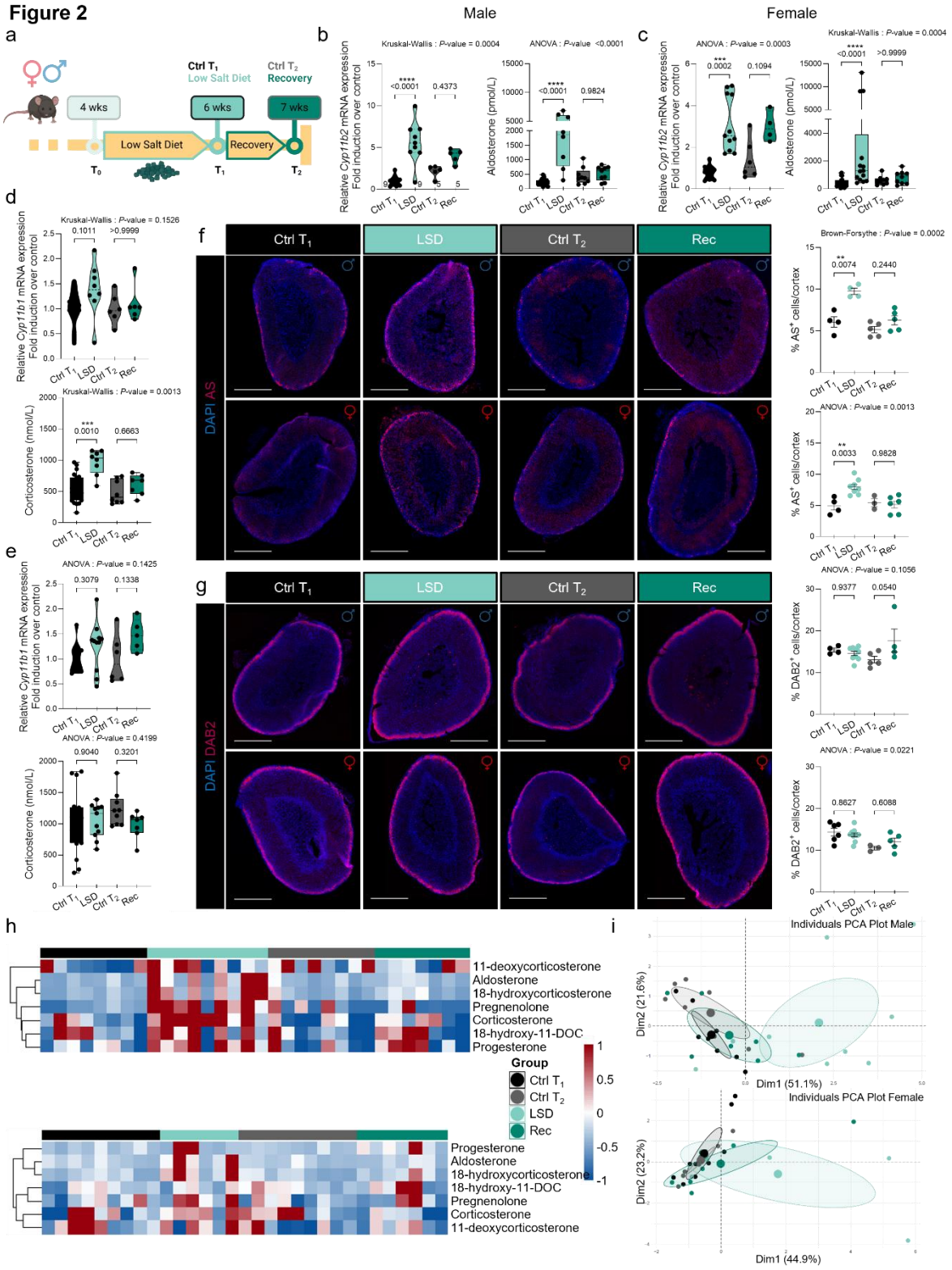

Figure 2. Effect of LSD on the adrenal cortex. (a). Schematic representation of the LSD administration regimen from 4 (T_0) to 6 weeks of age (T_1), followed by one week recovery to age 7 weeks (T_2). **(b-c).** Relative *Cyp11b2* mRNA expression measured by RT-qPCR and plasma aldosterone levels measured by LC-MS/MS at T_1 and T_2, in male **(b)** and female **(c)** *Cyp11b2*$^{+/Cre}$-*m*T*m*G mice. **(d-e).** RT-qPCR analysis of *Cyp11b1* expression and plasma corticosterone levels measured by LC-MS/MS at T_1 and T_2 of **(d)** male and **(e)** female

Cyp11b2$^{+/Cre}$-*m*T*m*G mice. **(f).** Immunofluorescent labelling of AS (ruby red) and quantification of %AS^{+} cells in the adrenal cortex of male (upper panel) and female (lower panel) mice at T_1 and T_2. **(g)**. Immunofluorescent labelling of DAB2 (ruby red) and quantification of the %DAB2^{+} cells in the adrenal cortex of male (upper panel) and female (lower panel) at T_1 and T_2. **(h).** Hierarchically clustered heatmaps of adrenal plasma steroid profiles of male (upper pannel) and female (lower pannel) mice at T_1 and T_2. **(i).** Principal component analysis (PCA) of adrenal plasma steroid profiles of male (upper pannel) and female (lower pannel) mice at T_1 and T_2. P values were obtained with Ordinary one-way ANOVA, followed by Šídák's multiple comparisons test or Kruskal-Wallis test followed by Dunn's multiple comparisons test, as indicated. Data are presented as means ± SEM. *P value < 0.05; **P value < 0.01; ***P value < 0.001.

Figure 3

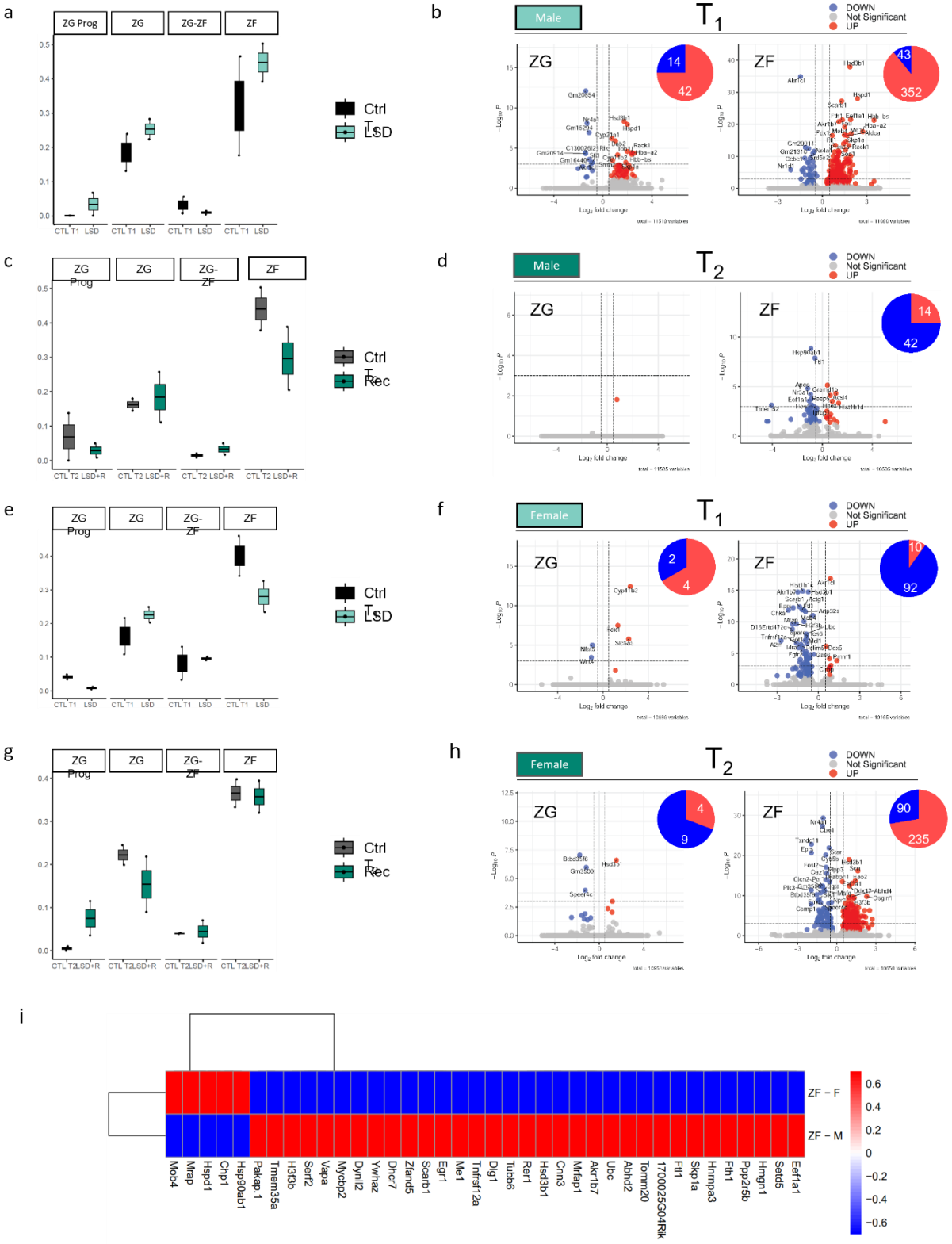

Figure 3. Effect of LSD on zone-specific cell composition and gene expression. (a, c). Cell cluster proportions of male *Cyp11b2*$^{+/Cre}$-*m*T*m*G mice at T_1 **(a)** and T_2 **(c)** following a LSD. **(b, d).** Volcano plots of differentially expressed genes (DEGs) in the ZG and ZF cell clusters of male *Cyp11b2*$^{+/Cre}$-*m*T*m*G mice at T_1 **(b)** and T_2 **(d)**, with chart pies summarizing the number of DEGs. **(e, g).** Cell cluster proportions of female *Cyp11b2*$^{+/Cre}$-*m*T*m*G mice at T_1 **(e)** and T_2

(g). **(f, h)**. Volcano plots of DEGs in the ZG and ZF cell clusters of female *Cyp11b2*$^{+/Cre}$-*m*T*m*G mice at T_1 **(f)** and T_2 **(h)**, with chart pie summarizing the DEGs. **(i).** Z-score hierarchical clustering heat map visualization representing the DEGs with opposite regulation in male and female *Cyp11b2*$^{+/Cre}$-*m*T*m*G male mice at T_1 in the ZF cluster. Volcano plots were generated starting from the unfiltered list of DEGs; upregulated, downregulated and not significant genes are respectively highlighted in blue, red and grey. Only the most significant genes (-Log10P > 1e-03) are labelled.

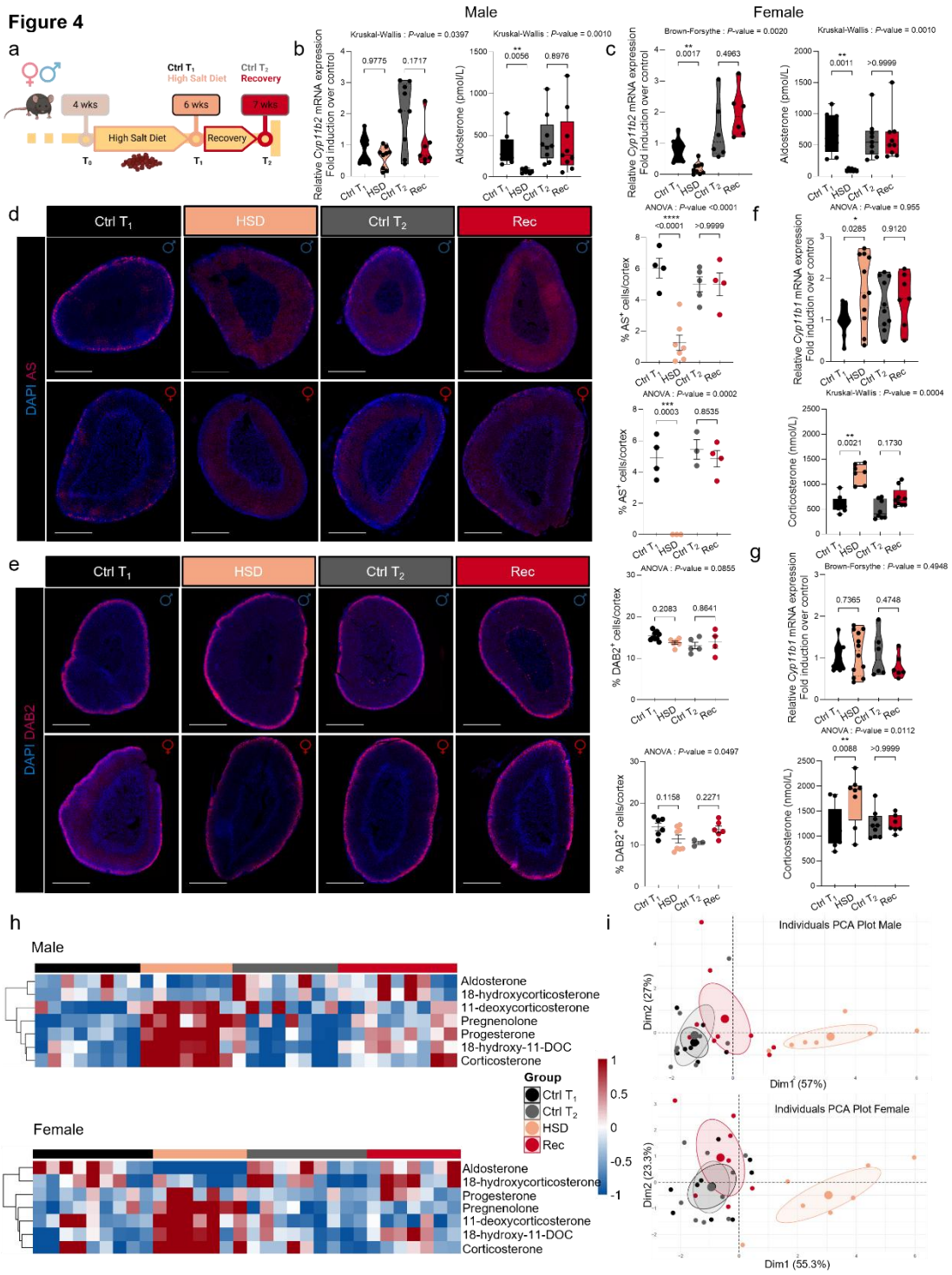

Figure 4. Effect of HSD on the adrenal cortex. (a) Schematic representation of the HSD administration regimen from 4 (T_0) to 6 weeks of age (T_1), followed by one week recovery to age 7 weeks (T_2). **(b-c)**. Relative *Cyp11b2* mRNA expression measured by RT-qPCR and plasma aldosterone levels measured by LC-MS/MS at T_1 and T_2, in male **(b)** and female **(c)** *Cyp11b2*$^{+/Cre}$-*m*T*m*G mice. **(d)** Immunofluorescent labelling of AS (ruby red) and quantification of the %AS$^+$ cells in the adrenal cortex of male (upper panel) and female (lower panel) mice at T_1 and T_2. **(e)**. Immunofluorescent labelling of DAB2 (ruby red) and quantification of the %DAB2$^+$ cells in the adrenal cortex of male (upper panel) and female (lower panel) at T_1 and T_2. **(f-g)**. RT-qPCR analysis for the *Cyp11b1* gene and plasma

corticosterone levels measured by LC-MS/MS at T_1 and T_2 in male **(f)** and female **(g)** *Cyp11b2*$^{+/Cre}$-*m*T*m*G mice. **(h)**. Hierarchically clustered heatmaps of adrenal plasma steroid profiles of male (upper pannel) and female (lower pannel) mice at T_1 and T_2. **(i).** Principal component analysis (PCAs) of adrenal plasma steroid profiles of male (upper pannel) and female (lower panel) mice at T_1 and T_2. P values were obtained with Ordinary one-way ANOVA, followed by Šídák's multiple comparisons test or Kruskal-Wallis test followed by adjusted with Dunn's multiple comparisons test or Brown-Forsythe ANOVA test followed by Dunnett's T3 multiple comparisons test, as indicated. Data are presented as means ± SEM. *P value < 0.05; **P value < 0.01; ***P value < 0.001.

Figure 5

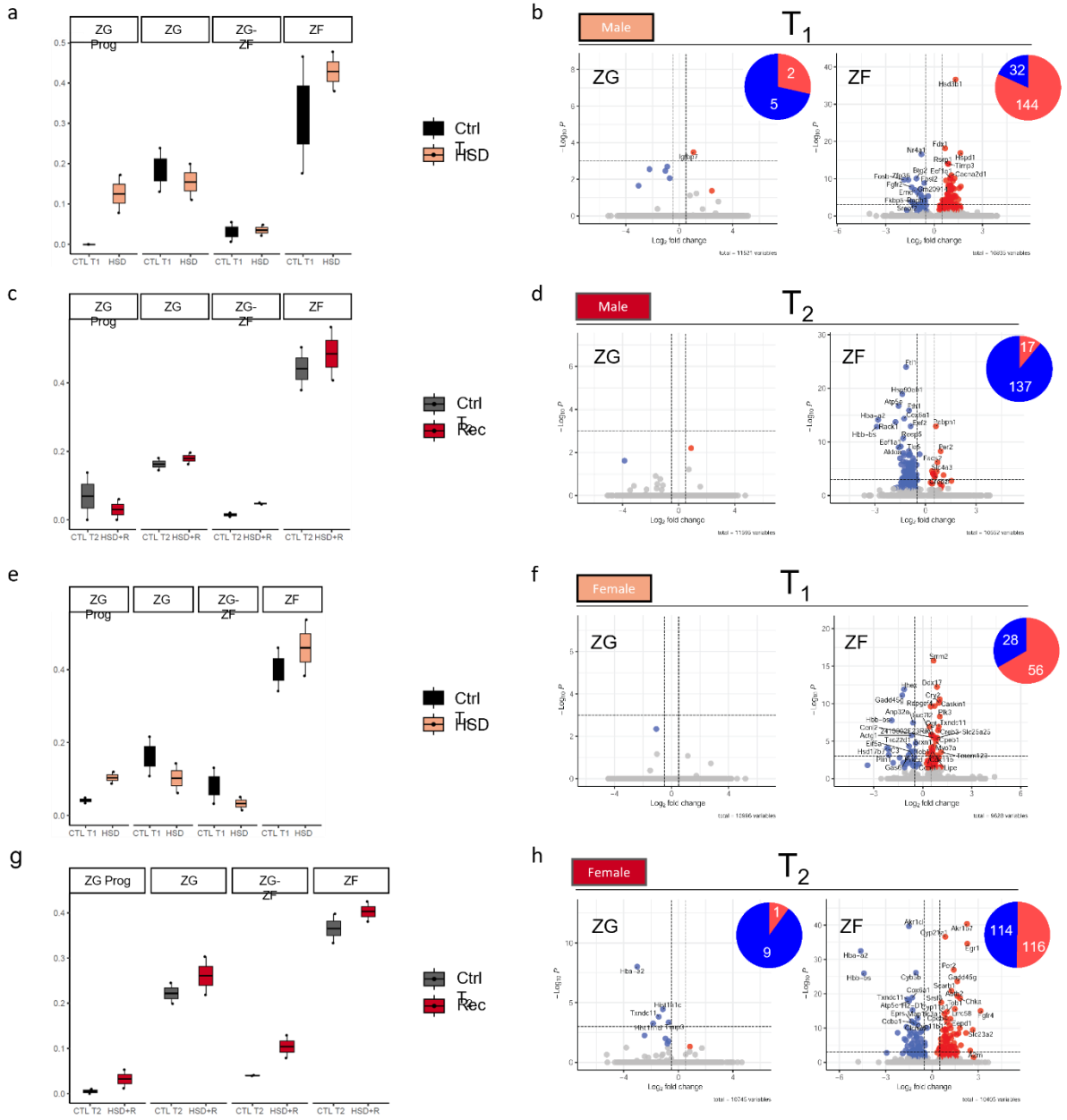

Figure 5. Effect of HSD on zone-specific gene expression and cell composition. (a, c). Cell cluster proportions of male *Cyp11b2*$^{+/Cre}$-*m*T*m*G mice at T_1 **(a)** and T_2 **(c)**. **(b, d).** Volcano plots of differentially expressed genes (DEGs) in the ZG and ZF cell clusters of male *Cyp11b2*$^{+/Cre}$-*m*T*m*G mice at T_1 **(b)** and T_2 **(d)**, with chart pies summarizing the number of DEGs. **(e, g).** Cell cluster proportions of female *Cyp11b2*$^{+/Cre}$-*m*T*m*G mice at T_1 **(e)** and T_2 **(g)**. **(f, h)**. Volcano plots of DEGs in the ZG and ZF cell clusters of female *Cyp11b2*$^{+/Cre}$-*m*T*m*G mice at T_1 **(f)** and T_2 **(h)**, with chart pie summarizing the DEGs. Volcano plots were generated starting from the unfiltered list of DEGs; upregulated, downregulated and not significant genes are respectively highlighted in blue, red and grey. Only the most significant genes (-Log10P > 1e-03) are labelled.

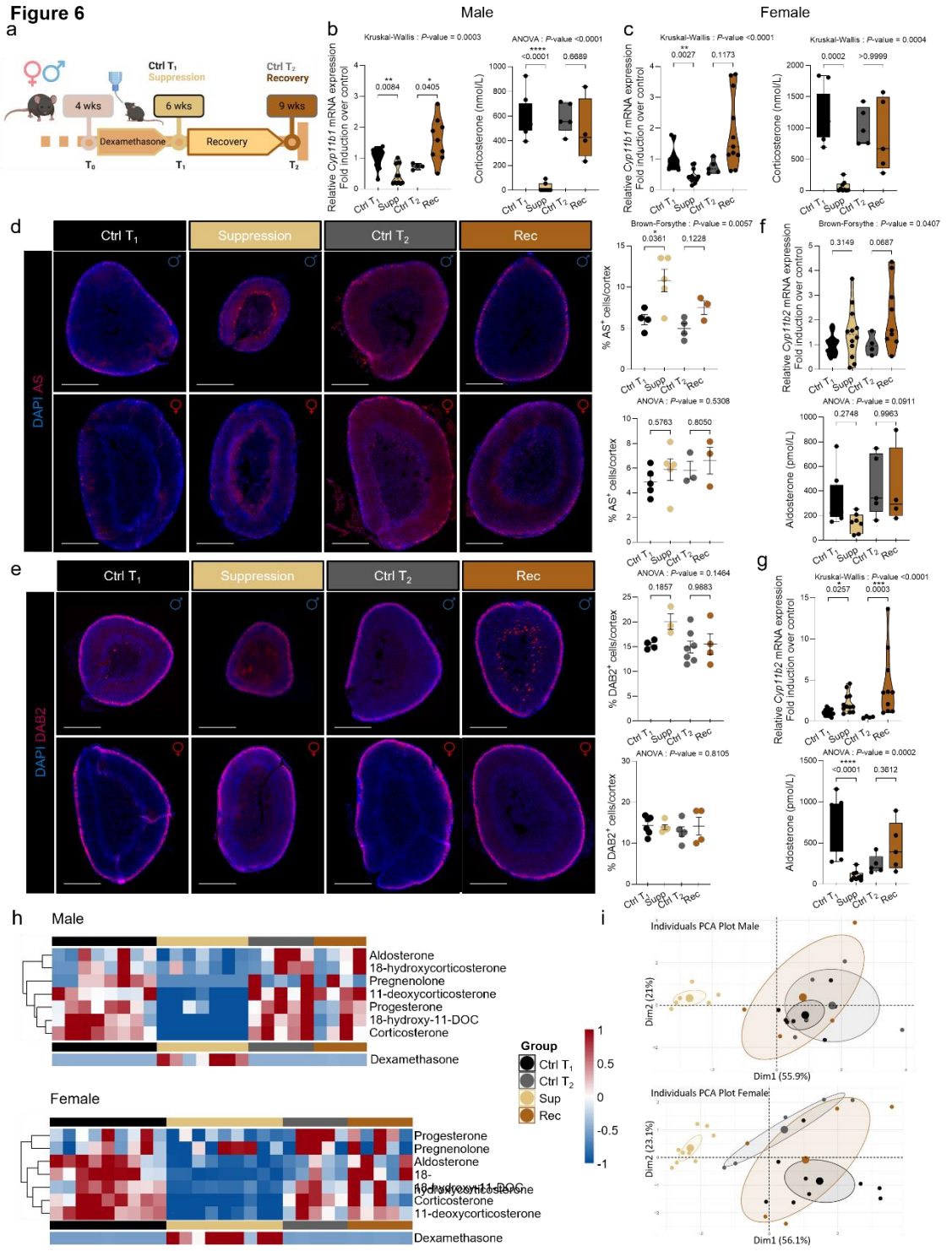

Figure 6. Effect of dexamethasone treatment on the adrenal cortex. (a) Schematic representation of the dexamethasone administration regimen from 4 (T_0) to 6 weeks of age (T_1), followed by 3 weeks recovery from age 6 weeks to 9 weeks (T_2). **(b-c)**. Relative *Cyp11b1* mRNA expression measured by RT-qPCR and plasma corticosterone levels measured by LC-MS/MS at T_1 and T_2, in male **(b)** and female **(c)** *Cyp11b2*$^{+/Cre}$-*m*T*m*G mice. **(d)** Immunofluorescent labelling of AS (ruby red) and quantification of the %AS$^+$ cells in the adrenal cortex of male (upper panel) and female (lower panel) at T_1 and T_2. **(e)**. Immunofluorescent labelling of DAB2 (ruby red) and quantification of the %DAB2$^+$ cells in the adrenal cortex of male (upper panel) and female (lower panel) at T_1 and T_2. **(f-g)**. RT-qPCR

analysis for the *Cyp11b2* gene and plasma aldosterone levels measured by LC-MS/MS at T_1 and T_2 in male **(f)** and female **(g)** *Cyp11b2*$^{+/Cre}$-*m*T*m*G mice. **(h)**. Hierarchically clustered heatmaps of adrenal plasma steroid profiles of male (upper panel) and female (lower panel) mice at T_1 and T_2. Measures of plasma dexamethasone concentrations are indicated below for each animal. **(i).** Principal component analysis (PCA) of adrenal plasma steroid profiles of male (upper panel) and female (lower panel) mice at T_1 and T_2. P values were obtained with Ordinary one-way ANOVA, followed by Šídák's multiple comparisons test or Kruskal-Wallis test followed by adjusted with Dunn's multiple comparisons test or Brown-Forsythe ANOVA test followed by Dunnett's T3 multiple comparisons test, as indicated. Data are presented as means +/- SEM. *P value < 0.05; **P value < 0.01; ***P value < 0.001.

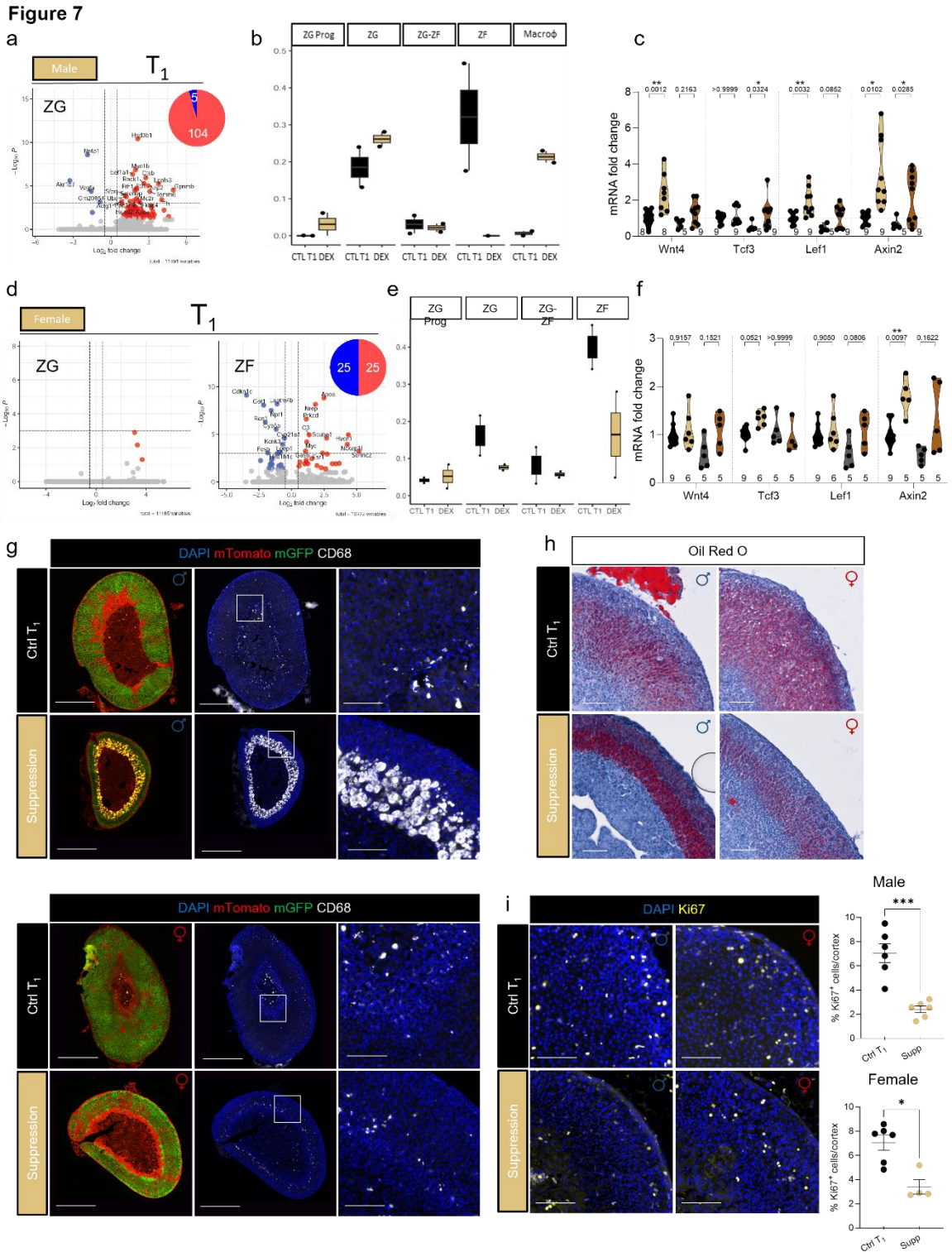

Figure 7. Effect of DEX treatment on zone-specific gene expression and cell composition. (a,d). Volcano plot of DEGs in the ZG cell cluster of male **(a)** and in the ZG and ZF cell clusters of female **(d)** *Cyp11b2*$^{+/Cre}$-*m*T*m*G mice at T_1, with chart pies summarizing the number of DEGs. **(b,e).** Cell cluster proportions of *Cyp11b2*$^{+/Cre}$-*m*T*m*G male **(b)** and female **(e)** mice at T_1. **(c, f)** Wnt4, Tcf3, Lef1 and Axin2 mRNA expression on male **(c)** and female **(f)** mice at T_1 and T_2. **(g).** Coimmunofluorescence of mGFP (green) with mTomato (red) and CD68 (white) of *Cyp11b2*$^{+/Cre}$-*m*T*m*G male (upper panel) and female (lower panel) mouse adrenals treated with dexamethasone (suppression) vs controls at T_1. Scale Bar: 500 μm left panels with entire

adrenals and 100 μm left pannel. White squares represent the magnification area in the lower panel. **(h).** Oil Red O staining of *Cyp11b2*$^{+/Cre}$-*m*T*m*G male (left panel) and female (right panel) mouse adrenals treated with dexamethasone (suppression) vs controls at T_1. Scale Bar: 100 μm. **(i).** Immunofluorescent labelling of Ki67 (yellow) and quantification of the %Ki67^{+} nuclei in the adrenal cortex of *Cyp11b2*$^{+/Cre}$-*m*T*m*G (upper panel) male and (lower panel) female mouse adrenals treated with dexamethasone vs controls at T_1, and quantification of the %Ki67^{+} nuclei in the adrenal cortex. Scale Bar: 100 μm. P values were obtained with Ordinary one-way ANOVA, followed by Šídák's multiple comparisons test or Kruskal-Wallis test followed by adjusted with Dunn's multiple comparisons test between the different time points. Data are shown as mean ± SEM. *P value < 0.05; **P value < 0.01; ***P value < 0.001.

Figure 8

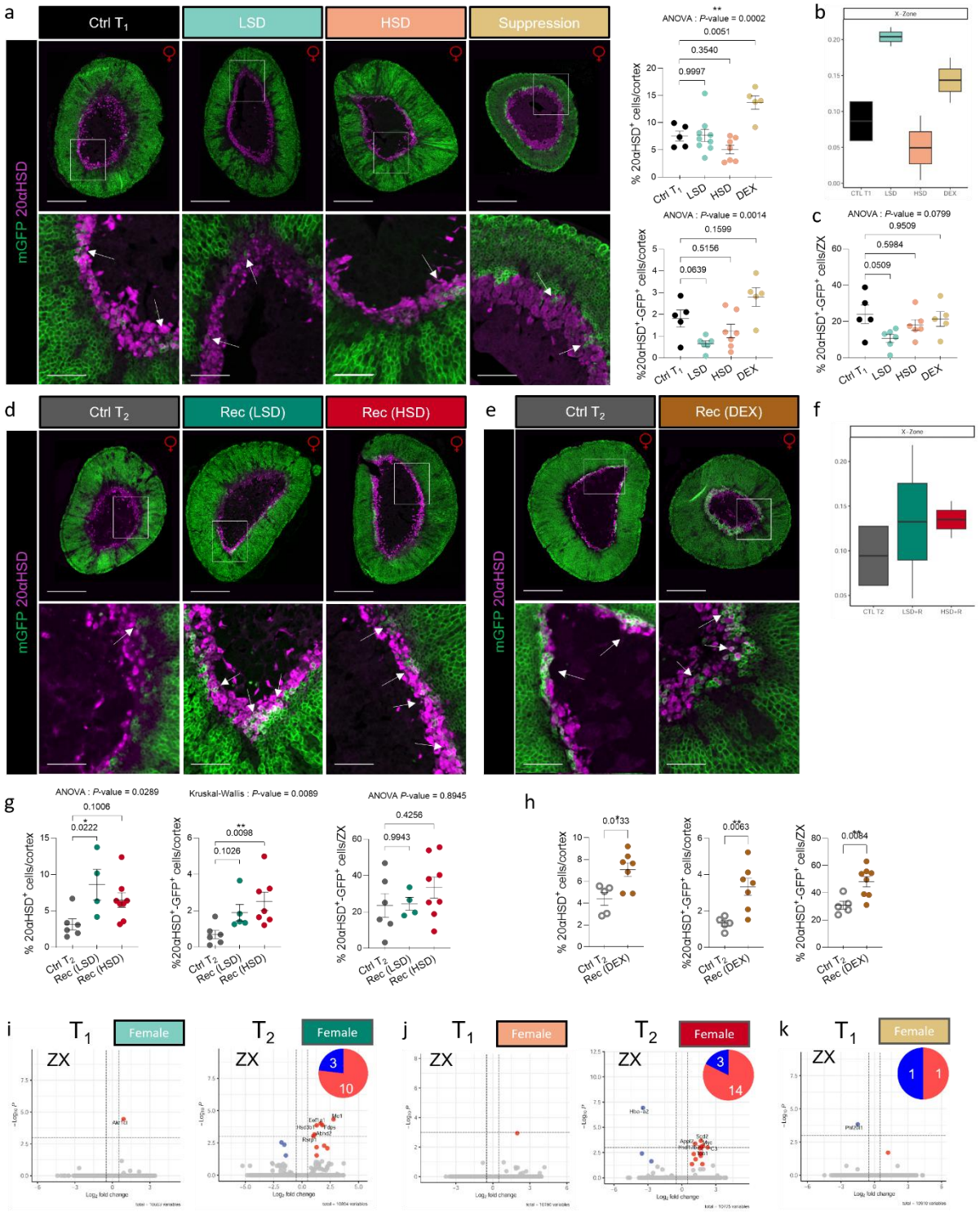

Figure 8. X-Zone plasticity in response to pathophysiological challenges. (a). Coimmunofluorescence of mGFP (green) and 20αHSD (purple) of *Cyp11b2*$^{+/Cre}$-*m*T*m*G female mice that underwent LSD, HSD and DEX treatment vs Ctrl T_1 and quantification of 20αHSD$^+$ and mGFP and 20αHSD double-positive cells in the adrenal cortex. mGFP and 20αHSD double-positive cells are indicated by white arrows in the lower panel magnified image. Scale Bar: 500 µm upper panels with entire adrenals and 100 µm lower panels. White squares represent the magnification area in the lower panel. **(b)**. ST ZX cluster proportions of *Cyp11b2*$^{+/Cre}$-female

mice that underwent LSD, HSD and DEX treatment vs Ctrl T_1. **(c).** Quantification of the mGFP and 20αHSD double-positive cells in the X-zone of *Cyp11b2*$^{+/Cre}$-*m*T*m*G female mice that underwent LSD, HSD and DXM vs Ctrl T_1. **(d)**. Coimmunofluorescence of mGFP (green) and 20αHSD (purple) of *Cyp11b2*$^{+/Cre}$-*m*T*m*G female mice that underwent LSD, HSD after a 1-week recovery period vs Ctrl T_2 (7 weeks old) mice. mGFP and 20αHSD double-positive cells are denoted by white arrows in the lower panel magnified image. The Ctrl T_2 image has been used on Figure 1d. Scale Bar: 500 μm upper panels with entire adrenals and 100 μm lower panel. White squares represent the magnification area in the lower panel. **(e).** Coimmunofluorescence of mGFP (green) and 20αHSD (purple) of *Cyp11b2*$^{+/Cre}$-*m*T*m*G female mice treated with DEX followed by 3-weeks recovery vs Ctrl T_2 (9 weeks old) mice. mGFP and 20αHSD double-positive cells are denoted by white arrows in the lower panel magnified image. Scale Bar: 500 μm upper panels with entire adrenals and 100 μm lower panel. White squares represent the magnification area in the lower panel. **(f).** ST ZX cluster proportions of *Cyp11b2*$^{+/Cre}$-female mice that underwent LSD, HSD and 1-week recovery period vs Ctrl T_2 (7 weeks old) mice. **(g)**. Quantification of 20αHSD$^+$, mGFP and 20αHSD double-positive cells in the adrenal cortex and X-zone of *Cyp11b2*$^{+/Cre}$-*m*T*m*G female mice that underwent LSD, HSD and 1-week recovery period vs Ctrl T_2 (7 weeks old) mice. **(h)**. Quantification of 20αHSD$^+$, mGFP and 20αHSD double-positive cells in the adrenal cortex and in the X-zone of *Cyp11b2*$^{+/Cre}$-*m*T*m*G female mice treated with DEX followed by 3-weeks recovery vs Ctrl T_2 (9 weeks old) mice. P values were obtained with Unpaired t test. **(i,j,k).** Volcano plot of DEGs in the X-zone cell cluster of *Cyp11b2*$^{+/Cre}$-*m*T*m*G female mice of mice fed a LSD **(i)** and HSD **(j)** at T_1 and T_2, and following DEX cohort at T_1 **(k)**, with chart pies summarizing the number of DEGs. P values were obtained with Ordinary one-way ANOVA, followed by Šídák's multiple comparisons test or Kruskal-Wallis test followed by adjusted with Dunn's multiple comparisons test or Brown-Forsythe ANOVA test followed by Dunnett's T3 multiple comparisons test, as indicated. Data are presented as means +/- SEM. *P value < 0.05; **P value < 0.01; ***P value < 0.001.

Sexually dimorphic interzonal crosstalk reshapes the adrenal cortex in response to pathophysiological challenges

Nicolo Faedda[1], Alaa B Abdellatif[1], Francesco Carbone[2], May Fayad[1], Bakhta Fedlaoui[1], Rita Chamoun[3], Romane L'Héritier[1], Ilaria Del Gaudio[1], Ourida Koual[1], Isabelle Giscos-Douriez[1], Stéphanie Baron[1,4], Ben Atkinson[5], Xiaomin Li[1], Linghui Kong[1], Yunling Xu[1], Eric Camerer[1], Mickael Menager[2], Fabio L. Fernandes-Rosa[1], Sheerazed Boulkroun[1], Maria-Christina Zennaro[1,6#]

[1]Université Paris Cité, PARCC, Inserm, Paris, France
[2]Université Paris Cité, Imagine Institute, Laboratory of Inflammatory Responses and Transcriptomic Networks in Diseases, Atip-Avenir Team, INSERM UMR 1163, 75015 Paris, France
[3]Cardiovascular Research Institute Maastricht (CARIM) and Heart & Vessels Center, Maastricht University Medical Center, Maastricht, The Netherlands.
[4]Assistance Publique-Hôpitaux de Paris, Hôpital Européen Georges Pompidou, Service de Physiologie, Paris, France
[5]Intelligent Imaging Innovations Ltd, 17 Westbourne Studios, W10 5JJ, London, UK
[6]Assistance Publique-Hôpitaux de Paris, Hôpital Européen Georges Pompidou, Service de Génétique, Paris, France

[#]Corresponding author
Address correspondence to:
Maria-Christina Zennaro, MD, PhD
Inserm, U970
Paris Cardiovascular Research Center – PARCC
56, rue Leblanc,
75015 Paris – France
Tel : +33 (0)1 53 98 80 42
Fax : + 33 (0)1 53 98 79 52
e-mail : maria-christina.zennaro@inserm.fr

Supplementary Figures and Tables

Figure S1

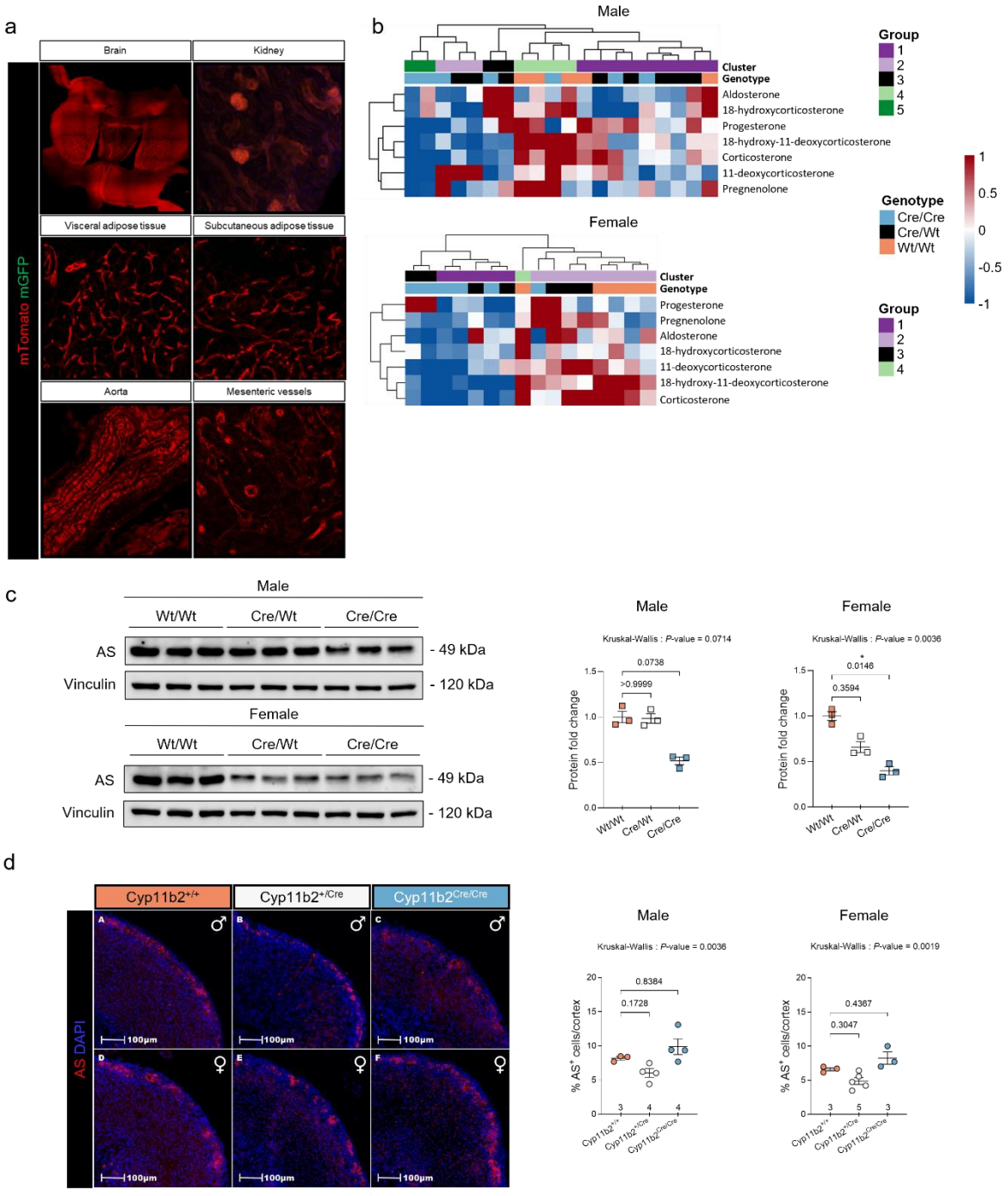

Figure S1. Characterization of the adrenal phenotype of the *Cyp11b2*^{Cre} mouse model. (a). Analysis of mGFP and mTomato expression in the brain, kidney, visceral and subcutaneous adipose tissue, aorta and mesenteric vessels of a 5-weeks old *Cyp11b2*$^{+/Cre}$-*m*T*m*G male mouse **(b).** Hierarchical clustering heat map visualization of plasma steroid profiles of *Cyp11b2*$^{+/+}$ (n=5), *Cyp11b2*$^{+/Cre}$ (n=8) and *Cyp11b2*$^{Cre/Cre}$ (n=7) male (upper pannel) and of *Cyp11b2*$^{+/+}$

(n=5), *Cyp11b2*$^{+/Cre}$ (n=5) and *Cyp11b2*$^{Cre/Cre}$ (n=6) female (lower pannel) mice of 6 weeks of age measured by LC-MS/MS. **(c).** Representative immunoblots and histograms showing Adosterone Synthase (AS) expression in wild type *Cyp11b2*$^{+/+}$, heterozygous *Cyp11b2*$^{+/Cre}$ and homozygous *Cyp11b2*$^{Cre/Cre}$ 6 weeks old mice of both sexes, relative to Vinculin. P values were obtained with Kruskal-Wallis test and adjusted with Dunn's multiple comparisons test. **(d).** Immunofluorescent labelling of AS (red) on adrenals from wild type *Cyp11b2*$^{+/+}$, heterozygous *Cyp11b2*$^{+/Cre}$ and homozygous *Cyp11b2*$^{Cre/Cre}$ 6 weeks old male and female mice. P values were obtained with Kruskal-Wallis test. Data are presented as mean values ± SEM. Data are presented as mean values +/- SEM. *P value < 0.05; **P value < 0.01; ***P value < 0.001.

Figure S2

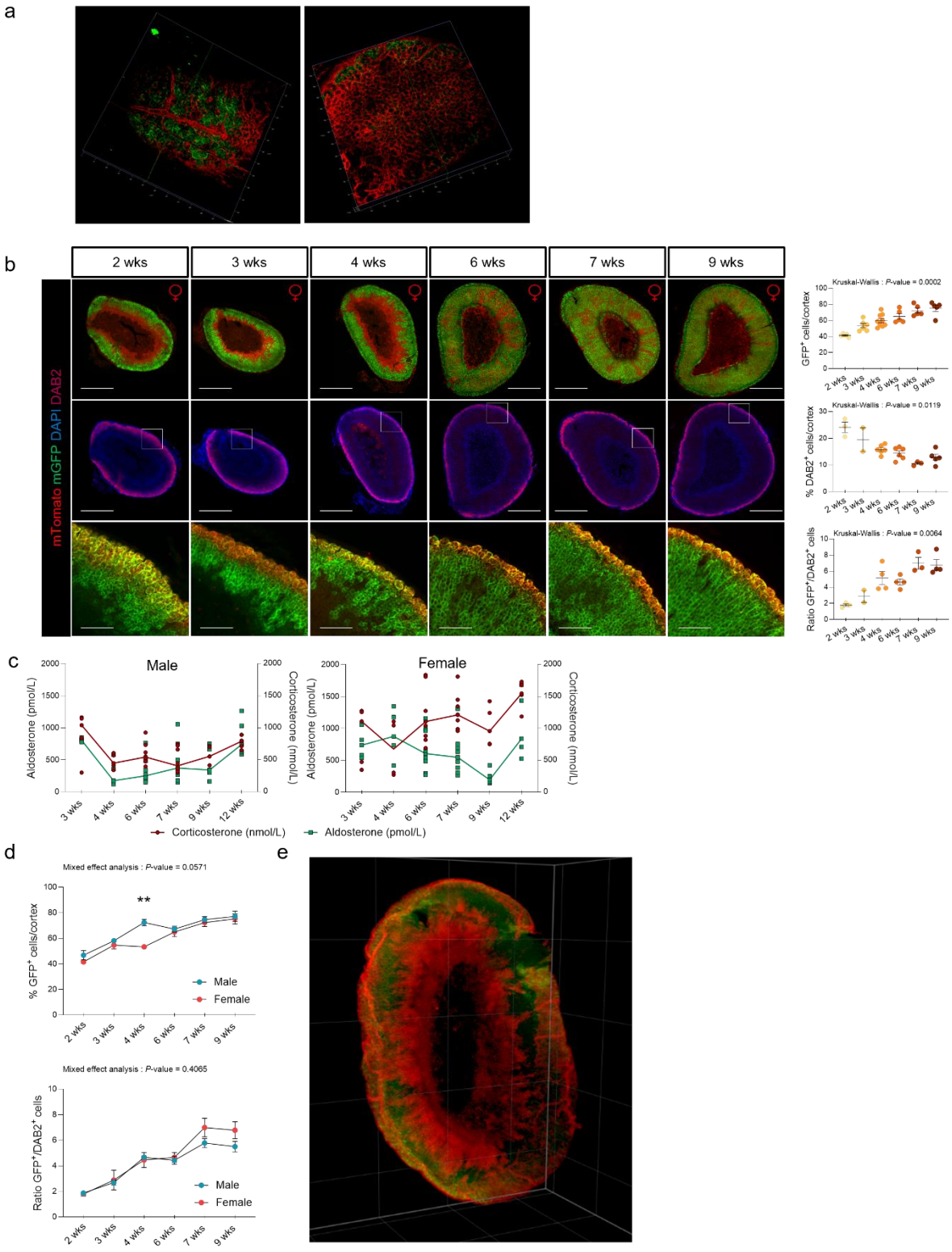

Figure S2. Transdifferentiation kinetics in *Cyp11b2*^{Cre}::*m*T*m*G mice. **(a).** Biphoton 3-D images of mGFP and mTomato expression of *Cyp11b2*$^{+/Cre}$-*m*T*m*G adrenals from a male mouse at postnatal day 1 (P1) after clarification; images represent superficial (left) and median (right) z-stacks of the adrenal. Specific mGFP is localized to the membrane, while unspecific

background signal is localized to the cytoplasm. **(b).** Coimmunofluorescence of mGFP (green) with Tomato (red) and DAB2 (ruby red) of *Cyp11b2*$^{+/Cre}$-*m*T*m*G female mice adrenals at 2, 3, 4, 6, 7 and 9 weeks of age and quantification of the DAB2^{+} cells, mGPF^{+} cells and analysis of cell lineage conversion expressed as the ratio of the number of cells expressing mGFP over the cortex area or the number of cells expressing DAB2. P values were obtained with Kruskal-Wallis test and adjusted with Dunn's multiple comparisons test. Scale Bar: 500 μm (upper panels),100 μm (lower pannels). White squares represent the magnification area in the lower panel. **(c).** Aldosterone and corticosterone plasma levels in male (left panel) and female (right panel) *Cyp11b2*$^{+/Cre}$-*m*T*m*G mice from 2 to 12 weeks of age. **(d).** Mixed effect analysis of cell lineage conversion by quantification of mGFP represented as %GFP^{+} cells/cortex (upper panel) or %GFP^{+} cells/%Dab2 $^{+}$ cells (lower panel) in male and female *Cyp11b2*$^{+/Cre}$ –*m*T*m*G mice at 2, 3, 4, 6, 7 and 9 weeks of age. Statistical analysis was performed using two-way analysis and adjusted with Šídák's multiple comparisons test. **(e)**. Volume rendering of a wholemount lightsheet fluorescence microscopy (LSFM) imaged, EZ Clear processed *Cyp11b2*$^{+/Cre}$-*m*T*m*G female 6 weeks old mouse adrenal tissue digitally sectioned along the longitudinal axis using Slide Book digital microscopy software. Data are shown as mean ± SEM. *P value < 0.05; **P value < 0.01; ***P value < 0.001.

Figure S3

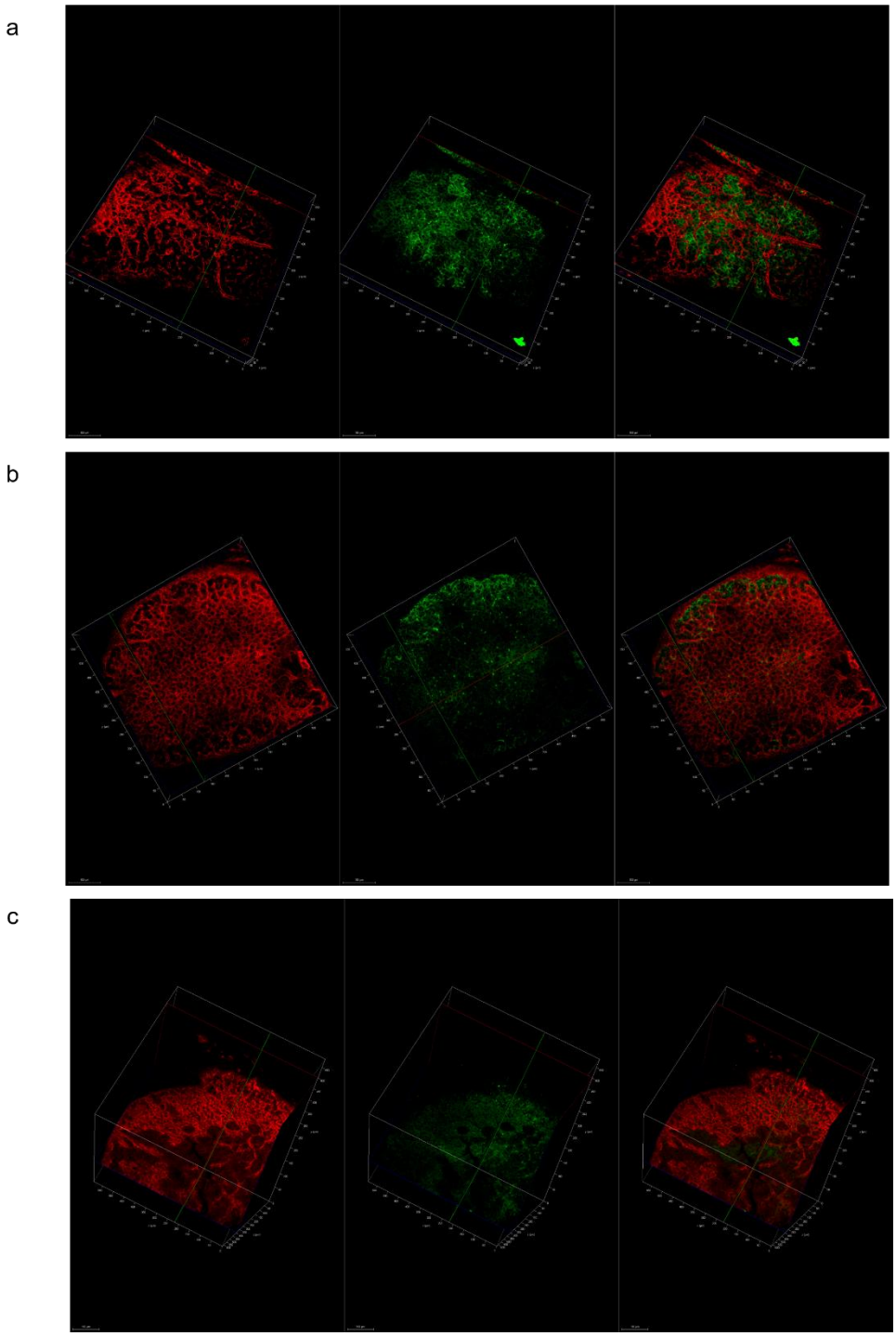

Figure S3. Transdifferentiation in *Cyp11b2*^{Cre}::*m*T*m*G mice at P1. **(a-c).** Biphoton 3D images of *Cyp11b2*$^{+/Cre}$-*m*T*m*G adrenals after clarification at postnatal day 1 (P1), with mTomato (left panel), mGFP (middle) and overlay (right panel). **(a).** Superficial z-stack of a *Cyp11b2*$^{+/Cre}$-*m*T*m*G mouse. **(b).** Median z-stack of a *Cyp11b2*$^{+/Cre}$-*m*T*m*G mouse. **(c).** Biphoton 3D images of *Cyp11b2*$^{+/+}$-*m*T*m*G control adrenal. Specific mGFP is localized to the membrane, while unspecific background signal is localized to the cytoplasm.

Figure S4

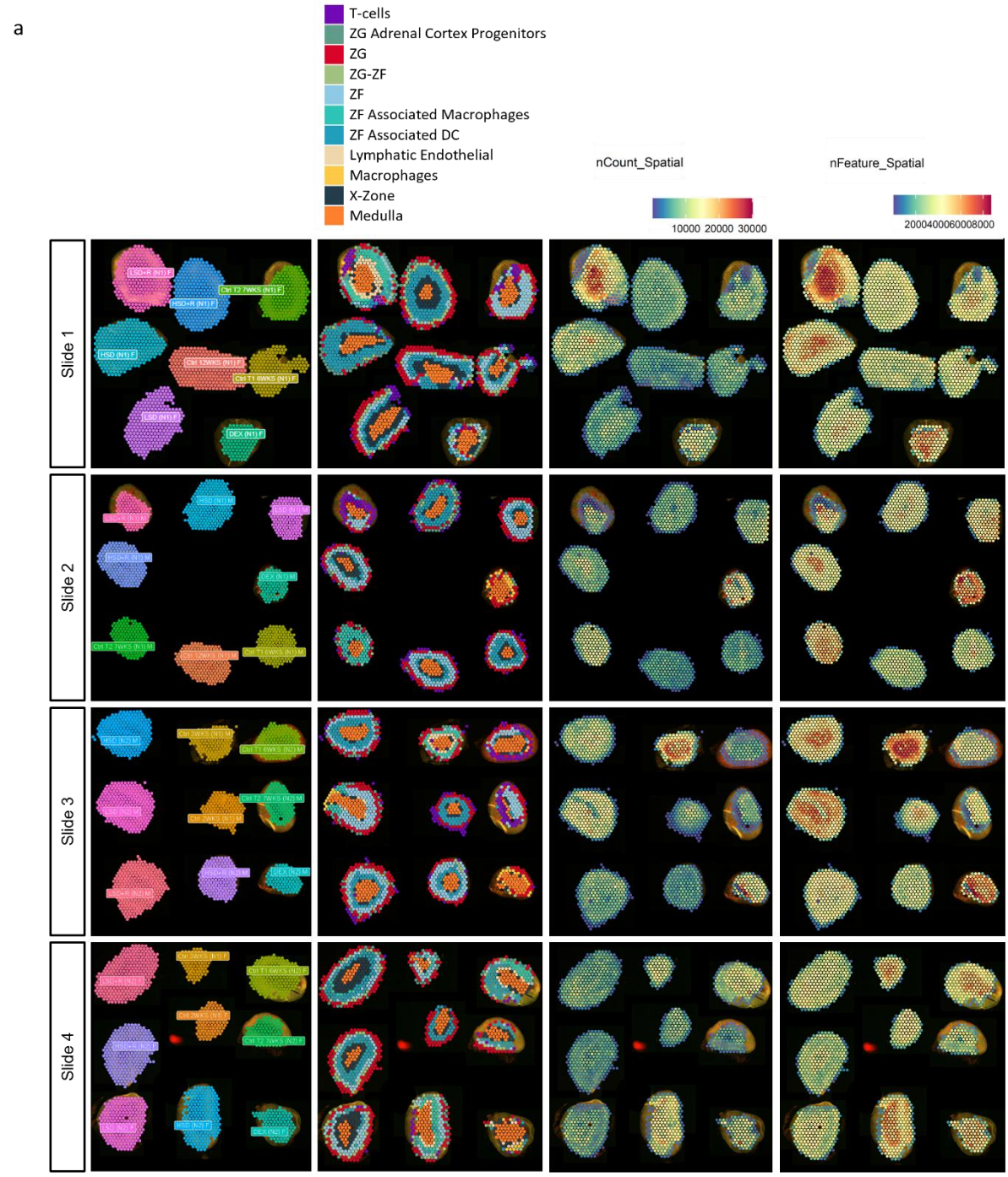

Figure S4. Spatial transcriptomic quality control. (a) Spatial arrangement of the different adrenal slices of control and treated mice and localization of the 11 cell clusters on the four 10x Visium slides with the number of unique transcripts (nCount) or unique genes (nFeature) per spatial spot.

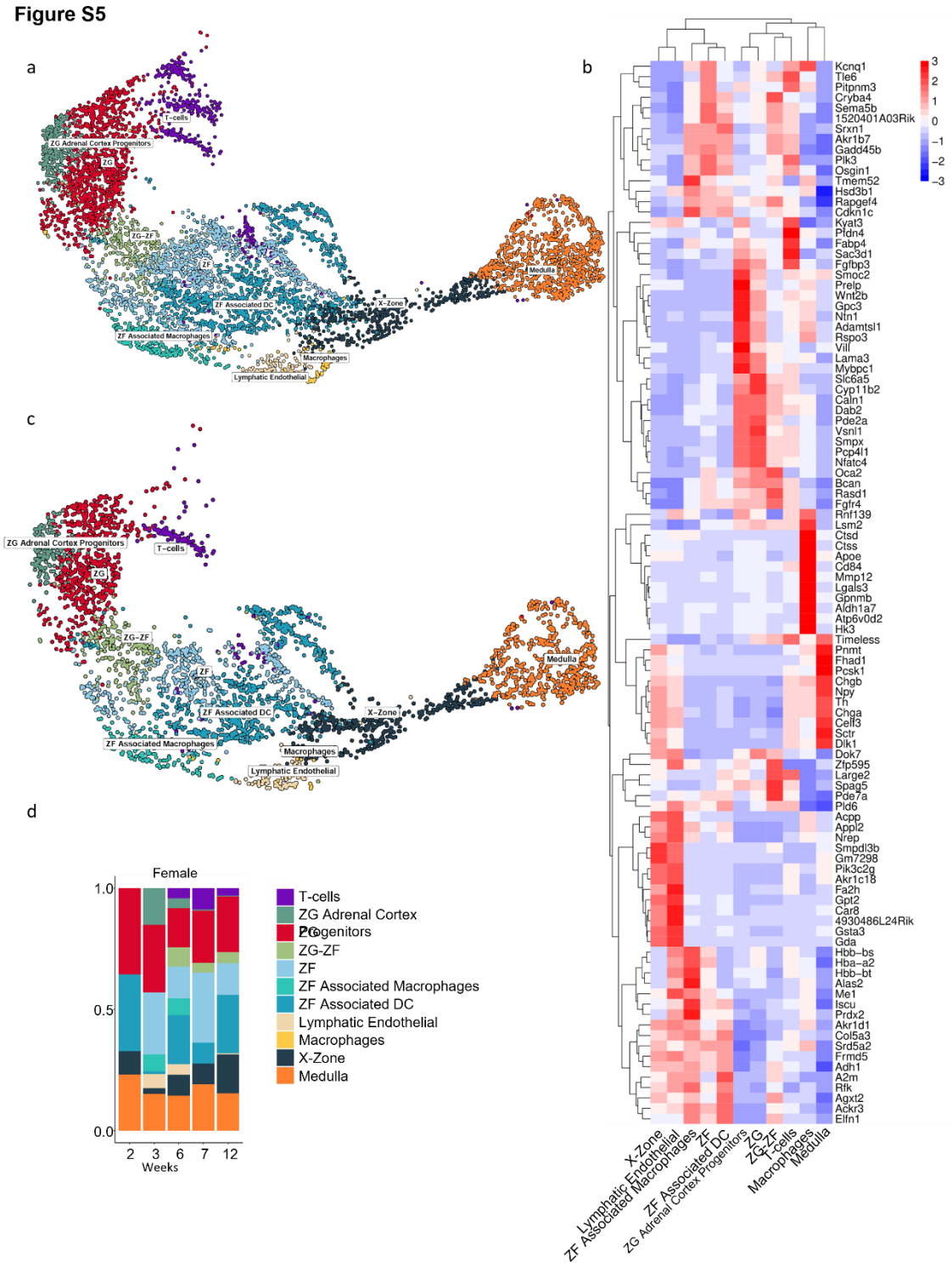

Figure S5. Adrenal spatial transcriptomic analysis at different ages. (a). General uMAP of the spots detected by the 4 10x Visium slides, all conditions and **(b).** Heatmap of the top differentially expressed genes (DEGs) in each of the different identified cell clusters. **(c)**. UMAP of adrenal cell clusters in control female *Cyp11b2*$^{+/Cre}$-*m*T*m*G mice of 2, 3, 6, 7 and 12 weeks of age. **(d).** Cell cluster proportion of control female *Cyp11b2*$^{+/Cre}$-*m*T*m*G mice of 2, 3, 6, 7 and 12 weeks of age.

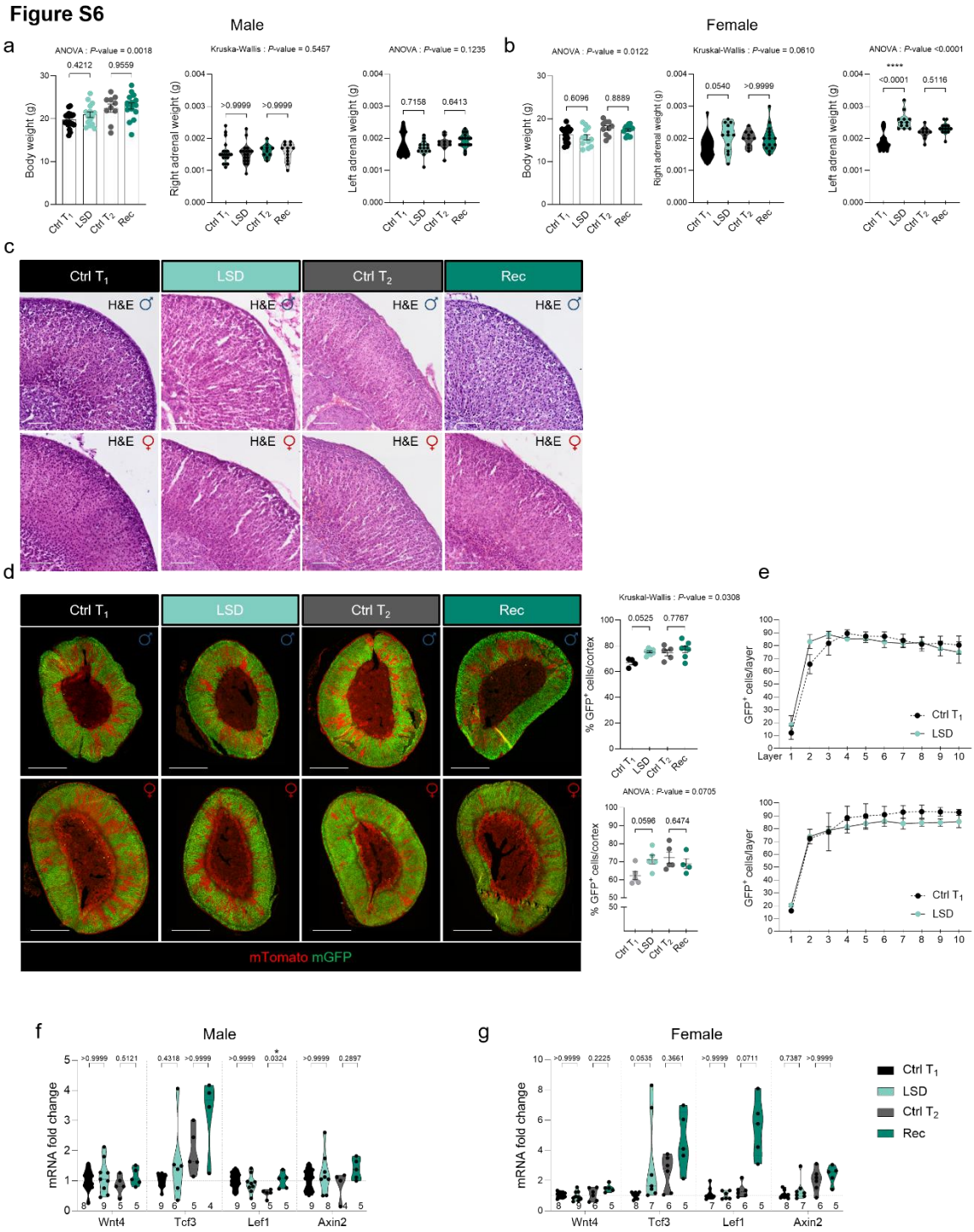

Figure S6. Effect of LSD on the adrenal cortex. (a-b). Body weight and absolute right and left adrenal mass of *Cyp11b2*$^{+/Cre}$-*m*T*m*G male **(a)** and female **(b)** mice fed with low salt diet from 4 to 6 weeks of age (T_1) and after a recovery period from 6 weeks to 7 weeks (T_2). **(c).** H&E staining of male and female, control and treated, *Cyp11b2*$^{+/Cre}$-*m*T*m*G mouse adrenals at T_1 and T_2. **(d).** Coimmunofluorescence of mGFP (green) with mTomato (red) and quantification of the mGPF$^+$ cells in the adrenal cortex of *Cyp11b2*$^{+/Cre}$-*m*T*m*G male (upper panel) and female

(lower panel) mice at T_1 and T_2. Scale Bar: 500 μm. **(e).** Analysis of the progression of mGFP+ cells along the adrenal cortex in the first 10 layers of *Cyp11b2*$^{+/Cre}$-*m*T*m*G male (upper panel, 10 layer) and female (lower pannel, 10 layers) mice fed with low salt diet from 4 to 6 weeks of age (T_1) and after a recovery period from 6 weeks to 7 weeks (T_2). Each layer has a thickness of 25 micron. **(f-g).** Effect of LSD on the expression of Wnt/β-catenin genes in male **(f)** and female **(g)** mice. P values were obtained with Ordinary one-way ANOVA, adjusted with Šídák's multiple comparisons test or with Kruskal-Wallis test and adjusted with Dunn's multiple comparisons test, as indicated. Data are presented as mean values ± SEM. *P value < 0.05; **P value < 0.01; ***P value < 0.001.

Figure S7

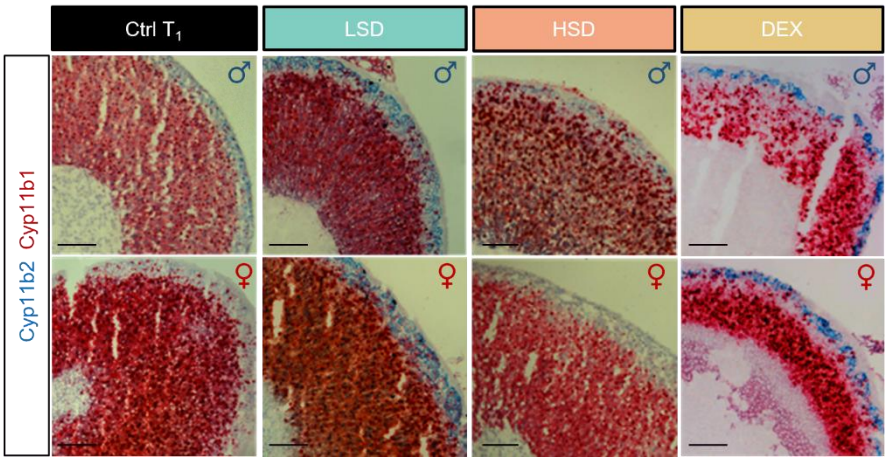

Figure S7. Effect of LSD, HSD and DXM treatment on Cyp11b2 and Cyp11b1 mRNA expression in the adrenal cortex. RNAscope in situ hybridization performed using one probe for *Cyp11b2* (blue) and one for *Cyp11b1* (red) in male and female mice fed a low salt (LSD) or high diet (HSD) for a two-week period, or submitted to DEX treatment. Scale Bar: 500 µm.

Figure S8

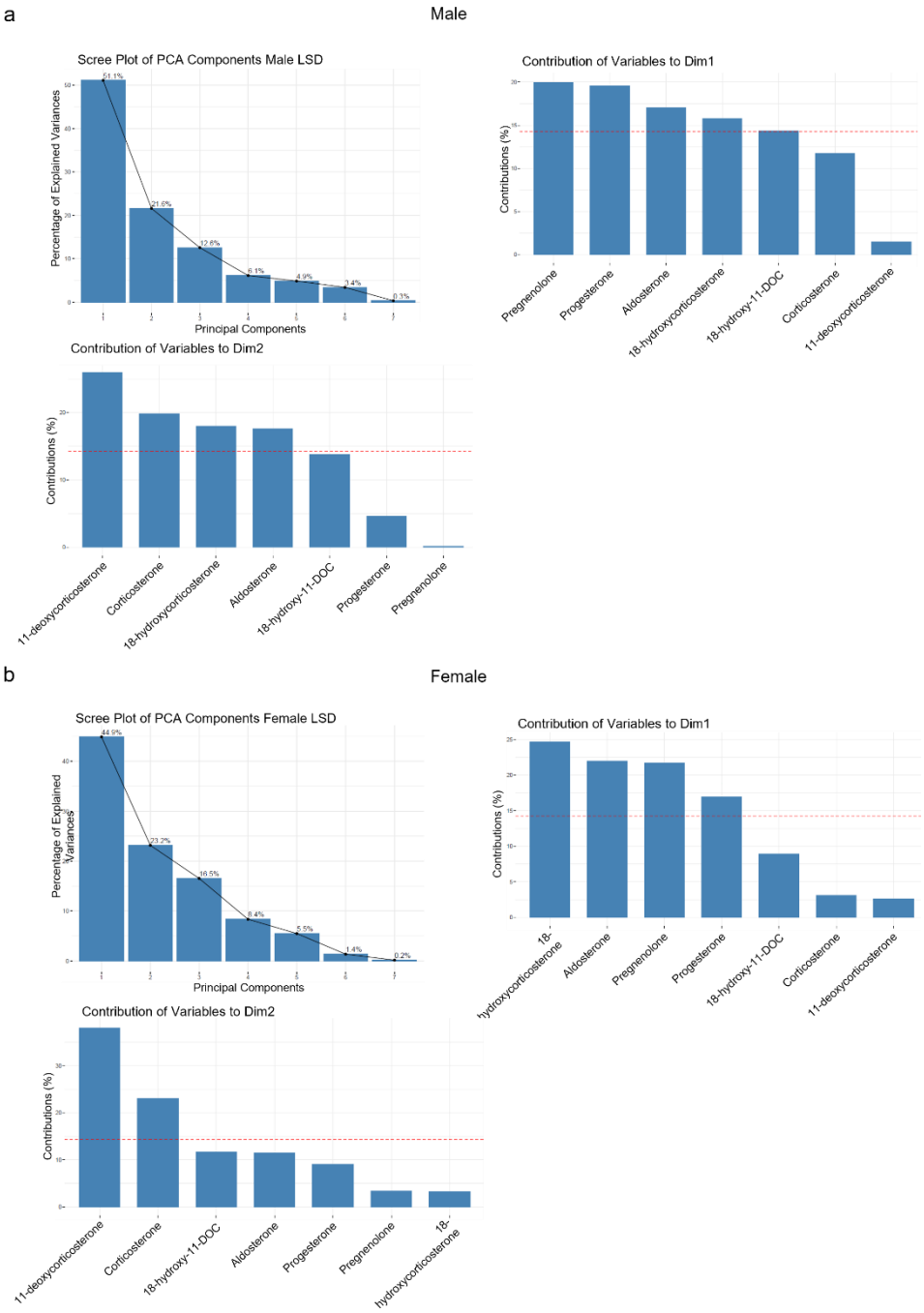

Figure S8. Characteristics of Principal component analysis (PCA) of adrenal plasma steroid profiles following a LSD. (a). Scree plot in which the x-axis shows the principal components (dimensions), which in this case are 7, and their contribution to variance of the Dim1 and Dim2 in male *Cyp11b2*$^{+/Cre}$-*m*T*m*G mice fed with LSD at T_1 and T_2 vs control littermates. **(b).** Scree plot in which the x-axis shows the principal components (dimensions) and their contribution to variance of Dim1 e Dim2 in female *Cyp11b2*$^{+/Cre}$-*m*T*m*G mice fed with LSD at T_1 and T_2 vs control littermates. PCA of plasma steroids revealed clear separation between control and LSD-fed mice along the first Dimension (Dim1) explaining 51.1% in males and 44.9% in females of the total variance.

Figure S9

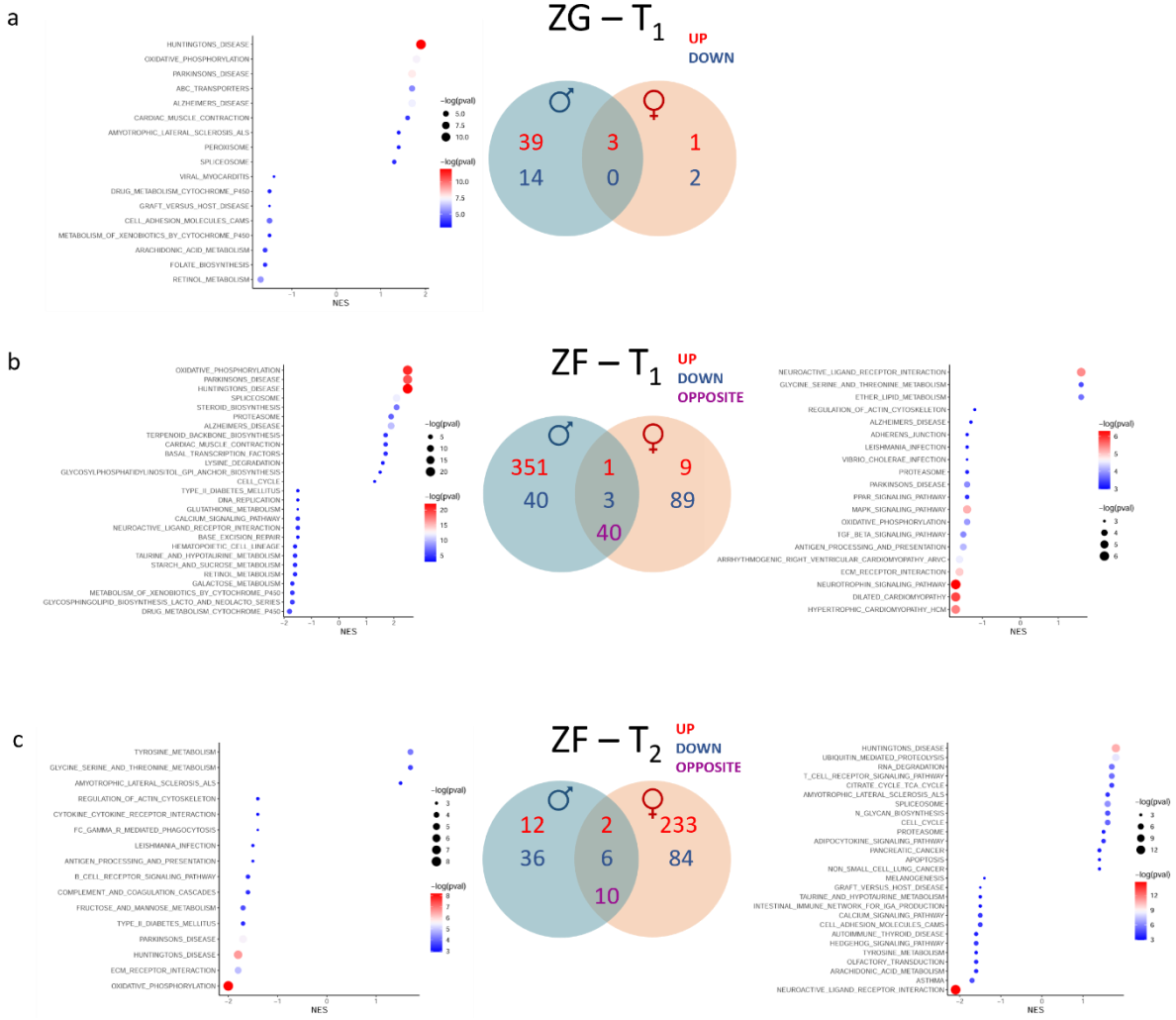

Figure S9. Effect of LSD on zone-specific gene expression. (a). Gene set enrichment analysis (GSEA) pathways from the KEGG database (adapted on mouse) of male *Cyp11b2*$^{+/Cre}$-*m*T*m*G LSD-treated mice vs Ctrl T_1 in the ZG cluster and Venn diagram illustrating the number of up and downregulated genes in male and female *Cyp11b2*$^{+/Cre}$-*m*T*m*G mice treated with LSD vs Ctrl T_1. **(b).** GSEA pathways from the KEGG database (adapted on mouse) of male (left panel) and female (right panel) *Cyp11b2*$^{+/Cre}$-*m*T*m*G LSD-treated mice vs Ctrl T_1 in the ZF cluster and Venn diagram illustrating the up and down and opposite regulated genes between males and females. **(c).** GSEA pathways from the KEGG database (adapted on mouse) of *Cyp11b2*$^{+/Cre}$-*m*T*m*G Recovery vs Ctrl T_2 male (left panel) and female (right panel) mice in the ZF cluster and Venn diagram illustrating the up and down and opposite regulated genes between males and females. Pathways were ordered by the NES (normalized enriched score) and only the top 20 up and down regulated pathways are visualized using dotplots. The color and size of the dots reflect the significance of the enrichment [-log(pval)].

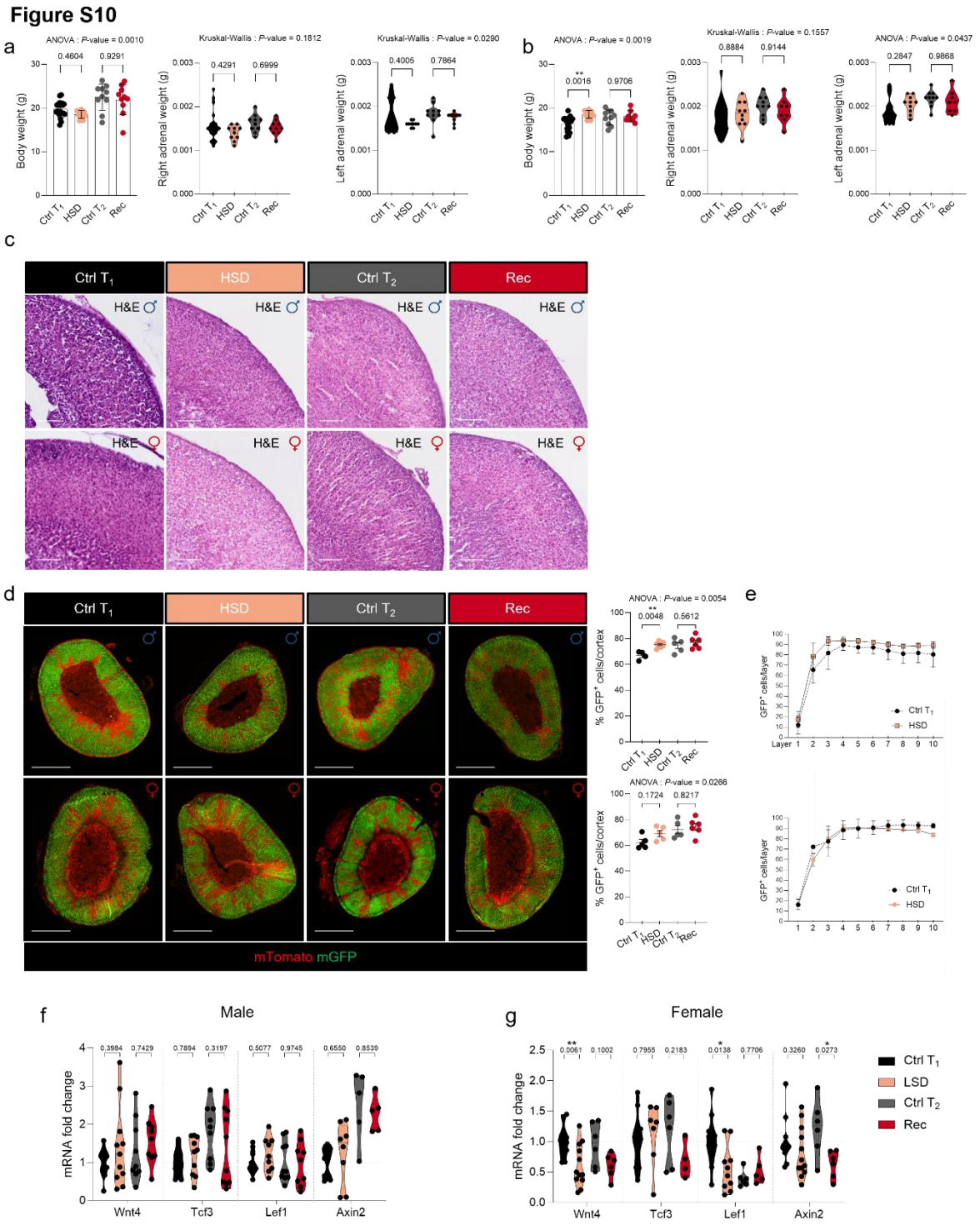

Figure S10. Effect of HSD on the adrenal cortex. (a, b) Body weight and absolute right and left adrenal weight of *Cyp11b2*$^{+/Cre}$-*m*T*m*G male **(a)** and female **(b)** mice fed with high salt diet from 4 to 6 weeks of age (T_1) and after a recovery period from 6 weeks to 7 weeks (T_2). **(c).** H&E staining of male (upper panel) and female (lower panel), control and treated, *Cyp11b2*$^{+/Cre}$-*m*T*m*G mouse adrenals at T_1 and T_2. **(d).** Coimmunofluorescence of mGFP (green) with Tomato (red) and quantification of the mGPF^{+} cells in the adrenal cortex of *Cyp11b2*$^{+/Cre}$-*m*T*m*G male (upper panel) and female (lower panel) mice at T_1 and T_2. Scale Bar: 500 µm. **(e).** Analysis of the progression of mGFP+ cells along the adrenal cortex layers of *Cyp11b2*$^{+/Cre}$-*m*T*m*G male (upper panel, 10 layer) and female (lower pannel, 10 layers) mice

fed with high salt diet from 4 to 6 weeks of age (T_1) and after a recovery period from 6 weeks to 7 weeks (T_2). Each layer has a thickness of 25 micron. **(f-g).** Effect of HSD on the expression of Wnt/β-catenin genes in male **(f)** and female **(g)** mice. P values were obtained with Ordinary one-way ANOVA, adjusted with Šídák's multiple comparisons test or with Kruskal-Wallis test and adjusted with Dunn's multiple comparisons test, as indicated. Data are presented as mean values ± SEM. *P value < 0.05; **P value < 0.01; ***P value < 0.001.

Figure S11

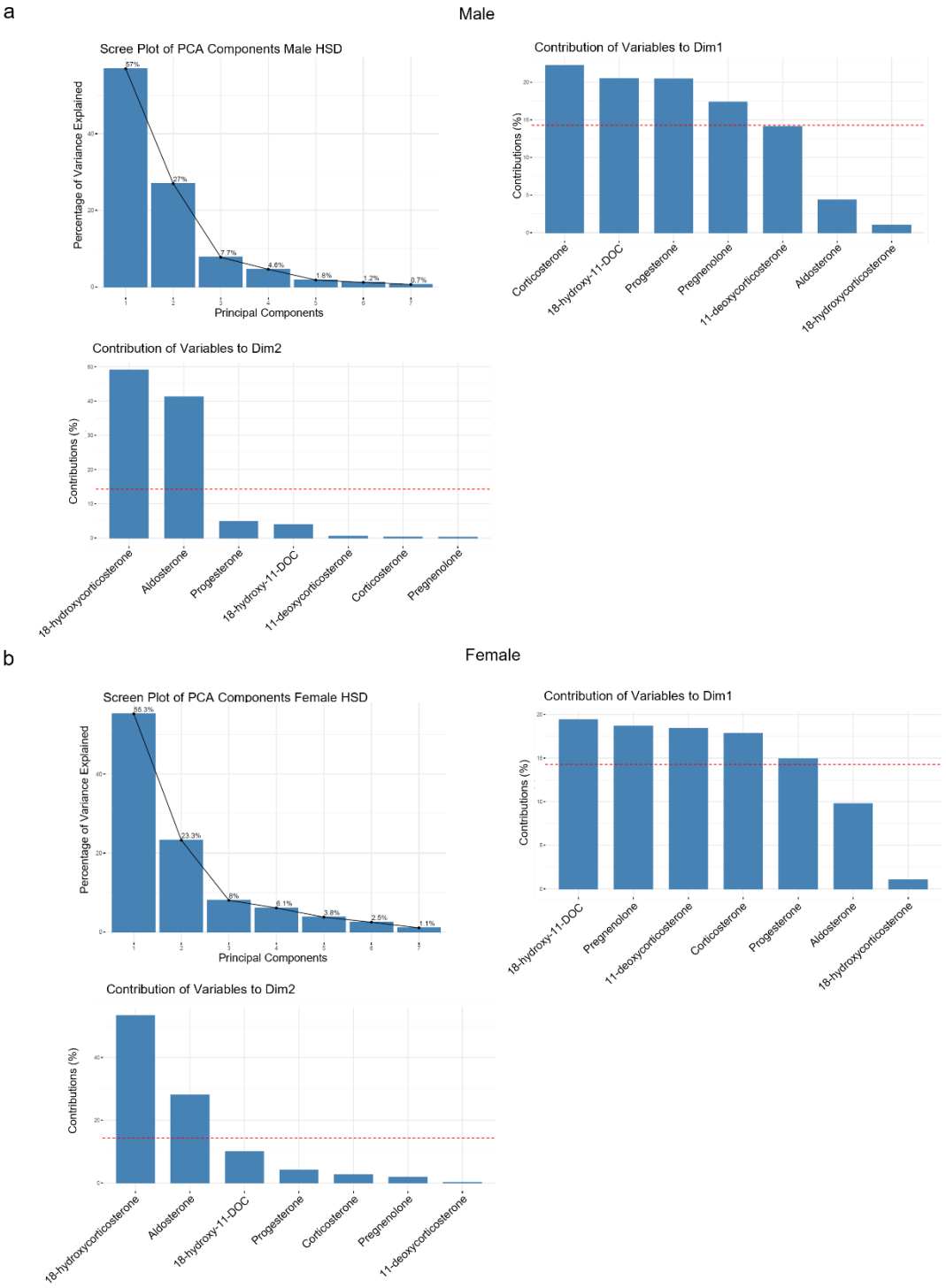

Figure S11. Characteristics of Principal component analysis (PCA) of adrenal plasma steroid profiles following a HSD. (a-b). Scree plot representing the principal components in relation to the percentage of explained variance and the respective contribution of single variables to dimensions 1 and 2 in male **(a)** and female **(b)** *Cyp11b2*$^{+/Cre}$-*m*T*m*G mice fed a HSD vs control littermates.

Figure S12

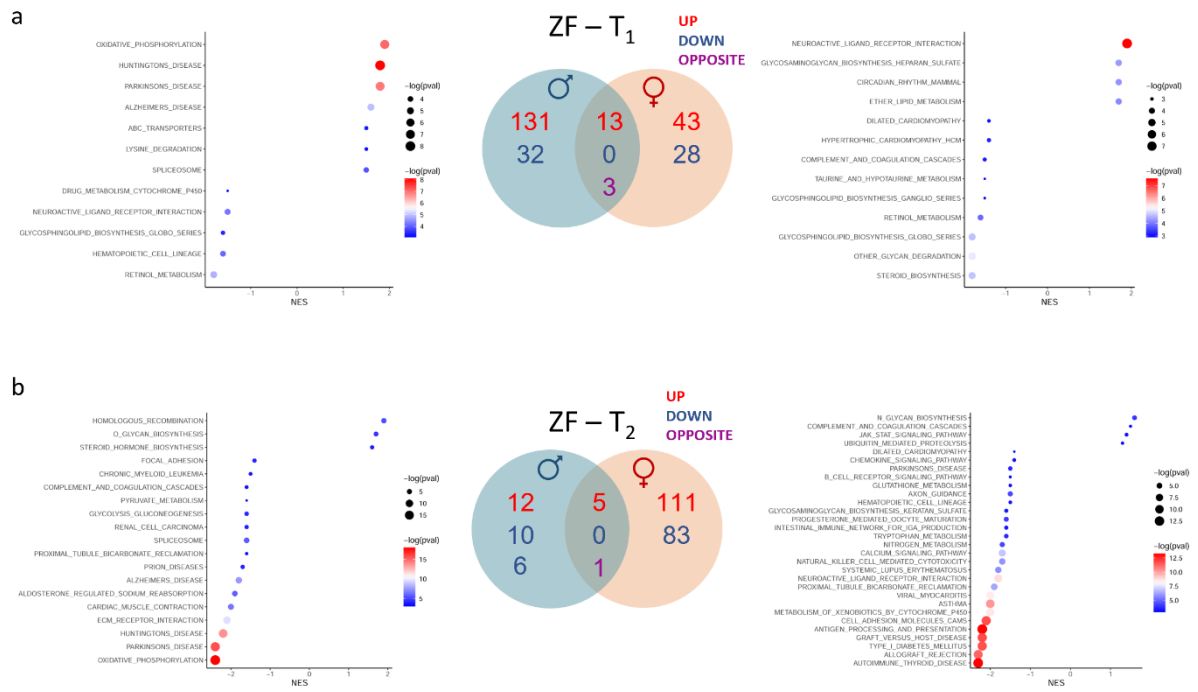

Figure S12. Effect of HSD on zone-specific gene expression. (a). Gene set enrichment analysis (GSEA) pathways from the KEGG database (adapted on mouse) of male (left panel) and female (right panel) *Cyp11b2*$^{+/Cre}$-*m*T*m*G HSD-treated mice vs Ctrl T_1 in the ZF cluster and Venn diagram illustrating the up and down and opposite regulated genes between males and females. **(b).** GSEA pathways from the KEGG database (adapted on mouse) of *Cyp11b2*$^{+/Cre}$-*m*T*m*G Rec vs Ctrl T_2 male (left panel) and female (right panel) mice in the ZF cluster and Venn diagram illustrating the up and down and opposite regulated genes between males and females. Pathways were ordered by the NES (normalized enriched score) and only the top 20 up and down regulated pathways are visualized using dotplots. The colour and size of the dots reflect the significance of the enrichment [-log(pval)].

Figure S13

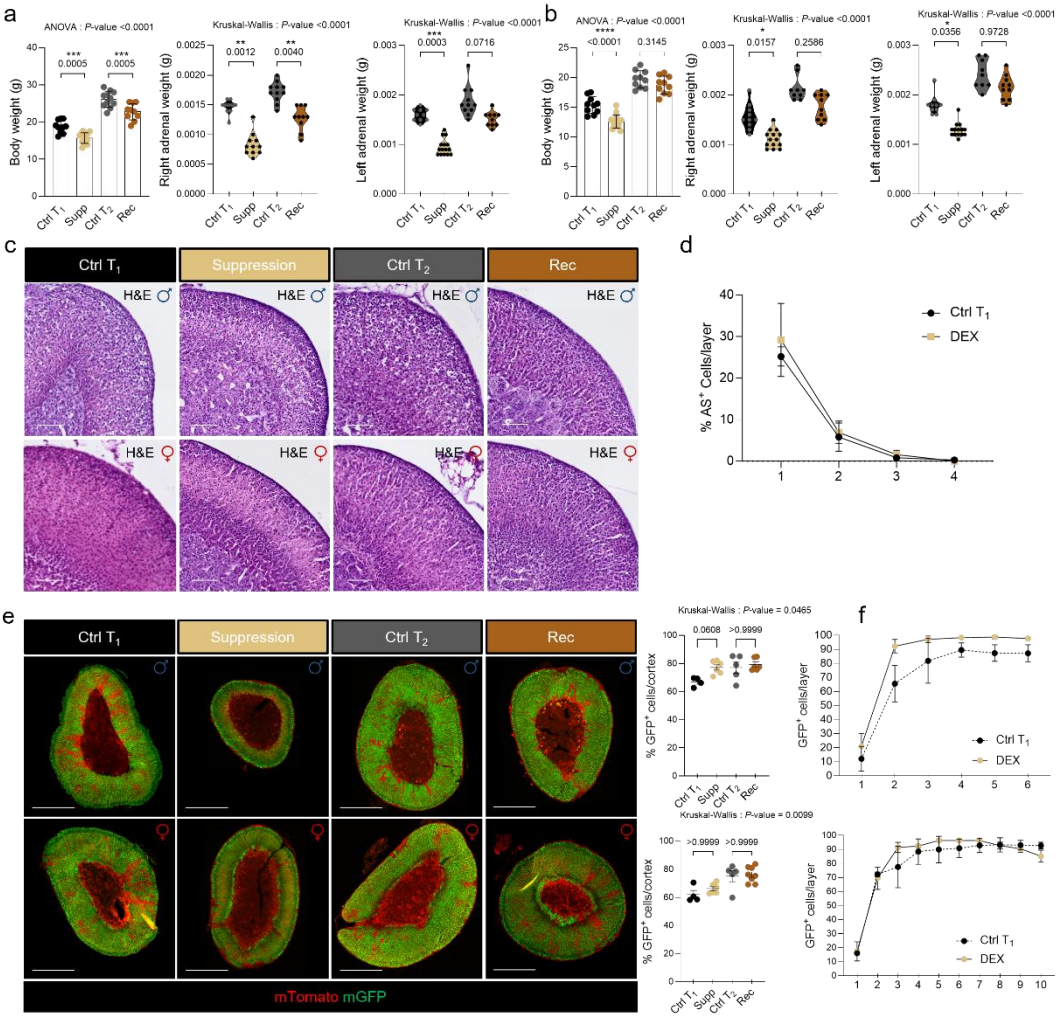

Figure S13. Effect of dexamethasone treatment on the adrenal cortex. Body weight and absolute right and left adrenal mass of *Cyp11b2*$^{+/Cre}$-*m*T*m*G male **(a)** and female **(a)** mice treated with dexamethasone (suppression) from 4 to 6 weeks of age (T_1) and after a recovery period from 6 weeks to 9 weeks (T_2). **(c).** H&E staining of male and female, control and treated, *Cyp11b2*$^{+/Cre}$-*m*T*m*G mouse adrenals at T_1 and T_2. **(d).** Quantification of AS$^+$ cells in the first 4 layers of the adrenal cortex of *Cyp11b2*$^{+/Cre}$-*m*T*m*G male mice treated with dexamethasone (DEX) from 4 to 6 weeks of age (T_1). Each layer has a thickness of 50 micron. **(e).** Coimmunofluorescence of mGFP (green) with mTomato (red) and quantification of the mGPF$^+$ cells in the adrenal cortex of *Cyp11b2*$^{+/Cre}$-*m*T*m*G (upper panel) male and (lower panel) female mice at T_1 and T_2. Scale Bar: 500 µm. **(f).** Analysis of the progression of mGFP+ cells along adrenal cortex layers of *Cyp11b2*$^{+/Cre}$-*m*T*m*G (upper panel, 6 layer) male and (lower pannel, 10 layer) female mice treated with DEX from 4 to 6 weeks of age (T_1) and after a recovery period from 6 weeks to 9 weeks (T_2). Each layer has a thickness of 25 micron; in males, only 6 layers could be quantified due to ZF atrophy. P values were obtained with Ordinary one-way ANOVA, adjusted with Šídák's multiple comparisons test or with Kruskal-Wallis test and adjusted with Dunn's multiple comparisons test, as indicated. Data are presented as mean values ±SEM. *P value < 0.05; **P value < 0.01; ***P value < 0.001.

Figure S14

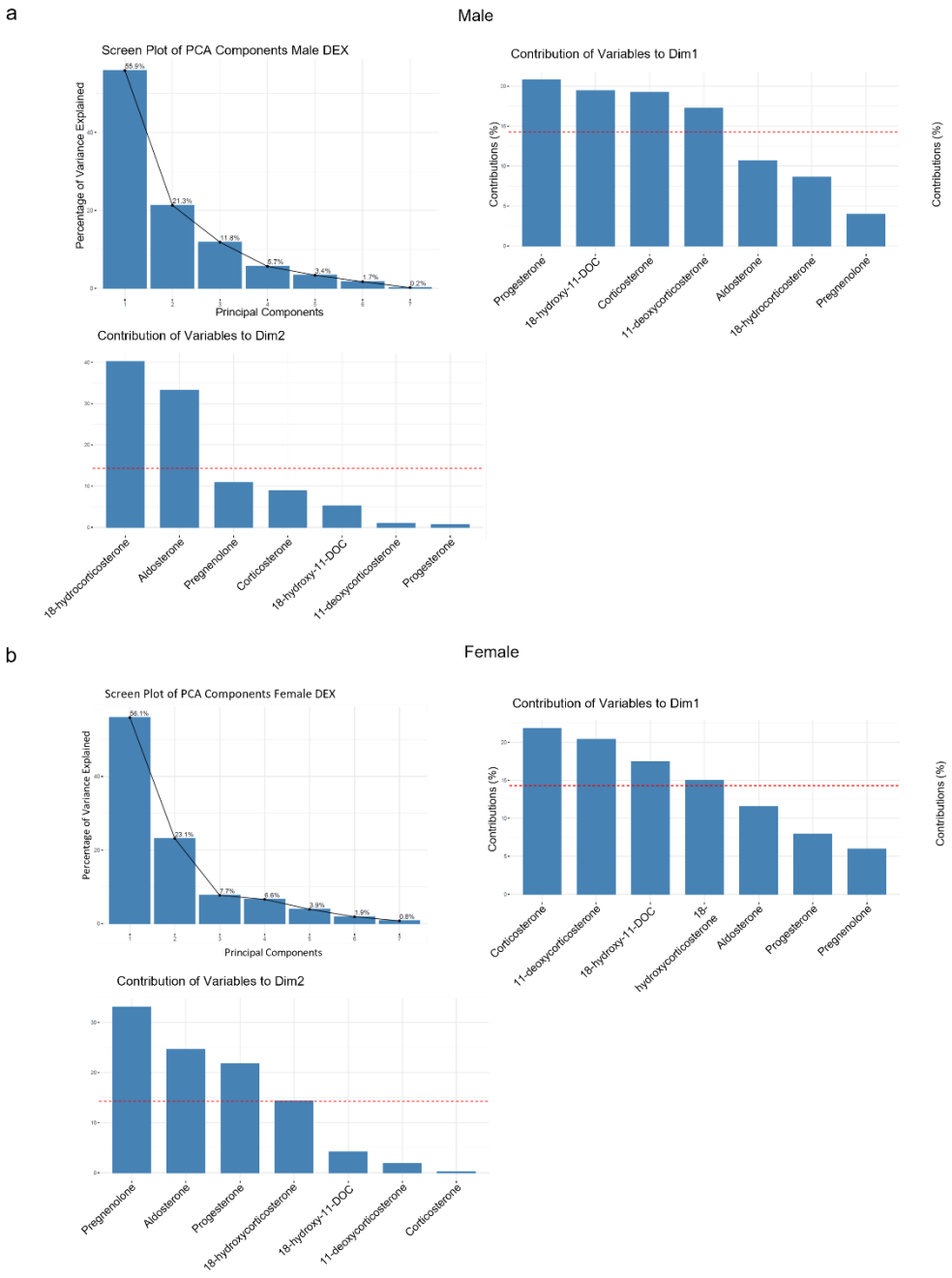

Figure S14. Characteristics of Principal component analysis (PCA) of adrenal plasma steroid profiles following DXM treatment. (a-b). Scree plot representing the principal components in relation to the percentage of explained variance and the respective contribution of single variables to dimensions 1 and 2 in male **(a)** and female **(b)** *Cyp11b2*$^{+/Cre}$-*m*T*m*G mice following DXM treatment vs control littermates. PCA shows clear separation between controls and DXM-treated mice along the first Dimension (Dim1), which explained 55.9% in males and 56.1% in females of the total variance, driven mainly by corticosterone, 11-deoxycorticosterone, 18-hydroxy-11-DOC, progesterone (only in males) and 18-hydrocorticosterone (only in females).

Figure S15

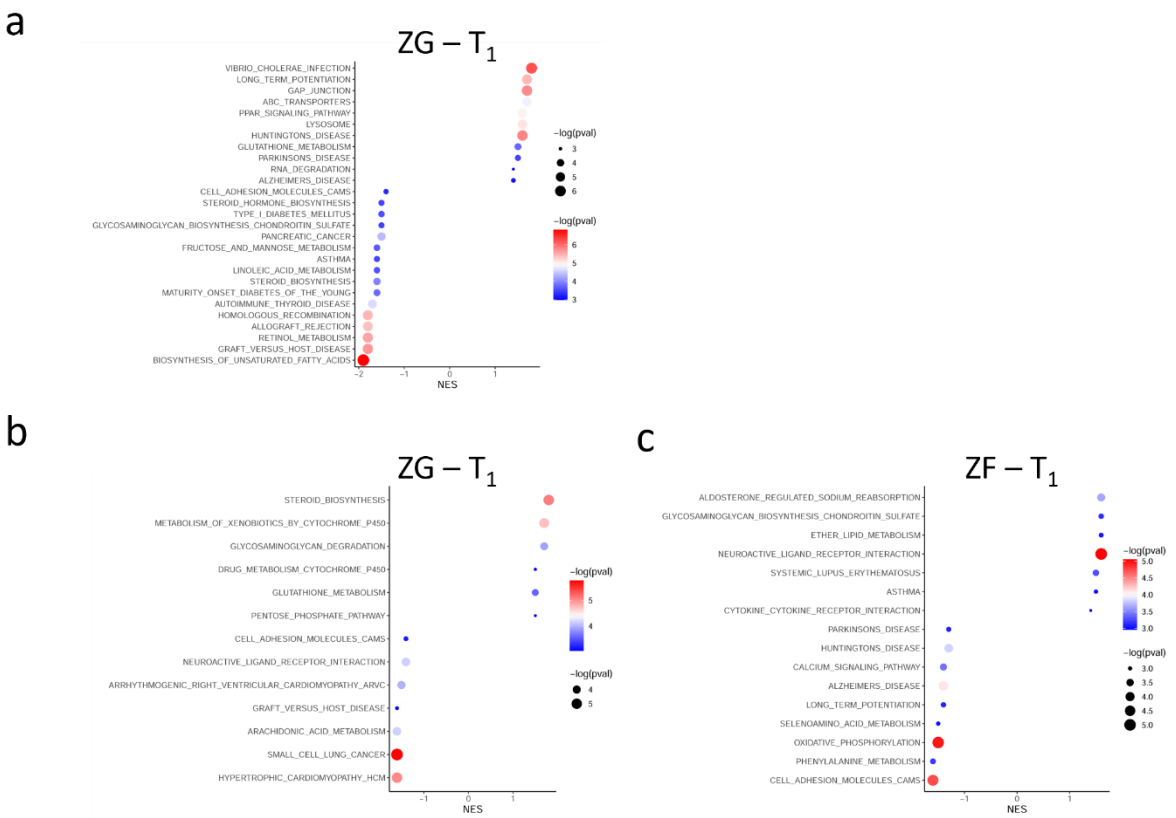

Figure S15. Effect of DEX treatment on zone-specific gene expression (a-b). Gene set enrichment analysis (GSEA) pathways from the KEGG database (adapted on mouse) of the ZG cluster of male **(a)** and female **(b)** *Cyp11b2*$^{+/Cre}$-*m*T*m*G DEX-treated vs Ctrl T_1 mice. **(c).** Gene set enrichment analysis (GSEA) pathways from the KEGG database (adapted on mouse) of female *Cyp11b2*$^{+/Cre}$-*m*T*m*G DEX-treated vs Ctrl T_1 mice in the ZF cluster.

Figure S16

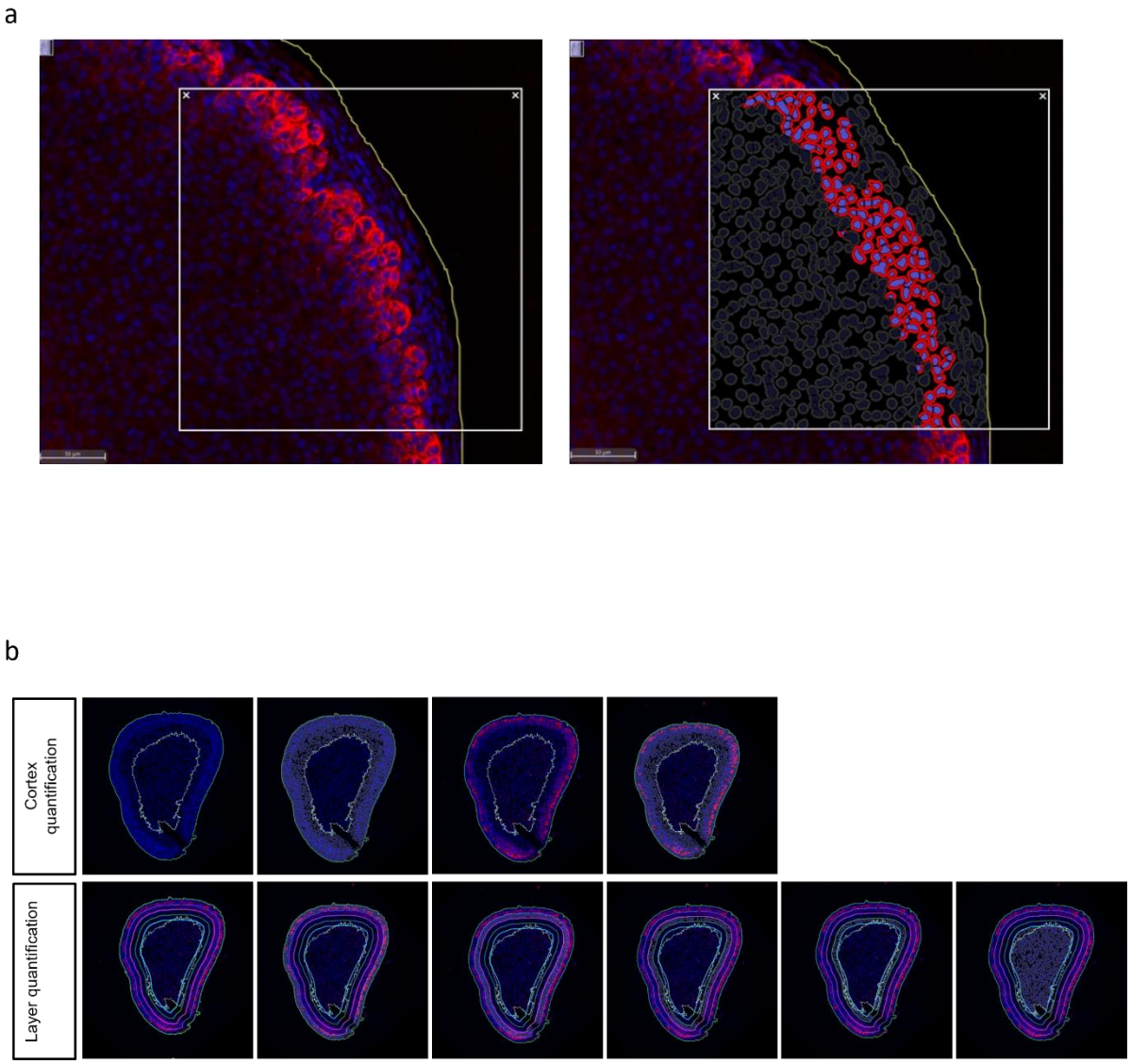

Figure S16. Quantification of immunolabeling signals in the adrenal cortex (a). Example of whole adrenal cortex DAB2^{+} cells quantification using HALO software (version 3.6.4134, Indica Labs) with the HighPlex Fl v4.2.14 module. **(b).** Example of adrenal cortex segmentation in 50 µm layers of a DEX-treated male mouse and quantification of DAB2^{+} cells using HALO software (version 3.6.4134, Indica Labs) with the HighPlex Fl v4.2.14 module.

Figure S17

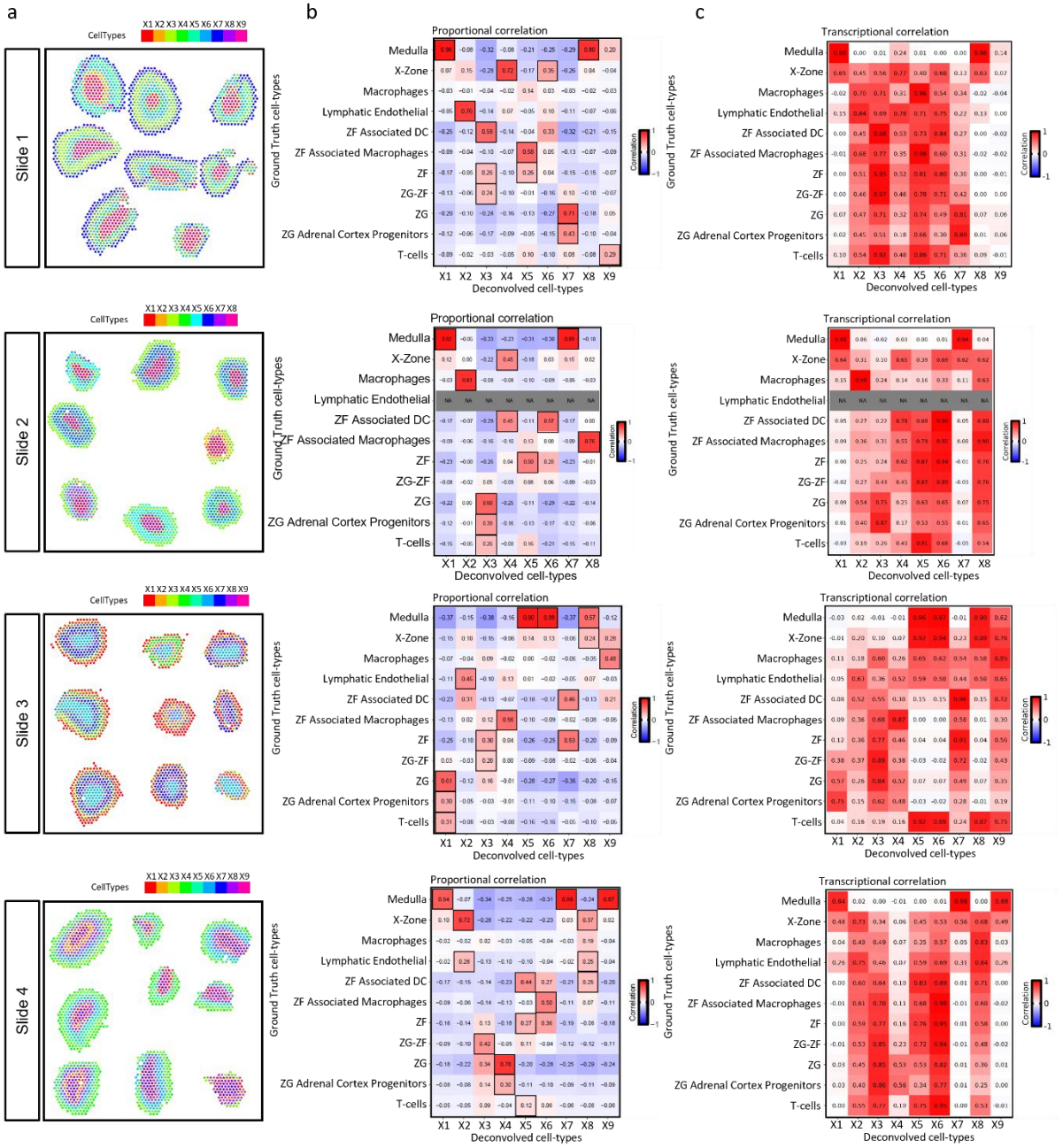

Figure S17. Deconvolution of spatial transcriptomic data. (a). Deconvolved cell-type proportions of adrenals ST data, displayed as pie charts for each ST spot. **(b).** Heatmap of Pearson's proportional correlations and transcriptional correlations between the deconvolved cell-type and ground truth cell-type proportions across spots. Matched deconvolved and ground truth cell types are boxed. **(c).** Heatmap of Pearson's transcriptional correlations between the deconvolved cell-type and ground truth cell-type proportions across spots.

14.2 Mineralocorticoid receptor inhibition in parietal epithelial cells prevents focal segmental glomerulosclerosis and crescentic glomerulonephritis

Lazareth H, Lenoir O, Garo F, Rocha A, Giscos-Douriez I, **Fayad M,** et al. Mineralocorticoid receptor inhibition in parietal epithelial cells prevents focal segmental glomerulosclerosis and crescentic glomerulonephritis. Kidney Int. 2025 Sep 24;S0085-2538(25)00748-3.

Mineralocorticoid receptor inhibition in parietal epithelial cells prevents focal segmental glomerulosclerosis and crescentic glomerulonephritis

OPEN

Hélène Lazareth[1,2,9], Olivia Lenoir[1,9], Florian Garo[1,3], Angélique Rocha[1], Isabelle Giscos-Douriez[1], May Fayad[1], Nasreddine Saidi[1], Léa Guyonnet[4,5], Alexandre Karras[1,2], Marcus J. Moeller[6], Carole Hénique-Gréciet[7], Maria-Christina Zennaro[1,8,10], Sheerazed Boulkroun[1,10] and Pierre-Louis Tharaux[1,10]

[1]Université Paris Cité, Inserm, Paris Cardiovascular Research Center - PARCC, F-75015, Paris, France; [2]Nephrology Department, Georges Pompidou European Hospital, Assistance Publique Hôpitaux de Paris, Université Paris Cité, Paris, France; [3]Nephrology-Dialysis-Apheresis Unit, Nîmes University Hospital, Nîmes, France; [4]Innovative Therapies in Haemostasis, INSERM, Université Paris Cité, F-75006, Paris, France; [5]Cytometry Platform, Institut Curie, Paris, France; [6]Division of Nephrology and Immunology, University Hospital of the Aachen University of Technology (RWTH), Internal Medicine II, Aachen, Germany; [7]INSERM U 955, Team 21, University Paris-Est-Créteil (UPEC), Créteil, France; and [8]Genetic Department, Georges Pompidou European Hospital, Assistance Publique Hôpitaux de Paris, Université Paris Cité, Paris, France

Abstract

Introduction: Focal segmental glomerulosclerosis (FSGS) is a common histological lesion in adults worldwide. It results from initial podocyte injury, followed by a maladaptive activation of glomerular parietal epithelial cells (PECs), which leads to progressive scarring of glomeruli. Abnormal PEC phenotype is also a hallmark of crescentic glomerulonephritides, another class of severe kidney diseases that complicate small vessel vasculitides. Current knowledge of the pathophysiological mechanisms leading to PEC activation is limited. Recent evidence indicates an active and destructive role for PECs in extra-capillary glomerular diseases. Therefore, targeting such maladaptive responses could represent a novel therapeutic option to prevent kidney failure in patients. Yet, druggable pathways to prevent or stop the pathogenic behavior of PECs are still elusive.

Methods: Here, we examined the role of the mineralocorticoid receptor signaling in PECs in two mouse models of glomerular disease involving PEC activation: a robust model of maladaptive FSGS with deoxycorticosterone acetate (DOCA)-salt administration with uninephrectomy, and nephrotoxic serum–induced crescentic glomerulonephritis.

Results: We demonstrate that targeting the mineralocorticoid receptor (MR) (Nr3c2) gene specifically in PECs prevents migration and proliferation after DOCA-salt administration with uninephrectomy. Remarkably, both MR deficiency in PECs and mineralocorticoid receptor pharmacological blockade using eplerenone were also effective in preventing extracapillary lesions and glomerular failure in nephrotoxic serum–induced crescentic glomerulonephritis. Additionally, we revealed a significant overlap between pathways triggered by heparin-binding EGF-like growth factor and its receptor signaling and MR signaling. This promoted the migration, proliferation, and epithelial-to-mesenchymal transition of PECs.

Conclusions: Together, our results highlight the common role of MR signaling in the pathophysiology of extra-capillary glomerulopathies, FSGS, and crescentic glomerulonephritis. This supports the use of MR antagonists as potential complementary therapeutic agents with original modes of action for severe diseases.

Kidney International (2025) ■, ■–■; https://doi.org/10.1016/j.kint.2025.07.037

KEYWORDS: chronic kidney disease; crescentic glomerulonephritis; focal segmental glomerulosclerosis; migration; mineralocorticoid receptor; parietal epithelial cells; podocytes

Copyright © 2025, International Society of Nephrology. Published by Elsevier Inc. This is an open access article under the CC BY license (http://creativecommons.org/licenses/by/4.0/).

Correspondence: *Pierre-Louis Tharaux or Maria-Christina Zennaro, Paris Cardiovascular Research Center, 56 rue Leblanc, 75015 Paris, France. E-mail: pierre-louis.tharaux@inserm.fr or maria-christina.zennaro@inserm.fr*

[9]HL and OL participated equally in the work.

[10]M-CZ, SB, and P-LT participated equally in the work.

Received 29 July 2024; revised 28 July 2025; accepted 31 July 2025

Focal segmental glomerulosclerosis (FSGS) represents the foremost primary glomerulopathy in adults in the United States and South America. FSGS is a histologic lesion accounting for approximately 15%–30% of primary glomerulopathy cases worldwide.[1–10] Irrespective of the underlying cause, the existing paradigm hypothesizes that after the initial triggering damage and loss of podocytes, the

Translational Statement

The 2021 Kidney Disease: Improving Global Outcomes guidelines recommend renin-angiotensin system blockade, optimal blood pressure management, and dietary salt restriction for treating maladaptive focal segmental glomerulosclerosis (FSGS), whereas primary FSGS should be treated primarily with high-dose oral glucocorticoids. Despite variable relapse rates, these strategies are often insufficient. In addition, there are currently no validated nephroprotective strategies that can be added to immunosuppression for the treatment of crescentic glomerulonephritis (CGN). The side effects of immunosuppressive drugs significantly impact patients' life expectancy and quality of life; complementary nephroprotective strategies are needed. Our research indicates that inhibiting mineralocorticoid receptor (MR) signaling can protect against glomerular damage by preventing the pathologic activation of parietal epithelial cells. These findings present a promising new avenue for clinical trials in the treatment of FSGS and CGN, highlighting the potential of MR antagonists in these diseases. Furthermore, use of glucocorticosteroids with minimal mineralocorticoid activity may be preferable in these contexts.

aberrant and pathologic activation of the parietal epithelial cells (PECs) results in ultimate glomerular destruction and scarring.[11–15] Similarly, crescentic glomerulonephritis (CGN) involves pathologic activation of PECs, which is more rapid and diffuse. Recently, we demonstrated that crescent- and FSGS-forming PECs are not passive bystanders but play a crucial role in glomerular tuft demolition and kidney failure.[16] Despite the varied origins of these disorders, one may wonder whether specific pathogenic cues that trigger PEC activation, along with the subsequent signaling pathways activated downstream of these signals, could be shared across this spectrum of diseases.[16–21] The PEC phenotype varies across different forms of FSGS, indicating that there may not be universal mechanisms for PEC activation or that various thresholds of common pathways exist. Delineating these will require further studies. Moreover, the term "activation" is somewhat vague and encompasses aberrant migration, proliferation, and extracellular matrix production by the PECs.[22–24] Other mechanisms, such as cell death or the release of inflammatory or signaling molecules by these cells, are also likely to play a significant role.

Mineralocorticoid receptor (MR) antagonists have recently emerged as potential therapeutic agents for preventing the progression of chronic kidney disease (CKD) progression.[25,26] Deoxycorticosterone acetate (DOCA), a synthetic mineralocorticosteroid, has been used to demonstrate the adverse effects of MR signaling in kidneys. Notably, the concomitant administration of DOCA and a high sodium diet (DOCA-salt model) causes hypertension and glomerulosclerosis, followed by diffuse tubular injury and interstitial fibrosis, as shown in animal models from the 1940s.[27–29] Although Selye[30] noted early that "both the parietal and visceral lamina of Bowman's capsule showed signs of hypertrophy and hyperplasia" in DOCA-intoxicated chick kidneys, the notion that nephron reduction and the DOCA-salt model induce maladaptive FSGS in rats[31] and mice[20,32] emerged only 30 years ago. Several studies have elucidated the mechanisms by which the aldosterone/MR axis orchestrates podocyte injury[33–37] and showed the beneficial impacts of MR antagonism on podocytes to limit CKD progression.[38–40]

Nonetheless, MR (or nuclear receptor subfamily 3 group C member 2 [NR3C2] signaling) was not investigated in severe extracapillary glomerular diseases. Moreover, it raises the question of why other experimental models of hypertension associated with high glomerular capillary pressure, such as angiotensin II or endothelin-1 infusion, do not induce FSGS, despite similar podocyte injuries observed in the DOCA-salt model. Given the central role of PECs in FSGS, we investigated whether MR directly influences PEC activation. To do this, we created a mouse model with an inducible PEC-selective MR deficiency. Our results showed that deletion of the MR (Nr3c2) gene in PECs ($MR^{\Delta PEC}$) impairs their activation and mitigates the renal dysfunction and sclerosis typically observed in the DOCA-salt model of FSGS. Furthermore, we observed a marked expression of MR in crescentic lesions from patients diagnosed with anti-neutrophil cytoplasmic antibody–associated vasculitis or lupus nephritis. To further explore this, we challenged $MR^{\Delta PEC}$ mice with the nephrotoxic nephritis (NTN) model of CGN. Surprisingly, these mice displayed marked protection against crescentic glomerular injury and kidney failure. Moreover, the administration of eplerenone, a selective MR antagonist, also prevented PEC pathogenic recruitment and renal failure in the NTN model.

Finally, transcriptomic analysis of heparin-binding EGF-like growth factor (HB-EGF)–treated PECs revealed a significant overlap between pathways triggered by HB-EGF/epidermal growth factor receptor (EGFR) signaling and aldosterone/MR signaling. Collectively, our work identifies the direct role of MR signaling in the pathogenic activation of PECs, highlighting potential pathways for therapeutic intervention in FSGS and CGN.

METHODS

Animals

Mice with PEC-specific deletion of the *Nr3c2* gene, coding for MR, were generated by crossing iPec-Cre mice,[41] which expresses CRE-recombinase exclusively in PEC after doxycycline induction, with *Nr3c2* floxed mice[42] and are named $MR^{\Delta PEC}$ in the article. Doxycycline hyclate (Sigma Aldrich) was administered *in* drinking water for 14 days (5% sucrose and 1 mg/ml doxycycline), followed by a washout for 1 week. Age-matched littermates that had no deletion of *Nr3c2* in any cells were used as "wild-type" (WT) controls. Animals were housed under standard specific pathogen-free conditions. All

mice were housed in individually ventilated cages (23 °C ± 2 °C, 50% ± 10% humidity, 12-hour light/dark cycle), with standard mouse feed and water *ad libitum*. Experiments were conducted according to the French veterinary guidelines and those formulated by the European Community for experimental animal use (L358-86/609EEC) and were approved by the Institut National de la Santé et de la Recherche Médicale, local University Research Ethics Committee and French Ministry of Research (APAFIS-# 25934). ARRIVE reporting guidelines were used to report animal experiments.[43]

Nephrotoxic nephritis model. NTN was induced in male mice (10–16 weeks of age) as previously reported.[16,44,45] Eplerenone was given by daily oral gavage at a dose of 100 mg/kg per day. This dose is commonly used in mice to investigate its effects on cardiovascular, renal, or endocrine systems, demonstrating efficacy without significant toxicity. This dose is considered pharmacologically active and safe for repeated administration in short- to medium-term studies without side effects.[46–49] Mice were killed after 14 days.

DOCA-salt model. Ten- to fifteen-week-old male mice underwent unilateral left nephrectomy via flank incision under isoflurane anesthesia and received 0.1 mg/kg buprenorphine twice daily for 2 days. They were divided into 2 groups receiving either DOCA or placebo. DOCA pellets (50 mg) and placebo pellets with 21-day release (Innovative Research of America) were implanted subcutaneously 2 weeks after uninephrectomy. A second pellet of DOCA or placebo was implanted 3 weeks after the first implant. All animals received 0.9% NaCl in drinking water *ad libitum*. Mice were killed after 4 weeks of DOCA or placebo treatment.

In situ hybridization

Sections of human AFA (alcohol formalin glacial acetic acid)-fixed paraffin-embedded biopsies (4-µm-thick) or kidney sections from MR^{WT} and $MR^{\Delta PEC}$ mice were processed for *in situ* hybridization using RNAcope-based "double Z" probe design with specific probes against human *NR3C2* (Bio-Techne, Hs-NR3C2, 434651, C1-probe) and human *CLDN1* (Bio-Techne, Hs-CLDN1-C2, 830731-C2) for the human biopsies, and mouse *Nr3c2* (Bio-Techne, Mm-Nr3c2-E5E6, 456321, C1-probe) and mouse *Cldn1*-C2 (Bio-Techne, Mm-Cldn1-C2, 865501-C2) for mouse samples. RNAscope for human and mouse samples was performed using the RNAscope 2.5 HD Duplex Detection (Advanced Cell Diagnostics).

Additional details on methodology are included in the Supplementary Methods.

RESULTS

Parietal epithelial cell–selective MR deficiency prevents PEC activation in experimental FSGS

First, we examined NR3C2 mRNA expression in PECs using publicly available databases finding low level of NR3C2 mRNA expression in the single nuclei RNA sequencing datasets from the Kidney Precision Medicine Project (Supplementary Figure S1A). Similarly, the Kidney Interactive Transcriptomics online analyzer also showed NR3C2 expression in PECs in human kidneys at similar levels to those in podocytes in 2 single-cell RNA sequencing datasets[50,51] (Supplementary Figure S1B and C). These data indicate that PECs express NR3C2 supporting our strategy to delete this gene selectively in PECs.

To decipher the function of MR signaling in PEC activation during maladaptive FSGS, we used a DOCA-salt treatment combined with uninephrectomy (UniNx) in mice with a PEC-specific *Nr3c2* gene deletion ($MR^{\Delta PEC}$) (Supplementary Figure S2A). Of note, at baseline, $MR^{\Delta PEC}$ mice displayed similar physiological parameters compared with control normal littermate mice, in particular urinary albumin-to-creatinine ratio (UACR) (Supplementary Figure S2B and Supplementary Table S1) and no glomerular abnormality (Supplementary Figure S2C and D). We conducted RNAcope-based *in situ* hybridization to examine the presence of MR/*Nr3c2* transcripts in PECs, which were identified by *Cldn1* expression. In normal control mouse kidneys, we observed detectable but rare *Nr3c2* transcripts in PECs. In contrast, $MR^{\Delta PEC}$ displayed minimal to no *Nr3c2* transcripts in PECs (Supplementary Figure S3). Interestingly, kidneys from DOCA-salt UniNx challenged WT animals exhibited more abundant *Nr3c2* transcripts in PECs than in baseline condition (Supplementary Figure S4A) with an apparent stable expression level in distal tubular sections (Supplementary Figure S4B). After 4 weeks of DOCA-salt treatment, UACR increased similarly in both groups. By week 7, WT mice showed a 6-fold increase in UACR, whereas the $MR^{\Delta PEC}$ group plateaued at a significantly lower level (Figure 1a and Supplementary Figure S5A). The difference in albuminuria was not due to systolic blood pressure, which was not statistically significant throughout the model (Supplementary Figure S5B). At this stage, renal function was significantly better preserved in $MR^{\Delta PEC}$ mice than in control mice (Figure 1b). We then analyzed the glomerular histologic lesions in this UniNx + DOCA-salt model (Figure 1c and d). Histologic analysis indicated a nonsignificant trend showing fewer glomeruli with FSGS lesions in $MR^{\Delta PEC}$ compared with WT group (Figure 1e). However, the most advanced stages of FSGS were significantly less severe in $MR^{\Delta PEC}$ animals, which exhibited a lower proportion of glomeruli with sclerosis affecting more than 50% of the glomerulus (Figure 1f). This finding is consistent with the significant difference in blood urea nitrogen levels. No histologic change was observed in the placebo group between $MR^{\Delta PEC}$ and WT mice (Supplementary Figure S6A–D).

Given that FSGS lesions imply PEC phenotype switch from a quiescent epithelial state to a change in polarity, migration, proliferation, and epithelial-mesenchymal transition (EMT), we analyzed PEC features in this model. Electron microscopy of kidneys of UniNx + DOCA-salt–treated mice revealed PECs with enlarged cytoplasm and cytoplasmic extension in WT mice, whereas PECs from $MR^{\Delta PEC}$ mice retained a normal flat cell shape (Figure 1g). No ultrastructural abnormality was observed in the placebo groups

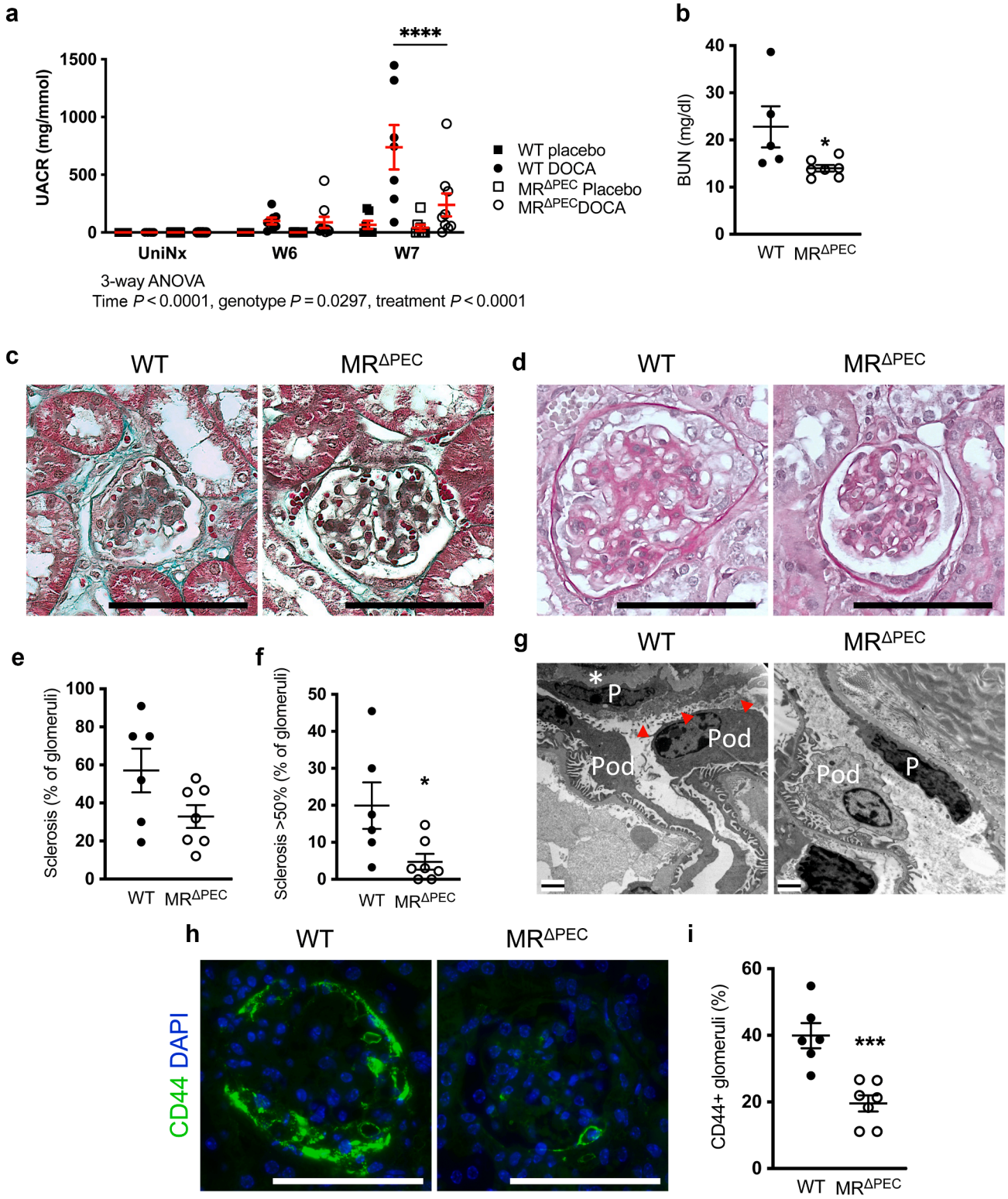

Figure 1 | Parietal epithelial cell (PEC)–selective mineralocorticoid receptor (MR) deficiency protects mice from focal segmental glomerulosclerosis (FSGS) lesions in the uninephrectomy (UniNx) + deoxycorticosterone acetate (DOCA)–salt FSGS model. (**a**) Urinary albumin-to-creatinine ratio (UACR) in PEC-Cre *Nr3c2*$^{wt/wt}$ (wild-type [WT]) and PEC-Cre *Nr3c2*$^{lox/lox}$ (MR$^{\Delta PEC}$) mice in the UniNx + DOCA-salt model. Data are shown as mean ± SEM. n = 6–7 mice. Three-way analysis of variance (ANOVA): time $P < 0.0001$, genotype $P = 0.0297$, treatment $P < 0.0001$, *post hoc* Fisher least significant difference test: $P < 0.0001$ for MR$^{\Delta PEC}$ DOCA versus WT DOCA at week 7 of DOCA. For clarity, only UACR after UniNx and at weeks 6 and 7 of the DOCA-salt model are shown, but the full dataset for UACR from week 1 to week 7 is shown in Supplementary Figure S3. (**b**) Blood urea nitrogen (BUN) (mg/dl) in WT and MR$^{\Delta PEC}$ mice after 7 weeks of UniNx + DOCA-salt. Data are shown as individual values and mean ± SEM. *t* test: * $P < 0.05$. (**c,d**) Masson trichrome (**c**) and periodic (continued)

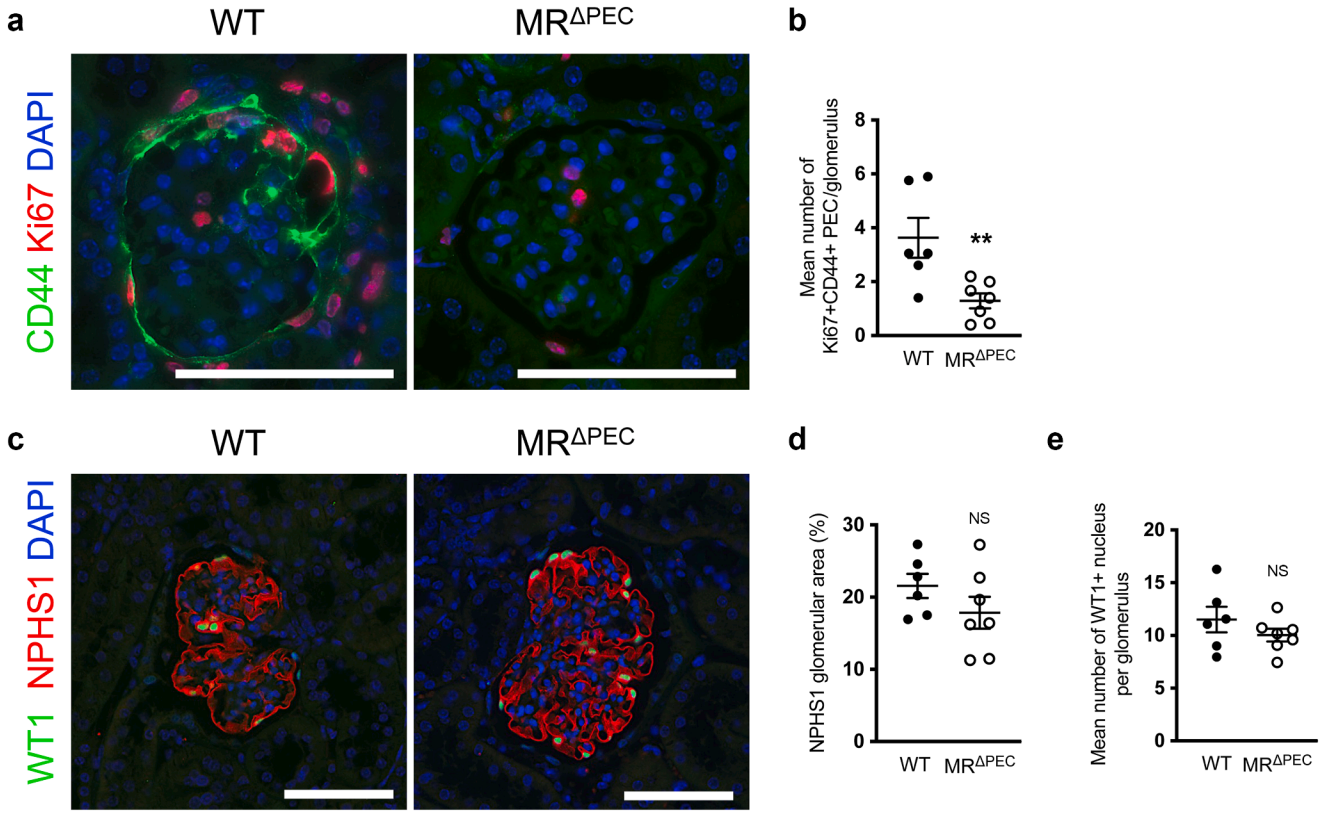

Figure 2 | Parietal epithelial cell (PEC)–selective mineralocorticoid receptor (MR) deficiency protects mice from PEC activation but not from podocyte injury in the uninephrectomy (UniNx) + deoxycorticosterone acetate (DOCA)–salt focal segmental glomerulosclerosis (FSGS) model. (**a**) Immunofluorescence stainings for CD44 (green), Ki67 (red), and 4′,6-diamidino-2-phenylindole (DAPI) (blue) on kidney sections in wild-type (WT) and $MR^{\Delta PEC}$ mice after 7 weeks of UniNx + DOCA-salt. Bar = 50 μm. (**b**) Quantification of the mean number of PEC expressing CD44 and Ki67 per glomerulus area on kidney sections from WT and $MR^{\Delta PEC}$ mice after 7 weeks of UniNx + DOCA-salt. Data are shown as individual values and mean ± SEM. n = 6 WT and 7 $MR^{\Delta PEC}$ mice. *t* test: $^{**}P < 0.01$. An average of 40 glomerular cross-sections per mouse were quantified. (**c**) Immunofluorescence for WT-1 (green), NPHS1 (red), and DAPI (blue) on kidney sections in WT and $MR^{\Delta PEC}$ mice after 7 weeks of UniNx + DOCA-salt. Bar = 50 μm. (**d,e**) Quantification of NPHS1+ glomerular area (**d**) and mean number of WT1+ cells per glomerular area (**e**) on kidney sections from WT and $MR^{\Delta PEC}$ mice after 7 weeks of UniNx + DOCA-salt. Data are shown as individual values and mean ± SEM. n = 6 WT and 7 $MR^{\Delta PEC}$ mice. Unpaired *t* test: $P = 0.21$ for (**d**) and $P = 0.28$ for (**e**). An average of 40 glomerular cross-sections per mouse were quantified. To optimize viewing of this image, please see the online version of this article at www.kidney-international.org.

(Supplementary Figure S6E). Finally, an expression of CD44, a marker of activated PECs,[52] was found in almost 40% of glomeruli in kidneys from UniNx + DOCA-salt–treated WT mice, whereas $MR^{\Delta PEC}$ had a significantly 2-fold lower percentage of glomeruli with CD44 expression (Figure 1h and i).

The determination of the percentage of PECs expressing Ki67, a marker of cell proliferation, revealed that $MR^{\Delta PEC}$ mice had significantly less proliferative PECs per glomeruli than WT mice in the UniNx + DOCA-salt model (Figure 2a and b). PEC-selective MR deficiency did not impact markers of mature differentiated podocytes (Figure 2c–e).

Taken together, our results demonstrated that MR deficiency in PECs restrained PEC activation and FSGS, thus highlighting MR signaling as one of the key pathologic mechanisms of PEC activation in the UniNx + DOCA-salt FSGS model.

Figure 1 | (continued) acid–Schiff (**d**) stainings on kidney sections from WT and $MR^{\Delta PEC}$ mice after 7 weeks of UniNx + DOCA-salt. Bar = 50 μm. (**e,f**) Quantifications of glomerulosclerosis (percentage of glomeruli) (**e**) and the percentage of glomeruli with sclerosis over 50% of the total glomerulus area (**f**) on kidney sections from WT and $MR^{\Delta PEC}$ mice after 7 weeks of UniNx + DOCA-salt. Data are shown as individual values and mean ± SEM. n = 6 WT and 7 $MR^{\Delta PEC}$ mice. *t* test: $^{*}P < 0.05$. (**g**) Transmission electron microscopy on kidney sections from WT and $MR^{\Delta PEC}$ mice after 7 weeks of UniNx + DOCA-salt. Bar = 1 μm. (**h**) Immunofluorescence staining for CD44 (green) and 4′,6-diamidino-2-phenylindole (DAPI) (blue) on kidney sections from WT and $MR^{\Delta PEC}$ mice after 7 weeks of UniNx + DOCA-salt. Bar = 50 μm. *Pod*, podocyte; *P*, parietal epithelial cell. *Enlarged Bowman's capsule basement membrane. Red arrowheads show enlarged PEC with microvilli. (**i**) Quantification of the percentage of glomeruli expressing CD44 in WT and $MR^{\Delta PEC}$ mice after 7 weeks of UniNx + DOCA-salt. Data are shown as individual values and mean ± *SEM* of n = 6 WT and 7 $MR^{\Delta PEC}$ mice. *t* test: $^{***}P < 0.001$. To optimize viewing of this image, please see the online version of this article at www.kidney-international.org.

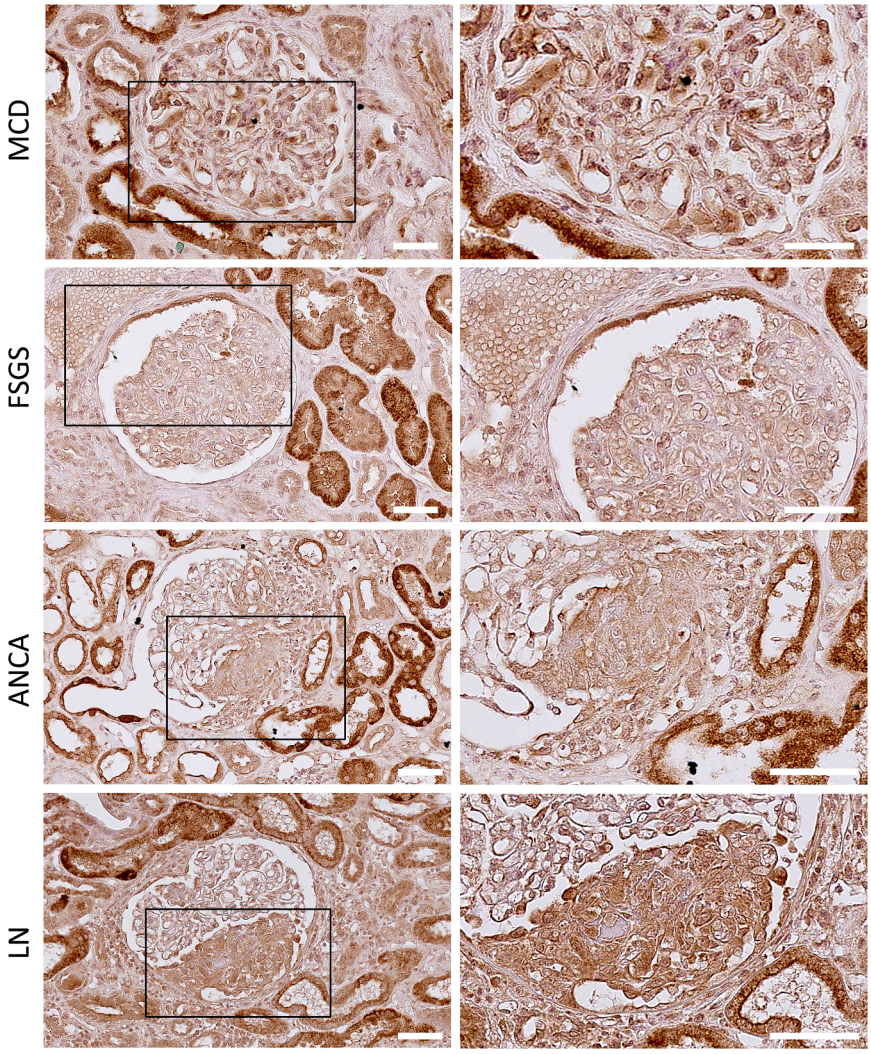

Figure 3 | Renal mineralocorticoid receptor (MR) expression in human kidneys. Representative images showing immunohistochemical staining of MR (brown) from pathologic human kidneys: minimal change disease (MCD), focal segmental glomerulosclerosis (FSGS), antineutrophil cytoplasmic antibody (ANCA) vasculitis, and lupus nephritis (LN). Note the intense constitutive staining in the distal tubules (positive control). Bar = 50 μm. To optimize viewing of this image, please see the online version of this article at www.kidney-international.org.

MR is expressed in activated PECs in human

We analyzed MR expression in kidney biopsies from patients with glomerular diseases. MR expression was investigated in kidney biopsies (Supplementary Tables S2 and S3). As shown in Figures 3 and 4 and Supplementary Figure S7, MR protein and mRNA expression were expressed in the distal convoluted tubules, and in glomerular cells, particularly podocytes and PECs, in patients with minimal change disease, FSGS, and CGN caused by antineutrophil cytoplasmic antibody–associated vasculitis and lupus nephritis. Of interest, immunoreactive MR expression was strong in extracapillary crescents in antineutrophil cytoplasmic antibody and lupus nephritis patients. Thus, we wondered whether MR signaling could activate PEC in CGN.

MR mediates renal injury in crescentic glomerulonephritis in mice

To assess the role of MR in the development of CGN in mice, we challenged WT and $MR^{\Delta PEC}$ mice with the nephrotoxic serum to induce the NTN model, a validated model of antibasement membrane glomerulonephritis in mice.[16,44,45] An additional group of WT mice was treated with eplerenone, an MR antagonist, to evaluate its potential therapeutic value. Both genetic and pharmacologic MR inhibition significantly prevented the rise in UACR in the NTN model (Figure 5a) and crucially preserved kidney function (Figure 5b and c). $MR^{\Delta PEC}$ mice and WT mice treated with eplerenone displayed less glomerular crescents than untreated WT mice, further confirming the beneficial effects of MR inhibition in this model (Figure 5d–f). Ultrastructure analysis by transmission electron microscopy showed glomerular basement membrane thickening, foot processes effacement, and filling of the urinary space with hypertrophied epithelial cells in WT mice, whereas $MR^{\Delta PEC}$ mice and WT mice treated with eplerenone had significantly preserved glomerular ultrastructure in the NTN model (Figure 5g).

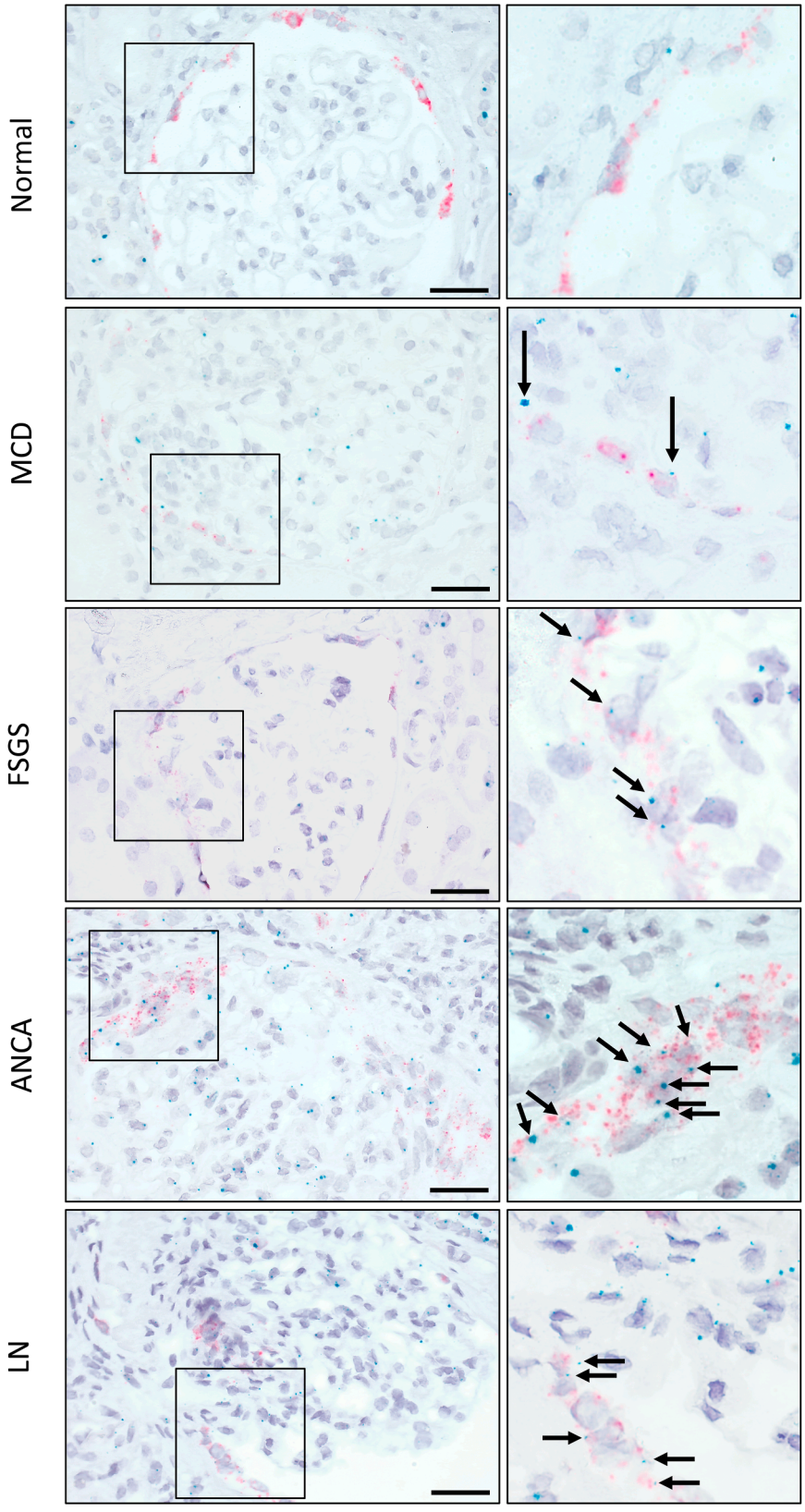

Figure 4| Representative images of combined RNAscope-based detection of mineralocorticoid receptor/nuclear receptor subfamily 3 group C member 2 (NR3C2) (cyan) and CLDN1 (pink) transcripts in normal and diseased kidneys with MCD or with extracapillary glomerulopathies. In normal kidneys and minimal change disease (MCD), parietal epithelial cells (PECs) identified by CLDN1 expression display very few NR3C2-associated signals, compared with distal tubular cell positive controls. In focal segmental glomerulosclerosis (FSGS), and even more in antineutrophil cytoplasmic antibody (ANCA)–associated vasculitis glomerulonephritis and lupus nephritis (continued)

Remarkably, PEC-selective MR deficiency and eplerenone treatment of WT mice prevented periglomerular infiltration of $CD3^+$ T lymphocytes in the NTN model (Figure 6a and b, Supplementary Figure S8). Not only did MR inhibition prevent T lymphocyte infiltration, but surprisingly, it prevented podocyte injury as shown by preserved NPHS1 glomerular expression and $WT1^+$ nuclei per glomerular area in $MR^{\Delta PEC}$ mice and WT mice treated with eplerenone (Figure 6c–e). Finally, both PEC-selective MR deficiency and eplerenone treatment of WT mice prevented PEC activation in the NTN model, as shown by a decreased proportion of $CD44^+$ glomeruli and decreased number of $CD4^+$ $Ki67^+$ PEC per glomeruli (Figure 6f–h).

Taken together, our results indicate a role of MR signaling in the pathologic PEC activation in CGN and demonstrate beneficial effects of eplerenone treatment on renal dysfunction in experimental CGN.

Eplerenone prevents HB-EGF–induced PEC migration and epithelial-mesenchymal transition

To address the mechanism of MR-mediated PEC activation, we assessed PEC migration in Ibidi chambers after treatment of cells with the promitotic and promigration factor HB-EGF and/or eplerenone. As previously reported,[16] HB-EGF promoted PEC migration. Although eplerenone did not affect unstimulated cells, it completely prevented HB-EGF–induced cell migration (Figure 7a). We previously demonstrated that HB-EGF–mediated PEC migration was associated with increased *Cd44* mRNA expression and decreased *Claudin1* mRNA expression.[16] We confirmed such changes; however, eplerenone partially or totally abolished the effect of HB-EGF on *Cd44* and *Pcna* and prevented EMT features, as shown by decreased *Snai1* and *Vimentin* mRNA expression (Figure 7b). Thus, MR antagonism with eplerenone prevents HB-EGF–mediated PEC migration and PEC proliferation through pathway independent of *Claudin1* regulation but involving CD44 and EMT.

MR signaling inhibition counteracts HB-EGF–mediated mRNA changes in PECs

To better understand the pathophysiological mechanisms by which MR inhibition prevents PEC activation in CGN and FSGS models, we performed RNA sequencing analyzes of murine PECs treated with HB-EGF and/or eplerenone. Principal component analysis showed segregation of HB-EGF–treated cells and HB-EGF + eplerenone–treated cells, whereas vehicle (dimethyl sulfoxide [DMSO])–treated cells and eplerenone-treated cells are not separated according to the 2 first principal components (Figure 8a).

MR antagonism induced significant mRNA expression modulation in HB-EGF–treated cells. We found 5215 differentially expressed genes (DEGs) (for adjusted $P < 0.05$) when comparing HB-EGF treatment versus vehicle treatment, among them 1709 with a log2 fold change <-1 or >1, and 2124 DEGs when comparing HB-EGF treatment versus HB-EGF + eplerenone treatment, 767 with a log2 fold change <-1 or >1 (Figure 8b and c, Supplementary Figure S9A–C, and Supplementary Tables S5 and S6). Among the 5215 DEGs enriched in the comparison of HB-EGF versus vehicle, 1949 were also commonly enriched in the comparison of HB-EGF versus HB-EGF + eplerenone (Figure 8d). This result indicates that eplerenone very significantly counteracts the HB-EGF profound and broad-spectrum shift of the transcriptome of the PEC, with inhibition of approximately 37% of the genes modulated by HB-EGF. Notably, RNA sequencing demonstrated that eplerenone significantly alleviated the HB-EGF–mediated transcriptional potentiation of recognized promitotic, motility, and cell adhesion pathways in PECs (*Egfr, Pdgfrb, Cd9, Pcna,* and *Itgb1*) and EMT (*Vim, Snail1,* and *Fn*) (Supplementary Figure S9C).

Next, we analyzed differentially regulated pathways using Gene Set Enrichment Analysis. We focused on the Hallmark, Biocarta, Reactome, and Wikipathways databases. Using a false discovery rate <25%, we identified 426 differentially regulated pathways in the comparison of HB-EGF treatment versus vehicle treatment and 362 differentially regulated pathways in the comparison of HB-EGF treatment versus HB-EGF + eplerenone treatment (Supplementary Tables S7 and S8). HB-EGF induced changes in pathways regulating cell cycle progression, DNA replication, DNA damage response, or apoptosis, such as G2/M checkpoints, E2F targets, Myc targets, Mtorc1, and P53 signaling pathways. EMT and transforming growth factor-β signaling pathways were also enriched in HB-EGF–treated cells. HB-EGF also promoted an inflammatory response, as shown by the enrichment of interferon alpha signaling, interferon gamma signaling, and tumor necrosis factor-α signaling pathways (Figure 8e and f). HB-EGF–stimulated PECs produce cytokine/chemokines that could contribute to immune cell recruitment, and eplerenone prevented HB-EGF-induced CCL2, CCL7, CCL9, CCL11, and CXCL13 mRNA expression (Supplementary Figure S9D).

Analysis of the Wikipathways, Reactome, and Biocarta databases confirmed HB-EGF effects on proliferation, cell death, extracellular matrix, and fibrosis with changes in collagen and metalloproteases synthesis pathways. Deep RNAseq also highlighted that HB-EGF regulates sensing to extracellular signals by regulating G-coupled protein Ca^{2+} receptor and tyrosine kinase receptor signaling. HB-EGF also regulated the focal adhesion, actin cytoskeleton, Rho GTPases, Rac GTPases, cell junction organization, and integrin pathways, supporting its effect on PEC migration.

Figure 4 | (continued) (LN) samples, activated PECs express several NR3C2 transcripts in the nucleus and cytoplasm in lesions areas. Of note, in the later in pathologic conditions, podocytes express NR3C2 as well. Bar = 20 μm. To optimize viewing of this image, please see the online version of this article at www.kidney-international.org.

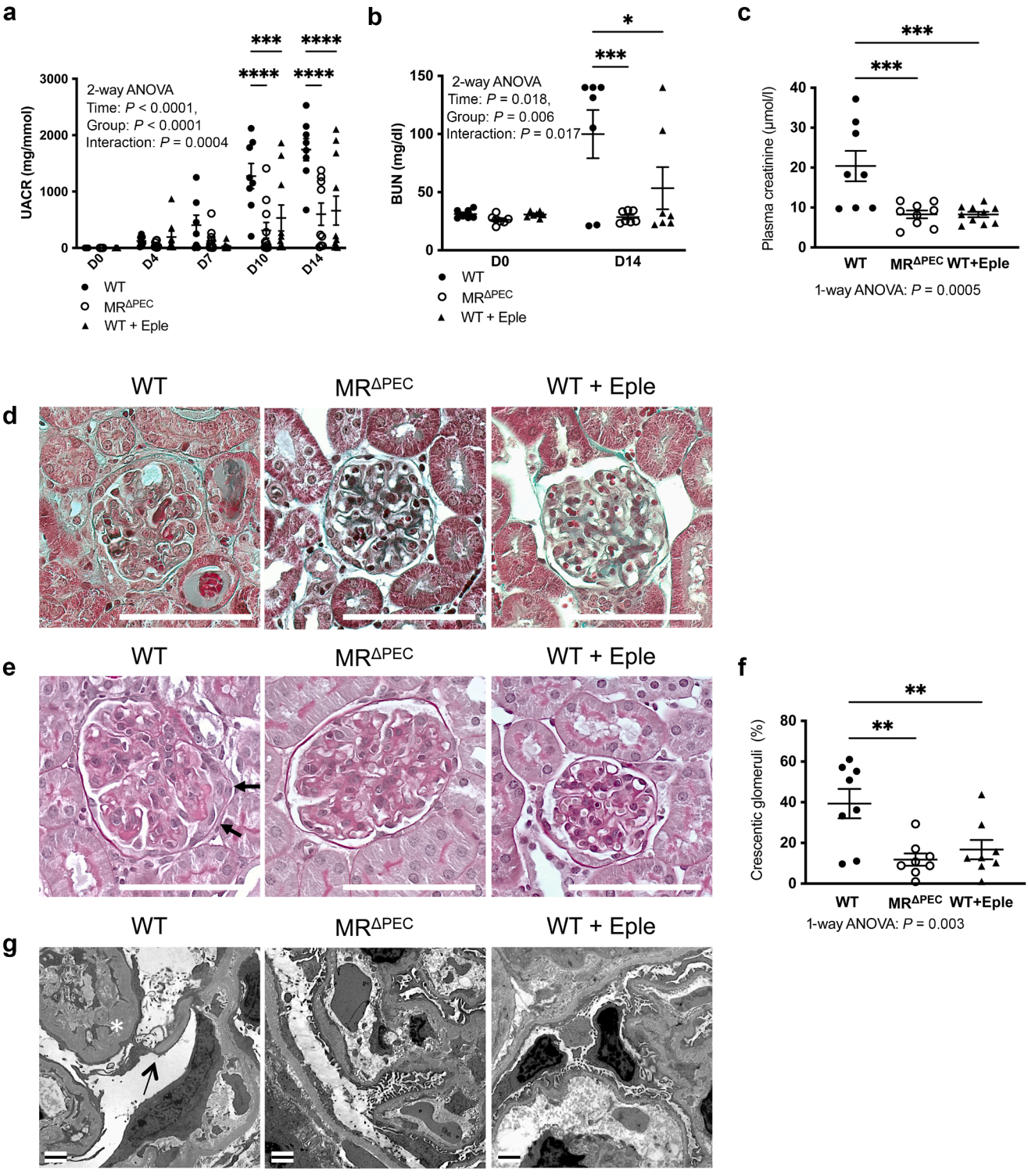

Figure 5 | Genetic and pharmacologic mineralocorticoid receptor (MR) inhibition prevent renal failure and preserve glomeruli in experimental crescentic glomerulonephritis. (**a**) Urinary albumin-to-creatinine ratio (UACR) in wild-type (WT) mice, $MR^{\Delta PEC}$ mice, and WT mice treated with eplerenone (Eple) during the time course of the nephrotoxic nephritis (NTN) model. Data are shown as mean ± SEM. n = 7–8 mice. Two-way analysis of variance (ANOVA): $P < 0.0001$ for time and group comparisons, $P = 0.0004$ for interaction. *Post hoc* Fisher least significant difference (LSD) test: $^{***}P < 0.001$, $^{****}P < 0.0001$. (**b**) Blood urea nitrogen (BUN) (mg/dl) at day 0 (D0) and day of sacrifice (D14) in WT mice, $MR^{\Delta PEC}$ mice, and WT mice treated with eplerenone during the NTN model. Data are shown as individual values and mean ± SEM. n = 7–8 mice. Two-way ANOVA: $P = 0.002$ for time, $P = 0.006$ for group, and $P = 0.01$. *Post hoc* Fisher LSD test: $^{*}P < 0.05$, $^{***}P < 0.001$. (**c**) Creatininemia (µmol/l) in WT mice, $MR^{\Delta PEC}$ mice, and WT mice treated with eplerenone at day 14 of the NTN model. Data are shown as individual values and mean ± SEM. n = 7–8 mice. One-way ANOVA: $P = 0.0005$, *post hoc* Fisher LSD test: $^{***}P < 0.001$. (**d,e**) Masson trichrome (**d**) and periodic acid–Schiff (**e**) stainings on kidney sections from WT mice, $MR^{\Delta PEC}$ mice, and WT mice (continued)

Remarkably, when we compared HB-EGF versus vehicle treatment and HB-EGF + eplerenone versus HB-EGF treatment, we found 324 common enriched pathways with opposite normalized enrichment scores (Figure 8e–g and Supplementary Table S8). This strongly supports the notion that eplerenone was able to counteract most of the HB-EGF effects in PECs.

DISCUSSION

The 2021 Kidney Disease: Improving Global Outcomes guidelines recommend using renin-angiotensin system blockade, optimal blood pressure control, and dietary salt restriction for patients with maladaptive FSGS. Conversely, primary FSGS should be addressed primarily with high-dose oral glucocorticoids as a first-line approach.[53] Although these therapeutic strategies demonstrate varying degrees of efficacy in some patients, characterized by differing relapse rates, they remain insufficient to meet our expectations. For primary FSGS and CGN, it is worth noting that using immunosuppressive agents carries significant side effects with unsatisfactory efficacy. Currently, numerous clinical trials are underway to test new molecules that consider the underlying etiology of the disease.[18,54–58] Intriguingly, none of the novel therapeutic approaches directly targets PECs. This absence is likely attributed to the relatively recent emergence of the role of PEC in FSGS progression.[14,24,59,60] Still, we have a limited understanding of the underlying pathologic mechanisms, and identifying targetable pathways associated with PEC involvement remains a challenge.[22,23]

We have recently made significant contributions to the understanding of the pathophysiological mechanisms governing the activation of PECs with the recent direct demonstration of the key pathogenic role of these cells in FSGS and, perhaps more spectacularly, in CGN.[16] Our work has revealed that the tetraspanin CD9 plays a pivotal role in coordinating the response of PECs to platelet-derived growth factor-BB and HB-EGF, thereby promoting changes in cell polarity, migration, and proliferation in both experimental FSGS and CGN.[16] Furthermore, we established the potential to mitigate glomerular damage and renal dysfunction by intercepting PEC activation. Remarkably, our findings also underscore that preventing PEC activation prevented podocyte depletion and mitigated renal inflammation and overall renal fibrosis in these models. Such work aligned with the important observation that increased CD44 expression leads to a prosclerotic and migratory PEC phenotype *in vitro* and *in vivo*, with fewer PECs migrating from Bowman's capsule to the glomerular tuft in *Cd44* knockout mice with experimental FSGS compared with WT mice.[52] We found increased NR3C2 mRNA and protein in PECs in FSGS, antineutrophil cytoplasmic antibody, and lupus nephritis samples but also, to a lesser extent, in minimal change disease samples compared with healthy kidneys. This suggests that the expression of MR in PECs is not a sufficient trigger for extracapillary lesions per se but may be an amplifier of FSGS or CGN mediators, which are nonexistent in minimal change disease.

Indeed, in the PEC-Cre mice, CRE is also expressed in certain tubular segments, as previously published, and we confirmed this observation using a PEC-Cre–driven ROSA-mTomato/mGFP reporter mouse model (Supplementary Figure S10). Although we cannot completely rule out the possibility of an effect from partial MR deletion in tubular cells due to some Cre activity in tubular cells, it is challenging to imagine how such an effect could significantly influence glomerular structure in models that primarily exhibit a glomerular initial mechanism of action. Moreover, the activity of PEC-Cre present in the distal tubules appears in a patchy and sparse manner, as shown with the PEC-Cre–driven ROSA-mTomato/mGFP reporter mouse model. We also observed no effect of PEC-Cre *Nr3c2* targeting on blood pressure regulation in the DOCA-salt model. This suggests that the limited expression of tubular CRE in PEC-Cre mice likely has a minimal impact on NR3C2 expression in the tubules. In contrast, the PEC-Cre–driven reporter GFP signal was detected in the vast majority of PECs across all glomeruli. This is consistent with RNAscope data, which show *Nr3c2* mRNA expression in tubules and podocytes, whereas its expression is almost undetectable in PECs in $MR^{\Delta PEC}$ mice.

Interestingly, MR signaling abrogation prevented CD44 expression in PECs *in vivo* in FSGS and CGN. *Cd9* mRNA expression was markedly inhibited by eplerenone despite HB-EGF stimulation. As we have demonstrated that CD9 is required for the induction of CD44 in PECs,[16] we hypothesize that MR signaling may command signaling upstream to the CD9-CD44 cascade for PEC activation.

Based on a series of clinical studies that have demonstrated that finerenone is protective in patients with diabetic kidney disease, the 2022 Kidney Disease: Improving Global Outcomes guidelines recommend the use of MR antagonists in diabetic patients with cardiorenal disease and albuminuria if the patients have normal serum K concentrations and mild estimated glomerular filtration rate decline.[61] The American Diabetes Association also recommended MR antagonist administration in diabetic patients with CKD.[62]

Figure 5 | (continued) treated with eplerenone at day 14 of the NTN model. Bar = 30 μm. The arrows indicate activated parietal epithelial cells (PECs) forming a pseudocrescent. (**f**) Quantification of crescents (%) in WT mice, $MR^{\Delta PEC}$ mice, and WT mice treated with eplerenone at day 14 of the NTN model. Data are shown as individual values and mean ± SEM. n = 7–8 mice. One-way ANOVA: $P = 0.003$, *post hoc* test: $^{**}P < 0.01$. (**g**) Transmission electronic microscopy showing glomerular ultrastructure in WT mice, $MR^{\Delta PEC}$ mice, and WT mice treated with eplerenone at day 14 of the NTN model. Bar = 2 μm. *Glomerular basement membrane thickening. Arrow shows PEC activation. To optimize viewing of this image, please see the online version of this article at www.kidney-international.org.

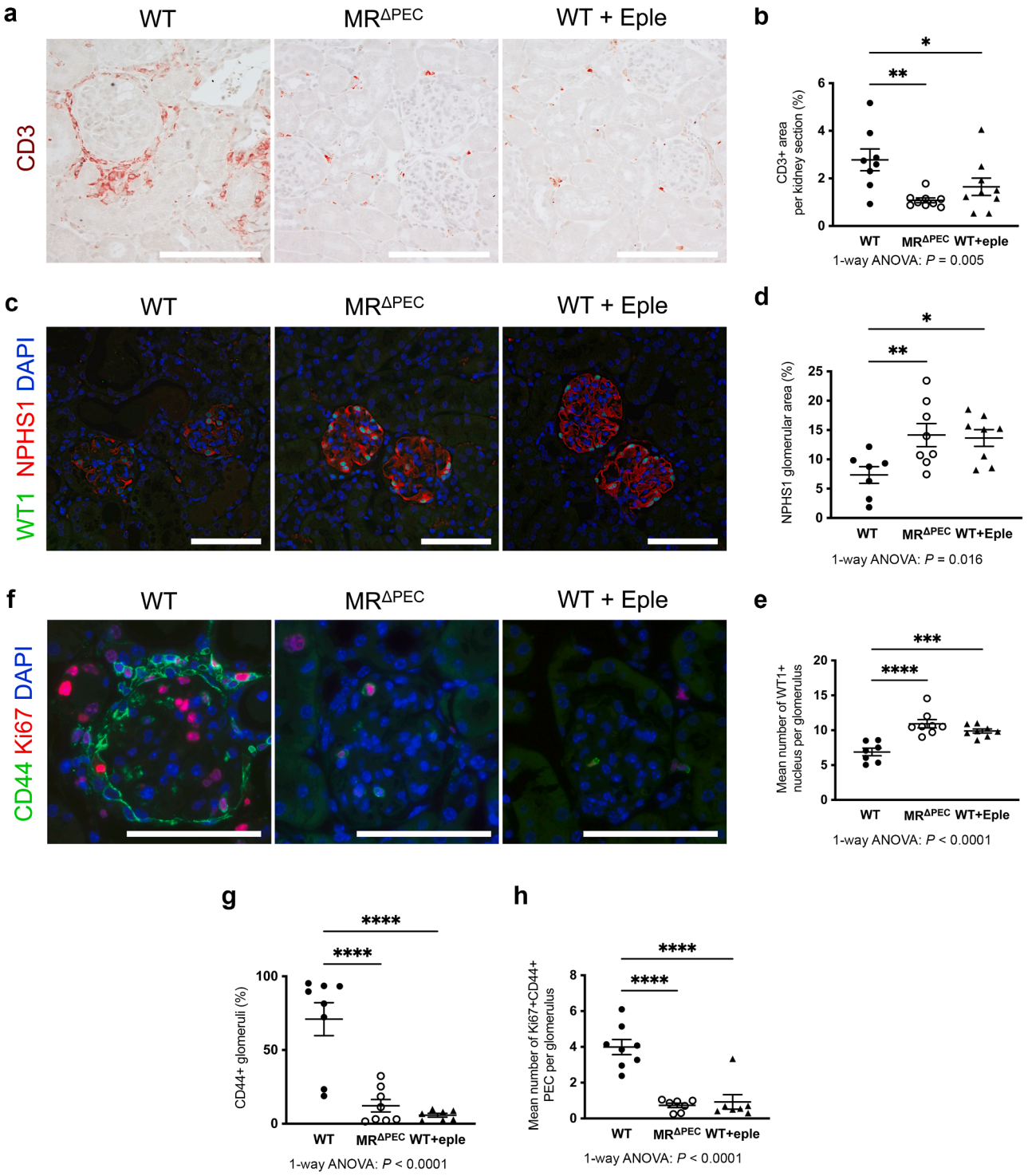

Figure 6 | Genetic and pharmacologic mineralocorticoid receptor (MR) inhibition prevents renal inflammation, podocyte loss, and parietal epithelial cell (PEC) activation in experimental crescentic glomerulonephritis. (**a**) Immunohistochemistry of CD3 on kidney sections of wild-type (WT) mice, $MR^{\Delta PEC}$ mice, and WT mice treated with eplerenone (Eple) at day 14 of the nephrotoxic nephritis (NTN) model. Bar = 50 μm. (**b**) Quantification of CD3+ area in kidneys from WT mice, $MR^{\Delta PEC}$ mice, and WT mice treated with eplerenone at day 14 of the NTN model. Data are shown as individual values and mean ± SEM. n = 7–8 mice. One-way analysis of variance (ANOVA): $P = 0.005$, *post hoc* Fisher least significant difference (LSD) test: $^{*}P < 0.05$, $^{**}P < 0.01$. (**c**) Immunofluorescence for NPHS1 (red), WT-1 (green), and 4′,6-diamidino-2-phenylindole (DAPI) (blue) on kidney sections from WT mice, $MR^{\Delta PEC}$ mice, and WT mice treated with eplerenone at day 14 of the NTN model. Bar = 50 μm. (**d**) Quantification of glomerular NPHS1 area on kidney sections from WT mice, $MR^{\Delta PEC}$ mice, and WT mice treated with eplerenone at day 14 of the NTN model. Data are shown as individual values and mean ± SEM. n = 7–8 mice. One-way ANOVA: $P = 0.016$, *post hoc* Fisher LSD test: $^{*}P < 0.05$. (**e**) Quantification of the glomerular expression of WT-1 on kidney sections of WT mice, $MR^{\Delta PEC}$ mice, and WT mice treated with eplerenone at day 14 of the NTN model. Data are shown as individual values and mean ± SEM. (continued)

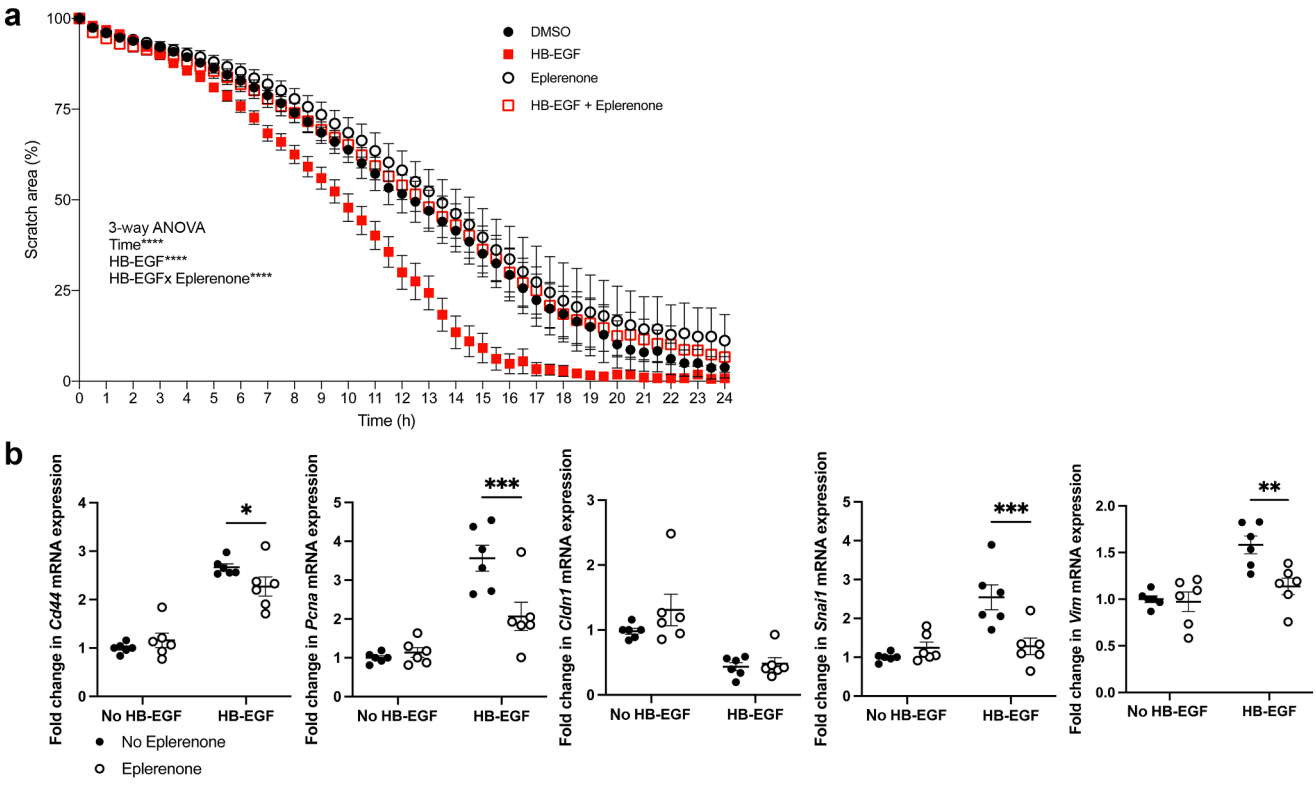

2-way ANOVA	Interaction	HB-EGF effect	Eplerenone effect
Cd44	0.0456	<0.0001	0.3705
Pcna	0.0045	<0.0001	0.0148
Cldn1	0.3125	<0.0001	0.1823
Snai1	0.0016	0.0011	0.0228
Vim	0.024	0.0003	0.0119

Figure 7 | Eplerenone inhibits heparin-binding EGF-like growth factor (HB-EGF)–mediated parietal epithelial cell (PEC) migration. (**a**) PEC migration assessment using Ibidi chambers under various conditions (vehicle [dimethyl sulfoxide {DMSO}], HB-EGF, eplerenone, or HB-EGF + eplerenone) during 24 hours. $P < 0.0001$ (****) using 3-way analysis of variance (ANOVA) for time****, HB-EGF****, and HB-EGF × eplerenone****. (**b**) Reverse transcription quantitative polymerase chain reaction analysis of *Cd44*, *Cldn1*, *Pcna*, *Snai1*, and *Vim* mRNA expressions (Supplementary Table S4) in PEC treated with DMSO, HB-EGF, eplerenone, or HB-EGF + eplerenone for 24 hours. Two-way ANOVA was performed, and post-test Fisher least significant difference was performed to test HB-EGF and eplerenone effects: HB-EGF versus DMSO, eplerenone versus DMSO, and eplerenone + HB-EGF versus HB-EGF. Only *P* values < 0.05 are shown. *$P < 0.05$, **$P < 0.01$, ***$P < 0.001$, ****$P < 0.0001$.

The potential for MR antagonists to provide renal protection in patients with nondiabetic CKD with proteinuria requires further investigation. Data supporting the use of mineralocorticoid receptor antagonist (MRA) in nondiabetic kidney disease, including FSGS cases, various glomerulonephritides, and chronic allograft nephropathy, are encouraging but not as robust as those in diabetic kidney disease.[63–68] Nonetheless, a recent retrospective study with a large sample size (n = 3195) and an extended follow-up period (median of 5.9 years) demonstrated that the use of MR antagonists (including steroidal MRAs) is significantly associated with a lower risk of initiating renal replacement therapy in a real-world CKD population, which included 42% of individuals without diabetes.[69] Finerenone is being evaluated in nondiabetic patients with stage 2–3 CKD, in 2 clinical trials, FIND-CKD (NCT05047263)[70] and CONFIDENCE (NCT05254002).[71] It is interesting to note that other MR antagonists are also being tested for the treatment of CKD. Our findings suggest that proper randomized controlled trials in nondiabetic CKD should distinguish

Figure 6 | (continued) n = 7–8 mice. One-way ANOVA: $P < 0.0001$, *post hoc* Fisher LSD test: ***$P < 0.001$, ****$P < 0.0001$. (**f**) Immunofluorescence for Ki67 (red), CD44 (green), and DAPI (blue) on kidney sections of WT mice, $MR^{\Delta PEC}$ mice, and WT mice treated with eplerenone at day 14 of the NTN model. Bar = 50 µm. (**g,h**) Quantification of the percentage of CD44 positive glomeruli (**g**) and of the mean number of PEC CD44+Ki67+ per glomerulus (**h**) in WT mice, $MR^{\Delta PEC}$ mice, and WT mice treated with eplerenone at day 14 of the NTN model. Data are shown as individual values and mean ± SEM. n = 7–8 mice. (**g**) One-way ANOVA: $P < 0.0001$, *post hoc* Fisher LSD test: ****$P < 0.0001$. (**h**) One-way ANOVA: $P < 0.0001$, *post hoc* Fisher LSD test: ****$P < 0.0001$. To optimize viewing of this image, please see the online version of this article at www.kidney-international.org.

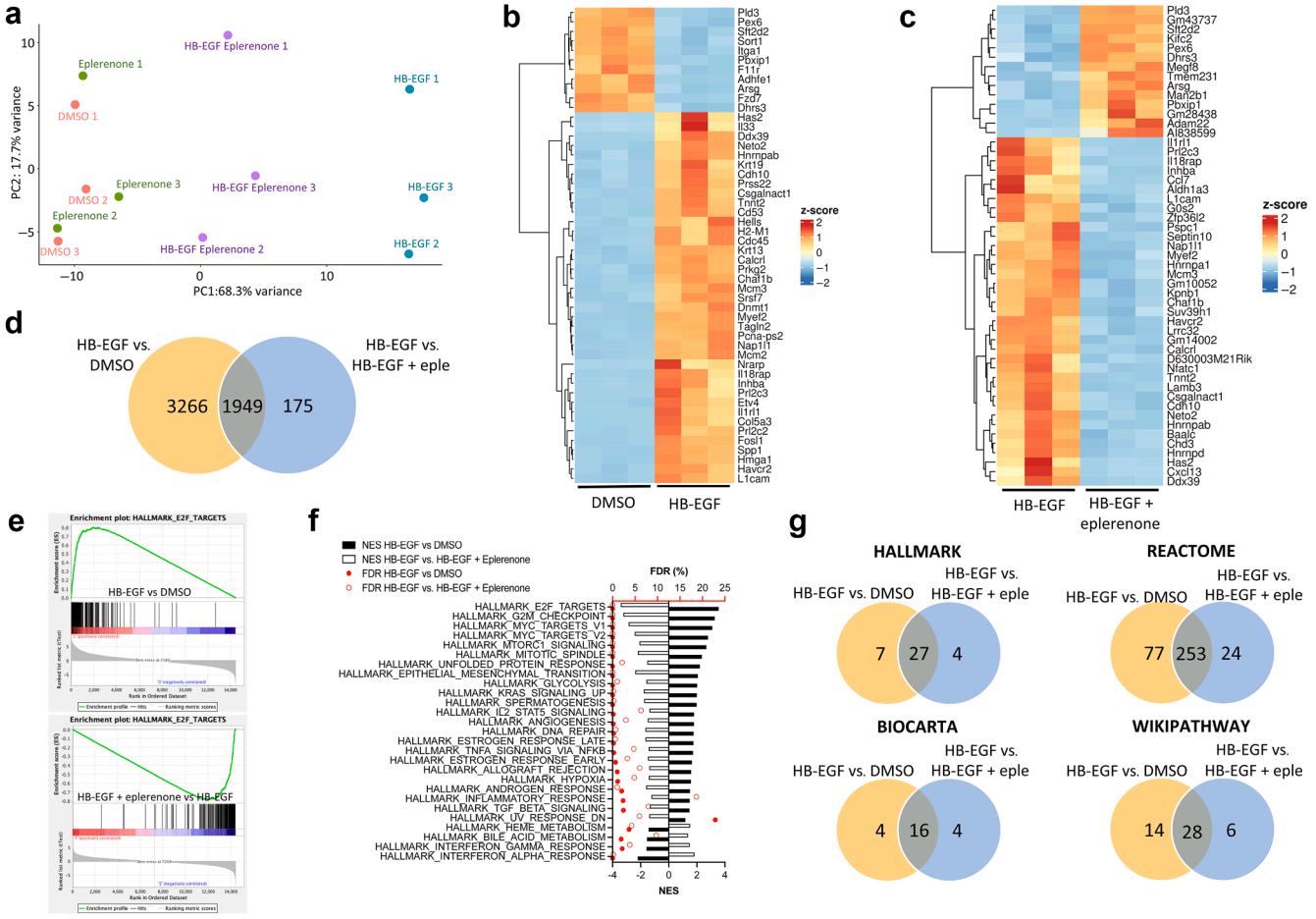

Figure 8 | RNA sequencing of parietal epithelial cell (PEC) treated with heparin-binding EGF-like growth factor (HB-EGF), eplerenone, HB-EGF + eplerenone, or dimethyl sulfoxide (DMSO) for 24 hours. (**a**) Principal component analysis. (**b**) Hierarchical clustering of the 50 most significantly differentially expressed genes in the comparison of HB-EGF versus vehicle (DMSO). (**c**) Hierarchical clustering of the 50 most significantly differentially expressed genes in the comparison of HB-EGF versus HB-EGF + eplerenone. (**d**) Among the 5215 differentially expressed genes (DEGs) enriched in the comparison of HB-EGF versus vehicle, 1949 were also commonly enriched in the comparison of HB-EGF versus HB-EGF + eplerenone. (**e**) Gene Set Enrichment Analysis (GSEA) Hallmark E2F Targets pathway enrichment plot in the comparisons of HB-EGF versus DMSO (upper panel) and HB-EGF + eplerenone versus HB-EGF (lower panel). (**f**) Representation graph of selected Hallmark pathways in the comparisons of HB-EGF versus DMSO and HB-EGF versus HB-EGF + eplerenone. Normalized enrichment scores (NES) are shown as bars and the false discovery rate (FDR) percentage are shown as red dots. (**g**) Visualization of common enriched pathways in the comparisons of HB-EGF versus DMSO and HB-EGF versus HB-EGF + eplerenone in the Hallmark, Biocarta, Wikipathways, and Reactome GSEA datasets.

FSGS or CGN from other diseases, as the mode of action of MR antagonism may be unique to extracapillary diseases. Notably, analysis of patients with CKD treated with spironolactone or eplerenone in combination with sodium-glucose cotransporter inhibitors supports the beneficial effects of MR antagonists on top of sodium-glucose cotransporter inhibitors in lowering UACR.[64,72] Importantly and reassuringly, the incidence of hyperkaliemia was low in these trials.

Our experiments have demonstrated that blocking MR signaling affects a significant mechanism in PEC activation, namely, PEC migration in response to HB-EGF. Eplerenone has multiple impacts on the kidney, influencing both podocytes and tubular cells[73,74] in addition to nonepithelial compartments.[75] In this study, we provide evidence that the genetic deletion of the MR receptor in PECs mimics the effects of eplerenone *in vivo*, supporting the notion that the impact of eplerenone is partially mediated through its action on PECs. These findings also suggest that glucocorticosteroids with minimal mineralocorticoid activity may be preferable in extracapillary diseases to minimize the risk of deleterious MR stimulation in PECs that express little hydroxysteroid 11-β dehydrogenase 2.

MR-signaling modulation affected several classical features of diseased PEC (e.g., CD44 expression, migration to the tuft, proliferation, and sclerosis). Surprisingly, PEC-selective MR deficiency and eplerenone treatment of WT mice prevented CD3+ T lymphocytes from infiltrating the periglomerular area in the NTN model. This suggests that activated PECs contribute to glomerular inflammation and that the MR may

play a role in establishing a proinflammatory phenotype in PECs, as evidenced by the profound influence MR has on EGFR-induced cytokine pathways *in vitro*.

A close interaction between genomic and nongenomic aldosterone signaling exists because MR can transactivate the EGFR and enhance its expression in various cell types.[76,77] In addition, we discovered a notable reverse interaction in PECs with several key EGFR-dependent transcriptome fingerprints and cellular behaviors that depend on MR signaling. Eplerenone blocked HB-EGF–mediated PEC migration and proliferation. HB-EGF regulates multiple proproliferative, promigration, and profibrotic pathways in PECs, and eplerenone dampened most of these effects revealing interplays between the HB-EGF/EGFR and MR signaling pathways. Notably, eplerenone influences more than 1900 mRNA modulated by HB-EGF, highlighting the broad and significant interaction of the MR with the EGFR cascades in pathophysiological conditions. We observed that some specific cell surface actors involved in PEC activation are controlled by MR signaling. Eplerenone inhibited HB-EGF–mediated *Cd9* mRNA induction. Eplerenone also inhibited HB-EGF–mediated *Pdgfrb*, *Egfr*, and *Itgb1* mRNA expression. Our experiments demonstrate that blocking MR signaling impacts PEC activation mechanisms, specifically PEC migration, proliferation, and the proinflammatory response to HB-EGF. We selected HB-EGF because it is a key driver of crescent formation[45] and a trigger for PEC activation.[16] However, multiple other mediators, such as platelet-derived growth factor, thrombin, and colony-stimulating factor-1, are also involved in extracapillary lesion formation. Future work will focus on the specific MR effects and interactions with these pathways.

Interestingly, transcriptional regulation of the EGFR by the MR and interactions between MR signaling and various surface receptors, such as the angiotensin II receptor I, the platelet-derived growth factor receptor, or the vascular endothelial growth factor receptor, has been demonstrated in other cell types.[78–80] Furthermore, direct interaction between MR and EGFR has been demonstrated.[81–86] Our finding expands beyond short-term signaling experiments to support the notion that intact MR signaling mediates actions of a multimolecular pathogenic platform for several hours *in vitro* if not days and weeks *in vivo*. Thus, we hypothesize that MR antagonism would then limit PEC activation by desensitizing cells to external deleterious signals.

In conclusion, we have shown that inhibiting MR signaling has a protective effect in 2 distinct classes of severe extracapillary glomerulopathies. This suggests that, despite differing initial triggers, common signaling pathways are activated, leading to the pathologic phenotype of the PECs. In addition to its reported profibrotic and hemodynamic effects, MR signaling exerts a direct role in the pathogenic activation of PECs, promoting glomerular leakage and sclerotic failure. Most importantly, the positive impact of blocking MR signaling in such cellular compartment highlights the potential for clinical trials targeting FSGS and CGN.

DISCLOSURE

AK received honoraria from AstraZeneca and Boehringer Ingelheim, which is unrelated to the present study. P-LT is cofounder of Detera Therapeutics and declared consulting fees from Travere Therapeutics Ireland Ltd. and Vifor, and received a grant from Alentis Therapeutics, which are unrelated to this work. All the other authors declared no competing interests.

DATA STATEMENT

All data are available in the main text or the Supplementary Materials. RNA sequencing datasets are available on GEO: GSE282359.

ACKNOWLEDGMENTS

We thank Gwendoline Luque, Nadege Pallatier, Nicolas Perez, Corina Suldac, and the ERI U970 team for assistance in animal care and handling; Nicolas Sorhaindo for biochemical measurements (ICB-IFR2, laboratoire de Biochimie, Hôpital Bichat, Paris, France); Corinne Lesaffre for histologic stainings (PH2I, histology platform PARCC, Paris, France); and Alain Schmitt and Jean-Marc Masse for transmission electron microscopy (Institut Cochin, Paris, France). We acknowledge administrative support from Véronique Oberweis, Bruno Pillard, and Cyrille Mahieux (PARCC, Paris, France).

FUNDING STATEMENT

This work was supported by the French Institute for Health and Medical Research (Inserm), a Consolidator Grant ERC grant (agreement no. 107037) from the European Research Council, and a Foundation pour la Recherche Médicale – "Equipe FRM 2019, VALID" grant (P-LT), and a grant from Université Paris Cité (2014–2016) (P-LT and M-CZ). The Assistance Publique des Hôpitaux de Paris-Ecole Polytechnique PhD fellowship program supported HL.

Supplementary material is available online at www.kidney-international.org.

REFERENCES

1. Gesualdo L, Di Palma AM, Morrone LF, et al. The Italian experience of the national registry of renal biopsies. *Kidney Int*. 2004;66:890–894.
2. Rivera F, Lopez-Gomez JM, Perez-Garcia R, et al. Frequency of renal pathology in Spain 1994–1999. *Nephrol Dial Transplant*. 2002;17:1594–1602.
3. Malafronte P, Mastroianni-Kirsztajn G, Betonico GN, et al. Paulista Registry of glomerulonephritis: 5-year data report. *Nephrol Dial Transplant*. 2006;21:3098–3105.
4. Bobart SA, Portalatin G, Sawaf H, et al. The Cleveland Clinic Kidney Biopsy Epidemiological Project. *Kidney360*. 2022;3:2077–2085.
5. Aroca-Martinez G, Gonzalez-Torres HJ, Dominguez-Vargas A, et al. Glomerular diseases in the Colombian Caribbean: data from the colombian nephropathy registry (NEFRORED(R)). *Saudi J Kidney Dis Transpl*. 2022;33:S18–S29.
6. Huang Y, Shi K, Zhu X, et al. Disease spectrum of 9 310 cases of renal biopsy pathological diagnosis from a single center in China. *Zhong Nan Da Xue Xue Bao Yi Xue Ban*. 2022;47:546–554.
7. Banode RK, Kimmatkar P, Bawankule C, et al. Kidney disease patterns diagnosed by kidney biopsy: a single-center experience from central India. *J Assoc Physicians India*. 2022;70:11–12.
8. Sim JJ, Batech M, Hever A, et al. Distribution of biopsy-proven presumed primary glomerulonephropathies in 2000–2011 among a racially and ethnically diverse US population. *Am J Kidney Dis*. 2016;68:533–544.
9. Hommos MS, De Vriese AS, Alexander MP, et al. The incidence of primary vs secondary focal segmental glomerulosclerosis: a clinicopathologic study. *Mayo Clin Proc*. 2017;92:1772–1781.
10. Rosenberg AZ, Kopp JB. Focal segmental glomerulosclerosis. *Clin J Am Soc Nephrol*. 2017;12:502–517.

11. Kim YH, Goyal M, Kurnit D, et al. Podocyte depletion and glomerulosclerosis have a direct relationship in the PAN-treated rat. *Kidney Int*. 2001;60:957–968.
12. Wharram BL, Goyal M, Wiggins JE, et al. Podocyte depletion causes glomerulosclerosis: diphtheria toxin-induced podocyte depletion in rats expressing human diphtheria toxin receptor transgene. *J Am Soc Nephrol*. 2005;16:2941–2952.
13. Fatima H, Moeller MJ, Smeets B, et al. Parietal epithelial cell activation marker in early recurrence of FSGS in the transplant. *Clin J Am Soc Nephrol*. 2012;7:1852–1858.
14. Shankland SJ, Smeets B, Pippin JW, et al. The emergence of the glomerular parietal epithelial cell. *Nat Rev Nephrol*. 2014;10:158–173.
15. Smeets B, Stucker F, Wetzels J, et al. Detection of activated parietal epithelial cells on the glomerular tuft distinguishes early focal segmental glomerulosclerosis from minimal change disease. *Am J Pathol*. 2014;184:3239–3248.
16. Lazareth H, Henique C, Lenoir O, et al. The tetraspanin CD9 controls migration and proliferation of parietal epithelial cells and glomerular disease progression. *Nat Commun*. 2019;10:3303.
17. Moeller MJ, Tharaux PL. Cellular regeneration of podocytes from parietal cells: the debate is still open. *Kidney Int*. 2019;96:542–544.
18. de Cos M, Meliambro K, Campbell KN. Novel treatment paradigms: focal segmental glomerulosclerosis. *Kidney Int Rep*. 2023;8:30–35.
19. Sun K, Xie Q, Hao CM. Mechanisms of scarring in focal segmental glomerulosclerosis. *Kidney Dis (Basel)*. 2021;7:350–358.
20. Smeets B, Kuppe C, Sicking EM, et al. Parietal epithelial cells participate in the formation of sclerotic lesions in focal segmental glomerulosclerosis. *J Am Soc Nephrol*. 2011;22:1262–1274.
21. Smeets B, Uhlig S, Fuss A, et al. Tracing the origin of glomerular extracapillary lesions from parietal epithelial cells. *J Am Soc Nephrol*. 2009;20:2604–2615.
22. Wong MN, Tharaux PL, Grahammer F, et al. Parietal epithelial cell dysfunction in crescentic glomerulonephritis. *Cell Tissue Res*. 2021;385:345–354.
23. Bronstein R, Pace J, Gowthaman Y, et al. Podocyte-parietal epithelial cell interdependence in glomerular development and disease. *J Am Soc Nephrol*. 2023;34:737–750.
24. Lazareth H, Lenoir O, Tharaux PL. Parietal epithelial cells role in repair versus scarring after glomerular injury. *Curr Opin Nephrol Hypertens*. 2020;29:293–301.
25. Epstein M, Kovesdy CP, Clase CM, et al. Aldosterone, mineralocorticoid receptor activation, and CKD: a review of evolving treatment paradigms. *Am J Kidney Dis*. 2022;80:658–666.
26. Fujii W, Shibata S. Mineralocorticoid receptor antagonists for preventing chronic kidney disease progression: current evidence and future challenges. *Int J Mol Sci*. 2023;24:7719.
27. Gavras H, Brunner HR, Laragh JH. Renin and aldosterone and the pathogenesis of hypertensive vascular damage. *Prog Cardiovasc Dis*. 1974;17:39–49.
28. Knowlton AI, Stoerk H. Influence of adrenal cortical steroids upon the blood pressure and the rate of progression of experimental nephritis in rats. *Endocrinology*. 1946;38:315–324.
29. Grundy HM, Simpson SA, Tait JF. Isolation of a highly active mineralocorticoid from beef adrenal extract. *Nature*. 1952;169:795–796.
30. Selye H. Production of nephrosclerosis by overdosage with desoxycorticosterone acetate. *Can Med Assoc J*. 1942;47:515–519.
31. Kretzler M, Koeppen-Hagemann I, Kriz W. Podocyte damage is a critical step in the development of glomerulosclerosis in the uninephrectomised-desoxycorticosterone hypertensive rat. *Virchows Arch*. 1994;425:181–193.
32. Raij L, Dalmasso AP, Staley NA, et al. Renal injury in DOCA-salt hypertensive C5-sufficient and C5-deficient mice. *Kidney Int*. 1989;36:582–592.
33. Yuan Y, Xu X, Zhao C, et al. The roles of oxidative stress, endoplasmic reticulum stress, and autophagy in aldosterone/mineralocorticoid receptor-induced podocyte injury. *Lab Invest*. 2015;95:1374–1386.
34. Bai M, Chen Y, Zhao M, et al. NLRP3 inflammasome activation contributes to aldosterone-induced podocyte injury. *Am J Physiol Renal Physiol*. 2017;312:F556–F564.
35. Li D, Lu Z, Xu Z, et al. Spironolactone promotes autophagy via inhibiting PI3K/AKT/mTOR signalling pathway and reduce adhesive capacity damage in podocytes under mechanical stress. *Biosci Rep*. 2016;36:e00355.
36. Chen C, Liang W, Jia J, et al. Aldosterone induces apoptosis in rat podocytes: role of PI3-K/Akt and p38MAPK signaling pathways. *Nephron Exp Nephrol*. 2009;113:e26–e34.
37. Shibata S, Nagase M, Yoshida S, et al. Podocyte as the target for aldosterone: roles of oxidative stress and Sgk1. *Hypertension*. 2007;49:355–364.
38. Nagase M, Shibata S, Yoshida S, et al. Podocyte injury underlies the glomerulopathy of Dahl salt-hypertensive rats and is reversed by aldosterone blocker. *Hypertension*. 2006;47:1084–1093.
39. Takagi N, Tanizawa T, Kon V, et al. Mineralocorticoid receptor blocker protects against podocyte-dependent glomerulosclerosis. *Nephron Extra*. 2012;2:17–26.
40. Nemeth Z, Kokeny G, Godo M, et al. Increased renoprotection with ACE inhibitor plus aldosterone antagonist as compared to monotherapies—the effect on podocytes. *Nephrol Dial Transplant*. 2009;24:3640–3651.
41. Appel D, Kershaw DB, Smeets B, et al. Recruitment of podocytes from glomerular parietal epithelial cells. *J Am Soc Nephrol*. 2009;20:333–343.
42. Berger S, Bleich M, Schmid W, et al. Mineralocorticoid receptor knockout mice: lessons on Na+ metabolism. *Kidney Int*. 2000;57:1295–1298.
43. Percie du Sert N, Ahluwalia A, Alam S, et al. Reporting animal research: explanation and elaboration for the ARRIVE guidelines 2.0. *PLoS Biol*. 2020;18:e3000411.
44. Henique C, Bollee G, Lenoir O, et al. Nuclear factor erythroid 2-related factor 2 drives podocyte-specific expression of peroxisome proliferator-activated receptor gamma essential for resistance to crescentic GN. *J Am Soc Nephrol*. 2016;27:172–188.
45. Bollee G, Flamant M, Schordan S, et al. Epidermal growth factor receptor promotes glomerular injury and renal failure in rapidly progressive crescentic glomerulonephritis. *Nat Med*. 2011;17:1242–1250.
46. Soulie M, Stephan Y, Durand M, et al. Benefit of combination therapy with dapagliflozin and eplerenone on cardiac function and fibrosis in rats with non-diabetic chronic kidney disease. *Sci Rep*. 2024;14:23955.
47. Zhang Q, Saito Y, Naya N, et al. The specific mineralocorticoid receptor blocker eplerenone attenuates left ventricular remodeling in mice lacking the gene encoding guanylyl cyclase-A. *Hypertens Res*. 2008;31:1251–1256.
48. Kurobe H, Hirata Y, Matsuoka Y, et al. Protective effects of selective mineralocorticoid receptor antagonist against aortic aneurysm progression in a novel murine model. *J Surg Res*. 2013;185:455–462.
49. Delyani JA, Rocha R, Cook CS, et al. Eplerenone: a selective aldosterone receptor antagonist (SARA). *Cardiovasc Drug Rev*. 2001;19:185–200.
50. Muto Y, Wilson PC, Ledru N, et al. Single cell transcriptional and chromatin accessibility profiling redefine cellular heterogeneity in the adult human kidney. *Nat Commun*. 2021;12:2190.
51. Wilson PC, Wu H, Kirita Y, et al. The single-cell transcriptomic landscape of early human diabetic nephropathy. *Proc Natl Acad Sci U S A*. 2019;116:19619–19625.
52. Roeder SS, Barnes TJ, Lee JS, et al. Activated ERK1/2 increases CD44 in glomerular parietal epithelial cells leading to matrix expansion. *Kidney Int*. 2017;91:896–913.
53. Kidney Disease: Improving Global Outcomes (KDIGO) Glomerular Diseases Work Group. KDIGO 2021 clinical practice guideline for the management of glomerular diseases. *Kidney Int*. 2021;100(4S):S1–S276.
54. De Vriese AS, Wetzels JF, Glassock RJ, et al. Therapeutic trials in adult FSGS: lessons learned and the road forward. *Nat Rev Nephrol*. 2021;17:619–630.
55. Lenoir O, Milon M, Virsolvy A, et al. Direct action of endothelin-1 on podocytes promotes diabetic glomerulosclerosis. *J Am Soc Nephrol*. 2014;25:1050–1062.
56. Rheault MN, Alpers CE, Barratt J, et al. Sparsentan versus irbesartan in focal segmental glomerulosclerosis. *N Engl J Med*. 2023;389:2436–2445.
57. Egbuna O, Zimmerman B, Manos G, et al. Inaxaplin for proteinuric kidney disease in persons with two APOL1 variants. *N Engl J Med*. 2023;388:969–979.
58. Morris AD, Floyd L, Woywodt A, et al. Rituximab in the treatment of primary FSGS: time for its use in routine clinical practice? *Clin Kidney J*. 2023;16:1199–1205.
59. Shankland SJ, Anders HJ, Romagnani P. Glomerular parietal epithelial cells in kidney physiology, pathology, and repair. *Curr Opin Nephrol Hypertens*. 2013;22:302–309.
60. Smeets B, Dijkman HB, Wetzels JF, et al. Lessons from studies on focal segmental glomerulosclerosis: an important role for parietal epithelial cells? *J Pathol*. 2006;210:263–272.

61. Kidney Disease: Improving Global Outcomes (KDIGO) Diabetes Work Group. KDIGO 2022 clinical practice guideline for diabetes management in chronic kidney disease. *Kidney Int*. 2022;102(5S):S1–S127.
62. ElSayed NA, Aleppo G, Aroda VR, et al. 11. Chronic kidney disease and risk management: standards of care in diabetes-2023. *Diabetes Care*. 2023;46:S191–S202.
63. Chrysostomou A, Becker G. Spironolactone in addition to ACE inhibition to reduce proteinuria in patients with chronic renal disease. *N Engl J Med*. 2001;345:925–926.
64. Provenzano M, Puchades MJ, Garofalo C, et al. Albuminuria-lowering effect of dapagliflozin, eplerenone, and their combination in patients with chronic kidney disease: a randomized crossover clinical trial. *J Am Soc Nephrol*. 2022;33:1569–1580.
65. Hu H, Cao M, Sun Y, et al. Efficacy and safety of eplerenone for treating chronic kidney disease: a meta-analysis. *Int J Hypertens*. 2023;2023:6683987.
66. Baskin E, Siddiqui MA, Gulleroglu K, et al. Long-term effect of eplerenone treatment in children with chronic allograft nephropathy. *Pediatr Transplant*. 2023;27:e14557.
67. Marup FH, Thomsen MB, Birn H. Additive effects of dapagliflozin and finerenone on albuminuria in non-diabetic CKD: an open-label randomized clinical trial. *Clin Kidney J*. 2024;17:sfad249.
68. Papasotiriou M, Georgopoulou GA, Mpratsiakou A, et al. A prospective study of eplerenone in the treatment of patients with glomerulonephritis. *Biomedicines*. 2023;11:3340.
69. Oka T, Sakaguchi Y, Hattori K, et al. Mineralocorticoid receptor antagonist use and hard renal outcomes in real-world patients with chronic kidney disease. *Hypertension*. 2022;79:679–689.
70. A Trial to Learn How Well Finerenone Works and How Safe it is in Adult Participants With Non-diabetic Chronic Kidney Disease (FIND-CKD). ClinicalTrials.gov identifier: NCT05047263. Updated September 29, 2025. Accessed October 15, 2025. https://clinicaltrials.gov/study/NCT05047263
71. A Study to Learn How Well the Treatment Combination of Finerenone and Empagliflozin Works and How Safe it is Compared to Each Treatment Alone in Adult Participants With Long-term Kidney Disease (Chronic Kidney Disease) and Type 2 Diabetes (CONFIDENCE). ClinicalTrials.gov identifier: NCT05254002. Updated March 18, 2025. Accessed October 15, 2025. https://clinicaltrials.gov/study/NCT05254002
72. Provenzano M, Jongs N, Vart P, et al. The kidney protective effects of the sodium-glucose cotransporter-2 inhibitor, dapagliflozin, are present in patients with CKD treated with mineralocorticoid receptor antagonists. *Kidney Int Rep*. 2022;7:436–443.
73. Ayuzawa N, Fujita T. The mineralocorticoid receptor in salt-sensitive hypertension and renal injury. *J Am Soc Nephrol*. 2021;32:279–289.
74. Shibata S, Nagase M, Yoshida S, et al. Modification of mineralocorticoid receptor function by Rac1 GTPase: implication in proteinuric kidney disease. *Nat Med*. 2008;14:1370–1376.
75. Nakamura T, Girerd S, Jaisser F, et al. Nonepithelial mineralocorticoid receptor activation as a determinant of kidney disease. *Kidney Int Suppl (2011)*. 2022;12:12–18.
76. Rickard AJ, Fuller PJ. Mineralocorticoid and epidermal growth factor receptors: partners in vivo. *Hypertension*. 2011;57:144–145.
77. Ruhs S, Nolze A, Hubschmann R, et al. 30 Years of the mineralocorticoid receptor: nongenomic effects via the mineralocorticoid receptor. *J Endocrinol*. 2017;234:T107–T124.
78. Stroedecke K, Meinel S, Markwardt F, et al. The mineralocorticoid receptor leads to increased expression of EGFR and T-type calcium channels that support HL-1 cell hypertrophy. *Sci Rep*. 2021;11:13229.
79. Krug AW, Grossmann C, Schuster C, et al. Aldosterone stimulates epidermal growth factor receptor expression. *J Biol Chem*. 2003;278:43060–43066.
80. Meinel S, Gekle M, Grossmann C. Mineralocorticoid receptor signaling: crosstalk with membrane receptors and other modulators. *Steroids*. 2014;91:3–10.
81. Gekle M, Freudinger R, Mildenberger S, et al. Aldosterone interaction with epidermal growth factor receptor signaling in MDCK cells. *Am J Physiol Renal Physiol*. 2002;282:F669–F679.
82. Mazak I, Fiebeler A, Muller DN, et al. Aldosterone potentiates angiotensin II-induced signaling in vascular smooth muscle cells. *Circulation*. 2004;109:2792–2800.
83. Grossmann C, Benesic A, Krug AW, et al. Human mineralocorticoid receptor expression renders cells responsive for nongenotropic aldosterone actions. *Mol Endocrinol*. 2005;19:1697–1710.
84. McEneaney V, Harvey BJ, Thomas W. Aldosterone rapidly activates protein kinase D via a mineralocorticoid receptor/EGFR trans-activation pathway in the M1 kidney CCD cell line. *J Steroid Biochem Mol Biol*. 2007;107:180–190.
85. Huang S, Zhang A, Ding G, et al. Aldosterone-induced mesangial cell proliferation is mediated by EGF receptor transactivation. *Am J Physiol Renal Physiol*. 2009;296:F1323–F1333.
86. Grossmann C, Husse B, Mildenberger S, et al. Colocalization of mineralocorticoid and EGF receptor at the plasma membrane. *Biochim Biophys Acta*. 2010;1803:584–590.

Supplementary Material

Supplementary Methods

Mouse blood pressure measurements and physiological assessments

Systolic blood pressure of mice was recorded by the tail-cuff method (Visitech Systems Inc., BP-2000). Ten measurements from each mouse were taken, and a mean value was determined. SBP was measured at baseline and then weekly until the end of the treatment period.

For urine collection, all mice were placed in metabolic cages with free access to water for 6-hour urine collection. Urinary creatinine, plasma creatinine, urinary and serum Na^+ K^+ Cl^-, and plasma urea concentrations were analyzed (Olympus, AU400) or iSTAT (Abbott, EC8+). Hemoglobin was measured on a HEMAVET 950FS robot. Urinary albumin excretion was measured using a ELISA assay (Crystal chem-80630).

iPec-Cre ROSA-mT/mG mice

Mice with specific PEC expression of membrane GFP were generated by crossing iPec-Cre mice [1] with ROSA-mTomato/mGFP (JAX:007676) mice. Doxycycline hyclate (Sigma Aldrich) was administered *in* drinking water for 14 days (5% sucrose and 1 mg/ml doxycycline), followed by a washout for 1 week. Nephrotoxic nephritis was induced in male mice (10–16 weeks of age) as previously reported [2-4]. Mice were sacrificed at 4 or 7 days after nephrotoxic serum injection. Kidneys were harvested and fixed in formol overnight, then tissue were immersed in 15% sucrose for 24h and frozen in -70°C isopropanol after embedding in OCT. Cryosections were then stained using DAPI. Slides were mounted using Fluoromount-G (Aviva Systems Biology, 0100-01). Images were acquired on a Zeiss AxioPhot microscope and ZEN software.

Study approval

The research involving human samples was approved after approval of the Ethics Evaluation Committee of Inserm (CEEI) (IRB00003888, FWA00005831). Codes were used to ensure the strict anonymity of patients. The study complies with the 2000 Declaration of Helsinki. Archived samples were only used after obtaining informed consent during routine clinical follow-up consultation in the HEGP hospital if not previously done at the time of the initial consultation. No sample was taken for the project itself; thus, the project did not modify the medical care of the patients.

Human renal biopsies

Acetic acid-formol-alcohol-fixed, paraffin-embedded renal tissue specimens were obtained from the Nephrology department of Hôpital Européen Georges Pompidou, Paris, France. Human tissue was used after informed consent by the patients and approval form and following the guidelines of the local Ethics Committee. Kidney biopsy specimens with sufficient tissue for immunohistochemical evaluation after completing the diagnosis workup were included (**Suppl Tables 2 and 3**).

Transmission Electron Microscopy Procedure

Small pieces of renal cortex (1 mm^3) were processed and analyzed as previously described [16].

Histology

Mouse kidneys sections were stained with Masson's trichrome, Periodic-Acid Schiff, or Sirius red staining. For immunofluorescence, kidney sections were stained with the following primary antibodies: anti-WT1 (Abcam, ab89901, 1:100), anti-CD44 (Abcam, ab119348, 1:100), anti-Ki67 (Thermofisher scientific, MA5-14520, 1:1000), anti-NPHS1 (Progen, GP-N2, 1:100). The following secondary antibodies were used: donkey anti-IgG (H+L) AF488-conjugated antibody (Life Technologies, A-11005, 1:400), donkey anti-rabbit IgG (H+L) AF594-conjugated antibody (A-21207, Life Technologies, 1:400), donkey anti-rat IgG (H+L) AF488-conjugated antibody (A-21208, Life Technologies, 1:400), goat anti-guinea-pig IgG (H+L) AF594-conjugated antibody (A-11076, Life Technologies, 1:400). The nuclei were stained with Hoechst 33342.

For immunohistochemistry, mouse kidney sections were stained with a mouse anti-CD3 antibody (Dako, A0452, 1:500) and incubated with Histofine® (Nichirei Biosciences, Japan) for 2 hours at room temperature. Staining was revealed with AEC reagent (DAKO), counterstained with hematoxylin QS (Vector, Burlingame, CA), and finalized with Permanent Aqueous Mounting Media (Innovex).

Human AFA-fixed paraffin-embedded biopsies were sectioned (4-*µm* thick) and processed for immunohistochemistry with a mouse anti-MR antibody (clone 1D5 kindly provided by Dr Gomez-Sanchez, 1:100)[5]. After incubation overnight at 4°C, sections were incubated 30 min with affinity-purified biotinylated horse anti-mouse (1/400, Vector laboratories) and then with an avidin-biotin peroxidase complex (Vectastain ABC Elite, Vector Laboratories) for 30 min.

To quantify histological lesions, all glomeruli of the renal section were blindly counted for crescents in the NTN model. In the DOCA-salt model, all glomeruli of the renal section were counted for glomeruli with FSGS lesions, glomeruli with sclerosis, and sclerotic lesions above 50% of the glomerular surface. Sirius red area was then quantified with automatic scanning of 13 randomly chosen cortical fields per mouse.

The number of podocytes and podocyte dedifferentiation were assessed respectively by the number of WT-1$^+$ cells or NPHS1$^+$ area per glomerular cross-section in an average of 40 glomerular cross-sections per mouse. Glomeruli with activated PEC were quantified as the percentage of glomeruli with CD44$^+$ cells surrounding the Bowman's capsule among the entire glomeruli of the renal section. The proliferation of PEC was evaluated by counting the number of Ki67$^+$ CD44$^+$ PEC per glomerulus in an average of 40 glomerular cross-sections per mouse. Quantification of CD3$^+$ area was performed on randomly chosen 6 cortical fields per mouse.

Cell culture

PEC cell line

Primary mouse PECs were cultured as previously described [6]. For gene and protein expression experiments, 3.10^6 cells were seeded in 24 wells plates in endothelial cell growth medium with 1% penicillin/streptomycin and 20% charcoal-stripped FBS. After 24h, the supplement mix was removed for 24h and then incubated for 24h with fresh supplement mix-deprived medium and 20% charcoal-stripped FBS with vehicle (DMSO), HB-EGF (20ng/ml), eplerenone (10^{-5}M) or HB-EGF (20ng/ml) + eplerenone (10^{-5}M) [7].

Migration in IBIDI chambers

Migration assay was performed using IBIDI chambers (n°80242) as published [2]. Cells were stimulated with either Endothelial cell basal medium without supplements with FBS 20% (control, DMSO) or with HB-EGF (20ng/ml), eplerenone (10^{-5}M), or HB-EGF (20ng/ml) + eplerenone (10^{-5}M) and a first round of photographs was taken (H0). Photographs were taken every 30 minutes during 24 hours. Areas of migration were measured by using NIS Element software.

RNA extraction and RT-qPCR

Total RNA and reverse transcription was performed using TRIzol reagent (Ambion, Life Technologies), DNase I Treatment (Life technologies) of 1μg of total RNA, and 500ng of total RNA (iScript reverse transcriptase, Bio-Rad). The qPCR was performed using SYBR Green (Sso Advanced Universal SYBR Green Supermix, Bio-Rad) on a C1000 touch thermal cycler Bio-Rad (CFX96 Real-Time System). The primers used for qPCR are described in **Supp Table 4**. Normalization for RNA quantity and reverse transcriptase efficiency was performed against three reference genes (geometric mean of the expression of 18S rRNA, Ubiquitin C, and β2-microglobulin) in accordance with the MIQE guidelines [8]. Standard curves were generated using serial dilutions from a cDNA pool of all samples of each experiment, yielding a correlation coefficient of at least 0.98 in all experiments. Data are reported as fold change over control.

RNA sequencing and pathway analysis

Gene expression profiles were determined for PEC treated for 24 hours with HB-EGF, eplerenone, and HB-EGF + eplerenone or vehicle. To construct the libraries, 250 ng of high-quality total RNA sample (RIN range between 6.6 and 9.8) was processed using Stranded mRNA Prep kit (Illumina).

Libraries were quantified by Q bit, and profiles were assessed using the DNA High Sensitivity LabChip kit on an Agilent Bioanalyzer. Libraries were sequenced on an Illumina Nextseq 500 instrument using 75 base-lengths read V2 chemistry in a paired-end mode.

After sequencing, a primary analysis based on AOZAN software (ENS, Paris) was applied to demultiplex and control the raw data quality (based on FastQC modules/version 0.11.5). Fastq files were then aligned using STAR algorithm (version 2.7.6a) on the Ensembl release 101 reference. Reads were then counted using RSEM (v1.3.1), and the statistical analyses on the read counts were performed with R (version 3.6.3) and the DESeq2 package (DESeq2_1.26.0) to determine the proportion of differentially expressed genes between two conditions. We used the standard DESeq2 normalization method with a pre-filter of reads and genes (reads uniquely mapped on the genome, or up to 10 different loci with a count adjustment, and genes with at least 10 reads in at least 3 different samples. Following the package recommendations, we used the Wald test with the contrast function and the Benjamini-Hochberg FDR control procedure to identify the differentially expressed genes. R scripts and parameters are available on the platform (https://github.com/GENOM-IC-Cochin/RNA-Seq_analysis). Datasets have been deposited on GEO. Different comparisons of gene sets were performed: vehicle vs. HB-EGF, vehicle vs. eplerenone, vehicle vs. HB-EGF + eplerenone, HB-EGF vs. eplerenone, HB-EGF vs HB-EGF + eplerenone and eplerenone vs HB-EGF + eplerenone vs eplerenone. Gene Set Enrichment Analysis (GSEA) was performed for pathway discovery [9, 10]. MSigDB gene set used were *Mus musculus* mh and m2 [11, 12]. We used gene set permutation as the GSEA user guide recommended for replicates <7 (https://www.gsea-msigdb.org/gsea/doc/GSEAUserGuideFrame.html).

Public databases

Single-cell RNA sequencing and Single-nuclei RNA sequencing data were extracted from public databases. For Kidney Precision Medicine Project (KPMP) (https://www.kpmp.org) [13], the results are based on the following datasets : DK114886, DK114861, DK114866, DK114870, DK114908, DK114915, DK114926, DK114920, DK114923, DK114933, and DK114937. Data was downloaded on September 4th, 2023. Other single-cell RNAseq data [14, 15] were extracted from the Kidney Interactive Transcriptomics analyzer (https://humphreyslab.com/SingleCell).

Statistics

Data are presented as individual values and means ± SEM. Statistical analyses were calculated by using GraphPad Prism software (GraphPad Software, La Jolla, CA). Comparisons between two groups were performed using Student t-tests when samples passed the Anderson-Darling and D'Agostino normality tests and F test for equality of variance. Otherwise, a non-parametric Mann-Whitney test was used. Comparisons between multiple groups were performed using one-way, two-way, or 3-way ANOVA and, when mentioned, followed by Fisher LSD multiple comparisons. A P *v*alue <0.05 was considered significant. * p<0.05, ** p<0.01, *** p<0.001, **** p<0.0001.

Figures Legends:

Supplementary Figure 1: *Nr3c2* mRNA in PECs in public human databases.

A. Expression in the single nucleus RNA sequencing datasets from the Kidney Precision Medicine Project (single-nucleus RNA-seq of the Adult Human Kidney dataset).

B-C. Expression in the single-nucleus RNA sequencing datasets from the Kidney Interactive Transcriptomics analyzer. From Wilson et al. 2019 (**B**) and Muto and Wilson 2021 (**C**), respectively.

Supplementary Figure 2: Basal description of mice lacking *Nr3c2* in PEC.

A. Genetic construction of Pec-Cre *Nr3c2*$^{wt/wt}$ (WT) and Pec-Cre *Nr3c2*$^{lox/lox}$ (MR$^{\Delta PEC}$) mice.

B. Basal urinary albumin-to-creatinine ratio of WT and MR$^{\Delta PEC}$ mice. Data are shown as individual values and mean ± sem. n= 18 mice per group.

C. Masson trichrome staining on kidney section of WT and MR$^{\Delta PEC}$ mice. Scale bar: 50 µm.

D. Transmission electron microscopy of kidney section of WT and MR$^{\Delta PEC}$ mice. Scale bar: 1µm.

Supplementary Figure 3: Basal MR expression in PEC of WT mice (WT) and mice lacking *Nr3c2* in PEC (MR$^{\Delta PEC}$).

RNAscope for *Nr3c2* mRNA (blue dots) and *Cldn1* mRNA (red staining) showing basal Nr3c2 mRNA expression in PEC of WT mice (left panel, WT) at low magnification (upper) and high magnification (lower left) and in mice lacking Nr3c2 in PEC (right panel, MR$^{\Delta PEC}$) at low magnification (upper) and high magnification (lower right). Arrows indicates Nr3c2 mRNA expression (blue dots). Scale bar: 20um

Supplementary Figure 4: MR expression in WT mice (WT) and mice lacking *Nr3c2* in PEC ($MR^{\Delta PEC}$) during DOCA salt model

A. RNAscope for *Nr3c2* mRNA (blue dots) and *Cldn1* mRNA (red staining) showing Nr3c2 mRNA expression during DOCA salt-model in PEC of WT mice (left and middle panel, WT) at low magnification (upper) and high magnification (lower left and middle) and in mice lacking Nr3c2 in PEC (right panel, $MR^{\Delta PEC}$) at low magnification (upper) and high magnification (lower right)

B. RNAscope for *Nr3c2* mRNA (blue dots) in tubules of WT mice (WT, left) and mice lacking Nr3c2 in PEC (right panel, $MR^{\Delta PEC}$) during DOCA-salt model showing preserved expression of *Nr3c2* mRNA in both mice. Arrows indicate *Nr3c2* mRNA expression (blue dots). Scale bar: 20μm.

Supplementary Figure 5: UniNx + DOCA-salt FSGS model, microalbuminuria and blood pressure.

A. Urinary albumin to creatinine ratio (ACR) in WT (placebo or DOCA) and $MR^{\Delta PEC}$ mice (placebo or DOCA) during DOCA salt model along time (basal, until week 7 (W7). **** $P < 0.0001$ between WT DOCA and $MR^{\Delta PEC}$ DOCA mice;

B. Blood pressure during DOCA model in WT and $MR^{\Delta PEC}$ mice mice at different time points (Day 0 (D0) : day of uninephrectomy) until seven weeks (W7) after uninephrectomy (UniNx) during DOCA-salt model. **** $P < 0.0001$ between WT (WT DOCA) and $MR^{\Delta PEC}$ ($MR^{\Delta PEC}$ DOCA) DOCA mice; $$$ $P < 0.001$, $$$$ $P < 0.0001$ between WT placebo (WT placebo) and WT DOCA (WT DOCA) mice; # $P < 0.05$, ####p<0.0001 between $MR^{\Delta PEC}$ placebo ($MR^{\Delta PEC}$ placebo) and $MR^{\Delta PEC}$ ($MR^{\Delta PEC}$DOCA) DOCA mice.

Supplementary Figure 6: Glomerular structure in DOCA salt model.

A. Masson Trichrome staining on kidney sections of WT and MR^{DPEC} mice with UniNx + salt and receiving placebo. Scale bar: 50 μm.

B. Transmission electron microscopy on kidney sections of WT and MR^{DPEC} mice with UniNx + salt and receiving placebo. Scale bar: 2μm in upper panel and 1μm in lower panel.

C. Sirius red staining on kidney section in WT and MR^{DPEC} mice with UniNx + salt and receiving placebo or DOCA. Scale bar: 50 μm.

D. Quantification of percentage of red sirius area over renal tissue. 1 way ANOVA: $$$$ $P < 0.0001$ between WT placebo and DOCA mice; ### $P < 0.001$ between MR^{DPEC} placebo and DOCA mice. **E.** Systolic blood pressure during DOCA in WT and MR^{DPEC} mice with UniNx + salt and receiving placebo or DOCA. 2 way ANOVA: **** $P < 0.0001$ between WT DOCA and MR^{DPEC} DOCA mice; $$$ $P < 0.001$, $$$$ $P < 0.0001$ between WT placebo and WT DOCA mice; # $P < 0.05$, ####p<0.0001 between MR^{DPEC} placebo and MR^{DPEC} mice.

Supplementary Figure 7:

A. RNAscope for *NR3C2* mRNA (blue dots) and *CLDN1* mRNA (red staining) showing *NR3C2* mRNA expression in distal convoluted tubules in human kidneys.

B. Quantification of the density of NR3C2 positive dots per 1000 pixel of PEC area per glomerulus in renal biopsies of patients with MCD (n=5 patients), FSGS (n= 4 patients), ANCA (n=3 patients) and Lupu nephritis (n=4 patients). 4 normal kidneys were used as control. Each dot represents a glomerulus.

Supplementary Figure 8: T cell infiltration in the NTN model.

Quantification of CD3+ area in kidneys from WT mice, $MR^{\Delta PEC}$ mice, and WT mice treated with eplerenone at day 14 of the NTN model. Data show the quantification of CD3+ area per kidney cortex section (left), CD3+ tubule-interstitial area per kidney cortex section (middle), and CD3+ periglomerular area per kidney cortex section (right). Data are shown as individual values and mean ± sem. n=7-8 mice. 1 way ANOVA: $P = 0.005$, post hoc Fisher LSD test: * $P < 0.05$, ** $P < 0.01$.

Supplementary Figure 9: Differentially expressed genes identified in PECs treated with eplerenone, DMSO, HB-EGF and HB-EGF with eplerenone.

A-B. Top 50 upregulated and downregulated genes in HB-EGF-treated PECs in comparison to DMSO-treated cells (**A**) and in HB-EGF + eplerenone-treated PECs in comparison to HB-EGF-treated PECs (**B**).

C. Normalized RNA counts for selected genes. 2-way ANOVA was performed and post-test Fisher LSD for testing eplerenone effect only: eplerenone vs. DMSO and eplerenone + HB-EGF vs. HB-EGF.
Only p value <0.05 are shown. * $P < 0.05$, ** $P < 0.01$, *** $P < 0.001$, *** $P < 0.0001$

D. Heatmap of cytokines and chemokines that are upregulated or downregulated in DMSO-treated, HB-EGF-treated, Eplerenone-treated and HB-EGF + eplerenone-treated PECs.

Supplementary Figure 10:

Representative photomicrograph of mTomato (red) and mGFP (green) expression in mouse kidneys from iPec-Cre mT/mG mice at baseline and after nephrotoxic serum injection at day 4 and day 7. Nuclei were counterstained with DAPI. CRE expression is observed in PECs in glomeruli as well as in some tubular cells. Scale bar: 50 μm.

Supplementary Table 1. Physiological parameters of wild-type and $MR^{\Delta PEC}$ mice.

	Wild-type	MR^{DPEC}	p-value
Systolic BP (mm Hg)	118.6 ± 3.47	118.9 ± 2.99	0.8977
Serum Na^+ (mmol/L)	146.9 ± 0.56	145.8 ± 0.40	0.1413
Serum K^+ (nmol/L)	4.35 ± 0.10	4.11 ± 0.15	0.0963
Serum Cl^- (mmol/L)	111.5 ± 0.49	110.3 ± 0.60	0.1545
Hemoglobin (g/dL)	13.26 ± 0.27	13.88 ± 0.23	0.1248
Urinary Albumin-to-Creatinine ratio	0.693 ± 0.15	0.586 ± 0.09	0.7134
Urinary Na^+/creatinine	40.2 ± 3.68	40.52 ± 4.47	0.8977
Urinary K^+/creatinine	41.84 ± 1.97	45.81 ± 1.46	0.1164
Urinary Cl^-/creatinine	27.12 ± 2.64	31.28 ± 3.13	0.3
Urinary Na^+/K^+	1.003 ± 0.122	0.904 ± 0.112	0.7477

Results are expressed as mean ± sem.

Supplementary Table 2. Clinical characteristics of patients whose kidney biopsies were used for MR immunochemistery.

Diagnosis	Sex	Age (years)	HTN	Serum creatinine (µmol/L)	eGFR (ml/min/1.73m^2)	Nephrotic Syndrome	PCR (g/mmol)	Hematuria	leukocyturia	Treatment at the time of KB
MCD	F	43n	na	na	na	na	na	na	na	na
MCD	F	18	na	na	na	na	na	na	na	na
MCD	M	46.5	0	1037	5	1	1.4	1	1	none
MCD	M	60.3	0	80	107	1	Na	0	0	none
MN	M	56.5	1	311	21	1	0.8	0	0	none
MN	M	45.3	0	82	99	1	0.6	0	0	none
Primary FSGS	M	24.3	0	127	78	1	0.571	0	0	none
Secondary FSGS	M	35.2	1	173	43	na	0.4	1	0	none
Secondary FSGS	M	53.4	0	150	39	0	0.1	1	0	na
IgAN + FSGS	M	33.8	1	236	30	0	na	1	0	none
IgAN + FSGS	M	30.9	0	280	25	0	0.4	1	0	none
Lupus	M	30.5	na	100	87	0	0.167	1	0	na
Lupus	F	24.2	1	200	34	1	0.4	1	0	Steroids 500 mg
Lupus	F	34.9	0	60	131	0	0.1	1	na	none
Lupus	M	24.5	0	150	55	1	1.2	na	na	Steroids 1mg/kg hydroxychloroquine
ANCA	M	53.6	na	200	32	0	0.2	1	0	na
ANCA	M	48.6	0	193	34	0	0.07	1	0	none
ANCA	M	81.1	1	112	53	0	0.15	1	1	none
ANCA	F	67.2	1	300	13	1	na	1	na	none

Abbreviations: ANCA: antineutrophilic cytoplasmic antibody vasculitis; eGFR: estimated glomerular filtration rate (according to CKD-EPI); F: female; FSGS: focal segmental glomerulosclerosis; HTN: hypertension; IgAN: IgA nephropathy; M: male; MCD: minimal change disease; MN: membranous nephropathy; PCR: Protein-to-creatinine ratio; KB: kidney biopsy; 1: yes; 0: no; na: not available

Supplementary Table 3. Clinical characteristics of patients whose kidney biopsies were used for RNAscope assessment of NR3C2 and CLDN1 expression.

Diagnosis	Sex	Age (years)	HTN	Serum creatinine (µmol/L)	eGFR	Nephrotic Syndrome	PCR (g/mmol)	Hematuria	leukocyturia	Treatment at time of KB
MCD	M	55	1	78	96	1	0.559	0	1	None
MCD	F	19	0	60	127	1	0.572	0	0	None
MCD	M	67	1	110	60	1	1.06	0	1	None
MCD	M	20	0	85	114	1	0.842	0	1	None
MCD	F	42	0	63	104	1	1.197	nc	Nc	None
Collapsing FSGS, HIV+, malaria, APOL1 G1/G1	M	53	0	1611	3	1	0.868	0	1	None
Collapsing FSGS, HIV -, APOL1 G1/G2	M	45	0	373	16	1	0.985	0	1	None
Primary FSGS	F	31	1	82	82	0	0.071	nc	nc	None
FSGS	M	39	1	113	70	0	0.109	0	0	None
Lupus class IV, Crescents	F	24	0	58	123	0	0.264	0	1	Steroids 15mg/d AZA + HCQ
Lupus class IV, Crescents	F	42	0	57	110	1	0.367	1	1	Steroids 10mg/d + MMF
Lupus class IV, Crescents	M	26	0	78	118	0	0.095	1	1	None
Lupus class III, Crescents	F	30	0	43	131	0	0.046	1	1	Steroids 4mg/d + HCQ
ANCA	M	56	0	102	71	0	0.062	1	1	Steroids 60 mg/d
ANCA	F	82	1	160	26	0	0.269	1	1	None
ANCA	M	70	0	333	15	0	0.247	1	1	Steroids 6 mg/d

Abbreviations: ANCA: antineutrophilic cytoplasmic antibody vasculitis; AZA: azathioprine; eGFR: estimated glomerular filtration rate according to CKD-EPI in ml/min/1.73m2; F: female; FSGS: focal segmental glomerulosclerosis; HCQ: hydroxychloroquine; HTN: hypertension; IgAN: IgA nephropathy; M: male; MCD: minimal change disease; MMF: mycophenolate mofetil; MN: membranous nephropathy; PCR: Protein-to-creatinine ratio; KB: kidney biopsy; 1: yes; 0: no; na: not available

Supplementary Table 4.

Gene symbol	Forward primer	Reverse primer
18S	CCCTGCCTTTGTACACACC	CGATCCGAGGGCCTCACTA
b2-microglobulin	ATTCACCCCCACTGAGACTG	TGCTATTTCTTTCTGCGTGC
Ubiquitin C	AGCCCAGTGTTACCACCAAG	ACCCAAGAACAAGCACAAG
Cd44	AGCTGACGAGACCCGGAATC	TCCCAGGAATGACGTCTCCA
Pcna	GGAGACAGTGGAGTGGCTTT	TGGATAAAGAAGAGGAGGCG
Cldn1	GATGTGGATGGCTGTCATTGG	CCATGCTGTGGCCACTAATGT
Snail	CTTGTGTCTGCACGACCTGT	AGTGGGAGCAGGAGAATGG
Vimentin	CCAACCTTTTCTTCCCTGAA	TGAGTGGGTGTCAACCAGAG

Supplementary Table 5. List of differentially expressed genes in PEC in response to 24h treatment with HB-EGF versus DMSO. (excel file)

Supplementary Table 6. List of differentially expressed genes in PEC in response to 24h treatment with HB-EGF versus HB-EGF + eplerenone. (excel file)

Supplementary Table 7. List of enriched pathways in PEC in response to 24h treatment with HB-EGF versus DMSO. (excel file)

Supplementary Table 8. List of enriched pathways in PEC in response to 24h treatment with HB-EGF versus HB-EGF + eplerenone. (excel file)

Supplementary information is available on Kidney International's website

Supplementary Figure 1

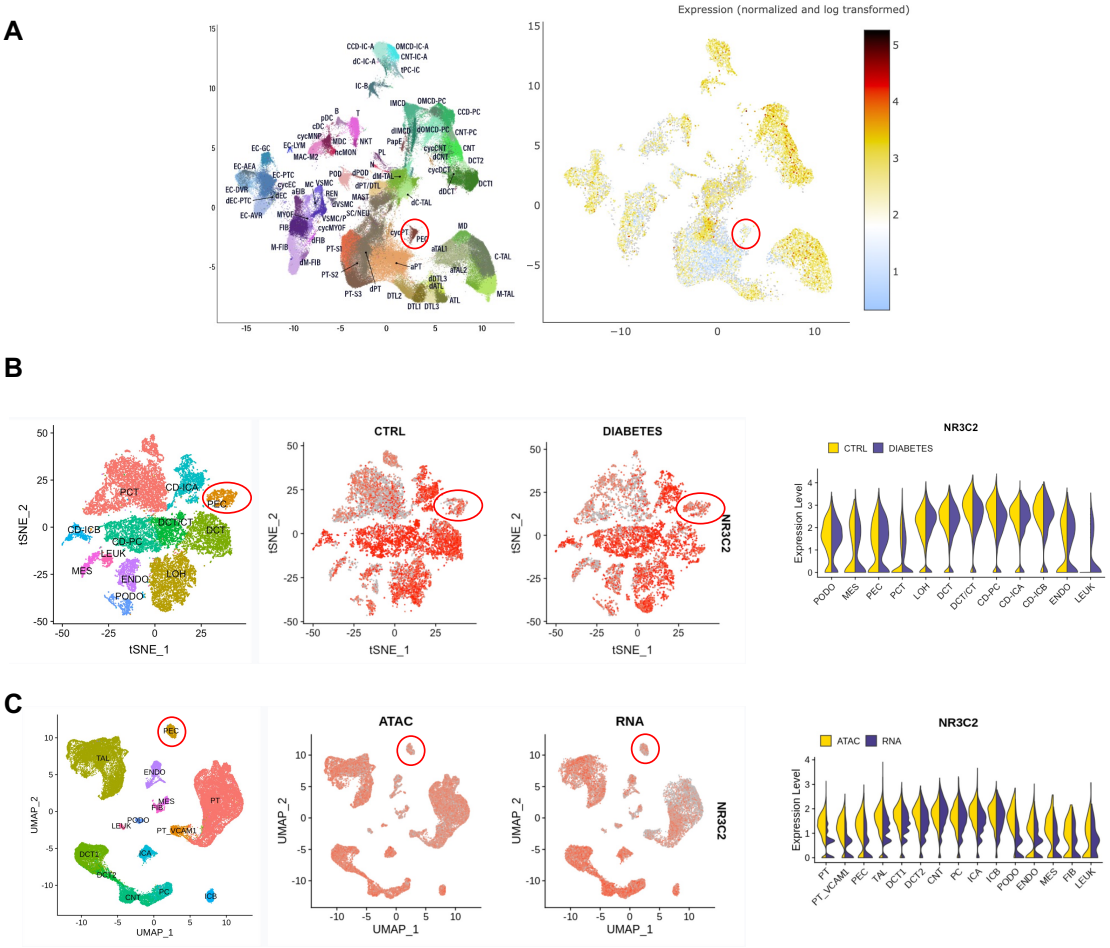

Supplementary Figure 2

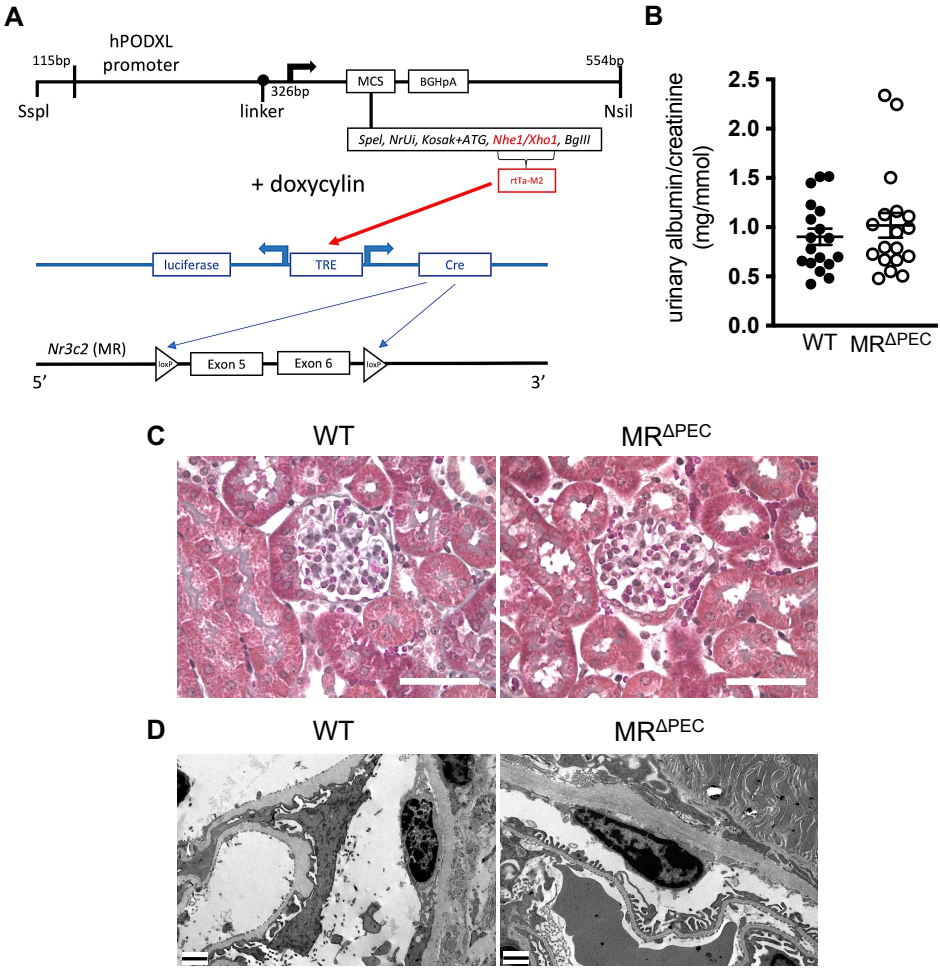

Supplementary Figure 3

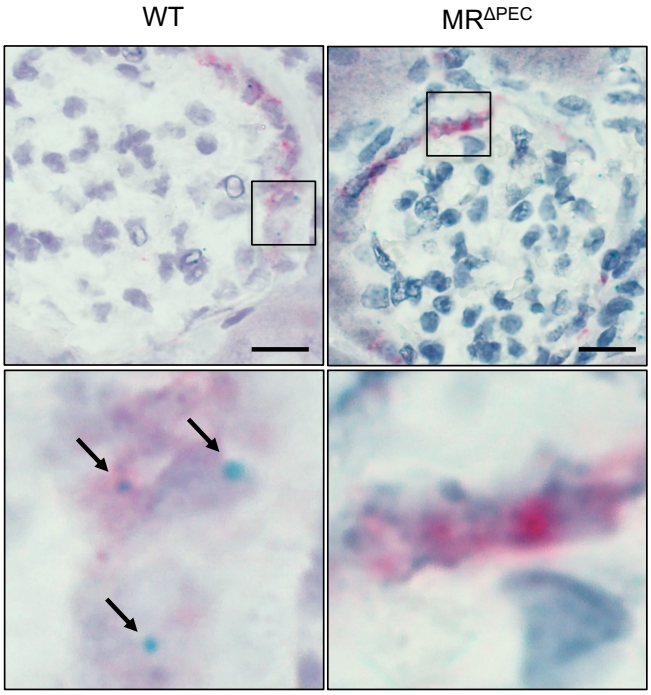

Supplementary Figure 4

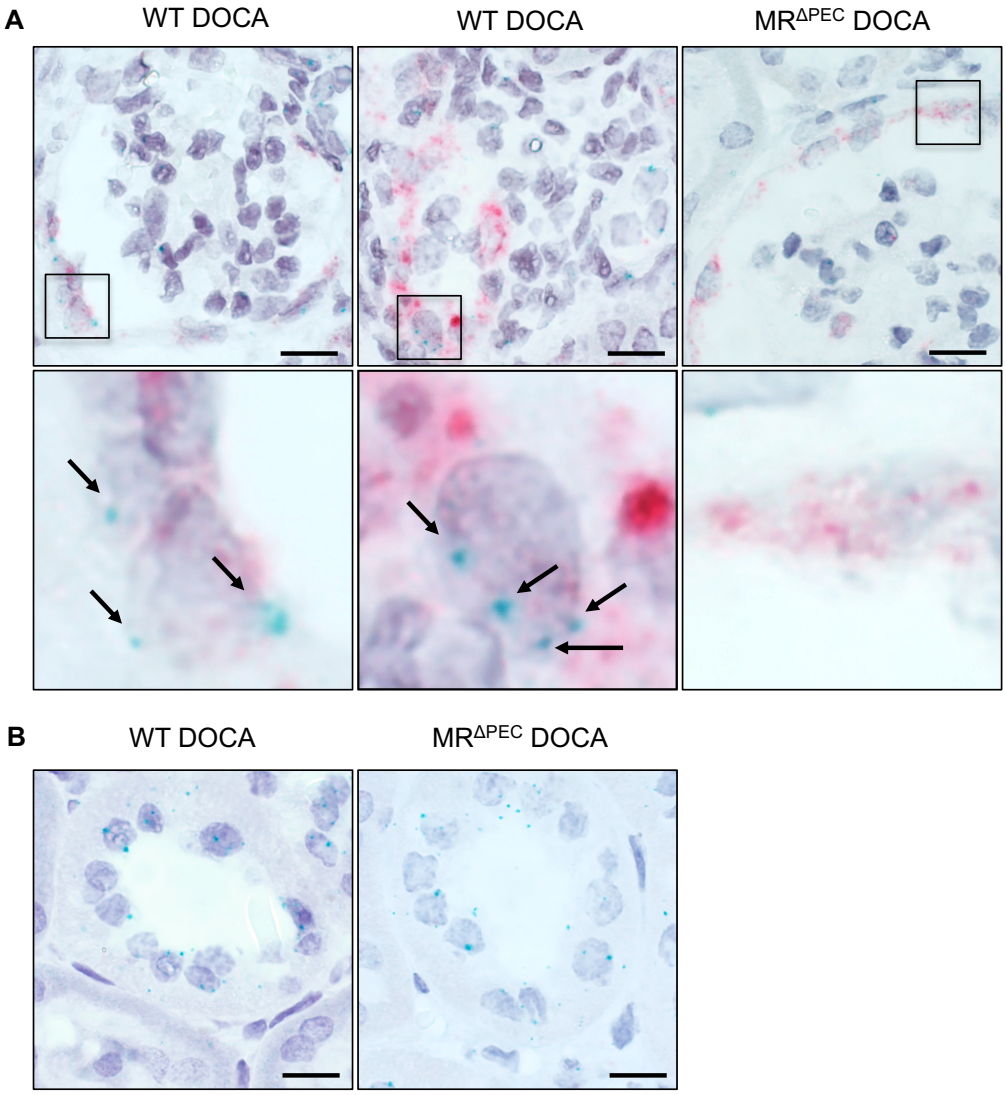

Supplementary Figure 5

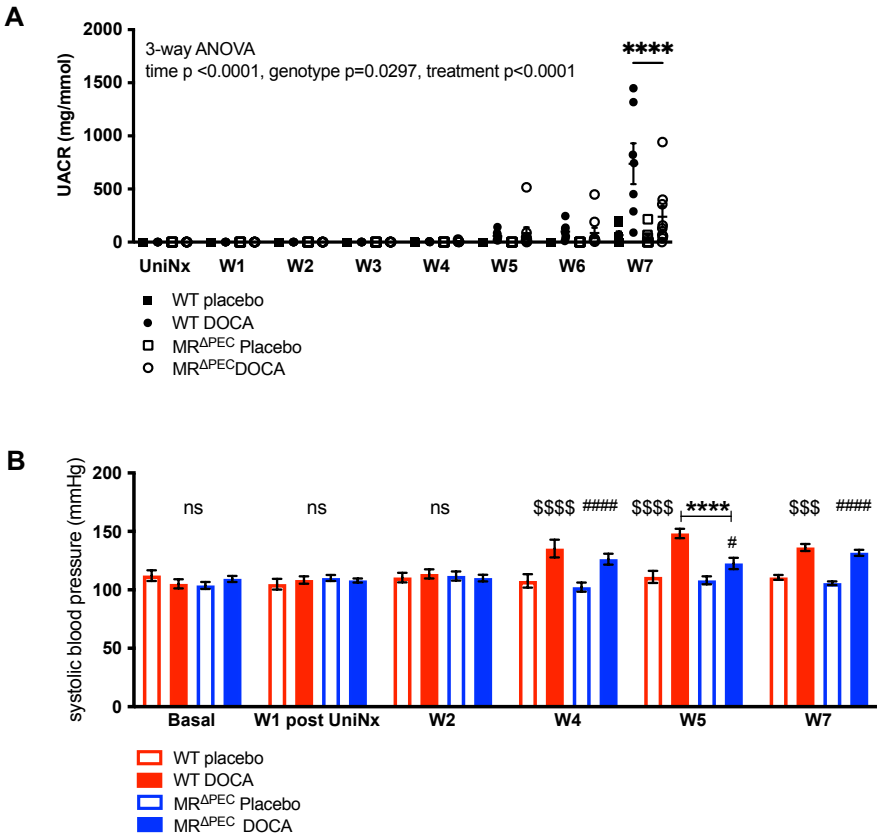

Supplementary Figure 6

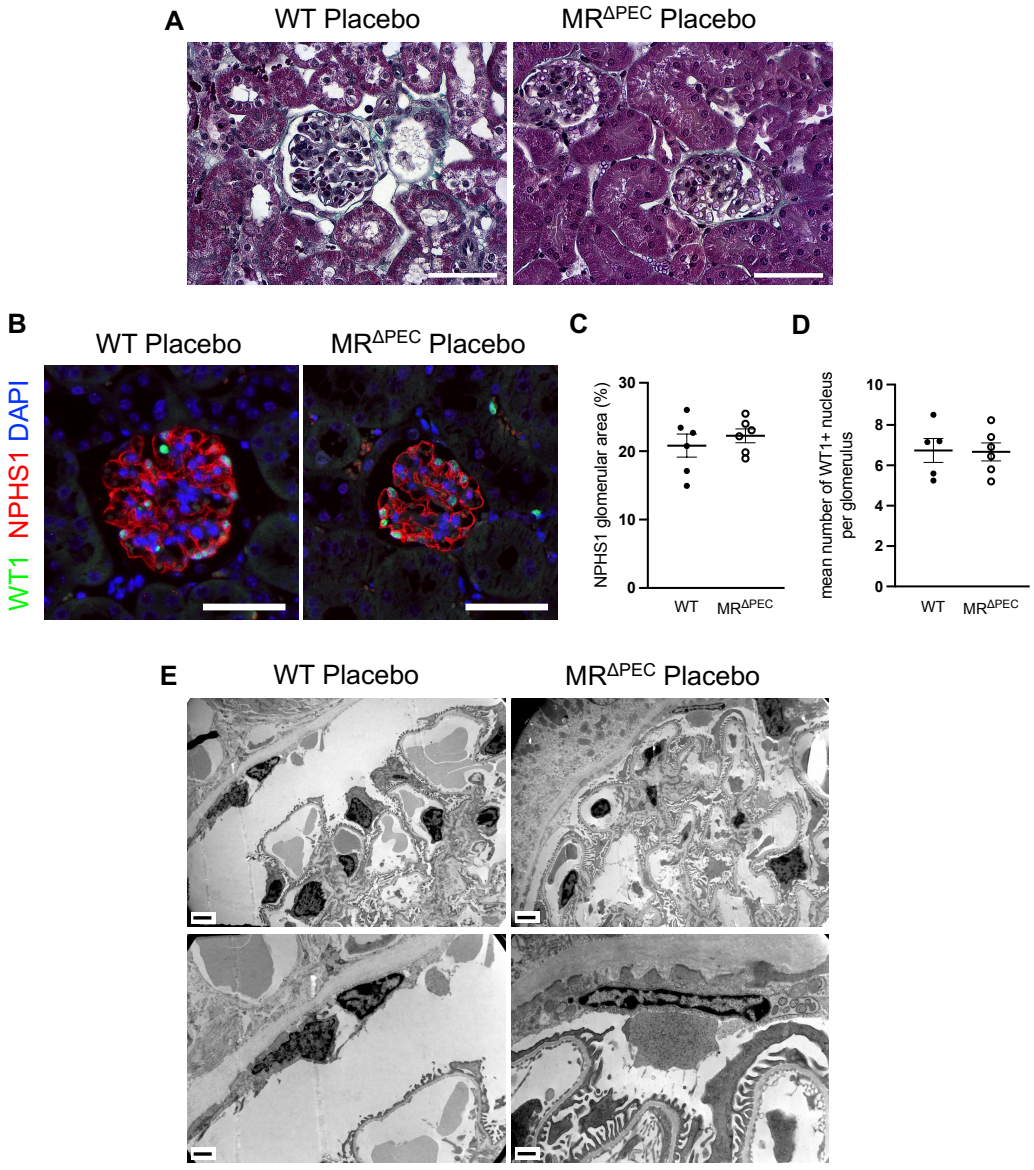

Supplementary Figure 7

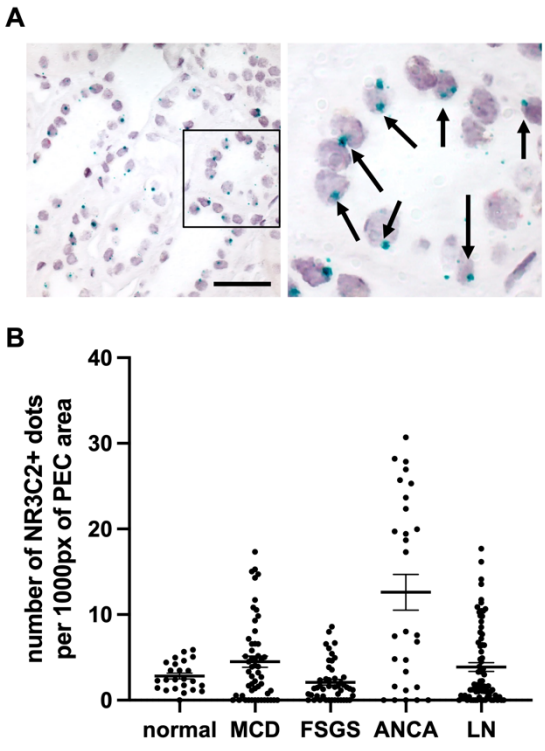

Supplementary Figure 8

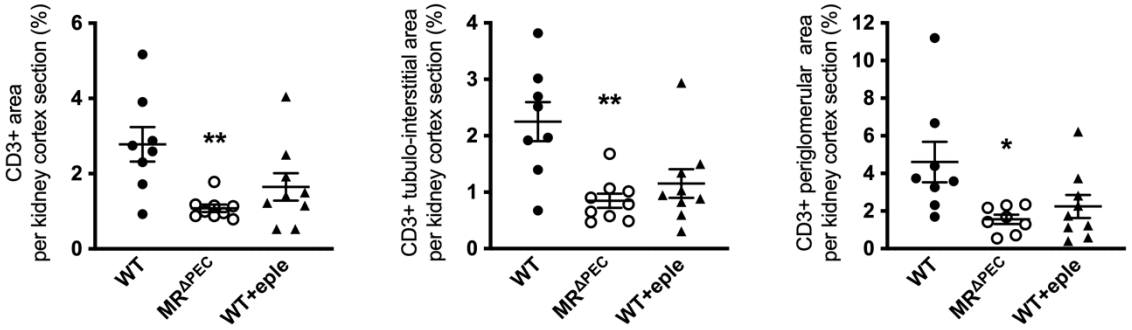

Supplementary Figure 9

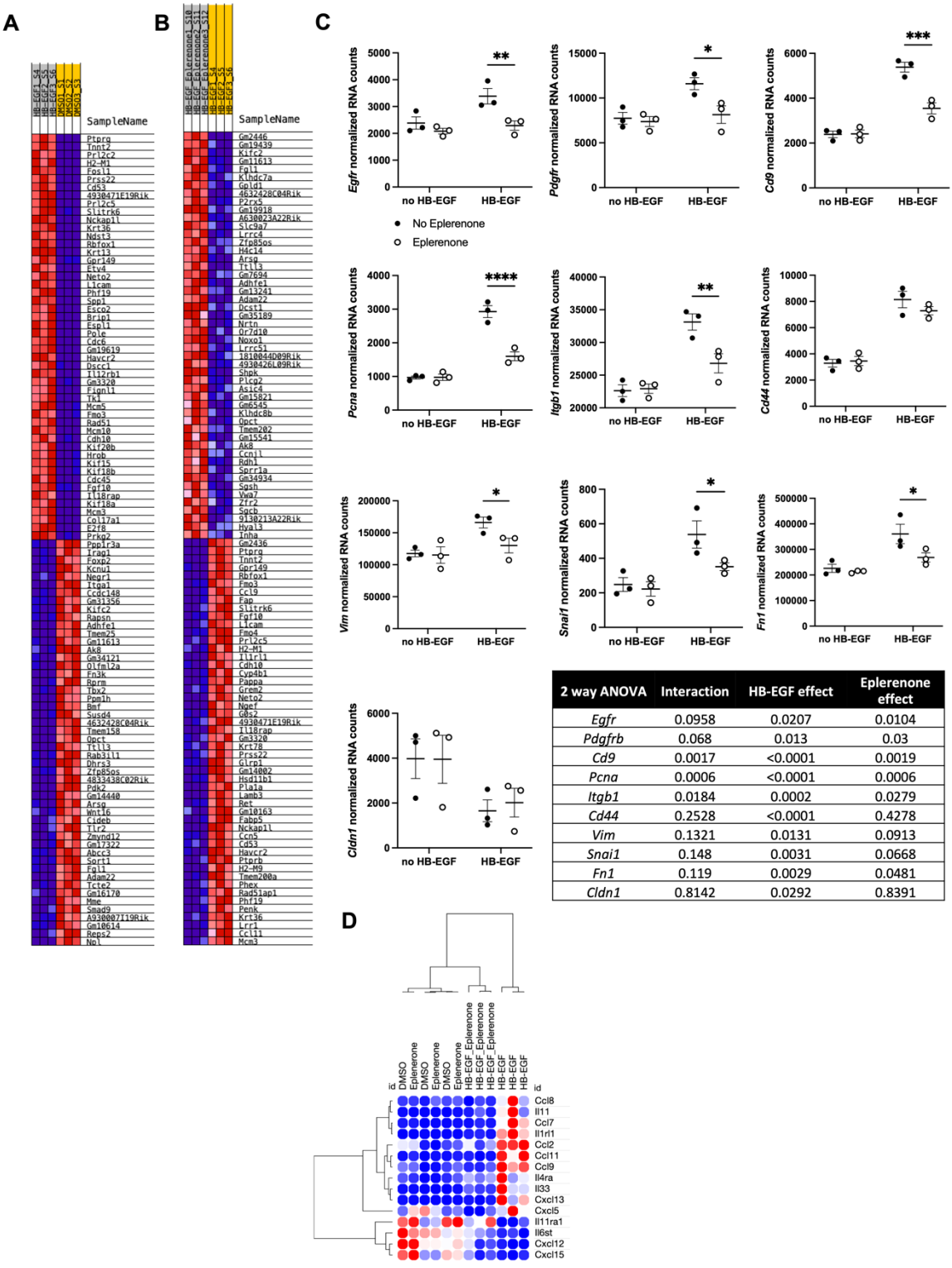

2 way ANOVA	Interaction	HB-EGF effect	Eplerenone effect
Egfr	0.0958	0.0207	0.0104
Pdgfrb	0.068	0.013	0.03
Cd9	0.0017	<0.0001	0.0019
Pcna	0.0006	<0.0001	0.0006
Itgb1	0.0184	0.0002	0.0279
Cd44	0.2528	<0.0001	0.4278
Vim	0.1321	0.0131	0.0913
Snai1	0.148	0.0031	0.0668
Fn1	0.119	0.0029	0.0481
Cldn1	0.8142	0.0292	0.8391

Supplementary Figure 10

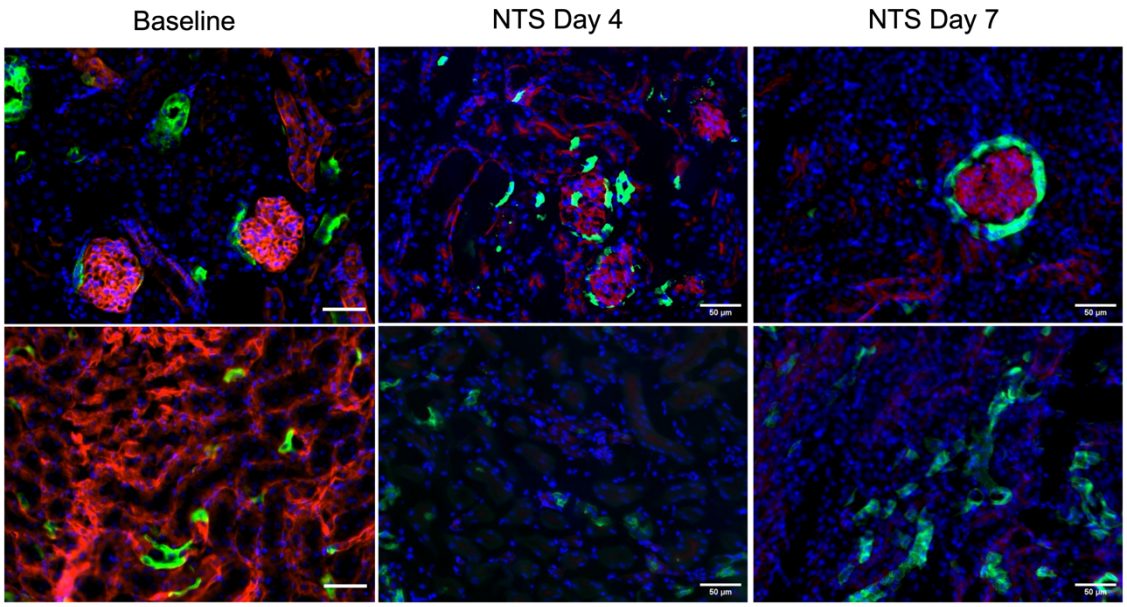

References

1. Appel D, Kershaw DB, Smeets B*, et al.* Recruitment of podocytes from glomerular parietal epithelial cells. *J Am Soc Nephrol* 2009; **20:** 333-343.

2. Lazareth H, Henique C, Lenoir O*, et al.* The tetraspanin CD9 controls migration and proliferation of parietal epithelial cells and glomerular disease progression. *Nat Commun* 2019; **10:** 3303.

3. Henique C, Bollee G, Lenoir O*, et al.* Nuclear Factor Erythroid 2-Related Factor 2 Drives Podocyte-Specific Expression of Peroxisome Proliferator-Activated Receptor gamma Essential for Resistance to Crescentic GN. *J Am Soc Nephrol* 2016; **27:** 172-188.

4. Bollee G, Flamant M, Schordan S*, et al.* Epidermal growth factor receptor promotes glomerular injury and renal failure in rapidly progressive crescentic glomerulonephritis. *Nat Med* 2011; **17:** 1242-1250.

5. Gomez-Sanchez CE, de Rodriguez AF, Romero DG*, et al.* Development of a panel of monoclonal antibodies against the mineralocorticoid receptor. *Endocrinology* 2006; **147:** 1343-1348.

6. Kabgani N, Grigoleit T, Schulte K*, et al.* Primary cultures of glomerular parietal epithelial cells or podocytes with proven origin. *PLoS One* 2012; **7:** e34907.

7. Hori Y, Touei D, Saitoh R*, et al.* The Aldosterone Receptor Antagonist Eplerenone Inhibits Isoproterenol-Induced Collagen-I and 11beta-HSD1 Expression in Rat Cardiac Fibroblasts and the Left Ventricle. *Biol Pharm Bull* 2017; **40:** 1716-1723.

8. Bustin SA, Benes V, Garson JA*, et al.* The MIQE guidelines: minimum information for publication of quantitative real-time PCR experiments. *Clin Chem* 2009; **55:** 611-622.

9. Mootha VK, Lindgren CM, Eriksson KF*, et al.* PGC-1alpha-responsive genes involved in oxidative phosphorylation are coordinately downregulated in human diabetes. *Nat Genet* 2003; **34:** 267-273.

10. Subramanian A, Tamayo P, Mootha VK*, et al.* Gene set enrichment analysis: a knowledge-based approach for interpreting genome-wide expression profiles. *Proc Natl Acad Sci U S A* 2005; **102:** 15545-15550.

11. Liberzon A, Birger C, Thorvaldsdottir H*, et al.* The Molecular Signatures Database (MSigDB) hallmark gene set collection. *Cell Syst* 2015; **1:** 417-425.

12. Liberzon A, Subramanian A, Pinchback R*, et al.* Molecular signatures database (MSigDB) 3.0. *Bioinformatics* 2011; **27:** 1739-1740.

13. Lake BB, Menon R, Winfree S*, et al.* An atlas of healthy and injured cell states and niches in the human kidney. *Nature* 2023; **619:** 585-594.

14. Muto Y, Wilson PC, Ledru N*, et al.* Single cell transcriptional and chromatin accessibility profiling redefine cellular heterogeneity in the adult human kidney. *Nat Commun* 2021; **12:** 2190.

15. Wilson PC, Wu H, Kirita Y*, et al.* The single-cell transcriptomic landscape of early human diabetic nephropathy. *Proc Natl Acad Sci U S A* 2019; **116:** 19619-19625.

14.3 Modulation of Calcium Signaling on Demand to Decipher the Molecular Mechanisms of Primary Aldosteronism

Fedlaoui B, Cosentino T, Al Sayed ZR, Alexandre Coelho R, Giscos-Douriez I, Faedda N, **Fayad M** et al. Modulation of Calcium Signaling on Demand to Decipher the Molecular Mechanisms of Primary Aldosteronism. Hypertension [Internet]. [cited 2025 Feb 14];0(0). Available from: https://www.ahajournals.org/doi/10.1161/HYPERTENSIONAHA.124.23295

Check for updates

Hypertension

ORIGINAL ARTICLE

Modulation of Calcium Signaling on Demand to Decipher the Molecular Mechanisms of Primary Aldosteronism

Bakhta Fedlaoui, Teresa Cosentino, Zeina R. Al Sayed, Rita Alexandre Coelho, Isabelle Giscos-Douriez, Nicolo Faedda, May Fayad, Jean-Sebastien Hulot, Christopher J. Magnus, Scott M. Sternson, Simon Travers-Allard, Stephanie Baron, David Penton, Fabio L. Fernandes-Rosa, Maria-Christina Zennaro, Sheerazed Boulkroun

BACKGROUND: Primary aldosteronism is the most common form of secondary hypertension. The most frequent genetic cause of aldosterone-producing adenomas is somatic mutations in the potassium channel KCNJ5. They affect the ion selectivity of the channel, with sodium influx leading to cell membrane depolarization and activation of calcium signaling, the major trigger for aldosterone biosynthesis.

METHODS: To investigate how *KCNJ5* mutations lead to the development of aldosterone-producing adenomas, we established an adrenocortical cell model in which sodium entry into the cells can be modulated on demand using chemogenetic tools [H295R-S2 α7-5HT3-R (α7-5HT3 receptor) cells]. We investigated their functional and molecular characteristics with regard to aldosterone biosynthesis and cell proliferation.

RESULTS: A clonal cell line with stable expression of the chimeric α7-5HT3-R in H295R-S2 (human adrenocortical carcinoma cell line, Strain 2) cells was obtained. Increased sodium entry through α7-5HT3-R upon stimulation with uPSEM-817 (uPharmacologically Selective Effector Molecule-817) led to cell membrane depolarization, opening of voltage-gated Ca^{2+} channels, and increased intracellular Ca^{2+} concentrations, resulting in the stimulation of *CYP11B2* expression and increased aldosterone biosynthesis. Increased intracellular sodium influx did not increase proliferation but rather induced apoptosis. RNA sequencing and steroidome analyses revealed unique profiles associated with Na^+ entry, with only partial overlap with Ang II (angiotensin II) or potassium-induced changes.

CONCLUSIONS: H295R-S2 α7-5HT3-R cells are a new model reproducing the major features of cells harboring *KCNJ5* mutations. Increased expression of *CYP11B2* and stimulation of the mineralocorticoid biosynthesis pathway are associated with a decrease of cell proliferation and an increase of apoptosis, indicating that additional events may be required for the development of aldosterone-producing adenomas. ***(Hypertension.* 2025;82:716–732. DOI: 10.1161/HYPERTENSIONAHA.124.23295.)** • **Supplement Material**.

GRAPHIC ABSTRACT: A graphic abstract is available for this article.

Key Words: adrenal cortex ■ calcium signaling ■ cell proliferation ■ mutation ■ potassium channels ■ sodium

Downloaded from http://ahajournals.org by on November 13, 2025

The adrenal gland consists of 2 distinct regions: the outer adrenal cortex and the inner adrenal medulla. The adrenal cortex is further divided into 3 zones, the zona glomerulosa (ZG), zona fasciculata, and zona reticularis, each specialized in hormone production due to the expression of specific enzymes. Among these hormones, aldosterone, produced by the adrenal ZG, plays an important role in regulating salt and fluid balance, thereby controlling arterial blood pressure. As a key component of the renin-angiotensin-aldosterone system,

Correspondence to: Sheerazed Boulkroun, INSERM, U970, Paris Cardiovascular Research Center–PARCC, 56, rue Leblanc, 75015 Paris, France. Email sheerazed.boulkroun@inserm.fr

Supplemental Material is available at https://www.ahajournals.org/doi/suppl/10.1161/HYPERTENSIONAHA.124.23295.
For Sources of Funding and Disclosures, see page 730.

© 2025 American Heart Association, Inc.

Hypertension is available at www.ahajournals.org/journal/hyp

NOVELTY AND RELEVANCE

What Is New?

Herein, we have developed a novel cell model in which intracellular Ca^{2+} concentration can be modulated on demand, through modulation of sodium entry, reproducing the major characteristics of cells harboring a *KCNJ5* mutation.

We demonstrate that Na^+ entry into the cells results, on one hand, in cell membrane depolarization, Ca^{2+} influx, activation of Ca^{2+} signaling leading to increased expression of *CYP11B2*, and stimulation of mineralocorticoid biosynthesis and, on the other hand, in a decrease in cell proliferation and an increase in apoptosis.

We show that Na^+ influx leads to a specific transcriptome signature that may explain some of the peculiar features of aldosterone-producing adenoma carrying *KCNJ5* mutations compared with other genetic abnormalities.

What Is Relevant?

While the role of *KCNJ5* mutations in promoting autonomous aldosterone biosynthesis has been clearly established, their role in promoting abnormal cell proliferation remains to be established. Our study demonstrates that *KCNJ5* mutations are not able to promote both autonomous aldosterone production and cell proliferation, suggesting that additional events may be required for adenoma development.

Clinical/Pathophysiological Implications?

This cellular model offers valuable new insights into the mechanisms leading to primary aldosteronism development, revealing novel processes involved in the disease and paving the way for new therapeutic approaches in primary aldosteronism.

Nonstandard Abbreviations and Acronyms

α7-5HT3-R	α7-5HT3 receptor
Ang II	angiotensin II
APA	aldosterone-producing adenoma
AT1R	Ang II type 1 receptor
AUC	area under the curve
Dab2	disabled-2
GIRK4	G-protein-gated inwardly rectifying K+ channel 4
NF-κB	nuclear factor-κB
PA	primary aldosteronism
TNFα	tumor necrosis factor-α
ZG	zona glomerulosa

its production is mainly stimulated by Ang II (angiotensin II), which increases in response to volume depletion, and elevated plasma potassium (K^+) levels.[1,2] Ang II signals through AT1R (Ang II type 1 receptor) and activates, via Gαq, an entire signaling cascade that leads to the release of Ca^{2+} from the endoplasmic reticulum. The stimulation by K^+ and to a less extent by Ang II results in ZG cell membrane depolarization and opening of voltage-gated calcium (Ca^{2+}) channels, leading to an increased intracellular Ca^{2+} concentration. The activation of Ca^{2+} signaling triggers a phosphorylation cascade that leads to increased transcription of *CYP11B2*, coding for aldosterone synthase and aldosterone biosynthesis.[1]

Deregulation of the mechanisms regulating adrenal aldosterone biosynthesis results in primary aldosteronism (PA). PA is the leading cause of secondary hypertension, affecting ≈5% to 10% of patients with hypertension and up to 20% of those with treatment resistant hypertension.[3–6] It is characterized by hypertension with elevated aldosterone levels, low plasma renin concentration, increased aldosterone-to-renin ratio, and is often associated with hypokalemia. The main subtypes of PA are bilateral adrenal hyperplasia and aldosterone-producing adenomas (APAs), accounting together for 95% of cases. PA is associated with an increased risk of cardiometabolic and renal complications[7] due to the major adverse effects of aldosterone excess; therefore, early diagnosis and appropriate treatment of PA are essential.

In the past decade, research has uncovered mutations in ion channels (*KCNJ5* [potassium inwardly rectifying channel subfamily J member 5],[8] *CACNA1D*,[9,10] *CACNA1H*,[11,12] *CLCN2*,[13,14] and *SLC30A1*[15]) and pumps (*ATP1A1*[9,16] and *ATP2B3*[16]), as principal causes of APAs and familial forms of PA. These mutations enhance either directly or indirectly intracellular Ca^{2+} concentrations, the main trigger for aldosterone biosynthesis. Notably, in the case of *KCNJ5*, which encodes GIRK4 (G-protein-gated inwardly rectifying K^+ channel 4), the majority of mutations cluster near the channel's ion-selective filter, leading to a loss of selectivity for K^+ ions in favor of an intracellular sodium (Na^+) influx.[8] These mutations lead to cell membrane depolarization, the opening of voltage-gated Ca^{2+} channels, an increase of intracellular Ca^{2+} concentration, activation of Ca^{2+} signaling pathways, and ultimately an increase of *CYP11B2* expression and aldosterone biosynthesis.[8]

While the role of *KCNJ5* mutations in autonomous aldosterone production has been well established, their role in modulating cell proliferation is still under debate.[17–20] The

Downloaded from http://ahajournals.org by on November 13, 2025

first objective of our study was, therefore, to investigate the role of *KCNJ5* mutations in regulating proliferative processes that could lead to adenoma development. The second objective was to determine whether changes in intracellular sodium balance could induce specific intracellular transcriptional profiles that could explain the peculiar pathological and biological features of adenoma carrying *KCNJ5* mutations. For this purpose, we used chemogenetic tools, which allow to manipulate specific ion fluxes via modified ion channels with pharmacologically selective properties, known as PSAM (pharmacologically selective actuator modules). PSAM, comprising mutated ligand-binding domains and selective ionic pore domains, respond to PSEM (pharmacologically selective effector molecules), inducing channel opening and allowing specific ions to flow through the activated channel.[21,22] Here, we used second-generation chemogenetic tools to establish a human adrenal cell model in which we could modulate sodium entry on demand, by introducing the α7-5HT3 chimeric receptor. This chimeric receptor consists of the ligand-binding domain of the α7 nicotinic acetylcholine receptor and the ionic pore domain of the serotonin receptor type 3. Importantly, the ligand-binding domain has been mutated to bind only the pharmacologically selective effector molecules and not the endogenous ligand.[21] Activation of α7-5HT3-R (α7-5HT3 receptor) by uPSEM-817 (uPharmacologically Selective Effector Molecule-817) was used to study the effect of Na^+ entry into the cells, mimicking molecular abnormalities observed in the presence of *KCNJ5* mutations. To determine the functional and molecular characteristics of this new cell model, we assessed changes in membrane potential, intracellular Ca^{2+} concentration, and impact on cell proliferation. Additionally, we conducted RNA-sequencing and steroidomic analyses following treatment with uPSEM-817, Ang II, and K^+.

METHODS

Data Availability

Expanded Materials and Methods are available in the Supplemental Material.

The data, analytic methods, and study materials that support the findings of this study are available from the corresponding author upon reasonable request.

Cell Culture and Electroporation

The H295R-S2 (human adrenocortical carcinoma cell line, Strain 2) cell line, a subclone of the H295R human adrenocortical carcinoma cell, was kindly provided by Dr William E. Rainey[23] and cultured in complete medium containing DMEM/Eagle F12 medium (1:1; GIBCO, Life Technologies) supplemented with 2% Ultroser G (Sartorius, France), 1% insulin/transferrin/selenium premix (BD Biosciences), 7.5 mmol/L HEPES (GIBCO), 1% penicillin and streptomycin (GIBCO, Life Technologies) and 20 mg/mL G418 (Thermo Fisher Scientific). Cells were maintained at 37 °C under a humid atmosphere of 95% air and 5% CO_2.

The α7-5HT3 chimeric receptor consists of the ligand-binding domain of the nicotinic receptor fused with the ionic pore domain of the serotonin receptor type 3. The sequence has been inserted into the pcDNA3.1 vector.[21]

Five million H295R-S2 cells were seeded into a 100-mm tissue culture dish. After 24 hours, the cells were trypsinized, counted, and 3.10^6 cells resuspended in 100 µL Nucleofector R solution and electroporated with 3 µg of plasmid (pcDNA3 containing or not containing α7-5HT3-R cDNA) using the Amaxa Nucleofector Kit R (Lonza) according to the manufacturer's instructions. After electroporation, the mixed populations were amplified under selection pressure with G418. Pure clones were isolated by picking clones after limited dilution of the cells to isolate 1 cell at an optimum distance from the other in a 200-mm diameter plate. Colonies were, afterward, isolated in wells and amplified for further characterization.

Statistics

The number of independent experiments (n) refers to the number of cells or dishes studied to calculate mean±SEM or median. The measurements were performed at different days and from different cell preparations using different cell passages to ensure the reproducibility of the experiments. For patch-clamp experiments, each cell was analyzed separately.

Data were analyzed in the Prism10 software (GraphPad, San Diego, CA) using the appropriate statistical tests as indicated in the text. The normality of the data distribution was checked using the Shapiro-Wilk test. Quantitative variables were reported as mean±SEM when a gaussian distribution was present or as medians and interquartile ranges when no gaussian distribution was present. Pairwise comparisons were conducted using unpaired *t* tests for normally distributed data and Mann-Whitney *U* tests for non-normally distributed data. For multiple comparisons, ANOVA followed by Bonferroni was applied when data presented a gaussian distribution while Kruskal-Wallis followed by Dunn test was used when non-gaussian distribution was present. $P<0.05$ was considered significant.

RESULTS

Characterization of a Cell Model Expressing the α7-5HT3-R

To assess the impact of modulating intracellular Na^+ concentration on adrenal cell function, we established stable expression of the chimeric α7-5HT3-R in H295R-S2 cells. This receptor was formed by combining the extracellular ligand-binding domain of the α7 nicotinic acetylcholine receptor and the ion pore domain of the serotonin receptor 5HT3.[21] Expression of *α7-5HT3-R* was investigated by quantitative reverse transcription PCR (RT-qPCR)[24] and found exclusively in cells transfected with the vector containing its genetic sequence (Figure S1A) but not in control cells transfected with an empty vector. Upon treatment with 12 mmol/L of K^+, both cell lines exhibited a rapid increase in intracellular Ca^{2+} concentration (Figure S1B). However, treatment with different

Downloaded from http://ahajournals.org by on November 13, 2025

concentrations of varenicline, a nicotinic receptor partial agonist and cholinergic agonist, resulted in a dose-dependent increase in intracellular Ca^{2+} concentration in cells expressing the α7-5HT3-R only (Figure S1B), indicating a specific effect on the chimeric receptor. This was associated with an increase in *CYP11B2* mRNA expression for varenicline concentrations ranging from 10^{-8} to 10^{-5} mol/L (Figure S1C).

To further characterize the cells expressing α7-5HT3-R, monoclonal cell populations were obtained via limiting dilution under antibiotic selection pressure. Among the 19 monoclonal cell populations selected, 6 showed *α7-5HT3-R* mRNA expression (Figure S1D), and in-depth characterization was performed on 3 of them, designated as clones 17, 24, and 42 (Figure 1). The expression of *α7-5HT3-R* mRNA was not statistically different between clones 17, 24, and 42 (Figure 1A).

Bright-field images revealed no discernible variations in cell morphology between control cells and the 3 selected clones (Figure 1B). Examination of the cellular localization of α7-5HT3-R using α-bungarotoxin, a peptide binding to the α-subunit of the nicotinic acetylcholine receptor, showed its presence on the cell surface of clones 17, 24, and 42 but not in control cells (Figure 1B). To ensure that the expression of α7-5HT3-R did not induce structural changes, we studied the expression of markers of cytoskeletal organization and of ZG cells. Phalloidin staining revealed similar actin organization in cells expressing an empty vector (control cells) or expressing α7-5HT3-R (Figure 1B). A similar staining was observed for Dab2 (disabled-2; Figure 1B), a protein marker of ZG cells expressed at the cell membrane.

Varenicline is a nicotinic receptor partial agonist and a cholinergic agonist, which may have nonspecific effects in our cell model. To avoid this, we compared the effect of varenicline to those of a drug, uPSEM-817, specifically designed to bind to α7-5HT3-R. Similar responses were obtained following uPSEM-817 and varenicline treatment in intracellular Ca^{2+} responses, both as traces (Figure S2A and S2C) and maximum of activation (Figure S2B and S2D).

α7-5HT3-R Activation by uPSEM-817 Induces Cell Membrane Depolarization and Increases Intracellular Ca^{2+} Content via Na^{+} Influx

Perforated patch-clamp recordings were conducted to assess the electrophysiological properties of 2 of the 3 clones expressing α7-5HT3-R and selected for further investigations (clones 17 and 42) in comparison

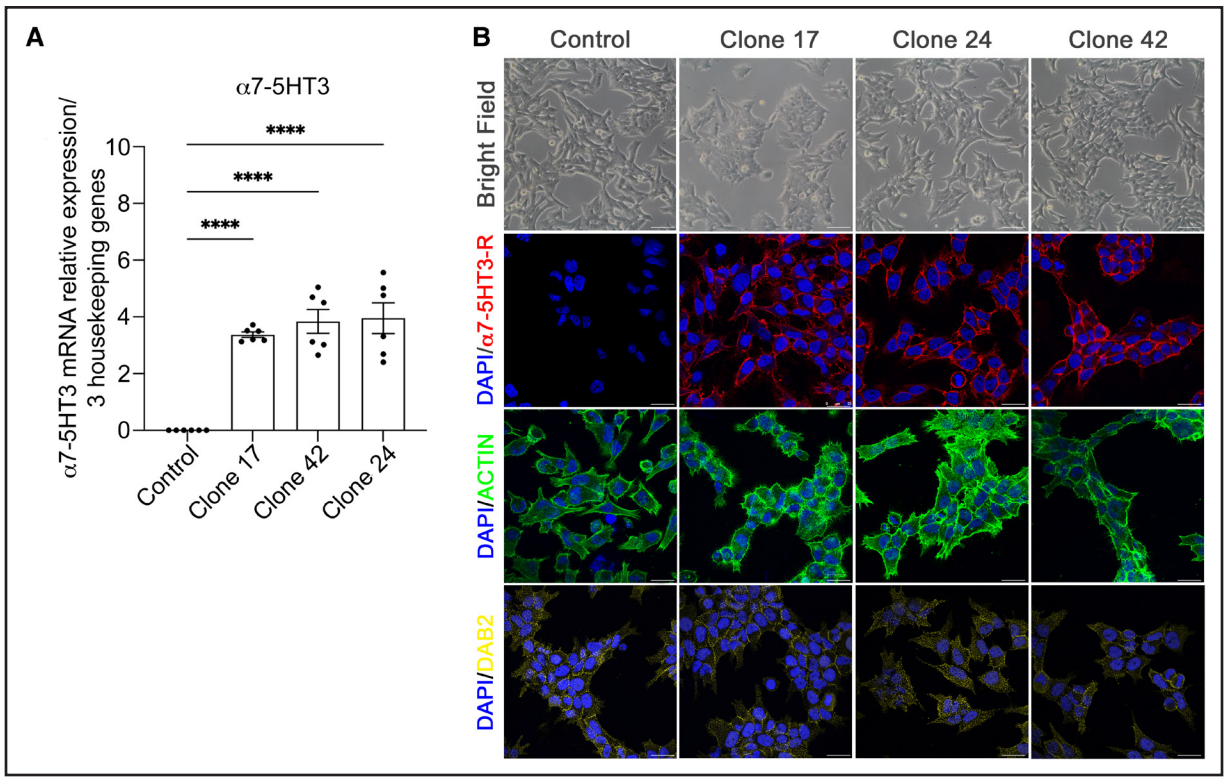

Figure 1. Morphological characterization of α7-5HT3-R (α7-5HT3 receptor)–expressing cells.
The expression of α7-5HT3-R was investigated in control cells, expressing an empty vector, and in 3 selected clones, 17, 24, and 42. **A**, mRNA expression of *α7-5HT3-R* was investigated by quantitative reverse transcription PCR (RT-qPCR), n=6 for each clone. **B**, Morphological characteristics of control and α7-5HT3-R–expressing cells were evaluated by immunofluorescence. Bright-field images revealed no structural difference between cells. DAPI (4′,6-diamidino-2-phenylindole) nuclear staining is shown in blue, α-bungarotoxin (α7-5HT3-R) in red, phalloidin (actin) in green, and Dab2 (disabled-2) in yellow. *P* values were determined by 1-way ANOVA followed by Bonferroni post hoc comparison tests, ****$P<0.0001$; bar represents 20 µm.

Downloaded from http://ahajournals.org by on November 13, 2025

to control cells. Control cells expressing an empty vector, as well as clones 17 and 42, displayed similar membrane hyperpolarization with membrane potentials of −60.83±1.2, −61.73±1.16, and −63.27±1.26, respectively (Figure 2A), indicating that α7-5HT3-R was not leaking ions.

All the clones responded to induction by Ang II, exhibiting membrane depolarization upon the application of

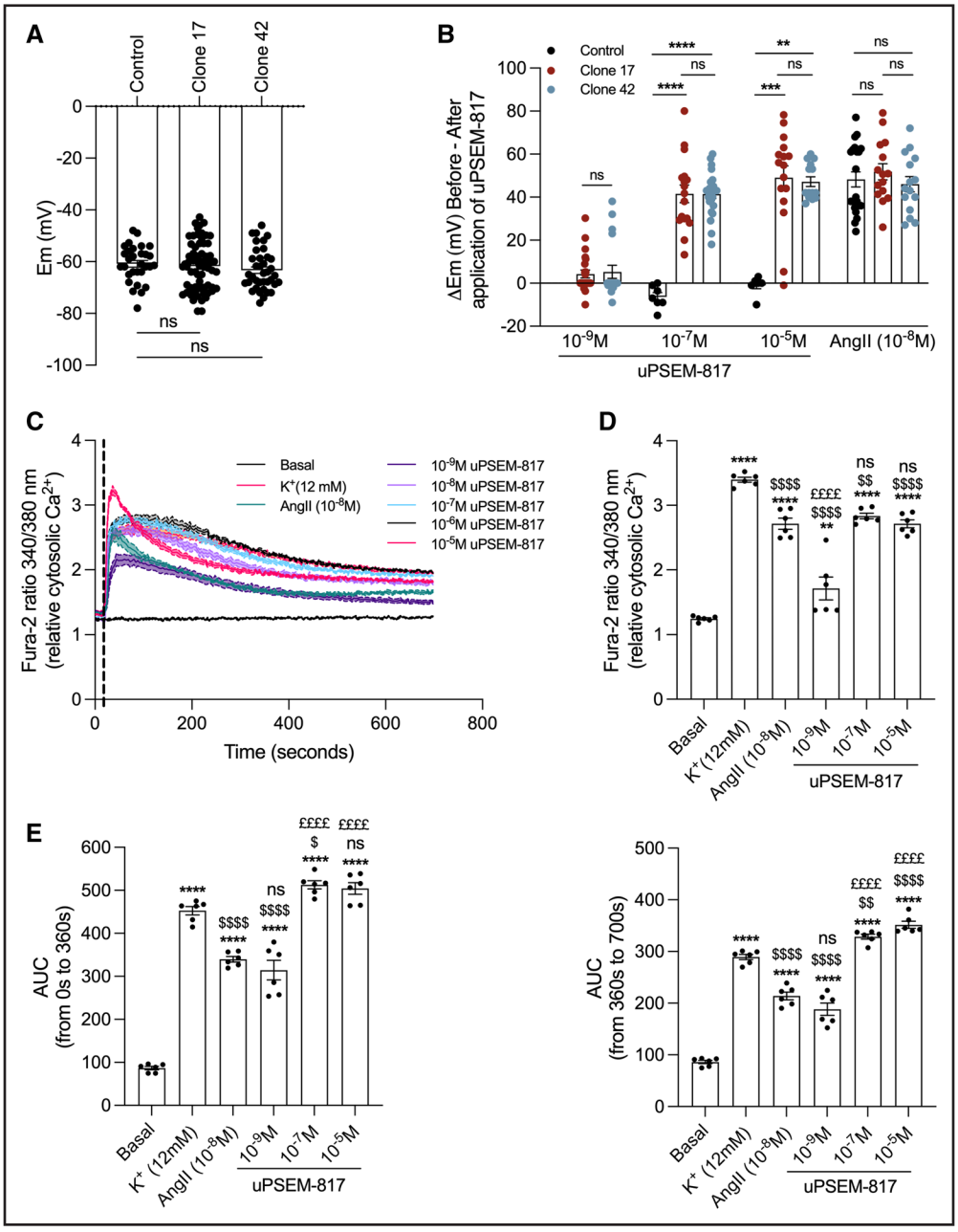

Figure 2. Functional characterization of α7-5HT3-R (α7-5HT3 receptor)–expressing cells.
A and **B**, Perforated patch-clamp experiments were performed on clones 17 and 42 to determine the membrane potential of cells in basal condition (n=15–21; **A**) or after stimulation with different concentrations of uPSEM-817 (uPharmacologically Selective Effector Molecule-817) (10^{-9}, 10^{-7}, and 10^{-5} mol/L) and Ang II (angiotensin II; 10^{-8} mol/L; n=7–23; **B**). **C**, Ca^{2+} entry into the cells was evaluated using Fura-2 AM (Fura-2-acetoxymethyl ester) assay for 700 s. Representative traces of intracellular Ca^{2+} responses to 10^{-8} mol/L Ang II, 12 mmol/L K^+, and 10^{-9} to 10^{-5} mol/L uPSEM-817 (clone 17); n=6. **D**, Determination of the maximum Fura-2 (ratiometric fluorescent dye which bind to free intracellular Ca^{2+}) ratio 340/380 nm in response to 10^{-8} mol/L Ang II, 12 mmol/L K^+, and 10^{-9}, 10^{-7}, and 10^{-5} mol/L uPSEM-817 (clone 17); n=6. **E**, Area under the curve (AUC) was determined to assess whether treatment with pharmacologically selective effector molecules (PSEMs) induced Ca^{2+} entry into the cells. The AUC was determined between 0 and 360 s to determine the intracellular Ca^{2+} variation during the peak response (**left**) and between 360 and 700 s to determine the steady-state response (**right**; clone 17); n=6. *P* values were determined by *t* test or 1-way ANOVA followed by Bonferroni post hoc comparison tests; *basal vs K^+, Ang II, or PSEM; $$K^+$$ vs Ang II or PSEM; £Ang II vs PSEM; $$P<0.05$$, $$$P<0.01$$, $$$$P<0.0001$$. £££££$P<0.0001$. ns. Ang II vs 10^{-9} mol/L PSEM (**left** and **right**), K^+ vs 10^{-5} mol/L PSEM (**right**). **$P<0.01$, ****$P<0.0001$. The dotted line indicates the time of injection of uPSEM-817, Ang II, or K^+.

Downloaded from http://ahajournals.org by on November 13, 2025

10^{-8} mol/L Ang II (ΔEm, 48.26±3.52, 51.81±3.73, and 46.00±3.51 for control cells; clones 17 and 42, respectively; Figure 2B). However, only clones 17 and 42 were responsive to 10^{-7} mol/L (ΔEm, 41.58±4.12 and 41.49±2.13 for clones 17 and 42, respectively) and 10^{-5} mol/L of uPSEM-817 (ΔEm, 49.03±5.51 and 47.19±2.24 for clones 17 and 42, respectively). The lower concentration of 10^{-9} mol/L uPSEM-817 did not consistently induce membrane depolarization (Figure 2B).

Electrophysiological measurements were performed using high-throughput automated patch-clamp to determine whether activation of α7-5HT3-R by uPSEM-817 increased Na^+ current. Repetitive stimulations using a voltage ramp from −100 to +20 mV that was used to calculate the reversal potential (ERev; Figure S3A), a surrogate of the resting membrane voltage, confirmed that uPSEM-817 induced depolarization of clones 24 and 42 compared with vehicle-treated cells (Figure S3B). Inward currents were measured at −100 mV as they correspond to positive charges (eg, Na^+ ions) entering the cells. Treatment with 10^{-6} mol/L of uPSEM-817 under extracellular Na^+ concentrations of 80 or 132.5 mmol/L activated a statistically significant inward current in clone 42 and a similar trend in clone 24 (Figure S3C). These results are consistent with an increase of Na^+ permeability when cells were treated with uPSEM-817.

To determine whether the membrane depolarization triggered by uPSEM-817 correlated with an increase in intracellular Ca^{2+} concentration, α7-5HT3-R–expressing cells were exposed to concentrations of uPSEM-817 ranging from 10^{-9} to 10^{-5} mol/L, as well as 12 mmol/L K^+ and 10^{-8} mol/L Ang II as positive controls (Figure 2C through 2E). The results are presented for clone 17 (Figure 2C through 2E), and similar results were obtained for clone 42 (Figure S4). Application of Ang II or K^+ led to a rapid increase in intracellular Ca^{2+} levels followed by a rapid decline without returning to baseline levels (Figure 2C; Figure S4A), occurring after similar response latency (data not shown). The maximum of activation (Figure 2D; Figure S4B) was significantly increased when cells were treated with Ang II or K^+. The areas under the curve (AUCs) at the peak (between 0 and 360 s; Figure 2E, left; Figure S4C) and at the steady-state response (between 0 and 700 s; Figure 2E, right; Figure S4D) were also significantly increased after K^+ or Ang II treatment, these increases being more important when cells were treated with K^+. Treatment with uPSEM-817 ranging from 10^{-9} to 10^{-5} mol/L also resulted in a similar rapid increase in intracellular Ca^{2+} content; this increase was more modest at 10^{-9} mol/L uPSEM-817 compared with higher concentrations of the compound. Interestingly, the decline following the peak was slower with uPSEM-817 compared with Ang II or K^+ (Figure 2C; Figure S4A). Maximum activation (Figure 2D; Figure S4B) and AUC at the peak (Figure 2E, left; Figure S4C) and at steady state (Figure 2E, right; Figure S4D) were lower in response to 10^{-9} mol/L of uPSEM-817 than with 10^{-7} and 10^{-5} mol/L uPSEM-817. Despite variations in Ca^{2+} content, while the maximum activations were comparable when cells were treated with Ang II, K^+, and 10^{-7} and 10^{-5} mol/L uPSEM-817, the AUCs at the steady state were significantly higher when cells were treated with 10^{-7} and 10^{-5} mol/L uPSEM-817 compared with Ang II and K^+. The sustained higher Ca^{2+} content when cells were treated with uPSEM-817 suggests the activation of different mechanisms compared with Ang II and K^+.

α7-5HT3-R Activation by uPSEM-817 Activates Steroidogenesis

The steroidome of clones 17, 24, and 42 was determined using the cell supernatant after 8 hours (Figure S5A and S5B) or 24 hours (Figure S5C and S5D) of treatment with 10^{-8} mol/L Ang II or 12 mmol/L K^+ as a positive control (Figure S5A and S5C) and uPSEM-817 ranging from 10^{-9} to 10^{-5} mol/L (Figure S5B and S5D), and the results are presented separately for each clone (Figure S5). Interestingly, despite similar modification in intracellular Ca^{2+} concentration, different profiles were obtained for the 3 different clones in response to Ang II, K^+, and uPSEM-817. However, they all converge toward a stimulation of steroid biosynthesis in response to uPSEM-817. Among the 19 steroids measured, only 14 were detectable after 8 and 24 hours of treatment. After 8 hours of treatment, an overall activation of steroid biosynthesis was observed in response to Ang II and K^+ (Figure S5A; Table). Similarly, uPSEM-817 at concentrations from 10^{-7} to 10^{-5} mol/L led to an increase in steroid biosynthesis, with no significant changes observed at 10^{-9} and 10^{-8} mol/L of uPSEM-817 (Figure S5B; Table). Interestingly, the increases in certain steroids due to uPSEM-817 were less pronounced compared with those induced by Ang II and K^+. After 24 hours of treatment, a significant decrease in the concentration of 2 steroid precursors, pregnenolone and progesterone, was observed in response to Ang II and K^+, while deoxycorticosterone, 17-hydroxyprogesterone, 17-hydroxypregnenolone, pregnenolone, and progesterone concentrations remained elevated in response to uPSEM-817 (Table). Aldosterone biosynthesis was highly stimulated by Ang II and K^+ and to a lesser extent by uPSEM-817. While no effect was observed after 8 hours of treatment, after 24 hours, the concentration of 18-oxocortisol was significantly increased in response to K^+, and a trend was also observed in response to Ang II and for all the concentrations of uPSEM-817. The concentrations of 18-hydroxycortisol were undetectable in all tested conditions.

Downloaded from http://ahajournals.org by on November 13, 2025

Table. Steroid Profiles in H295R-S2 Cells Expressing α7-5HT3-R in Response to Ang II (10^{-8} mol/L), K^+ (12 mmol/L), and uPSEM-817 (10^{-9} to 10^{-5} mol/L)

Characteristics	Time	Ang II (10^{-8} mol/L)	K^+ (12 mmol/L)	PSEM (10^{-9} mol/L)	PSEM (10^{-8} mol/L)	PSEM (10^{-7} mol/L)	PSEM (10^{-6} mol/L)	PSEM (10^{-5} mol/L)
Pregnenolone	8 h	2.622±0.176*	2.458±0.203*	1.071±0.025	1.035±0.024	1.269±0.031*	1.254±0.037†	1.489±0.066*
	24 h	0.441±0.023*	0.813±0.038	1.031±0.036	1.045±0.041	1.485±0.206	1.419±0.157‡	1.643±0.065†
Progesterone	8 h	4.005±0.366*	3.112±0.296§	1.167±0.020	1.150±0.016	1.422±0.065†	1.453±0.065*	1.652±0.077*
	24 h	0.330±0.022*	0.533±0.036*	1.058±0.058	1.002±0.056	1.165±0.045	1.115±0.052	1.196±0.048‡
11-deoxycorticosterone	8 h	4.100±0.478†	3.811±0.350§	1.025±0.046	0.981±0.060	1.272±0.049‡	1.241±0.039‡	1.378±0.060§
	24 h	0.409±0.044*	0.828±0.051	1.055±0.040	1.012±0.024	1.219±0.041§	1.197±0.056§	1.349±0.048*
18-hydroxy 11-deoxycorticosterone	8 h	2.761±0.205†	2.585±0.238§	1.122±0.019	1.114±0.023	1.260±0.055†	1.353±0.064*	1.455±0,038*
	24 h	2.467±0.193*	2.235±0.198*	0.982±0.038	0.973±0.034	1.234±0.041‡	1.271±0.081	1.404±0,101§
Corticosterone	8 h	2.515±0.179*	2.424±0.245*	1.108±0.035	1.148±0.036	1.294±0.074	1.090±0.187	1.021±0.188
	24 h	2.329±0.268*	1.983±0.183§	0.984±0.051	1.002±0.055	1.169±0.033‡	1.174±0.032§	1.302±0.026*
18-hydroxycortisol	8 h	0.794±0.090	0.921±0.112	0.944±0.057	0.754±0.126	0.910±0.053	0.894±0.037	1314±0.249
	24 h	2.200±0.575	8.049±2.958§	2.203±0.557	2.241±0.595	3.047±1.206	2.126±0.691	2.086±0.622
18-oxocortisol	8 h	1.046±0.094	1.131±0.126	0.937±0.043	0.798±0.075	0.929±0.028	1.068±0.102	1.633±0.355
	24 h	2.200±0.575	8.049±2.958§	2.203±0.557	2.241±0.595	3.047±1.206	2.126±0.691	2.086±0.622
18-hydroxycorticosterone	8 h	1.927±0.172†	2.088±0.156*	1.125±0.033	1.125±0.052	1.231±0.051‡	1.003±0.108	0.835±0.063
	24 h	3.496±0.400*	2.456±0.341§	0.989±0.074	1.004±0.094	1.177±0.157	0.891±0.102	0.818±0.085
Aldosterone	8 h	2.454±0.238§	2.580±0.273†	0.914±0.040	0.927±0,038	1.024±0.054	1.187±0.063	1.388±0.062
	24 h	12.13±4.007*	6.046±1.657§	0.946±0.043	1.035±0.082	1.495±0.211	1.459±0.138§	1.436±0.135§
17-hydroxyprogesterone	8 h	2.761±0.351*	2.535±0.242†	1.187±0.027‡	1.141±0.035	1.334±0.059*	1.325±0.051*	1.589±0.041*
	24 h	0.243±0.009*	0.896±0.034§	1.052±0.038	0.975±0.041	1.068±0.034	1.049±0.032	1.230±0.030§
11-deoxycortisol	8 h	1.586±0.147†	1.706±0.105†	1.026±0.033	0.995±0.056	1.087±0.038	1.064±0.035	1.079±0.039
	24 h	1.065±0.046	0.626±0.064*	1.016±0.025	0.985±0.030	1.096±0.041	1.073±0.052	1.060±0.046
Cortisol	8 h	1.093±0.061	1.066±0.056	1.119±0.082	1.157±0.058	1.126±0.081	1.051±0.057	1.003±0.055
	24 h	2.541±0.310*	1.923±0.251§	0.974±0.033	1.034±0.041	1.161±0.080	1.194±0.095	1.199±0.076
21-deoxycortisol	8 h	1.546±0.135‡	1.443±0.139	1.046±0.074	1.059±0.146	0.968±0.143	0.926±0.163	1.863±0.548
	24 h	0.852±0.121	1.954±0.115*	1.151±0.120	1.107±0.098	1.345±0.162	1.195±0.073	0.941±0.122
Delta-4-androstenedione	8 h	1.450±0.123‡	1.541±0.131§	1.001±0.033	0.978±0.085	1.113±0.039	1.069±0.034	1.246±0.038§
	24 h	0.482±0.046*	1.146±0.055	1.049±0.032	1.003±0.027	1.098±0.047	0.985±0.039	1.104±0.041

Results are expressed as fold induction over untreated cells expressing α7-5HT3-R (set as 1, not shown) and represent mean±SEM of the 3 clones, compared with ANOVA followed by Bonferroni when data presented for gaussian distribution and Kruskal-Wallis followed by Dunn test for non-gaussian distribution. Cells treated with Ang II and K^+ and cells treated with uPSEM-817 (PSEM) were analyzed separately. n=9 per condition except for 18-oxocortisol (n=6) and 18-hydroxycortisol (n=6). α7-5HT3-R indicates α7-5HT3 receptor; Ang II, angiotensin II; H295R-S2, human adrenocortical carcinoma cell line, strain 2; PSEM, pharmacologically selective effector molecule; and uPSEM-817, uPharmacologically Selective Effector Molecule-817.

*P≤0.0001, †P≤0.001, ‡P≤0.05, §P≤0.01.

T- and L-Type Channels Are Both Involved in Ca^{2+} Entry Into the Cells in Response to uPSEM-817

Both T- and L-type voltage-gated Ca^{2+} channels have been shown to be involved in aldosterone biosynthesis regulation by modulating intracellular Ca^{2+} concentrations.[25,26] We evaluated the effect of a 2-hour pretreatment with 10^{-6} mol/L of the L-type Ca^{2+} channel blocker nifedipine or 10^{-6} mol/L of the T-type Ca^{2+} channel blocker mibefradil on the modulation of intracellular Ca^{2+} content in response to 10^{-8} mol/L Ang II, 12 mmol/L K^+, and increasing concentrations of uPSEM-817 (Figure 3A through 3C). Interestingly, pretreatment of the cells with nifedipine or mibefradil partially abolished Ca^{2+} entry into the cells after treatment with K^+ and uPSEM-817, as revealed by lower peak (Figure 3A and 3B) and decreased AUC (representing the modifications of intracellular Ca^{2+} concentrations, illustrating activation of Ca^{2+} signaling; Figure 3C). In contrast, nifedipine and mibefradil had no effect on the initial entry of Ca^{2+} into the cell in response to Ang II (Figure 3B), and only nifedipine pretreatment led to a significant decrease in the AUC (Figure 3A through 3C). These results indicate that both T- and L-type Ca^{2+} channels are mobilized to allow Ca^{2+} entry into the cells in response to K^+ and uPSEM-817, a mobilization that appears to be greater than in response to Ang II.

To determine whether the differences observed in the modulation of intracellular Ca^{2+} concentration in response

Downloaded from http://ahajournals.org by on November 13, 2025

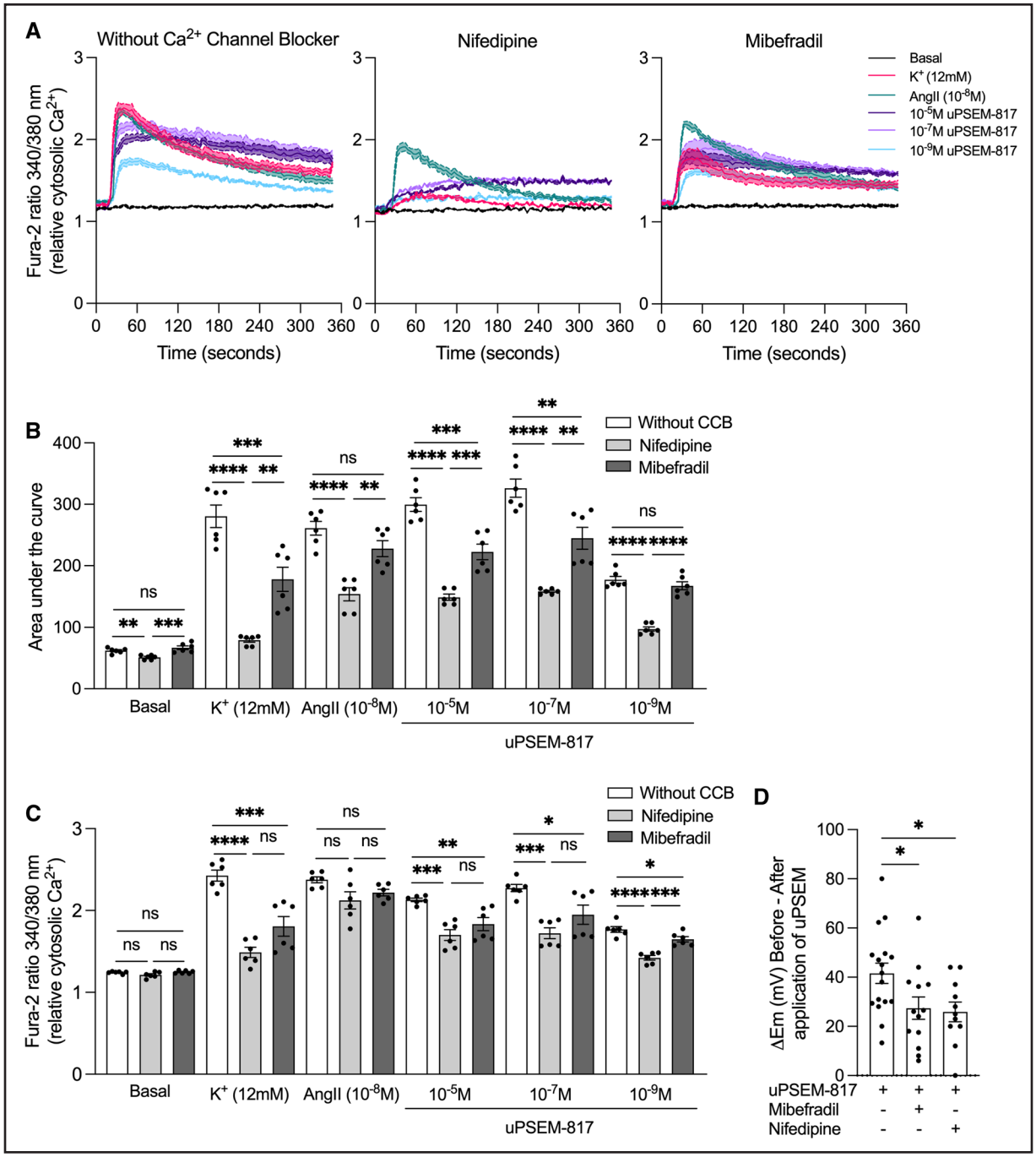

Figure 3. Inhibition of Ca2+ entry using nifedipine or mibefradil.
A, Representative traces of intracellular Ca^{2+} responses to 10^{-8} mol/L Ang II (angiotensin II), 12 mmol/L K^+, and 10^{-9}, 10^{-7}, and 10^{-5} mol/L uPSEM-817 (uPharmacologically Selective Effector Molecule-817) after pretreatment with nifedipine (**left**) or mibefradil (**right**; clone 17); n=6. **B**, Determination of the maximum Fura-2 (ratiometric fluorescent dye which bind to free intracellular Ca^{2+}) ratio 340/380 nm in response to uPSEM-817, Ang II, and K^+ after pretreatment with nifedipine (light grey) or mibefradil (dark grey) or without pretreatment (white; clone 17); n=6. **C**, Illustration of $[Ca^{2+}]_i$ signaling, illustrated by the determination of the area under the curve assessed for 360 s, in response to uPSEM-817, Ang II, and K^+ after pretreatment with nifedipine (light grey) or mibefradil (dark grey) or without pretreatment (white; clone 17); n=6. **D**, Patch-clamp recordings of cells treated with uPSEM-817 and nifedipine or mibefradil (clone 17). n=11 to 17; *P* values were determined by 1-way ANOVA followed by Bonferroni post hoc comparison tests;*$P<0.05$, **$P<0.01$, ***$P<0.001$, ****$P<0.0001$. CCB indicates Ca^{2+} channel blocker.

to Ca^{2+} channel blockers and uPSEM-817 cotreatment were due to differences in cell membrane depolarization, we performed patch-clamp analyses (Figure 3D). Before the administration of 10^{-7} mol/L uPSEM-817, we treated each patched cell with 10^{-6} mol/L mibefradil or with 10^{-6} mol/L nifedipine. These blockers were applied

Downloaded from http://ahajournals.org by on November 13, 2025

locally using an ejector solution. The results displayed a range of responses among cells: in certain instances, the blockers effectively suppressed depolarization, returning the membrane potential to a state near its baseline (ΔEM, ≈0); while in other cases, the membrane remained depolarized, albeit to a lesser degree than when exposed exclusively to 10^{-7} mol/L uPSEM-817 (Figure 3D).

α7-5HT3-R Activation by uPSEM-817 Led to a Decrease in Cell Proliferation and an Increase of Apoptosis

To evaluate the impact of elevated intracellular Ca^{2+} concentration on cell proliferation, cells were treated with 12 mmol/L K^+ or 10^{-9} to 10^{-5} mol/L uPSEM-817 for 24 and 72 hours. The number of viable proliferating cells was determined using a colorimetric method. Although following 24 hours of treatment, cell proliferation remained unaffected by K^+ or uPSEM-817 treatment, a decrease in cell proliferation was observed after 72 hours of treatment with the higher concentration of uPSEM-817 (Figure 4A).

To explore the impact on cell cycle progression of Ang II, K^+, and uPSEM-817 treatment, we assessed the cell cycle phase distribution using propidium iodide staining and cytometric analysis at 8, 24, 48, and 72 hours. Treatment with Ang II for 8 hours resulted in a reduction in the percentage of cells in the G1 phase and in an increase in the percentage of cells in G2 compared with untreated cells suggesting an increase in cell proliferation (Figure 4B). After 24 hours of Ang II treatment, an increase in the percentage of cells in the G1 phase and a decrease in the S phase was also observed. Longer exposure to Ang II had no effect on the distribution of cells across different phases of the cell cycle. In response to K^+ treatment, a similar pattern was observed with a decrease in the percentage of cells in G1 and an increase in G2 after 8 hours. While no alterations in cell distribution were noted after 24 hours of K^+ treatment, an increase in the percentage of cells in G1 and a decrease in the percentage of cells in G2 was observed (Figure 4B). Conversely, treatment with uPSEM-817 did not affect cell distribution among the different phases compared with untreated cells (Figure 4C). We assessed the effect of uPSEM-817 on apoptosis by determining the proportion of cells in the sub-G1 phase. The sub-G1 phase reflects DNA fragmentation, which occurs in the late stage of apoptosis. Similar to what was observed for cell proliferation results, no effect was observed when cells were treated with uPSEM-817, Ang II, and K^+ for 24 hours (Figure 4D, left). At 72 hours, a significant increase in the percentage of cells in the sub-G1 phase was observed in response to K^+, Ang II, and uPSEM-817 (10^{-7} mol/L; Figure 4D, right), indicating an increase in cell apoptosis.

α7-5HT3-R Activation by uPSEM-817 Results in the Activation of Specific Pathways

To gain insight into the impact of modulating intracellular Na^+ concentration in cells expressing α7-5HT3-R, we conducted RNA-sequencing analysis on these cells (clones 17, 24, and 42) following treatment with 10^{-7} mol/L uPSEM-817 for 8 hours (Figures S6 and S7) and 24 hours (Figure 5; Figure S8). Hierarchical clustering effectively segregated cells treated for 8 and 24 hours from untreated cells (Figures S6A, S7A, and S8A; Figure 5A). After 8 hours of treatment, we identified 28 differentially expressed genes with a fold change of at least 0.5; 18 upregulated genes (64.29%) and 10 downregulated genes (35.71%; Table S2). Gene ontology analyses unveiled 18 specific enriched biological processes in uPSEM-817–treated cells (Figure S6B; Table S3), primarily related to Ca^{2+} ion transport and signaling pathways, cell adhesion, and aldosterone synthesis and secretion. Following 24 hours of treatment, 30 genes were differentially expressed with a fold change of at least 0.5, with 22 (73.33%) genes upregulated and 8 (26.67%) genes downregulated (Figure 5B; Table S4).[27,28] Enriched pathways included protein regulation of GTPase activity, Ras (Rat sarcoma virus) protein signal transduction, and aldosterone synthesis and regulation (Figure 5B; Table S5). These analyses were completed by using the gene set enrichment analysis and Hallmark database that provides information on the most universal cellular mechanisms (Figures S7 and S8). Using a false discovery rate <25%, we identified 6 differentially regulated pathways after 8 hours of treatment with pharmacologically selective effector molecules and 7 after 24 hours. After 8 hours of treatment, TNFα (tumor necrosis factor-α) signaling via NF-κB (nuclear factor-κB) and coagulation pathway were found enriched in basal condition (Figure S7B), whereas Kras (v-Ki-ras2 Kirstenb rat sarcoma viral oncogene homolog) signaling, heme metabolism, UV response, and interferon-α response were found to be enriched in response to uPSEM-817 (Figure S7C). After 24 hours of treatment (Figure S8), only TNFα signaling via the NF-κB pathway (Figure S8B) was enriched in basal condition, and Myc proto-oncogene targets, oxidative phosphorylation, DNA repair apical surface, unfolded protein response, and G2/M checkpoint pathways were enriched after uPSEM-817 treatment (Figure S8C).

To identify genes and pathways specifically regulated by modulation of intracellular Na^+ concentration, we also performed RNA sequencing on α7-5HT3-R–expressing cells treated with 12 mmol/L K^+ and 10^{-8} mol/L Ang II for 8 and 24 hours (Figures S6 and S9; Figure 5). After 8 hours of treatment, 4932 genes were differentially expressed in response to Ang II and 728 in response to K^+ (Figure S6C and S6G; Tables S6 and S7). Gene ontology analyses[27,28] for 8 hours of Ang II treatment revealed

Downloaded from http://ahajournals.org by on November 13, 2025

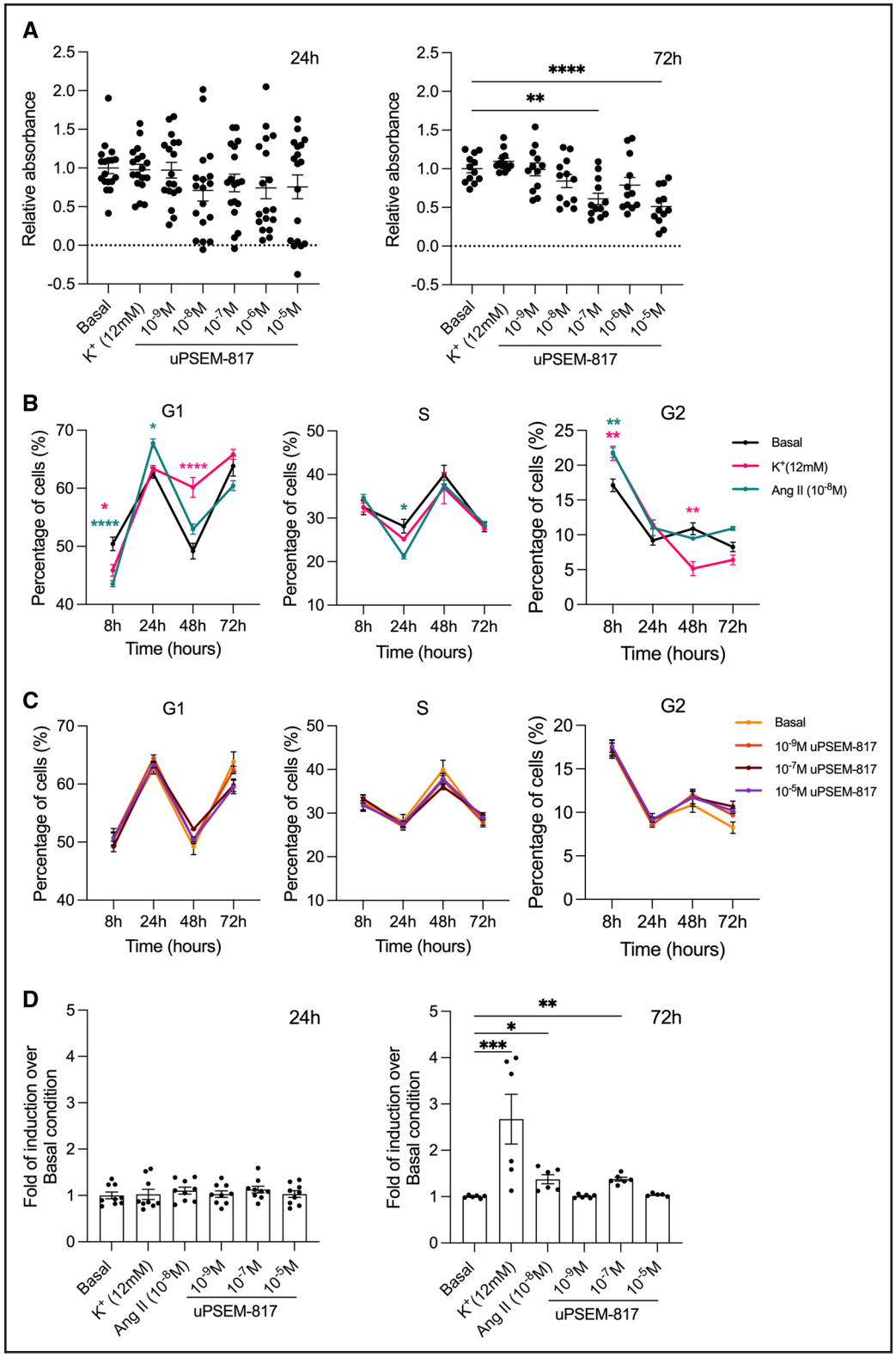

Figure 4. Effect of uPSEM-817 on cell proliferation and apoptosis.
A, Cell viability was measured on cells treated for 24 or 72 hours with 12 mmol/L K^+ or uPSEM-817 (uPharmacologically Selective Effector Molecule-817) by MTS (3-(4,5-Dimethylthiazol-2-yl)-5-(3-carboxymethoxyphenyl)-2-(4-sulfophenyl)-2 H-tetrazolium) assay (clone 17). **B**, Cell cycle distribution measured by FACS (Fluorescence-Activated Cell Sorting) using propidium iodide in response to 10^{-8} mol/L Ang II (angiotensin II) and 12 mmol/L K^+ (**top**), and 10^{-9}, 10^{-7}, and 10^{-5} mol/L uPSEM-817 (**bottom**; clone 17). **C**, Apoptosis determined by the proportion of cells in the sub-G1 phase (clone 17). **D**, Proportion of cells in the sub-G1 phase after 24 hours (**left**) or 72 hours (**right**) in response to 12 mmol/L K^+, 10^{-8} mol/L Ang II, and 10^{-9}, 10^{-7}, and 10^{-5} mol/L uPSEM-817. n=6 (cell cycle), n=12 (proliferation); *P* values were determined by 1-way ANOVA followed by Bonferroni post hoc comparison tests,*$P<0.05$, **$P<0.01$, ***$P<0.001$, ****$P<0.0001$.

Downloaded from http://ahajournals.org by on November 13, 2025

ORIGINAL ARTICLE

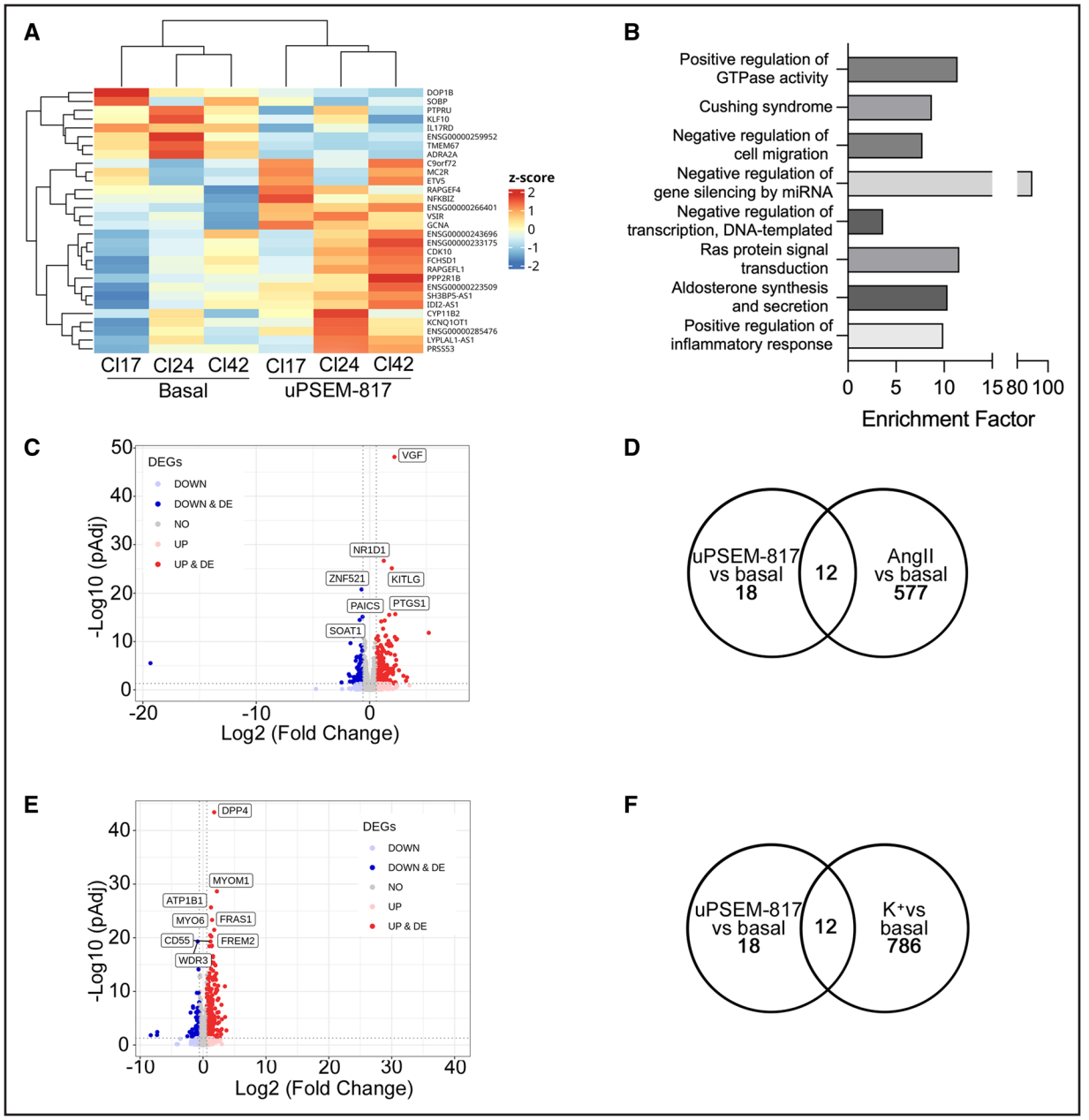

Figure 5. Gene expression profiles of H295R-S2 (Human adrenocortical carcinoma cell line, Strain 2) α7-5HT3-R (α7-5HT3 receptor) cells treated 24 hours with 10^{-7} mol/L uPSEM-817 (uPharmacologically Selective Effector Molecule-817), 10^{-8} mol/L Ang II (angiotensin II), or 12 mmol/L K^+.

A, Hierarchical clustering of samples using the 28 differentially expressed genes (DEGs) in cells treated or not with 10^{-7} mol/L uPSEM-817. **B**, Biological process enrichments determined using the list of DEGs in cells treated or not with 10^{-7} mol/L uPSEM-817. **C**, Volcano plot showing the 4932 DEGs in response to 10^{-8} mol/L Ang II. DEGs are highlighted as blue (downregulated) or red (upregulated) dots. **D**, Venn diagram representing the common and different genes differentially expressed in response to 10^{-8} mol/L Ang II and 10^{-7} mol/L uPSEM-817. **E**, Volcano plot showing the 728 DEGs in response to 12 mmol/L K^+. The *x* axis is the log2-fold change between the 2 conditions; the adjusted *P* value based on $-\log_{10}$ is reported on the *y* axis. Genes significantly different are highlighted as blue (downregulated in cells treated with 12 mmol/L K^+) or red (upregulated in cells treated with 12 mmol/L K^+) dots. **F**, Venn diagram representing the common and different genes differentially expressed in response to 12 mmol/L K^+ and 10^{-7} mol/L uPSEM-817.

enrichment in 390 different pathways (Table S8), with significant involvement in the regulation of reticulum activity, negative regulation of cell growth, and aldosterone, cortisol, and parathyroid hormone synthesis and secretion (Figure S6D). Eight hours of treatment with K^+ resulted in enrichment of 211 pathways (Table S9), including membrane depolarization during action potential, Ca^{2+} and Na^+ ion transport, and circadian rhythm (Figure S6H). Interestingly, both Ang II and K^+ treatment led to enrichment in positive regulation of transcription and MAPK (Mitogen-Activated Protein Kinase) signaling pathways. Among the 28 differentially expressed genes

Downloaded from http://ahajournals.org by on November 13, 2025

in response to uPSEM-817, 17 were common to Ang II (*OLFML2B*, *RGPD6*, *LMOD1*, *MAT1A*, *MC2R*, *CA2*, *CACNA1C*, *EGFR*, *ETV5*, *TNXB*, *PFKP*, *antisense to WASF3*, *antisense to ERVW-1* and *PEX1*, *PPP2R1B*, *LYPLAL1-AS1*, *LONRF2*, and *ST6GALNAC6*; Figure S6E) and 12 to K^+ (*OLFML2B*, *LMOD1*, *MAT1A*, *MC2R*, *CA2*, *CACNA1C*, *ATP8B4*, *ETV5 PFKP*, *PPP2R1B*, *LYPLAL1-AS1*, and *LONRF2*; Figure S6I). Among the 18 enriched pathways in response to uPSEM-817, 9 were commonly enriched in response to Ang II (Figure S6F) and 5 in response to K^+ (Figure S6J). Most importantly, 11 genes were specifically regulated by uPSEM-817 when compared with Ang II (*HPX*, *EPHA10*, *ATP8B4*, *HHIP*, *MICAL1*, *RBMS2*, *E9PAM4*, *H7C2Y5*, *TP53TG3B*, *DUXAP8*, and *RNVU1-7*) and 16 when compared with K^+ (*HPX*, *antisense to WASF3*, *EPHA10*, *HHIP*, *ST6GALNAC6*, antisense to *ERVW-1* and *PEX1*, *EGFR*, *MICAL1*, *TNXB*, *RGPD6*, *RBMS2*, *E9PAM4*, *H7C2Y5*, *TP53TG3B*, *DUXAP8*, and *RNVU1-7*). This allowed us to define a specific Na^+-induced signature composed of 10 genes (*HPX*, *EPHA10*, *HHIP*, *MICAL1*, *RBMS2*, *E9PAM4*, *H7C2Y5*, *TP53TG3B, DUXAP8*, and *RNVU1-7*; Figure S10).

After 24 hours of treatment, 589 genes were statistically differentially expressed in response to Ang II (Figure 5C and 5D; Table S10). Among them, 12 were common to uPSEM-817 (*SOBP*, *ADRA2A*, *ETV5*, *antisense to DLGAP1*, *VSIR*, *GCNA*, *FCHSD1*, *RAPGEFL1*, *PPP2R1B*, *CYP11B2*, *LYPLAL1-AS1*, and *PRSS53*); 146 pathways were specifically enriched in response to Ang II and 2 (Cushing syndrome and aldosterone synthesis and secretion) were commonly enriched in response to Ang II and uPSEM-817 (Figure S9B; Table S11). Interestingly, enriched pathways included those associated with cell adhesion and extracellular matrix organization (Figure S9A). K^+ treatment for 24 hours led to the regulation of 798 genes (Figure S7A; Figure 5F; Table S12); among them, 12 were common to uPSEM-817 (*KLF10*, *ADRA2A*, *C9ORF72*, *MC2R*, *ETV5*, *RAPGEF4*, *VSIR*, *GCNA*, *FCHSD1*, *PPP2R1B*, *CYP11B2*, and *LYPLAL1-AS1*). Similarly, enriched pathways included those associated with cell adhesion and extracellular matrix organization (Figure S9C; Table S13). Five of the 8 enriched pathways identified in response to uPSEM-817 treatment were also commonly enriched in response to K^+ (Figure S9D). These common pathways involved positive regulation of GTPase activity, Cushing syndrome, negative regulation of cell migration, Ras protein signal transduction, and aldosterone synthesis and secretion. Notably, Cushing syndrome and aldosterone biosynthesis and secretion pathways were also commonly enriched between uPSEM-817 and Ang II. We were able to define a 24-hour sodium-specific signature composed by 14 genes (*FMNL1-AS1*, *IDI2-AS1*, *WHAMMP1*, *MUSTN1-ITIH4 readthrough*, *NFKBIZ*, *KCNQ1OT1*, *SH3BP5-AS1*, CDK10, *PTPRU*, *IL17RD*, *TMEM67*, *MAZ-AS*, *DOP1B*, and 1 unknown sequence; Figure S11).

The list of differentially expressed genes was compared with their expression in 11 control adrenals and 123 APAs retrieved from transcriptomic data[29] (Tables S14 and S15). Of these 123 APAs, 50 carried a mutation in the *KCNJ5* gene and 73 in another APA driver gene; the comparison was, therefore, made between the 11 control adrenals, the 50 APAs with a mutation in the *KCNJ5* gene, and the 73 APAs without a mutation in the *KCNJ5* gene. After 8 hours of treatment with 10^{-7} mol/L of uPSEM-817, among the 55 identified genes that were significantly differentially expressed without consideration of the fold change, the expression of 49 genes was found in our transcriptomic data from control adrenals and APAs and could be retrieved. In these data, no expression was detected for 5 genes, and of the remaining 44 genes, 13 were also found to be differentially expressed in APAs compared with control adrenals (Table S12), 2 only in APAs with a *KCNJ5* mutation (*HPX* and *WHRN*) and 3 in APAs without *KCNJ5* mutation (*ETV5*, *GPAM*, and *OLFML2B*). Interestingly, among the 13 genes differentially expressed in APAs independently of the mutational status, 4 were found to be upregulated (*CACNA1C*, *ATP2B2*, *VDR*, and *EPHA10*) and 1 downregulated (*RGPD6*) in both APAs and α7-5HT3-R cells, whereas 6 genes were found to be upregulated in α7-5HT3-R cells but downregulated in APAs (*PPP2R1B*, *LONRF2*, *ATP8B4*, *TNXB*, *ITGA7*, and *HSPA12A*), independently of the mutational status and 2 downregulated in response to uPSEM-817 but upregulated in all APAs (*TMEM200A* and *ELL2*). Similarly, after 24 hours of treatment, among the 73 genes identified, genes that were significantly differentially expressed regardless of the fold change, the expression of 64 genes could be retrieved from our transcriptomic data. No expression was found for 10 genes, and among the remaining 54 genes, 15 were also found to be differentially expressed in APAs compared with control adrenals (Table S13). Among these 15 genes, 3 were found to be commonly upregulated in both α7-5HT3-R cells and APAs (*FCHSD1*, *CACNA1C*, and *TTN1*) and 1 downregulated (*KLF10*) whereas 2 were found to be upregulated in α7-5HT3-R cells and downregulated in APAs, independently of the mutational status (*PPP2R1B* and *NEAT1*), and 4 downregulated in α7-5HT3-R cells and upregulated in all APAs (*STMN3*, *FIBCD1*, *FSCN1*, and *CCDC71L*). Interestingly, 3 genes were found to be significantly regulated only in APAs without KCNJ5 mutations, 2 downregulated in α7-5HT3-R cells but upregulated in APAs (*ETV5* and *CEP170*), and 1 downregulated in both (*NR2F2*); 2 genes were found to be significantly regulated only in APAs with KCNJ5 mutations, 1 downregulated in α7-5HT3-R cells but upregulated in APAs (*NFKBI2*), and 1 downregulated in both (*ABHD2*). Interestingly, none of the genes commonly regulated in α7-5HT3-R cells and APAs belongs to the Na^+ signature defined after 8 and 24 hours of treatment,

Downloaded from http://ahajournals.org by on November 13, 2025

suggesting that they are probably involved in the early phase of APA development.

DISCUSSION

Somatic *KCNJ5* mutations are the most frequent genetic abnormalities found in APAs with a prevalence between 43% and 75% of cases. APAs with *KCNJ5* mutations are more frequent in women and at younger age[29,30] and are characterized by hybrid steroid production and larger adenoma size.[31] Expression of mutated *KCNJ5* in adrenocortical cells leads to increased aldosterone production without increasing cell proliferation,[17,19] raising the question as to whether those mutations are sufficient to lead to both increased aldosterone production and adenoma formation. Here, we describe the development of an adrenocortical cell model that recapitulates the main features of *KCNJ5* mutations, by modulating on demand sodium entry into the cells using chemogenetic tools. Increased sodium entry through the chimeric α7-5HT3-R upon stimulation with uPSEM-817 led to cell membrane depolarization, opening of voltage-gated Ca^{2+} channels and increased intracellular Ca^{2+} concentrations, resulting in the stimulation of *CYP11B2* expression and increased aldosterone biosynthesis.

The steroid response of H295R-S2 α7-5HT3-R cells to Ang II is similar to that described in H295R cells,[32] with an early and transitory increase of pregnenolone, progesterone, and 11-deoxycorticosterone and a late and sustained production of aldosterone and corticosterone.[32] In contrast, sodium entry into the cells induced by uPSEM-817 led to a specific steroid profile only partially overlapping with that induced by Ang II and K^+. In particular, we observed a prolonged induction of early steroid precursors and deoxycorticosterone, suggesting an action on both early and late steps of aldosterone biosynthesis, as well as a delayed and smaller induction of aldosterone biosynthesis; there was no induction of glucocorticoid biosynthesis in H295R-S2 α7-5HT3-R cells. An increase of 18-oxocortisol and 18-hydroxycortisol was also observed in response to uPSEM-817 in 2 of the 3 clones, suggesting production of hybrid steroids in response to increased intracellular Na^+ concentration. This is consistent with results reported for the overexpression of KCNJ5 harboring the p.Tyr158Ala mutation in HAC15 (Human Adrenocortical Carcinoma cell line) cells resulting in a significant increase of both 18-hydroxycortisol and 18-oxocortisol.[18,33] However, despite similar depolarization of the cells in response to uPSEM-817 or Ang II, our data suggest a delayed activation of mineralocorticoid biosynthesis in response to the modulation of intracellular Na^+ concentration compared with Ang II and K^+ that could be due to the activation of specific signaling pathways. This hypothesis is supported by our finding of a specific gene expression signature associated with Na^+ influx into the cells.

Interestingly, gene expression analysis revealed expression of *KCNJ5* in H295R-S2 α7-5HT3-R cells (Figure S12A), which remains unchanged after uPSEM-817 treatment. In this context, Na^+ may act as an activator for the KCNJ5 channel[34] by binding to the C-terminal part of the channel, near a region also sensitive to $PtdIns(4,5)P_2$, enhancing the sensitivity of the channels to $PtdIns(4,5)P_2$.[35] The interaction of $PtdIns(4,5)P_2$ with the C-terminal part of GIRK4 has been shown to regulate its opening by stabilizing the structure of the pore.[35] The resulting K^+ extrusion may attenuate the activation of Ca^{2+} signaling and explain the delayed increase in aldosterone biosynthesis observed in response to uPSEM-817.

If the role of *KCNJ5* mutations in inducing aldosterone biosynthesis has been clearly established, their role in promoting abnormal cell proliferation is still a matter of debate. In our model, we demonstrated that Na^+ entry into the cells lead to decreased cell proliferation and increased apoptosis. This is in accordance with previous studies showing that expression of *KCNJ5* mutants in adrenocortical cells resulted in decreased cell proliferation associated in some cases with increased apoptosis.[18,20] Choi et al[8] postulated that the activation of Ca^{2+} signaling induced by *KCNJ5* mutations is responsible for both increased aldosterone biosynthesis and cell proliferation, and indeed some studies also reported an association between *KCNJ5* mutations and larger adenoma size[29,30] and a positive correlation between the expression of Ki67, a marker of cell proliferation, and the diameter of APA harboring *KCNJ5* mutations.[20] Specific factors overexpressed in APA harboring *KCNJ5* mutations[36,37] have been suggested to possibly counteract the pro-apoptotic effect of these mutations,[20] suggesting the existence of compensatory mechanisms maintaining cell proliferation over long term. In particular, expression of *TDGF1* and *VSNL1*, 2 genes with anti-apoptotic properties, was found to be upregulated in *KCNJ5* mutated APAs.[38,39] However, in our cell model, the expression of *VSNL1* was not modified (Figure S12B) and *TDGF1* was not expressed at all. The increased expression of these genes may be a later event secondary to the development of an APA to compensate for Na^+-induced cell death. Moreover, signaling pathway analyses revealed downregulation of genes involved in the G2/M checkpoint pathway and in the progression through the cell division cycle, probably contributing to the decrease of cell proliferation observed in our model. Alternatively, our data suggest that other mechanisms may be responsible for abnormal cell proliferation, leading to the development of APA. These include the presence of 2 hits, 1 responsible for cell proliferation and the other for autonomous aldosterone production. Recently, we and others identified risk alleles associated to PA in genome-wide association studies. Within the identified genetic loci, some genes appear to modulate adrenal cortex homeostasis and may

Downloaded from http://ahajournals.org by on November 13, 2025

affect cell proliferation, eventually generating a propitious environment leading to the occurrence of somatic mutations.[40,41] The 2 models are not mutually exclusive and may be linked together by mechanisms that remain to be identified. Finally, in FH-III (Familial Hyperaldosteronism type III) it cannot be ruled out that Na^+ entry induced by *KCNJ5* mutations may have an impact on cell proliferation during adrenal development, which could explain the bilateral hyperplasia observed in severe cases.[8,19]

Ang II and potassium both stimulate aldosterone biosynthesis by activating Ca^{2+} signaling, but through different mechanisms, resulting in only a partial overlap in the genes they induce. Similarly, uPSEM-817, by increasing intracellular Na^+ levels, induces membrane depolarization, which like potassium, leads to opening of voltage-gated Ca^{2+} channels and increase of intracellular Ca^{2+} concentration. However, uPSEM-817 also has unique effects, which account for the partial overlap in the differentially expressed genes induced by these 3 compounds. Gene expression profiles allowed us to identify a sodium-induced gene signature composed of 10 genes after 8 hours of treatment with uPSEM-817 (Figure S9) and 14 genes after 24 hours of treatment (Figure S10). Interestingly, among these lists of genes, some are involved in cell cycle regulation, proliferation, and apoptosis. Hence, the expression of *RBMS2* and *PTPRU*, 2 genes involved in the control of cell cycle progression[42] and cell proliferation,[43,44] respectively, was decreased after 8 or 24 hours while the expression of *CDK10* (Cyclin Dependent Kinase 10), a Cdc2 (Cell division control protein 2)-related kinase involved in the regulation of the G2/M phase of the cell cycle, was increased. However, the role of CDK10 in regulating cell proliferation is not clear, as some studies suggest a role of CDK10 in cell proliferation activation,[45–47] while others report a tumor suppressor role for CDK10 through inhibition of cell proliferation.[48,49] The identification of these genes in the Na^+ signature supports our results showing an inhibitory effect of uPSEM-817 on cell proliferation. Among the genes belonging to the Na^+ signature after 8 hours of treatment with uPSEM-817, *HPX* expression was found to be upregulated. *HPX* encodes hemopexin, a protein with high binding affinity for heme. Interestingly, CYP11B2 and other cytochrome P450 enzymes use heme as a cofactor required for their activity. The availability of heme has been shown to affect aldosterone and corticosterone biosynthesis in rats.[50] Our transcriptomic data revealed a significant increase of *HPX* expression in APAs harboring a *KCNJ5* mutation,[29] and a recent study also reported increased expression of *HPX* associated with CpG hypomethylation[51] in APAs compared with the adjacent adrenal gland, suggesting a role of *HPX* in APA development potentially through the regulation of aldosterone biosynthesis. Similarly, the expression of *MC2R*, the melanocortin 2 receptor, was found to be increased in APAs associated with CpG hypomethylation.[51] Gene expression profiling of H295R-S2 α7-5HT3-R cells treated with Ang II, K^+, or uPSEM-817 also revealed a significant increase of *MC2R* expression; and a previous study reported higher expression of *MC2R* in APAs compared with control adrenals.[52] Finally, a recent work of our laboratory shows that expression of *MC2R* in APAs was more frequently found in regions expressing CYP11B2,[53] suggesting a potential role in regulating aldosterone biosynthesis. Moreover, the existence of a continuum of PA and dysregulated aldosterone production, prominently influenced by ACTH (adrenocorticotropic hormone), has recently been described.[54]

In conclusion, we demonstrate that H295R-S2 α7-5HT3-R cells are a new cell model in which intracellular Ca^{2+} concentration can be modulated on demand, reproducing the major features of cells harboring *KCNJ5* mutations. The stimulation of Na^+ entry into the cells leads to cell membrane depolarization, Ca^{2+} entry into the cells, activation of Ca^{2+} signaling, increased expression of *CYP11B2*, and stimulation of the mineralocorticoid biosynthesis pathway. This is associated with a decrease of cell proliferation and an increase of apoptosis, indicating that additional events may be required for the development of APA. RNA sequencing revealed that Na^+ entry into the cells is responsible for a specific transcriptomic signature that may explain some of the features of APA carrying *KCNJ5* mutations. This cellular model thus provides important new insight into the mechanisms leading to PA development, uncovering new mechanisms involved in the disease, thereby paving the way for new therapeutic approaches in PA.

The strengths of our study are multiple. First, the model provides a novel and highly valuable tool for studying the early events that occur following a mutational event leading to Na^+ entry into the cells, such as mutations affecting *KCNJ5*[8] but also mutations affecting *SLC30A1*,[15] *ATP1A1*,[9,16] and *MCOLN3*.[55] Second, the cell model allows following dynamic changes in cell proliferation and function and to explore molecular mechanisms and specific transcriptional changes induced by mutations in PA. Importantly, these events cannot be studied in human tissues from patients with APAs, as they only provide a snapshot at a given moment of the development of the disease. Indeed, we were able to show that while modification of steroid biosynthesis occurs rapidly, alterations in the cellular sodium balance result in reduced cell proliferation and increased apoptosis, in accordance with data from the literature.[18] However, we cannot exclude the possibility that, at a later stage of development of APA, the constitutive activation of Ca^{2+} signaling might stimulate cell proliferation. Another significant finding of our study was the identification of specific pathways and signatures associated with the modification of the Na^+ influx. While some pathways, such as aldosterone biosynthesis and secretion, calcium signaling, and cell proliferation, were further explored, others remain to be

Downloaded from http://ahajournals.org by on November 13, 2025

investigated and will be the scope of future research. Moreover, this innovative cellular model offers a valuable tool for evaluating the molecular effects of novel therapeutic strategies for PA, particularly the application of novel aldosterone synthase inhibitors.

Limitations of our study are related to possible biases in interpreting proliferation studies in our model. Indeed, these cells are generated from H295R-S2 cells, which derive from an adrenocortical adenoma carrying TP53 (Tumor protein P53) and β-catenin mutations. Because β-catenin signaling is known to promote cell proliferation in various tumors, this model may be suboptimal for investigating positive effects on proliferation. Nevertheless, we have demonstrated that the activation of Ca^{2+} signaling, through modulation of Na^{+} entry into the cells, is achievable within this context. Therefore, the presence of β-catenin mutations does not pose an obstacle to these specific investigations. An additional limitation may be the lack of the microenvironment of steroidogenic cells; further studies in integrated mouse models will be necessary to establish the natural history of PA development.

PERSPECTIVES

Using a chemogenetic approach allowing the modulation of sodium influx on demand, we have generated a new cell model that replicates the main characteristics of *KCNJ5*-mutated APAs and provides new insights into the mechanisms responsible for their development. Our results show that modulation of intracellular ionic balance leads to cell membrane depolarization, activation of Ca^{2+} signaling, and enhanced steroid biosynthesis, associated with a decrease in cell viability and an increase in apoptosis, indicating that additional events may be required for the development of an APA with a *KCNJ5* mutation.

This innovative model could be used to test the molecular impact of new treatments for PA in vitro. Additionally, applying this chemogenetic approach could also enable the development of a new inducible mouse model of PA, providing a valuable tool for dissecting the mechanisms underlying APA development and for evaluating new therapeutic strategies.

ARTICLE INFORMATION

Received May 06, 2024; accepted January 27, 2025.

Affiliations

Université Paris Cité, INSERM, PARCC (Paris Cardiovascular Research Center), France (B.F., T.C., Z.R.A.S., I.G.-D., N.F., M.F., J.-S.H., S.T.-A., F.L.F.-R., M.-C.Z., S. Boulkroun). Electrophysiology Facility, University of Zurich, Switzerland (R.A.C., D.P.). CIC1418 and DMU CARTE (J.-S.H.), Service de Physiologie (S.T.-A., S. Baron), and Service de Génétique (M.-C.Z.), Assistance Publique Hôpitaux de Paris, Hôpital Européen Georges Pompidou, France. Department of Neurosciences, Howard Hughes Medical Institute, University of California San Diego (C.J.M., S.M.S.).

Sources of Funding

This work was funded through institutional support from INSERM (Institut National de la Santé et de la Recherche Médicale), by Agence Nationale pour la Recherche (ANR-18-CE93-0003-01), Fondation pour la Recherche Médicale (EQU201903007864), the European Union Horizon 2020 research and innovation program under the Marie Sklodowska-Curie grant agreement number 954798 (MINDSHIFT Innovative Training Network), for which M.-C. Zennaro is the principal investigator, and by a grant from the Leducq Foundation (18CVD05) for J.-S. Hulot. Research in the laboratory of D. Penton was financed by the Swiss National Foundation for Science (CRSII-222773) and by the University Research Priority Program (URPP) of the University of Zurich ITINERARE-Innovative Therapies in Rare Diseases.

Disclosures

None.

Supplemental Material

Supplemental Materials and Methods
Tables S1–S15
Figures S1–S13

REFERENCES

1. Spat A, Hunyady L. Control of aldosterone secretion: a model for convergence in cellular signaling pathways. *Physiol Rev*. 2004;84:489–539. doi: 10.1152/physrev.00030.2003
2. Fernandes-Rosa FL, Boulkroun S, Zennaro M-C. Genetic and genomic mechanisms of primary aldosteronism. *Trends Mol Med*. 2020;26:819–832. doi: 10.1016/j.molmed.2020.05.005
3. Hannemann A, Bidlingmaier M, Friedrich N, Manolopoulou J, Spyroglou A, Volzke H, Beuschlein F, Seissler J, Rettig R, Felix SB, et al. Screening for primary aldosteronism in hypertensive subjects: results from two German epidemiological studies. *Eur J Endocrinol*. 2012;167:7–15. doi: 10.1530/EJE-11-1013
4. Monticone S, Burrello J, Tizzani D, Bertello C, Viola A, Buffolo F, Gabetti L, Mengozzi G, Williams TA, Rabbia F, et al. Prevalence and clinical manifestations of primary aldosteronism encountered in primary care practice. *J Am Coll Cardiol*. 2017;69:1811–1820. doi: 10.1016/j.jacc.2017.01.052
5. Käyser SC, Dekkers T, Groenewoud HJ, van der Wilt GJ, Carel Bakx J, van der Wel MC, Hermus AR, Lenders JW, Deinum J. Study heterogeneity and estimation of prevalence of primary aldosteronism: a systematic review and meta-regression analysis. *J Clin Endocrinol Metab*. 2016;101:2826–2835. doi: 10.1210/jc.2016-1472
6. Xu Z, Yang J, Hu J, Song Y, He W, Luo T, Cheng Q, Ma L, Luo R, Fuller PJ, et al; Chongqing Primary Aldosteronism Study (CONPASS) Group. Primary aldosteronism in patients in china with recently detected hypertension. *J Am Coll Cardiol*. 2020;75:1913–1922. doi: 10.1016/j.jacc.2020.02.052
7. Savard S, Amar L, Plouin PF, Steichen O. Cardiovascular complications associated with primary aldosteronism: a controlled cross-sectional study. *Hypertension*. 2013;62:331–336. doi: 10.1161/HYPERTENSIONAHA.113.01060
8. Choi M, Scholl UI, Yue P, Bjorklund P, Zhao B, Nelson-Williams C, Ji W, Cho Y, Patel A, Men CJ, et al. K+ channel mutations in adrenal aldosterone-producing adenomas and hereditary hypertension. *Science*. 2011;331:768–772. doi: 10.1126/science.1198785
9. Azizan EA, Poulsen H, Tuluc P, Zhou J, Clausen MV, Lieb A, Maniero C, Garg S, Bochukova EG, Zhao W, et al. Somatic mutations in ATP1A1 and CACNA1D underlie a common subtype of adrenal hypertension. *Nat Genet*. 2013;45:1055–1060. doi: 10.1038/ng.2716
10. Scholl UI, Goh G, Stolting G, de Oliveira RC, Choi M, Overton JD, Fonseca AL, Korah R, Starker LF, Kunstman JW, et al. Somatic and germline CACNA1D calcium channel mutations in aldosterone-producing adenomas and primary aldosteronism. *Nat Genet*. 2013;45:1050–1054. doi: 10.1038/ng.2695
11. Scholl UI, Stolting G, Nelson-Williams C, Vichot AA, Choi M, Loring E, Prasad ML, Goh G, Carling T, Juhlin CC, et al. Recurrent gain of function mutation in calcium channel CACNA1H causes early-onset hypertension with primary aldosteronism. *Elife*. 2015;4:e06315. doi: 10.7554/eLife.06315
12. Daniil G, Fernandes-Rosa FL, Chemin J, Blesneac I, Beltrand J, Polak M, Jeunemaitre X, Boulkroun S, Amar L, Strom TM, et al. CACNA1H mutations are associated with different forms of primary aldosteronism. *EBioMedicine*. 2016;13:225–236. doi: 10.1016/j.ebiom.2016.10.002
13. Fernandes-Rosa FL, Daniil G, Orozco IJ, Göppner C, El Zein R, Jain V, Boulkroun S, Jeunemaitre X, Amar L, Lefebvre H, et al. A gain-of-function

Downloaded from http://ahajournals.org by on November 13, 2025

mutation in the CLCN2 chloride channel gene causes primary aldosteronism. *Nat Genet*. 2018;50:355–361. doi: 10.1038/s41588-018-0053-8
14. Scholl UI, Stolting G, Schewe J, Thiel A, Tan H, Nelson-Williams C, Vichot AA, Jin SC, Loring E, Untiet V, et al. CLCN2 chloride channel mutations in familial hyperaldosteronism type II. *Nat Genet*. 2018;50:349–354. doi: 10.1038/s41588-018-0048-5
15. Rege J, Bandulik S, Nanba K, Kosmann C, Blinder AR, Plain A, Vats P, Kumar-Sinha C, Lerario AM, Else T, et al. Somatic SLC30A1 mutations altering zinc transporter ZnT1 cause aldosterone-producing adenomas and primary aldosteronism. *Nat Genet*. 2023;55:1623–1631. doi: 10.1038/s41588-023-01498-5
16. Beuschlein F, Boulkroun S, Osswald A, Wieland T, Nielsen HN, Lichtenauer UD, Penton D, Schack VR, Amar L, Fischer E, et al. Somatic mutations in ATP1A1 and ATP2B3 lead to aldosterone-producing adenomas and secondary hypertension. *Nat Genet*. 2013;45:440–4, 444e1. doi: 10.1038/ng.2550
17. Scholl UI, Nelson-Williams C, Yue P, Grekin R, Wyatt RJ, Dillon MJ, Couch R, Hammer LK, Harley FL, Farhi A, et al. Hypertension with or without adrenal hyperplasia due to different inherited mutations in the potassium channel KCNJ5. *Proc Natl Acad Sci USA*. 2012;109:2533–2538. doi: 10.1073/pnas.1121407109
18. Oki K, Plonczynski MW, Luis LM, Gomez-Sanchez EP, Gomez-Sanchez CE. Potassium channel mutant KCNJ5 T158A expression in HAC-15 cells increases aldosterone synthesis. *Endocrinology*. 2012;153:1774–1782.
19. Mulatero P, Tauber P, Zennaro MC, Monticone S, Lang K, Beuschlein F, Fischer E, Tizzani D, Pallauf A, Viola A, et al. KCNJ5 mutations in European families with nonglucocorticoid remediable familial hyperaldosteronism. *Hypertension*. 2012;59:235–240. doi: 10.1161/HYPERTENSIONAHA.111.183996
20. Yang Y, Gomez-Sanchez CE, Jaquin D, Aristizabal Prada ET, Meyer LS, Knosel T, Schneider H, Beuschlein F, Reincke M, Williams TA. Primary aldosteronism: KCNJ5 mutations and adrenocortical cell growth. *Hypertension*. 2019;74:809–816. doi: 10.1161/HYPERTENSIONAHA.119.13476
21. Magnus CJ, Lee PH, Atasoy D, Su HH, Looger LL, Sternson SM. Chemical and genetic engineering of selective ion channel-ligand interactions. *Science*. 2011;333:1292–1296. doi: 10.1126/science.1206606
22. Magnus CJ, Lee PH, Bonaventura J, Zemla R, Gomez JL, Ramirez MH, Hu X, Galvan A, Basu J, Michaelides M, et al. Ultrapotent chemogenetics for research and potential clinical applications. *Science*. 2019;364:eaav5282. doi: 10.1126/science.aav5282
23. Wang T, Rowland JG, Parmar J, Nesterova M, Seki T, Rainey WE. Comparison of aldosterone production among human adrenocortical cell lines. *Horm Metab Res*. 2012;44:245–250. doi: 10.1055/s-0031-1298019
24. Bustin SA, Benes V, Garson JA, Hellemans J, Huggett J, Kubista M, Mueller R, Nolan T, Pfaffl MW, Shipley GL, et al. The MIQE guidelines: minimum information for publication of quantitative real-time PCR experiments. *Clin Chem*. 2009;55:611–622. doi: 10.1373/clinchem.2008.112797
25. Yang T, He M, Zhang H, Barrett PQ, Hu C. L- and T-type calcium channels control aldosterone production from human adrenals. *J Endocrinol*. 2020;244:237–247. doi: 10.1530/JOE-19-0259
26. Barrett PQ, Guagliardo NA, Klein PM, Hu C, Breault DT, Beenhakker MP. Role of voltage-gated calcium channels in the regulation of aldosterone production from zona glomerulosa cells of the adrenal cortex. *J Physiol*. 2016;594:5851–5860. doi: 10.1113/JP271896
27. Sherman BT, Hao M, Qiu J, Jiao X, Baseler MW, Lane HC, Imamichi T, Chang W. DAVID: a web server for functional enrichment analysis and functional annotation of gene lists (2021 update). *Nucleic Acids Res*. 2022;50:W216–W221.
28. Huang DW, Sherman BT, Lempicki RA. Systematic and integrative analysis of large gene lists using DAVID bioinformatics resources. *Nat Protoc*. 2009;4:44–57. doi: 10.1038/nprot.2008.211
29. Boulkroun S, Beuschlein F, Rossi GP, Golib-Dzib JF, Fischer E, Amar L, Mulatero P, Samson-Couterie B, Hahner S, Quinkler M, et al. Prevalence, clinical, and molecular correlates of KCNJ5 mutations in primary aldosteronism. *Hypertension*. 2012;59:592–598. doi: 10.1161/HYPERTENSIONAHA.111.186478
30. Fernandes-Rosa FL, Williams TA, Riester A, Steichen O, Beuschlein F, Boulkroun S, Strom TM, Monticone S, Amar L, Meatchi T, et al. Genetic spectrum and clinical correlates of somatic mutations in aldosterone-producing adenoma. *Hypertension*. 2014;64:354–361. doi: 10.1161/HYPERTENSIONAHA.114.03419
31. Lenzini L, Rossitto G, Maiolino G, Letizia C, Funder JW, Rossi GP. A meta-analysis of somatic KCNJ5 K(+) channel mutations in 1636 patients with an aldosterone-producing adenoma. *J Clin Endocrinol Metab*. 2015;100:E1089–E1095. doi: 10.1210/jc.2015-2149
32. Mangelis A, Dieterich P, Peitzsch M, Richter S, Jühlen R, Hübner A, Willenberg HS, Deussen A, Lenders JWM, Eisenhofer G. Computational analysis of liquid chromatography-tandem mass spectrometric steroid profiling in NCI H295R cells following angiotensin II, forskolin and abiraterone treatment. *J Steroid Biochem Mol Biol*. 2016;155:67–75. doi: 10.1016/j.jsbmb.2015.09.038
33. Hattangady NG, Karashima S, Yuan L, Ponce-Balbuena D, Jalife J, Gomez-Sanchez CE, Auchus RJ, Rainey WE, Else T. Mutated KCNJ5 activates the acute and chronic regulatory steps in aldosterone production. *J Mol Endocrinol*. 2016;57:1–11. doi: 10.1530/JME-15-0324
34. Sui JL, Chan KW, Logothetis DE. Na+ activation of the muscarinic K+ channel by a G-protein-independent mechanism. *J Gen Physiol*. 1996;108:381–391. doi: 10.1085/jgp.108.5.381
35. Rosenhouse-Dantsker A, Sui JL, Zhao Q, Rusinova R, Rodríguez-Menchaca AA, Zhang Z, Logothetis DE. A sodium-mediated structural switch that controls the sensitivity of Kir channels to PtdIns(4,5)P(2). *Nat Chem Biol*. 2008;4:624–631. doi: 10.1038/nchembio.112
36. Azizan EA, Lam BY, Newhouse SJ, Zhou J, Kuc RE, Clarke J, Happerfield L, Marker A, Hoffman GJ, Brown MJ. Microarray, qPCR, and KCNJ5 sequencing of aldosterone-producing adenomas reveal differences in genotype and phenotype between zona glomerulosa- and zona fasciculata-like tumors. *J Clin Endocrinol Metab*. 2012;97:E819–E829. doi: 10.1210/jc.2011-2965
37. Akerstrom T, Willenberg HS, Cupisti K, Ip J, Backman S, Moser A, Maharjan R, Robinson B, Iwen KA, Dralle H, et al. Novel somatic mutations and distinct molecular signature in aldosterone-producing adenomas. *Endocr Relat Cancer*. 2015;22:735–744. doi: 10.1530/ERC-15-0321
38. Williams TA, Monticone S, Morello F, Liew CC, Mengozzi G, Pilon C, Asioli S, Sapino A, Veglio F, Mulatero P. Teratocarcinoma-derived growth factor-1 is upregulated in aldosterone-producing adenomas and increases aldosterone secretion and inhibits apoptosis in vitro. *Hypertension*. 2010;55:1468–1475. doi: 10.1161/HYPERTENSIONAHA.110.150318
39. Williams TA, Monticone S, Crudo V, Warth R, Veglio F, Mulatero P. Visinin-like 1 is upregulated in aldosterone-producing adenomas with KCNJ5 mutations and protects from calcium-induced apoptosis. *Hypertension*. 2012;59:833–839. doi: 10.1161/HYPERTENSIONAHA.111.188532
40. Le Floch E, Cosentino T, Larsen CK, Beuschlein F, Reincke M, Amar L, Rossi G-P, De Sousa K, Baron S, Chantalat S, et al. Identification of risk loci for primary aldosteronism in genome-wide association studies. *Nat Commun*. 2022;13:5198. doi: 10.1038/s41467-022-32896-8
41. Naito T, Inoue K, Sonehara K, Baba R, Kodama T, Otagaki Y, Okada A, Itcho K, Kobuke K, Kishimoto S, et al; BioBank Japan. Genetic risk of primary aldosteronism and its contribution to hypertension: a cross-ancestry meta-analysis of genome-wide association studies. *Circulation*. 2023;147:1097–1109. doi: 10.1161/CIRCULATIONAHA.122.062349
42. Sun X, Hu Y, Wu J, Shi L, Zhu L, Xi P-W, Wei J-F, Ding Q. RBMS2 inhibits the proliferation by stabilizing P21 mRNA in breast cancer. *J Exp Clin Cancer Res*. 2018;37:298. doi: 10.1186/s13046-018-0968-z
43. Zhu Z, Liu Y, Li K, Liu J, Wang H, Sun B, Xiong Z, Jiang H, Zheng J, Hu Z. Protein tyrosine phosphatase receptor U (PTPRU) is required for glioma growth and motility. *Carcinogenesis*. 2014;35:1901–1910. doi: 10.1093/carcin/bgu123
44. Liu Y, Zhu Z, Xiong Z, Zheng J, Hu Z, Qiu J. Knockdown of protein tyrosine phosphatase receptor U inhibits growth and motility of gastric cancer cells. *Int J Clin Exp Pathol*. 2014;7:5750–5761.
45. Li S, MacLachlan TK, De Luca A, Claudio PP, Condorelli G, Giordano A. The cdc-2-related kinase, PISSLRE, is essential for cell growth and acts in G2 phase of the cell cycle. *Cancer Res*. 1995;55:3992–3995.
46. Poon SSS, Wong JT, Saunders DN, Ma QC, McKinney S, Fee J, Aparicio SAJR. Intensity calibration and automated cell cycle gating for high-throughput image-based siRNA screens of mammalian cells. *Cytometry A*. 2008;73:904–917. doi: 10.1002/cyto.a.20624
47. Guen VJ, Gamble C, Perez DE, Bourassa S, Zappel H, Gärtner J, Lees JA, Colas P. STAR syndrome-associated CDK10/cyclin M regulates actin network architecture and ciliogenesis. *Cell Cycle*. 2016;15:678–688. doi: 10.1080/15384101.2016.1147632
48. Yu J-H, Zhong X-Y, Zhang W-G, Wang Z-D, Dong Q, Tai S, Li H, Cui Y-F. CDK10 functions as a tumor suppressor gene and regulates survivability of biliary tract cancer cells. *Oncol Rep*. 2012;27:1266–1276. doi: 10.3892/or.2011.1617
49. Zhong X, Xu X, Yu J, Jiang G, Yu Y, Tai S, Wang Z, Cui Y. Clinical and biological significance of Cdk10 in hepatocellular carcinoma. *Gene*. 2012;498:68–74. doi: 10.1016/j.gene.2012.01.022
50. Martini CN, Vaena de Avalos SG, Romero DG, San Martin de Viale L, Vila MC. Heme availability affects corticosterone and aldosterone

Downloaded from http://ahajournals.org by on November 13, 2025

biosynthesis in rat adrenal. *Steroids*. 1997;62:767–770. doi: 10.1016/s0039-128x(97)00074-3
51. Murakami M, Yoshimoto T, Nakabayashi K, Tsuchiya K, Minami I, Bouchi R, Izumiyama H, Fujii Y, Abe K, Tayama C, et al. Integration of transcriptome and methylome analysis of aldosterone-producing adenomas. *Eur J Endocrinol*. 2015;173:185–195. doi: 10.1530/EJE-15-0148
52. Ye P, Mariniello B, Mantero F, Shibata H, Rainey WE. G-protein-coupled receptors in aldosterone-producing adenomas: a potential cause of hyperaldosteronism. *J Endocrinol*. 2007;195:39–48. doi: 10.1677/JOE-07-0037
53. De Sousa K, Abdellatif AB, Giscos-Douriez I, Meatchi T, Amar L, Fernandes-Rosa FL, Boulkroun S, Zennaro M-C. Colocalization of Wnt/β-catenin and ACTH signaling pathways and paracrine regulation in aldosterone-producing adenoma. *J Clin Endocrinol Metab*. 2022;107:419–434. doi: 10.1210/clinem/dgab707
54. Parksook WW, Brown JM, Omata K, Tezuka Y, Ono Y, Satoh F, Tsai LC, Niebuhr Y, Milks J, Moore A, et al. The spectrum of dysregulated aldosterone production: an international human physiology study. *J Clin Endocrinol Metab*. 2024;109:2220–2232. doi: 10.1210/clinem/dgae145
55. van Rooyen D, Bandulik S, Coon G, Laukemper M, Kumar-Sinha C, Udager AM, Lee C, Wachtel H, Cohen DL, Luther JM, et al. Somatic mutations in *MCOLN3* in aldosterone-producing adenomas cause primary aldosteronism. *bioRxiv*. Preprint posted online October 23, 2024. doi: 10.1101/2024.10.20.619295

Downloaded from http://ahajournals.org by on November 13, 2025

15 Book Chapter

15.1 MicroRNAs in aldosterone production and action

MacKenzie SM, Birch LA, Lamprou S, Rezvanisanijouybari P, **Fayad M,** Zennaro MC, et al. MicroRNAs in aldosterone production and action. Vitam Horm. 2024;124:137–63.

CHAPTER FOUR

MicroRNAs in aldosterone production and action☆

Scott M. MacKenzie[a,*], Lara A. Birch[a], Stelios Lamprou[a], Parisa Rezvanisanijouybari[a], May Fayad[a,b], Maria-Christina Zennaro[b,c], and Eleanor Davies[a]

[a]School of Cardiovascular and Metabolic Health, BHF Glasgow Cardiovascular Research Centre, University of Glasgow, Glasgow, United Kingdom
[b]Université Paris Cité, PARCC, INSERM, Paris, France
[c]Assistance Publique-Hôpitaux de Paris, Hôpital Européen Georges Pompidou, Service de Génétique, Paris, France
*Corresponding author. e-mail address: scott.mackenzie@glasgow.ac.uk

Contents

1. Aldosterone 139
   1.1 Aldosterone synthesis 139
   1.2 Regulation of aldosterone secretion 140
   1.3 Primary aldosteronism 142
2. MicroRNA 143
   2.1 Gene silencing 144
   2.2 Extracellular/circulating miRNA 145
3. The role of microRNA in aldosterone production 145
4. The role of microRNA in aldosterone action 148
   4.1 Renal 149
   4.2 Cardiac 151
   4.3 Vascular 151
   4.4 Brain 152
5. Circulating microRNAs and their role in aldosterone-associated diagnostics 153
References 156

☆ S.M.M., M.-C.Z. and E.D. are members of the EU ENS@T-HT (633983) and HT-ADVANCE (101095407) research consortia. L.A.B. is funded by a British Heart Foundation PhD studentship (FS/4yPhD/F/20/34127). S.L. is funded by a PhD studentship through the Medical Research Council Precision Medicine DTP programme (MR/N013166/1). P.R. and M.F. are funded by the European Union's Horizon 2020 research and innovation programme under the Marie Sklodowska-Curie grant agreement No. 954798 (MINDSHIFT ITN), for which M.-C.Z. and E.D. are principal investigators.

Vitamins and Hormones, Volume 124
ISSN 0083-6729, https://doi.org/10.1016/bs.vh.2023.07.001
Copyright © 2024 Elsevier Inc. All rights are reserved, including those for text and data mining, AI training, and similar technologies.

Abstract

Aldosterone is a cardiovascular hormone with a key role in blood pressure regulation, among other processes, mediated through its targeting of the mineralocorticoid receptor in the renal tubule and selected other tissues. Its secretion from the adrenal gland is a highly controlled process subject to regulatory influence from the renin–angiotensin system and the hypothalamic–pituitary–adrenal axis. MicroRNAs are small endogenous non-coding RNA molecules capable of regulating gene expression post-transcriptionally through stimulation of mRNA degradation or suppression of translation. Several studies have now identified that microRNA levels are changed in cases of aldosterone dysregulation and that microRNAs are capable of regulating the expression of various genes involved in aldosterone production and action. In this article we summarise the major studies concerning this topic. We also discuss the potential role for circulating microRNAs as diagnostic biomarkers for primary aldosteronism, a highly treatable form of secondary hypertension, which would be highly desirable given the current underdiagnosis of this condition.

Regulation of the genome is a complex process influenced by many biochemical pathways and molecular entities. While the role of transcription factors in gene expression is well established (Adcock & Caramori, 2009), other molecules are also key to regulating genes, both pre- and post-transcriptionally. These include the small (~25 nucleotide) non-coding RNAs collectively known as microRNAs (miRNAs). Since their initial discovery in *Caenorhabditis elegans* 30 years ago (Lee, Feinbaum, & Ambros, 1993), our understanding of how this RNA class is synthesised and its involvement in a wide range of physiological and pathological processes has greatly expanded. Following initial confirmation that miRNAs do not code for protein (Lee, Feinbaum, & Ambros, 2004), subsequent research revealed that they are able to silence genes by binding the 3′ untranslated region (UTR) of specific target messenger RNAs (mRNA), thereby promoting either the transcript's decay or inhibiting its translation (Huntzinger & Izaurralde, 2011). Thus, miRNAs are important post-transcriptional regulators of gene expression (Ha & Kim, 2014). Moreover, it has been illustrated that miRNAs are secreted actively or passively outside the cellular space, which makes them an excellent mediator candidate for cellular communication and potential viable biomarkers for human disease (Huang, 2017).

Given that approximately 60% of human genes are estimated to be regulated by up to 2300 miRNAs (Alles et al., 2019; Friedman, Farh, Burge, & Bartel, 2009), it was inevitable that their impact on all major biological systems would be assessed, and this has included studies of miRNAs' role in

the secretion and action of the major mineralocorticoid hormone, aldosterone. Subject to the influence of multiple regulatory systems, fine control of aldosterone secretion is crucial; its dysregulation can have serious consequences as evidenced by conditions such as primary aldosteronism (PA) (MacKenzie, Kralingen, & Davies, 2018). In this chapter, we discuss the evidence that miRNA is a significant player in the processes underlying aldosterone production and action in health and disease.

1. Aldosterone

Aldosterone is the major human mineralocorticoid hormone, synthesised within the cortex of the adrenal gland. It acts principally in the distal tubule of the kidney where activation of its receptor, the mineralocorticoid receptor (MR), modulates water balance and blood pressure by regulating the expression of proteins involved in sodium reabsorption and potassium excretion (Xing, Lerario, Rainey, & Hammer, 2015). However, MR is much more widely expressed than this, which can have serious consequences when aldosterone is in excess. As well as promoting renal fibrosis, high levels of aldosterone can result in atherosclerotic plaques, arterial stiffness and calcification in the vascular system and stimulate fibrosis and myocardial hypertrophy in the heart owing to the presence of MR in each of these tissues (Buffolo, Tetti, Mulatero, & Monticone, 2022). Inflammation is an important part of these processes and arises from activation of the MR present in macrophages and T cells within these tissues (Barrera-Chimal, Bonnard, & Jaisser, 2022).

1.1 Aldosterone synthesis

The human adrenal cortex secretes 3 principal categories of steroid hormone: mineralocorticoids, glucocorticoids and adrenal androgens. The cortex consists of three functionally differentiated zones: the zona glomerulosa (ZG), the zona fasciculata (ZF) and the zona reticularis (ZR). Due to this functional zonation arising from differential expression of steroidogenic enzymes, each zone is responsible for the principal secretion of a specific steroid hormone. Using cholesterol as a precursor, steroid hormone synthesis progresses through a series of enzymatic steps involving members of the cytochrome P450 (CYP) and hydroxysteroid dehydrogenase families of enzymes located either in cellular mitochondrial membranes or the endoplasmic reticulum (ER) (Fig. 1).

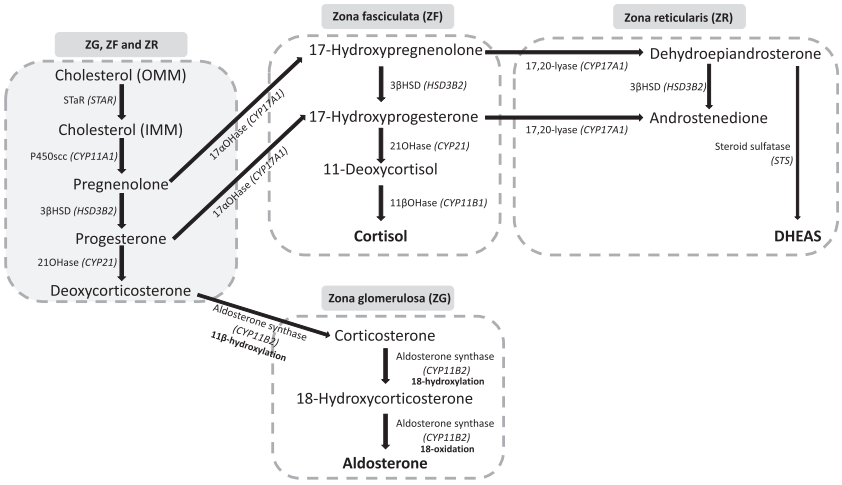

Fig. 1 Summary of the major steroidogenic pathways of the adrenal cortex within the three adrenocortical zones. Names of the enzymes mediating each stage are shown alongside the name of the corresponding gene in brackets.

Aldosterone is produced within the ZG, which is the sole adrenocortical area to express the *CYP11B2* gene. The gene product, the aldosterone synthase enzyme or CYP11B2 (Cytochrome P450 family 11 subfamily B member 2), catalyses the last 3 stages of aldosterone biosynthesis: hydroxylation at the C11 position of deoxycorticosterone to produce corticosterone, followed by hydroxylation at the C18 position, producing 18-hydroxycorticosterone and, finally, oxidation of the hydroxyl group at C18, which results in aldosterone (Connell & Davies, 2005; Fernandes-Rosa, Boulkroun, & Zennaro, 2020).

1.2 Regulation of aldosterone secretion

The major regulators underlying aldosterone biosynthesis in normal physiology are the renin–angiotensin–aldosterone system (RAAS), extracellular potassium concentration and the hypothalamic–pituitary–adrenal axis (MacKenzie et al., 2018).

1.2.1 The renin–angiotensin–aldosterone system (RAAS)

The primary stimulus for aldosterone biosynthesis is angiotensin II (AngII), via the renin angiotensin aldosterone system (RAAS) (Fig. 2). Activation of the RAAS is triggered by reductions in sodium concentration or intravascular pressure/volume. Renin and its substrate angiotensinogen are secreted into the circulation by the kidney and liver, respectively. Cleavage of circulating angiotensinogen by renin results in angiotensin I, which is rapidly converted

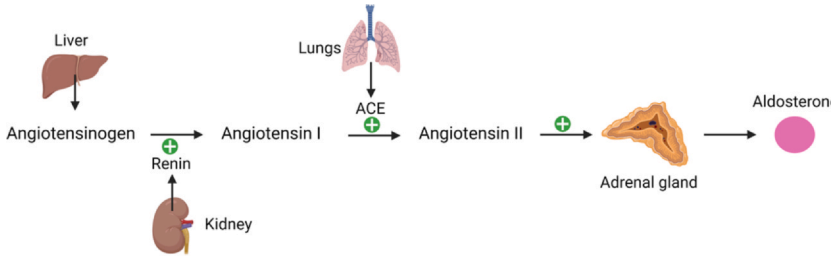

Fig. 2 Summary of aldosterone stimulation by components of the renin–angiotensin–aldosterone system (RAAS). Created with BioRender.com.

by angiotensin converting enzyme (ACE) in the lung to angiotensin II (AngII). AngII binding of the angiotensin II type I receptor (AT1R) leads to massive Ca^{2+} release from the ER by increased formation of inositol triphosphate (IP3). AngII also inhibits the TWIK-related acid-sensitive potassium (TASK) channel and GIRK4, encoded by the Potassium Voltage-Gated channel subfamily J member 5 (*KCNJ5*) gene, as well as the Na^+/K^+-ATPase pump, the α1 subunit of which is encoded by the *ATP1A1* gene (ATPase Na^+/K^+ Transporting Subunit Alpha 1). The net effect is depolarisation of the cell membrane due to the increased intracellular calcium concentrations that follow the opening of voltage-dependent calcium channels (Bandulik, Penton, Barhanin, & Warth, 2010).

1.2.2 Extracellular potassium concentration

Increases in extracellular potassium concentrations also serve as a stimulus for aldosterone biosynthesis. ZG cells have a hyperpolarised membrane potential close to the potassium equilibrium potential. K^+ stimulation results in ZG cell membrane depolarisation and the opening of voltage-gated calcium channels, increasing intracellular Ca^{2+} concentration, which activates calcium signalling. Activation of the calcium signalling pathway triggers a phosphorylation cascade, involving calmodulin and calmodulin-dependent kinase I/IV, leading to the activation of specific transcription factors that bind the promoter region and stimulate transcription of *CYP11B2*, thereby increasing aldosterone biosynthesis (Bandulik et al., 2010; Spät, Hunyady, & Szanda, 2016).

1.2.3 The hypothalamic–pituitary–adrenal (HPA) axis

Although primarily the major regulator of cortisol secretion, activation of the stress-responsive HPA can also stimulate aldosterone biosynthesis. HPA activation results in release of corticotropic hormone (ACTH), which can target the arenal cortex to induce aldosterone production via cAMP signalling.

ACTH binds the melanocortin type 2 receptor (MC2R), which is coupled to a Gαs protein. This binding activates adenylate cyclase and induces an increase in the concentration of cyclic adenosine monophosphate (cAMP) that activates protein kinase A (PKA). PKA then phosphorylates numerous transcription factors including cAMP responsive element binding protein (CREB), permitting its translocation to the nucleus. PKA also stimulates calcium influx through the phosphorylation of L-type voltage-gated calcium channels, again increasing intracellular calcium concentration to stimulate aldosterone production (Spät et al., 2016). ACTH also regulates *CYP11B2* gene expression through the phosphorylation of CREB, which binds the gene promoter at CRE response elements (Gallo-Payet, 2016).

1.3 Primary aldosteronism

Primary aldosteronism (PA) is the most common form of secondary hypertension with an estimated prevalence of 5% of hypertensive patients; this can rise to 10–20% of patients referred to specialist centres (Hannemann & Wallaschofski, 2011) and 20% of patients with resistant hypertension (Douma et al., 2008).

PA results from dysregulation of the mechanisms controlling aldosterone production in the adrenal cortex and leads to inappropriately high levels of aldosterone in the circulation. PA is characterised by hypertension due to the elevated aldosterone and is associated with renin suppression and thus an elevated aldosterone/renin ratio, as well as hypokalemia and metabolic alkalosis in some cases (Funder et al., 2016).

PA is most commonly caused either by an aldosterone-producing adenoma (APA) of the adrenal cortex or else by bilateral adrenal hyperplasia (BAH). The development of immunohistochemistry (IHC)-guided next-generation sequencing (NGS) of aldosterone synthase has in recent years allowed 88–93% of somatic mutations in APAs to be identified (Nanba et al., 2018; Sousa et al., 2020) and these have been found to affect genes encoding the ion channels *KCNJ5* (Choi et al., 2011), *CACNA1D* (Azizan et al., 2013; Scholl et al., 2013), *CACNA1H* (Nanba et al., 2020) and *CLCN2* (Dutta et al., 2019) as well as genes encoding *ATP1A1,* which codes for the α1 subunit of the Na^+/K^+-ATPase pump (Azizan et al., 2013; Beuschlein et al., 2013), *ATP2B3,* which encodes the membrane calcium pump (PMCA3) (Beuschlein et al., 2013), and *CTNNB1,* which encodes β-catenin (Åkerström et al., 2016). Recently, double mutations affecting CTNNB1 and GNAQ/GNA11 were identified in APA occurring at puberty, pregnancy and menopause (Zhou et al., 2021). Germline mutations

were identified in familial forms of PA, enabling classification into 4 forms of familial hyperaldosteronism (FH) that together represent < 5% of diagnosed PA cases (Zennaro, Boulkroun, & Fernandes-Rosa, 2020). FH-I is the result of a chimeric *CYP11B1-CYP11B2* gene, in which *CYP11B2* expression is under the control of the regulatory regions of *CYP11B1*, resulting in glucocorticoid remediable aldosteronism. FH-II is due to mutations in *CLCN2*, FH-III to mutations in *KCNJ5* and FH-IV to mutations in *CACNA1H*. These mutations lead to constitutively depolarised ZG cell membranes or directly to increased intracellular Ca^{2+} concentrations that activate Ca^{2+} signalling, promote expression of *CYP11B2* and stimulate biosynthesis of aldosterone (Fernandes-Rosa et al., 2020).

2. MicroRNA

The process of miRNA biogenesis begins in the nucleus with transcription of the non-protein coding genes that code for the precursor miRNA form, pri-miRNA, which is a double-stranded transcript with a distinctive hairpin-looped structure (Han et al., 2004). Mature single-stranded miRNA is formed from this precursor through a pathway facilitated by the microprocessor complex. This protein complex first recognises specific methylated parts of the pri-miRNA with the aid of the RNA binding protein DiGeorge Syndrome Critical Region 8 (DGCR8) and promotes its cleavage by the Drosha ribonuclease to leave a newly formed premature miRNA (pre-miRNA), which is shorter in length but retains the hairpin structure.

The next stages of miRNA processing take place in the cytoplasm following transport of pre-miRNAs from the nucleus in a process catalysed by Exportin-5 (Okada et al., 2009). There the pre-miRNA is further cleaved by Dicer. This is an RNAse III enzyme that removes the looped structure from the pre-miRNA to leave a mature double-stranded miRNA (Zhang, Kolb, Jaskiewicz, Westhof, & Filipowicz, 2004). Consisting of two strands, this duplex gives rise to two different mature forms of each miRNA. Specifically, the 5′–3′ strand forms the '5p' miRNA whereas the 3′–5′ strand becomes the '3p' miRNA. However, each strand is not treated equally. While both strands can be taken up by the four Argonaute proteins (AGO1–4) (Yoda et al., 2010), the form that is loaded preferentially on to the AGO proteins is highly dependent on the tissue, cell line and cellular environment. However, their selection is mainly influenced by the thermodynamic stability

at the 5′ end of the mature transcript; the strand (5p or 3p) with lower stability at its 5′ end is loaded on to the AGO1–4 complex and is referred to as the guide strand, while the other is known as the passenger strand (Meijer, Smith, & Bushell, 2014). It is the guide strand that is responsible for targeting mRNA and promoting its degradation (Ha & Kim, 2014).

The naming of miRNAs generally follows particular conventions. A mature miRNA of specific sequence is assigned a unique identification number (e.g. miR-1, miR-2, etc.) and a prefix can be added denoting the host species (e.g. '*mmu*' for mouse and '*hsa*' for human), along with a suffix to convey the arm of the pre-miR strand from which the mature miRNA is derived (e.g. hsa-miR-121-3p). Letters can also be added to the miRNA ID number to denote mature sequences that are extremely similar (e.g. hsa-miR-23a-3p and hsa-miR-23b-3p). Finally, in recognition of the fact that different genomic loci can give rise to mature miRNAs that are identical in sequence, such loci and miRNA precursors can be differentiated numerically (e.g. hsa-miR-16-1 and hsa-miR-16-2). Although some exceptions do apply to this system for specific miRNAs or across different organisms, these rules generally hold for the miRNAs described here (Ambros et al., 2003).

2.1 Gene silencing

As mentioned previously, miRNAs predominantly bind target mRNAs at the 3′ UTR (Ha & Kim, 2014). This binding can result in translational repression, mRNA deadenylation and decapping (Huntzinger & Izaurralde, 2011). The targeting process is catalysed by the minimal miRNA-induced silencing complex (mi-RISC) which contains the guide strand and AGO complex and determines target specificity through interactions with miRNA response elements (MREs) on the target mRNA (Kawamata & Tomari, 2010).

MRE complementarity with the guide miRNA sequence determines whether AGO2-dependent slicing or mi-RISC mediated translational inhibition and mRNA decay occurs (Kawamata & Tomari, 2010). Most MREs contain small sequence complementarity mismatches with the guide miRNA, precluding AGO2 endonuclease activity, which requires no mismatches (Jo et al., 2015). As a result, mi-RISC mediated translational inhibition and mRNA decay are favoured. Formation of a silencing mi-RISC complex involves recruitment of GW182 proteins and other effector proteins, including poly(A)-deadenylase complexes and decapping proteins, which are responsible for promoting the mRNA degradation (Behm-Ansmant et al., 2006).

2.2 Extracellular/circulating miRNA

Although the principal mode of miRNA action occurs within the cell where it was transcribed, it has been shown that miRNAs can be transported actively between cell lines through the secretion of extracellular vesicles (Valadi et al., 2007). Also, they have been observed to migrate through cell lines as miRNA–protein complexes and even released in the fluids secreted following cellular damage. Furthermore, miRNAs can form complexes with high and low-density lipoproteins and access cells via the bloodstream, targeting mRNAs and thereby regulating the gene expression of distant cells in an endocrine manner (Vickers, Palmisano, Shoucri, Shamburek, & Remaley, 2011).

Such circulating miRNAs (cir-miRNA) have been studied extensively since, aside from their potential functional effects, they hold great potential to serve as viable biomarkers for human disease. This is favoured by their tolerance to ribonuclease activity—which renders them highly stable molecules (Mitchell et al., 2008)—and the fact that they can be obtained from human fluids (e.g., blood samples) with minimal invasiveness (Weber et al., 2010). Several studies have shown levels of various cir-miRNAs in cardiovascular disease (CVD) patients to be differentially expressed, implying that these molecules are involved in the pathophysiology of certain conditions and that changes in their expression might be measured to monitor and diagnose patients more quickly and efficiently (Jiang et al., 2014; Schulte et al., 2015; Shan et al., 2015).

3. The role of microRNA in aldosterone production

As described previously, aldosterone is synthesised through a series of enzymatic reactions, which begins with conversion of cholesterol to pregnenolone by the P450scc (side-chain cleavage) enzyme and ends with the aldosterone synthase enzyme. Expression of these enzymes is subject to tight regulation which is key, particularly in the final stages, to secreting appropriate levels of aldosterone. Any changes that lead to increased expression of aldosterone synthase, as in primary aldosteronism, will cause severe hypertension and, consequently, cardiovascular disease and organ damage (Connell, MacKenzie, Freel, Fraser, & Davies, 2008). It is now clear that components of the aldosterone steroidogenic pathway are subject to post-transcriptional regulation by miRNAs (Azhar, Dong, Shen, Hu, & Kraemer, 2019). The effect of miRNAs on the expression of the steroidogenic enzymes and, consequently, on steroid hormone levels has been confirmed by several studies.

In 2013, Robertson et al. found that Dicer 1 knockdown (i.e. non-specific disruption of cellular microRNA production) increased *CYP11B2* (aldosterone synthase) mRNA levels in the human adrenocortical cell line, H295R. This indicated a role for miRNAs in the regulation of adrenal steroidogenesis. More specifically, we then found levels of miR-24 and miR-10b to be downregulated in human aldosterone-producing adenoma relative to nontumorous adrenal cortex and further demonstrated that miR-24 could affect aldosterone levels in adrenocortical cells through its direct modulation of *CYP11B2* expression; supplementation of miR-24 levels reduced the cellular levels of *CYP11B2* mRNA and aldosterone secretion, while inhibition of miR-24 action had the opposite effects (Robertson et al., 2013). A study by Nusrin et al. shortly after showed a similar effect by miR-10b in H295R cells (Nusrin et al., 2014). Interestingly, they also demonstrated that hypoxia of H295R cells induces expression of miR-10b, accompanied by a decrease in aldosterone synthase enzyme levels and, somewhat paradoxically, a marked increase in *CYP11B2* mRNA. They proposed that this could be due to miR-10b acting on *CYP11B2* through a translational repression pathway rather than via mRNA degradation. Separately, Maharjan et al. showed miR-766 binds *CYP11B2* mRNA at a polymorphic site within its 3'UTR although, being polymorphic, this site can only be bound in one of its alternative allelic forms (Maharjan, Mopidevi, Kaw, Puri, & Kumar, 2014).

Subsequently, Robertson et al. again used Dicer1 knockdown in H295R cells to explore effects on other components of the aldosterone steroidogenic pathway and found that it increased mRNA levels for *CYP11A1*, *CYP21A1*, and *CYP17A1*, in addition to the previously-reported *CYP11B2*. Furthermore, analysis of steroid secretion following Dicer1 knockdown showed significant increases in cortisol, corticosterone, 11-deoxycorticosterone, 18-deoxycorticosterone, and aldosterone (Robertson et al., 2017). This indicated miRNA action at multiple points in the steroidogenic pathway, acting to prevent overproduction of its constituent enzymes and thereby limit aldosterone secretion. Focusing on individual miRNAs, we also identified direct regulatory effects of miR-125a-5p on *CYP11B2* expression and of miR-320a-3p on *CYP11A1* and *CYP17A1* expression.

MiRNA regulation of cholesterol supply to the steroidogenic pathway, mediated by the steroidogenic acute regulatory (StAR) protein, may also be of importance, and this was reported to be the case in the mouse adrenocortical cell line Y1, where *StAR* mRNA is directly targeted by miR-132 (Hu, Shen, Kraemer, & Azhar, 2017).

Looking beyond the steroidogenic pathway itself, studies have also examined miRNA effects on components of the major regulatory systems that control aldosterone secretion including, most importantly, the RAAS (see above). AngII increases blood pressure by direct vasoconstriction, stimulation of aldosterone secretion from the zona glomerulosa, and increased sodium and water reabsorption via actions on the nephron (Riet et al., 2015). Several studies show the RAAS system to be regulated by miRNAs—and vice versa—with miRNAs involved at every stage of the RAAS cascade (Butterworth & Rosa, 2019).

One of the earliest studies of miRNA and aldosterone by Romero and colleagues showed that stimulation of H295R cells with AngII increased miR-21 expression. Overexpression of miRNA-21 in H295R was found to increase aldosterone levels and cell proliferation, suggestive of a role for this miRNA in RAAS regulation of aldosterone secretion (Romero, Plonczynski, Carvajal, Gomez-Sanchez, & Gomez-Sanchez, 2008).

Looking at renin regulation, studies of the HEK293 kidney cell line showed miR-181a and miR-663 to be capable of binding the 3′-UTR of *REN* mRNA to regulate its expression. Levels of these two miRNAs are reduced in the kidneys of hypertensive patients relative to their normotensive counterparts (Marques et al., 2011). A subsequent study involving transfection of mouse kidneys with miR-181a mimic reported significant reduction in renin mRNA levels and diastolic blood pressure (Jackson et al., 2020).

Work by Kemp et al. showed miR-483-3p to be capable of regulating the RAAS at multiple points. Luciferase reporter gene analysis demonstrated that this miRNA can act directly on the 3′-UTRs of mRNA encoding angiotensinogen, ACE-1, ACE-2 and the receptor AT2R; the inhibitory effects of miR-483-3p was reversed by the presence of its antagomir (Kemp et al., 2014). This ability to influence the RAAS pathway at so many points is suggestive of potentially significant roles for even single miRNAs within a complex system, but each component is likely to have multiple regulators, as is known to be the case for ACE1 and ACE2 (Boettger et al., 2009; Chen, Xu, Yu, Chang, & Zhong, 2015; Gu et al., 2014; Lambert et al., 2014). Given their roles at multiple stages of the RAAS, Butterworth argues persuasively that miRNAs fine-tune protein levels in aldosterone-responsive cells and integrating the signals created by aldosterone action at multiple levels in order to provide a feedback mechanism that ultimately dampens its effects (Butterworth & Rosa, 2019; Butterworth, 2015).

A recent study by Novák et al. (2022) investigated the polymorphism rs7079 located in the 3'UTR of the angiotensinogen (AGT) gene and its possible links to coronary artery disease. Comparison showed patients of CC genotype displayed CAD symptoms at an earlier age than those with AA and CA genotypes, and also were more likely to present with restenosis (Novák et al., 2022). The authors suggested a link to previous studies which demonstrated that binding of miR-31 and miR-584 at the area encompassing this SNP was stronger for the C allele than for the A allele (Mopidevi, Ponnala, & Kumar, 2013; Wu et al., 2019). They hypothesised that stronger binding of these miRNAs in CC individuals might leave less available for regulating expression of nitric oxide synthase, but this will require further study. Regardless, it directs us to consider the effect of polymorphic variation on the efficiency of miRNA targeting.

The role of miRNA-136 in the development of hypertension (EH) and its potential use as a biomarker for the diagnosis of essential hypertension was investigated by Chu et al. Levels of miRNA-136 were found to be decreased in the peripheral blood of essential hypertensive patients when compared to healthy controls (Chu, Li, Jia, Diao, & Li, 2020). The study also found that serum levels of RAAS biomarkers (ACE activity, renin, Ang II, and aldosterone) were upregulated in patients with EH compared to healthy subjects. A negative correlation was observed between microRNA-136 levels and those of RAAS biomarkers, indicating that microRNA-136 may have an overall inhibitory effect on the RAAS system and therefore play a role in the development of primary hypertension. However, it appears unlikely that this would be due to a direct effect of miRNA-136 on each of these RAAS elements and no evidence is supplied to support this. Furthermore, it is not clear whether this correlation is causative.

In conclusion, it is apparent that miRNAs participate in the regulation of aldosterone secretion at many levels. The picture that is emerging is complex and still only partial, but it does point to a significant role for miRNA in determining circulating aldosterone levels.

4. The role of microRNA in aldosterone action

In addition to their effects on its production, miRNAs are also important effectors of aldosterone action with the ability to target multiple genes within a single pathway. The primary receptor and effector of classical

aldosterone action is the mineralocorticoid receptor (MR). Mechanisms of aldosterone action are broadly defined as being of two types: genomic or rapid non-genomic. Genomic effects of aldosterone begin with the binding, dimerisation and translocation of MR to the nucleus. Acting as a transcription factor, MR then mediates the regulation of hundreds of genes to promote water and sodium reabsorption in the kidney. Rapid non-genomic actions of aldosterone, on the other hand, can occur in either an MR-dependent or independent manner via protein-protein interactions, ions and reactive oxygen species (Parksook & Williams, 2023).

While the MR is highly distributed throughout kidney epithelia, it is also expressed in the vasculature (McCurley et al., 2012), heart (Mihailidou, Le, Mardini, & Funder, 2009), brain (Gomez-Sanchez, Gomez-Sanchez, Plonczynski, & Gomez-Sanchez, 2010) and adipose tissue (Caprio et al., 2007), so consequences of aldosterone action can also be sought in these tissues. Expression of the MR itself is known to be regulated by miRNA, with hundreds of predicted miRNA binding sites located across its large 3′ untranslated region. Moreover, the MR—in its role as transcription factor—can initiate or repress the production of aldosterone-sensitive miRNAs.

The significant role of miRNAs in the execution of aldosterone action has been highlighted in several in vitro and in vivo studies that encompass the traditional role of aldosterone and the MR in the maintenance of salt/water homeostasis in the kidney and vasculature as well as additional roles in the heart and brain. In the brain, aldosterone has diverse effects ranging from memory, learning and mood to salt appetite and baroreceptor reflex. Although conferring a subtle effect, altered expression of miRNAs and dysregulation of aldosterone action has been observed in models of cardiovascular disease. However, there remain gaps and contradictions in the current literature regarding miRNA regulation of aldosterone action. Further validation studies of miRNA targeting, and action are vital to fully elucidating the role of miRNAs in aldosterone action and the extent of their effect (not least in the many MR-expressing cell types and tissues not represented below), but the most significant findings to date are summarised in the following sections.

4.1 Renal

Several studies have demonstrated the regulation of aldosterone effectors including epithelial sodium channel (ENaC) by aldosterone-sensitive miRs. The miR-23-24-27 cluster is highly responsive to aldosterone stimulation, with

increased expression enhancing Na^+ transport in a mouse cortical collecting duct cell line. miR-27 was found to have the greatest impact on ENaC action; membrane tracking protein intersectin-2 (Itsn-2) was identified as a potential target of miR-27, but further research is needed to fully delineate this relationship (Liu et al., 2017). Similarly, levels of miR-335-3p, miR-290-5p and miR-1983 are decreased in the mouse cortical collecting duct with a concomitant reduction in ENaC-mediated sodium transport (Edinger et al., 2014). Two independent studies have found levels of the miR-466 family to be decreased upon aldosterone stimulation of a mouse cortical collecting duct cell line; MR and SGK1 are direct targets of miR-466. Inhibition of miR-466 in mouse kidney cortical collecting duct epithelial cells significantly increased MR and SGK1 protein expression resulting in elevated ENaC transport (Jacobs et al., 2016; Ozbaki-Yagan, Liu, Bodnar, Ho, & Butterworth, 2020). This is supported by in vivo experiments that increased miR-466 levels in the distal nephrons of mice on low Na^+ diet. Overall, these studies demonstrate the importance of miRNAs in renal homeostasis and sodium/water balance, dysregulation of which results in disease.

Aldosterone is well-established as being pro-fibrotic and several studies having demonstrated a plausible role for miRNAs in potentiating these effects. In the kidney, miR-34c-5p levels increased significantly with aldosterone treatment. Several predicted target genes of miR-34c-5p are members of the Wnt/b-catenin signalling pathway, responsible for driving fibrosis and calcium release (Park et al., 2018). Calcification is a hallmark of end-stage renal disease, with aldosterone-specific miRNAs shown to contribute to vascular smooth muscle cell (VSMC) calcification. Similar to its role in fibrosis, overexpression of miR-34-b/c ameliorated aldosterone-induced VSMC calcification (Hao, Zhang, Cong, Ren, & Hao, 2016). The MR as a transcription factor has also been shown to promote production of the long non-coding RNA TUG1 in human kidney cells. TUG1 binds and suppresses miR-29b-3p, resulting in increased extracellular matrix deposition and fibrosis. This highlights the potential of MR to regulate miRNAs while also being subject to miRNA regulation (Zhang et al., 2021). In diabetic kidney disease, miR-16-5p promotes fibroblast activation in patients' kidneys. Aldosterone does not achieve this by direct activation of fibroblasts: rather, epithelial-derived extracellular vesicles containing an enriched cargo that highly expresses miR-196b-5p have been shown to activate the fibroblasts (Hu et al., 2020). Taken together, these miRNAs regulate several pathways driving aldosterone-induced renal fibrosis.

4.2 Cardiac

MiRNAs have been shown to maintain cardiac function and dysregulation of their levels have been implicated in several cardiac pathologies including cardiac hypertrophy, fibrosis, myocardial infarction, and atrial fibrillation. MiR-181 is a potential regulatory miRNA of the aldosterone-MR pathway. Overexpression of miR-181 by AAV9 delivery post-MI improves cardiac function and decreases cardiomyocyte size, with in vivo knock-out models resulting in impaired cardiac function and pathogenic remodelling. This suggests a cardioprotective role for the aldosterone-sensitive miR-181 (Garg et al., 2020). MiR-21 is well-defined as having an essential role in cardiac pathophysiologies, showing sensitivity to aldosterone in both an MR-dependent and independent manner (Kumarswamy, Volkmann, & Thum, 2011). Expression of miR-21 is typically low in the heart but is upregulated with end-stage heart disease and atrial fibrillation. Aldosterone stimulates cardiac miR-21 expression, which confers a potentially cardioprotective effect. Several studies show that downregulation of miR-21 exacerbates cardiac dysfunction in models of aldosterone excess (Ball et al., 2017). Moreover, complete genetic ablation increases cardiac hypertrophy with poor outcomes in models of hypertension (Syed et al., 2018). Conversely, miR-21 has been shown to enhance pathogenic remodelling and fibrosis in atrial fibrillation by downregulation of anti-fibrotic Sprouty-1 in cardiac fibroblasts (Lavall et al., 2014). Due to the involvement of miR-21 in fibrosis its levels are often measured as a marker of fibrosis. Indeed, several studies have demonstrated reduction in miR-21 to be a marker for anti-fibrotic effects, as observed in treatment with aldosterone synthesis antagonist torsemide (Adam et al., 2015) and MR antagonist finerenone (Lavall et al., 2019), where pathogenic remodelling and fibrosis were inhibited.

4.3 Vascular

Aldosterone and the MR have essential roles in maintaining sodium water balance, disruption of which results in increased blood volume and hypertension that damages the vasculature. Hypertension is the single most important risk factor for cardiovascular disease with miRNAs conferring a subtle but significant effect on blood pressure regulation. 3'-UTR luciferase reporter gene construct studies showed miRNAs miR-124-3p and miR-135-5p directly bind MR-encoding *NR3C2* mRNA. However, as no change was observed in levels of *NR3C2* mRNA this regulation is thought to occur through translational inhibition of the MR. Both miR-124-3p and miR-135-5p are significantly downregulated in the

plasma of hypertensive patients. When levels of miR-124-3p and miR-135-5p expression were increased following inhibition of lncRNA MALAT1 in HUVEC cells, MR protein levels were reduced and cell proliferation was inhibited (Luo, Wang, Hu, & Wu, 2020; Sõber, Laan, & Annilo, 2010).

Resistant hypertension is high blood pressure that responds poorly to treatment and is commonly observed in patients with elevated plasma aldosterone. In a comparison of resistant hypertension relative to essential hypertension, miR-21 was found to be significantly upregulated and to correlate with plasma aldosterone levels (Kara et al., 2021). However, no underlying molecular mechanism has been described.

MiR-155 is identified as a profoundly dysregulated miRNA in ageing mouse vessels. Increased MR levels within resistance vessels have been linked to the observed decrease in vascular miR-155 and also to rises in the vascular expression of calcium channel Cav1.2 and angiotensin II receptor type 1 (Kara et al., 2021). In the vasculature miR-29b has been highlighted as a regulator of the VSMC phenotype switch, promoting migration and proliferation associated with aldosterone-induced vascular remodelling during hypertension. However, the effect was found to be exclusive to VSMCs with no change in endothelial cells, indicating a cell-specific impact of aldosterone on the vasculature (Bretschneider et al., 2016).

4.4 Brain

MR is highly distributed throughout the brain, with its highest concentrations in the hippocampus and amygdala. Brain MR is thought to hold dual roles, involving cognitive function, memory and behaviour within the limbic system and vasopressin release, salt appetite and baroreceptor response in the brain stem (Paul, Wingenfeld, Otte, & Meijer, 2022). In the brain, corticosterone is the primary MR ligand but aldosterone binding still occurs at highly aldosterone-selective MR in the brain stem. MiRs-135a-5p and miR-135b-5p have been highlighted as negative regulators of brain MR with roles in stress response and post-stroke outcomes. In the amygdala, miR-135-5p and miR-124-3p directly binding *NR3C2* mRNA alters MR expression. In response to stress, these miRs are negatively regulated, resulting in inappropriate MR expression and a potential role in early stress response (Mannironi et al., 2013). MiR-124-3p is a neuronal-specific miR, implying its role in the aldosterone action and regulation of MR is confined to the brain. In the context of stroke, miR-135a-5p was identified as neuroprotective, attenuating oxidative stress, inflammation, and apoptosis in oxygen-glucose

deprivation models of stroke (Wang & Hu, 2021). Similar effects were seen with the delivery of miR-135b-5p to rodent stroke models; its overexpression alleviated post-stroke cognitive dysfunction, inflammation, and neuronal apoptosis (Huang, Wang, & Ouyang, 2020). Finally, miR-766-3p was found to negatively regulate *NR3C2*. Sponging of miR-776-3p by long non-coding RNA exacerbates cerebral ischaemia, suggesting that MR, potentially regulated by miR-776-3p, propagates ischaemic damage (Cai et al., 2019).

5. Circulating microRNAs and their role in aldosterone-associated diagnostics

The studies detailed above clearly demonstrate firstly a role for miRNAs in the regulation of aldosterone secretion by the adrenal gland and, secondly, that dysregulation of miRNA levels in various tissues results from aldosterone excess and its associated effects. These findings add weight to the hypothesis that circ-miRNA levels, resulting from the passage of miRNAs from these tissues into the bloodstream—either actively or passively—might represent a viable biomarker in the diagnosis of conditions associated with aldosterone dysregulation, most notably PA.

There is no doubt that improved tools are required in order to identify and treat the potentially huge number of individuals currently believed to be at increased cardiovascular risk owing to undiagnosed aldosterone excess. In spite of the advances made over the last decade in identifying the mutations that drive aldosterone-producing adenoma, there is a systemic failure to screen hypertensive patients for PA, which is compounded by the fact that such screening and confirmatory tests are protracted and technically demanding, limiting the numbers that can realistically be diagnosed (Funder, 2021). The development of a more straightforward, biomarker-based test would deliver considerable health and economic benefits for this readily treatable condition. Biomarkers are required to be highly specific and sensitive for the condition being tested while also being readily sampled from accessible tissues or bodily fluids and accurately detected by reliable assays. Confirmation of the stability of cir-miRNA in plasma and serum established the principle that these nucleic acids could serve as biomarkers for cancers (Mitchell et al., 2008) or, by extension, any condition that results in disruption to the miRNA transcriptome, including diabetes, Alzheimer's disease and cardiovascular disease in its various forms, including hypertension (Wu et al., 2021).

For conditions relating to the adrenal cortex and/or disruption of aldosterone secretion and action, such as PA, the initial challenge is to confirm whether changes at the local tissue level lead to detectable and reproducible changes to levels of specific miRNAs in the circulation. At the simplest level, Kara et al. were able to establish a positive correlation between levels of aldosterone and circulating miR-21 levels ($p < 0.05$; $r = 0.339$) in a study population consisting of newly-diagnosed hypertensives, resistant hypertensives and healthy controls (Kara et al., 2021). In their small population of resistant hypertensives ($n = 20$), cir-miRNA-21 levels alone could predict resistant hypertension with a 95% sensitivity and 71% specificity. This finding tallies with a large body of previous research that links hsa-miR-21 expression to hypertension (Li, Wei, & Wang, 2018).

Although such demonstrations of single miRNA associations with aldosterone-related characteristics have value, it is likely that any truly viable diagnostic tool will combine measurement of multiple 'feature' cir-miRNAs into a defined signature that can dramatically improve the diagnostic sensitivity and specificity achievable with just a single biomarker. This was the rationale behind the ENSAT-HT project, which sought to assemble the most informative diagnostic signature for a range of endocrine hypertension conditions from a variety of biological measurements or 'omics' (e.g. urine and plasma steroids, circulating miRNAs, plasma small metabolites, etc.). Owing to the complexity of such a multiomic approach, machine learning was utilised in order to define the most informative diagnostic signatures from the extremely large number of possible combinations. Specifically, the study sought to generate diagnostic multiomics signatures that distinguish essential hypertension patients from those with pheochromocytoma/functional paraganglioma (PPGL), Cushing's syndrome and—of greatest relevance here—PA. Definition of such a biomarker-based signature able to distinguish essential hypertensives from those with PA would clearly be of great benefit in addressing the current low diagnosis rate—and therefore effective treatment—for PA. Our role in this project was to use a realtime quantitative RT-PCR-based approach to quantify 173 potential feature circ-miRNAs, the most informative of which would be incorporated into the machine learning-generated signatures. For the initial 'retrospective' stage of the study, circ-miRNAs and the other omic measurements were conducted in 108 essential hypertensive patients and 100 PA patients (in addition to PPGL, Cushing's syndrome and normotensive participants). This generated an optimal multiomic signature capable of distinguishing PA from essential hypertension with a sensitivity of 95% and a specificity of 85.7% (balanced accuracy: 90.4%); this signature included 15 feature circ-miRNAs alongside

other omic measurements (Reel et al., 2022). Utilising only circ-miRNA data, the optimal signature for essential hypertension vs. PA achieved a sensitivity of 95% and specificity of 76.2% (balanced accuracy: 85.6%); this model incorporated measurements of 27 feature circ-miRNAs. Cir-miRNAs common to both of these signatures include hsa-miR-660-5p, hsa-miR-363-3p, hsa-miR-328-3p, hsa-miR-32-5p, hsa-miR-25-3p, hsa-miR-19a-3p, hsa-miR-19b-3p, hsa-miR-185-5p, hsa-miR-16-5p, hsa-miR-15a-5p, hsa-miR-15b-3p, hsa-miR-155-5p, hsa-let-7d-3p and hsa-let-7b-5p. Of these, hsa-miR-15a-5p has previously been reported to circulate at higher levels in patients with hypertension relative to those with hypertension and chronic kidney disease (Nandakumar et al., 2017) but, based on the existing literature, no obvious associations of these miRNAs with PA-related pathways is apparent, due probably in large part to the lack of prior research on this topic. Detailed bioinformatic pathway analysis of these findings is now ongoing to establish and prioritise further research into these miRNAs. The reproducibility of these findings has also been tested under the 'prospective' phase of the ENSAT-HT project and results are currently being analysed ahead of publication. While there is undoubted potential in using circ-miRNAs as diagnostic biomarkers, their successful and widespread utilisation rests on overcoming various technical limitations such as normalisation of data and accurate, reproducible measurement of markers that show relatively small dynamic range while performing cost-effective assays that can be performed on equipment available to the majority of clinical laboratories (MacKenzie et al., 2021). Studies over the next few years will play a large part in determining the practicality of this approach, and will include the HT-ADVANCE project, which started in 2023 and tests the ENSAT-HT diagnostic signature within a clinical trial setting.

A more specific approach to diagnosing PA has been taken by Decmann et al. who sought to distinguish two of its distinct subtypes, APA and BAH, using circ-miRNA. Initial RNA-seq of 16 APA and 14 BAH patients initially identified 50 differentially-expressed circ-miRNAs. Validation of 4 of the most statistically significant of these using the more robust quantitative realtime RT-PCR methodology in a further 93 samples confirmed upregulation of hsa-mir-30e-5p, hsa-miR-30d-5p and hsa-miR-7-5p in BAH relative to APA (Decmann et al., 2019). Individually, each of these was shown by ROC analysis to have specificities and sensitivities of approximately 60% when distinguishing BAH from APA, although it is not clear to what extent these figures could be improved by combining these circ-miRNAs into a single diagnostic test, possibly alongside others of the initial 50 miRNAs that might be validated by RT-PCR. The authors

noted that previous studies that have highlighted these 3 miRNAs have unclear relevance to the pathogenesis of PA, but this probably speaks as much to the general lack of miRNA research in this area as anything else.

Of course, the potential value of such circ-miRNAs lies not only in their diagnostic use but also in what they might tell us about the development and progression of PA. Future study will not only centre on which cir-miRNAs are dysregulated in PA but why that is the case and what—if any—impact these have on the regulation of aldosterone excess or its actions on various target tissues. While such effects can only be confirmed through careful verification of these effects both in vitro and in vivo, bioinformatic analysis also has a major role to play in helping to direct and focus such studies on those microRNAs, tissues and pathways most likely to be of consequence. Further interest and complication will arise as we learn more of circulating microRNAs and the relative extent to which they are the result of leakage from dying cells or the product of active secretion; the latter raises the prospect, already demonstrated in certain circumstances (Shan et al., 2015), that circ-miRNAs may be components of a hormone-like signalling system, secreted from one tissue and then carried by the circulation to target organs where they can act (Bär, Thum, & Gonzalo-Calvo, 2019). Whether the levels of such miRNAs in the circulation are truly capable of significant physiological action remains to be seen but is a live and highly interesting topic for investigation.

References

Adam, O., Zimmer, C., Hanke, N., Hartmann, R. W., Klemmer, B., Böhm, M., & Laufs, U. (2015). Inhibition of aldosterone synthase (CYP11B2) by torasemide prevents atrial fibrosis and atrial fibrillation in mice. *Journal of Molecular and Cellular Cardiology, 85*, 140–150. https://doi.org/10.1016/j.yjmcc.2015.05.019.

Adcock, I. M., & Caramori, G. (2009). *Asthma and COPD. Part IV: Inflammatory Mediators and Pathways* (2nd ed.,). 373–380. https://doi.org/10.1016/b978-0-12-374001-4.00031-6.

Åkerström, T., Maharjan, R., Willenberg, H. S., Cupisti, K., Ip, J., Moser, A., ... Björklund, P. (2016). Activating mutations in CTNNB1 in aldosterone producing adenomas. *Scientific Reports, 6*(1), 19546. https://doi.org/10.1038/srep19546.

Alles, J., Fehlmann, T., Fischer, U., Backes, C., Galata, V., Minet, M., ... Meese, E. (2019). An estimate of the total number of true human miRNAs. *Nucleic Acids Research, 47*(7), 3353–3364. https://doi.org/10.1093/nar/gkz097.

Ambros, V., Bartel, B., Bartel, D. P., Burge, C. P., Carrington, J. C., Chen, X., ... Tuschl, T. (2003). A uniform system for microRNA annotation. *RNA (New York, N. Y.), 9*(3), 277–279. https://doi.org/10.1261/rna.2183803.

Azhar, S., Dong, D., Shen, W.-J., Hu, Z., & Kraemer, F. B. (2019). The role of miRNAs in regulating adrenal/gonadal steroidogenesis. *Journal of Molecular Endocrinology, 1*(aop), R21–R43. https://doi.org/10.1530/jme-19-0105.

Azizan, E. A. B., Poulsen, H., Tuluc, P., Zhou, J., Clausen, M. V., Lieb, A., ... Brown, M. J. (2013). Somatic mutations in ATP1A1 and CACNA1D underlie a common subtype of adrenal hypertension. *Nature Genetics, 45*(9), 1055–1060. https://doi.org/10.1038/ng.2716.

Ball, J. P., Syed, M., Marañon, R. O., Hall, M. E., KC, R., Reckelhoff, J. F., ... Romero, D. G. (2017). Role and regulation of microRNAs in aldosterone-mediated cardiac injury and dysfunction in male rats. *Endocrinology, 158*(6), 1859–1874. https://doi.org/10.1210/en.2016-1707.

Bandulik, S., Penton, D., Barhanin, J., & Warth, R. (2010). TASK1 and TASK3 potassium channels: Determinants of aldosterone secretion and adrenocortical zonation. *Hormone and Metabolic Research, 42*(06), 450–457. https://doi.org/10.1055/s-0029-1243601.

Bär, C., Thum, T., & Gonzalo-Calvo, D. de (2019). Circulating miRNAs as mediators in cell-to-cell communication. *Epigenomics, 11*(2), 111–113. https://doi.org/10.2217/epi-2018-0183.

Barrera-Chimal, J., Bonnard, B., & Jaisser, F. (2022). Roles of mineralocorticoid receptors in cardiovascular and cardiorenal diseases. *Annual Review of Physiology, 84*(1), 585–610. https://doi.org/10.1146/annurev-physiol-060821-013950.

Behm-Ansmant, I., Rehwinkel, J., Doerks, T., Stark, A., Bork, P., & Izaurralde, E. (2006). mRNA degradation by miRNAs and GW182 requires both CCR4:NOT deadenylase and DCP1:DCP2 decapping complexes. *Genes & Development, 20*(14), 1885–1898. https://doi.org/10.1101/gad.1424106.

Beuschlein, F., Boulkroun, S., Osswald, A., Wieland, T., Nielsen, H. N., Lichtenauer, U. D., ... Reincke, M. (2013). Somatic mutations in ATP1A1 and ATP2B3 lead to aldosterone-producing adenomas and secondary hypertension. *Nature Genetics, 45*(4), 440–444. https://doi.org/10.1038/ng.2550.

Boettger, T., Beetz, N., Kostin, S., Schneider, J., Krüger, M., Hein, L., & Braun, T. (2009). Acquisition of the contractile phenotype by murine arterial smooth muscle cells depends on the Mir143/145 gene cluster. *Journal of Clinical Investigation, 119*(9), 2634–2647. https://doi.org/10.1172/jci38864.

Bretschneider, M., Busch, B., Mueller, D., Nolze, A., Schreier, B., Gekle, M., & Grossmann, C. (2016). Activated mineralocorticoid receptor regulates micro-RNA-29b in vascular smooth muscle cells. *FASEB Journal: Official Publication of the Federation of American Societies for Experimental Biology, 30*(4), 1610–1622. https://doi.org/10.1096/fj.15-271254.

Buffolo, F., Tetti, M., Mulatero, P., & Monticone, S. (2022). Aldosterone as a mediator of cardiovascular damage. *Hypertension, 79*(9), 1899–1911. https://doi.org/10.1161/hypertensionaha.122.17964.

Butterworth, M. B. (2015). MicroRNAs and the regulation of aldosterone signaling in the kidney. *American Journal of Physiology. Cell Physiology, 308*(7), C521–C527. https://doi.org/10.1152/ajpcell.00026.2015.

Butterworth, M. B., & Rosa, D. A. D. L. (2019). Regulation of aldosterone signaling by microRNAs. *Vitamins and Hormones, 109*, 69–103. https://doi.org/10.1016/bs.vh.2018.09.002.

Cai, J., Shangguan, S., Li, G., Cai, Y., Chen, Y., Ma, G., ... Deng, Y. (2019). Knockdown of lncRNA Gm11974 protect against cerebral ischemic reperfusion through miR-766-3p/NR3C2 axis. *Artificial Cells, Nanomedicine, and Biotechnology, 47*(1), 3847–3853. https://doi.org/10.1080/21691401.2019.1666859.

Caprio, M., Fève, B., Claës, A., Viengchareun, S., Lombès, M., & Zennaro, M.-C. (2007). Pivotal role of the mineralocorticoid receptor in corticosteroid-induced adipogenesis. *The FASEB Journal, 21*(9), 2185–2194. https://doi.org/10.1096/fj.06-7970com.

Chen, L.-J., Xu, R., Yu, H.-M., Chang, Q., & Zhong, J.-C. (2015). The ACE2/Apelin signaling, microRNAs, and hypertension. *International Journal of Hypertension, 2015*, 896861. https://doi.org/10.1155/2015/896861.

Choi, M., Scholl, U. I., Yue, P., Björklund, P., Zhao, B., Nelson-Williams, C., ... Lifton, R. P. (2011). K+ Channel mutations in adrenal aldosterone-producing adenomas and hereditary hypertension. *Science (New York, N. Y.), 331*(6018), 768–772. https://doi.org/10.1126/science.1198785.

Chu, H.-T., Li, L., Jia, M., Diao, L.-L., & Li, Z.-B. (2020). Correlation between serum microRNA-136 levels and RAAS biochemical markers in patients with essential hypertension. *European Review for Medical and Pharmacological Sciences, 24*(22), 11761–11767. https://doi.org/10.26355/eurrev_202011_23828.

Connell, J. M. C., & Davies, E. (2005). The new biology of aldosterone. *Journal of Endocrinology, 186*(1), 1–20. https://doi.org/10.1677/joe.1.06017.

Connell, J. M. C., MacKenzie, S. M., Freel, E. M., Fraser, R., & Davies, E. (2008). A lifetime of aldosterone excess: Long-term consequences of altered regulation of aldosterone production for cardiovascular function. *Endocrine Reviews, 29*(2), 133–154. https://doi.org/10.1210/er.2007-0030.

Decmann, A., Nyírö, G., Darvasi, O., Turai, P., Bancos, I., Kaur, R. J., ... Igaz, P. (2019). Circulating miRNA expression profiling in primary aldosteronism. *Frontiers in Endocrinology, 10*, 739. https://doi.org/10.3389/fendo.2019.00739.

Douma, S., Petidis, K., Doumas, M., Papaefthimiou, P., Triantafyllou, A., Kartali, N., ... Zamboulis, C. (2008). Prevalence of primary hyperaldosteronism in resistant hypertension: A retrospective observational study. *The Lancet, 371*(9628), 1921–1926. https://doi.org/10.1016/s0140-6736(08)60834-x.

Dutta, R. K., Arnesen, T., Heie, A., Walz, M., Alesina, P., Söderkvist, P., & Gimm, O. (2019). A somatic mutation in CLCN2 identified in a sporadic aldosterone-producing adenoma. *European Journal of Endocrinology, 181*(5), K37–K41. https://doi.org/10.1530/eje-19-0377.

Edinger, R. S., Coronnello, C., Bodnar, A. J., LaFramboise, W. A., Benos, P. V., Ho, J., ... Labarca, M. (2014). Aldosterone regulates microRNAs in the cortical collecting duct to alter sodium transport. *Journal of the American Society of Nephrology: JASN, 25*(11), 2445–2457. https://doi.org/10.1681/asn.2013090931.

Fernandes-Rosa, F. L., Boulkroun, S., & Zennaro, M.-C. (2020). Genetic and genomic mechanisms of primary aldosteronism. *Trends in Molecular Medicine, 26*(9), 819–832. https://doi.org/10.1016/j.molmed.2020.05.005.

Friedman, R. C., Farh, K. K.-H., Burge, C. B., & Bartel, D. P. (2009). Most mammalian mRNAs are conserved targets of microRNAs. *Genome Research, 19*(1), 92–105. https://doi.org/10.1101/gr.082701.108.

Funder, J. (2021). Primary aldosteronism. *Trends in Cardiovascular Medicine, 32*(4), 228–233. https://doi.org/10.1016/j.tcm.2021.03.005.

Funder, J. W., Carey, R. M., Mantero, F., Murad, M. H., Reincke, M., Shibata, H., ... Young, W. F. (2016). The management of primary aldosteronism: Case detection, diagnosis, and treatment: An Endocrine Society Clinical Practice guideline. *The Journal of Clinical Endocrinology & Metabolism, 101*(5), 1889–1916. https://doi.org/10.1210/jc.2015-4061.

Gallo-Payet, N. (2016). 60 YEARS OF POMC: Adrenal and extra-adrenal functions of ACTH. *Journal of Molecular Endocrinology, 56*(4), T135–T156. https://doi.org/10.1530/jme-15-0257.

Garg, A., Foinquinos, A., Jung, M., Janssen-Peters, H., Biss, S., Bauersachs, J., ... Thum, T. (2020). MiRNA-181a is a novel regulator of aldosterone–mineralocorticoid receptor-mediated cardiac remodelling. *European Journal of Heart Failure, 22*(8), 1366–1377. https://doi.org/10.1002/ejhf.1813.

Gomez-Sanchez, E. P., Gomez-Sanchez, C. M., Plonczynski, M., & Gomez-Sanchez, C. E. (2010). Aldosterone synthesis in the brain contributes to Dahl salt-sensitive rat hypertension. *Experimental Physiology, 95*(1), 120–130. https://doi.org/10.1113/expphysiol.2009.048900.

Gu, Q., Wang, B., Zhang, X.-F., Ma, Y.-P., Liu, J.-D., & Wang, X.-Z. (2014). Contribution of renin–angiotensin system to exercise-induced attenuation of aortic remodeling and improvement of endothelial function in spontaneously hypertensive rats. *Cardiovascular Pathology, 23*(5), 298–305. https://doi.org/10.1016/j.carpath.2014.05.006.

Ha, M., & Kim, V. N. (2014). Regulation of microRNA biogenesis. *Nature Reviews. Molecular Cell Biology, 15*(8), 509–524. https://doi.org/10.1038/nrm3838.

Han, J., Lee, Y., Yeom, K.-H., Kim, Y.-K., Jin, H., & Kim, V. N. (2004). The Drosha-DGCR8 complex in primary microRNA processing. *Genes & Development, 18*(24), 3016–3027. https://doi.org/10.1101/gad.1262504.

Hannemann, A., & Wallaschofski, H. (2011). Prevalence of primary aldosteronism in patient's cohorts and in population-based studies–A review of the current literature. *Hormone and Metabolic Research = Hormon- Und Stoffwechselforschung = Hormones et Metabolisme, 44*(3), 157–162. https://doi.org/10.1055/s-0031-1295438.

Hao, J., Zhang, L., Cong, G., Ren, L., & Hao, L. (2016). MicroRNA-34b/c inhibits aldosterone-induced vascular smooth muscle cell calcification via a SATB2/Runx2 pathway. *Cell and Tissue Research, 366*(3), 733–746. https://doi.org/10.1007/s00441-016-2469-8.

Hu, R., Li, X., Peng, C., Gao, R., Ma, L., Hu, J., ... Yang, S. (2020). miR-196b-5p-enriched extracellular vesicles from tubular epithelial cells mediated aldosterone-induced renal fibrosis in mice with diabetes. *BMJ Open Diabetes Research & Care, 8*(1), e001101. https://doi.org/10.1136/bmjdrc-2019-001101.

Hu, Z., Shen, W.-J., Kraemer, F. B., & Azhar, S. (2017). Regulation of adrenal and ovarian steroidogenesis by miR-132. *Journal of Molecular Endocrinology, 59*(3), 269–283. https://doi.org/10.1530/jme-17-0011.

Huang, W. (2017). MicroRNAs: Biomarkers, diagnostics, and therapeutics. *Methods in Molecular Biology (Clifton, N. J.), 1617*, 57–67. https://doi.org/10.1007/978-1-4939-7046-9_4.

Huang, Y., Wang, Y., & Ouyang, Y. (2020). Elevated microRNA-135b-5p relieves neuronal injury and inflammation in post-stroke cognitive impairment by targeting NR3C2. *International Journal of Neuroscience, 132*(1), 58–66. https://doi.org/10.1080/00207454.2020.1802265.

Huntzinger, E., & Izaurralde, E. (2011). Gene silencing by microRNAs: Contributions of translational repression and mRNA decay. *Nature Reviews. Genetics, 12*(2), 99–110. https://doi.org/10.1038/nrg2936.

Jackson, K. L., Gueguen, C., Lim, K., Eikelis, N., Stevenson, E. R., Charchar, F. J., ... Head, G. A. (2020). Neural suppression of miRNA-181a in the kidney elevates renin expression and exacerbates hypertension in Schlager mice. *Hypertension Research, 43*(11), 1152–1164. https://doi.org/10.1038/s41440-020-0453-x.

Jacobs, M. E., Kathpalia, P. P., Chen, Y., Thomas, S. V., Noonan, E. J., & Pao, A. C. (2016). SGK1 regulation by miR-466g in cortical collecting duct cells. *American Journal of Physiology-Renal Physiology, 310*(11), F1251–F1257. https://doi.org/10.1152/ajprenal.00024.2016.

Jiang, Y., Wang, H., Cao, H., Wang, C., Zhang, L., Wang, H., ... Cai, J. (2014). Peripheral blood miRNAs as a biomarker for chronic cardiovascular diseases. *Scientific Reports, 4*(1), 5026. https://doi.org/10.1038/srep05026.

Jo, M. H., Shin, S., Jung, S.-R., Kim, E., Song, J.-J., & Hohng, S. (2015). Human Argonaute 2 has diverse reaction pathways on target RNAs. *Molecular Cell, 59*(1), 117–124. https://doi.org/10.1016/j.molcel.2015.04.027.

Kara, S. P., Ozkan, G., Yılmaz, A., Bayrakçı, N., Güzel, S., & Geyik, E. (2021). MicroRNA 21 and microRNA 155 levels in resistant hypertension, and their relationships with aldosterone. *Renal Failure, 43*(1), 676–683. https://doi.org/10.1080/0886022x.2021.1915800.

Kawamata, T., & Tomari, Y. (2010). Making RISC. *Trends in Biochemical Sciences, 35*(7), 368–376. https://doi.org/10.1016/j.tibs.2010.03.009.

Kemp, J. R., Unal, H., Desnoyer, R., Yue, H., Bhatnagar, A., & Karnik, S. S. (2014). Angiotensin II-regulated microRNA 483-3p directly targets multiple components of the renin-angiotensin system. *Journal of Molecular and Cellular Cardiology, 75*, 25–39. https://doi.org/10.1016/j.yjmcc.2014.06.008.

Kumarswamy, R., Volkmann, I., & Thum, T. (2011). Regulation and function of miRNA-21 in health and disease. *RNA Biology, 8*(5), 706–713. https://doi.org/10.4161/rna.8.5.16154.

Lambert, D. W., Lambert, L. A., Clarke, N. E., Hooper, N. M., Porter, K. E., & Turner, A. J. (2014). Angiotensin-converting enzyme 2 is subject to post-transcriptional regulation by miR-421. *Clinical Science, 127*(4), 243–249. https://doi.org/10.1042/cs20130420.

Lavall, D., Jacobs, N., Mahfoud, F., Kolkhof, P., Böhm, M., & Laufs, U. (2019). The non-steroidal mineralocorticoid receptor antagonist finerenone prevents cardiac fibrotic remodeling. *Biochemical Pharmacology, 168*, 173–183. https://doi.org/10.1016/j.bcp.2019.07.001.

Lavall, D., Selzer, C., Schuster, P., Lenski, M., Adam, O., Schäfers, H.-J., … Laufs, U. (2014). The mineralocorticoid receptor promotes fibrotic remodeling in atrial fibrillation. *Journal of Biological Chemistry, 289*(10), 6656–6668. https://doi.org/10.1074/jbc.m113.519256.

Lee, R. C., Feinbaum, R. L., & Ambros, V. (1993). The C. elegans heterochronic gene lin-4 encodes small RNAs with antisense complementarity to lin-14. *Cell, 75*(5), 843–854. https://doi.org/10.1016/0092-8674(93)90529-y.

Lee, R., Feinbaum, R., & Ambros, V. (2004). A short history of a short RNA. *Cell, 116*(2 Suppl), S89–S92. https://doi.org/10.1016/s0092-8674(04)00035-2.

Li, X., Wei, Y., & Wang, Z. (2018). microRNA-21 and hypertension. *Hypertension Research, 41*(9), 649–661. https://doi.org/10.1038/s41440-018-0071-z.

Liu, X., Edinger, R. S., Klemens, C. A., Phua, Y. L., Bodnar, A. J., LaFramboise, W. A., … Butterworth, M. B. (2017). A microRNA cluster miR-23–24–27 is upregulated by aldosterone in the distal kidney nephron where it alters sodium transport. *Journal of Cellular Physiology, 232*(6), 1306–1317. https://doi.org/10.1002/jcp.25599.

Luo, L., Wang, Y., Hu, P., & Wu, J. (2020). Long non-coding RNA metastasis associated lung adenocarcinoma transcript 1 (MALAT1) promotes hypertension by modulating the Hsa-miR-124-3p/nuclear receptor subfamily 3, group C, member 2 (NR3C2) and Hsa-miR-135a-5p/NR3C2 axis. *Medical Science Monitor: International Medical Journal of Experimental and Clinical Research, 26*, e920478. https://doi.org/10.12659/msm.920478.

MacKenzie, S. M., Kralingen, J. C. van, & Davies, E. (2018). Regulation of aldosterone secretion. *Vitamins and Hormones, 109*, 241–263. https://doi.org/10.1016/bs.vh.2018.07.001.

MacKenzie, S. M., Saunders, H., Kralingen, J. C., Van, Robertson, S., Riddell, A., Zennaro, M.-C., & Davies, E. (2021). Circulating microRNAs as diagnostic markers in primary aldosteronism. *Cancers, 13*(21), 5312. https://doi.org/10.3390/cancers13215312.

Maharjan, S., Mopidevi, B., Kaw, M. K., Puri, N., & Kumar, A. (2014). Human aldosterone synthase gene polymorphism promotes miRNA binding and regulates gene expression. *Physiological Genomics, 46*(24), 860–865. https://doi.org/10.1152/physiolgenomics.00084.2014.

Mannironi, C., Camon, J., Vito, F. D., Biundo, A., Stefano, M. E. D., Persiconi, I., … Presutti, C. (2013). Acute stress alters amygdala microRNA miR-135a and miR-124 expression: Inferences for corticosteroid dependent stress response. *PLoS One, 8*(9), e73385. https://doi.org/10.1371/journal.pone.0073385.

Marques, F. Z., Campain, A. E., Tomaszewski, M., Zukowska-Szczechowska, E., Yang, Y. H. J., Charchar, F. J., & Morris, B. J. (2011). Gene expression profiling reveals renin mRNA overexpression in human hypertensive kidneys and a role for microRNAs. *Hypertension, 58*(6), 1093–1098. https://doi.org/10.1161/hypertensionaha.111.180729.

McCurley, A., Pires, P. W., Bender, S. B., Aronovitz, M., Zhao, M. J., Metzger, D., … Jaffe, I. Z. (2012). Direct regulation of blood pressure by smooth muscle cell mineralocorticoid receptors. *Nature Medicine, 18*(9), 1429–1433. https://doi.org/10.1038/nm.2891.

Meijer, H. A., Smith, E. M., & Bushell, M. (2014). Regulation of miRNA strand selection: Follow the leader. *Biochemical Society Transactions, 42*(4), 1135–1140. https://doi.org/10.1042/bst20140142.

Mihailidou, A. S., Le, T. Y. L., Mardini, M., & Funder, J. W. (2009). Glucocorticoids activate cardiac mineralocorticoid receptors during experimental myocardial infarction. *Hypertension, 54*(6), 1306–1312. https://doi.org/10.1161/hypertensionaha.109.136242.

Mitchell, P. S., Parkin, R. K., Kroh, E. M., Fritz, B. R., Wyman, S. K., Pogosova-Agadjanyan, E. L., ... Tewari, M. (2008). Circulating microRNAs as stable blood-based markers for cancer detection. *Proceedings of the National Academy of Sciences, 105*(30), 10513–10518. https://doi.org/10.1073/pnas.0804549105.

Mopidevi, B., Ponnala, M., & Kumar, A. (2013). Human angiotensinogen +11525C/A polymorphism modulates its gene expression through microRNA binding. *Physiological Genomics, 45*(19), 901–906. https://doi.org/10.1152/physiolgenomics.00056.2013.

Nanba, K., Blinder, A. R., Rege, J., Hattangady, N. G., Else, T., Liu, C.-J., ... Rainey, W. E. (2020). Somatic CACNA1H mutation as a cause of aldosterone-producing adenoma. *Hypertension, 75*(3), 645–649. https://doi.org/10.1161/hypertensionaha.119.14349.

Nanba, K., Omata, K., Else, T., Beck, P. C. C., Nanba, A. T., Turcu, A. F., ... Rainey, W. E. (2018). Targeted molecular characterization of aldosterone-producing adenomas in White Americans. *The Journal of Clinical Endocrinology and Metabolism, 103*(10), 3869–3876. https://doi.org/10.1210/jc.2018-01004.

Nandakumar, P., Tin, A., Grove, M. L., Ma, J., Boerwinkle, E., Coresh, J., & Chakravarti, A. (2017). MicroRNAs in the miR-17 and miR-15 families are downregulated in chronic kidney disease with hypertension. *PLoS One, 12*(8), e0176734. https://doi.org/10.1371/journal.pone.0176734.

Novák, J., Maceková, S., Héžová, R., Máchal, J., Zlámal, F., Hlinomaz, O., ... Bienertová-Vašků, J. (2022). Polymorphism rs7079 in miR-31/-584 binding site in angiotensinogen gene associates with earlier onset of coronary artery disease in central European population. *Genes, 13*(11), 1981. https://doi.org/10.3390/genes13111981.

Nusrin, S., Tong, S. K. H., Chaturvedi, G., Wu, R. S. S., Giesy, J. P., & Kong, R. Y. C. (2014). Regulation of CYP11B1 and CYP11B2 steroidogenic genes by hypoxia-inducible miR-10b in H295R cells. *Marine Pollution Bulletin, 85*(2), 344–351. https://doi.org/10.1016/j.marpolbul.2014.04.002.

Okada, C., Yamashita, E., Lee, S. J., Shibata, S., Katahira, J., Nakagawa, A., ... Tsukihara, T. (2009). A high-resolution structure of the pre-microRNA nuclear export machinery. *Science (New York, N. Y.), 326*(5957), 1275–1279. https://doi.org/10.1126/science.1178705.

Ozbaki-Yagan, N., Liu, X., Bodnar, A. J., Ho, J., & Butterworth, M. B. (2020). Aldosterone-induced microRNAs act as feedback regulators of mineralocorticoid receptor signaling in kidney epithelia. *The FASEB Journal, 34*(9), 11714–11728. https://doi.org/10.1096/fj.201902254rr.

Park, E.-J., Jung, H. J., Choi, H.-J., Cho, J.-I., Park, H.-J., & Kwon, T.-H. (2018). miR-34c-5p and CaMKII are involved in aldosterone-induced fibrosis in kidney collecting duct cells. *American Journal of, 314*(3), F329–F342. https://doi.org/10.1152/ajprenal.00358.2017.

Parksook, W. W., & Williams, G. H. (2023). Aldosterone and cardiovascular diseases. *Cardiovascular Research, 119*(1), 28–44. https://doi.org/10.1093/cvr/cvac027.

Paul, S. N., Wingenfeld, K., Otte, C., & Meijer, O. C. (2022). Brain mineralocorticoid receptor in health and disease: From molecular signalling to cognitive and emotional function. *British Journal of Pharmacology, 179*(13), 3205–3219. https://doi.org/10.1111/bph.15835.

Reel, P. S., Reel, S., Kralingen, J. C., Van, Langton, K., Lang, K., Erlic, Z., ... Jefferson, E. (2022). Machine learning for classification of hypertension subtypes using multi-omics:

A multi-centre, retrospective, data-driven study. *EBioMedicine, 84*, 104276. https://doi.org/10.1016/j.ebiom.2022.104276.

Riet, L. T., Esch, J. H. M. V., Roks, A. J. M., Meiracker, A. H. V. D., & Danser, A. H. J. (2015). Hypertension. *Circulation Research, 116*(6), 960–975. https://doi.org/10.1161/circresaha.116.303587.

Robertson, S., Diver, L. A., Alvarez-Madrazo, S., Livie, C., Ejaz, A., Fraser, R., ... Davies, E. (2017). Regulation of corticosteroidogenic genes by MicroRNAs. *International Journal of Endocrinology, 2017*(6), 2021903–2021911. https://doi.org/10.1155/2017/2021903.

Robertson, S., MacKenzie, S. M., Alvarez-Madrazo, S., Diver, L. A., Lin, J., Stewart, P. M., ... Davies, E. (2013). MicroRNA-24 is a novel regulator of aldosterone and cortisol production in the human adrenal cortex. *Hypertension, 62*(3), 572–578. https://doi.org/10.1161/hypertensionaha.113.01102.

Romero, D. G., Plonczynski, M. W., Carvajal, C. A., Gomez-Sanchez, E. P., & Gomez-Sanchez, C. E. (2008). Microribonucleic acid-21 increases aldosterone secretion and proliferation in H295R human adrenocortical cells. *Endocrinology, 149*(5), 2477–2483. https://doi.org/10.1210/en.2007-1686.

Scholl, U. I., Goh, G., Stölting, G., Oliveira, R. C., de, Choi, M., Overton, J. D., ... Lifton, R. P. (2013). Somatic and germline CACNA1D calcium channel mutations in aldosterone-producing adenomas and primary aldosteronism. *Nature Genetics, 45*(9), 1050–1054. https://doi.org/10.1038/ng.2695.

Schulte, C., Molz, S., Appelbaum, S., Karakas, M., Ojeda, F., Lau, D. M., ... Zeller, T. (2015). miRNA-197 and miRNA-223 predict cardiovascular death in a cohort of patients with symptomatic coronary artery disease. *PLoS One, 10*(12), e0145930. https://doi.org/10.1371/journal.pone.0145930.

Shan, Z., Qin, S., Li, W., Wu, W., Yang, J., Chu, M., ... Zhang, C. (2015). An endocrine genetic signal between blood cells and vascular smooth muscle cells role of MicroRNA-223 in smooth muscle function and atherogenesis. *Journal of the American College of Cardiology, 65*(23), 2526–2537. https://doi.org/10.1016/j.jacc.2015.03.570.

Sõber, S., Laan, M., & Annilo, T. (2010). MicroRNAs miR-124 and miR-135a are potential regulators of the mineralocorticoid receptor gene (NR3C2) expression. *Biochemical and Biophysical Research Communications, 391*(1), 727–732. https://doi.org/10.1016/j.bbrc.2009.11.128.

Sousa, K. D., Boulkroun, S., Baron, S., Nanba, K., Wack, M., Rainey, W. E., ... Zennaro, M.-C. (2020). Genetic, cellular, and molecular heterogeneity in adrenals with aldosterone-producing adenoma. *Hypertension, 75*(4), 1034–1044. https://doi.org/10.1161/hypertensionaha.119.14177.

Spät, A., Hunyady, L., & Szanda, G. (2016). Signaling interactions in the adrenal cortex. *Frontiers in Endocrinology, 7*, 17. https://doi.org/10.3389/fendo.2016.00017.

Syed, M., Ball, J. P., Mathis, K. W., Hall, M. E., Ryan, M. J., Rothenberg, M. E., ... Romero, D. G. (2018). MicroRNA-21 ablation exacerbates aldosterone-mediated cardiac injury, remodeling, and dysfunction. *American Journal of Physiology-Endocrinology and Metabolism, 315*(6), E1154–E1167. https://doi.org/10.1152/ajpendo.00155.2018.

Valadi, H., Ekström, K., Bossios, A., Sjöstrand, M., Lee, J. J., & Lötvall, J. O. (2007). Exosome-mediated transfer of mRNAs and microRNAs is a novel mechanism of genetic exchange between cells. *Nature Cell Biology, 9*(6), 654–659. https://doi.org/10.1038/ncb1596.

Vickers, K. C., Palmisano, B. T., Shoucri, B. M., Shamburek, R. D., & Remaley, A. T. (2011). MicroRNAs are transported in plasma and delivered to recipient cells by high-density lipoproteins. *Nature Cell Biology, 13*(4), 423–433. https://doi.org/10.1038/ncb2210.

Wang, C., & Hu, F. (2021). Long noncoding RNA SOX2OT silencing alleviates cerebral ischemia-reperfusion injury via miR-135a-5p-mediated NR3C2 inhibition. *Brain Research Bulletin, 173*, 193–202. https://doi.org/10.1016/j.brainresbull.2021.05.018.

Weber, J. A., Baxter, D. H., Zhang, S., Huang, D. Y., Huang, K. H., Lee, M. J., ... Wang, K. (2010). The microRNA spectrum in 12 body fluids. *Clinical Chemistry, 56*(11), 1733–1741. https://doi.org/10.1373/clinchem.2010.147405.

Wu, Y., Wang, M., Zhang, J., Sun, N., & Li, C. (2019). A new model of the mechanism underlying lead poisoning: SNP in miRNA target region influence the AGT expression level. *Hereditas, 156*(1), 6. https://doi.org/10.1186/s41065-019-0084-x.

Wu, Y., Li, Q., Zhang, R., Dai, X., Chen, W., & Xing, D. (2021). Circulating microRNAs: Biomarkers of disease. *Clinica Chimica Acta, 516*, 46–54. https://doi.org/10.1016/j.cca.2021.01.008.

Xing, Y., Lerario, A. M., Rainey, W., & Hammer, G. D. (2015). Development of adrenal cortex zonation. *Endocrinology and Metabolism Clinics of North America, 44*(2), 243–274. https://doi.org/10.1016/j.ecl.2015.02.001.

Yoda, M., Kawamata, T., Paroo, Z., Ye, X., Iwasaki, S., Liu, Q., & Tomari, Y. (2010). ATP-dependent human RISC assembly pathways. *Nature Structural & Molecular Biology, 17*(1), 17–23. https://doi.org/10.1038/nsmb.1733.

Zennaro, M.-C., Boulkroun, S., & Fernandes-Rosa, F. L. (2020). Pathogenesis and treatment of primary aldosteronism. *Nature Reviews Endocrinology, 16*(10), 578–589. https://doi.org/10.1038/s41574-020-0382-4.

Zhang, H., Kolb, F. A., Jaskiewicz, L., Westhof, E., & Filipowicz, W. (2004). Single processing center models for human dicer and bacterial RNase III. *Cell, 118*(1), 57–68. https://doi.org/10.1016/j.cell.2004.06.017.

Zhang, J., Zhang, Y., Gao, J., Wang, M., Li, X., Cui, Z., & Fu, G. (2021). Long noncoding RNA Tug1 promotes angiotensin II–induced renal fibrosis by binding to mineralocorticoid receptor and negatively regulating MicroR-29b-3p. *Hypertension, 78*(3), 693–705. https://doi.org/10.1161/hypertensionaha.120.16395.

Zhou, J., Azizan, E. A. B., Cabrera, C. P., Fernandes-Rosa, F. L., Boulkroun, S., Argentesi, G., ... Brown, M. J. (2021). Somatic mutations of GNA11 and GNAQ in CTNNB1-mutant aldosterone-producing adenomas presenting in puberty, pregnancy or menopause. *Nature Genetics, 53*(9), 1360–1372. https://doi.org/10.1038/s41588-021-00906-y.

16 Scientific review

16.1 Genetics mechanisms of primary aldosteronism

Under submission

Genetics mechanisms of primary aldosteronism

May Fayad[1*], Nicolo Faedda[1*], Teresa Cosentino[1*], Sheerazed Boulkroun[1], Fabio L. Fernandes-Rosa[1$#], Maria-Christina Zennaro[1,2$#]

[1]Université de Paris, PARCC, Inserm, Paris, France
[2]Assistance Publique-Hôpitaux de Paris, Hôpital Européen Georges Pompidou, Service de Génétique, Paris, France

*,$These authors contributed equally to this work

Affiliations:
[1] Université Paris Cité, PARCC, Inserm,
[2]Assistance Publique-Hôpitaux de Paris, Hôpital Européen Georges Pompidou, Service de Génétique, Paris, France

Corresponding author:
Maria-Christina Zennaro, MD, PhD
INSERM, U970
Paris Cardiovascular Research Center – PARCC
56, rue Leblanc,
75015 Paris – France
Tel : +33 (0)1 53 98 80 42
Fax : + 33 (0)1 53 98 79 52
e-mail: maria-christina.zennaro@inserm.fr

Fabio Fernandes Rosa, MD, PhD
INSERM, U970
Paris Cardiovascular Research Center – PARCC
56, rue Leblanc,
75015 Paris – France
Tel : +33 (0)1 53 98 80 42
Fax : + 33 (0)1 53 98 79 52
e-mail: fabio.fernandes-rosa@inserm.fr

Number of figures and tables:

Abstract (<200 words, unstructured)

Keywords: Primary aldosteronism; hypertension; adrenal gland; aldosterone; mineralocorticoid; genetics

INTRODUCTION

High blood pressure is one of the main cardiovascular risk factors affecting about 25% of the world's adult population (2017). Although there are a wide range of approved drugs for hypertension treatment, in two thirds of hypertensive patients, optimal blood pressure control is not achieved. Primary Aldosteronism (PA), also known as Conn's syndrome, is the most common form of secondary arterial hypertension, with a prevalence of ~6% of hypertensive patients in primary care and 10%-20% of hypertensive patients referred to specialist care [1–3]. PA is characterized by autonomous production of aldosterone by the adrenal glands, from one or both adrenal glands. Aldosterone overproduction leads to sodium retention and increase urinary excretion of potassium and protons, resulting in elevated blood pressure, occasional hypokalaemia and metabolic alkalosis [4]. There are two forms of PA, sporadic and familial, the latter being transmitted in an autosomal dominant manner while sporadic forms are the most frequent forms of PA, found in 95% of patients, and mainly due to unilateral aldosterone-producing adenoma (APA) or bilateral adrenal hyperplasia (BAH). Clinical suspicion of PA arises in the presence of specific criteria: blood pressure (BP) > 150/100 obtained after three daily measurements ; BP > 140/90 resistant to three conventional antihypertensive drugs, including a diuretic or BP < 140/90 controlled by the use of four or more antihypertensive drugs; hypertension and hypokalemia; hypertension and adrenal incidentaloma; hypertension and sleep apnea; hypertension and family history of early-onset hypertension or cerebrovascular events at a young age (<40 years); hypertensive individuals with first-degree relatives with PA. Biochemical diagnosis of PA is based on increased concentrations of plasma aldosterone in the presence of low levels of plasma renin, resulting in an elevated aldosterone to renin ratio. The diagnosis of PA is confirmed by different dynamic tests, the most common being the oral salt loading or the captopril test. Adrenal CT and adrenal vein sampling (AVS) are performed to differentiate unilateral from bilateral PA [4].

Patients with PA present increased cardiovascular morbidity compared to essential hypertensive oneswith similar blood pressure values but with normal aldosterone levels [5,6]. This is due to the direct effects of aldosterone on cardiovascular tissues [7–9]. Furthermore, PA remains an underdiagnosed condition, with less than 2% of high-risk patients tested for PA, and much less than 1% ever diagnosed and appropriately treated with mineralocorticoid receptor antagonists.

Enormous progress has been made in recent years to unravel the genetic basis of PA. Somatic and germline mutations in genes coding for ion channels (*KCNJ5*, *CACNA1D*, *CACNA1H*, *CLCN2, SLC30A1*) and ATPases (*ATP1A1*, *ATP2B3*), were identified in APA and familial forms of PA, demonstrating the central role of calcium signaling in the pathogenesis of PA [10]. In addition,

somatic mutations in *CTNNB1*, alone or co-occurring with *GNA11*/*GNAQ* were identified in APAs from patients with a particular form of PA [11–13], and recently an additional mechanism leading to APA and linked to mutations in the cell adhesion molecule gene *CADM1* has been discovered [14].The identification of the genetic mechanisms leading to PA development may provide new options for better diagnosis and eventually for targeted treatment. In this review we describe the actual knowledge on the genetics of PA and discuss the pathogenic mechanisms underlying autonomous aldosterone production and APA development.

Aldosterone biosynthesis

Aldosterone is a steroid hormone produced by the zona glomerulosa (ZG) of the adrenal cortex which in humans consists of three functionally distinct concentric layers. The functional properties of each adrenal layers depend on the expression of specific enzymes and the ability of response to unique regulatory stimuli [15]. Aldosterone plays an important role in regulating electrolyte homeostasis and blood pressure, and influencing the function of the cardiovascular system by acting on the heart, vessels and central nervous system [16,17]. Aldosterone regulates blood pressure, through changes in sodium and potassium balance, by interacting with the mineralocorticoid receptor (MR), a ligand-dependent transcription factor located in the epithelial cells of the distal nephron. When activated, MR induces the transcription of genes encoding for proteins involved in the regulation of transepithelial sodium transport, such as the epithelial sodium channel ENaC and the Na^+,K^+-ATPase pump, thus leading to Na^+ reabsorption and K^+ excretion [18].

The primary precursor of aldosterone is cholesterol which can derive from a variety of sources and undergoes a series of transformations regulated by specific enzymes. The transformation begins with the passage of cholesterol from the outer membrane to the inner membrane of the mitochondrion, a process regulated by steroidogenic acute regulatory protein (StAR). In the inner membrane of the mitochondrion, cholesterol is converted into pregnenolone by the cholesterol side-chain cleavage enzyme (encoded by *CYP11A1)*. Pregnenolone passively diffuses into the endoplasmic reticulum and is converted into progesterone *by* the 3β-hydroxysteroid dehydrogenase (3βHSD) enzyme (encoded by *HSD3B2* in the adrenal glands and gonades). Progesterone is hydroxylated to deoxycorticosterone (DOC) by the 21-hydroxylase enzyme (encoded by *CYP21A2)*. Finally, aldosterone biosynthesis is completed in the mitochondrion, where DOC undergoes 11β- and 18-hydroxylation, followed by 18-methyl oxidation. These reactions are mediated by the enzyme aldosterone synthase (encoded by *CYP11B2*) [19,20].

The main trigger for aldosterone biosynthesis is the activation of intracellular calcium signaling in the cells of ZG, which is mainly induced by AngII, through the renin-angiotensin system, and by

extracellular K^+ levels [15]. Aldosterone biosynthesis is increased during acute or chronic sodium depletion or in cases of fluid loss, orthostatic position, potassium-rich dietary load, and tissue damage resulting in hyperkalemia. The renin-angiotensin system translates changes in renal perfusion and sodium concentration, perceived at the level of the renal tubule, into changes in the production of aldosterone by the adrenal cortex to regulate volume and electrolyte homeostasis. In ZG cells, AngII binds the AT1 receptor (Angiotensin type 1 receptor), activating the Gαq-phospholipase C-mediated pathway. This leads to an increase in the concentration of inositol 1,4,5-triphosphate (IP3) and 1,2-diacylglycerol (DAG), finally resulting in release of calcium from the endoplasmic reticulum and in increase of intracellular calcium concentration. AngII also inhibits TASK (TWIK-related acid sensitive) and GIRK4 potassium channels and the Na^+,K^+ATPase pump leading to cell membrane depolarisation. The depolarization induces the opening of voltage-dependent calcium channels, also resulting in increased intracellular calcium concentration [21]. ZG cells have a high conductance for K^+ and are maintained in a hyperpolarized state due to the expression of a high number of potassium channels [22] and the Na^+,K^+ATPase pump. Increased extracellular K^+ inhibits K^+ channels, leading to cell membrane depolarization, opening of voltage-dependent calcium channels and increasing in intracellular Ca^{2+} concentrations [15]. Increase in intracellular calcium concentration induced by either AngII or potassium leads to activation of Ca^{2+} signaling, which increases aldosterone biosynthesis by activating transcription factors, in particular the nuclear receptor subfamily 4 group A members 1 and 2 (NURR77 or NGF1B and NURR1), the cyclic AMP-dependent transcription factor ATF-1 and CREB, which increase expression of *CYP11B2*, Additionally, Increased Ca^{2+} signaling also activate early and intermediary steps of adrenal steroidogenesis [15,20,21].

Genetics of PA

The technological development enabling the analysis of the coding sequences of all genes (exome) or the entire genome allowed an enormous progress on the knowledge of the genetic basis of PA. It can now be stated that almost all Conn's adenomas carry a somatic mutation in one of the genes involved in the disease, and four different forms of familial hyperaldosteronism (FH) have been defined based on the subjacent genetic defect. These findings open important perspectives for the management of patients in the context of familial forms, but also to consider the identification of surrogate markers for the presence of APAs carrying certain mutations and the development of targeted treatments.

CYP11B1/CYP11B2 chimeric gene and FH-I

The *CYP11B1/CYP11B2* chimeric gene, which is inherited in an autosomal dominant manner, was the first genetic defect associated with PA, causing FH-I (glucocorticoid remediable aldosteronism)[23,24]. FH-I, accounts for approximately 1% of PA cases, but its frequency is increasing in pediatric hypertensive cohorts[25–27]. The disease is characterized by an early hypertension, associated with the biological features of PA, as well as elevated levels of the hybrid steroids 18-hydroxycortisol and 18-oxocortisol. Remarkably, hyperaldosteronism is suppressible by dexamethasone [28,29]. The chimeric *CYP11B1/CYP11B2* gene results from an unequal crossing over and contains the regulatory regions of the *CYP11B1* (encoding 11β-hydroxylase responsible for cortisol synthesis) and the coding regions of the *CYP11B2* (encoding aldosterone synthase. The aldosterone synthase is found ectopically expressed in the zona fasciculata and its expression is regulated mainly by the ACTH with the same circadian rhythm as cortisol [23,24]. Patients with FH-I exhibit increased cardiovascular risk, with end organ damage that may occur before patients become hypertensive [30] and frequent cerebrovascular events in young subjects [31].

<u>*KCNJ5* Mutations in APA and FH-III</u>

The *KCNJ5* gene encodes the potassium channel GIRK4, a member of the family of trimeric G protein coupled inward rectifier K^+ channels (GIRK). It is mainly expressed in the ZG of the adrenal cortex. Somatic mutations in *KCNJ5* gene were identified in APA and germline mutations are responsible for familial hyperaldosteronism type III (FH-III) [32]. The great majority of *KCNJ5* genetic variations detected so far are located in or near the selectivity filter [33]. These mutations result in a loss of selectivity of the channel for K^+ that permissively allows the passage of Na^+ resulting in membrane depolarisation, opening of voltage-dependent Ca^{2+} channels, influx of Ca^{2+}, and thus increased intracytoplasmic calcium concentration leading to activation of the Ca^{2+} signaling pathway and aldosterone production [32,34,35]. Somatic and germline *KCNJ5* mutations located far from the selectivity filter were also identified in patients with PA [36–38]. It was suggested that these mutations are loss-of-function and lead to a decrease in GIRK4 expression in the cell membrane [39,40], however their role in PA pathogenesis is not proved. Somatic mutations in *KCNJ5* are the most frequent genetic defect identified in APA, with a frequency ranging from 40% in European cohorts until 70% in patients from East Asia [41–46]. *KCNJ5* somatic mutations are more frequent in APA from female and young patients [43,44,47,48]. They were associated with higher aldosterone levels, larger tumour size and higher plasma concentrations of hybrid steroids 18-oxocortisol and 18-hydroxycortisol [44,49–51]. Histologically, APA carrying *KCNJ5* mutations are mainly composed by large clear cells resembling ZF cells [36,43], with higher percentage of cells expressing *CYP11B1*

and lower *CYP11B2* in comparison with APAs carrying other mutations [51]. In addition, GIRK4 expression in *KCNJ5*-mutated APA is decreased in comparison with the adjacent ZG [52–54]. In vitro studies have suggested that *KCNJ5* mutations may have an effect on cell growth and this effect is determined by the expression level of the mutated channel [54].

Germline *KCNJ5* mutations are associated with the familial hyperaldosteronism type III (FH-III) [32]. FH-III was originally described as a severe early onset form of PA, usually before the age of 20, associated with resistant hypertension, profound hypokalemia, and high urinary concentrations of the steroid hybrids 18-oxocortisol and 18-hydroxycortisol, due to massive bilateral adrenal hyperplasia requiring adrenalectomy for blood pressure control [55]. Since the identification of germline *KCNJ5* mutations in families with PA, variable severity of hyperaldosteronism was observed among FH III kindreds [56–59]. The analysis of the adrenal glands of FH-III patients showed adrenal enlargement and loss of zonation with expression of aldosterone-synthase observed throughout the adrenal cortex. Interestingly, co-expression of aldosterone synthase with 11β hydroxylase, 17α hydroxylase, or both, was often observed in these adrenals, explaining the increased concentrations of hybrid steroids [60].

CACNA1D mutations in APA and PASNA

The *CACNA1D* gene encodes the α1 subunit of the L-type calcium channel Cav1.3. It is composed of four homologous domains (I to IV), and each domain has six transmembrane segments (S1 to S6), and mediate calcium influx into the cell after cell membrane depolarization [61]. Mutations in the Cav1.3 channel affect highly conserved amino acids in different regions of the protein, inducing a change in voltage sensitivity, and the channel opening at more negative voltages and increased Ca^{2+} influx [62,63]. *CACNA1D* somatic mutations were found from 10% of APAs using targeted Sanger sequencing until 27% in studies performing CYP11B2 IHC-guided NGS [43,51,64], and their frequency is higher in African-American patients (42%)[64]. *CACNA1D* mutations were mainly observed in APA of male patients and were initially associated with small tumours [43,63], however, this association was not observed in studies using *CYP11B2* IHC guided NGS [51]. De novo germline *CACNA1D* mutations were identified in two children with severe form of hyperaldosteronism associated with complex neurologic disorder (PASNA, primary aldosteronism seizures and neurological abnormalities) [62]. Other two cases of PASNA were identified, including one patient with associated hyperinsulinemia [65,66].

CACNA1H mutations in FH-IV and APA

CACNA1H encodes the pore-forming α1 subunit of the T-type voltage-dependent calcium channel Cav3.2. Recurrent germline mutations in *CACNA1H* gene are responsible of FH-IV. The recurrent germline mutation (p.Met1549Val) was identified in five patients with early-onset PA, two of them exhibited developmental delay or attention deficit disorder [67]. Although adrenal imaging of the patients did not show adrenal abnormalities, histological examination of one patient showed micronodular adrenal hyperplasia. A de novo germline *CACNA1H* mutation affecting the same codon (p.Met1549Ile) was identified in a patient with early onset primary aldosteronism associated with multiplex development disorder. Germline *CACNA1H* mutations were also identified in patients with mild PA and different phenotypic presentation, suggesting that *CACNA1H* might be a susceptibility gene for PA [68]. Mutations in Cav3.2 cause slower activation and deactivation of the channel that persists over time leading to increased intracellular calcium concentration [67,68]. Recently, somatic *CACNA1H* mutations were also identified [51].

Somatic *ATP1A1* and *ATP2B3* mutations

ATP1A1 encodes for the α1 subunit of the Na^+,K^+ ATPase pump. This pump is a member of the P-type ATPase family, and consists of three subunits: α, β and γ. The α subunit, which is catalytic and responsible for ion binding, consists of ten trans-membrane domains (M1-M10) and two intracytoplasmic tails (C- and N-terminals) [69]. Somatic mutations in the *ATP1A1* gene have been identified in the M1, M4 and M9 domains, which are essential for K^+ binding [70]. The frequency of ATP1A1 mutations ranges from 8 to 17% of APA [51,64]. Somatic mutations in *ATP1A1* lead to loss of pump activity and inward sodium or proton leak, leading to cell membrane depolarization. Modifications of intracellular calcium concentrations were not observed in experiments performed in adrenocortical NCI-H295R cells which rather suggested a mechanism involving intracellular acidification [71]. The pathogenic mechanisms involved in stimulating aldosterone production is not completely understood and may result from alterations in multiple pathways. Recently, the results of a *in vitro* study performed in HAC15 adrenocortical cancer cells suggested that a common *ATP1A1* may also stimulate cell proliferation [72].

The *ATP2B3* gene encodes the Ca^{2+} ATPase isoform 3 (PMCA3: Plasma Membrane Ca^{2+} ATPase 3) pump. PMCA3 consists of 10 trans-membrane domains (M1-M10), a large loop and two cytoplasmic ends. Somatic mutations in *ATP2B3* gene were identified in 1.7-10% of APA, with higher frequency in studies performing IHC-guided NGS [43,51,64,70,73]. *ATP2B3* mutations identified so far are inframe deletions in the M4 domain, which is crucial for both Ca^{2+} binding and proximity to the catalytic core of the pump [70]. These mutations reduce the pump's ability to extrude Ca^{2+}, resulting

in an increase in intracytoplasmic calcium concentration [70,74]. Other proposed mechanisms is the loss of Na^+ through the pump causing membrane depolarization and the opening of voltage-dependent Ca^{2+} channels [74].

CLCN2 Mutations in FH-II and APA

CLCN2 encodes the chloride channel ClC-2, which plays a role in ion homeostasis by opening in response to membrane hyperpolarisation, hyposmotic cell swelling and acidic extracellular pH [75]. A germline mutation in *CLCN2* was identified in in a large Australian family with FH-II identified and three other PA pedigrees segregating with the disease [76]. In addition, four different germline *CLCN2* mutations were identified in unrelated patients with early-onset PA [76]. Concomitantly, a de novo germline *CLCN2* mutation was identified in a 9 years-old patient with a severe PA. *CLCN2* mutations lead to increased chloride conductance and chloride efflux causing cell membrane depolarization, resulting in calcium signaling activation and increased expression of *CYP11B2* [77]. The pathogenesis of the *CLCN2* mutations were confirmed in two studies with different knock-in mouse models, both providing important insights regarding the role of chloride channels in PA development [78,79]. Recently, somatic *CLCN2* mutations were also described in small number of APA from different centers [80–82].

CTNNB1 Mutations alone and co-occurring with *GNA11*/*GNAQ*

CTNNB1 encodes the β-catenin, part of the Wnt/βcatenin signaling pathway which has been shown to play an important role in adrenal cortex development and aldosterone biosynthesis [83,84]. Wnt protein binds to its receptor Frizzled, inhibiting the phosphorylation of ßcatenin, thereby preventing its destruction at the proteasome, and allowing it to translocate into the nucleus and induce the expression of Wnt target genes [85]. Somatic *CTNNB1* mutations were described in 2-5% of APA [11,47,86]. Although the low frequency of *CTNNB1* mutations, the Wnt/βcatenin signaling pathway is active in approximately 70% of APAs, independently from the mutational status [51,83]. and are apparently [12].

It has been shown that *CTNNB1* mutations are more frequent in women and associated, in some cases, with overexpression of the gonadotropin-releasing hormone receptor (LHCGR) and gonadotropin-releasing hormone receptor (GNRHR) in APA, with PA onset during pregnancy or menopause [12]. Recently, a study further explored these findings and demonstrated that *CTNNB1* mutations are associated with GNAQ/11 mutations in APA of patients with PA during puberty, pregnancy or menopause [13]. The GNAQ and GNA11 genes encode the Gαq/11 subunits of G proteins associated

with membrane G protein-coupled receptors. They are associated with the response to angiotensin II via its AT1 receptor and stimulate the phospholipase C/inositol triphosphate signaling pathway and the increase of intracellular calcium. The presence of these mutations is associated with a very specific gene expression profile, with increased expression of the LH and HCG receptor, thus linking hormonal changes occurring at puberty, pregnancy and menopause to the development of APA in these patients [13]. Although the frequency of this form of PA is not known, it would appear not to be an uncommon entity, especially at puberty, which strongly supports screening for PA and searching for APA in young patients with hypertension.

CADM1 Mutations

CADM1 encodes for the cell adhesion molecule 1, which is a molecule present at gap junctions and is involved in intracellular communication. Mutations in *CADM1* gene were identified in six patients. These mutations (p.Gly379Arg and p.Val380Arg) are located in the membrane dimerization domain of the protein. APAs carrying these mutations show high expression of *CYP11B2* and low expression of *CYP11B1*. In vitro studies showed that expression of a mutated form of *CADM1* in H295R adrenal cortical cells induced an increase in *CYP11B1* expression and aldosterone biosynthesis. The authors showed that this effect was associated with inhibition of intercellular communication via gap junctions [14].

SLC30A1 Mutations

SLC30A1 (Solute carrier family 30 member 1) gene encodes the ubiquitous zinc efux transporter ZnT1 (zinc transporter 1) which functions as a Zn^{2+}/Ca^{2+} and/or Zn^{2+}/H^{+} exchanger. It is expressed in all tissues and cell types examined to date, consistent with its primary function as a zinc exporter in the body [87]. *SLC30A1* belongs to a large superfamily of transporters known as CDFs (Cation Diffusion Facilitators) and is part of the SLC30 subfamily comprising 10 members grouped based on gene sequence homology. ZnT1 consists of six transmembrane domains with a histidine/serine-rich loop between domains M4 and M5. The N-terminal and C-terminal domains are localized intracellularly [88]. Recurrent deletions of seven amino acids (p.Leu51_Ala57del and p.Leu49_Leu55del) have recently been identified in five APAs. These deletions are located in the transmembrane domain II, close to the zinc-binding site (His43 and Asp47), probably leading to abnormal ion transport. Functional analyses carried out in HAC15 adrenal cortical cells revealed abnormal Na^{+} conductivity, leading to cell membrane depolarization, opening of voltage-dependent

calcium (Ca^{2+}) channels and increased intracellular Ca^{2+} concentrations, resulting in stimulation of *CYP11B2* mRNA expression and aldosterone biosynthesis [89]

Genetic susceptibility

Genome-wide association studies (GWAS) have identified genetic variants associated with primary aldosteronism. Recently, two susceptibility genes for PA, *CASZ1* and *RXFP2*, that were previously linked to blood pressure and to resistant hypertension [90,91], were identified. Overexpression of these genes in adrenocortical cells showed a modification in mineralocorticoid output under basal and stimulated conditions, without affecting cortisol synthesis. In parallel, a decreased expression of aldosterone synthase, the enzyme responsible for the last steps of aldosterone synthase, was observed. Interestingly, these shared loci are found in both APAs and in bilateral adrenal hyperplasia which suggests a continuum between the two conditions [92]. The discovery of the involvement of *CASZ1* and *RXFP2* in the development of PA unveiled a new perspective for the diagnosis and treatment of PA.

APA development

The enormous progress made in recent years has indicated that PA is a heterogeneous disease caused by genetic defects in one or more factors involved in the regulation of aldosterone synthesis, in which activation of calcium signaling plays a central role [33]. Although the link between somatic mutations and aldosterone production have been established [32,34,62,63,70], their involvement in cell proliferation and APA formation remains to be demonstrated. Two models of APA development were proposed: 1) a two-hit model with one hit is responsible by cell proliferation and nodulation and a second hit is responsible by aldosterone autonomous production [93] and 2) a model where APA may derive from aldosterone producing cell clusters (APCC) [94]. These two hypotheses could co-exist and both contribute to the development of APAs.

APCC, also called aldosterone-producing micronodules [95], have been described in 2010 as a subcapsular cluster of cells composed of ZG-like cells in the outer part and of columnar ZF-like cells in the inner part [94,96]. Disabled 2 (DAB2), a marker of ZG cells is expressed only in the outer part of the APCCs and both, the outer and the inner part, express CYP11B2 but not *CYP11B1,* suggesting that APCC could be an intermediate phenotype between ZG and ZF [96]. It has also been shown that APCCs have a particular transcriptional profile similar to ZG, but with an enhanced capacity to produce aldosterone [97]. Interestingly, APCCs harbor somatic mutations in APA-driver genes in both normal adrenals and adrenals with APA [51,97]. Furthermore, it was suggested that APCCs may

participate in the pathogenesis of bilateral PA, with an accumulation and enlargement of APCCs in both adrenals, the majority carrying *CACNA1D* mutations [98]. It has been suggested that APCCs could be a precursor population of cells that can progress to APA [97,99,100]. In this case, a somatic mutation in one of the APA driver genes occurring in ZG leads to the formation of aldosterone-producing cell clusters (APCC), followed, through the development of APCC-to-APA translational lesions (pAATL), to APA formation. pAATL lesions were detected by histological analysis of an adrenal with multiple adrenocortical micronodules from two patients with APA [100]. They consist in a subcapsular APCC-like structure (APCC-like) and an inner-APA-like structure (mAPA-like) without well-defined histological border [100]. The search for APA driver genes was performed in both portions of pAATL to determine whether they could constitute intermediate structures between APCC and APA. In one case 2 different *KCNJ5* mutations were found within the same adrenal, one in a suspected aldosterone producing nodule and the second one only in the mAPA-like portion of pAATL. This suggests different origins for the aldosterone producing nodule and the mAPA and a transdifferentiation of APCC cells into a mAPA like phenotype due to the *KCNJ5* mutation [100]. In the second case, the same *ATP1A1* mutation was found in both APCC-like and mAPA like portions, suggesting a clonal origin of the entire structure [100]. The precise mechanism leading to the development of APCC into a pAATL and APA remains to be identified.

The 'two-hit model' of APA development is based on the hypothesis that a first event leads to cell proliferation and nodule formation and a second involves specific hormone secretion. It has been shown that adrenal cortex remodeling including increased nodulation, ZG hyperplasia and reduced vascularization and are frequent features of adrenals carrying an APA [96]. Also, both the APA and the adjacent ZG exhibit stem cell/precursor characteristics, indicating that the re-expression of genes involved in fetal adrenal development could underlie the excessive proliferation of ZG cells and the formation of APA [101]. The presence of different somatic mutations in APA-driver genes identified in different nodules within the same multinodular adrenal suggested that the somatic mutations may be second events occurring in a previously remodeled adrenal cortex [53,102]. In addition, in some APA with heterogeneous expression of CYP11B2, somatic mutations were observed only in the aldosterone synthase positive region of the APA [103]. The two-hit model for APA formation was also supported by a case report of a patient with early-onset and severe hypertension harbouring a germline heterozygous *APC* gene mutation associated, in the resected multinodular adrenal, to biallelic *APC* inactivation due to a loss of heterozygosity in all adrenal nodules, but a somatic *KCNJ5* mutation only in one nodule expressing aldosterone synthase [104]. The inactivation of *APC* induces a constitutive activation of the Wnt/β-catenin pathway, being the first event leading to abnormal cell proliferation and nodule formation, followed by the KCNJ5 mutation which drives the specific

hormonal production. The recent identification of the co-occurrence of *CTNNB1* and *GNAQ/GNA11* somatic mutations in APA of patients with PA presenting during puberty, pregnancy or menopause, also suggests two different genetic hits may lead to both cell proliferation and aldosterone production [13].

Wnt/β-catenin and ACTH/cAMP/PKA signaling pathways, together with paracrine factors play an important role in steroidogenesis and adrenal development. These factors may also drive the development of aldosterone producing structures and the intratumoral heterogeneity observed in APA. ACTH regulates aldosterone production by stimulation of cyclic adenosine monophosphate (cAMP) / protein kinase A pathway, leading to the phosphorylation of CREB and increased StAR expression [20,105]. Recently, it has been shown that β-catenin was activated in cells expressing aldosterone synthase, together with high expression of MC2R. In APCCs, in addition to the activation of β-catenin, strong expression of pCREB was also observed, suggesting that APCC may represent intermediate cellular structures between ZG and ZF [51]. Paracrine regulation of aldosterone production in the adrenal cortex and APAs is mediated by factors released by chromaffin cells, endothelial cells, nerve fibers, and immune cells [106–109]. Intraadrenal mast cells stimulates aldosterone secretion through release of serotonin (5-HT) and activation of 5-HT type 4 receptors (5-HT4R, almost exclusively expressed in the ZG) leading to the atimulation of the cAMP/PKA pathway and opening of membrane calcium channels [110–112]. In a large series of APAs, it was observed an increase of mast cell density in comparison with normal adrenals [106]. This was confirmed in a recent study that shown an abundance of mast cells in APAs and also in APCCs. The mast cells were mainly localized in zones expressing aldosterone synthase, suggesting that mast cells may induce proliferation of ZG cells and play a role on the secretion of mineralocorticoids [113]. Taken together, these results showed that aldosterone-producing structures in adrenals with APAs share common molecular characteristics and cellular environments, independently of the type of mutation, suggesting common developmental mechanisms [113].

Ferroptosis has been also proposed as a potential mechanism playing a role in APA development [114]. Ferroptosis is an iron-dependent form of regulated cell death, due to the accumulation of redox-active iron, lipid hydroperoxides, and oxidized polyunsaturated fatty acid-containing phospholipids [115,116]. The adrenocortical cells are sensitive to ferroptosis due to redox imbalance caused by electron leakage by cytochrome P450 enzymes and reactive oxygen species generation [117–119]. *BEX1* (encoding the Brain-expressed X-linked protein) was previously identified as a differentially expressed gene with increased expression in adenomas with *CACNA1D* or *ATP1A1* mutations [63] and appears to be over-expressed in small tumours compared to large ones [114]. In vitro experiments showed that *BEX1* may play a role in cell proliferation and thus nodulation by protecting

adrenocortical cells from cell death by ferroptosis. This protection from ferroptosis may induce a response to increased steroidogenesis and oxidative stress, providing growth advantage for ZG cells with aldosterone overproduction compared adjacent cells [114].

Conclusions and Perspectives

In the last decade, the identification of mutations in genes coding for ion channels and ATPases placed the intracellular ionic balance and the activation of calcium signaling as the central pathogenic mechanisms of PA. The development of new techniques to identify somatic mutations in APAs, as the use of CYP11B2 immunohistochemistry-guided NGS, allowed the identification of somatic mutations in the great majority of APAs. The identification of germline mutations in genes coding for ion channels established a new classification of familial forms of PA based on the underlying genetic defect. Some questions concerning the genetic basis of PA, the development of APAs, and the impact of the genetic findings on PA patients care are still open. The first issue concerns the identification of new genes responsible for APA. Since APA-driver mutations are identified in more than 85% of APAs, new genes responsible for APA discovery in the future will impact small number of APAs, as observed recently for *CLCN2* and *CACNA1H* somatic mutations [80,81,120]. However, many cases of familial and inherited PA remain unexplained. In this case the investigation of patients with early-onset PA may provide the identification of germline mutations in novel genes, a strategy successfully used for the identification of the genetics of familial PA [32,67,76,77].

The knowledge of the genetic basis of PA open new perspectives for patient care. First of all, it would be crucial to identify surrogate markers of the somatic mutations in APAs before adrenalectomy. Some clinical, epidemiologic and biochemical characteristics were observed in association with specific genetic status [43,48] and the frequency of somatic mutations is variable accordingly to the ethnic background [64,121]. In addition, it was demonstrated that a distinct steroid signature in adrenal venous or peripheral plasma was able to differentiate the APA genotype [50]. The identification of a particular group of patients with APA, manifesting during adolescence, pregnancy and menopause was possible due to the identification of the co-occurrence of somatic mutations in *CTNNB1* and GNA11/Q genes [13]. Pharmacologically, In vitro studies have shown that mutated GIRK4 channels can be blocked by calcium blockers and by macrolide antibiotics [122,123]. Ex-vivo experiments in cells isolated from APA with KCNJ5 mutations confirm that macrolides may decrease *CYP11B2* expression and aldosterone production in these cells [124]. These findings open new and exciting perspectives for PA targeted diagnosis and treatment.

Concerning APA development, APAs and APCCs share somatic mutations in the same genes [97]. In addition, different mutational events in APCC and micronodules within the same adrenal with APA were observed and opens new perspectives for the understanding of the pathogenic mechanisms leading to APA development [51]. Genetic and histological studies performed in adrenals of patients with APA without biochemical cure after adrenalectomy indicated common mechanisms underlying BAH and APA [125]. This is in line with the possibility of a continuum between low renin hypertension, BAH and APA, as suggested by different authors. Furthermore, in adrenals with BAH, APCCs are increased in number and carry somatic mutations [98], as observed in adrenals with APA, normal adrenals, and also in multinodular adrenals in patients with PA. In this case, APCCs would be the link between all these different phenotypes and the somatic genetic background may be the driver for the development of these structures and PA predisposition.

CONFLICT OF INTEREST

No potential conflict of interest relevant to this article was reported.

ACKNOWLEDGMENTS

The laboratory is funded by institutional support from INSERM, by the Agence Nationale pour la Recherche (ANR-18-CE93-0003-01), the Fondation pour la Recherche Médicale (EQU201903007864), the European Union's Horizon 2020 research and innovation programme under the Marie Sklodowska-Curie grant agreement No. 954798 (MINDSHIFT ITN).

REFERENCES

1. Hannemann A, Wallaschofski H. Prevalence of primary aldosteronism in patient's cohorts and in population-based studies--a review of the current literature. Horm Metab Res. 2012 Mar;44(3):157–62.

2. Monticone S, Burrello J, Tizzani D, Bertello C, Viola A, Buffolo F, et al. Prevalence and Clinical Manifestations of Primary Aldosteronism Encountered in Primary Care Practice. J Am Coll Cardiol. 2017 Apr 11;69(14):1811–20.

3. Vaidya A, Brown JM, Carey RM, Siddiqui M, Williams GH. The Unrecognized Prevalence of Primary Aldosteronism. Ann Intern Med. 2020 Oct 20;173(8):683.

4. Funder JW, Carey RM, Mantero F, Murad MH, Reincke M, Shibata H, et al. The Management of Primary Aldosteronism: Case Detection, Diagnosis, and Treatment: An Endocrine Society Clinical Practice Guideline. J Clin Endocrinol Metab. 2016 May;101(5):1889–916.

5. Savard S, Amar L, Plouin PF, Steichen O. Cardiovascular complications associated with primary aldosteronism: a controlled cross-sectional study. Hypertension. 2013 Aug;62(2):331–6.

6. Monticone S, D'Ascenzo F, Moretti C, Williams TA, Veglio F, Gaita F, et al. Cardiovascular events and target organ damage in primary aldosteronism compared with essential hypertension: a systematic review and meta-analysis. Lancet Diabetes Endocrinol. 2018 Jan;6(1):41–50.

7. Rossi GP, Sacchetto A, Pavan E, Palatini P, Graniero GR, Canali C, et al. Remodeling of the left ventricle in primary aldosteronism due to Conn's adenoma. Circulation. 1997 Mar 18;95(6):1471–8.

8. Em F, Pb M, Ra W, Ep M, K A, Hj D, et al. Demonstration of blood pressure-independent noninfarct myocardial fibrosis in primary aldosteronism: a cardiac magnetic resonance imaging study. Circulation Cardiovascular imaging [Internet]. 2012 Nov [cited 2024 Oct 13];5(6). Available from: https://pubmed.ncbi.nlm.nih.gov/23019275/

9. Nj B. Aldosterone and end-organ damage. Current opinion in nephrology and hypertension [Internet]. 2005 May [cited 2024 Oct 13];14(3). Available from: https://pubmed.ncbi.nlm.nih.gov/15821416/

10. Zennaro MC, Boulkroun S, Fernandes-Rosa FL. Pathogenesis and treatment of primary aldosteronism. Nat Rev Endocrinol. 2020 Oct;16(10):578–89.

11. Åkerström T, Maharjan R, Sven Willenberg H, Cupisti K, Ip J, Moser A, et al. Activating mutations in CTNNB1 in aldosterone producing adenomas. Sci Rep. 2016 Jan 27;6:19546.

12. Teo AED, Garg S, Shaikh LH, Zhou J, Karet Frankl FE, Gurnell M, et al. Pregnancy, Primary Aldosteronism, and Adrenal CTNNB1 Mutations. N Engl J Med. 2015 Oct 8;373(15):1429–36.

13. Zhou J, Azizan EAB, Cabrera CP, Fernandes-Rosa FL, Boulkroun S, Argentesi G, et al. Somatic mutations of GNA11 and GNAQ in CTNNB1-mutant aldosterone-producing adenomas presenting in puberty, pregnancy or menopause. Nat Genet. 2021 Sep;53(9):1360–72.

14. X W, Eab A, E G, S G, M H, Cp C, et al. Somatic mutations of CADM1 in aldosterone-producing adenomas and gap junction-dependent regulation of aldosterone production. Nature genetics [Internet]. 2023 Jun [cited 2024 Oct 13];55(6). Available from: https://pubmed.ncbi.nlm.nih.gov/37291193/

15. Spät A, Hunyady L. Control of aldosterone secretion: a model for convergence in cellular signaling pathways. Physiol Rev. 2004 Apr;84(2):489–539.

16. Jd S. New ideas about aldosterone signaling in epithelia. American journal of physiology Renal physiology [Internet]. 2002 Apr [cited 2024 Oct 13];282(4). Available from: https://pubmed.ncbi.nlm.nih.gov/11880316/

17. F J, N F. Emerging Roles of the Mineralocorticoid Receptor in Pathology: Toward New Paradigms in Clinical Pharmacology. Pharmacological reviews [Internet]. 2016 Jan [cited 2024 Oct 13];68(1). Available from: https://pubmed.ncbi.nlm.nih.gov/26668301/

18. Loffing J, Kaissling B. Sodium and calcium transport pathways along the mammalian distal nephron: from rabbit to human. Am J Physiol Renal Physiol. 2003 Apr;284(4):F628-643.

19. Miller WL, Auchus RJ. The molecular biology, biochemistry, and physiology of human steroidogenesis and its disorders. Endocr Rev. 2011 Feb;32(1):81–151.

20. Hattangady NG, Olala LO, Bollag WB, Rainey WE. Acute and chronic regulation of aldosterone production. Mol Cell Endocrinol. 2012 Mar 24;350(2):151–62.

21. A S, L H, G S. Signaling Interactions in the Adrenal Cortex. Frontiers in endocrinology [Internet]. 2016 Feb 29 [cited 2024 Oct 13];7. Available from: https://pubmed.ncbi.nlm.nih.gov/26973596/

22. Bandulik S, Penton D, Barhanin J, Warth R. TASK1 and TASK3 potassium channels: determinants of aldosterone secretion and adrenocortical zonation. Horm Metab Res. 2010 Jun;42(6):450–7.

23. Lifton RP, Dluhy RG, Powers M, Rich GM, Cook S, Ulick S, et al. A chimaeric 11 beta-hydroxylase/aldosterone synthase gene causes glucocorticoid-remediable aldosteronism and human hypertension. Nature. 1992 Jan 16;355(6357):262–5.

24. L P, Km C, L S, Jm C, Pw S, Mi N, et al. Glucocorticoid-suppressible hyperaldosteronism results from hybrid genes created by unequal crossovers between CYP11B1 and CYP11B2. Proceedings of the National Academy of Sciences of the United States of America [Internet]. 1992 Sep 1 [cited 2024 Oct 13];89(17). Available from: https://pubmed.ncbi.nlm.nih.gov/1518866/

25. P M, D T, A V, C B, S M, G M, et al. Prevalence and characteristics of familial hyperaldosteronism: the PATOGEN study (Primary Aldosteronism in TOrino-GENetic forms). Hypertension (Dallas, Tex : 1979) [Internet]. 2011 Nov [cited 2024 Oct 13];58(5). Available from: https://pubmed.ncbi.nlm.nih.gov/21876069/

26. M A, A MA, Ca C, C C, H G, R B, et al. Frequency of familial hyperaldosteronism type 1 in a hypertensive pediatric population: clinical and biochemical presentation. Hypertension (Dallas, Tex : 1979) [Internet]. 2011 Jun [cited 2024 Oct 13];57(6). Available from: https://pubmed.ncbi.nlm.nih.gov/21502562/

27. Pallauf A, Schirpenbach C, Zwermann O, Fischer E, Morak M, Holinski-Feder E, et al. The prevalence of familial hyperaldosteronism in apparently sporadic primary aldosteronism in Germany: a single center experience. Horm Metab Res. 2012 Mar;44(3):215–20.

28. Sutherland DJ, Ruse JL, Laidlaw JC. Hypertension, increased aldosterone secretion and low plasma renin activity relieved by dexamethasone. Can Med Assoc J. 1966 Nov 26;95(22):1109–19.

29. F H, Rg D. Glucocorticoid-remediable aldosteronism. Endocrinology and metabolism clinics of North America [Internet]. 2011 Jun [cited 2024 Oct 13];40(2). Available from: https://pubmed.ncbi.nlm.nih.gov/21565670/

30. Stowasser M, Sharman J, Leano R, Gordon RD, Ward G, Cowley D, et al. Evidence for abnormal left ventricular structure and function in normotensive individuals with familial hyperaldosteronism type I. J Clin Endocrinol Metab. 2005 Sep;90(9):5070–6.

31. Litchfield WR, Anderson BF, Weiss RJ, Lifton RP, Dluhy RG. Intracranial aneurysm and hemorrhagic stroke in glucocorticoid-remediable aldosteronism. Hypertension. 1998 Jan;31(1 Pt 2):445–50.

32. Choi M, Scholl UI, Yue P, Björklund P, Zhao B, Nelson-Williams C, et al. K+ channel mutations in adrenal aldosterone-producing adenomas and hereditary hypertension. Science. 2011 Feb 11;331(6018):768–72.

33. Zennaro MC, Boulkroun S, Fernandes-Rosa F. Genetic Causes of Functional Adrenocortical Adenomas. Endocr Rev. 2017 Dec 1;38(6):516–37.

34. Oki K, Plonczynski MW, Lam ML, Gomez-Sanchez EP, Gomez-Sanchez CE. The potassium channel, Kir3.4 participates in angiotensin II-stimulated aldosterone production by a human adrenocortical cell line. Endocrinology. 2012 Sep;153(9):4328–35.

35. Oki K, Plonczynski MW, Luis Lam M, Gomez-Sanchez EP, Gomez-Sanchez CE. Potassium channel mutant KCNJ5 T158A expression in HAC-15 cells increases aldosterone synthesis. Endocrinology. 2012 Apr;153(4):1774–82.

36. M M, Ea A, Mj B, Km O. Characterization of a novel somatic KCNJ5 mutation delI157 in an aldosterone-producing adenoma. Journal of hypertension [Internet]. 2012 Sep [cited 2024 Oct 13];30(9). Available from: https://pubmed.ncbi.nlm.nih.gov/22743686/

37. Murthy M, Xu S, Massimo G, Wolley M, Gordon RD, Stowasser M, et al. Role for germline mutations and a rare coding single nucleotide polymorphism within the KCNJ5 potassium channel in a large cohort of sporadic cases of primary aldosteronism. Hypertension. 2014 Apr;63(4):783–9.

38. E C, A S, T K, C M, Da H, Mm H, et al. A novel point mutation in the KCNJ5 gene causing primary hyperaldosteronism and early-onset autosomal dominant hypertension. The Journal of clinical endocrinology and metabolism [Internet]. 2012 Aug [cited 2024 Oct 13];97(8). Available from: https://pubmed.ncbi.nlm.nih.gov/22628607/

39. Cheng CJ, Sung CC, Wu ST, Lin YC, Sytwu HK, Huang CL, et al. Novel KCNJ5 mutations in sporadic aldosterone-producing adenoma reduce Kir3.4 membrane abundance. J Clin Endocrinol Metab. 2015 Jan;100(1):E155-163.

40. B S, R HJ, Hp R, N T, Ak B, N D. A revised mechanism of action of hyperaldosteronism-linked mutations in cytosolic domains of GIRK4 (KCNJ5). The Journal of physiology [Internet]. 2022 Mar [cited 2024 Oct 13];600(6). Available from: https://pubmed.ncbi.nlm.nih.gov/34957562/

41. Vc W, Kh H, Ky P, Yc T, Ch W, Sm W, et al. Prevalence and clinical correlates of somatic mutation in aldosterone producing adenoma-Taiwanese population. Scientific reports [Internet]. 2015 Jun 12 [cited 2024 Oct 13];5. Available from: https://pubmed.ncbi.nlm.nih.gov/26066391/

42. Kitamoto T, Suematsu S, Matsuzawa Y, Saito J, Omura M, Nishikawa T. Comparison of cardiovascular complications in patients with and without KCNJ5 gene mutations harboring aldosterone-producing adenomas. J Atheroscler Thromb. 2015;22(2):191–200.

43. Fernandes-Rosa FL, Williams TA, Riester A, Steichen O, Beuschlein F, Boulkroun S, et al. Genetic spectrum and clinical correlates of somatic mutations in aldosterone-producing adenoma. Hypertension. 2014 Aug;64(2):354–61.

44. Lenzini L, Rossitto G, Maiolino G, Letizia C, Funder JW, Rossi GP. A Meta-Analysis of Somatic KCNJ5 K(+) Channel Mutations In 1636 Patients With an Aldosterone-Producing Adenoma. J Clin Endocrinol Metab. 2015 Aug;100(8):E1089-1095.

45. Taguchi R, Yamada M, Nakajima Y, Satoh T, Hashimoto K, Shibusawa N, et al. Expression and mutations of KCNJ5 mRNA in Japanese patients with aldosterone-producing adenomas. J Clin Endocrinol Metab. 2012 Apr;97(4):1311–9.

46. Zheng FF, Zhu LM, Nie AF, Li XY, Lin JR, Zhang K, et al. Clinical characteristics of somatic mutations in Chinese patients with aldosterone-producing adenoma. Hypertension. 2015 Mar;65(3):622–8.

47. Scholl UI, Healy JM, Thiel A, Fonseca AL, Brown TC, Kunstman JW, et al. Novel somatic mutations in primary hyperaldosteronism are related to the clinical, radiological and pathological phenotype. Clin Endocrinol (Oxf). 2015 Dec;83(6):779–89.

48. Boulkroun S, Beuschlein F, Rossi GP, Golib-Dzib JF, Fischer E, Amar L, et al. Prevalence, clinical, and molecular correlates of KCNJ5 mutations in primary aldosteronism. Hypertension. 2012 Mar;59(3):592–8.

49. Tezuka Y, Yamazaki Y, Kitada M, Morimoto R, Kudo M, Seiji K, et al. 18-Oxocortisol Synthesis in Aldosterone-Producing Adrenocortical Adenoma and Significance of KCNJ5 Mutation Status. Hypertension. 2019 Jun;73(6):1283–90.

50. Williams TA, Peitzsch M, Dietz AS, Dekkers T, Bidlingmaier M, Riester A, et al. Genotype-Specific Steroid Profiles Associated With Aldosterone-Producing Adenomas. Hypertension. 2016 Jan;67(1):139–45.

51. K DS, S B, S B, K N, M W, We R, et al. Genetic, Cellular, and Molecular Heterogeneity in Adrenals With Aldosterone-Producing Adenoma. Hypertension (Dallas, Tex : 1979) [Internet]. 2020 Apr [cited 2024 Oct 13];75(4). Available from: https://pubmed.ncbi.nlm.nih.gov/32114847/

52. Boulkroun S, Golib Dzib JF, Samson-Couterie B, Rosa FLF, Rickard AJ, Meatchi T, et al. KCNJ5 mutations in aldosterone producing adenoma and relationship with adrenal cortex remodeling. Mol Cell Endocrinol. 2013 May 22;371(1–2):221–7.

53. Fernandes-Rosa FL, Amar L, Tissier F, Bertherat J, Meatchi T, Zennaro MC, et al. Functional histopathological markers of aldosterone producing adenoma and somatic KCNJ5 mutations. Mol Cell Endocrinol. 2015 Jun 15;408:220–6.

54. Y Y, Ce GS, D J, Et AP, Ls M, T K, et al. Primary Aldosteronism: KCNJ5 Mutations and Adrenocortical Cell Growth. Hypertension (Dallas, Tex : 1979) [Internet]. 2019 Oct [cited 2024 Oct 13];74(4). Available from: https://pubmed.ncbi.nlm.nih.gov/31446799/

55. Geller DS, Zhang J, Wisgerhof MV, Shackleton C, Kashgarian M, Lifton RP. A novel form of human mendelian hypertension featuring nonglucocorticoid-remediable aldosteronism. J Clin Endocrinol Metab. 2008 Aug;93(8):3117–23.

56. Mulatero P, Tauber P, Zennaro MC, Monticone S, Lang K, Beuschlein F, et al. KCNJ5 mutations in European families with nonglucocorticoid remediable familial hyperaldosteronism. Hypertension. 2012 Feb;59(2):235–40.

57. S M, Ng H, D P, Cm I, Ma E, Ta W, et al. a Novel Y152C KCNJ5 mutation responsible for familial hyperaldosteronism type III. The Journal of clinical endocrinology and metabolism [Internet]. 2013 Nov [cited 2024 Oct 13];98(11). Available from: https://pubmed.ncbi.nlm.nih.gov/24037882/

58. Mulatero P, Monticone S, Rainey WE, Veglio F, Williams TA. Role of KCNJ5 in familial and sporadic primary aldosteronism. Nat Rev Endocrinol. 2013 Feb;9(2):104–12.

59. Adachi M, Muroya K, Asakura Y, Sugiyama K, Homma K, Hasegawa T. Discordant genotype-phenotype correlation in familial hyperaldosteronism type III with KCNJ5 gene mutation: A patient report and review of the literature. Hormone research in paediatrics. 2014 Jan 1;82(2):138–42.

60. Ce GS, X Q, Ep GS, H S, Mo B, M W. Disordered zonal and cellular CYP11B2 enzyme expression in familial hyperaldosteronism type 3. Molecular and cellular endocrinology [Internet]. 2017 Jan 5 [cited 2024 Oct 13];439. Available from: https://pubmed.ncbi.nlm.nih.gov/27793677/

61. Catterall WA. Signaling complexes of voltage-gated sodium and calcium channels. Neurosci Lett. 2010 Dec 10;486(2):107–16.

62. Scholl UI, Goh G, Stölting G, de Oliveira RC, Choi M, Overton JD, et al. Somatic and germline CACNA1D calcium channel mutations in aldosterone-producing adenomas and primary aldosteronism. Nat Genet. 2013 Sep;45(9):1050–4.

63. Ea A, H P, P T, J Z, Mv C, A L, et al. Somatic mutations in ATP1A1 and CACNA1D underlie a common subtype of adrenal hypertension. Nature genetics [Internet]. 2013 Sep [cited 2024 Oct 13];45(9). Available from: https://pubmed.ncbi.nlm.nih.gov/23913004/

64. Nanba K, Omata K, Else T, Beck PCC, Nanba AT, Turcu AF, et al. Targeted Molecular Characterization of Aldosterone-Producing Adenomas in White Americans. J Clin Endocrinol Metab. 2018 Oct 1;103(10):3869–76.

65. Semenova NA, Ryzhkova OR, Strokova TV, Taran NN. [The third case report a patient with primary aldosteronism, seizures, and neurologic abnormalities (PASNA) syndrome de novo variant mutations in the CACNA1D gene]. Zh Nevrol Psikhiatr Im S S Korsakova. 2018;118(12):49–52.

66. De Mingo Alemany MC, Mifsud Grau L, Moreno Macián F, Ferrer Lorente B, León Cariñena S. A de novo CACNA1D missense mutation in a patient with congenital hyperinsulinism, primary hyperaldosteronism and hypotonia. Channels (Austin). 2020 Dec;14(1):175–80.

67. Scholl UI, Stölting G, Nelson-Williams C, Vichot AA, Choi M, Loring E, et al. Recurrent gain of function mutation in calcium channel CACNA1H causes early-onset hypertension with primary aldosteronism. Elife. 2015 Apr 24;4:e06315.

68. Daniil G, Fernandes-Rosa FL, Chemin J, Blesneac I, Beltrand J, Polak M, et al. CACNA1H Mutations Are Associated With Different Forms of Primary Aldosteronism. EBioMedicine. 2016 Nov;13:225–36.

69. Jh K. Biochemistry of Na,K-ATPase. Annual review of biochemistry [Internet]. 2002 [cited 2024 Oct 13];71. Available from: https://pubmed.ncbi.nlm.nih.gov/12045105/

70. Beuschlein F, Boulkroun S, Osswald A, Wieland T, Nielsen HN, Lichtenauer UD, et al. Somatic mutations in ATP1A1 and ATP2B3 lead to aldosterone-producing adenomas and secondary hypertension. Nat Genet. 2013 Apr;45(4):440–4, 444e1-2.

71. Stindl J, Tauber P, Sterner C, Tegtmeier I, Warth R, Bandulik S. Pathogenesis of Adrenal Aldosterone-Producing Adenomas Carrying Mutations of the Na(+)/K(+)-ATPase. Endocrinology. 2015 Dec;156(12):4582–91.

72. Kobuke K, Oki K, Gomez-Sanchez CE, Gomez-Sanchez EP, Itcho K, Ohno H, et al. ATP1A1 Mutant in Aldosterone-Producing Adenoma Leads to Cell Proliferation. Int J Mol Sci. 2021 Oct 12;22(20):10981.

73. T Å, Hs W, K C, J I, S B, A M, et al. Novel somatic mutations and distinct molecular signature in aldosterone-producing adenomas. Endocrine-related cancer [Internet]. 2015 Oct [cited 2024 Oct 13];22(5). Available from: https://pubmed.ncbi.nlm.nih.gov/26285814/

74. Tauber P, Aichinger B, Christ C, Stindl J, Rhayem Y, Beuschlein F, et al. Cellular Pathophysiology of an Adrenal Adenoma-Associated Mutant of the Plasma Membrane Ca(2+)-ATPase ATP2B3. Endocrinology. 2016 Jun;157(6):2489–99.

75. Jentsch TJ, Pusch M. CLC Chloride Channels and Transporters: Structure, Function, Physiology, and Disease. Physiol Rev. 2018 Jul 1;98(3):1493–590.

76. Scholl UI, Stölting G, Schewe J, Thiel A, Tan H, Nelson-Williams C, et al. CLCN2 chloride channel mutations in familial hyperaldosteronism type II. Nat Genet. 2018 Mar;50(3):349–54.

77. Fernandes-Rosa FL, Daniil G, Orozco IJ, Göppner C, El Zein R, Jain V, et al. A gain-of-function mutation in the CLCN2 chloride channel gene causes primary aldosteronism. Nat Genet. 2018 Mar;50(3):355–61.

78. J S, E S, S F, L M, J P, Dn M, et al. Elevated aldosterone and blood pressure in a mouse model of familial hyperaldosteronism with ClC-2 mutation. Nature communications [Internet]. 2019 Nov 14 [cited 2024 Oct 13];10(1). Available from: https://pubmed.ncbi.nlm.nih.gov/31727896/

79. Göppner C, Orozco IJ, Hoegg-Beiler MB, Soria AH, Hübner CA, Fernandes-Rosa FL, et al. Pathogenesis of hypertension in a mouse model for human CLCN2 related hyperaldosteronism. Nat Commun. 2019 Oct 15;10(1):4678.

80. Dutta RK, Arnesen T, Heie A, Walz M, Alesina P, Söderkvist P, et al. A somatic mutation in CLCN2 identified in a sporadic aldosterone-producing adenoma. Eur J Endocrinol. 2019 Nov;181(5):K37–41.

81. Rege J, Nanba K, Blinder AR, Plaska S, Udager AM, Vats P, et al. Identification of Somatic Mutations in CLCN2 in Aldosterone-Producing Adenomas. J Endocr Soc. 2020 Oct 1;4(10):bvaa123.

82. Wu CH, Peng KY, Hwang DY, Lin YH, Wu VC, Chueh JS. Novel Mutations Detection with Next-Generation Sequencing and Its Association with Clinical Outcome in Unilateral Primary Aldosteronism. Biomedicines. 2021 Sep 6;9(9):1167.

83. Berthon A, Drelon C, Ragazzon B, Boulkroun S, Tissier F, Amar L, et al. WNT/β-catenin signalling is activated in aldosterone-producing adenomas and controls aldosterone production. Hum Mol Genet. 2014 Feb 15;23(4):889–905.

84. Pignatti E, Leng S, Yuchi Y, Borges KS, Guagliardo NA, Shah MS, et al. Beta-Catenin Causes Adrenal Hyperplasia by Blocking Zonal Transdifferentiation. Cell Rep. 2020 Apr 21;31(3):107524.

85. El Wakil A, Lalli E. The Wnt/beta-catenin pathway in adrenocortical development and cancer. Mol Cell Endocrinol. 2011 Jan 30;332(1–2):32–7.

86. Tadjine M, Lampron A, Ouadi L, Bourdeau I. Frequent mutations of beta-catenin gene in sporadic secreting adrenocortical adenomas. Clin Endocrinol (Oxf). 2008 Feb;68(2):264–70.

87. Sl K, B L. Zn transporter levels and localization change throughout lactation in rat mammary gland and are regulated by Zn in mammary cells. The Journal of nutrition [Internet]. 2003 Nov [cited 2024 Oct 13];133(11). Available from: https://pubmed.ncbi.nlm.nih.gov/14608047/

88. Huang L, Tepaamorndech S. The SLC30 family of zinc transporters - a review of current understanding of their biological and pathophysiological roles. Mol Aspects Med. 2013;34(2–3):548–60.

89. Rege J, Bandulik S, Nanba K, Kosmann C, Blinder AR, Plain A, et al. Somatic SLC30A1 mutations altering zinc transporter ZnT1 cause aldosterone-producing adenomas and primary aldosteronism. Nat Genet. 2023 Oct;55(10):1623–31.

90. Takeuchi F, Isono M, Katsuya T, Yamamoto K, Yokota M, Sugiyama T, et al. Blood pressure and hypertension are associated with 7 loci in the Japanese population. Circulation. 2010 Jun 1;121(21):2302–9.

91. Irvin MR, Sitlani CM, Floyd JS, Psaty BM, Bis JC, Wiggins KL, et al. Genome-Wide Association Study of Apparent Treatment-Resistant Hypertension in the CHARGE Consortium: The CHARGE Pharmacogenetics Working Group. American Journal of Hypertension. 2019 Nov 15;32(12):1146–53.

92. Le Floch E, Cosentino T, Larsen CK, Beuschlein F, Reincke M, Amar L, et al. Identification of risk loci for primary aldosteronism in genome-wide association studies. Nat Commun. 2022 Sep 3;13(1):5198.

93. Ce GS, Ep GS. Mutations of the potassium channel KCNJ5 causing aldosterone-producing adenomas: one or two hits? Hypertension (Dallas, Tex : 1979) [Internet]. 2012 Feb [cited 2024 Oct 13];59(2). Available from: https://pubmed.ncbi.nlm.nih.gov/22203746/

94. K N, K N, D L, T K, M O, S M, et al. Adrenocortical zonation in humans under normal and pathological conditions. The Journal of clinical endocrinology and metabolism [Internet]. 2010 May [cited 2024 Oct 13];95(5). Available from: https://pubmed.ncbi.nlm.nih.gov/20200334/

95. Williams TA, Gomez-Sanchez CE, Rainey WE, Giordano TJ, Lam AK, Marker A, et al. International Histopathology Consensus for Unilateral Primary Aldosteronism. J Clin Endocrinol Metab. 2021 Jan 1;106(1):42–54.

96. Boulkroun S, Samson-Couterie B, Dzib JFG, Lefebvre H, Louiset E, Amar L, et al. Adrenal cortex remodeling and functional zona glomerulosa hyperplasia in primary aldosteronism. Hypertension. 2010 Nov;56(5):885–92.

97. Nishimoto K, Tomlins SA, Kuick R, Cani AK, Giordano TJ, Hovelson DH, et al. Aldosterone-stimulating somatic gene mutations are common in normal adrenal glands. Proc Natl Acad Sci U S A. 2015 Aug 18;112(33):E4591-4599.

98. Omata K, Satoh F, Morimoto R, Ito S, Yamazaki Y, Nakamura Y, et al. Cellular and Genetic Causes of Idiopathic Hyperaldosteronism. Hypertension. 2018 Oct;72(4):874–80.

99. Nishimoto K, Koga M, Seki T, Oki K, Gomez-Sanchez EP, Gomez-Sanchez CE, et al. Immunohistochemistry of aldosterone synthase leads the way to the pathogenesis of primary aldosteronism. Mol Cell Endocrinol. 2017 Feb 5;441:124–33.

100. Nishimoto K, Seki T, Kurihara I, Yokota K, Omura M, Nishikawa T, et al. Case Report: Nodule Development From Subcapsular Aldosterone-Producing Cell Clusters Causes Hyperaldosteronism. J Clin Endocrinol Metab. 2016 Jan;101(1):6–9.

101. Boulkroun S, Samson-Couterie B, Golib-Dzib JF, Amar L, Plouin PF, Sibony M, et al. Aldosterone-producing adenoma formation in the adrenal cortex involves expression of stem/progenitor cell markers. Endocrinology. 2011 Dec;152(12):4753–63.

102. T D, M ter M, Jw L, Ar H, L SK, Jf L, et al. Adrenal nodularity and somatic mutations in primary aldosteronism: one node is the culprit? The Journal of clinical endocrinology and metabolism [Internet]. 2014 Jul [cited 2024 Oct 13];99(7). Available from: https://pubmed.ncbi.nlm.nih.gov/24758183/

103. Nanba K, Chen AX, Omata K, Vinco M, Giordano TJ, Else T, et al. Molecular Heterogeneity in Aldosterone-Producing Adenomas. J Clin Endocrinol Metab. 2016 Mar;101(3):999–1007.

104. J V, F FR, J GD, P L, M DP, C T, et al. Aldosterone-Producing Adenoma With a Somatic KCNJ5 Mutation Revealing APC-Dependent Familial Adenomatous Polyposis. The Journal of clinical endocrinology and metabolism [Internet]. 2016 Nov [cited 2024 Oct 13];101(11). Available from: https://pubmed.ncbi.nlm.nih.gov/27648962/

105. Jm C, E D. The new biology of aldosterone. The Journal of endocrinology [Internet]. 2005 Jul [cited 2024 Oct 13];186(1). Available from: https://pubmed.ncbi.nlm.nih.gov/16002531/

106. Duparc C, Moreau L, Dzib JFG, Boyer HG, Tetsi Nomigni M, Boutelet I, et al. Mast cell hyperplasia is associated with aldosterone hypersecretion in a subset of aldosterone-producing adenomas. J Clin Endocrinol Metab. 2015 Apr;100(4):E550-560.

107. M EB, Jp H, Sr B, Wa S, Gp V. Intraadrenal interactions in the regulation of adrenocortical steroidogenesis. Endocrine reviews [Internet]. 1998 Apr [cited 2024 Oct 13];19(2). Available from: https://pubmed.ncbi.nlm.nih.gov/9570034/

108. Wils J, Duparc C, Cailleux AF, Lopez AG, Guiheneuf C, Boutelet I, et al. The neuropeptide substance P regulates aldosterone secretion in human adrenals. Nat Commun. 2020 May 29;11(1):2673.

109. Ag L, C D, A N, M C, H L, E L. Role of Mast Cells in the Control of Aldosterone Secretion. Hormone and metabolic research = Hormon- und Stoffwechselforschung = Hormones et metabolisme [Internet]. 2020 Jun [cited 2024 Oct 13];52(6). Available from: https://pubmed.ncbi.nlm.nih.gov/32215882/

110. Lefebvre H, Compagnon P, Contesse V, Delarue C, Thuillez C, Vaudry H, et al. Production and metabolism of serotonin (5-HT) by the human adrenal cortex: paracrine stimulation of aldosterone secretion by 5-HT. J Clin Endocrinol Metab. 2001 Oct;86(10):5001–7.

111. Lefebvre H, Contesse V, Delarue C, Soubrane C, Legrand A, Kuhn JM, et al. Effect of the serotonin-4 receptor agonist zacopride on aldosterone secretion from the human adrenal cortex: in vivo and in vitro studies. J Clin Endocrinol Metab. 1993 Dec;77(6):1662–6.

112. Contesse V, Lefebvre H, Lenglet S, Kuhn JM, Delarue C, Vaudry H. Role of 5-HT in the regulation of the brain-pituitary-adrenal axis: effects of 5-HT on adrenocortical cells. Can J Physiol Pharmacol. 2000 Dec;78(12):967–83.

113. De Sousa K, Abdellatif AB, Giscos-Douriez I, Meatchi T, Amar L, Fernandes-Rosa FL, et al. Colocalization of Wnt/β-Catenin and ACTH Signaling Pathways and Paracrine Regulation in Aldosterone-producing Adenoma. J Clin Endocrinol Metab. 2022 Jan 18;107(2):419–34.

114. Yang Y, Tetti M, Vohra T, Adolf C, Seissler J, Hristov M, et al. BEX1 Is Differentially Expressed in Aldosterone-Producing Adenomas and Protects Human Adrenocortical Cells From Ferroptosis. Hypertension. 2021 May 5;77(5):1647–58.

115. Dixon SJ, Lemberg KM, Lamprecht MR, Skouta R, Zaitsev EM, Gleason CE, et al. Ferroptosis: an iron-dependent form of nonapoptotic cell death. Cell. 2012 May 25;149(5):1060–72.

116. Stockwell BR, Friedmann Angeli JP, Bayir H, Bush AI, Conrad M, Dixon SJ, et al. Ferroptosis: A Regulated Cell Death Nexus Linking Metabolism, Redox Biology, and Disease. Cell. 2017 Oct 5;171(2):273–85.

117. Rapoport R, Sklan D, Hanukoglu I. Electron leakage from the adrenal cortex mitochondrial P450scc and P450c11 systems: NADPH and steroid dependence. Arch Biochem Biophys. 1995 Mar 10;317(2):412–6.

118. Prasad R, Kowalczyk JC, Meimaridou E, Storr HL, Metherell LA. Oxidative stress and adrenocortical insufficiency. J Endocrinol. 2014 Jun;221(3):R63-73.

119. Zou Y, Li H, Graham ET, Deik AA, Eaton JK, Wang W, et al. Cytochrome P450 oxidoreductase contributes to phospholipid peroxidation in ferroptosis. Nat Chem Biol. 2020 Mar;16(3):302–9.

120. Nanba K, Blinder AR, Rege J, Hattangady NG, Else T, Liu CJ, et al. Somatic CACNA1H Mutation As a Cause of Aldosterone-Producing Adenoma. Hypertension. 2020 Mar;75(3):645–9.

121. K N, K O, Ce GS, Ca S, Ap D, M S, et al. Genetic Characteristics of Aldosterone-Producing Adenomas in Blacks. Hypertension (Dallas, Tex : 1979) [Internet]. 2019 Apr [cited 2024 Oct 13];73(4). Available from: https://pubmed.ncbi.nlm.nih.gov/30739536/

122. Tauber P, Penton D, Stindl J, Humberg E, Tegtmeier I, Sterner C, et al. Pharmacology and pathophysiology of mutated KCNJ5 found in adrenal aldosterone-producing adenomas. Endocrinology. 2014 Apr;155(4):1353–62.

123. Scholl UI, Abriola L, Zhang C, Reimer EN, Plummer M, Kazmierczak BI, et al. Macrolides selectively inhibit mutant KCNJ5 potassium channels that cause aldosterone-producing adenoma. J Clin Invest. 2017 Jun 30;127(7):2739–50.

124. Caroccia B, Prisco S, Seccia TM, Piazza M, Maiolino G, Rossi GP. Macrolides Blunt Aldosterone Biosynthesis: A Proof-of-Concept Study in KCNJ5 Mutated Adenoma Cells Ex Vivo. Hypertension. 2017 Dec;70(6):1238–42.

125. Hacini I, De Sousa K, Boulkroun S, Meatchi T, Amar L, Zennaro MC, et al. Somatic mutations in adrenals from patients with primary aldosteronism not cured after adrenalectomy suggest common pathogenic mechanisms between unilateral and bilateral disease. Eur J Endocrinol. 2021 Aug 3;185(3):405–12.

FIGURE LEGENDS

Fig. 1. Overview of the molecular mechanisms driving aldosterone-producing adenomas (APAs). Somatic mutations in genes such as KCNJ5, ATP1A1, CLCN2, SLC30A1 and MCOLN3 disrupt ion transport, leading to membrane depolarization and increased intracellular calcium, which stimulates aldosterone synthesis. Activating mutations in calcium channel genes (CACNA1D, CACNA1H) or pumps (ATP2B3) directly promote increased intracellular calcium concentrations and upregulate CYP11B2 expression. Alterations in GNA11 and GNAQ result in constitutive G-protein signalling, while CTNNB1 mutations activate Wnt/β-catenin pathways, contributing to both hormone production and cell proliferation. CADM1 mutations increase aldosterone production by interfering with cell–cell communication.

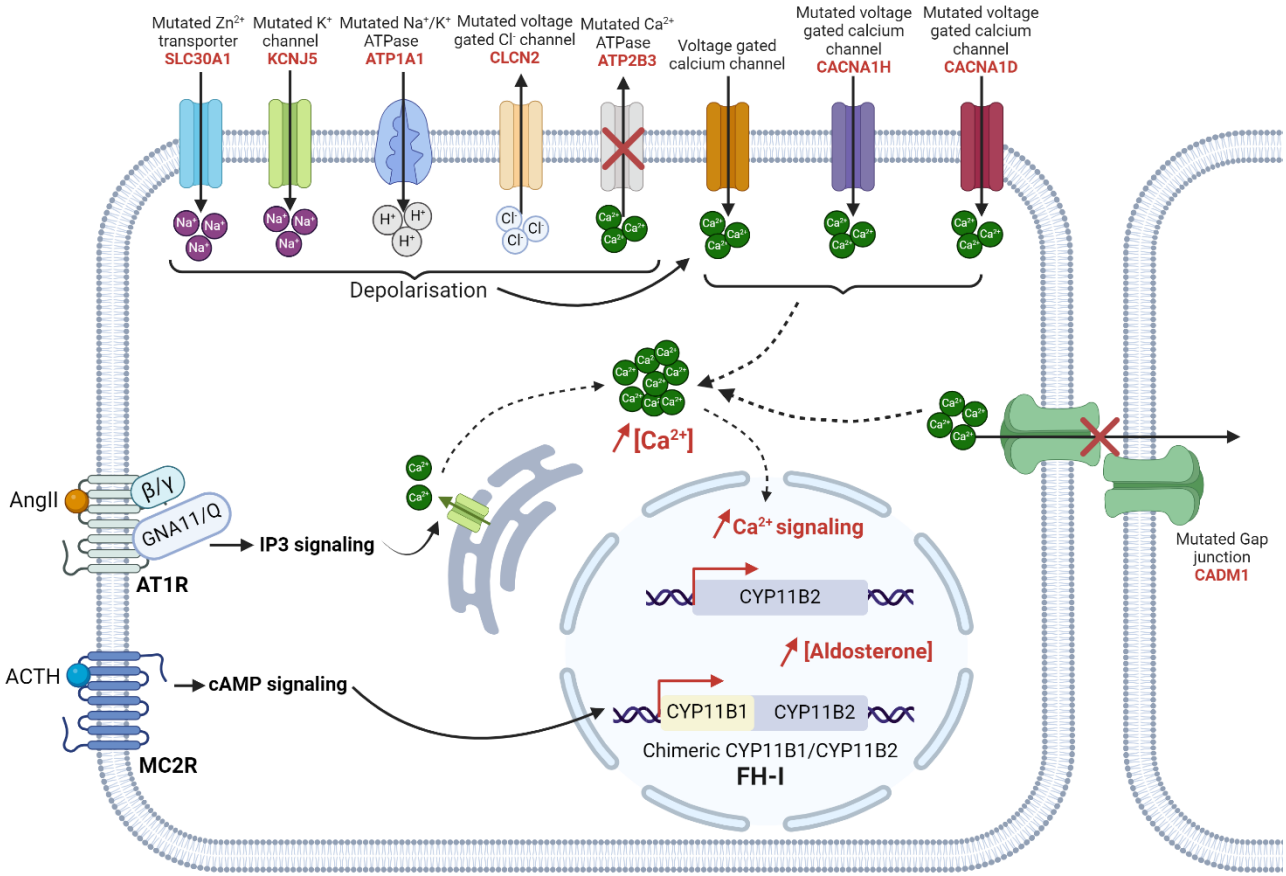

17 Hot off the press

17.1 Insights into the mechanisms of inhibition of aldosterone production by mutant atrial natriuretic peptide (MANP)

Hypertension News. International Society of Hypertension; September 2022. Opus 70. DOI: 10.30824/2209-1

HOT OFF THE PRESS

Insights into the mechanisms of inhibition of aldosterone production by mutant atrial natriuretic peptide (MANP)

MAY FAYAD
MARIA-CHRISTINA ZENNARO
Université Paris Cité, Inserm, PARCC,
F-75015 Paris, France





DOI: 10.30824/2209-3

In this study, Chen et al investigated the molecular mechanisms of aldosterone inhibition by mutant atrial natriuretic peptide (MANP), a novel atrial natriuretic peptide (ANP) analog, in the human adrenal cortical cell line H295R[1].

Aldosterone is one of the major hormones contributing to blood pressure regulation and a potent sodium-retaining factor in the organism. Excessive aldosterone leads to hypertension, but also facilitates pathophysiologic fibrosis, and organ remodeling in the heart, vasculature, and kidney, contributing to heart failure and chronic kidney disease. Mineralocorticoid receptor antagonists have been used for decades to lower blood pressure in resistant hypertension and primary aldosteronism, and have shown potent effects in reducing morbi-mortality in heart failure. However, given that they increase aldosterone levels by a counter-regulatory mechanism, drug development efforts have focused on direct aldosterone inhibition.

ANP is a cardiac hormone involved in blood pressure homeostasis through vasodilation and natriuretic actions via activation of pGC-A (particulate guanylyl cyclase A receptor) and production of the second messenger cGMP. ANP is also an endogenous inhibitor of aldosterone production[2]. However, the therapeutic use of ANP is limited because of its instability due to degradation by neprilysin. Recently, MANP, a novel ANP analog, has been engineered to overcome this limitation. MANP possesses a more potent aldosterone inhibitory action than ANP *in vivo* and is reported to be resistant to neprilysin degradation[3]. MANP is now entering into phase 2 clinical trial after it was shown to lower blood pressure in a phase 1 clinical study in patients with resistant hypertension[4]. The mechanisms whereby the natriuretic peptides (NP) lower aldosterone has not been clearly elucidated. It has been suggested that this effect may be mediated by pGC-A activation, while other studies suggested that this inhibition is caused by the NP clearance receptor (NPRC). Therefore, this work aimed to better understand the mechanisms of aldosterone inhibition by natriuretic peptides.

The authors demonstrated the presence of pGC-A and NPRC in human adrenocortical H295R cells, and showed that treatment of these cells with MANP increased the production of cGMP in a dose-dependent manner. Aldosterone production in H295R cells stimulated by ANGII or KCl was reduced by treatment with MANP. Similarly, MANP treatment also suppressed aldosterone production stimulated by forskolin (a direct activator of adenylyl cyclase producing cAMP). In order to investigate if NPRC also inhibits aldosterone biosynthesis, H295R cells were treated with the NPRC-specific agonist cANF and antagonist AP-811. cANF did not suppress aldosterone production and AP-811 did not affect the inhibitory effect of MANP.

cGMP-AM, a non-specific cGMP analog, mimicked MANP's aldosterone-suppressive effects in H295R cells. Since PKG and PDEs are two important downstream protein targets of cGMP, the authors explored which one is responsible for the aldosterone-mediated inhibition of MANP. PKG activator did not lower aldosterone levels and PKG inhibitor had no effect on the aldosterone decrease induced by MANP. In contrast, they observed reversal of the inhibitory effect of MANP when using a nonspecific PDE inhibitor and they showed that this effect was mediated through PDE2 and not PDE3. They further showed that MANP treatment 10 minutes before forskolin stimulation reduced cAMP levels suggesting an activation of PDE2. MANP also lowered intracellular Ca^{2+} levels following AngII stimulation, as well as expression of *CYP11B2*, the gene encoding aldosterone synthase, and this effect was reversed by the PDE2 inhibitor Bay 60-7550. These results were confirmed by *in vivo* studies showing that the expression of *CYP11B2* was higher in homozygous PDE2 knockout mouse embryos compared to wild-type mice.

In summary, this study demonstrated that MANP inhibits aldosterone production via the pGC-A/cGMP/PDE2 pathway and plays an important role in reducing aldosterone and CYP11B2 levels, therefore highlighting the therapeutic potential of MANP in treating hypertension. Additional potential approaches may target an increase of cGMP and PDE2 activity, the increase of endogenous NPs through neprilysin inhibitors or exogenous NP administration.

References

1. Chen Y, Iyer SR, Nikolaev VO, Naro F, Pellegrini M, Cardarelli S, Ma X, Lee HC, Burnett JC Jr. MANP (Mutant Atrial Natriuretic Peptide) Activation of the cGMP (3',5', Cyclic Guanosine Monophosphate) Inhibits Aldosterone via PDE2 (Phosphodiesterase 2) and Cytochrome p450 Family 11 Subfamily b Member 2 in H295R Cells and in Mice. Hypertension. 2022 Jun 8:101161HYPERTENSIONAHA12118906. doi: 10.1161/HYPERTENSIONAHA.121.18906. Epub ahead of print. PMID: 35674049.

2. Atarashi K, Mulrow PJ, Franco-Saenz R. Effect of atrial peptides on aldosterone production. J Clin Invest. 1985;76:1807–18101. doi: 10.1172/JCI112172

3. Dickey DM, Yoder AR, Potter LR. A familial mutation renders atrial natriuretic peptide resistant to proteolytic degradation. J Biol Chem. 2009; 284:19196–19202. doi: 10.1074/jbc.M109.010777

4. Chen HHW, Iyer SR, Sangaralingham J, Cannone V, Burnett JC. A first-in-human study Of MANP: a novel atrial natriuretic peptide analogue in human hypertension. Hypertension. 2021;78:1859–1867. doi: 10.1161/HYPERTENSIONAHA.121.17159.

May Fayad - may.fayad@inserm.fr

Maria-Christina Zennaro - maria-christina.zennaro@inserm.fr

